UC San Diego

UC San Diego Electronic Theses and Dissertations

Title

Behavior of post-installed anchors in reinforced concrete shear walls of different aspect ratios subjected to simulated seismic loads

Permalink

https://escholarship.org/uc/item/4f80g4r3

Author

Faraone, Gloria

Publication Date

2021

Peer reviewed|Thesis/dissertation

eScholarship.org Powered by the California Digital Library
University of California

UNIVERSITY OF CALIFORNIA SAN DIEGO

Behavior of post-installed anchors in reinforced concrete shear walls of different aspect ratios subjected to simulated seismic loads

A dissertation submitted in partial satisfaction of the
requirements for the degree
Doctor of Philosophy

in

Structural Engineering

by

Gloria Faraone

Committee in charge:

Professor Tara C. Hutchinson, Chair
Professor Joel Conte
Professor William Hodgkiss
Professor Gilberto Mosqueda
Professor Peter Shearer

2021

Copyright
Gloria Faraone, 2021
All rights reserved.

The dissertation of Gloria Faraone is approved, and it is acceptable in quality and form for publication on microfilm and electronically.

University of California San Diego

2021

DEDICATION

This dissertation is dedicated to my family.

EPIGRAPH

Ma che poss'io, Signor, s'a me non vieni

coll'usata ineffabil cortesia?

But how can I do that, Lord, if you don't come to me

with your usual ineffable graciousness?

Rime, Michelangelo Buonarroti

TABLE OF CONTENTS

Dissertation Approval Page . . . iii

Dedication . . . iv

Epigraph . . . v

Table of Contents . . . vi

List of Figures . . . x

List of Tables . . . xxiv

Glossary of Terms . . . xxvi

Acknowledgments . . . xxvii

Vita . . . xxx

Abstract of the Dissertation . . . xxxii

Chapter 1 Introduction . . . 1
- 1.1 Motivation . . . 1
- 1.2 Scope . . . 2
- 1.3 Post-Installed Anchors for Seismic Applications . . . 3
- 1.4 Scope of Dissertation . . . 9
- 1.5 Background . . . 10
  - 1.5.1 Anchorage Types and Failure Mechanisms . . . 11
  - 1.5.2 Influence of Cracks on Anchor Behavior . . . 13
  - 1.5.3 Brief History of Seismic Anchorage Qualification . . . 18
  - 1.5.4 Implementation of Seismic Anchorage Qualification within Design Codes . . . 20
  - 1.5.5 Behavior of Slender Reinforced Concrete Shear Walls . . . 22
  - 1.5.6 Code-based Crack Widths . . . 32
  - 1.5.7 Behavior of Squat Reinforced Concrete Shear Walls . . . 34
  - 1.5.8 Plastic Hinge Length in RC Shear Walls . . . 48
- 1.6 Summary Remarks . . . 52
- 1.7 Organization of Dissertation . . . 53

Chapter 2 Slender Wall Test Program . . . 55
- 2.1 Motivation . . . 55
  - 2.1.1 Previous Experimental Investigations . . . 56
  - 2.1.2 Scope of the Slender Wall Test Program . . . 57
  - 2.1.3 Research Significance . . . 59
- 2.2 Wall Details and Construction . . . 60
  - 2.2.1 Program Overview . . . 60
  - 2.2.2 Design of the Wall and Description of Test . . . 60

2.2.3 Test Setup and Instrumentation . . . 64
2.2.4 Test Procedure . . . 66
2.3 Experimental Results . . . 67
2.3.1 Wall Global Response . . . 67
2.3.2 Damage Evolution . . . 68
2.3.3 Estimated Crack Spacing . . . 73
2.3.4 Components of Lateral Displacement . . . 74
2.3.5 Vertical Wall Displacement . . . 75
2.3.6 Plastic Hinge Zone Evolution . . . 76
2.4 Summary Remarks . . . 78
2.5 Acknowledgment of Publications . . . 79

Chapter 3 Squat Wall Test Program . . . 80
3.1 Motivation . . . 81
3.2 Relating Design to Damage . . . 81
3.2.1 Scope of this Test Program . . . 83
3.2.2 Research Significance . . . 84
3.3 Experimental Investigation . . . 84
3.3.1 Program Overview . . . 84
3.3.2 Design and Description of Test Walls . . . 85
3.3.3 Test Setup and Instrumentation . . . 86
3.3.4 Test Procedure . . . 87
3.4 Experimental Results . . . 92
3.4.1 Global Response . . . 92
3.4.2 Drift Ratios at Performance Limits . . . 95
3.4.3 Damage Evolution . . . 99
3.4.4 Estimated Crack Spacing . . . 105
3.4.5 Base Curvature and Estimation of Plastic Hinge Length . . . 105
3.4.6 Components of Lateral Displacement . . . 112
3.5 Comparison of Strength Predictions with Available Analytical Models . . . 114
3.5.1 Strut-and-Tie Model . . . 114
3.5.2 Shear Strength Prediction . . . 115
3.6 Summary Remarks . . . 119
3.7 Acknowledgment of Publications . . . 120

Chapter 4 Response of Anchors in Cracked Concrete . . . 122
4.1 Introduction . . . 123
4.1.1 Research Significance . . . 125
4.2 Experimental Investigation . . . 126
4.2.1 Description of the Post-Installed Anchors . . . 126
4.2.2 Anchor Axial Loading Setup . . . 129
4.2.3 Anchor Load History . . . 132
4.2.4 Reference Tests and Characterization of Anchor Behavior . . . 133
4.3 Experimental Results and Discussion . . . 137
4.3.1 Crack Pattern and Anchor Behavior . . . 137
4.3.2 Anchor Load and Displacement Histories . . . 150
4.3.3 Anchor Residual Capacity Following Wall Cyclic Test . . . 161

4.4 Summary Remarks . . . 171
4.5 Acknowledgment of Publications . . . 174

Chapter 5 Numerical Analysis of Reinforced Concrete Shear Wall Test Specimens . . . 175
5.1 Scope . . . 175
5.2 Introduction . . . 176
5.2.1 Description of the Numerical Model . . . 180
5.3 Model Validation . . . 185
5.3.1 Description of the Wall Models . . . 185
5.4 Analysis of the Results . . . 190
5.4.1 Global Response . . . 190
5.4.2 Local Response . . . 198
5.5 Summary Remarks . . . 215
5.6 Acknowledgment of Publications . . . 215

Chapter 6 Numerical Parametric Study . . . 217
6.1 Introduction . . . 217
6.2 Description of the Numerical Wall Models . . . 218
6.2.1 Load Protocol . . . 221
6.2.2 Justification for the Parametric Wall Models . . . 222
6.3 Results of the Parametric Study . . . 227
6.3.1 Hysteresis Curves . . . 227
6.3.2 Damage Characterization of Walls with Different AR . . . 237
6.3.3 Consideration of Estimated Crack Widths . . . 260
6.3.4 Damage Distribution as a Function of Building Height . . . 263
6.4 Summary Remarks . . . 265
6.5 Acknowledgment of Publications . . . 266

Chapter 7 Conclusions and Future Work . . . 267
7.1 Motivation for this Research . . . 267
7.2 Adopted Approach . . . 268
7.3 Research Significance . . . 269
7.4 Primary Conclusions . . . 270
7.4.1 Experimental Program: Wall Tests and Anchor Tests . . . 270
7.4.2 Numerical Program: Validation and Parametric Study . . . 274
7.5 Recommendations for Future Research . . . 276

Appendix A Slender and Squat Wall Test Specimens: Design Calculations . . . 279
A.1 Slender Wall Design . . . 279
A.1.1 Load Combinations . . . 280
A.1.2 Design Loads . . . 281
A.1.3 Actions at the Base of the Slender Wall . . . 283
A.2 Squat Walls Design . . . 284
A.2.1 Design Loads . . . 284
A.2.2 Actions at the Base of the Squat Wall . . . 285

Appendix B Materials Related Data: Wall Test Specimens . . . 287
B.1 Slender Wall . . . 287
B.1.1 Tests on Concrete . . . 287
B.1.2 Tests on reinforcing bars . . . 292
B.2 Squat Walls . . . 292
B.2.1 Tests on concrete . . . 293
B.2.2 Tests on reinforcing bars . . . 294

Appendix C Crack Width Histories: Wall Test Specimens . . . 297

Appendix D Anchor Seismic Demand and Capacity . . . 310

Appendix E Anchor Response Data: Wall Test Specimens . . . 312
E.1 Anchor Response during Wall Cyclic Tests . . . 312
E.1.1 Anchors in Wall SL7.5 . . . 315
E.1.2 Anchors in Wall SQ7.5 . . . 380
E.1.3 Anchors in Wall SQ0 . . . 452
E.2 Anchor Residual Capacity Curves . . . 527
E.2.1 Slender Wall SL7.5 . . . 527
E.2.2 Wall SQ7.5 . . . 547
E.2.3 Wall SQ0 . . . 555

Appendix F Structure from Motion Data . . . 562

Appendix G Sample Code Used in the Numerical Validation Study . . . 570

Bibliography . . . 575

LIST OF FIGURES

Figure 1.1: Schematic of typical structural and nonstructural anchor applications 3
Figure 1.2: Photographs of typical structural and nonstructural anchor applications 4
Figure 1.3: Minimum recommended performance categories for anchors 5
Figure 1.4: Inelastic force-deformation curve showing the R factor 7
Figure 1.5: Common post-installed anchor types and load transfer mechanisms 12
Figure 1.6: Actions acting on an anchor during seismic loading 12
Figure 1.7: Failure modes associated with tension loading 14
Figure 1.8: Results of crack width study on flexural reinforced concrete members 16
Figure 1.9: Crack patterns at the end of the tests by Dazio et al. (2009) 24
Figure 1.10: Crack patterns at the end of the tests by Tran (2012) 26
Figure 1.11: Crack patterns at the end of the tests by Lu et al. (2016) 29
Figure 1.12: Maximum crack width at yield of the reinforcement in rectangular shear walls . 31
Figure 1.13: Wall specimen failed in diagonal tension, tested by Hidalgo et al. 2001 35
Figure 1.14: Graphical representation of the diagonal compression failure mode 36
Figure 1.15: Graphical representation of shear sliding failure mode 37
Figure 1.16: Crack patterns of walls with AR=1 at the end of the tests by Salonikios et al. (1999) 40
Figure 1.17: Crack patterns at the end of the tests by Greifenhagen and Lestuzzi (2005) . . . 41
Figure 1.18: Typical crack patterns at the end of the tests by Carrillo and Alcocer (2012) . . . 43
Figure 1.19: Maximum measured shear crack width versus estimated displacement ductility . 46
Figure 1.20: Schematic representation of the plastic hinge length and plastic hinge zone . . . 48

Figure 2.1: Maximum crack width at yield of rectangular wall specimens 58
Figure 2.2: Moment-axial force interaction diagram 62
Figure 2.3: Elevation and cross section details of the slender full-scale wall 63
Figure 2.4: Annotated photograph of test setup 64
Figure 2.5: Schematic of test setup 65
Figure 2.6: Global sensors on the wall 66
Figure 2.7: Displacement protocol 67
Figure 2.8: Lateral load versus top wall displacement 68
Figure 2.9: Evolution of the crack pattern at key drift ratios 69
Figure 2.10: Photographs of wall faces at the end of the test 71
Figure 2.11: Photographs of South and North boundaries at the end of the test 72
Figure 2.12: Top flexural and shear displacement contributions to total lateral displacement and shear to flexure displacement ratio versus wall drift ratio 74
Figure 2.13: Vertical growth versus drift ratio 75
Figure 2.14: Curvature profile versus normalized wall height 76
Figure 2.15: Estimated plastic hinge length values 77

Figure 3.1: Detailing of AR=1 walls 89
Figure 3.2: Moment-axial force interaction diagram 90
Figure 3.3: Annotated photographs of test setup 90
Figure 3.4: Layout of linear variable displacement transducers used to capture distortion of walls 91
Figure 3.5: Displacement protocol utilized in the tests 91

Figure 3.6: Lateral load versus top wall displacement (and drift ratio) 94
Figure 3.7: ASCE 41 (2014) envelope compared to experimental backbone curves 96
Figure 3.8: Characterization of lateral load and drift ratio at performance limit states and comparison between experimental performance drift versus FEMA 356 (2000) drift . 97
Figure 3.9: Photographs and sketches of the crack pattern of wall SQ7.5 102
Figure 3.10: Photographs and sketches of the crack pattern of wall SQ0 103
Figure 3.11: Photographs and sketches of the crack pattern at the end of the wall test 104
Figure 3.12: Curvature diagram estimated from gauges measurements in the wall tested with axial load 106
Figure 3.13: Curvature diagram estimated from gauges measurements in the wall tested without axial load 107
Figure 3.14: Comparison of curvature values measured during the wall tests at achieved drift amplitudes normalized by yield curvature X_y 108
Figure 3.15: Flexural and shear displacement contributions to total lateral displacement at top of wall Δ 113
Figure 3.16: Strut and tie model (adapted from Hwang et al. 2001) 115
Figure 3.17: Experimental envelope curve compared to shear strength predicted by the Krolicki et al. (2011) model 118

Figure 4.1: Schematic showing the effect of cracks on anchors 127
Figure 4.2: Slender wall SL7.5 tested with axial load 128
Figure 4.3: Squat wall SQ7.5 tested with axial load 129
Figure 4.4: Squat wall SQ0 tested without axial load 130
Figure 4.5: Annotated photograph of the anchor load setup (typical) 131
Figure 4.6: Typical anchor axial load history, from installation and application of the target load to wall cycling 133
Figure 4.7: Reference test setup and failure cones 135
Figure 4.8: Reference tests in uncracked concrete of the anchors installed in the slender wall 135
Figure 4.9: Reference tests in uncracked concrete of the anchors installed in the squat walls . 136
Figure 4.10: Crack pattern at the end of the slender wall SL7.5 test 138
Figure 4.11: Crack pattern at the end of the squat SQ7.5 and SQ0 wall tests 139
Figure 4.12: Photograph of the residual crack pattern in wall SL7.5 143
Figure 4.13: Photograph of the residual crack pattern in wall SQ7.5 144
Figure 4.14: Photograph of the residual crack pattern in wall SQ0 145
Figure 4.15: Categorization of residual cracking around anchor locations 146
Figure 4.16: Select anchor locations and intersecting crack pattern at the end of the wall SL7.5 cyclic test 147
Figure 4.17: Select anchor locations and intersecting crack pattern of anchor B2 in wall SQ7.5 148
Figure 4.18: Select anchor locations and intersecting crack pattern of anchor B6 in wall SQ0 . 149
Figure 4.19: Summary of anchor response during wall cyclic tests 155
Figure 4.20: Bonded anchor D3 in wall SL7.5 156
Figure 4.21: Torque-controlled expansion anchor B6 in wall SL7.5 157
Figure 4.22: Torque-controlled expansion anchor B2 in wall SQ7.5 158
Figure 4.23: Torque-controlled expansion anchor B6 in wall SQ0 159
Figure 4.24: Comparison of anchor load reduction at key performance drift levels 160
Figure 4.25: Annotated photograph of the tension to failure test assembly 161

Figure 4.26: Photograph of the West face of the SL7.5 wall following tension to failure tests on twenty-two bonded and torque-controlled expansion anchors 162
Figure 4.27: Photograph of the East face of the SQ7.5 wall following tension to failure tests on fourteen torque-controlled expansion anchors 163
Figure 4.28: Photograph of the West face of the SQ0 wall following tension to failure tests on eleven torque-controlled expansion anchors 164
Figure 4.29: Anchor tension to failure test results of slender wall SL7.5 165
Figure 4.30: Anchor tension to failure test results of squat walls SQ7.5 and SQ0 166
Figure 4.31: Anchor tension to failure test overall results 167
Figure 4.32: Anchor residual load-displacement curve of bonded anchor B1 in slender wall SL7.5 169
Figure 4.33: Anchor residual load-displacement curve of torque-controlled expansion anchor D4 in slender wall SL7.5 170
Figure 4.34: Comparison of results of anchor B6 tested to failure in wall SQ7.5 and wall SQ0 171

Figure 5.1: Representation of the SFI-MVLEM model. 180
Figure 5.2: Stress-strain field in the finite panel 182
Figure 5.3: Material constitutive models. 184
Figure 5.4: Elevation view of the full-scale walls 187
Figure 5.5: Cross section view. Note these are (a) SL7.5 and (b) SQ7.5 and SQ0 walls described in Chapters 2 and 3. Units in inches [1 in =25.4 mm; 1 kip =4.45 kN] 188
Figure 5.6: Test setup and displacement protocol. Additional details in in Chapters 2 and 3 . 189
Figure 5.7: Schematic representation of the dense meshes of walls AR2-8-BE and AR1-BE (typical) 189
Figure 5.8: Numerical and experimental lateral load vs. drift ratio 190
Figure 5.9: Crack pattern at 2% drift ratio in wall AR1-0-BE 191
Figure 5.10: Detail of the damage in the toe of wall AR1-0-BE at 2% drift ratio 192
Figure 5.11: Detail of the damage in the toes of wall AR2-8-BE at 2% drift ratio 192
Figure 5.12: Detail of the toe on the push side of wall AR1-8-BE at 1.2% drift ratio. Circles highlight the ruptured longitudinal reinforcing bars 193
Figure 5.13: Cumulative hysteretic energy vs. cumulative top displacement 194
Figure 5.14: Secant stiffness degradation (log scale) vs drift imposed at the top 194
Figure 5.15: Example calculation of secant stiffness 195
Figure 5.16: Cyclic degradation effect on the hysteresis curves 197
Figure 5.17: Shear and flexural components to top lateral displacement predicted by the FEMs and measured during the tests 200
Figure 5.18: Representation of an equivalent element 201
Figure 5.19: Effect of mesh size on crack pattern for the slender wall model AR2-8-BE at key performance drift ratios 203
Figure 5.20: Effect of mesh size on crack pattern for the squat wall model without applied axial load AR1-0-BE at key performance drift ratios 204
Figure 5.21: Effect of mesh size on crack pattern for the squat wall model with applied axial load AR1-8-BE at key performance drift ratios 205
Figure 5.22: Wall AR2-8-BE- Comparison of experimental and numerical crack patterns, obtained using two different concrete models 210
Figure 5.23: Wall AR1-0-BE- Comparison of experimental and numerical crack patterns, obtained using two different concrete models 211

Figure 5.24: Wall AR1-8-BE- Comparison of experimental and numerical crack patterns, obtained using two different concrete models 213
Figure 5.25: Comparison of numerical and experimental crack patterns at 0.5% (left), 1.0% (center) and 2.0% (right) 214

Figure 6.1: Buildings configurations with bearing walls of different aspect ratios (ARs) . . . 219
Figure 6.2: Lateral load versus drift ratio curves of AR=2 wall models with different levels of transverse confinement in the boundary elements 222
Figure 6.3: AR= 2, Axial Load Ratio = 0% wall models with different levels of transverse confinement in the boundary elements. Estimated damage prediction at 0.5%, 1% and 2% drift ratios 224
Figure 6.4: AR= 2, Axial Load Ratio = 8% wall models with different levels of transverse confinement in the boundary elements. Estimated damage prediction at 0.5%, 1% and 2% drift ratios 225
Figure 6.5: Hysteresis curves predicted by numerical models with minimum amount of horizontal and vertical reinforcement by code (0.25% in ACI 318 2019) 226
Figure 6.6: Lateral load versus drift hysteresis curves of AR=1 wall models 229
Figure 6.7: Lateral load versus drift hysteresis curves of AR=2 wall models 230
Figure 6.8: Lateral load versus drift hysteresis curves of AR=4 wall models 231
Figure 6.9: Normalized lateral strength of the wall models as a function of axial load ratio . 233
Figure 6.10: Normalized equivalent damping of wall models as a function of the applied axial load for different aspect ratios 235
Figure 6.11: Effect of α_{dow} parameter on wall response 236
Figure 6.12: Crack pattern at **0.5% drift ratio** predicted by the **AR=1** wall models with **boundary elements** and different axial load ratios 238
Figure 6.13: Crack pattern at **1% drift ratio** predicted by the **AR=1** wall models with **boundary elements** and different axial load ratios 239
Figure 6.14: Crack pattern at **2% drift ratio** predicted by the **AR=1** wall models with **boundary elements** and different axial load ratios 240
Figure 6.15: Crack pattern at **0.5% drift ratio** predicted by the **AR=1** wall models with distributed reinforcement, i.e., "**noBE**", and different axial load ratios 241
Figure 6.16: Crack pattern at **1% drift ratio** predicted by the **AR=1** wall models with distributed reinforcement, i.e., "**noBE**", and different axial load ratios 242
Figure 6.17: Crack pattern at **2% drift ratio** predicted by the **AR=1** wall models with distributed reinforcement, i.e., "**noBE**", and different axial load ratios 243
Figure 6.18: Summary of predicted crack pattern for **AR=1** wall models at **2% drift ratio** . . 244
Figure 6.19: Crack pattern at **0.5% drift ratio** predicted by the **AR=2** wall models with **boundary elements** and different axial load ratios 246
Figure 6.20: Crack pattern at **1% drift ratio** predicted by the **AR=2** wall models with **boundary elements** and different axial load ratios 247
Figure 6.21: Crack pattern at **2% drift ratio** predicted by the **AR=2** wall models with **boundary elements** and different axial load ratios 248
Figure 6.22: Crack pattern at **0.5% drift ratio** predicted by the **AR=2** wall models with distributed reinforcement, i.e., "**noBE**", and different axial load ratios 249
Figure 6.23: Crack pattern at **1% drift ratio** predicted by the **AR=2** wall models with distributed reinforcement, i.e., "**noBE**", and different axial load ratios 250

Figure 6.24: Crack pattern at **2% drift ratio** predicted by the **AR=2** wall models with distributed reinforcement, i.e., "**noBE**", and different axial load ratios 251
Figure 6.25: Crack pattern at **0.5% drift ratio** predicted by the **AR=4** wall models with **boundary elements** and different axial load ratios 252
Figure 6.26: Crack pattern at **1% drift ratio** predicted by the **AR=4** wall models with **boundary elements** and different axial load ratios 253
Figure 6.27: Crack pattern at **2% drift ratio** predicted by the **AR=4** wall models with **boundary elements** and different axial load ratios 254
Figure 6.28: Crack pattern at **0.5% drift ratio** predicted by the **AR=4** wall models with distributed reinforcement, i.e., "**noBE**", and different axial load ratios 255
Figure 6.29: Crack pattern at **1% drift ratio** predicted by the **AR=4** wall models with distributed reinforcement, i.e., "**noBE**", and different axial load ratios 256
Figure 6.30: Crack pattern at **2% drift ratio** predicted by the **AR=4** wall models with distributed reinforcement, i.e., "**noBE**", and different axial load ratios 257
Figure 6.31: Summary of predicted crack pattern for **AR=2** wall models at **2% drift ratio** . . 258
Figure 6.32: Summary of predicted crack pattern for **AR=4** wall models at **2% drift ratio** . 259
Figure 6.33: Maximum crack width at yield of the reinforcement in rectangular shear walls . 261
Figure 6.34: Maximum elevation normalized by the wall height of elements in the minor, moderate, and severe crack width bins versus applied axial load ratio at the Collapse Prevention limit state 262
Figure 6.35: Graphic representation of maximum elevation of cracked elements as predicted by the wall model 262

Figure B.1: Design concrete mix 288
Figure B.2: Unconfined Compression Tests 289
Figure B.3: Strain Stress relationship at 28 days 289
Figure B.4: Split test 290
Figure B.5: Strain Stress relationship 292
Figure B.6: Three tested cylinders at the end of the test 293
Figure B.7: Strain Stress relationship for the three cylinders at 28 days. Note: displacement slip occurred at the beginning of the tests, which affected strain measurement 294
Figure B.8: # 4 Transverse reinforcing bars: Strain Stress relationship 295
Figure B.9: # 5 Longitudinal reinforcing bars: Strain Stress relationship 296

Figure C.1: Wall SL7.5. Location of crack width sensors 298
Figure C.2: Wall SQ7.5. Location of crack width sensors 298
Figure C.3: Wall SQ0. Location of crack width sensors 299
Figure C.4: Crack width history of sensor DCR01 in the slender wall SL7.5. Maximum measured crack width = 5.2 mm and residual measured crack width = 2.3 mm 300
Figure C.5: Crack width history of sensor DCR02 installed in slender wall SL7.5. Maximum measured crack width = 2.2 mm and residual measured crack width = 0.61 mm . 301
Figure C.6: Crack width history of sensor DCR03 installed in slender wall SL7.5. Maximum measured crack width = 2.8 mm and residual measured crack width = 0.68 mm . 302
Figure C.7: Crack width history of sensor DCR04 installed in slender wall SL7.5. Maximum measured crack width = 5.0 mm and residual measured crack width = 1.0 mm . 303
Figure C.8: Crack width history, photograph and location of sensor CR1 installed in wall SQ7.5 304
Figure C.9: Crack width history, photograph and location of sensor CR2 installed in wall SQ7.5 304

Figure C.10: Crack width history, photograph and location of sensor CR3 installed in wall SQ7.5 305
Figure C.11: Crack width history, photograph and location of sensor CR4 installed in wall SQ7.5 305
Figure C.12: Crack width history, photograph and location of sensor CR5 installed in wall SQ7.5 306
Figure C.13: Crack width history, photograph and location of sensor CR6 installed in wall SQ7.5 306
Figure C.14: Crack width history, photograph and location of sensor CR1 installed in wall SQ0 307
Figure C.15: Crack width history, photograph and location of sensor CR2 installed in wall SQ0 307
Figure C.16: Crack width history, photograph and location of sensor CR3 installed in wall SQ0 308
Figure C.17: Crack width history, photograph and location of sensor CR4 installed in wall SQ0 308
Figure C.18: Crack width history, photograph and location of sensor CR5 installed in wall SQ0 309
Figure C.19: Crack width history, photograph and location of sensor CR6 installed in wall SQ0 309

Figure E.1: Bonded anchor A1 in wall SL7.5: location and photographs 316
Figure E.2: Bonded anchor A1 in wall SL7.5: measured load and displacement histories and wall drift ratio history 317
Figure E.3: Bonded anchor A2 in wall SL7.5: location and photographs 318
Figure E.4: Bonded anchor A2 in wall SL7.5: measured load and displacement histories and wall drift ratio history 319
Figure E.5: Bonded anchor A3 in wall SL7.5: location and photographs 320
Figure E.6: Bonded anchor A3 in wall SL7.5: measured load and displacement histories and wall drift ratio history. 321
Figure E.7: Expansion anchor A4 in wall SL7.5: location and photographs 322
Figure E.8: Expansion anchor A4 in wall SL7.5: measured load and displacement histories and wall drift ratio history 323
Figure E.9: Expansion anchor A5 in wall SL7.5: location and photographs 324
Figure E.10: Expansion anchor A5 in wall SL7.5: measured load and displacement histories and wall drift ratio history 325
Figure E.11: Expansion anchor A6 in wall SL7.5: location and photographs 326
Figure E.12: Expansion anchor A6 in wall SL7.5: measured load and displacement histories and wall drift ratio history 327
Figure E.13: Bonded anchor B1 in wall SL7.5: location and photographs 328
Figure E.14: Bonded anchor B1 in wall SL7.5: measured load and displacement histories and wall drift ratio history 329
Figure E.15: Bonded anchor B2 in wall SL7.5: location and photographs 330
Figure E.16: Bonded anchor B2 in wall SL7.5: measured load and displacement histories and wall drift ratio history 331
Figure E.17: Bonded anchor B3 in wall SL7.5: location and photographs 332
Figure E.18: Bonded anchor B3 in wall SL7.5: measured load and displacement histories and wall drift ratio history 333
Figure E.19: Expansion anchor B4 in wall SL7.5: location and photographs 334
Figure E.20: Expansion anchor B4 in wall SL7.5: measured load and displacement histories and wall drift ratio history 335
Figure E.21: Expansion anchor B5 in wall SL7.5: location and photographs 336
Figure E.22: Expansion anchor B5 in wall SL7.5: measured load and displacement histories and wall drift ratio history 337
Figure E.23: Expansion anchor B6 in wall SL7.5: location and photographs 338
Figure E.24: Expansion anchor B6 in wall SL7.5: measured load and displacement histories and wall drift ratio history 339

Figure E.25: Bonded anchor C1 in wall SL7.5: location and photographs 340
Figure E.26: Bonded anchor C1 in wall SL7.5: measured load and displacement histories and wall drift ratio history 341
Figure E.27: Bonded anchor C2 in wall SL7.5: location and photographs 342
Figure E.28: Bonded anchor C2 in wall SL7.5: measured load and displacement histories and wall drift ratio history 343
Figure E.29: Bonded anchor C3 in wall SL7.5: location and photographs 344
Figure E.30: Bonded anchor C3 in wall SL7.5: measured load and displacement histories and wall drift ratio history 345
Figure E.31: Expansion anchor C4 in wall SL7.5: location and photographs 346
Figure E.32: Expansion anchor C4 in wall SL7.5: measured load and displacement histories and wall drift ratio history 347
Figure E.33: Expansion anchor C5 in wall SL7.5: location and photographs 348
Figure E.34: Expansion anchor C5 in wall SL7.5: measured load and displacement histories and wall drift ratio history 349
Figure E.35: Expansion anchor C6 in wall SL7.5: location and photographs 350
Figure E.36: Expansion anchor C6 in wall SL7.5: measured load and displacement histories and wall drift ratio history 351
Figure E.37: Bonded anchor D1 in wall SL7.5: location and photographs 352
Figure E.38: Bonded anchor D1 in wall SL7.5: measured load and displacement histories and wall drift ratio history 353
Figure E.39: Bonded anchor D2 in wall SL7.5: location and photographs 354
Figure E.40: Bonded anchor D2 in wall SL7.5: measured load and displacement histories and wall drift ratio history 355
Figure E.41: Bonded anchor D3 in wall SL7.5: location and photographs 356
Figure E.42: Bonded anchor D3 in wall SL7.5: measured load and displacement histories and wall drift ratio history 357
Figure E.43: Expansion anchor D4 in wall SL7.5: location and photographs 358
Figure E.44: Expansion anchor D4 in wall SL7.5: measured load and displacement histories and wall drift ratio history 359
Figure E.45: Expansion anchor D5 in wall SL7.5: location and photographs 360
Figure E.46: Expansion anchor D5 in wall SL7.5: measured load and displacement histories and wall drift ratio history 361
Figure E.47: Expansion anchor D6 in wall SL7.5: location and photographs 362
Figure E.48: Expansion anchor D6 in wall SL7.5: measured load and displacement histories and wall drift ratio history 363
Figure E.49: Bonded anchor E1 in wall SL7.5: location and photographs 364
Figure E.50: Bonded anchor E1 in wall SL7.5: measured load and displacement histories and wall drift ratio history 365
Figure E.51: Bonded anchor E2 in wall SL7.5: location and photographs 366
Figure E.52: Bonded anchor E2 in wall SL7.5: measured load and displacement histories and wall drift ratio history 367
Figure E.53: Bonded anchor E3 in wall SL7.5: location and photographs 368
Figure E.54: Bonded anchor E3 in wall SL7.5: measured load and displacement histories and wall drift ratio history 369
Figure E.55: Expansion anchor E4 in wall SL7.5: location and photographs 370

Figure E.56: Expansion anchor E4 in wall SL7.5: measured load and displacement histories and wall drift ratio history . . . 371
Figure E.57: Expansion anchor E5 in wall SL7.5: location and photographs. . . . 372
Figure E.58: Expansion anchor E5 in wall SL7.5: measured load and displacement histories and wall drift ratio history. . . . 373
Figure E.59: Expansion anchor E6 in wall SL7.5: location and photographs. . . . 374
Figure E.60: Expansion anchor E6 in wall SL7.5: measured load and displacement histories and wall drift ratio history. . . . 375
Figure E.61: Bonded anchors F1, F2 and F3 in wall SL7.5: location and photographs . . . 376
Figure E.62: Bonded anchors F1, F2 and F3 in wall SL7.5: measured displacement histories . 377
Figure E.63: Expansion anchors F4, F5 and F6 in wall SL7.5: location and photographs . . . 378
Figure E.64: Expansion anchor F4, F5 and F6 in wall SL7.5: measured displacement histories 379
Figure E.65: Location and photograph of anchor A1 in wall SQ7.5 . . . 381
Figure E.66: Wall SQ7.5: photographs showing the crack evolution around anchor A1 . . . 382
Figure E.67: Wall SQ7.5, anchor A1: measured load and displacement histories and wall drift history . . . 383
Figure E.68: Location and photograph of anchor A2 in wall SQ7.5 . . . 385
Figure E.69: Wall SQ7.5: photographs showing the crack evolution around anchor A2 . . . 386
Figure E.70: Wall SQ7.5, anchor A2: measured load and displacement histories and wall drift history . . . 387
Figure E.71: Location and photograph of anchor A3 in wall SQ7.5 . . . 389
Figure E.72: Wall SQ7.5: photographs showing the crack evolution around anchor A3 . . . 390
Figure E.73: Wall SQ7.5, anchor A3: measured load and displacement histories and wall drift history . . . 391
Figure E.74: Location and photograph of anchor A4 in wall SQ7.5 . . . 393
Figure E.75: Wall SQ7.5: photographs showing the crack evolution around anchor A4 . . . 394
Figure E.76: Wall SQ7.5, anchor A4: measured load and displacement histories and wall drift history . . . 395
Figure E.77: Location and photograph of anchor A5 in wall SQ7.5 . . . 397
Figure E.78: Wall SQ7.5: photographs showing the crack evolution around anchor A5 . . . 398
Figure E.79: Wall SQ7.5, anchor A5: measured load and displacement histories and wall drift history . . . 399
Figure E.80: Location and photograph of anchor A6 in wall SQ7.5 . . . 401
Figure E.81: Wall SQ7.5: photographs showing the crack evolution around anchor A6 . . . 402
Figure E.82: Wall SQ7.5, anchor A6: measured load and displacement histories and wall drift history . . . 403
Figure E.83: Location and photograph of anchor B1 in wall SQ7.5 . . . 405
Figure E.84: Wall SQ7.5: photographs showing the crack evolution around anchor B1 . . . 406
Figure E.85: Wall SQ7.5, anchor B1: measured load and displacement histories and wall drift history . . . 407
Figure E.86: Location and photograph of anchor B2 in wall SQ7.5 . . . 409
Figure E.87: Wall SQ7.5: photographs showing the crack evolution around anchor B2 . . . 410
Figure E.88: Wall SQ7.5, anchor B2: measured load and displacement histories and wall drift history . . . 411
Figure E.89: Location and photograph of anchor B3 in wall SQ7.5 . . . 413
Figure E.90: Wall SQ7.5: photographs showing the crack evolution around anchor B3 . . . 414

Figure E.91: Wall SQ7.5, anchor B3: measured load and displacement histories and wall drift history . . . 415
Figure E.92: Location and photograph of anchor B4 in wall SQ7.5 . . . 417
Figure E.93: Wall SQ7.5: photographs showing the crack evolution around anchor B4 . . . 418
Figure E.94: Wall SQ7.5, anchor B4: measured load and displacement histories and wall drift history . . . 419
Figure E.95: Location and photograph of anchor B5 in wall SQ7.5 . . . 421
Figure E.96: Wall SQ7.5: photographs showing the crack evolution around anchor B5 . . . 422
Figure E.97: Wall SQ7.5, anchor B5: measured load and displacement histories and wall drift history . . . 423
Figure E.98: Location and photograph of anchor B6 in wall SQ7.5. . . . 425
Figure E.99: Wall SQ7.5: photographs showing the crack evolution around anchor B6 . . . 426
Figure E.100: Wall SQ7.5 anchor B6: measured load and displacement histories and wall drift history . . . 427
Figure E.101: Location and photograph of anchor C1 in wall SQ7.5 . . . 429
Figure E.102: Wall SQ7.5: photographs showing the crack evolution around anchor C1 . . . 430
Figure E.103: Wall SQ7.5, anchor C1: measured load and displacement histories and wall drift history . . . 431
Figure E.104: Location and photograph of anchor C2 in wall SQ7.5 . . . 433
Figure E.105: Wall SQ7.5: photographs showing the crack evolution around anchor C2 . . . 434
Figure E.106: Wall SQ7.5, anchor C2: measured load and displacement histories and wall drift history . . . 435
Figure E.107: Location and photograph of anchor C3 in wall SQ7.5 . . . 437
Figure E.108: Wall SQ7.5: photographs showing the crack evolution around anchor C3 . . . 438
Figure E.109: Wall SQ7.5, anchor C3: measured load and displacement histories and wall drift history . . . 439
Figure E.110: Location and photograph of anchor C4 in wall SQ7.5 . . . 441
Figure E.111: Wall SQ7.5: photographs showing the crack evolution around anchor C4 . . . 442
Figure E.112: Wall SQ7.5, anchor C4: measured load and displacement histories and wall drift history . . . 443
Figure E.113: Location and photograph of anchor C5 in wall SQ7.5 . . . 445
Figure E.114: Wall SQ7.5: photographs showing the crack evolution around anchor C5 . . . 446
Figure E.115: Wall SQ7.5, anchor C5: measured load and displacement histories and wall drift history . . . 447
Figure E.116: Location and photograph of anchor C6 in wall SQ7.5. . . . 449
Figure E.117: Wall SQ7.5: photographs showing the crack evolution around anchor C6 . . . 450
Figure E.118: Wall SQ7.5, anchor C6: measured load and displacement histories and wall drift history . . . 451
Figure E.119: Location and photograph of anchor A1 in wall SQ0 . . . 453
Figure E.120: Wall SQ0: photographs showing the crack evolution around anchor A1 . . . 454
Figure E.121: Wall SQ0, anchor A1: measured load and displacement histories and wall drift history . . . 455
Figure E.122: Location and photograph of anchor A2 in wall SQ0 . . . 457
Figure E.123: Wall SQ0: photographs showing the crack evolution around anchor A2 . . . 458
Figure E.124: Wall SQ0, anchor A2: measured load and displacement histories and wall drift history . . . 459

Figure E.125: Location and photograph of anchor A3 in wall SQ0 461
Figure E.126: Wall SQ0: photographs showing the crack evolution around anchor A3 462
Figure E.127: Wall SQ0, anchor A3: measured load and displacement histories and wall drift history 463
Figure E.128: Location and photograph of anchor A4 in wall SQ0 465
Figure E.129: Wall SQ0: photographs showing the crack evolution around anchor A4 466
Figure E.130: Wall SQ0, anchor A4: measured load and displacement histories and wall drift history 467
Figure E.131: Location and photograph of anchor A5 in wall SQ0 469
Figure E.132: Wall SQ0: photographs showing the crack evolution around anchor A5 470
Figure E.133: Wall SQ0, anchor A5: measured load and displacement histories and wall drift history 471
Figure E.134: Location and photograph of anchor A6 in wall SQ0 473
Figure E.135: Wall SQ0: photographs showing the crack evolution around anchor A6 474
Figure E.136: Wall SQ0, anchor A6: measured load and displacement histories and wall drift history 475
Figure E.137: Wall SQ0: photographs showing the crack evolution around row A during the last three drift demands 476
Figure E.138: Location and photograph of anchor B1 in wall SQ0 478
Figure E.139: Wall SQ0: photographs showing the crack evolution around anchor B1 479
Figure E.140: Wall SQ0, anchor B1: measured load and displacement histories and wall drift history 480
Figure E.141: Location and photograph of anchor B2 in wall SQ0 482
Figure E.142: Wall SQ0: photographs showing the crack evolution around anchor B2 483
Figure E.143: Wall SQ0, anchor B2: measured load and displacement histories and wall drift history 484
Figure E.144: Location and photograph of anchor B3 in wall SQ0 486
Figure E.145: Wall SQ0: photographs showing the crack evolution around anchor B3 487
Figure E.146: Wall SQ0, anchor B3: measured load and displacement histories and wall drift history 488
Figure E.147: Location and photograph of anchor B4 in wall SQ0 490
Figure E.148: Wall SQ0: photographs showing the crack evolution around anchor B4 491
Figure E.149: Wall SQ0, anchor B4: measured load and displacement histories and wall drift history 492
Figure E.150: Location and photograph of anchor B5 in wall SQ0 494
Figure E.151: Wall SQ0: photographs showing the crack evolution around anchor B5. 495
Figure E.152: Wall SQ0, anchor B5: measured load and displacement histories and wall drift history. 496
Figure E.153: Location and photograph of anchor B6 in wall SQ0 498
Figure E.154: Wall SQ0: photographs showing the crack evolution around anchor B6 499
Figure E.155: Wall SQ0, anchor B6: measured load and displacement histories and wall drift history 500
Figure E.156: Wall SQ0: photographs showing the crack evolution around row B during the last three drift demands 501
Figure E.157: Location and photograph of anchor C1 in wall SQ0 503
Figure E.158: Wall SQ0: photographs showing the crack evolution around anchor C1 504

Figure E.159: Wall SQ0, anchor C1: measured load and displacement histories and wall drift history . . . 505
Figure E.160: Location and photograph of anchor C2 in wall SQ0 . . . 507
Figure E.161: Wall SQ0: photographs showing the crack evolution around anchor C2 . . . 508
Figure E.162: Wall SQ0, anchor C2: measured load and displacement histories and wall drift history . . . 509
Figure E.163: Location and photograph of anchor C3 in wall SQ0 . . . 511
Figure E.164: Wall SQ0: photographs showing the crack evolution around anchor C3 . . . 512
Figure E.165: Wall SQ0, anchor C3: measured load and displacement histories and wall drift history . . . 513
Figure E.166: Location and photograph of anchor C4 in wall SQ0 . . . 515
Figure E.167: Wall SQ0: photographs showing the crack evolution around anchor C4 . . . 516
Figure E.168: Wall SQ0, anchor C4: measured load and displacement histories and wall drift history . . . 517
Figure E.169: Location and photograph of anchor C5 in wall SQ0 . . . 519
Figure E.170: Wall SQ0: photographs showing the crack evolution around anchor C5 . . . 520
Figure E.171: Wall SQ0, anchor C5: measured load and displacement histories and wall drift history . . . 521
Figure E.172: Location and photograph of anchor C6 in wall SQ0 . . . 523
Figure E.173: Wall SQ0: photographs showing the crack evolution around anchor C6 . . . 524
Figure E.174: Wall SQ0, anchor C6: measured load and displacement histories and wall drift history . . . 525
Figure E.175: Wall SQ0: photographs showing the crack evolution around row C during the last three drift demands . . . 526
Figure E.176: Anchor A1 in wall SL7.5: Load-displacement pullout curve and photographs of the cone of failure and of the pulled anchor . . . 528
Figure E.177: Anchor A2 in wall SL7.5: Load-displacement pullout curve and photographs of the cone of failure and of the pulled anchor . . . 528
Figure E.178: Anchor A3 in wall SL7.5: Load-displacement pullout curve and photographs of the cone of failure and of the pulled anchor . . . 529
Figure E.179: Anchor B1 in wall SL7.5: Load-displacement pullout curve and photographs of the cone of failure and of the pulled anchor . . . 529
Figure E.180: Anchor B2 in wall SL7.5: Load-displacement pullout curve and photographs of the cone of failure and of the pulled anchor . . . 530
Figure E.181: Anchor C1 in wall SL7.5: Load-displacement pullout curve and photographs of the cone of failure and of the pulled anchor . . . 530
Figure E.182: Anchor C3 in wall SL7.5: Load-displacement pullout curve and photographs of the cone of failure and of the pulled anchor . . . 531
Figure E.183: Anchor D2 in wall SL7.5: Load-displacement pullout curve and photographs of the cone of failure and of the pulled anchor . . . 531
Figure E.184: Anchor D3 in wall SL7.5: Load-displacement pullout curve and photographs of the cone of failure and of the pulled anchor . . . 532
Figure E.185: Anchor F1 in wall SL7.5: Load-displacement pullout curve and photographs of the cone of failure and of the pulled anchor . . . 532
Figure E.186: Anchor F2 in wall SL7.5: Load-displacement pullout curve and photographs of the cone of failure and of the pulled anchor . . . 533

Figure E.187: Statistics of residual capacities of bonded anchors in no visible cracks in wall SL7.5 533
Figure E.188: Statistics of residual capacities of bonded anchors in one or more shear cracks in wall SL7.5 534
Figure E.189: Statistics of residual capacities of bonded anchors in one or more tension cracks in wall SL7.5 535
Figure E.190: Statistics of residual capacities of bonded anchors in diagonal crossing shear cracks wall SL7.5 536
Figure E.191: Anchor B4 in wall SL7.5: Load-displacement pullout curve and photographs of the cone of failure and of the pulled anchor 537
Figure E.192: Anchor B5 in wall SL7.5: Load-displacement pullout curve and photographs of the cone of failure and of the pulled anchor 537
Figure E.193: Anchor B6 in wall SL7.5: Load-displacement pullout curve and photographs of the cone of failure and of the pulled anchor 538
Figure E.194: Anchor C4 in wall SL7.5: Load-displacement pullout curve and photographs of the cone of failure and of the pulled anchor 538
Figure E.195: Anchor C5 in wall SL7.5: Load-displacement pullout curve and photographs of the cone of failure and of the pulled anchor 539
Figure E.196: Anchor C6 in wall SL7.5: Load-displacement pullout curve and photographs of the cone of failure and of the pulled anchor 539
Figure E.197: Anchor D4 in wall SL7.5: Load-displacement pullout curve and photographs of the cone of failure and of the pulled anchor 540
Figure E.198: Anchor D5 in wall SL7.5: Load-displacement pullout curve and photographs of the cone of failure and of the pulled anchor 540
Figure E.199: Anchor D6 in wall SL7.5: Load-displacement pullout curve and photographs of the cone of failure and of the pulled anchor 541
Figure E.200: Anchor E4 in wall SL7.5: Load-displacement pullout curve and photographs of the cone of failure and of the pulled anchor 541
Figure E.201: Anchor E5 in wall SL7.5: Load-displacement pullout curve and photographs of the cone of failure and of the pulled anchor 542
Figure E.202: Summary and statistics of the residual capacities of expansion anchors in no visible cracks in wall SL7.5 543
Figure E.203: Summary and statistics of the residual capacities of expansion anchors in one or more shear cracks in wall SL7.5 544
Figure E.204: Summary and statistics of the residual capacities of expansion anchors in one or more tension cracks in wall SL7.5 545
Figure E.205: Summary and statistics of the residual capacities of expansion anchors in diagonal crossing shear cracks in wall SL7.5 546
Figure E.206: Anchor A2 in wall SQ7.5: load-displacement pullout curve and photographs of the cone of failure and of the pulled anchor 547
Figure E.207: Anchor A6 in wall SQ7.5: load-displacement pullout curve and photographs of the cone of failure and of the pulled anchor 548
Figure E.208: Anchor B1 in wall SQ7.5: load-displacement pullout curve and photographs of the cone of failure and of the pulled anchor 548
Figure E.209: Anchor B2 in wall SQ7.5: load-displacement pullout curve and photographs of the cone of failure and of the pulled anchor 549

Figure E.210: Anchor B3 in wall SQ7.5: load-displacement pullout curve and photographs of the cone of failure and of the pulled anchor 549
Figure E.211: Anchor B4 in wall SQ7.5: load-displacement pullout curve and photographs of the cone of failure and of the pulled anchor 550
Figure E.212: Anchor B5 in wall SQ7.5: load-displacement pullout curve and photographs of the cone of failure and of the pulled anchor 550
Figure E.213: Anchor B6 in wall SQ7.5: load-displacement pullout curve and photographs of the cone of failure and of the pulled anchor 551
Figure E.214: Anchor C1 in wall SQ7.5: load-displacement pullout curve and photographs of the cone of failure and of the pulled anchor 551
Figure E.215: Anchor C2 in wall SQ7.5: load-displacement pullout curve and photographs of the cone of failure and of the pulled anchor 552
Figure E.216: Anchor C3 in wall SQ7.5: load-displacement pullout curve and photographs of the cone of failure and of the pulled anchor 552
Figure E.217: Anchor C4 in wall SQ7.5: load-displacement pullout curve and photographs of the cone of failure and of the pulled anchor 553
Figure E.218: Anchor C5 in wall SQ7.5: load-displacement pullout curve and photographs of the cone of failure and of the pulled anchor 553
Figure E.219: Anchor C6 in wall SQ7.5: load-displacement pullout curve and photographs of the cone of failure and of the pulled anchor 554
Figure E.220: Wall SQ7.5: summary of normalized data and comparison with anchor reference tests results 554
Figure E.221: Wall SQ0: anchor B1 load-displacement pullout curve and photographs of the cone of failure and of the pulled anchor 555
Figure E.222: Wall SQ0: anchor B2 load-displacement pullout curve and photographs of the cone of failure and of the pulled anchor 556
Figure E.223: Wall SQ0: anchor B3 load-displacement pullout curve and photographs of the cone of failure and of the pulled anchor 556
Figure E.224: Wall SQ0: anchor B4 load-displacement pullout curve and photographs of the cone of failure and of the pulled anchor 557
Figure E.225: Wall SQ0: anchor B5 load-displacement pullout curve and photographs of the cone of failure and of the pulled anchor 557
Figure E.226: Wall SQ0: anchor B6 load-displacement pullout curve and photographs of the cone of failure and of the pulled anchor 558
Figure E.227: Wall SQ0: anchor C1 load-displacement pullout curve and photographs of the cone of failure and of the pulled anchor 558
Figure E.228: Wall SQ0: anchor C2 load-displacement pullout curve and photographs of the cone of failure and of the pulled anchor 559
Figure E.229: Wall SQ0: anchor C3 load-displacement pullout curve and photographs of the cone of failure and of the pulled anchor 559
Figure E.230: Wall SQ0: anchor C4 load-displacement pullout curve and photographs of the cone of failure and of the pulled anchor 560
Figure E.231: Wall SQ0: anchor C6 load-displacement pullout curve and photographs of the cone of failure and of the pulled anchor 560
Figure E.232: Wall SQ0: summary of normalized data and comparison with anchor reference tests results 561

Figure F.1: SfM model of wall SQ7.5- front view of West face 563
Figure F.2: SfM model of wall SQ7.5- front view of East face (anchor face) 564
Figure F.3: SfM model of wall SQ7.5- isometric view from South-West 565
Figure F.4: SfM model of wall SQ7.5- isometric view from North-East 566
Figure F.5: SfM model of wall SQ0- front view of West face (anchor face) 567
Figure F.6: SfM model of wall SQ0- front view of East face 568
Figure F.7: SfM model of wall SQ0- isometric view from South-West 569

LIST OF TABLES

Table 1.1: Classification of structures according to ductility 7
Table 1.2: Structural ductility factors, from ASCE/SEI 7-16 (2016) and CEN (2004) 8
Table 1.3: Revised anchor mapping table 9
Table 1.4: Reference data considered in Fig. 1.12 32
Table 1.5: Damage evaluation of concrete shear walls according to measured crack width . . 33
Table 1.6: Reference data considered in Fig. 1.19 47

Table 2.1: Test results summary 68
Table 2.2: Empirical equations adopted to estimate the plastic hinge length in rectangular walls 78

Table 3.1: Drift ratio δ (%) corresponding to performance limit states for RC shear walls adopted by various codes and in the literature 83
Table 3.2: Summary of experimental results. [1 kip= 4.45 kN; 1 in= 25.4 mm] 93
Table 3.3: Summary of experimental results. [1 kip= 4.45 kN; 1 in= 25.4 mm] 98

Table 4.1: Anchor installation and design parameters 131

Table 5.1: Geometric and material properties of the tested full-scale walls 186
Table 5.2: Crack width ranges related to shear wall and anchor performance 207

Table 6.1: Matrix of wall models considered in the numerical parametric study 220
Table 6.2: Equivalent hysteretic damping values predicted by wall models absent axial load . 235

Table A.1: Summary of the Dead Loads assumed in the design of the slender wall 281
Table A.2: Superimposed Live Loads on the slender wall* 281
Table A.3: Gravity load on the slender wall specimen 282
Table A.4: Effective seismic weight per floor of the slender wall specimen 283
Table A.5: Seismic design story shear of the slender wall specimen 283
Table A.6: Summary of the Dead Loads assumed in the design of the squat walls 285
Table A.7: Superimposed Live Loads on the squat wall* 285
Table A.8: Gravity loads on the squat wall specimen 286
Table A.9: Seismic design story shear of the squat wall specimen 286

Table B.1: Compressive strength and strain at peak stress at 28 days 288
Table B.2: Split test results at 28 days 291
Table B.3: Average yield and ultimate strengths of reinforcement from tension test 292
Table B.4: Compressive strength and strain at peak stress at 28 days 294
Table B.5: Split test results at 28 days 295
Table B.6: Average yield and ultimate strengths of reinforcement from tension test 296

Table E.1: Crack width measured around the anchor plates during the cyclic test of wall SQ7.5 313
Table E.2: Crack width measured around the anchor plates during the cyclic test of wall SQ0 314

GLOSSARY OF TERMS

This section defines the acronyms, variables and selected nomenclature used in this dissertation. It is noted that the notation used in the design process of the walls, described in Chapters 2 and 3 and in Appendix A, follows the design codes ASCE/SEI 7-16 (2016) and ACI 318 (2019), which can be consulted for further details.

Acronyms/Abbreviation

R	Response Modification Coefficient
AR	Aspect Ratio
ASPC	Anchor Seismic Performance Category
BA	Bonded anchor
BE	Wall Boundary Element
DR	Wall Drift Ratio
EA	Expansion anchor
PC	Performance Category
RC	Reinforced Concrete

Greek Symbols

δ	Drift Ratio [%]
Δ_f	Flexural Component of the Lateral Displacement
Δ_s	Shear Component of the Lateral Displacement

Typical Parameters

d	Anchor diameter
H_w	Wall Height

h_{ef} Embedment depth

L_p Equivalent Plastic Hinge Length

L_w Wall Length

L_{pz} Plastic Hinge Zone Length

T Anchor tension load

T^* Normalized tension load on the anchor

t_w Wall Thickness

T_i Initial tension load on the anchor (at the beginning of the cyclic test on the wall)

$T_{u,50}$ 50% ultimate tension load

T_u Ultimate tension load

w_r Residual crack width

w_{max} Maximum crack width

w Crack Width

ACKNOWLEDGMENTS

This research was partially funded by Hilti Corporation through the *Hilti Seismic Project (HSP)* and material and technical assistance was provided by Hilti North America. Technical oversight of the project was provided by Dr. Ulrich Bourgund, Mr. John F. Silva, Dr. Roberto Piccinin and Dr. Kenton McBride. The financial and technical support of these organizations and individuals is gratefully acknowledged. Opinions, findings and conclusions are those of the author and do not necessary reflect the views of the sponsoring organizations.

I would like to thank my doctoral committee for their time, support and guidance. Thanks to Professors Joel Conte and Gilberto Mosqueda for the stimulating discussions and for the best Engineering classes I ever had in my academic path. Thanks to Professors William Hodgkiss and Peter Shearer, who guided me in my out-of-department sequence with inspiring lectures and exceptional availability. In particular, I would like to profoundly thank my advisor, Professor Tara Hutchinson, for trusting in me and in my abilities, and for guiding me through my doctoral studies. I am not only thankful for her technical support, but also for her incredibly human touch always showed in every occasion. I am grateful for her constant feedback and suggestions, for her time and patience, for her encouragements to always be exceptionally good at any task, and finally for showing me how to live a well-balanced life. Things like the "daily morning Research Huddle", a smile, a cup of coffee together, and a "don't forget to have a walk or a yoga stretch today!" make her the best advisor I could have possibly asked for.

I express my gratitude to the Hilti Corporation for the time and money invested on this project. In particular, I would like to thank Mr. John Silva and Dr. Roberto Piccinin for accompanying me step by step through the different phases of the project, for sharing their knowledge with me and for taking time to physically participate to the laboratory work and testing phases. I am also particularly thankful to Dr. Kenton McBride for having fun with me in the lab and for his thoughtful and precious insight.

The work presented herein was performed in the Powell Structural Laboratories with the help of the amazing laboratory staff. I am deeply thankful to Darren Mckay, Dr. Christopher Latham, Michael Sanders, Abdullah Hamid, Noah Aldrich and Andrew Sander for their fundamental help during the experimental work, from the very beginning (when all we had was a sketch of the test setup) to the demolition and disposal of the concrete specimens. I am particularly thankful to Noah Aldrich and Andrew Sander for spending several of their weekends in the laboratories to advance construction of the test specimens

and for keeping up with our tough testing schedule. I also gratefully acknowledge the undergraduates and graduate students who assisted the laboratory staff- undergraduates Melissa Patel, Madison Williams, Kim-Chi Nguyen, Marvin Machado, Angel Gonzales, Jesus Perez, Gustavo Ramirez, Javi Puyat and Jaysen Zapata were helpful in preparing the reinforced concrete walls and the test setup. Graduate visiting students Lorenzo Moschetti and Elisabetta Barzi assisted me during construction and testing and shared with me happy moments in the laboratories. Ph.D. students Michael Morano, Amanpreet Singh, Brandon Schiller and Sergio Suarez as well as Dr. Xiang Wang and Long Wang were extremely helpful in the instrumentation setup during testing. Moreover, I deeply thank Professor Falko Kuster, Eric Lo, Megulo Abebe and Luca De Vivo from the CHEI team lead by Professor Falko Kuster for assisting me in recording and image processing after the tests.

I would like to thank all my friends at UC San Diego, especially Dr. Elide Pantoli, Leticia Maria Nocko, Radhavi Abeysiridara, Chaiane Wiggers De Souza, Marco Pasetto, Marco Pigazzini, Simone Sternini, Andreas Koutras, Georgios Moutsanidis and Konstantinos Anagnostopoulos, and the staff of the Structural Engineering department, particularly Sandra De Sousa, Joana Halnez, Yvonne Wollmann, Julie Storing and Lindsay Walton, for their precious attention to my overall well-being.

All of my work is dedicated to my family, my mother Daniela, my father Giorgio, and my sister Giulia. Thank you for unconditionally supporting me, encouraging me, and making me feel so loved, even from so far apart. I send a huge "Grazie" to you! And I am deeply grateful for having Giorgio here by my side. Thank you for sharing these years with me!

Chapter 2 contains material published in the following journal paper: Faraone, G., Hutchinson, T. C., Piccinin, R., and Silva, J., 2019, "Cyclic Lateral Load Response of a Full-Scale Flexure-Dominated Shear Wall" *ACI Structural Journal*. V. 116, No. 6, pp. 281-292. The dissertation author was the primary author on this paper. Chapter 2 also contains material published in the following report: Faraone, G. and Hutchinson, T. C., 2018, "Behavior of post-installed anchors in reinforced concrete shear walls subjected to cyclic lateral loading. Part I: slender wall test program" *Structural Systems Research Project Report SSRP- 2018/05*, UC San Diego. The dissertation author was the primary author on this report.

Chapter 3 contains material submitted for publication in the following journal paper: Faraone, G., Hutchinson, T. C., Piccinin, R., and Silva, J. (2021). "Seismic Performance of Varying Aspect Ratio Full-Scale Concrete Walls," ACI Structural Journal (under review). The dissertation author was

the primary author on this paper. Chapter 3 also contains material published in the following report: Faraone, G. and Hutchinson, T. C., 2021, "Behavior of post-installed anchors in reinforced concrete shear walls subjected to cyclic lateral loading. Part II: squat walls test program," *Structural Systems Research Project Report SSRP- 2021/01*, UC San Diego. The dissertation author was the primary author on this report.

Chapter 4 in part contains material published in the following journal paper: Faraone, G., Hutchinson, T. C., Piccinin, R., and Silva, J., 2019, "Performance of Post-Installed Anchors in a Progressively Damaged Concrete Shear Wall," *ACI Structural Journal*. V. 116, No. 6, pp. 293-306. In part contains material submitted for publication in the following journal paper: Faraone, G., Hutchinson, T. C., Piccinin, R., and Silva, J. (2021). "Anchor Performance in Cyclically Loaded Shear Walls," ACI Structural Journal (under review). The dissertation author was the primary author on these papers.

Chapter 5 contains material published in the following conference papers: Faraone, G., Moschetti L., and Hutchinson T. C., 2018, "Numerical Prediction of the In-Plane Cyclic Behavior of Reinforced Concrete Shear Walls," Proceedings of the 11th National Conference on Earthquake Engineering, Los Angeles, CA and Faraone, G., and Hutchinson T. C., 2018, "Numerical Prediction of the Behavior of Reinforced Concrete Shear Walls under In-Plane Cyclic Loading, with Particular Focus on Assessing Local Cracking Response," Proceedings of the 2018 ASCE Structures Congress, Fort Worth, Texas. In addition, Chapter 5, in part is currently being prepared for submission for publication of the material: Faraone, G., Hutchinson, T. C., Piccinin, R., and Silva, J., "Numerical Prediction of the Response of Full-Scale Laterally Loaded Concrete Shear Walls." The dissertation author was the primary investigator and author of this material.

Chapter 6, in part is currently being prepared for submission for publication of the material: Faraone, G., Hutchinson, T. C., Piccinin, R., and Silva, J., "Evolution of Simulated Seismic Damage in Concrete Shear Walls of Varying Aspect Ratios." The dissertation author was the primary investigator and author of this material.

VITA

EDUCATION

2012	B. S. in Civil Engineering *cum laude*, University of Bologna, Italy
2015	M. S. in Structural Engineering *cum laude*, University of Bologna, Italy
2021	Ph. D. in Structural Engineering, University of California San Diego

LICENSES AND CERTIFICATIONS

2015	Italian Professional Engineering License, University of Bologna, Italy

TEACHING AND ADVISING EXPERIENCE

2018-2021	Teaching Assistant, University of California San Diego
2020	Graduate Student Teaching Associate for SE - Solid Mechanics - University of California San Diego

SCHOLARSHIPS AND AWARDS

2015-2016	Structural Engineering Department Fellowship
2017-2020	Hilti Fellowship

PUBLICATIONS

Peer-reviewed journal articles

Wang, X., Faraone, G., Hutchinson, T. C., Piccinin R., Silva F. J., and Kuester, F., (In Review) "Laser-based Damage Assessment Methodology of Reinforced Concrete Shear Walls with Post-installed Anchors", *Engineering Structures Elsevier*.

Faraone, G., Hutchinson, T. C., Piccinin R., and Silva F. J., (In Review) "Seismic Performance of Varying Aspect Ratio Full-Scale Concrete Walls", *ACI Structural Journal*.

Faraone, G., Hutchinson, T. C., Piccinin R., and Silva F. J., (In Review) "Anchor Performance in Cyclically Loaded Shear Walls", *ACI Structural Journal*.

Faraone, G., Hutchinson, T.C., Piccinin, R., and Silva, J., 2019, "Discussion 116-S55 of *Size Effect of Squat Shear Walls Extrapolated by Microplane Model M7. Paper by M. Rasoolinejad and Z. P. Bažant* from the May 2019 ACI Structural Journal", *ACI Structural Journal*. V. 117, No. 2, pp. 304-307

Faraone, G., Hutchinson, T. C., Piccinin, R., and Silva, J., 2019, "Cyclic Lateral Load Response of a Full-Scale Flexure Dominated Shear Wall", *ACI Structural Journal*. V. 116, No. 6, pp. 281-292. DOI:10.14359/51718068

Faraone, G., Hutchinson, T. C., Piccinin, R., and Silva, J., 2019, "Performance of Post-Installed Anchors in a Progressively Damaged Concrete Shear Wall," *ACI Structural Journal*. V. 116, No. 6, pp. 293-306. DOI:10.14359/51718069

Refereed conference papers

Faraone, G., Hutchinson, T. C., Piccinin, R., and Silva, J., 2020, "Damage Patterns in Squat and Flexural RC Shear Walls," Proceedings of the 2020 ASCE Structures Congress, St. Louis, Missouri

Faraone, G., Hutchinson, T. C., Piccinin, R., and Silva, J., 2019, "Back-Estimated Ductility and Response Modification Coefficient (*R* factor) for Concrete Shear Walls", Proceedings of the 5th Workshop on The New Boundaries of Structural Concrete, ACI Italian Chapter, Milan, Italy

Faraone, G., Moschetti L., and Hutchinson T. C., 2018, "Numerical Prediction of the In-Plane Cyclic Behavior of Reinforced Concrete Shear Walls," Proceedings of the 11th National Conference on Earthquake Engineering, Los Angeles, CA

Faraone, G., and Hutchinson T. C., 2018, "Numerical Prediction of the Behavior of Reinforced Concrete Shear Walls under In-Plane Cyclic Loading, with Particular Focus on Assessing Local Cracking Response," Proceedings of the 2018 ASCE Structures Congress, Fort Worth, Texas

ABSTRACT OF THE DISSERTATION

Behavior of post-installed anchors in reinforced concrete shear walls of different aspect ratios subjected to simulated seismic loads

by

Gloria Faraone

Doctor of Philosophy in Structural Engineering

University of California San Diego, 2021

Professor Tara C. Hutchinson, Chair

Reinforced concrete shear walls are commonly used to provide lateral strength and stiffness to concrete buildings in seismic regions. Typically installed in the wall face, mechanical anchors are responsible for connecting various nonstructural systems to the main structure. During an earthquake, anchors in reinforced concrete structural elements need to retain their strength and stiffness, despite the inevitable presence of cracks and damage in the concrete, developed as a consequence of the lateral cyclic loading. Anticipating damage to the concrete, which will naturally influence anchor response, current guidelines to qualify anchors for seismic applications require adequate performance in cracked concrete to assure minimal anchor load loss. However, these guidelines are based on anchor performance in pure flexural cracks, as this is the typical damage condition occurring in reinforced concrete frame elements,

which has been studied for decades. The response of anchors to a mix of flexure and shear cracks, i.e., the complex situation realized in shear-flexure structural components such as shear walls, however, has largely not been studied.

To address the paucity of data regarding anchor behavior in cracked concrete, the behavior of anchors installed horizontally in three full-scale reinforced concrete shear walls with different aspect ratios (wall height/length) is studied in this dissertation. Notably, two types of post-installed anchors were investigated in these tests, namely: i) expansion anchors and ii) bonded anchors. One slender and two identical low-aspect ratio walls were designed according to current U.S. design codes. Simulated seismic loading was imposed at the top of the wall using an equivalent cyclic displacement history, while uniform compression was applied on the slender and one of the two identical low-aspect ratio shear walls. One of the low aspect ratio walls was tested without axial compression to investigate its effect on the anchor response. Anchors were continuously loaded to their design tension while the walls were cycled. The slender full-scale wall failed in a predominantly flexural mode, precipitated by buckling and fracture of the boundary reinforcement. The two identical full-scale low-aspect ratio walls failed in a mixed flexure-shear response, with severe web concrete crushing and buckling and rupture of the boundary reinforcement. Anchor axial load and displacement data, continually measured during the wall cyclic tests, confirmed the sensitivity of the performance of anchors amidst the presence of a variety of cracked concrete conditions, especially in walls prone to develop large shear stress and shear induced damage when subjected to lateral cyclic loads. Following the wall cyclic tests, tension failure tests performed on the anchors indicated that their residual tension load capacity was significantly compromised by concrete damage. Such damage was concentrated in specific wall regions, such as the boundary elements and the plastic hinge region in slender walls, or along the diagonal struts, the boundary elements and near the base of low-aspect ratio walls. Of the two types of anchors tested, expansion anchors observed the most significant load loss (and consequentially axial displacement) in the presence of both the wall cyclic loading and the residual tests on the anchors themselves.

Following the experimental program, a multiple vertical line finite element model was used to predict the response of each of the tested full-scale shear walls. Numerical analyses cross-comparison with test results demonstrated a high level of accuracy of the selected modeling approach. As such, an expanded parametric study was conducted to understand the extent of severe concrete strains on the crack

distribution and width, using a smeared crack approach. Wall models designed for the parametric study were intended to explore different geometry, reinforcement and axial compression to study the damage distribution within the wall elevation. Crack pattern distribution plots developed using the parametric study results were used to identify regions where anchors would be vulnerable to load loss upon achievement of service, design and severe seismic damage. Ultimately, the findings from this dissertation shed light on the vulnerability of anchors placed in reinforced concrete shear walls, where damage in the form of mixed mode cracking and spalling can be expected. Future design guidelines would benefit from precluding crack sensitive anchors in the most highly damaged regions of these essential lateral force resisting components of the structural system.

Chapter 1

Introduction

1.1 Motivation

Reinforced concrete (RC) shear walls are commonly used in concrete buildings to provide lateral strength and stiffness to carry lateral loads imposed by, e.g., wind or earthquake scenarios. Additionally, structural walls are often the main anchorage material for nonstructural components and systems, such as electrical, mechanical, plumbing or contents, connected via mechanical concrete anchors. The integrity of the concrete is essential to provide a secure bond between anchorage and concrete within the structural element. However, during an earthquake, RC shear walls may develop shear and flexural cracks, thus the anchors will need to continue to serve their function despite the presence of those evolving cracks. Several studies demonstrate the vulnerability of anchorage to cyclic opening and closing of cracks in the event of a seismic action. However, cracks and anchor interaction were previously investigated in reinforced concrete frame elements only and no experimental evidence on the behavior of anchors in planar reinforced concrete structural elements exists so far. Post-installed anchors are widely used in seismic applications, and they are often installed in reinforced concrete members, which exhibit coupled shear and flexure responses, but their response to shear and x-type (crossing) cracks, i.e., the more complex situation realized in shear-flexure structural components, has largely been neglected.

1.2 Scope

To investigate the behavior of anchors in evolving shear and tension cracks, one slender and two squat, full-scale concrete shear walls, typical of a two-story and one-story office building, respectively, were designed according to present U.S. design codes. Post-installed mechanical anchors were installed in one face of each full-scale wall, and constantly loaded to their seismic design tension load through a special load assembly. The effects of a seismic event on the walls and consequently on the anchors were simulated through the application of an equivalent cyclic displacement history at the top of the walls. Anchor load and displacement data, monitored during the wall cyclic tests, reflected the instants of crack opening nearby the anchors, and showed a weakened anchor performance in damaged concrete. All three shear walls showed significant ductility capacity, failing in pure flexure or mixed shear-flexure modes anticipated by buckling and fracture of the reinforcing bars in the boundary elements. Complementary numerical modeling of the test walls is conducted in an effort to define best practices to facilitate robust prediction of shear wall cyclic response. Finally, the numerical model is extended to a parametric study involving a wide range of detailed and aspect ratio walls.

This work focuses on enriching the literature of reinforced concrete shear wall experimental data by documenting the local and global response of these unique full-scale walls. Since they served primarily as a vehicle to provide representative boundary conditions to post-installed anchors during simulated seismic loads, particular focus is given to documenting the evolving crack pattern. In addition, central to this work is the behavior of post-installed anchors in progressively damaged concrete. All prior experimental studies on anchor seismic performance have thus far been conducted with anchors placed vertically. The behavior of post-installed anchors, installed horizontally in commonly utilized reinforced concrete shear walls is investigated for the first time in this unique research project. Two types of post-installed anchors were considered, namely: torque-controlled expansion and bonded anchors, for their different bonding mechanism. The measured axial load and displacement of the anchors during the simulated wall cyclic damage evolution confirm the sensitivity of the performance of mechanically expanded anchors amidst the presence of a variety of cracked concrete conditions. Failure tests conducted following the wall lateral cyclic history demonstrate that severe concrete damage significantly reduced residual anchor load capacity. Finally, the numerical study highlighted those regions where significant

concrete damage and large crack widths in reinforced concrete shear walls are expected to impact anchor response.

1.3 Post-Installed Anchors for Seismic Applications

Anchors are commonly used to fix nonstructural components and structural systems to concrete elements. In this regard, post-installed anchors are appealing as they can be installed anytime after concrete curing by drilling the proper installation hole in the concrete component. Due to their ease of installation, flexibility, and wide applicability, post-installed anchors are often used by designers and contractors. Anchors applications may be multiple within a building, as anchors often support heating, ventilating, or air conditioning components, mechanical-electrical-plumbing, fire suppression system piping or architectural components as façades, partition walls and ceilings. As an example, Figs. 1.1 and 1.2 show a schematic representation of anchors in a concrete building and photographs of typical applications, respectively. Particularly, Fig. 1.2 shows examples of horizontal anchor installations. To this regard, an informal survey performed to define the scope of this dissertation indicated that more than half of the global applications of anchors involves the connection of nonstructural components to concrete elements and that about 57% of these applications require horizontal anchor installation.

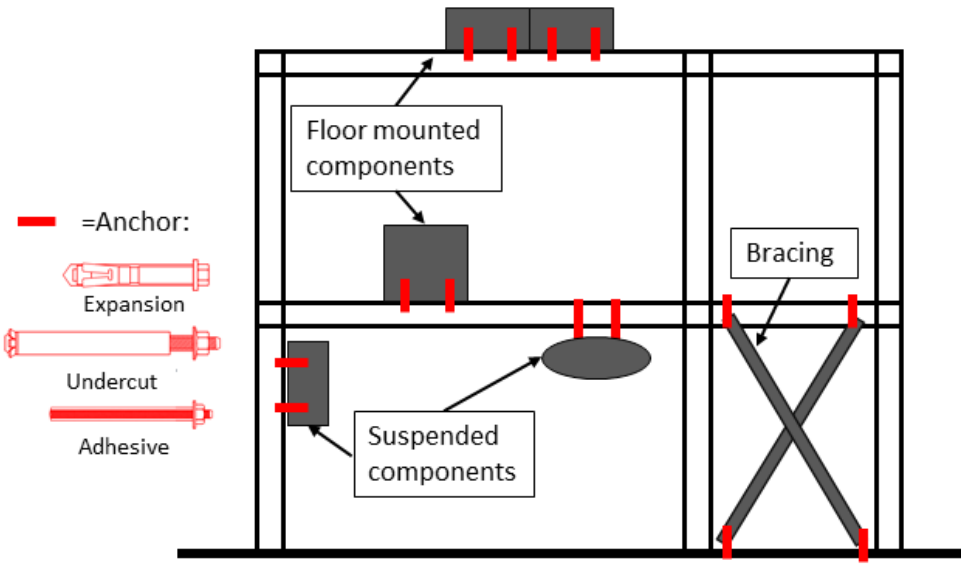


Figure 1.1: Schematic of typical structural and nonstructural anchor applications. Reproduced after Mahrenholtz (2012)

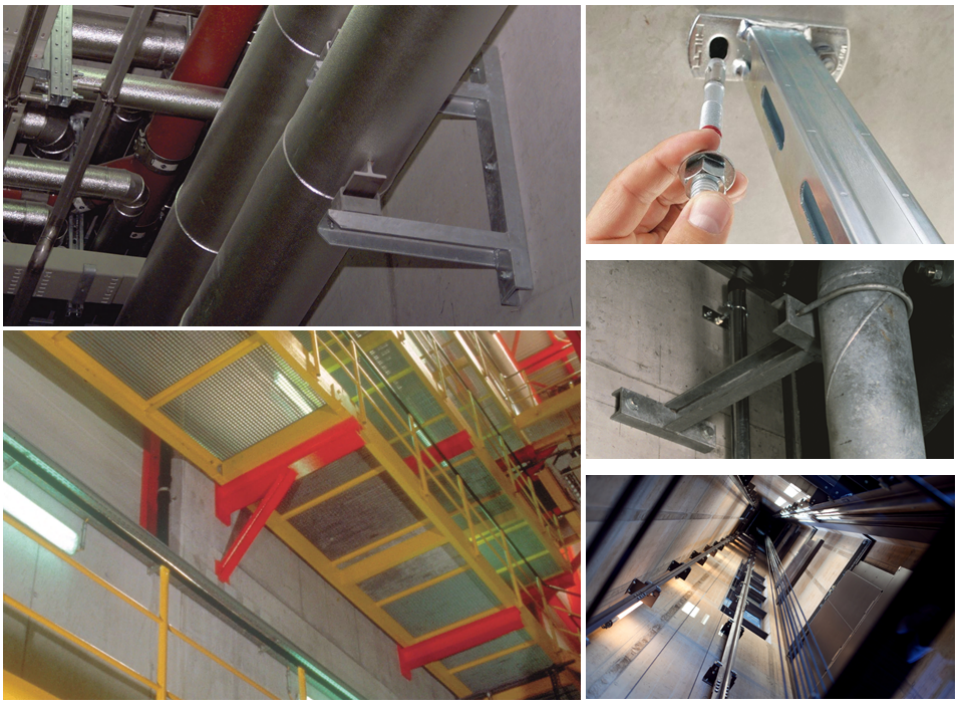


Figure 1.2: Photographs of typical structural and nonstructural anchor applications. Source: *https://www.hilti.com/*

During a seismic event, concrete structures respond to the ground motion through deformations, which result in concrete degradation and cracking in the structural elements where anchors are often installed. Notably, since cracks will reasonably intersect anchor location (see e.g., Lotze 1987) affecting anchor performance, it is conservative to assume that anchors are always located in a crack. In addition, these cracks may open and close cyclically as the concrete structure responds to the ground motion, adding cyclic crack width history conditions to the cyclic anchor load demand. To avoid the failure of the connection, it is necessary that anchors maintain a safe load transfer between the cracked concrete structure and the connected component. Hence, anchor performance needs to be regulated to address the safety of anchors in seismic conditions. In recognition of this, several researchers in the past decade contributed to the development of current performance qualification guidelines, such as the ETAG 001 (EOTA 2013c) in Europe and the ACI 355.2 (ACI 355 2019) in the U.S. (see, e.g., Wood et al. 2010, Mahrenholtz 2012, Mahrenholtz et al. 2016, Mahrenholtz et al. 2017). These qualification guidelines specify the required test setup to verify anchor performance and evaluate test results. Anchors are qualified to be used in seismic applications if they pass prescribed simulated seismic tests in tension and shear

load in both cracked and uncracked concrete.

Current European Anchor Qualification Procedures (EOTA TR 045 2013) classify anchors in three Performance Categories (PCs) on the basis of their performance, as it is reported in Fig. 1.3. The underlying assumption in this table is that concrete damage and large crack widths are expected in buildings located in seismic regions where design ground accelerations are larger than in regions of low seismicity. The ground acceleration of the building site and the importance class of the building are used to identify two anchor seismic performance categories with different acceptable probability of failure in cracked concrete. Central to these categories is the determination of the maximum expected crack width, distribution, and type of cracks surrounding the anchors. In particular, the definition of class C2 in Fig. 1.3 is essentially centered around crack widths which are assumed to occur in flexure dominated elements at inelastic response levels (Hoehler 2006).

Seismicity		***Importance Class acc. to EN 1998-1:2004, 4.2.5***			
	$a_g \cdot S$ [2)]	***I***	***II***	***III***	***IV***
Very low[1)]	$a_g \cdot S \leq 0{,}05$ g	*ETAG 001 Part 1 to Part 5*			
Low[1)]	$0{,}05\ g < a_g \cdot S \leq 0{,}1\ g$	*C1*	*C1* [3)] *or C2* [4)]		*C2*
	$a_g \cdot S > 0{,}1$ g	*C1*	*C2*		

[1)] *Definition according to EN 1998-1:2004, 3.2.1.*

[2)] $a_g = \gamma_1 \cdot a_{gR}$ *Design ground acceleration on type A ground (Ground types as defined in EN 1998-1:2004, Table 3.1);*

γ_1 *= importance factor (see EN 1998-1:2004, 4.2.5);*

a_{gR} *= reference peak ground acceleration on type A ground (see EN 1998-1:2004, 3.2.1);*

S = *Soil factor (see e.g. EN 1998-1:2004, 3.2.2).*

[3)] *C1 for fixing non-structural elements to structures*

[4)] *C2 for fixing structural elements to structures*

Figure 1.3: Minimum recommended performance categories for anchors under seismic actions, from EOTA (2013b)

Similar to EOTA TR 045 (2013), ACI 355 (2019) prescribes testing and evaluation requirements for post-installed mechanical anchors intended for use in concrete design under the provisions of ACI 318 (2019). Evaluation tests and selected criteria are defined to determine whether anchors are acceptable for use in uncracked concrete only, or in cracked concrete as well ACI 355 (2019). Three anchor categories are defined on the basis of the anchor capacity as determined from the prescribed tests. These anchor performance categories are then used by ACI 318 (2019) to assign capacity reduction factors

and other design parameters. However, unlike EOTA TR 045 (2013), ACI 318 (2019) does not address the probability of seismic damage and cracks expected in the main concrete element, where anchors are installed.

With the objective of mapping the recommended European performance categories to U.S. guidelines, the link between the CEN (2004) and ASCE/SEI 7-16 (2016) design codes is here discussed and a new anchor qualification table has been proposed. In the European Design Codes CEN (2004), the importance class of the building accounts for the degree of risk to human life, health and welfare associated with the seismic damage. Buildings are classified as low risk structures if they are of minor importance for public safety, as opposed to the essential facilities, which could pose substantial hazard to the community in the eventuality of failure. In the U.S. Design Code ASCE/SEI 7-16 (2016) the same concept is expressed in nearly identical terms with the Risk Category of the building, which defines different Seismic Design Categories (SDCs) to different levels of seismicity of the site. In both codes, this classification leads to particular design procedures based on the development of ductility, i.e., the capacity of the structure to undergo plastic deformations, required to ensure sufficient seismic resistance. In the Eurocode 8, three classes of ductility are defined on the basis of the seismicity of the site and on the importance of the building (CEN 2004). A behavior factor q is then defined for each type of structure and level of ductility to reduce the elastic spectrum used in linear analysis to calculate design forces. In other terms, through the q factor the design forces are reduced to account for plastic deformation and energy absorption within the structure, namely: 1) DCL (Ductility Class Low), which does not require capacity design of the structure (q = 1.5), 2) DCM (Medium), which allows high levels of ductility ($1.5 < q < 4$), and 3) DCH (Ductility Class High), which requires the capacity design criteria and local ductility to be met ($q > 4$). Table 1.1 summarizes the classification of structures according to their ductility, according to both the European and the U.S. codes. In the U.S. code ASCE/SEI 7-16 (2016), seismic design must be observed for SDCs C to F only, and the associated level of ductility is expressed by the Response Modification Coefficient, commonly indicated as R factor. This factor is used in the lateral force seismic design procedure to reduce the design forces accordingly to the expected level of ductility (see Fig. 1.4). It is noted that the R factor is considered the direct relative of the q factor, as similar values can be found for each structural components, see e.g., Table 1.2 for concrete shear walls.

In general, ductile structures, which are able to undergo large deformations and dissipate energy

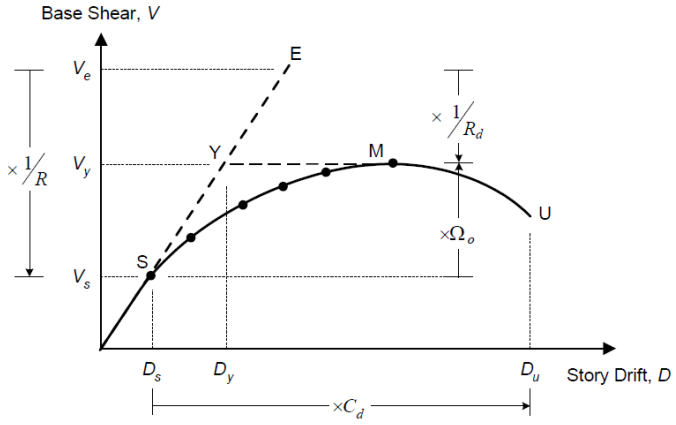


Figure 1.4: Inelastic force-deformation curve showing the use of the R factor in seismic design. Figure from SEAOC Seismology Committee (2008)

Table 1.1: Classification of structures according to ductility

Category	**Eurocode 8 (2004)**	**ASCE 7-16 (2016)**
High dissipative structures	High ductility	Special
Medium dissipative structures	Medium ductility	Intermediate
Low dissipative structures	Low ductility	Ordinary

beyond the elastic limit, are associated with a large R factor. Thus, seismic design forces can be noticeably reduced since a large amount of the incoming energy will be dissipated by the structure itself. On the opposite side, brittle and fragile structures have a smaller R factor, as they are not able to develop a flexural mechanism to dissipate energy and they may fail with little or no notice. Reinforced concrete shear walls, for example, are associated with low R factors due to their high stiffness, and their failure modes include both shear and flexural cracking in a different extent. Table 1.2 reports the reduction coefficients associated to concrete shear walls from both the ASCE/SEI 7-16 (2016) and CEN (2004) codes for low and high ductility classes, denoted by "ordinary" and "special", respectively in ASCE/SEI 7-16 (2016) and by DCM and DCH, respectively, in CEN (2004) (see Table 1.1). It is also noted that lower ductility is expected for shear wall systems carrying a major portion of the gravity loads ("bearing wall systems") than for building wall systems, designed to carry only lateral loads, and a similar reduction is expressed in CEN (2004) as well.

The analysis of the two design codes presented so far demonstrates a strong link between CEN

Table 1.2: Structural ductility factors, from ASCE/SEI 7-16 (2016) and CEN (2004)

ASCE 7-16 (2016)		**Eurocode 8 (2004)**	
Type of Component	**R**	**Type of Component**	q
Bearing Wall Systems		**Wall Systems**	
Ordinary RC Shear Wall	**4**	DCM	**3**
Special RC Shear Wall	**5**	DCH	$\mathbf{4 \leq q \leq 4.8}$
Building Wall Systems		**Coupled Wall Systems / Dual Systems**	
Ordinary RC Shear Wall	**5**	DCM	$\mathbf{3 \leq q \leq 3.6}$
Special RC Shear Wall	**6**	DCH	$\mathbf{4.5 \leq q \leq 5.4}$

(2004) and ASCE/SEI 7-16 (2016), and a new anchor qualification table developed on Fig. 1.3 can be introduced in terms of the U.S. design parameters. The new anchor classification should consider the potential amount of the structure's inelastic behavior, which is related to the R factor or Behavior Coefficient q, considering that in reinforced concrete members ductility, i.e., plastic displacement and deformation, predictably comes with cracking. However, the performance of the anchors is inevitably affected by the occurring of cracks in the event of an earthquake, when the reinforced concrete member is stressed beyond the elastic limit. Research has shown that both axial stiffness and strength of anchors located in flexural cracks are reduced (Eligehausen et al. 2006). Therefore, the new anchor classification proposed by Silva (2016) in Table 1.3 uses the three U.S. design parameters described earlier to define the Anchor Seismic Performance Category (ASPC), namely: 1) the Risk Category, 2) the Seismic Design Category (SDC) and 3) the Response Modification Coefficient R. Similar to the classification in Fig. 1.3, these proposed ASPCs are indirectly related to the seismic demand on the building through the SDC and the R factor of the structural element provides an estimate of the cracking conditions. In addition, the risk category of the building provides information on the probability of failure of each anchor performance category. This proposed classification accounts for the structure ductility, as opposed to EOTA (2013b), which only implicitly considers the expected ductility of reinforced concrete frame-type structures in the definition of class C2. It is also noted that the ductility of frame structures is relatively high with respect to reinforced concrete shear walls, as discussed earlier. Hence, Table 1.3 includes information regarding the R factor of the building. However, the expected crack width is currently weakly related to the type of structure and level of inelastic behavior, expressed by the R factor, and experiments should be performed to define this link. The crack width values currently adopted in the qualification guidelines as

representative of the serviceability and suitability levels, 0.5 mm and 0.8 mm, were largely derived from studies of frame-braced systems, i.e., with an assumed R=8. Thus, they may not adequately capture the expected design earthquake demands at the anchorage locations in mixed shear-flexural members. No data exists regarding anchor performance in mixed cracking mode components. Therefore, this study addresses the performance of anchors in reinforced concrete shear walls, with an assumed R=5. The full-scale wall experiments and the numerical analyses presented in this dissertation are intended to characterize wall damage and anchor response.

Table 1.3: Revised mapping table by J. F. Silva (2016)

Anchor Seismic Performance Category (ASPC)			
Seismic Design Category	**Risk Category**	**Response Modification Coefficient**	
		R ≤ 5	**R** > 5
A	I, II, III, IV	ASPC 1	ASPC 1
B	I	ASPC 1	ASPC 1
	II,III	ASPC 1	ASPC 2
	IV	ASPC 2	ASPC 2
C, D	I	ASPC 2	ASPC 2
	II,III	ASPC 2	ASPC 3
	IV	ASPC 3	ASPC 3
E	I	ASPC 2	ASPC 2
	II,III	ASPC 2	ASPC 3
F	IV	ASPC 3	ASPC 3

1.4 Scope of Dissertation

The work described in this dissertation consists of shear walls and anchors tests conducted in the Powell Structural Laboratories at the University of California San Diego (UCSD). In addition, complementary numerical modeling of the tests specimens is conducted to define best practices when predicting shear wall cyclic response. The numerical model is then extended to an extensive parametric study involving a wide range of detailed and aspect ratio walls to identify regions of severe damage.

The experimental part of this work includes testing of three reinforced concrete shear walls with post-installed anchors. Since the anchors cannot be scaled, full-scale walls were designed and tested. The thickness of the walls was chosen in such a way to 1) avoid buckling, 2) accommodate anchor embedment depth without splitting/blow through, 3) generate a damage/crack pattern various enough to have several

tension, shear and X cracks distributed all over the walls. One flexural wall specimen investigated the behavior of anchors installed in R=5 reinforced concrete walls, cyclically loaded laterally at pseudo-static rate. The developed crack pattern intersected the anchors installed in one face of the slender wall, and added uncontrolled opening and closing crack width histories to the nominally constant tension load imposed on each anchor, as to reproduce real field conditions in the event of seismic actions. Additional insight regarding anchor response in varying types of intersecting cracks, especially with a predominant shear character was obtained with two squat wall specimen tests. In these tests, post-installed anchors were installed in two identical full-scale squat walls, which were subjected to lateral cyclic load and to different levels of constant axial load. Similar to the flexural wall specimen, the anchors were installed on one side of each squat wall at the beginning of the test, before applying any load to the walls. In all three tests the anchors were loaded in tension by means of a self-reacting loading assembly, which induced only minimal out of plane tension load and moment on the wall. Anchor pullout to failure tests were performed at the end of the application of the displacement history on the walls, to determine the residual strength of the anchors. This work was supported by anchor reference tests, which served to characterize the mechanical behavior of the anchors in uncracked and unconfined conditions.

This test program was accompanied by numerical modeling of the walls response. A finite element model able to capture the coupled shear-flexure response typical of shear walls was validated against experimental data. This validation study proved the model to be sufficiently robust and to predict the global wall response and crack evolution with reasonable accuracy. An extensive parametric study was then performed considering a wide range of walls to predict the regions where damage concentrates in shear walls with varied geometry and detailing design, and where anchor installation is not recommended.

1.5 Background

This section intends to frame the new contributions of the research presented in this dissertation, by introducing key concepts and summarizing previous experimental research regarding the performance of anchors in cracked concrete and of reinforced concrete structural walls subjected to simulated seismic loading, with a focus on the crack response.

1.5.1 Anchorage Types and Failure Mechanisms

Mechanical anchors connect nonstructural components and systems to concrete elements. Mechanical anchors, usually made of carbon steel, stainless steel or malleable cast iron, can be placed in the structural elements before the concrete is poured (cast-in anchors) or they can be placed into drilled holes in concrete after concrete curing (post-installed anchors). In this research post-installed mechanical anchors are considered due to their flexibility with regard to placement. Typically, post-installed anchors develop anchoring stresses according to three main types of mechanism, as reported in EOTA (2013c) and represented in Fig.1.7, namely:

- **Expansion**: when a tensile force applied to the anchor is transferred to the concrete by friction and some keying between an expanded sleeve and the concrete. The expansion can be achieved by means of a torque acting on the screw or bolt, or by means of deformation, through impacts acting on the sleeve or cone.

- **Undercut**: when the anchor sleeve is hammered or rotated into a drilled undercut hole, which provides mechanical interlock.

- **Bonded**: when mortar bonds the threaded rods or other types of anchor elements to the sides of the drilled hole. Tensile loads are transmitted to the concrete via bond stresses between the anchor and the mortar and the mortar and the concrete face of the drilled hole. The embedded metal parts may be either of carbon steel or stainless steel and the mortar may be made primarily of resin, cement or a combination of both as a binding material.

Anchors can be loaded in shear, when the axis of action of the force is transverse to the anchor's axis, in tension, when the axis of action of the force is parallel to the anchor's axis, or in a combination of shear and tension. In the presence of these forces, the cyclic opening of cracks in the anchor location diminishes the potential for load transfer of the anchor. To address this realistic scenario, experiments on anchors should not only subject them to constant forces, but also consider replicating this boundary conditions. Fig. 1.6 schematically shows the actions acting on an anchor during a seismic event (Hoehler 2006). In this schematic, anchors connect a secondary structure, such as a suspended nonstructural component, to the primary structure, i.e., a beam of the concrete moment frame structure. The displacement of

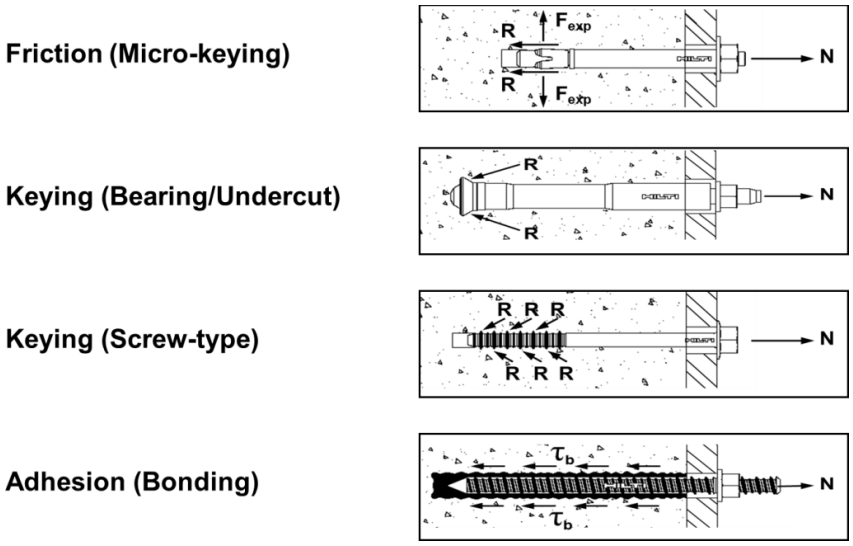


Figure 1.5: Common post-installed anchor types and load transfer mechanisms. Source: *https://www.hilti.com/*

the concrete frame generates tension and shear forces on the anchors, and cyclic crack opening modify anchor boundary conditions.

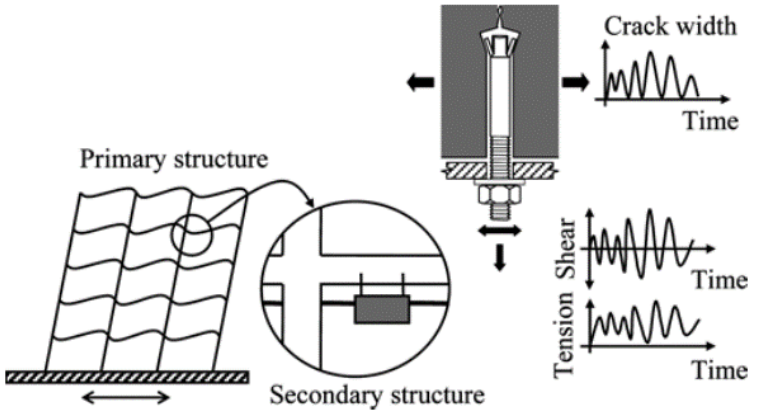


Figure 1.6: Actions acting on an anchor during seismic loading. Figure from Hoehler (2006)

Basic anchor design approach follows ACI 318 (2019), where additional requirements are specified for anchors in structures assigned to Seismic Design Categories C, D, E, or F. Since seismic design generally assumes yielding of the concrete structural elements, cracks cannot be neglected when determining anchor strength. In particular, ACI 318 (2019) reduces anchor nominal tensile strengths associated with concrete failure modes (determined as for ACI 355 2019) to account for increased cracking and spalling in the concrete resulting from seismic actions.

When the external load on the anchor exceeds the anchoring stresses developed within the embedded anchor part and the concrete, the anchor may fail, i.e., it may loose its anchoring force and be completely or partially ejected from the concrete hole in which it was installed. Various anchor failure modes can be observed, depending on the applied anchor load, on the type of anchoring mechanism and on the conditions of the surrounding concrete, see Cook (1993), Cook and Konz (2001), Cattaneo (2007) and ACI 318 (2019). When anchors are loaded in tension, five main failure modes may occur:

1. **Steel failure**, when the steel elements yield and fracture as the strength of the concrete is higher;

2. **Concrete cone failure**, when the concrete surrounding the anchor fails. The failure cone propagates from the head of the anchor to concrete surface in a radial circular cone at approximately 35 degrees (breakout cone). The failure is influenced by concrete strength, aggregates maximum size and type.

3. **Pull-out**, when the anchor pulls out of the drilled hole without a significant concrete breakout, as the anchor has lost frictional resistance or bearing strength;

4. **Pull-through**, when the anchor pulls through the expansion element (typically the sleeve).

5. **Splitting failure**, when splitting cracks open because the anchor expansion forces have exceed the tensile strength of the concrete.

1.5.2 Influence of Cracks on Anchor Behavior

During a seismic event, anchors are subjected to a combination of cyclic tension and shear forces and they may be located in cracks, which can open and close several times during the earthquake, while the structure in which they are located is deforming. The seismic behavior of anchors depends on the type of load transfer mechanisms, diameter or embedment of the anchor, and, remarkably, on the type of imposed action, such as direction of application, amplitude, rate and number of cycles. In addition, the state of the surrounding concrete (i.e., cracked, uncracked) and the crack behavior (i.e., number of cycles) severely compromise anchor seismic behavior and should be considered (Hoehler 2006). Anchor behavior in cracked concrete is significantly different from its behavior in uncracked concrete. The relation between anchors and cracks was studied by several researchers in the 1980s, with much work from

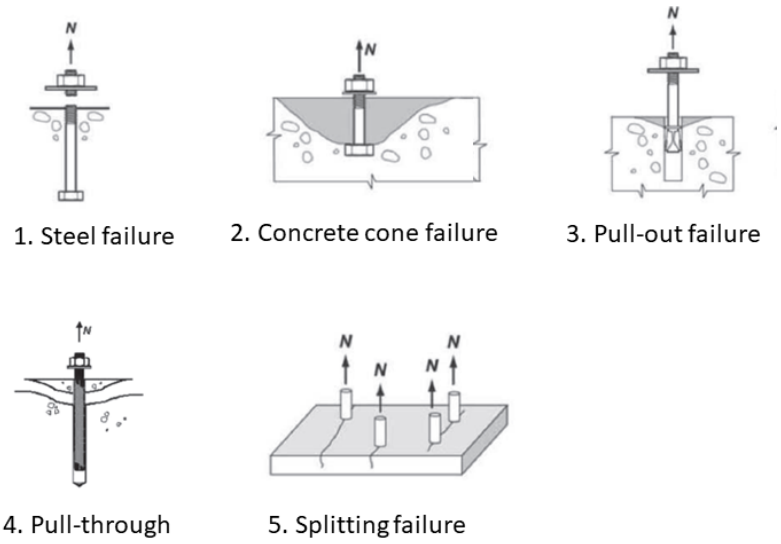


Figure 1.7: Failure modes associated with tension loading: 1. Steel failure 2. Concrete cone failure 3. Pull-out 4. Pull-through 5. Splitting failure. Figure from ACI 318 (2014)

the University of Stuttgart. Early research focused on anchor performance in static open cracks, and only recently the opening and closing of cracks with maximum 0.3 mm width were considered. It is noted that this crack width value is representative of anchor service conditions, i.e., when loads are determined without load factors, thus not representative of seismic conditions. The aforementioned research contributions conducted at the University of Stuttgart are reported in this section in chronological order, as discussed in Hoehler (2006).

Rehm and Lehmann (1982) demonstrate that anchor displacement increases as a result of crack opening and closing, in a different way for different anchor types and crack widths. Incipient failure of the anchors occurred when the displacement increased as a function of the number of crack cycles. Similarly, Cannon (1981) studied the performance of expansion anchors in cracked beams, concluding that the presence of flexural cracking at the anchor location determined the performance of anchors. In particular, the intersection of flexural cracks with loaded expansion anchors eliminated the installation preload and produced nonlinear anchor axial load-displacement response. Cannon (1981) concluded that the performance of anchors under cyclic loading depends on the magnitude of the applied load, the presence of intersecting cracks, and the rigidity or flexibility of the attachment. He also noted that the crack's trajectory coincided with anchor location at almost all times. Finally, Lotze (1993) applied a uniform moment to a RC beam with installed anchors to study the influence of the anchors on the

crack pattern development. He studied several stress discontinuities, including externally loaded anchors and drilled holes without anchors. In all cases, the discontinuity attracted the cracks, acting as a stress concentrator. Other experimental and theoretical research showed that anchors may even induce cracking (Hoehler 2006). Thus, in general, design of anchors should be based on the assumption that concrete is cracked.

Amongst the earliest contributions to understanding the impact of cycling cracking, the work of Seghezzi (1985) noted that residual crack width influenced the displacement behavior of axially loaded anchors. In particular, anchors in cracks, which were not completely closed, showed an increase in the displacement as a function of the number of crack cycles. In similar fashion, Furche (1994) tested several types of anchors subjected to applied constant axial tension in cracks cycling from 0.1 mm to 0.3 mm and concluded that the load required for crack closure depends on the splitting force generated by the anchors. Moreover, the anchors which did not fail during the crack cycling were tested to failure in a static 0.3 mm-wide crack and they showed a significant residual strength. Anchors not suitable for use in cracked concrete were characterized by large displacements. When the axial load was not sufficient to overcome the available bond resistance, the anchor remained bonded to one side of the crack interface.

In the same years, Eligehausen and Balogh (1995) discussed the behavior of different types of anchors in cracked reinforced concrete. During crack opening they note that significant changes in the load-displacement behavior of the anchor are observed. The variations depend on the anchoring mechanism of the type of anchor and affect the stiffness, ultimate load capacity and possibly the failure mode of the anchor. The load-bearing capacity could observe a 30% reduction and more in small static (non-cycled) crack widths. Similarly, Eligehausen and Hoehler (2003) performed a parametric study on reinforced concrete flexural members to determine the maximum crack width to test anchors. To develop fasteners qualification tests, indeed, crack widths have to be independent of a specific performance state or intensity of earthquake motion. To put a reliable boundary on the expected crack width for the purpose of testing of fastenings, the location of fasteners should be limited outside of the plastic hinge zones, where plastic deformation is expected to occur. In 2005, ACI 318 adopted the limitation on the placement of fasteners outside of plastic hinge zones, (a) to avoid the negative effect of a reduction in the embedment depth due to spalling of concrete and (b) because the large crack widths inside the plastic hinge length make fastening there impractical. Outside of the zone of plastic deformation, the maximum

crack opening width for fastenings is the one closest to the point where yielding occurs, and it is independent of the performance state. This is the maximum crack opening width for which anchors should be qualified. Eligehausen and Hoehler (2003) concluded that in flexural members the crack width at yielding varies between 0.3 mm and 0.9 mm, for both serviceability and suitability levels, as it is shown in Fig.1.8.

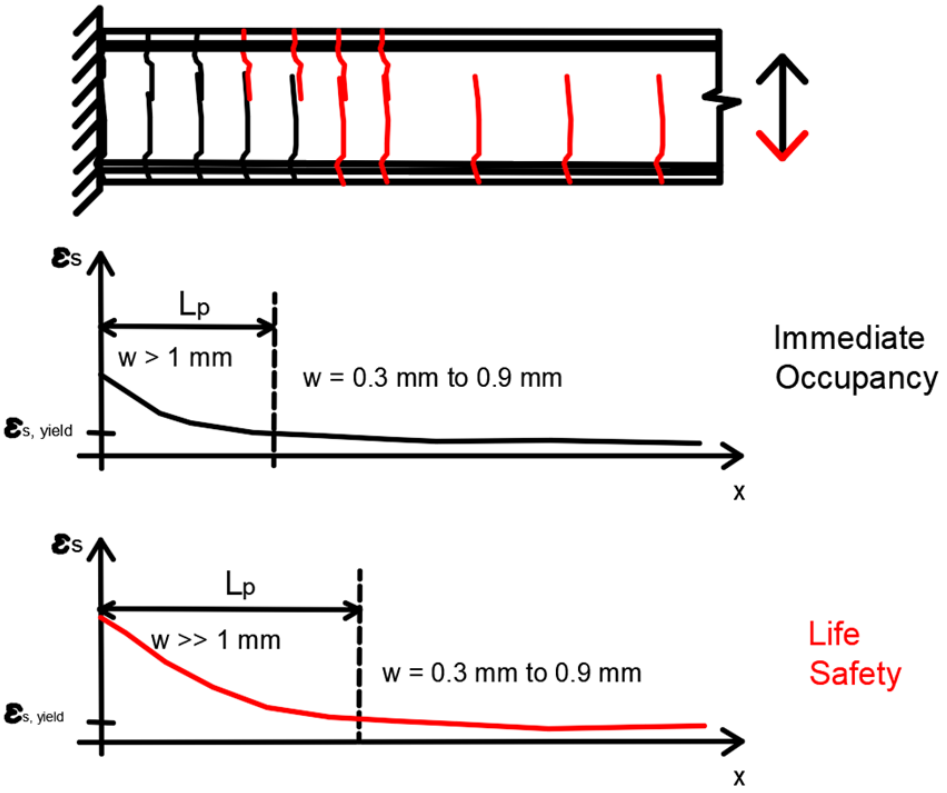


Figure 1.8: Results of crack width study by Eligehausen and Hoehler (2003) on flexural reinforced concrete members. Figure modified after Eligehausen and Hoehler (2003)

Debates on the maximum crack width to be considered were still ongoing when Hoehler (2006) investigated the maximum crack width that can occur outside of the plastic hinge zone in reinforced concrete beams and columns using several different analytical methods, when the reinforcement steel in the RC component reaches the tension yield strain. The maximum characteristic crack widths within the plastic hinge length ranged from 0.89 mm to 4.92 mm for the Immediate Occupancy (which corresponds to the serviceability level) and 1.88 mm to 11.84 mm at the Life Safety performance level (which can be compared to the suitability level). The maximum calculated crack widths near yield at the Immediate Occupancy (serviceability level) was 1.07 mm and 1.01 mm at the Life Safety (suitability level). These

cracks were not dependent on the performance state, since the reinforcement steel strain is near yield in both cases. However, Hoehler (2006) conducted tests opening the cracks by Δw= 0.8 mm. In addition, Hoehler (2006) developed several tests setup and procedures to investigate both cast-in and post-installed fastener behavior in wide cycled cracks, where full crack closure occurred. Since fasteners during an earthquake are subjected to both crack cycling and load cycling at dynamic rates, the primary objectives of the tests were (a) to compare the relative performance of different fastener types under representative seismic crack cycling conditions, (b) to investigate the influence of loading sequence and rate and shape of crack cycles, and (c) to establish a testing procedure for a seismic crack cycling test. Regarding the behavior of anchors in cracks, results on the tests performed with headed studs, expansion anchors, undercut anchors and screw anchors (sizes M10 to M20) showed that fasteners can resists repeated seismic crack cycles (with maximum crack width set to 0.8 mm) in many cases without significant reduction of the residual strength.

Watkins (2011) investigated the effect of seismic actions on the Nonstructural Components and Systems (NCSs) anchored via mechanical anchorage to concrete frame structures, with particular attention to the effect of dynamic cyclic cracking. Apart from the system identification tests, the experiments were focused on the relationship between amplitude of anchor loading and corresponding crack width. When the dynamic test was concluded, failure tests were performed on epoxy, torque controlled expansion, drop-in and undercut anchor types in cyclically cracked concrete. Results from the shake table tests showed that in some cases the maximum anchor load exceeded the uncracked capacity from monotonic reference tests. Watkins suggested that, besides natural variability, the increase in anchor strength was probably due to strain rate effects as well as compaction of the concrete around the anchor bearing surface. Moreover, the load-displacement relationship under dynamic inertial loading and crack cycling was generally bound by the monotonic reference test envelope for both load and displacement for all anchor types tested. Results from the failure tests showed that the anchor load at failure for tests conducted in cracked cyclic concrete was generally approximately equal to the mean ultimate axial load capacity obtained from monotonic reference tests in statically open cracks. The tests supported the code philosophy of using the reference anchor monotonic strength in cracked concrete with statically open cracks.

Mahrenholtz (2012) tested a variety of anchors of different types and manufacturers under conditions they were not qualified for, such as the maximum crack width of 0.8 mm, significantly larger

than 0.5 mm specified in effective guidelines (ETAG 001 of 2006 and ACI 355.2 of 2007). Mahrenholtz (2012) used the stepwise increasing test protocols proposed in Wood et al. (2010) to check their suitability for anchor qualifications. The research program was aimed to answer some of the open questions left by previous authors on the effect of high loading rate on anchor behavior, the definition of anchor ductility, and the calculation of a seismic group factor. In particular, Mahrenholtz (2012) addressed the issue related to the definition of crack widths applicable for seismic tests in the suitability and serviceability levels. A crack width of 0.8 mm was generally accepted as the maximum crack width which may occur before yielding of the reinforcement just outside the plastic hinge zone and it was assumed in this study to represent extreme conditions (suitability level), whereas 0.5 mm cracks were considered as moderate and therefore associated with the serviceability level. Mahrenholtz (2012) performed simultaneous load and crack cycling tests for the first time, according to a unified test protocol for both serviceability and suitability demand levels. Results showed that large accumulated axial anchor displacement during crack cycling tests were critical for the performance of anchors loaded in tension. Low fatigue cycles, instead, made shear load cycling tests critical for the seismic performance of anchors, which were not affected by the crack width. Together with the results of research conducted at the University of California San Diego (Eligehausen et al. 2010), Mahrenholtz (2012) results led to a proposal for the seismic amendment of the European anchor qualification guideline, which is included in the current version of ETAG 001-Annex E EOTA (2013b).

1.5.3 Brief History of Seismic Anchorage Qualification

A brief history of the evolution of anchor guidelines and some general remarks on the approach of anchor qualification is here summarized from Silva (2001). The focus is on the situation in the U.S. and Europe, for which the Anchor Qualification Guidelines evolved almost in parallel.

In the 1970s, the U.S. nuclear industry began encouraging ductile steel failure of anchorages for seismic applications. Anchors were regulated by separate sets of reports issued by three model code agencies in U.S., namely, the Building Officials and Code Administrators International Inc. (BOCA), the International Conference of Building Officials (ICBO) and Southern Building Code Congress International, Inc. (SBCCI), on the basis of the allowable stress design. The global factor of safety was set equal to 4 for inspected work and one-third increase for seismic applications was permitted.

In the 1980s, anchor bolt design provisions were included in the Code Requirements for Nuclear Safety Related Structures issue by the American Concrete Institute (ACI). Outside of the nuclear industry, the International Conference of Building Officials (ICBO) established guidelines for the evaluation of expansion anchors in the ICBO-ES-AC01. Seismic qualifications were included without special tests in recognition for "short term loads".

Awareness of the importance of anchorage behavior was elevated due to the many anchor failures occurring during the 1994 Northridge Earthquake. In particular, seismic qualification of post-installed anchors was called to question. As a result, the Concrete and Masonry Anchor Manufacturers Association (CAMA) was formed, and in 1995 the standard AC58 for adhesive anchors was issued (ICC 1995). It included seismic tests based loosely on Canadian Standard (CAN3-N287.2-M82 1991). Both AC01 and AC106 guidelines for expansion and screw anchors, respectively, were later modified to include seismic tests. It is notable, however, that in these standards, all tests were performed in uncracked concrete. In addition, mechanical post-installed anchors were not permitted for seismic applications.

In 1997, in Europe ETAG 001 (EOTA 2013c) was implemented as the first guideline for European Technical Approval of Metal Anchors for Use in Concrete. The EOTA guideline assessed anchors to be used in cracked and uncracked concrete, but it was limited to anchors subjected to static or quasi-static actions only. To this point, EOTA guidelines did not include seismic qualification tests. However, in 2001, in the U.S. the first ACI standard for mechanical anchor qualification, ACI 355.2 (2001), included seismic tests qualification requirements for testing in cracks and evaluation requirements for post-installed anchors. The guideline for the Qualification of Post-Installed Mechanical Anchors in Concrete was applicable to post-installed mechanical anchors intended for use in structural applications, as covered by the design guideline (ACI 318 2011). This guideline was based on strength design and the Concrete Capacity Design (CCD) method was applied to determine the concrete capacity, and most importantly, it included provisions for cracked concrete. ACI 318-02 introduced cast-in and mechanical anchor design provisions in Appendix D (ACI 318-02). In this code version, seismic design requirements now included requirement for anchors to be qualified for ACI 355.2 (ACI 355 2019).

In 2010, in the U.S., the first ACI standard for adhesive anchors, ACI 355.4 (ACI 355 2011), was developed concurrently with design provisions in ACI 318 (2011). Seismic qualifications were the same as those of ACI 355.2 (ACI 355 2019). In 2012, in Europe, ETAG 001 - Annex E EOTA (2013c)

was adopted. These improved seismic qualification procedures were largely based on Hilti-sponsored research at the University of California San Diego and at the University of Stuttgart (IWB). In this effort, anchors were categorized according to their performance into one non-seismic performance category and two seismic performance categories, C1 and C2, as a function of seismicity of the site and class of importance of the building (see Fig.1.3). Seismic performance category C1 is intended to apply to lower seismic demands and only for nonstructural applications. In this case, anchor capacity is defined in terms of strength and tests are conducted in 0.5 mm wide cracks. Seismic performance category C2 is more demanding, and it is required in buildings of higher importance class, since it adds a level of safety for applications in severe earthquake regions. It defines the capacity in terms of strength and deformation and requires tests to be conducted in 0.8 mm wide cracks. Tests for qualification of anchors under category C1 verify the functioning under pulsating tension load and under alternating shear load. Tests for qualification of anchors under category C2 include the reference tension tests and the reference shear tests both in low and high strength concrete. They also verify the functioning under pulsating tension load, under alternating shear load and the functioning with tension load under varying crack width, from 0.00 mm to 0.8 mm. These tests are the results of research efforts by Wood et al. (2010), Mahrenholtz (2012), Mahrenholtz et al. (2016), Mahrenholtz et al. (2017).

1.5.4 Implementation of Seismic Anchorage Qualification within Design Codes

General technical approvals regulate the application of the vast majority of all post-installed anchors in use. Independent laboratories perform the qualification tests required for a general technical approval, as indicated in the anchor qualification guidelines, such as ETAG 001 Annex A, EOTA (2013a) in Europe, or ACI 355.2 (ACI 355 2019), in U.S. These qualification guidelines prescribe how to perform qualification tests, with detailed specifications on the test setup, and how to evaluate test results. The responsible authority grants the technical approval (ETA - *European Technical Approval* in Europe or ESR - *Evaluation Service Report* in US), which specifies characteristic resistance and minimum anchor spacing, on the basis of the results of the qualification tests.

Anchor design is regulated by design codes, which establish the boundary conditions to be represented in qualification tests and they generally refer to anchor qualification guidelines as a prerequisite. In Europe, design of anchors is specified in Annex C of the ETAG 001, EOTA (2010) and in the U.S.

anchor design is regulated by ACI 318 (2019). Seismic anchorage qualifications are, hence, implemented in design codes. Noting that anchor design is related to the boundary conditions provided by the structural element to which is attached, it looks reasonable to link anchor performance to the building response, usually defined by the R factor. Since previous studies focused on the response of reinforced concrete frame elements, this dissertation will look at reinforced concrete shear walls. To frame this work, background on shear walls behavior is presented in the next sections.

1.5.5 Behavior of Slender Reinforced Concrete Shear Walls

Reinforced concrete (RC) structural walls resist lateral loads in RC buildings, by providing sufficient strength and stiffness against wind and/or earthquake loading. Wall response to lateral loads may vary accordingly to their geometry. The global behavior of RC shear walls is typically characterized by flexural and shear contributions, combined to a different extent, as it was observed in numerous experimental studies. Three main types of RC shear walls and correspondent typical response to lateral loading are identified on the basis of the aspect ratio (AR: H_w/L_w): 1) squat walls, 2) flexural walls and 3) intermediate walls, for which the typical behavior transitions between the extremes. If slender flexural walls are characterized as those with an AR $\geq$ 2.5, the AR limiting value for walls to be classified as squat is not clearly defined in literature. NEHRP provision (Moehle et al. 2011) states that "walls with very low aspect ratios ($H_w/L_w \leq 0.5$) tend to resist lateral forces through a diagonal strut mechanism in which concrete and distributed horizontal and vertical reinforcement resist shear". However, AR limiting values of 1.5 and 2 are also common in the literature: Massone et al. (2009), Tran (2012) and Kolozvari et al. (2014) defined shear dominated RC walls with AR $\leq$ 1.5, together with ACI 318 (2011). Instead Paulay et al. (1982), the Canadian concrete code CSA (2004) and CEN (2004) stated that walls with AR $<$ 2 are prone to show shear dominated behavior. The shear-flexure interaction is not only influenced by the geometry, but also by the detailing of the cross section, the material properties and the applied axial load on the wall, as previous experimental programs on RC shear wall show. The applied axial load is usually expressed in terms of axial load ratio, defined as the ratio between the applied axial load and the section capacity, which is calculated as $A_g f'_c$, with A_g = cross-sectional area of the wall and f'_c = specified concrete compressive strength. Some of the main contributions on the behavior of various RC shear walls are reported in the following sections.

Beyer et al. (2008)

Beyer et al. (2008) gathered data from quasi-static cyclic tests on 34 slender structural RC walls to examine the shear deformations in rectangular and non shear walls and to provide estimates of the expected shear deformations in walls controlled by flexure. This study was part of an experimental campaign to understand the behavior of U-shaped walls under simulated seismic loads.

The analysis of the experimental results showed that, after cracking of concrete and yielding of

longitudinal reinforcement, the shear strain is not evenly distributed over a wall height and section, even if the shear force in a cantilever wall subjected to a point force at the top is constant over the height. In addition, this study showed that the shear deformations can reach the 20% of the flexural deformations of cantilever walls in the inelastic range, and can be larger for shorter walls. Moreover, in walls forming a flexural hinge and a stable shear-transfer mechanism, the ratio of shear-to-flexural displacements remains approximately constant over the entire ductility range, once the walls have reached their nominal strength. As the opposite, if the shear transfer mechanism is significantly degrading, the shear-to-flexural displacement ratio tends to increase, as the shear deformations increase.

Dazio et al. (2009)

Dazio et al. (2009) conducted an experimental research program on the ductility level of vertical reinforcement on deformation response and failure mechanism of RC shear walls. Six half-scale models 5.9 inches thick, 78.7 inches long and 179.5 or 177.9 inches tall, with shear span ratios of 2.28 or 2.26 were tested under cyclic loading at the Swiss Federal Institute of Technology in Zurich. The applied axial load levels ranged from 0.051 to 0.128 $A_g f'_c$, where A_g is the cross-sectional area of the wall and f'_c is the specified concrete compressive strength, which ranged from approximately 5.5 to 6.7 ksi. The specimen walls were designed according to the European Code for regions of moderate seismicity in Central Europe (CEN 2004).

Results showed that the amount and the ductility properties of the vertical reinforcement affect the global ductility of the wall specimen. In particular, walls with low longitudinal reinforcement ratios had reduced flexure-shear cracking. Moreover, walls with greater moment strength due to axial load developed a less extended crack pattern in proximity of the yield strength. Fig. 1.9 shows the different crack patterns developed at the end of the test by each specimen. Focus on the shear contribution to the total displacement showed that shear deformations continue to occur after flexural yielding, keeping the shear to flexural displacement ratio almost constant between 5 to 15% throughout all the ductility history. Crack widths were measured at the end of the test in five different locations along the wall length within the plastic hinge length. Results for the ductile specimen showed maximum crack width of 3.5 mm.



Figure 1.9: Crack patterns at the end of the tests by Dazio et al. (2009)

Birely (2012)

Birely (2012) designed a four-specimen test matrix to investigate the effect of the splicing and layout of the longitudinal reinforcement and the impact of the lateral load distribution on the shear demand. The walls, 6 inches thick, 120 inches long and 144 inches tall, were designed to represent a modern planar wall according to the U.S. design codes (ACI 318 2011), all but one with spliced vertical reinforcement. A combination of axial load, moment and shear were applied at the top of the wall to simulate the demands resulting from the upper stories of the prototype structure.

Results showed that damage always initiated at the top of the splice, suggesting that splices impact wall's performance. Moreover, the lower the effective height was, the lower resulted the drift capacity, characterized by a sudden loss of strength.

Tran (2012)

Tran (2012) tested five cantilever walls, three with AR= 2.0 and two with AR= 1.5 at the University of California Los Angeles, to investigate the nonlinear cyclic response of moderate-aspect ratio cantilever structural walls. These approximately one-half-scale walls, subjected to combined constant axial load and reversed cyclic lateral loading, were 5.9 inches thick and 48 inches long, with lateral load applied either 72 or 96 inches above the wall-foundation block interface. Two axial load levels were applied, $0.10\,A_g f'_c$ and $0.025\,A_g f'_c$, where A_g is the cross-sectional area of the wall and f'_c is the specified concrete compressive strength. The specimens were designed to yield in flexure at a lateral load of approximately 80-90% of the nominal shear strength, with web horizontal and vertical reinforcement ratios exceeding the minimum coded value of 0.0025. Two levels of average shear stress at nominal flexure capacity were considered, between approximately 4 and 8 $\sqrt{f'_c}$ psi.

Test results showed various failure modes correlated to the shear stress level. In walls with moderate shear stress level, failure was initiated by concrete crushing and buckling of boundary longitudinal reinforcement (diagonal tension failure), whereas in walls with high shear stress level, strength loss was caused by large diagonal concrete compression, which lead to out-of-plane buckling of special boundary elements. To monitor the damage, Tran (2012) reported the crack widths at peak lateral displacement and the residual crack width at zero lateral load of a dozen of numbered horizontal flexural and diagonal shear cracks on each wall specimen under both positive and negative loading, within the plastic hinge

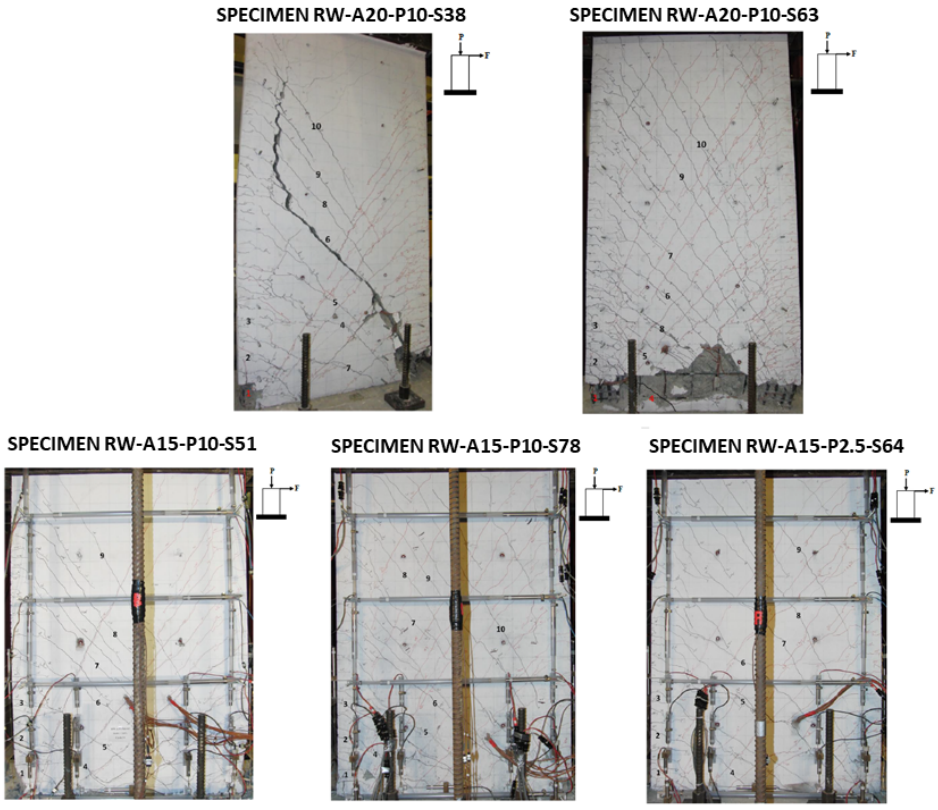


Figure 1.10: Crack patterns at the end of the test by Tran (2012)

zone. Fig.1.10 shows the different crack patterns developed at the end of the test for each specimen. At 3% drift ratio the maximum and average absolute crack widths were 3.5 mm and 3 mm, respectively. The maximum and average residual crack widths were 1.25 mm and 0.8 mm respectively.

Jiang et al. (2013)

Jiang et al. (2013) conducted an experimental study on RC shear wall specimens of common use in seismic regions in China, to define the damage levels corresponding to different performance levels. To assess the damage of RC shear wall under horizontal cyclic loading three main design parameters were studied, namely: 1) the axial load ratio, 2) the transverse reinforcement ratio of boundary elements and 3) the cross-section shape. Jiang et al. (2013) tested seven I-shaped, T-shaped and rectangular wall specimens, which were 39.4 inches long, 78.7 inches tall, and 3.9 inches thick. These specimens had horizontal and vertical reinforcement ratios of 0.66% and longitudinal reinforcement ratios of 1.25% and 1.51% were used in the five I-shaped wall specimens and in the T-shaped and rectangular wall specimens,

respectively. Constant axial load ratios of 0.1, 0.2 and 0.3 were applied to the wall specimens. The walls were designed in line with the Chinese seismic design code. The maximum crack width and maximum residual crack width values were measured at peak horizontal force or displacement and at zero force, within each loading and unloading cycle. After the specimens reached the ultimate state, crack widths could not be measured due to severe concrete spalling. The initial damage occurred in form of horizontal cracks appearing at the bottom of the boundary element. Diagonal cracks on the web were generally observed immediately after the initial yielding of the longitudinal reinforcement. The maximum crack width in the I-shaped and rectangular specimen at buckling of longitudinal reinforcement measured 2.50 mm and 1.63 mm respectively.

Results showed that the maximum crack and maximum residual crack width values increased monotonically with the increase in the drift level, consistently in all tested specimens. Both maximum transient crack width and maximum residual crack width values decreased with increase in the axial load ratio, demonstrating the restraining effect of the axial load on crack opening. An increase in the axial load ratio not only reduced the maximum crack width, it also effectively promoted crack closure during unloading. However, with the accumulation of damage, the ability of the cracks to effectively close was reduced due to the deterioration of the material. Nonetheless, the axial load ratio was also seen to influence the propagation of damage. Jiang et al. (2013) observed an increase in the height of concrete spalling, with the increase in applied axial load. The shear component of the global displacement was also observed to increase with increasing deformation and damage due to an increase in axial load. However, Jiang et al. (2013) observed a decrease in the displacement ductility of the walls, with an increase in applied axial load.

Lu et al. (2016)

Lu et al. (2016) investigated RC shear walls with low vertical reinforcement ratio, which were expected to exhibit low ductility during earthquakes. The six, approximately half scale, tested walls were typical of multistory RC walls in regions with moderate seismicity in New Zealand, with different shear span ratio, axial load and reinforcement ties in the wall boundary elements. The 5.9 inches thick, 55.1 inches long and 110.2 inches tall wall specimens were designed with limited ductile detailing requirements and with the current minimum vertical reinforcement, which is 0.53% for 5800 psi specified

concrete strength and 43,511 psi reinforcement yield strength according to NZS 3101:2006. The applied axial load ratios of 0, 3.5 and 6.6%, selected to reflect the current practice in New Zealand, were not large enough to require confinement reinforcement. The vertical reinforcement ratio was too low to require anti buckling ties, which were placed in two specimens to investigate their contribution to the spread of plasticity.

Dataset summarizing the experimental results of the tests (Henry 2019) confirmed that the plasticity was concentrated at the base, within the plastic hinge region. The lateral-load response showed limited drift capacity and premature reinforcement buckling or fracture, as only few main flexural cracks developed at the wall base. Crack widths measured at the end of the test within the plastic hinge length reached 27 mm close to the wall base, as Fig.1.11 shows. It was observed that crack widths were slightly larger in the specimens with no transverse reinforcement.

Effect of Axial Load on the Seismic Behavior of Walls

Select tests presented in the previous sections demonstrate the effect of the axial load on the shear wall response. To focus specifically on the impact of axial load on shear wall response, additional research programs and main conclusions are reported in this section. Remarkably, Zhang and Wang (2000), Su and Wong (2007) and Alarcon et al. (2014) comprehensively investigated the effect of axial load ratio on the shear-flexure interaction characterizing the shear wall response, as illustrated in the following paragraphs. However, it is noted that current U.S. design codes (e.g., ACI 318 2019) do not take into account the effect of axial load on the wall strength capacity equation.

Several research programs investigated the effect of axial load on the seismic behavior of walls. Surveys on existing buildings in Chile and Hong Kong (Su and Wong 2007, Alarcon et al. 2014) show that relatively large amount of axial load acts on concrete shear walls. In particular, slender walls in tall concrete buildings usually carry about 10%-20% of their section capacity in axial load during service loads conditions, and about 20% - 30% if earthquake loads are also considered. Under certain circumstances, however, these may be much greater, for example Alarcon et al. (2014) showed that the axial load ratio on RC shear walls increases on average by 50% when earthquake loads are added to the gravity loads. Generally, axial load affects the crack pattern and damage evolution, failure mode and ductility of RC walls (Zhang and Wang 2000). It is expected that large axial loads delay the onset of initial

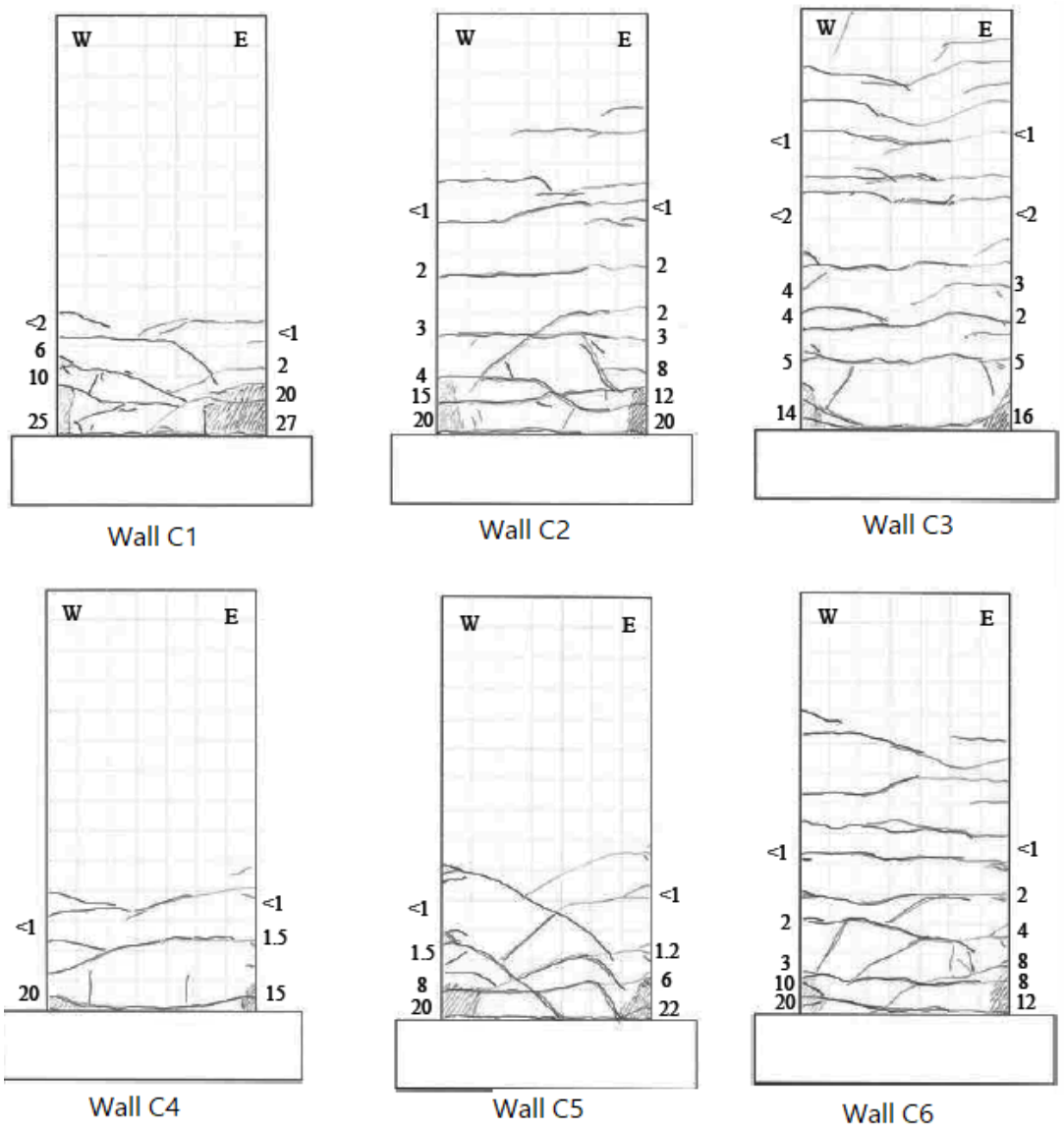


Figure 1.11: Crack patterns at the end of the tests by Lu et al. (2016). Crack widths in mm [1 in = 25.4 mm]

cracking and yield and decrease the displacement demand at which bar buckling and concrete crushing occur, leading to a reduction in displacement ductility. The studies by Zhang and Wang (2000), Su and Wong (2007) and Alarcon et al. (2014) cited before are illustrated in chronological order in the following paragraphs for completeness.

Zhang and Wang (2000) tested four isolated cantilever walls with different axial load ratios to investigate its effect on the post-yielding behavior of shear walls. All four walls had AR=2.5. Experimental results showed that axial load ratio has a detrimental effect on the energy dissipation of the walls. Walls tested with the high axial load ratio of 35% of the section capacity exhibited an undesirable out-of-plane buckling failure mode in the post-yield region and low ductility. On the contrary, walls tested with 25% axial load ratio observed a more favorable boundary elements failure mode and relatively high ductility.

Su and Wong (2007) tested quarter scale slender walls to investigate the effect of axial load and confinement of the cross section on their response. These three wall specimens had an aspect ratio AR = 4 to be representative of the typical mid-rise residential buildings in Hong Kong. The authors also performed survey for residential buildings in Hong Kong to find that common values of axial load ratio are larger than 30% of the section capacity in shear wall structures at working condition and these values can increase up to 50% in ultimate load conditions. The initial axial load ratios of 25% and 50% of the cross section capacity were decreased throughout the test. Su and Wong (2007) observed that the axial load applied to the wall specimen significantly influences the deformability and the failure mode, and that the rotation ductility decreases for increasing axial load. Moreover, an increase in axial load negatively affects the strength degradation and energy dissipation of reinforced concrete walls. Su and Wong (2007) conclude that the axial load ratio is an important factor in the life safety and collapse prevention performance criteria and therefore it should be carefully addressed in the design phase.

More recently, Alarcon et al. (2014) tested three half-scale slender wall specimens without boundary confinement to reproduce the failure modes observed in the Chilean earthquake. Three different values of axial load ratios were applied, namely 35%, 25% and 15% of the section capacity. Results showed that the displacement capacity of the wall with higher axial load ratio was almost half of the wall specimen with the lowest axial load.

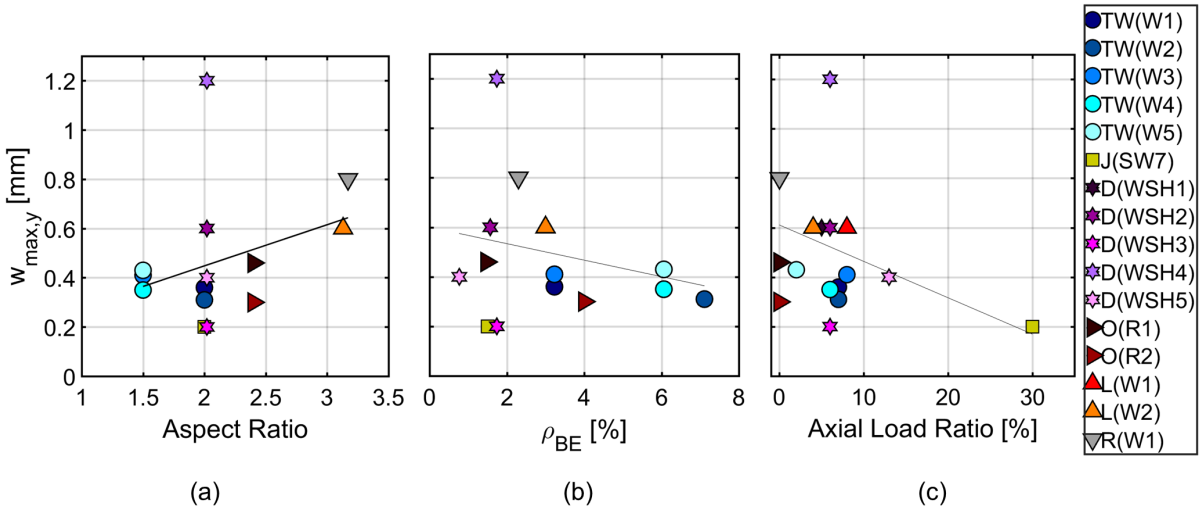


Figure 1.12: Maximum crack width at yield of the reinforcement in rectangular shear walls as a function of (a) the Aspect Ratio, (b) the reinforcement ratio in the boundary elements ρ_{BE}, and (c) the Axial Load Ratio. See Table 1.4 for mapping with legend nomenclature

Summary of Experimental Research on Flexural Shear Walls

The research programs presented in the previous sections highlight the flexural dominated characteristics of walls with AR $\geq$ 2 under simulated seismic loads. The majority of the wall specimens failed in a flexure dominated mode, anticipated by bar buckling and concrete crushing. These wall specimens also showed large deformation capacity, demonstrating the notable ductility properties of this type of walls, which usually concentrate the plastic strains at the wall base, within the plastic hinge length. Another main conclusion of the tests summarized in the previous sections regards the shear and flexural components of the response of these AR $\geq$ 2 wall specimens. In particular, shear deformations can reach the 20% of the flexural deformations of cantilever walls in the inelastic range. However, larger values at large ductility demands are measured when the shear-transfer mechanism of the wall is not stable. Degrading concrete damage is often observed in these walls, enhanced by absence of axial compression load, which is shown to facilitate cracks closing. To further elaborate on cracks formation, some useful considerations on the measured crack width at yield are drawn from these research programs and presented in the following.

Regarding the crack width amplitude, a global perspective of the state of the art is presented in Fig.1.12. Key data referred to rectangular cross section walls subjected to cyclic lateral loading is represented versus the maximum crack width experienced at measured yield of the reinforcement during

the test. Fig.1.12 shows the maximum measured crack width at yield of the reinforcement as a function of (a) the Aspect Ratio (AR), (b) the reinforcement ratio in the boundary elements ρ_{BE} and (c) the axial load ratio in rectangular shear walls previously tested in the literature (see Table 1.4 for reference). Data quite consistently demonstrate a linear trend in all three cases. The maximum crack width at yield $w_{max,y}$ increases with the slenderness of the wall and decreases when large compression axial load is applied to the wall. The axial compression load is therefore helpful in reducing the crack width at yield of the reinforcement, even if, at later stages, it may induce severe damage, as discussed in the following section. In addition, crack width values at yield are controlled by the amount of reinforcement in the boundary elements, and data suggest that crack width can be reduced by increasing ρ_{BE}. Wall specimens with heavily reinforced boundary elements are more likely to develop a more extensive crack pattern, with consequently smaller crack widths.

Table 1.4: Reference data considered in Fig. 1.12

Short name	Reference
TW(W1-W5)	Tran (2012)
J(SW7)	Jiang et al. (2013)
D(WSH1-WSH5)	Dazio et al. (2009)
O(R1-R2)	Oesterle et al. (1976)
L(W1-W2)	Lu et al. (2016)
R(W1)	Riva et al. (2003)

1.5.6 Code-based Crack Widths

Besides the results of scaled wall specimens tested in the literature, FEMA 306 (ATC-43 1998) provides information regarding expected crack widths in RC shear walls, as reported in Table 1.5. In comparison with experimental evidence, these codified values are very large. It is hypothesized that such large code suggestions are intended to provide values at and below which the performance target of the structure is capable of withstanding collapse in scenario earthquakes, absent serious loss of capacity. Although these values were defined for a different scope, they are reported here for completeness. It is observed in Table 1.5 that shear crack width amplitudes are expected to be smaller than flexural cracks when the same level of damage is considered. This observation suggests that large shear cracks could be detrimental for the structural stability of RC shear walls.

Table 1.5: Damage evaluation of concrete shear walls according to measured crack width. Suggested crack width ranges per FEMA 306 (ATC-43 1998)

Behavioral mode	**Severity**	**Flexural crack width** w [mm]	**Shear crack width** w [mm]
Ductile Flexure mode	Minor	$w < 6.4$	$w < 3.2$
	Moderate	$w < 6.4$	-
	Severe	N/A	N/A
Flexure/Diagonal tension mode	Minor	$w < 4.8$	$w < 1.6$
	Moderate	$w < 6.4$	$w < 3.2$
	Severe	-	$w < 9.5$
Flexure/Web crushing mode	Minor	$w < 4.8$	$w < 1.6$
	Moderate	$w < 6.4$	$w < 3.2$
	Severe	-	-
Flexure/Sliding shear shear	Minor	$w < 6.4$	$w < 3.2$
	Moderate	N/A	N/A
	Severe	$w < 9.5$	-

1.5.7 Behavior of Squat Reinforced Concrete Shear Walls

Low aspect ratio, or squat, RC shear walls are more often described by their normalized moment M to shear V ratio, $M/(VL_w) \leq 1.5$, where L_w is the wall length. They are commonly used in low-rise construction as the primary lateral load resisting system in regions of medium to high seismic risk. They are also used in high-rise structures to enhance the lateral strength of the building, though often only extending over the first few stories above the foundation level. Their behavior is typically dominated by shear, as opposed to slender RC shear walls, alternatively classified as having an $M/(VL_w) \geq 2$. In the latter case, response under lateral forces is normally controlled by flexure. In many low-rise buildings, the height of the cantilever shear walls is less than its length and the assessment of the flexural and shear strength and appropriate reinforcement cannot be based on conventional techniques applicable to taller walls. Low-rise shear walls normally carry only very small gravity loads, and thus their beneficial effect is usually ignored. The flexural steel demand will also be small in most cases for their relatively large available internal lever arm. Usually, it is more practical to distribute the vertical (i.e, flexural) reinforcement uniformly over the full length of the wall, allowing only a nominal increase at the vertical edges. The corresponding loss of ductility for seismic loading is not likely to be of great importance mainly because properly detailed squat shear walls can absorb most of the seismic demand in the elastic range absent significant flexural reinforcement needs. In general, it is good design practice to avoid shear failures in favor of a more ductile flexural response even for squat shear walls.

Typical Failure Modes of Squat Walls

As outlined in Paulay et al. (1981), three main categories of squat walls are identified on the basis of their response to simulated seismic loads, namely: 1) elastic, 2) rocking and 3) ductile walls. Elastic walls are strong enough to respond elastically to the largest earthquake likely to occur, whereas rocking walls respond to lateral loads with overturning actions or rocking. More commonly, squat walls are not designed to respond elastically to design level accelerations, and they need ductility to respond to lateral forces (ductile walls).

Ductile cantilever squat walls transmit a significant portion of shear force imposed at the top of the wall directly to their foundation by diagonal compression (Barda 1972). Shear failure is therefore likely to develop in the form of diagonal tension or compression, especially when the applied reversed

cyclic loading produces strength and stiffness degradation. In the case of ductile squat shear walls, three typical shear failure modes may be observed, namely: 1) diagonal tension, 2) diagonal compression and 3) sliding shear, described as below.

1. **Diagonal tension failure** occurs when the provided horizontal shear reinforcement is not sufficient to transfer the shear force. One or more wide inclined cracks per loading direction generate a corner-to-corner diagonal tension failure plane (usually at 45°). This mechanism may be prevented by providing horizontal shear reinforcement to transfer a larger shear force than the one producing significant flexural yielding. Fig.1.13 shows the typical wide cracks in a specimen that failed in diagonal tension, tested by Hidalgo et al. (2001).

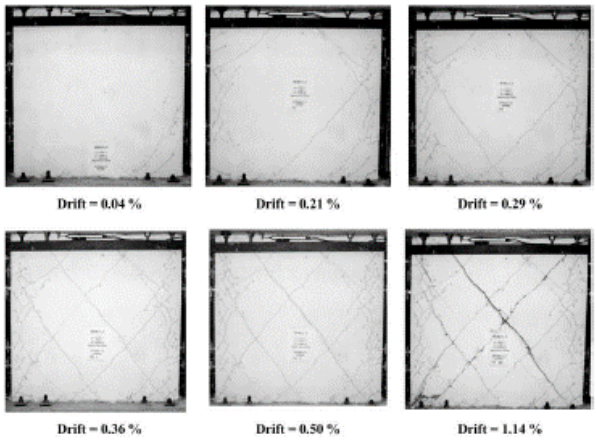
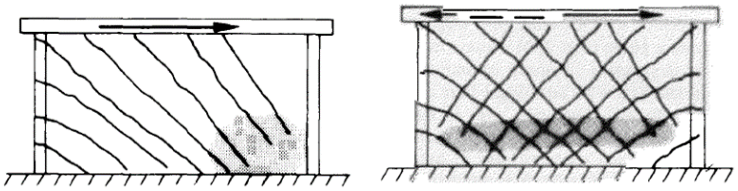


Figure 1.13: Wall specimen failed in diagonal tension, tested by Hidalgo et al. (2001). Photo courtesy of Hidalgo et al. (2001)

2. **Diagonal compression failure** occurs when the concrete strength is reduced by a series of diagonal intersecting cracks, cyclically opening and closing under reversed loading. The crushing of the concrete may easily spread over the entire length of the wall producing a dramatic and irrevocable loss of strength. This mechanism of failure, more common in barbell and flanged walls, may occur after adequate horizontal reinforcement is placed to prevent the development of diagonal tension, described above. This undesirable brittle failure mode may be avoided by limiting the maximum shear strength to the wall's flexural strength. Fig.1.14 shows the typical damage pattern and the mechanism of a diagonal compression failure. Confined boundary elements may help in redistributing the inelasticity along the wall height, and in preventing the reduction of axial

strength following concrete spalling. In general, damage is not redistributed along the boundary element but rather localizes in a reduced region of the wall if the confinement is poor. A brittle compression failure induced by concrete crushing and buckling of vertical reinforcement may then occur.



(a) Diagonal compression failure under monotonic loading

(b) Diagonal compression failure under reversed cyclic loading

Figure 1.14: Graphical representation of the diagonal compression failure mode, from Paulay et al. (1981)

3. **Sliding shear failure** occurs following reversed cyclic loading when interconnected flexural cracks generate a continuous and approximately horizontal shear path (plane of potential sliding). With subsequent inelastic load reversals, the shear friction mechanism along this plane deteriorates, together with the bond along the vertical bars. Eventually, concrete crushing between cracks spreads over the wall length in a narrow band, weakening the plane at the base. The principal mode of shear transfer along the base in this case is the buckling of vertical bars. The sliding displacement noticeably reduces the stiffness of the squat wall, resulting in early failure of the structural wall. Sliding shear failure may be avoided by providing diagonal reinforcement crossing the sliding plane (Paulay et al. 1981). Fig.1.15 shows the typical damage pattern and the mechanism of a sliding shear failure, from Paulay et al. (1981).

The understanding of the three typical failure modes described above is also subject of past research on squat walls, as summarized in the next section. These research effort on the behavior of low aspect ratio walls under cyclic lateral loads provide insight on best design practices to avoid undesirable failure modes and to increase ductility capacity of low-rise walls.

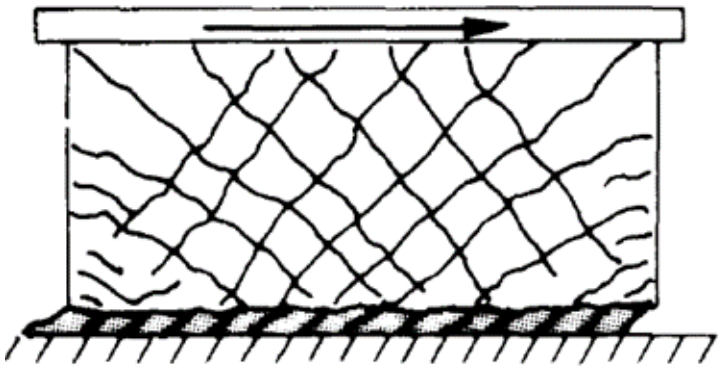


Figure 1.15: Graphical representation of shear sliding failure mode, from Paulay et al. (1981)

Paulay et al. (1981)

Most notably, the early research on the response of squat walls to lateral forces was guided by Paulay et al. (1981). To investigate the energy dissipation through flexural yielding in squat shear walls subjected to reversed cyclic loading and to establish the maximum attainable displacement ductility, Paulay et al. (1981) tested four specimens with AR=0.5. Two of these wall specimens had 118 inches by 3.9 inches rectangular cross section whereas the remaining two had flanges. All specimens were designed to have approximately the same flexural capacity with a corresponding nominal shear stress of about 7.2 $\sqrt{f'_c}$ psi. Vertical reinforcement was uniformly distributed in a single layer centered in the wall and additional vertical reinforcement was placed at the boundaries of the wall specimens. Sufficient horizontal reinforcement was also provided to avoid diagonal tension failure. Since particular attention was given to the shear deformation contribution to the total lateral displacement to reduce the sliding shear displacement, one wall specimen of each type of cross section was supplied with additional diagonal reinforcement to compare its response to the conventionally reinforced wall specimen. Horizontal load corresponding to the onset of yielding in the outermost vertical tension bar was applied in the first cycle. All the subsequent displacements were applied as even multiples of the effective yield displacement, obtained from an elasto-plastic idealization of the load-deflection behavior. The displacement protocol imposed two complete cycles at each displacement amplitude. No axial load other than the wall specimen self-weight was considered.

Test results showed that it is possible to ensure a predominantly flexural behavior involving the yielding of the flexural reinforcement in squat shear walls. Significant energy can be dissipated by

the formation of a plastic hinge if the shear failure modes of diagonal compression and/or tension are preliminary avoided by providing sufficient shear strength (at least equal to the shear demand imposed by the flexural overstrength). It was also observed that flanged walls are more susceptible to fail by sliding shear, which is the most significant cause of loss of strength and stiffness. Moreover, the severity of sliding shear was seen to increase with decreasing vertical reinforcement (which provides dowel shear resistance) and with a decrease in the flexural compression zone of the wall section over which the bulk of the shear would need to be transferred by shear friction. Overall, crossing diagonal bars were seen to improve the seismic response of squat walls, even if they could not help in preventing sliding shear failure in these tests, for the small amount of diagonal steel provided. However, it was also noted that significant additional energy dissipation occurred thanks to the yielding of the diagonal reinforcement, when slip displacements occurred. Finally, recommendations were made for the amount of shear force to be resisted by diagonal reinforcement.

Lefas et al. (1990)

Almost a decade later than the fundamental contribution by Paulay et al. (1981), Lefas et al. (1990) integrated previous research on squat walls, investigating the effect the axial load on their response. To characterize the behavior of RC squat shear walls, without neglecting the axial load, Lefas et al. (1990) tested thirteen 1.4 scale wall models with constant thickness and AR=1 and AR=2 under the combined action of axial horizontal load. The aim of these tests was to investigate the effect of the aspect ratio, the axial load, the concrete strength, and the amount of web horizontal reinforcement on wall behavior. Wall specimens represented the critical story element of a structural wall system with a rectangular cross section. Wall specimens with AR=1 were 29.5 inches wide x 29.5 inches high x 2.8 inches thick. Vertical reinforcement was designed in compliance with the recommendations of ACI Building Code ACI 318-83 and placed in a double layer configuration. The horizontal reinforcement was also Code compliant, except for one wall specimen, which was designed with significantly less reinforcement than that specified in the Code to investigate its effect on the behavior of the wall specimen when subjected to monotonic lateral load. Three levels of axial load were constantly applied, namely, 0.0, 0.1 and 0.2 of the uniaxial compressive strength of the wall cross section. The lateral load was monotonically increased at a small rate to failure.

Test results showed that axial compression increased the horizontal load carrying capacity of the wall specimens and reduced both their vertical and horizontal displacements. Conversely, the wall with no axial load exhibited a more ductile response. Lefas et al. (1990) also observed that the shear capacity is not affected by the horizontal reinforcement and that the strength and deformational response of the wall specimens are independent of the uniaxial concrete strength characteristics within a range of 4,000 to 8,000 psi. Shear resistance was found to be associated with the development of triaxial compressive stress conditions within the compressive zone near the base. The failure of the wall specimens occurred due to nearly vertical splitting of the compressive zone with a wider failure region in smaller AR wall specimens. In particular, damage to the compressive zone was greater for the walls with lower aspect ratios and increasing axial load. It was also noted that the increase in the axial load did not affect the maximum compressive strain but reduced the maximum recorder tensile steel strain.

Salonikios et al. (1999)

Lefas et al. (1990) shed light on the effect of axial load on monotonically loaded squat walls. However, information regarding the response of cyclically loaded squat walls with different axial load levels was scarce. The first comprehensive study on this topic was conducted by Salonikios et al. (1999), who also addressed the problem of cyclic shear in squat walls to assess the validity of design provisions both in Europe and in the U.S. The experimental program involved eleven 1:2.5 scale wall specimens, six with $M/(VL_w) = 1.5$ and five with $M/(VL_w) = 1.0$, detailed according to the provisions of the Eurocodes. Wall section was 3.9 x 47.2 inches^2 and to achieve the required aspect ratios, specimen heights of 47 and 71 inches were selected. The longitudinal reinforcement ratio in the boundary elements observed the minimum 1% by the European Code. Reinforcement was placed in two layers. The five $M/(VL_w) = 1.0$ wall specimens differed for some details of the reinforcement layout, namely the presence of diagonal bars, intersecting at two different heights from the wall-footing interface, the presence of cross ties along the web or the presence of an additional third layer of reinforcement (both vertical and horizontal) in the middle of the cross section. An axial load of 7% of the cross sectional capacity was applied to one of the five wall specimens with AR=1. Three cycles in load control mode were initially applied to the wall specimens to investigate the elastic range, followed by three cycles at each ductility level in displacement control mode until failure.

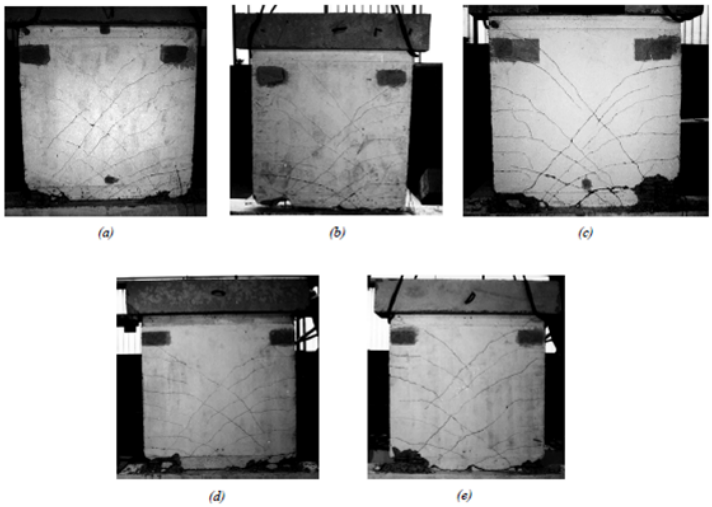


Figure 1.16: Crack patterns of walls with AR=1 at the end of the tests by Salonikios et al. (1999)

Test results showed that all the tested specimens failed in predominantly flexure mode, characterized by concrete crushing and reinforcement buckling at the confined edges, see Fig. 1.16. Moderate diagonal cracking of the web and sliding shear at the base did not significantly affect the failure mechanism. It was concluded that the diagonal reinforcement produces an overall superior behavior of the wall specimens, and it also reduces the global amount of reinforcement by about 15%. It was also shown that axial load reduces the sliding at the base and allows more energy to be dissipated, by reducing the pinched shape in the hysteresis loops.

Greifenhagen and Lestuzzi (2005)

The squat walls tested by Salonikios et al. (1999), presented in the previous section, were designed with boundary elements, as is common practice for ductile flexural elements. Completing the perspective on the best detailing practices for cyclically loaded squat walls, Greifenhagen and Lestuzzi (2005) considered, instead, wall specimens without boundary elements. Greifenhagen and Lestuzzi (2005) tested four wall specimens not designed for seismic loads to investigate the performance of lightly reinforced concrete shear walls under reversed static cyclic loading. The 1:3 scale specimens represented the lower portion of a shear wall of an existing building. The minimum amount of vertical and horizontal reinforcement was placed in two layers in all wall specimens, with the exception of one specimen, for which no horizontal reinforcement was provided. No boundary elements were designed. Force and

displacement controlled cycles were applied to simulate seismic action. Because of the limited capacity of the actuators, the vertical force was decreased twice during the loading history of the wall specimens.

Test results showed that the damage accumulates near the base of the wall, degrading the concrete in sliding, compression and tensile straining, see Fig. 1.17. Greifenhagen and Lestuzzi (2005) concluded that shear walls only designed for gravity loads can have drift capacity greater than 1%, as the drift capacity depends on the axial force ratio and on the arrangement of the vertical reinforcement. It is also observed that cantilever shear walls, without rotation restraint at the top, are less prone to brittle shear failures, as opposed to walls with fixed top ends.

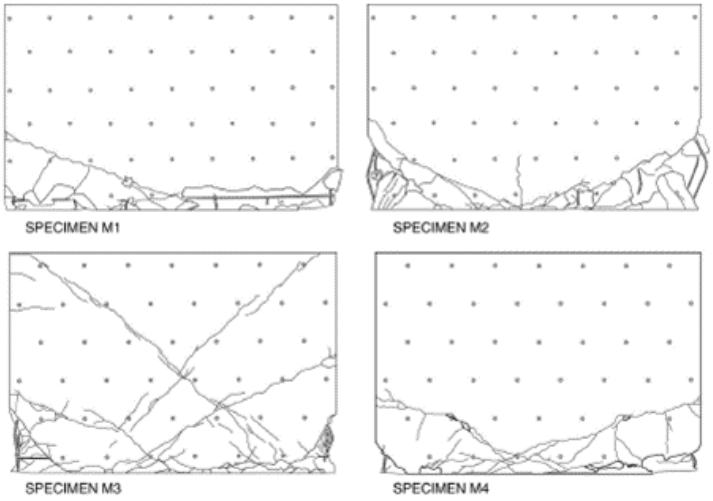


Figure 1.17: Crack patterns at the end of the tests by Greifenhagen and Lestuzzi (2005)

Kuang and Ho (2008)

Similar to Greifenhagen and Lestuzzi (2005), an investigation on the effect of reinforcement detailing on the response of low aspect ratio walls under equivalent seismic loads was carried out by Kuang and Ho (2008). The eight large-scale, squat RC squat walls specimens, with AR=1.0 and 1.5, tested under reversed cyclic loading by Kuang and Ho (2008), were purposely designed according to the British Standard Regulation (BSI 1997) absent seismic detailing. All the specimens had the same rectangular cross section of 47 x 4 inches, with wall panel heights of 47 inches or 71 inches, corresponding to ARs of 1.0 and 1.5, respectively. A vertical load of about 12% of the wall section capacity was applied, before two complete cycles of reversed loading at multiples of the ductility factor were applied.

Test results showed that a displacement ductility of 2.5 to 3.0 may generally be achieved for walls without boundary confinement. Hence, ordinary squat shear walls designed and detailed without seismic considerations may not sufficiently satisfy the ductility demand for shear wall building structures with limited ductility in a region of moderate seismicity. As recommended by Park (1998), a ductility factor of approximately 3 is recommended in this case. Displacement ductility factors ranging from 4.5 to 5.0 can be achieved by simply modifying the current non seismic design practice of reinforcement details, by adding, for example, boundary confinement zones at the edges of the wall or adding cross ties throughout the cross section.

Hidalgo et al. (2002) and Carrillo and Alcocer (2012)

Contemporary to the European studies by Greifenhagen and Lestuzzi (2005) and Kuang and Ho (2008), in Latin American countries, the occurrence of the 1985 Chilean earthquake motivated more studies the behavior of typical low-rise RC wall housing in Chile (Hidalgo et al. 2002 and Carrillo and Alcocer 2012). To study the shear mode failure of typical Chilean walls, Hidalgo et al. (2002), for example, tested twenty-six full-scale specimens with shear span between 0.35 and 1.00, designed according to ACI 318-99 with sufficient boundary reinforcement to prevent flexural failure. Due to the reduced thickness of walls, ranging approximately from 3.1 to 4.7 inches, the horizontal and vertical reinforcement were placed in one layer only. Test parameters were the AR of the walls, the amount of vertical and horizontal distributed reinforcement and the compressive strength of concrete. Cyclic horizontal displacement of increasing amplitude was applied at mid-height of the wall specimen, until the lateral strength had dropped to approximately 75% of the maximum value. Since it was observed that low-cycle fatigue is not significant, only two cycles at each amplitude were applied. All the tests included zero axial load except for the wall specimens' self-weight. Results showed that the deformation capacity of specimens gets smaller as the shear span ratio decreases. Cracking was observed to occur at drift ratios of 0.1%, while drift at maximum strength varied between 0.2% and 0.8%. Wall specimens failed at drifts between 0.3% and 1.3%. It was also observed that the strength deterioration increased in smaller shear span ratio specimens with the decreasing of the horizontal and vertical reinforcement amount. No information regarding the effect of the axial load were collected in this study.

To complement Hidalgo et al. (2002) research on typical low-rise RC wall housing in Chile with

information on the axial load effect, Carrillo and Alcocer (2012) tested thirty-nine full scale isolated cantilever walls to simulate the 2010 design of concrete walls and construction practice in Latin American countries. The experimental program included the following variables: AR=0.5, 1.0, 2.0, the presence of openings and windows, the type of concrete (normal-weight, light-weight, self-consolidating), the web reinforcement ratio (0, 50, 100% of the minimum required by Code ACI 318 2011) and the type of reinforcement (deformed bars or welded-wire mesh). Reinforcement was placed in a single layer and boundary elements were designed to prevent flexural failure before shear failure. Wall specimens were tested under a quasi-static reversed cyclic loading history, and an axial compressive stress of about 2% of the section capacity was applied on top of the specimens and kept constant during testing. The lateral load was applied in load control until cracking, and it was switched to displacement control after that. Two cycles per increment were applied. Typical crack patterns at the end of the tests are reported in Fig. 1.18. Results showed that the shear strength of the walls with half of the minimum reinforcement ratio was comparable to the walls complying with minimum reinforcement ratio recommendations. Thus, it was concluded that the minimum web reinforcement ratio is over conservative to prevent the diagonal tension cracking in low seismic zones.

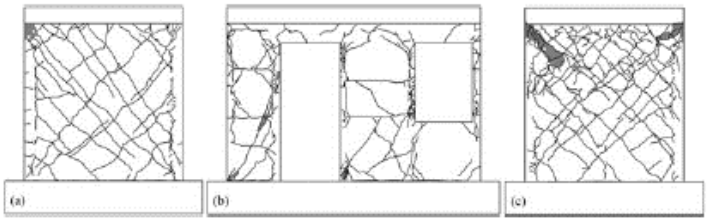


Figure 1.18: Typical crack patterns at the end of the tests by Carrillo and Alcocer (2012)

Orakcal et al. (2009)

In addition to the Chilean lightly reinforced squat walls, another type of vulnerable low-aspect ratio shear walls is found in older California buildings (1960s), which show windows and openings in reinforced concrete walls. The behavior of these typical wall segments in this type of old buildings is considered in the study carried out by Orakcal et al. (2009) at the University of California Los Angeles. To investigate shear failure modes, Orakcal et al. (2009) tested 3/4 scale AR=0.9 lightly reinforced wall specimens, and AR=1.0 lightly reinforced spandrel specimens. Specifically, four different types of span-

drels were tested, varying the amount or properties of the reinforcement and the location of a weakened plane joint. The wall piers had, instead, identical reinforcement placed in one layer, and they were tested under axial load levels of 0, 5 and 10% of their axial load capacity. The lateral load was applied at mid-height of the specimens to simulate the actual boundary conditions of a wall segment in a building, with rotation prevented at both bottom and top of the segment. Three full cycles were applied at each amplitude.

At the end of the tests the observed damage in both the axially loaded wall piers showed cracks at 45° and axial collapse due to progressive concrete crushing and concrete spalling in the web region. Web bars buckled along the primary diagonal plane and boundary longitudinal bars buckled outward. The wall piers without axial load showed cracks at 45° and axial collapse due to progressive concrete crushing and concrete spalling in the web region. Overall, the piers were governed by shear deformations associated with diagonal cracking, followed by widening and sliding along diagonal cracks. Degradation of the lateral load capacity was associated with crushing of concrete close to the center of the wall, where the constraining effect of top and bottom beams are minimized.

Looi et al. (2017)

Complementing the work of Orakcal et al. (2009), Looi et al. (2017) investigated the effect of the axial load on low-aspect ratio walls, which are usually found in tall buildings with vertical irregularities. These low-aspect ratio walls are usually segments of slender walls and therefore they carry large values of axial loads, being at the base of tall buildings, and if not properly detailed, they may fail in shear or compression before the development of a plastic hinge. To assess the performance of low-aspect ratio walls subjected to large values of axial load ratio, Looi et al. (2017) considered four AR=1 reduced-scale wall specimens, with 2% reinforcement ratio in the longitudinal and transverse direction, as typical of a sub-structure building. The wall specimens were tested with axial load ratios in the 10% - 40% range, namely 12%, 22%, 38% and 44%.

Results show that the amount of applied axial load has several effects on the wall response to lateral loads, manifested in the developed crack pattern, failure mode and capacity of deformability. The axial load ratio also influenced the type of out-of-plane buckling. Considerable out of plane deformations were observed in all tested wall specimens. However, in walls with low axial load ratios the out-of-plane

deformation developed without causing severe degradation to the global axial capacity. On the contrary, when large axial load is applied, the out-of-plane deformation occurs with the axial failure (buckling instability caused by compression), unless the boundary elements are well confined. In other words, low values of compression give a limited local buckling allowing for a load redistribution on the other bars without producing axial failure. Conversely, large values of applied axial load are responsible for the global buckling of the reinforcement, characterized by a visible buckling length, which can dangerously lead to a "pancake failure", i.e., the collapse of building floors one atop the other.

Summary of Experimental Research on Squat Shear Walls

The research programs reviewed in the previous sections highlight important response characteristics observed from testing of walls with AR $\leq$ 1 subjected to simulated seismic loads. As expected for this type of wall, the tests confirmed that the deformation capacity attained by the wall specimens is small, and that it decreases with the aspect ratio of the wall in lightly reinforced wall specimens. Similarly, the ductility capacity of squat walls not seismically detailed can be small and may not satisfy the ductility demand for shear wall building structures. Regarding the typical damage developed by the squat walls tested, it is observed that the detailing, the ductility properties, and the axial load applied to the specimens significantly affect the spread of concrete damage. In this regard, test results show that the amount of applied axial load has several effects on the wall response to lateral loads, manifested in the developed crack pattern, failure mode and deformation capacity. Axial load ratio in general reduces the displacement ductility of wall specimens, however, it provides a margin of resistance against sliding shear failure and restrains crack opening and extension. However, despite the significant amount of literature on RC squat shear walls, the relation between crack widths and axial load ratio is not well defined, largely due to the scarcity of information on crack width values during and/or at the end of the test. Nonetheless, the maximum shear crack width values were measured for select specimens tested by Paulay et al. (1981), Salonikios et al. (1999) and Orakcal et al. (2009), see Table 1.6, and represented in Fig.1.19. In the later, the maximum measured crack width is plotted versus the estimated displacement ductility of the considered wall specimens. The trend line suggests smaller crack widths are associated with larger ductility values. This may be explained considering that wide damage distribution and therefore smaller crack widths are expected in wall specimens with large ductility, as opposed to low ductility

walls, which usually exhibit brittle failures, with damage concentrated in a few large cracks. It is noted, however, that the available data are not sufficient to define a clear trend and more experimental evidence is required.

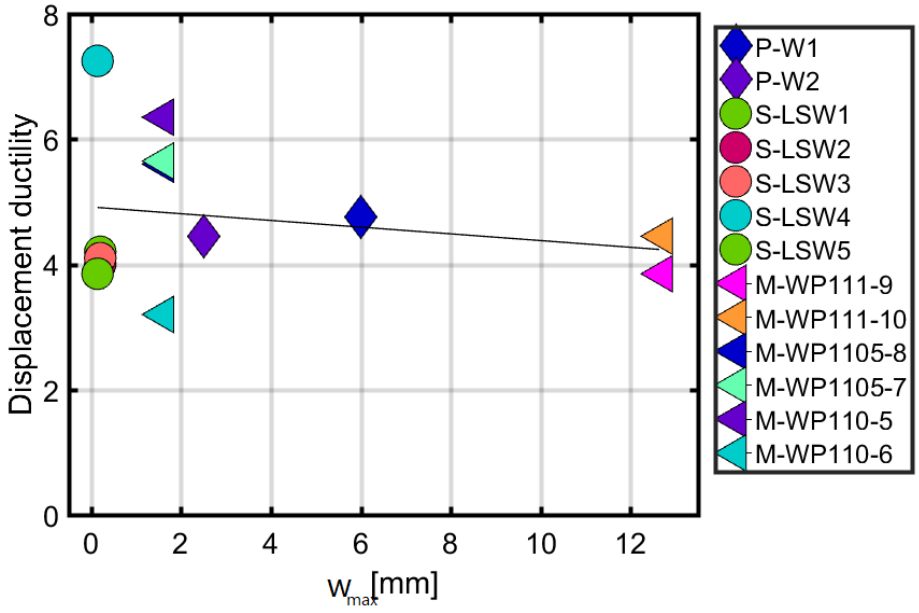


Figure 1.19: Maximum measured shear crack width versus estimated displacement ductility. See Table 1.6 for mapping with legend nomenclature

Regarding the displacement ductility, however, it was observed that it is possible to ensure a predominantly flexural response involving the yielding of the flexural reinforcement. Moreover, confined boundary elements at the wall ends increase shear resistance, as they facilitate the development of triaxial compressive stresses within the compressive zone near the base. These observations stress the importance of a proper detailing of low-aspect ratio walls to satisfy the ductility demands of building structures. To this end, the following section illustrates commonly adopted squat wall design practices from the European and the U.S. design codes, as discussed in Salonikios et al. (2000).

Comparison of Design Codes

It is instructive to compare the present European and U.S. design codes, particular to issues important for squat shear walls. Initially, it is noted that U.S. design codes (ACI 318 2019) refers to the aspect ratio (AR= wall height to length ratio) to distinguish between different wall behaviors whereas the

Table 1.6: Reference data considered in Fig. 1.19

Short name	Reference	Aspect ratio
P-W1	Paulay et al. (1981)	0.5
P-W2	Paulay et al. (1981)	0.5
S-LSW1	Salonikios et al. (1999)	1.0
S-LSW2	Salonikios et al. (1999)	1.0
S-LSW3	Salonikios et al. (1999)	1.0
S-LSW4	Salonikios et al. (1999)	1.0
S-LSW5	Salonikios et al. (1999)	1.0
M-WP111-9	Orakcal et al. (2009)	0.4
M-WP111-10	Orakcal et al. (2009)	0.4
M-WP1105-8	Orakcal et al. (2009)	0.4
M-WP1105-7	Orakcal et al. (2009)	0.4
M-WP110-5	Orakcal et al. (2009)	0.4
M-WP110-6	Orakcal et al. (2009)	0.4

European Code (CEN 2004) refers to the shear span ratio. The latter results in a more rational criteria to distinguish between slender and squat walls, since it accounts for the loading conditions imposed on the wall. However, ACI 318 (2019) recognizes the increased shear strength of walls with low AR by specifying a higher concrete contribution of 3 $\sqrt{f'_c}$ psi for AR $\leq$ 1.5. The European code does not account for increased concrete contribution in low AR walls, but provides an equation to calculate the shear strength of low AR walls, which only considers the horizontal reinforcement in resisting the shear. To this regard, the U.S. design code (ACI 318 2019) reports that for AR $<$ 2 the vertical reinforcement ratio should not be less than the horizontal reinforcement ratio. In addition, the U.S. design code (ACI 318 2019) recognizes the increased shear capacity of low aspect ratio shear walls (AR $\leq$ 1.5) by means of a larger value of the α_c coefficient (α_c =3.0 versus α_c = 2.0 for AR $\geq$ 2.0) in the shear strength equation in ACI 318 (2019):

$$V_n = A_c(\alpha_c \sqrt{f'_c} + \rho_h f_y) \tag{1.1}$$

and ACI 318 (2019) the margin against the sliding shear failure mode is addressed by the limiting upper bound of 8 $\sqrt{f'_c}$ psi for the nominal shear stress. The European code, instead, prescribes explicit calculation of the resistance against diagonal tension and sliding shear failure modes by considering the dowel action of vertical bars, the shear resistance of the diagonal bars (if any) and the friction. CEN (2004) also suggests to provide diagonal bars to carry half the design shear at the base.

1.5.8 Plastic Hinge Length in RC Shear Walls

A brief summary of the state of the art regarding the understanding and estimation of the plastic hinge length in RC shear walls is here presented, as the plastic hinge region will be the most significantly damaged, thus avoiding anchor placement in these regions is essential. Notably, current anchor qualification procedures (EOTA TR 045 2013, ACI 355 2019) prohibit anchor installation within the plastic hinge length. Although the concept of plastic hinge length is reasonably understood for concrete beams and columns, the definition of plastic hinge length is ill defined for concrete shear walls. Nonetheless, in principle, the physical length over which reinforcement is at or beyond yielding is commonly referred to as the *plastic hinge zone*. The plastic hinge is defined, therefore, as the length of equivalent uniform inelastic curvature, typically assumed as half of the *plastic hinge zone*, see the schematic in Fig.1.20.

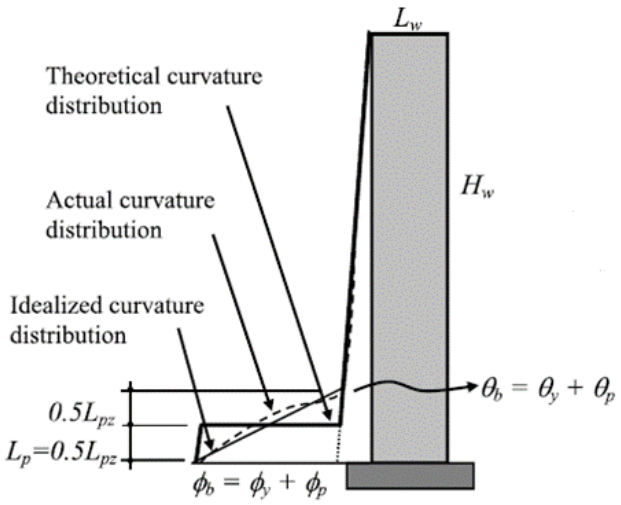


Figure 1.20: Schematic representation of the plastic hinge length L_p and plastic hinge zone L_{pz}. Figure courtesy of Kazaz (2013)

To characterize this zone of plasticity, the effort of Hines et al. (2004), as applied to well confined bridge columns, is of interest. According to Hines et al. (2004), the spread of plasticity depends mainly on:

- the **Moment gradient** M_{max}/M_y, where M_{max} is the maximum moment experienced by the member and M_y is the yielding moment. This term reflects the fact that the transition between the yield moment and ultimate moment in a member is proportional to the member's shear span M/V. A

member with shorter shear span is expected to show a reduced spread of plasticity. This effect is accounted for when non linear material properties are considered and it is assumed that plane sections before bending remain plane after bending.

- the **Tension shift**, which refers to the tendency of flexural tensile forces to be almost constant over a small region at the base, before they can be adequately transferred to the compressed region by a inclined struts. Tension shift depends on the diameter of the longitudinal bars and on its steel yield strength. This concept invalidates the assumption that plane sections remain plane.

- the **Strain penetration**, which refers to the fact that longitudinal bar strains can reach significant inelastic levels into the foundation and a fixed end rotation at the base of the footing can occur.

Thus, the plastic hinge length formulation should include the three contributions above. Common forms are reported below:

1. Mattock et al. (1976) offer the following:

$$L_p = \alpha \cdot L + \beta \cdot D + \xi \cdot f_y \cdot d_b \tag{1.2}$$

where L is the member shear span (maximum moment to zero moment length), D is the member depth (cross section) and d_b is the bar diameter of the longitudinal reinforcement. The plastic hinge length of beams based on Mattock et al. (1976) is found with the coefficients α = 0.05, β =0.5, ξ = 0. Priestley et al. (1996) suggested different coefficients to apply Equation (1.2) to shear walls. According to Priestley et al. (1996), the coefficients for shear walls are α = 0.08, β =0, ξ = 0.022.

2. Paulay and Uzumeri (1975) offer the following:

$$L_p = \alpha \cdot 0.8 \cdot L_w + \beta \cdot H_w \tag{1.3}$$

An upper-bound estimate, according to Joint ACI-ASCE Committee 428 (1968), is obtained with $\alpha = 0.5$ and $\beta = 0.10$. Paulay and Priestley (1993) recommended analysts use α = 0.25 and β=0.044 to obtain a lower bound estimate. It is noted that for a given H_w/L_w ratio, L_p depends only on wall length L_w. For a typical value of $H_w/L_w = 7$ the upper bound plastic hinge is $0.5 \cdot L_w$,

as it is commonly assumed. Over the range of H_w/L_w from 5 to 12, L_p varies from $0.4 \cdot L_w$ to $1.6 \cdot L_w$, with the lower and upper bound α and β values used.

3. Paulay and Priestley (1992) subsequently simplified Equation (1.3) as:

$$L_p = 0.2 \cdot L_w + 0.07 \cdot (M/V) \tag{1.4}$$

which is based on research specifically applicable to walls.

4. Bohl and Adebar (2011) suggested a lower bound estimation of plastic hinge length in isolated walls as:

$$L_p = (0.2 \cdot L_w + 0.05 \cdot (M/V))(1 - 1.5P/f'_c A_g) \leq 0.8 L_w \tag{1.5}$$

where P is axial load (compression is positive) and $P/f'_c A_g$ is the axial load ratio. The shear span M/V can be either determined from analysis or estimated as $0.7H_w$, if the hinging at the base of a shear wall is due to a first-mode distribution of forces. However, the maximum curvature at the base of a shear wall in a tall building (more than 10 stories high) is strongly influenced by the higher modes (Bohl and Adebar 2011).

5. Kazaz (2013) performed regression analysis to derive:

$$L_p = 0.27 \cdot L_w \left(1 - \frac{P}{A_w \cdot f'_c}\right)\left(1 - \frac{f_y \cdot \rho_{sh}}{f'_c}\right)\left(\frac{M/V}{L_w}\right)^{0.45} \tag{1.6}$$

Moreover, deriving the plastic hinge length in a form similar to the previous equations in the literature Kazaz (2013) obtained:

$$L_p = 0.143 \cdot L_w + 0.072(M/V) \tag{1.7}$$

These analytical expressions were derived using the results of comprehensive nonlinear finite element analyses within the parametric study carried on in Kazaz (2013). The accuracy and reliability of the proposed plastic hinge length equations were evaluated using the available shear wall test results.

It is notable, however, that a simplistic estimate of the anticipated plastic hinge length L_p of the wall is often taken as:

$$L_p = 0.5 \cdot L_w \tag{1.8}$$

Equation (1.8) is suggested by Park and Paulay (1975), based on observations from beam tests. However, it has become common practice to assume that the plastic hinge length L_p of a concrete wall varies from 0.5 to 1.0 times the larger horizontal dimension of the wall L_w. This assumption is used as a lower-bound estimate of L_p to make a safe estimate of the displacement capacity from the curvature capacity and it was used to derive an expression introduced in ACI 318-99, which also accounts for maximum compression strain depth in a wall without confinement reinforcement. However, Kazaz (2013) noted that Equation (1.8) underestimates the plastic hinge length as the wall length increases and shear effects become predominant.

As a result of the aforementioned and other research, various plastic hinge length expressions are found in design codes:

- **ASCE/SEI 41** ASCE 41 (2014): $L_p = 0.5 \cdot L_w$ but less than one story height for shear walls;
- **NZ 3101.1.2006** P 3101 Concrete Design Committee (2006): in case of out of plane loading:

$$L_p \text{ lesser of} \begin{cases} t_w, & \text{if } t_w \leq 200mm \\ 0.5t_w, & \text{if } t_w \geq 500mm \\ \text{larger of} \begin{cases} 0.25M/V \\ 0.5t_w, \quad \text{if } t_w \geq 500 \text{ mm or } t_w \leq 200mm \end{cases} \end{cases} \tag{1.9}$$

In case of in plane loading:

$$L_p \text{ lesser of} \begin{cases} 0.5 \cdot L_w \\ 0.15 \cdot M/V \end{cases} \tag{1.10}$$

- **Eurocode 8** CEN (2004):

$$L_p = 0.1 \cdot L + 0.17 \cdot D + 0.24 \cdot \frac{f_y \cdot d_b}{\sqrt{f_c}} \tag{1.11}$$

or, for members with detailing for earthquake resistance and no lapping of longitudinal bars near the section where yielding is expected,

$$L_p = 1/30 \cdot L + 0.2 \cdot D + 0.11 \cdot \frac{f_y \cdot d_b}{\sqrt{f_c}} \tag{1.12}$$

where d_b is the mean diameter of the tension reinforcement, and f_c and f_y in MPa. Whether to use Equation (1.11) or (1.12) depends on how the enhancement of strength and deformation capacity of concrete due to confinement is taken into account in the calculation of the ultimate curvature of the end section. Note that the critical region above the base of the wall, where special detailing specifications apply, may be estimated as $h_{cr} = max[L_w, H_w/6]$, but $h_{cr} \leq 2L_w$ and less or equal than one clear story height.

1.6 Summary Remarks

The purpose and motivation of this dissertation are explained in this Chapter. In addition, a comprehensive literature review related to the response of reinforced concrete shear walls under cyclic loading and to the behavior of anchors in cracked concrete is provided to backup this work.

Central to this dissertation is the behavior of post-installed anchors in seismic regions. Post-installed anchors are widely used to connect nonstructural component and systems to concrete buildings, which can deform significantly under seismic loads and develop plastic deformations and cracks. Anchors, however, perform poorly in cracked concrete, as they rely on the integrity of the concrete surrounding the installation hole to develop their anchoring mechanism. Previous research on anchors and cracks demonstrated that anchor performance is affected by the crack width value measured nearby the anchor location, and by the cyclic opening and closing of cracks in anchor's vicinity. However, anchors should remain functional in cracks and damaged concrete condition, and to account for this, qualification guidelines (EOTA TR 045 2013) suggested testing in cracked concrete. However, only flexural cracks,

typical of flexure dominated reinforced concrete members, were considered in the definition of these tests, neglecting the shear characteristics of cracks. In particular, other types of structural concrete members, such as concrete walls, may develop various cracking responses when laterally cycled. To address this observation, testing of anchors in full-scale reinforced concrete shear walls and robust numerical analyses are needed. To provide varying boundary conditions to the anchors, full-scale walls with the anchors installed in one face are tested under simulated seismic loads and varied constant levels of axial load. Moreover, different aspect ratios of the walls are considered to explore a wide range of cyclic opening and closing of cracks at the anchor location. Anchor performance during lateral wall cycling is then assessed and residual anchor load capacity is measured at the end of the wall tests. Guidance on anchor installation in concrete shear walls is offered after comprehensive numerical analyses. Complementary numerical simulations are performed within the study presented in this dissertation to identify the best practices when predicting concrete shear walls cyclic response. Finally, the numerical model is extended to a parametric study involving a wide range of detailed and aspect ratio walls to identify regions of accumulated damage and large cracks prohibiting anchor installation.

1.7 Organization of Dissertation

The research efforts presented in this dissertation are organized within Chapters 2 - 6 as follows:

- Chapters 2 and 3 present the slender (AR=2) and the squat (AR=1) full-scale walls design and test setup. Experimental data summarizing the wall specimens' response to simulated earthquake loads are also analyzed and discussed in detail, with a focus on the wall damage evolution and crack pattern, as this particularly has implications on the anchor capacity.

- Chapter 4 presents the anchor load and displacement data measured during the wall tests. Seventy-two total post-installed anchors were installed in the three full-scale walls, counting two types of anchoring mechanisms typically used in practical shear wall applications. During the wall cycling tests, the full-scale walls described in previous Chapters imposed unique boundary conditions to the anchors installed in the walls' faces. Anchor load reduction and measured displacement of these anchors is compared in Chapter 4 and related to the amount of concrete damage exhibited by the walls. Finally, residual anchor load capacity is assessed at the end of the wall cycling via

tension to failure tests and compared to the reference anchor capacity in uncracked concrete.

- Chapter 5 presents the validation of a numerical nonlinear finite element method developed to predict wall response. Validation against full-scale walls develops confidence in the model, which can hence be used to extend the experimental data on the response and the damage evolution of various concrete walls. The work presented in Chapter 5 develops best practices for assessing global and local response of concrete shear walls, particularly in form of comparison with crack patterns using the smeared crack assumption.

- Chapter 6 presents numerical efforts to expand the experimental data to various types of wall geometry and detailing. Predicting the wall seismic response and identifying the wall damage under simulated seismic loads is important to design anchor location to fasten nonstructural components and systems to structural elements.

- Chapter 7 summarizes major findings and contributions of the work presented in this dissertation and highlights additional work needed in the future.

- Appendices contain additional material useful to integrate the main body of the dissertation. In particular, Appendices A and B support Chapters 2 and 3 documenting the shear wall specimens' design calculations and the construction material data obtained from tests on concrete and reinforcing bars. Similarly, Appendices D, C and E support Chapter 4 reporting information on anchor seismic load and capacity, crack width histories, and anchor response data measured during the wall tests. In addition, Appendix F shows the final wall damage after anchor tension to failure tests, obtained using the Structure from Motion technique. Finally, Appendix G shows an example code used to perform the numerical validation effort and the parametric study presented in Chapters 5 and 6, respectively.

Chapter 2

Slender Wall Test Program

To investigate the behavior of post-installed anchors in walls that develop shear-flexural cracks, a slender full-scale wall typical of a two-story building was designed according to U.S. design codes. Seismic loading was imposed on the wall through an equivalent cyclic displacement history applied at the wall top. The specimen failed in flexure, precipitated by buckling and fracture of the boundary reinforcement. The local and global response of this full-scale wall is documented herein, with particular emphasis on the evolution of cracking. Such cracks result in the boundary conditions to the anchors, whose behavior is discussed in Chapter 4.

2.1 Motivation

Reinforced concrete (RC) shear walls provide sufficient lateral strength and stiffness against wind and/or earthquake loading to RC buildings. The global behavior of RC shear walls is typically characterized via a combination of flexural and shear contributions. As a result, the types of response to lateral loads are categorized according to the aspect ratio (AR) of the wall (defined as wall height/length). On one extreme, a squat wall with a low AR ($\leq$ 1) tends to behave in a shear-dominated mode. On the other extreme, slender walls, with a high AR ($\geq$ 2) exhibit flexure-dominated behavior. Naturally, intermediate walls respond in a coupled shear-flexure mode. In this investigation the focus is on slender, flexure-dominated shear walls. In a follow-up study, squat, shear-dominated walls, as well as axial load amplitude, are investigated (see Chapter 3). The presence of damage in concrete walls may significantly

affect the strength of anchors embedded in the wall. However, the magnitude of strength reduction will be sensitive to the nature and location of the cracks that develop. In the context of post-installed anchors (such as expansion anchors, adhesive anchors), stress fields are induced by the anchor during installation, and these can be a source of crack initiation prior to and during the imposition of earthquake loads. It is therefore important to understand cracking and damage as it evolves in concrete shear walls to determine the influence of wall damage on anchors behavior and vice versa. This may have implications for anchor qualification and for guidelines regarding the location of anchors in walls.

2.1.1 Previous Experimental Investigations

Prior large-scale lateral cyclic RC shear wall test programs of interest to the current program are reviewed in Chapter 1. In this section particular attention is given to three large-scale test programs, which include well-documented observations on crack characteristics. These wall specimens were designed according to recent codes and practices, thus they serve as a guide in the design of the present specimen and baseline for comparison.

An experimental program by Dazio et al. (2009) involved testing of six half-scale RC wall specimens, designed according to the European code with AR=2. These specimens had dimensions of 79 inches long, 159 inches tall and 6 inches thick. Varied longitudinal reinforcement ratios were selected (0.27-0.54% in the web and 0.67-1.54% in the boundary elements), while the horizontal reinforcement ratio was constant at 0.25% for all specimens. The applied axial load ranged from 5% to 13% of the gross cross-sectional capacity. Test results showed that the quantity of the longitudinal reinforcement offered the most pronounced effect on the global ductility, the crack pattern and the failure mode (Dazio et al. 2009).

Similarly, Tran and Wallace (2015) tested five half scale cantilever walls designed according to US practice, three with an AR=2.0 and two with an AR=1.5, to investigate the inelastic response of high aspect ratio cantilever walls. The 6 inches thick and 48 inches long walls had reversed cyclic lateral load applied at either 72 or 96 inches above the wall-foundation block interface. Two constant design axial load ratios were applied, namely 10% and 2.5% of the gross sectional capacity, and two levels of average shear stress at nominal flexure capacity were considered. Test results showed various failure modes, from diagonal tension failure to diagonal compression failure, according to the level of shear stress (Tran and

Wallace 2015).

Jiang et al. (2013) tested scaled RC shear walls reflecting common design practice in China to define the damage levels corresponding to different performance levels. The seven I-shaped, T-shaped and rectangular specimens, 39 inches long, 79 inches tall and 4 inches thick walls, were designed with a horizontal reinforcement ratio of 0.66%. The vertical reinforcement ratio was 1.25% for the five I-shaped specimens and 1.51% for the T-shaped and rectangular specimens. Results showed that the maximum crack width decreased with increasing axial load and demonstrated the remarkable restraining effect of axial load on crack opening (Jiang et al. 2013).

The aforementioned test programs were cross-compared to understand the impact of select design parameters on the maximum crack width at yield $w_{max,y}$. The maximum crack width is an important parameter when considering the behavior of anchors in the wall. Of particular interest are the values of $w_{max,y}$ as a function of aspect ratio AR, boundary element reinforcing ρ_{BE}, and the axial compression applied during the test. Particularly, the axial load ratio $\frac{P}{f'_c A_g}$, defined as the ratio of the applied axial load, P, to the section capacity, $f'_c A_g$, was selected as a control parameter for its known influence on crack opening (Jiang et al. 2013). Fig. 2.1 shows that the maximum crack width at yield ranged between 0.2 mm to 1.2 mm, with about 75% of the specimens exhibiting a maximum crack width at yield of less than 0.5 mm. The wall specimen with no boundary confinement in Dazio et al. (2009) experienced the largest cracks at yielding with reported values of 1.2 mm, for the lack of confinement and the relatively low ρ_{BE}. Maximum crack width at yield generally increases with an increasing aspect ratio of the specimens. Conversely, large values of axial load ratio or large amounts of reinforcement in the boundaries reduced the width of cracks at yield, as indicated by the trend lines in Fig. 2.1.

2.1.2 Scope of the Slender Wall Test Program

The analysis of data represented in Fig. 2.1 guided the design of a full-scale shear wall constructed and tested at the University of California San Diego. To capture a common design scenario, the aspect ratio of the wall was selected as 2.0, and the boundary element reinforcing ratio $\rho_{BE} \approx 2\%$ was defined. A target 10% axial load ratio was also selected in consultation with experts in the field of reinforced concrete (Ghosh 2016), data in the literature (e.g., Fig. 2.1) and surveys on multistory building walls (Birely 2012). ACI 318 (2014) was adopted to design a ductile wall specimen, with the intent of

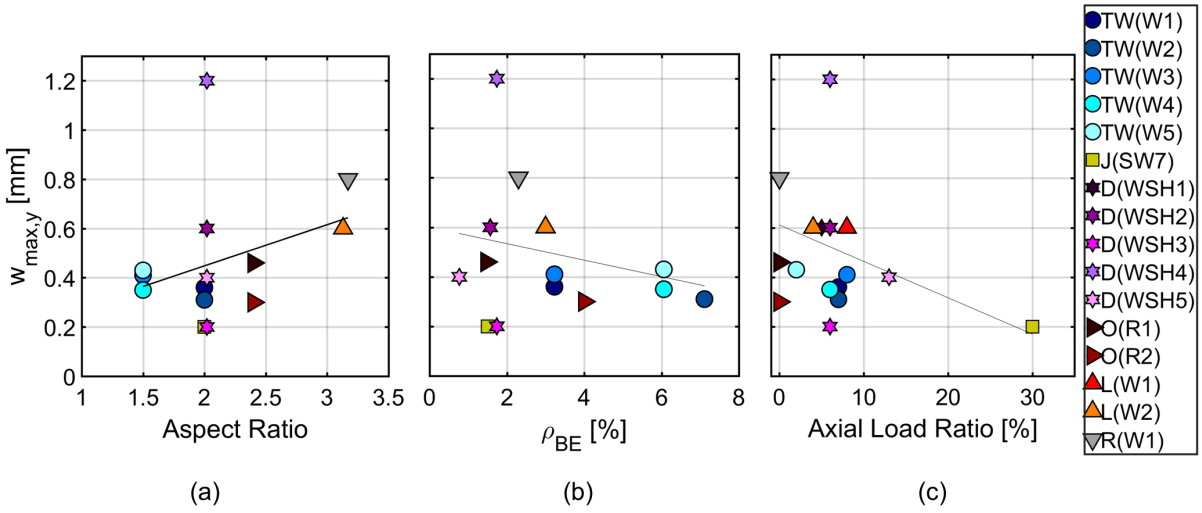


Figure 2.1: Maximum crack width at yield versus (a): aspect ratio AR; (b): reinforcement ratio in boundary elements ρ_{BE}; and (c) axial load ratio of rectangular section shear walls. Note: Axial load ratio defined as axial load P divided by sectional compressive capacity (i.e., cross section area $A_g \cdot f'_c$). See Table 1.4 for mapping with legend nomenclature

developing a widespread flexural dominated crack pattern under the action of lateral load. In this context, the contemporary design philosophy of RC shear walls focuses on the presence of boundary elements, i.e., the heavily reinforced and confined zones at the ends of a wall, which may enhance the wall strength and increase the energy dissipated as the wall behaves inelastically. Moreover, an increased reinforcement ratio at the wall boundaries is known to promote yielding over a greater wall height and to better distribute the flexural cracks. An increased lateral displacement capacity with respect to a wall with distributed longitudinal bars is also expected (Moehle et al. 2011). The design of the wall was supported by conducting nonlinear numerical analyses with the open source program OpenSees (McKenna et al. 2000). In this work, an improved version of the multiple vertical line element model (MVLEM) was selected from the available numerical tools in OpenSees. The SFI-MVLEM, a fiber-based model described in Chapter 5, was first calibrated against wall specimens from the literature, as documented in Faraone and Hutchinson (2018), and a sensitivity study was then performed. With confidence in the model, a parametric study was undertaken to systematically study the impact of various design parameters on the global crack pattern in the wall with the goal of obtaining predicted stabilized cracks extending a significant length up the height of the wall. In what follows, the final designed and tested wall and key results regarding its global and local response are described. The experimental observations of this unique full-

scale shear wall behavior are of focus in the present Chapter. Chapter 5 compares these wall test results with predictions obtained via finite element modeling, while Chapter 4 presents the findings related to the performance of the anchors installed within the wall.

2.1.3 Research Significance

The maximum expected crack width, distribution, and type of cracks in RC shear walls as related to global response parameters, such as drift and strength, provide an important indicator of damage, which in turn is relevant for anchors installed within the walls. To this end, a unique full-scale RC shear wall, designed as a ductile component according to current design codes, was tested under simulated seismic loading and the evolution of cracking and damage carefully documented. Thirty-six anchors, installed along the breadth and height of the specimen, were thus subjected to the evolving cracked concrete conditions.

2.2 Wall Details and Construction

2.2.1 Program Overview

A full-scale, slender, $AR = 2$ RC shear wall was designed, constructed and tested under combined constant compression and reversed cyclic lateral loading. Unique to previous full-scale RC wall tests, this specimen was intended to assist with understanding the performance of concrete anchorage in evolving concrete cracks. For this purpose, one face of the wall was instrumented to monitor the global response of the full-scale slender wall, while anchors were installed in the other face to inspect their behavior in progressively damaged concrete. The results of the performance of the anchors installed in these walls are cross-compared and used to elicit insight into the implications of the presence of progressively developing seismic-induced cracks on anchor load capacity in Chapter 4. Wall design and description of the test setup is reported in the following sections. Additional information on the wall design calculations and material tests are summarized in Appendix A and Appendix B, respectively, while other data and results of this test are exhaustively described in Faraone and Hutchinson (2018).

2.2.2 Design of the Wall and Description of Test

The wall was designed in accordance with the most recent design codes at the time of construction (ACI 318 2014, ASCE/SEI 7-16 2016) and assuming a 2-story office prototype building. The baseline size of the prototypical load bearing RC wall was 24 ft tall by 8 ft long. Considering the resultant lateral load applied at 2/3 of the total height, the physical specimen was constructed with a height of 16 ft. The prototype building was assumed located in downtown Los Angeles (34.040° N, 118.247 ° W), at a site class D, with mapped spectral response acceleration values, $S_{DS} = 1.555g$ and $S_{D1} = 0.819g$, taken from the USGS website (USGS, 2018). The design was based on the response modification factor R=5, assigned to bearing wall systems with special reinforced concrete shear walls (ASCE/SEI 7-16 2016). Ordinary normal weight concrete with specified compressive strength of 5 ksi and deformed reinforcing bars ASTM A615, grade 60, satisfying the requirements of ACI 318 (2014), were used in concert with conventional practice. Seismic load combinations produced the governing axial load, moment and shear at the base of the wall. The governing shear, V_u= 77 kips, was used to determine the minimum thickness of the wall by limiting the average shear stress in the wall to $3\sqrt{f'_c}$. However, the minimum thickness

was controlled by the slenderness limitations, included in ACI 318 (2014), expressed by $\frac{l_u}{16} = 12$ inches, where l_u is the unsupported height of the wall, i.e., 16 ft. The 12 inches thick wall was estimated to experience less than $\sqrt{f'_c}$ average shear stress. The embedment depth of the anchors was also satisfied by the selected thickness. The governing axial load, P_u= 154 kips, and moment at the base of the wall, M_u= 1490 kip-ft, were used to determine the layout of the vertical reinforcement, namely $9-$#6 bars in the boundary elements and $14-$#6 bars in the web region, spaced 8 inches on center (Fig. 2.3). The web reinforcement ratio, ρ_v= 1%, satisfied the minimum ρ_v= 0.25% in ACI 318 (2014), §18.10.2.1, and lap splicing of the vertical reinforcement was avoided. The flexural strength of the wall at P_u was estimated to be M_n= 4331 kip-ft and the top shear at the flexural strength resulted $V@M_n$ = 271 kips. The shear demand at the base of the wall, V_u^*=284 kips, was calculated considering the probable flexural strength, M_{pr}= 5002 kip-ft, obtained with an amplified reinforcement strength of 1.25 f_y= 75 ksi, see the axial force moment interaction diagram in Fig. 2.2. A shear amplification factor, ω= 1.1, was also included in the calculation of V_u^* to account for inelastic dynamic effects. For the shear capacity equation in ACI 318 (2014) §18.10.4.1, the required amount of horizontal reinforcement to satisfy the shear demand was 0.3% (greater than the minimum by code, ρ_h= 0.25%), which was provided by #4@6 inches on center. The resulting shear strength was V_n= 543 kips.

Sliding shear resistance was verified according to ACI 318 (2014) §22.9.4.2, under the undesirable assumptions of not roughened surface and absence of axial load, despite the wall-footing interface was roughened, as prescribed in ACI 318 (2014), and 500 kips of axial load (corresponding roughly to 10% axial load ratio) were constantly applied during the wall test. Finally, boundary elements were detailed according to ACI 318 (2014) §18.10.6. Noteworthy ACI 318 (2011) did not require special boundary elements for the specimen in object, but ACI 318 (2014) did trigger the need for special confined boundary zones in the wall, due to the prescribed smaller lower limit of the ultimate design drift with respect to the previous version (see Ghosh 2016). Transverse confinement was provided by #4 tie sets 4 inches on center, and the horizontal reinforcement was anchored inside the confined core, see Fig. 2.3. The confined boundaries were detailed to extend 18 inches horizontally and 96 inches vertically from the critical section, see Fig. 2.3. The average material characteristics were determined from material tests on the day of the wall cyclic test. The average concrete strength as determined on concrete cylinder compression tests was f'_c = 6 ksi. The average yield and tensile strength of the longitudinal

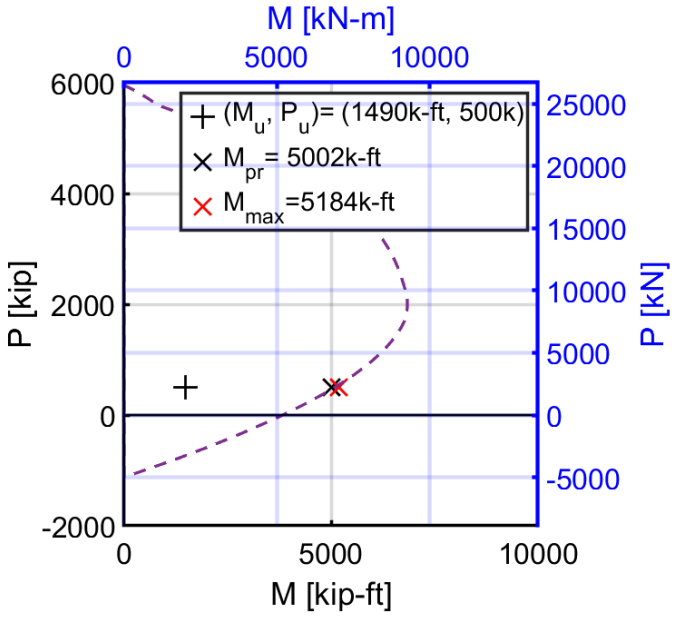


Figure 2.2: Moment-axial force interaction diagram. Probable moment strength, M_{pr}, determined using a tensile strength of 1.25 f_y, and maximum moment, M_{max}, from the wall test are also shown. [1 in = 25.4 mm, 1 kip =4.45 kN]

reinforcing bars of the wall were 73 ksi and 101 ksi, respectively. Additional information on material tests is reported in Appendix B.

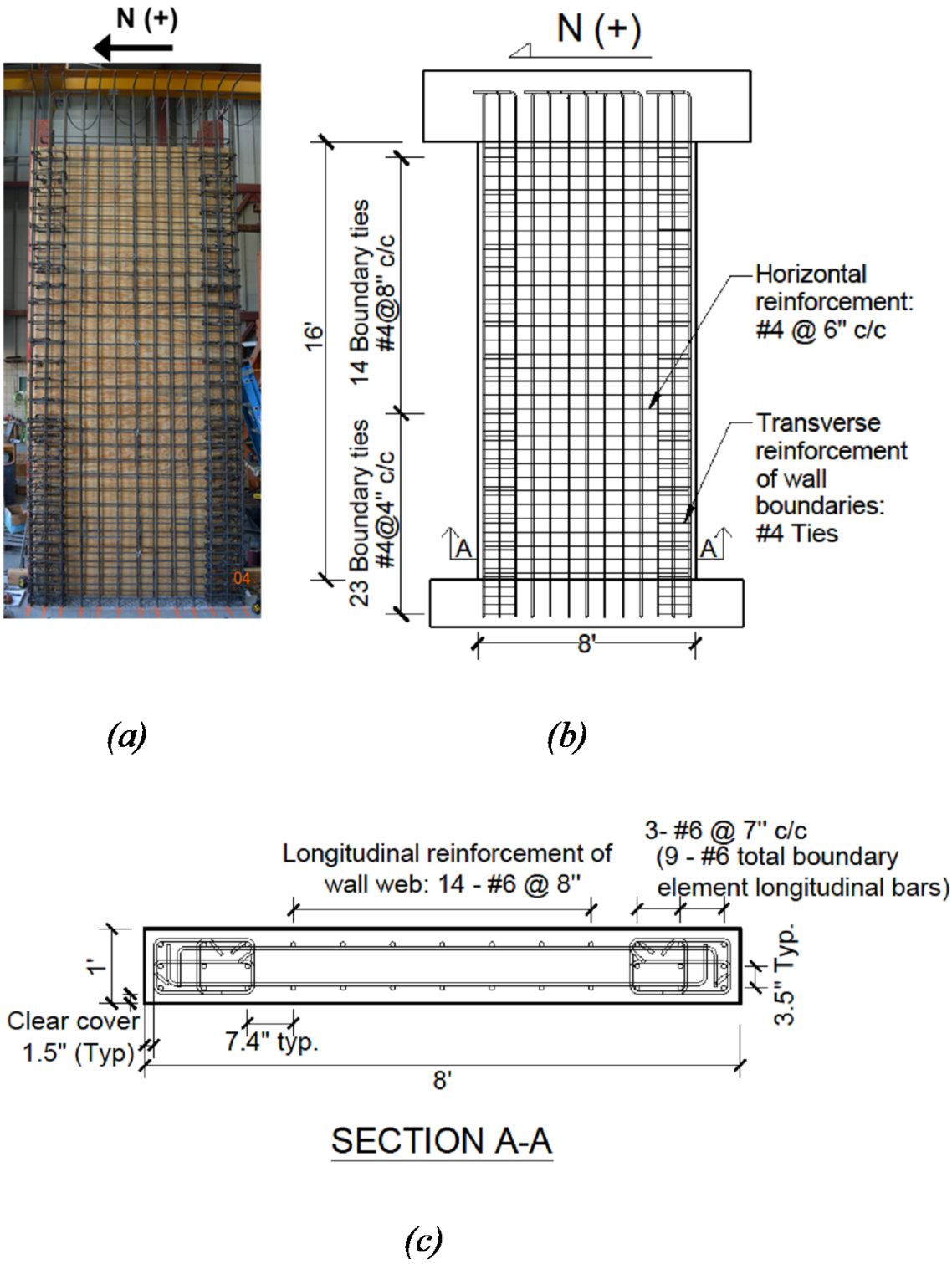


Figure 2.3: (a) Photograph of the reinforcement cage during construction, (b) elevation drawing and (c) cross section reinforcement details

2.2.3 Test Setup and Instrumentation

The full-scale wall was tested in its normal vertical position, see the annotated photograph in Fig. 2.4 and the schematic of this test setup in plan and elevation view in Fig. 2.5. The wall was connected to the strong floor via post-tensioning through an RC footing. The height of the footing was dictated by the necessary development length of the wall longitudinal reinforcement and it was designed to resist the potential for tension splitting introduced by the post-tensioning system, and to counteract sliding and uplift during the wall cyclic test.

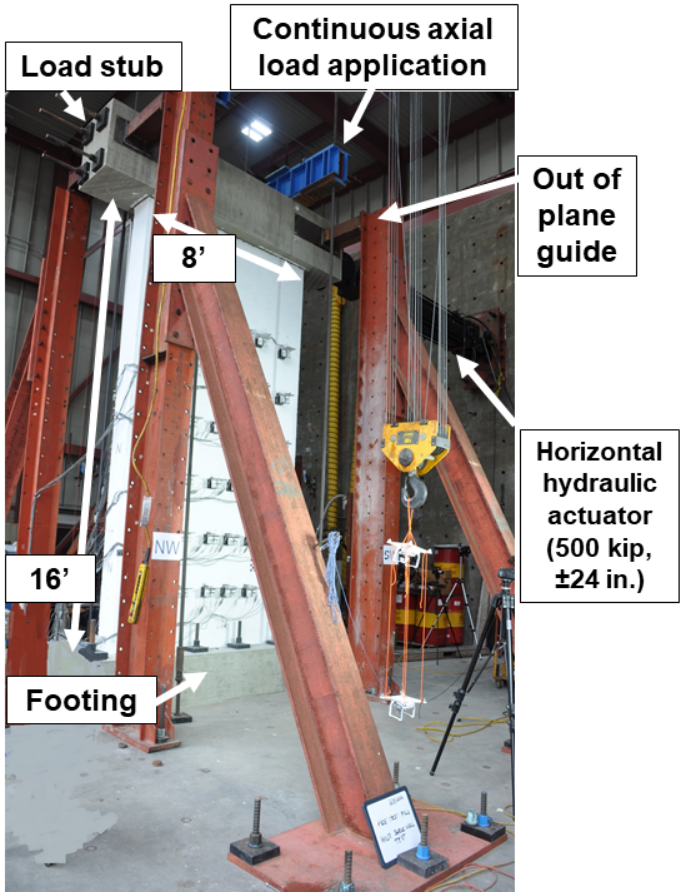


Figure 2.4: Annotated photograph of test setup (Northwest view). [1 in = 25.4 mm, 1 kip =4.45 kN]

The lateral load was applied by a 500 kips hydraulic actuator, attached to the strong wall to one end and to the RC post-tensioned load stub at the top of the wall to the other end, as shown in Figs. 2.4 and 2.5. Out-of-plane guides prevented wall twisting during the lateral load application. Four post-tensioned threaded rods transferred 125 kips each of axial load from the top of the load stub to the wall,

through two steel spreader beams mounted transversely on top of the load stub, see Fig. 2.5(a). Axial load was applied prior to imposing lateral displacement and it was held constant, sans small variations due to the rotation of the rods at very large lateral displacements of the wall.

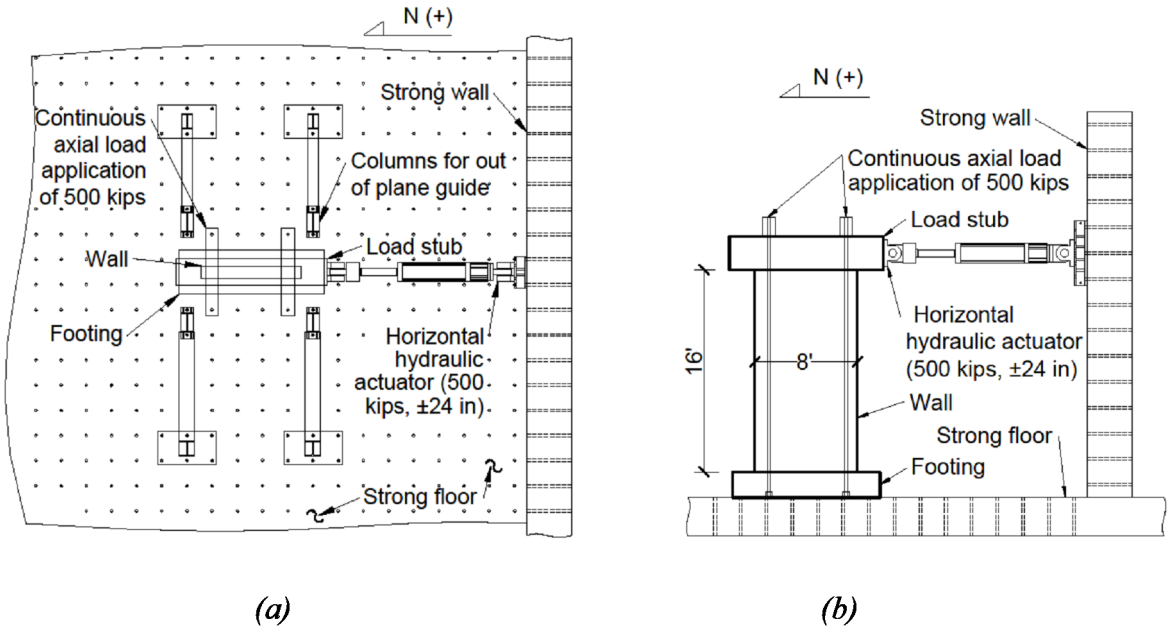


Figure 2.5: Schematic of test setup- (a) plan view and (b) elevation. [1 in = 25.4 mm, 1 kip =4.45 kN]

Twenty-six linear potentiometers, installed on the East face of the wall as shown in Fig. 2.6, measured wall displacements, uplift, and sliding during the wall cyclic test. The test wall was divided into three sections with at least one pair of vertical and diagonal displacement gauges each. The lower 0.5 L_w= 4 ft, which is the theoretical plastic hinge length for ACI 318 (2014), was instrumented with three pairs of vertical sensors to better capture the anticipated nonlinear strain profile within the most damaged region. Strain gauges measured the local strains in the reinforcing bars at fifty-two locations, placed within the cross section, up to about 6 ft from the wall-footing interface. Crack widths were measured at discrete locations during the test. Namely, high precision linear potentiometers were used to measure the crack width histories at four locations close to the anchors within the theoretical plastic hinge length. In addition, eight manual crack width sensors were installed close to other anchors outside of the theoretical plastic hinge length. The crack width sensors were installed upon the first visual presence of hair line cracks during the early stages of lateral loading of the wall.

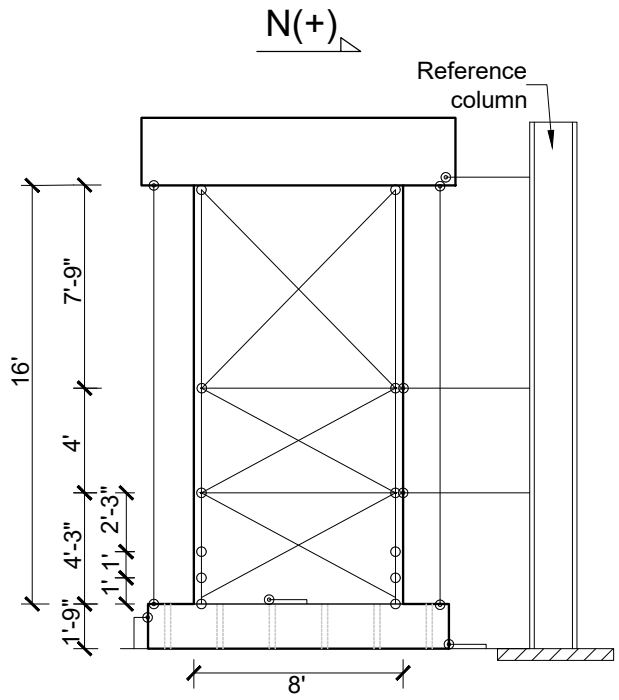


Figure 2.6: Global sensors on the wall: linear potentiometers in the East wall elevation. Note: Theoretical plastic hinge length = 0.5 L_w (L_w = wall length = 8') [1 in = 25.4 mm, 1 kip =4.45 kN]

2.2.4 Test Procedure

The adopted displacement protocol followed ACI 374 (2013) recommendations, see Fig. 2.7. Namely, three cycles per amplitude were imposed within the linear, quasi-linear, expected yield, and up to 1.0% (four times the expected yield) drift amplitudes. Subsequently, severe damage was anticipated, therefore the drift ratio was incremented by twice the predicted yield drift. The displacement-controlled protocol was intended to continue at increasing 0.5% increments until at least a 20% drop in load capacity was realized. The final protocol involved three cycles at 0.125%, 0.25%, 0.50%, 0.75%, 1.0% drift and two cycles at 1.50%, 2.0% and 2.5% drift as shown in Fig. 2.7. Significant load reduction was realized during the final cycle at 3.0% drift. Visual inspections were performed at the first cycle of each drift amplitude and in each of the North (+) and South (-) directions, and at zero drift following completion of a cycle amplitude group. Open cracks were marked during each displacement hold, while loads in the anchors were reviewed, and if needed reloaded to the target tension load.

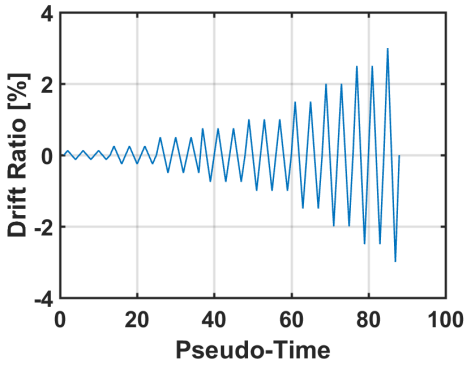


Figure 2.7: Displacement protocol adopted from ACI 374 (2013)

2.3 Experimental Results

Analysis and interpretation of test results is presented in this section. Additional information on crack width values measured during the test is summarized in Appendix C, while other data is exhaustively described in Faraone and Hutchinson (2018).

2.3.1 Wall Global Response

The global response of the wall is characterized by presentation of its lateral force versus drift ratio response, see Fig. 2.8, which also includes annotation of the first yielding and strength. Table 2.1 summarizes important response parameters, namely the lateral strength and displacement at the first observed crack, at the first measured yield of the boundary longitudinal reinforcement, at strength and at 3% drift ratio. The latter value of 3% was selected to offer an indication of the strength reduction of the wall at final failure. It is noted that the estimated first yield was 0.25%, while the first yield as measured by discrete strain gauges (Table 2.1) occurred at 0.4 and 0.5% in the North (+) and South (-) directions, respectively. For the purposes of subsequent discussions, the theoretically estimated first yield of 0.25% was utilized in recognition of the discrete locations of strain gauges.

The hysteresis in Fig. 2.8 also offers an opportunity to assess the stiffness of the wall and compare it with design-based estimates. At first observed wall cracking for example, the average (of North (+) and South (-) directions) cracked stiffness was about 1371 kip/in, while at first yield the average stiffness had softened by 54%, to about 634 kip/in. The experimental stiffness at first crack compares well with the commonly adopted value of $EI_{cr} = 0.5EI_g$. Finally, the maximum lateral load was approximately

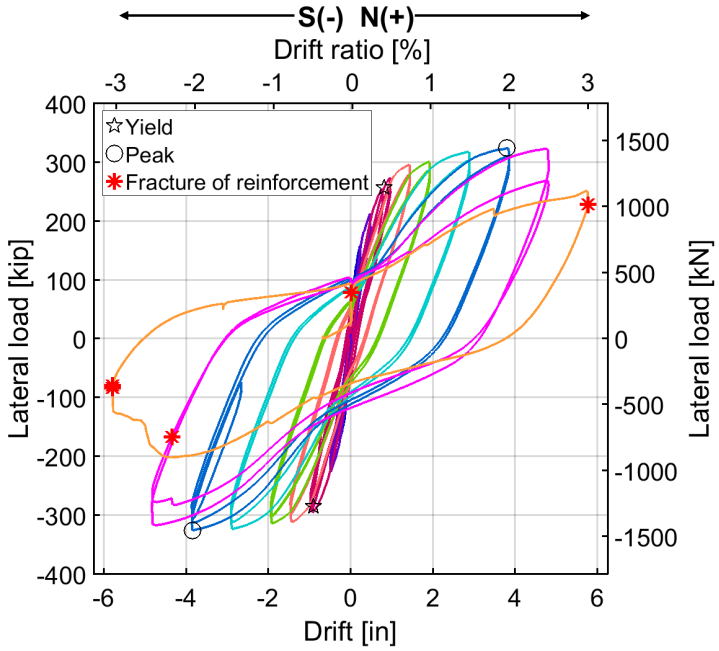


Figure 2.8: Lateral load versus top wall displacement (and drift ratio) [1 in =25.4 mm, 1 kip =4.45 kN]

$0.6V_n$, with V_n being the expected shear strength of the cross section and approximately 1.04 $V@M_{pr}$, where M_{pr} was the probable flexural strength of the wall (Fig. 2.2).

Table 2.1: Test results summary

Loading Direction	First crack[1]		Yield[2]		Strength		3% Drift Ratio	
	V [kip][3]	Δ [in][4]	V [kip][3]	Δ [in][4]	V [kip][3]	Δ [in][4]	V [kip][3]	Δ [in][4]
North (+)	145	0.21	257	0.82	324	3.84	252	5.73
South (-)	167	0.24	292	0.98	326	3.84	123	5.76

[1] : instance of first observable crack

[2] : first yield from measured strain in reinforcing bars

[3] : 1 kip = 4.45 kN

[4] : 1 in = 25.4 mm

2.3.2 Damage Evolution

The evolution of damage in the wall was characterized by documenting the pattern and width of cracks and correlating these aspects with the yield drift ratio. Fig. 2.9 addresses this by sequentially presenting a visual of the crack pattern at increasing values of drift ratio, reported as a fraction of the

yield drift ratio. It is noted that Fig. 2.9 was generated by manual marking over photographs taken at the corresponding drift ratios. These plots show that the cracks are a mix of nearly pure flexural cracks at the ends of the wall, shifting towards shear cracks approaching the interior of the wall, and overlapping shear 'X' cracks within the middle regions of the wall. Moreover, the evolution articulated in Fig. 2.9 demonstrates that very early in the displacement protocol ($\approx 2\delta_y$, where δ_y = theoretical yield drift ratio), cracks have extended approximately 70% the height of the wall (H_w).

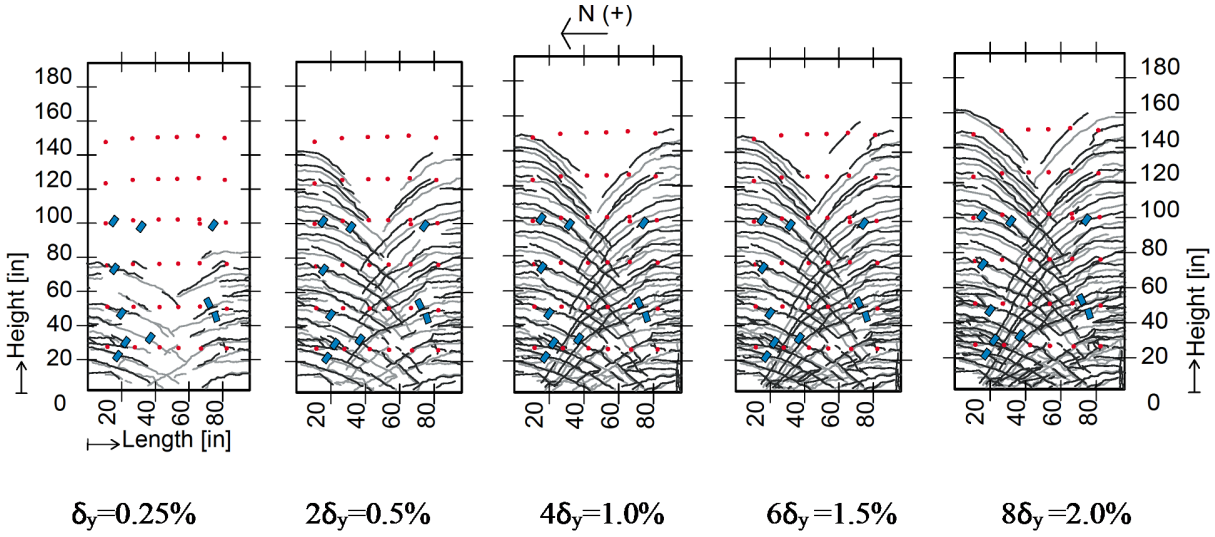


Figure 2.9: Evolution of the crack pattern reproduced using photographs taken at key drift ratios. Dark lines and light gray lines represent cracks on the West (anchors side) and East (no anchors) faces, respectively. Crack width sensors (blue boxes) and anchors (red circles) are also shown. [1 in =25.4 mm]

Though not depicted in Fig. 2.9, it is noted that initial cracking occurred at 0.125% drift level ($\approx \frac{\delta_y}{2}$) in the North and South toes of the wall, where horizontal flexural cracks extended vertically up to 45 inches ($\approx 20\%H_w$) from the wall-footing interface, with an average spacing of 8 inches and a maximum crack width of 0.25 mm. During subsequent cycles, three major diagonal cracks propagated from the wall toes (boundary elements) towards the middle of the wall. Estimated first yield occurred at about 0.25% drift ratio ($\approx \delta_y$) at a lateral load of 213 kips and the first couple of shear cracks intersected forming an interior 'X' on the East face of the wall, see Fig. 2.9. Flexure and shear cracks extended about 80 inches ($\approx 40\%H_w$) from the wall-footing interface and a maximum crack width of 0.5 mm was measured near the South toe of the wall. Diagonal and horizontal cracks continued to extend as the top drift ratio increased. Extensive concrete spalling occurred at 1.5% drift ratio ($\approx 6\delta_y$). On the South end, where a maximum crack width of 5 mm was measured, concrete spalling extended vertically approximately

10 inches ($\approx 5\%H_w$) from the wall-footing interface. At this stage minimal cover precluded visibility of the longitudinal reinforcing bars, however, as the drift amplitude increased to 2% drift ratio ($\approx 8\delta_y$), concrete spalling continued from the wall base at the South toe, and at the force at strength V_{max} = 324 kips, spalling extended 25 inches ($\approx 10\%H_w$) from the wall-footing interface. Large cracks, with widths up to 12 mm and a stabilized spacing between 5-6 inches were realized at this phase of the testing. Beyond 2% drift ratio ($\approx 8\delta_y$), the maximum elevation of cracks and damage did not change, however the width of all cracks grew substantially. Visible signs of buckling of the reinforcement were recognized at 2.5% drift ratio ($\approx 10\delta_y$) in the South boundary region of the wall. During the second cycle to this target amplitude, one longitudinal reinforcing bar ruptured at about 10 inches from the wall base, where during previous cycles the local bar curvature was the largest. During the final cycle to a target 3% drift ratio ($\approx 10\delta_y$), the lateral capacity dropped to 23% of strength, due to rupture of several other reinforcing bars, both in the North and South boundary elements. Ten longitudinal reinforcing bars (out of eighteen) fractured in total within the two end boundaries, see Figs. 2.10 and 2.11. The wall failed in flexure and the test ended with a residual drift ratio of 0.4% (0.7 inches) in the negative direction (South). At the end of the test, the region of surface spalling and subsequent crushed concrete extended vertically as high as 29 inches ($\approx 15\%H_w$) and horizontally for about half of the wall length, see Fig. 2.10.

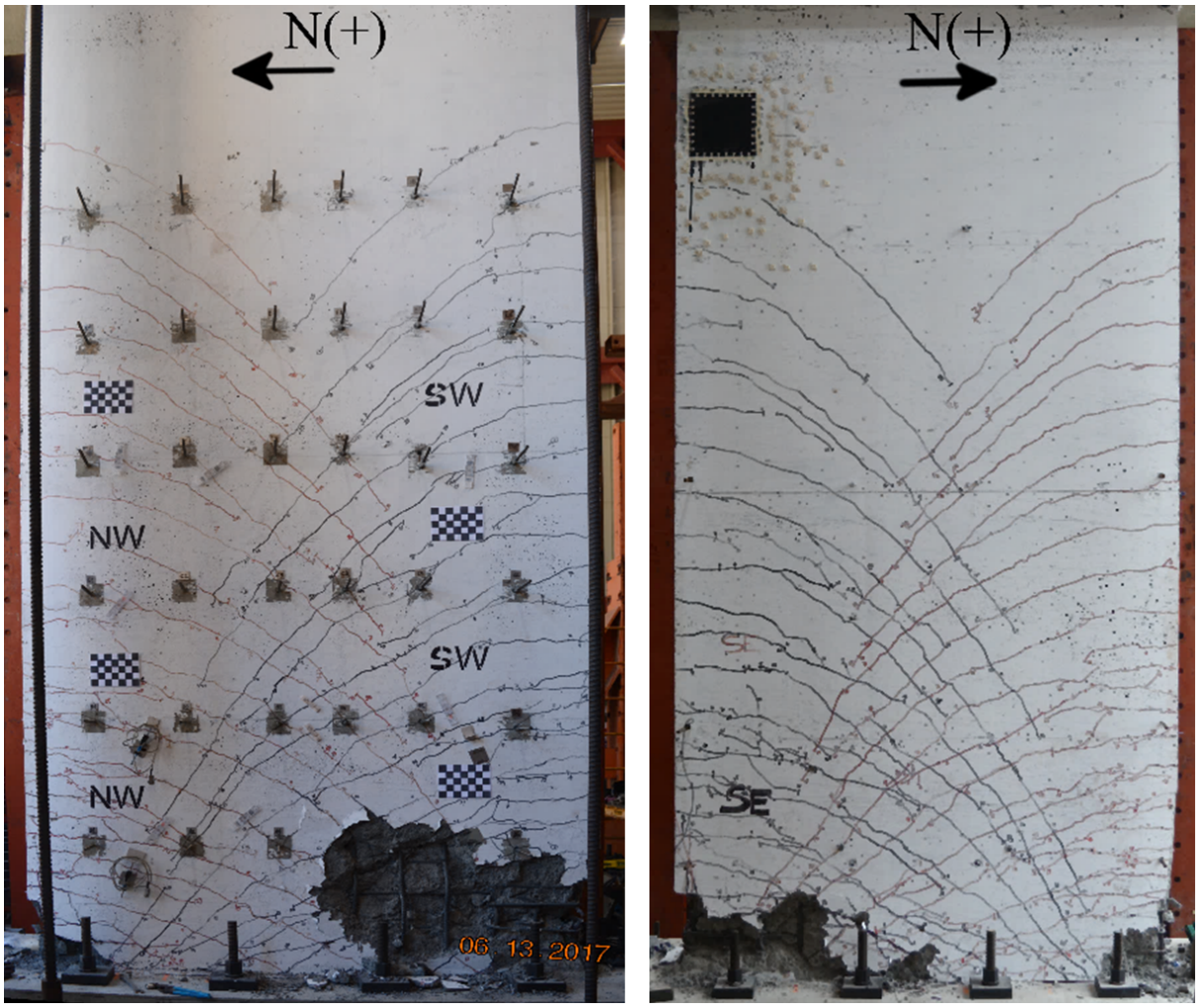


Figure 2.10: Photographs of (*left*) "anchor side" and (*right*) "no anchor side" wall faces at the end of the test. Residual drift δ_r=0.4% in the negative direction (South)

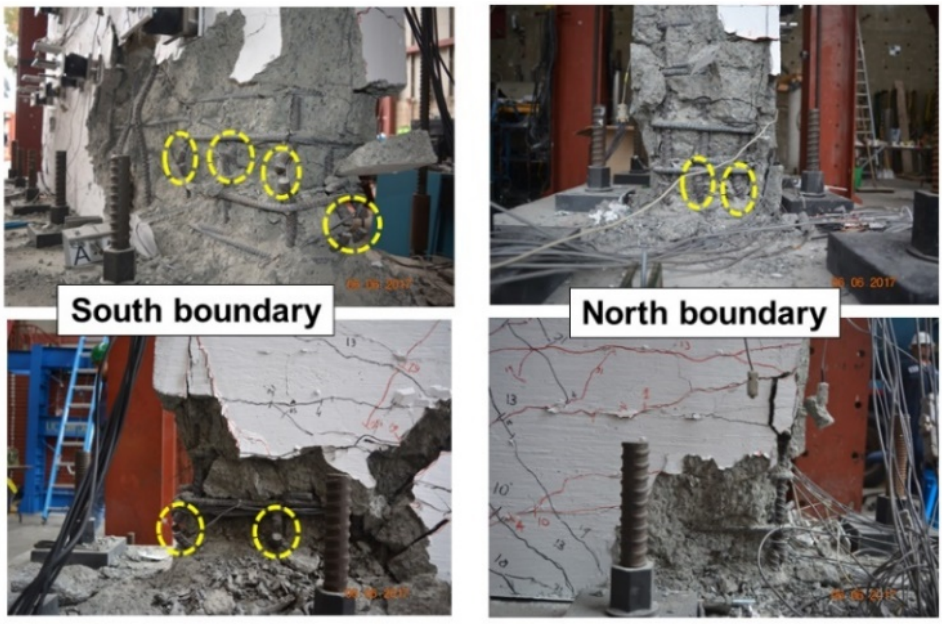


Figure 2.11: Photographs of South and North boundaries showing the fractured boundary longitudinal reinforcement at the end of the test (top row: end view, bottom row: wall face view)

2.3.3 Estimated Crack Spacing

The measured stabilized crack spacing, averaged on the two wall faces, was about 6 inches. It is noted that the crack pattern characteristics were overall similar in the two faces of the wall, despite the presence of the anchors in one face. Indeed, cracks evolved almost simultaneously on the two faces of the wall. It is noted however that the trajectory of select cracks were attracted by the field discontinuities afforded by the placement of the anchors, though this disruption was minor and a more or less similar pattern evolved on both faces, as it is evident in comparing the overlapping the two faces' crack patterns in Fig. 2.9. The average stabilized crack spacing observed in the test in the boundary elements of the wall specimen can be compared with empirical estimates available in design codes, considering the boundary element as a singular isolated column. It is noted that these estimated values were compared to the crack spacing as measured at the end of the wall test. The two estimates are also in ACI 224.R-01 (2001):

- European code (EC2) CEN (2008):

$$s_{r,av} = k_3 c + k_1 k_2 k_4 \phi / \rho_{BE} = 11 inches \tag{2.1}$$

  where k_3 =3.4, c is the cover, k_1 = 0.8 for deformed bars, k_2 = 0.8, being the boundary elements subjected to both tension and flexure, and k_4 = 0.25 to obtain an average estimation of the crack spacing.

- European Model Code for Concrete Structures CEB-FIP:

$$s_{r,av} = \frac{2\phi}{3(3.6\rho_{BE})} = 7 inches \tag{2.2}$$

The CEN (2008) slightly underestimates, with a larger value, the crack spacing, while the CEB-FIP expression aligns with the measured stabilized crack spacing of the full-scale RC wall. Nonetheless, both expressions offer reasonable estimates, despite the fact they were developed for beams where the spacing is associated with tension cracking only.

2.3.4 Components of Lateral Displacement

It is useful to understand the relative contributions of flexural, shear and sliding displacement components to the total lateral displacement of the wall. Notably however, the sliding between the wall and the footing was negligible during the entirety of the wall cyclic test. Flexural and shear components of the lateral displacement on the other hand are expected to be large contributors, and in this case were determined using the displacement sensors placed in an X configuration in the instrumented (no anchor) face of the wall (Fig. 2.6), using the methodology presented in Massone and Wallace (2004). Shear and flexural contributions to wall lateral top displacement are plotted in Fig. 2.12 versus the drift ratio. Values were computed at both positive and negative peaks of the first cycle at each wall drift amplitude. These analyses show that the flexural deformations accounted for about 80% of the lateral displacement and consequently the shear contribution to the total displacement were limited to about 20%. The shear displacement contribution reached a maximum value of about 35% of the total during the very last cycle of the test, when significant strength degradation occurred, and multiple reinforcing bars fractured. The shear to flexure displacement components ratio, Δ_s/Δ_f was almost constant at about 15%, over the 1% to 2.5% drift ratio range indicating predominately flexural behavior of the wall, see Fig. 2.12. This is consistent with prior studies, (e.g., Dazio et al. 2009; Beyer et al. 2011) who observed this ratio to vary between 10-30%.

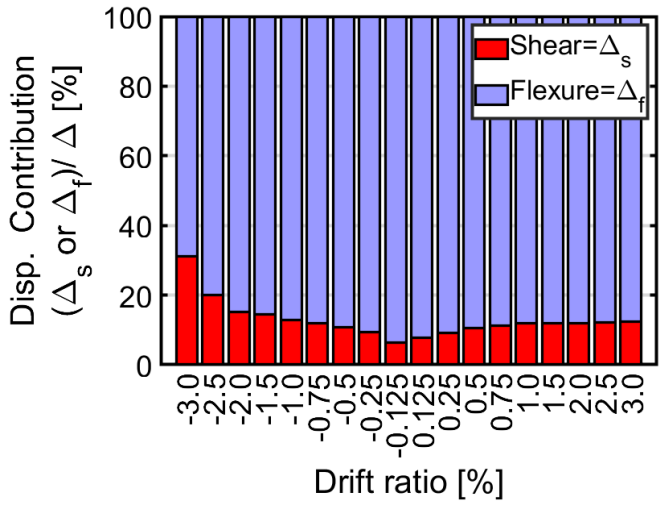


Figure 2.12: Top flexural and shear displacement contributions to total lateral displacement and shear to flexure displacement ratio versus wall drift ratio. Values computed at both positive and negative peaks of the first cycle at each wall drift amplitude

2.3.5 Vertical Wall Displacement

Vertical displacement gauges were used to measure the displacement at the end of the wall during the application of lateral cyclic loading. Notably, a non-negligible permanent residual vertical elongation of about 2.4 inches was recorded at the end of the test, as shown in Fig. 2.13. The elongation and subsequent fracture of the reinforcement ensued appreciable plastic deformation of the wall during testing and inevitably enhanced the vertical distortion. During the cycles at the last two drift amplitudes, when the reinforcing bars fractured, the vertical growth increased by five times the value at the end of 2% drift ratio.

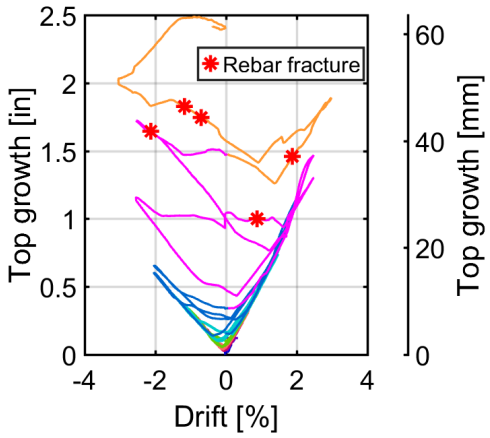


Figure 2.13: Vertical growth versus drift ratio

2.3.6 Plastic Hinge Zone Evolution

The length of the plastic hinge zone, L_{pz}, defined as the length over which the plasticity spreads, was estimated as the height above the footing where the curvature was equal to the yield curvature (Calvi et al. 2008):

$$\chi_y = 2\varepsilon_y / L_w = 6.x10^{-5} 1/in (\approx 2.51/km) \tag{2.3}$$

where ε_y is the yield strain of the reinforcement (= 0.3% in/in from material tests). The curvature profile, shown in Fig. 2.14, was estimated from the vertical and horizontal displacement gauges measurements. From the curvature profile, the plastic zone extends approximately up to 0.5 H_w and thus $L_p \approx 0.5 L_w$, being $H_w = 2L_w$. The maximum base curvature was measured to be about $1.5x10^{-3} 1/in$ [$\approx 24\chi_y$] at the end of the wall test.

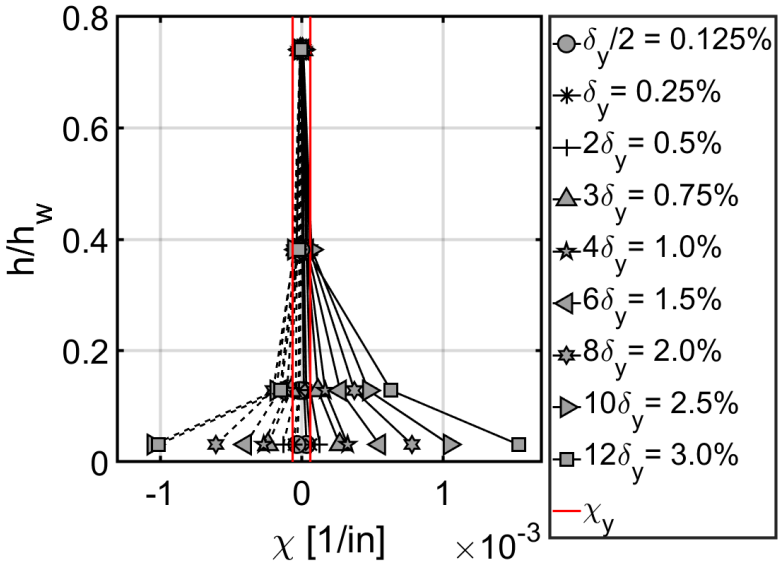


Figure 2.14: Curvature profile versus normalized wall height. [1 in= 25.4 mm]

For comparison, the plastic hinge length was also calculated using several empirical formulations from the literature, see Table 2.2. The value $L_p \approx 0.5 L_w$ by Park and Paulay (1975) was conservatively assumed as the theoretical plastic hinge length in the analysis of the anchor response. Fig. 2.15 graphically shows the results of the various analytical expressions. It is noted that the various expressions offer a lower bound to the plastic hinge length. Fig. 2.15 shows that the mean value of all the estimations in

Fig. 2.15 approximately extends as high as the spalled concrete region. The dotted line at 0.5 L_w in Fig. 2.15(b), instead, visually identifies the plastic hinge length as the height at which the steepest diagonal crack (extending from the base compression zone) intercepts the centroid of the boundary element, as it is suggested by Oesterle et al. (1976) in the presence of diagonal cracking. The considered analytical expressions were also applied to estimate the plastic hinge length of moderate scale wall specimens available in the literature (half-scale wall specimens WSH2-WSH6 tested by Dazio et al. (2009) and 1/3 scale R1 and R2 wall specimens tested by Oesterle et al. (1976), see Chapter 1). The success of these estimates compared with that measured by the various researchers and the present test program, is compared in Fig. 2.15(c). In general, the analytical expressions consistently provide a lower bound estimate of the plastic hinge length with the measured values approximately equal or greater than the maximum analytical value.

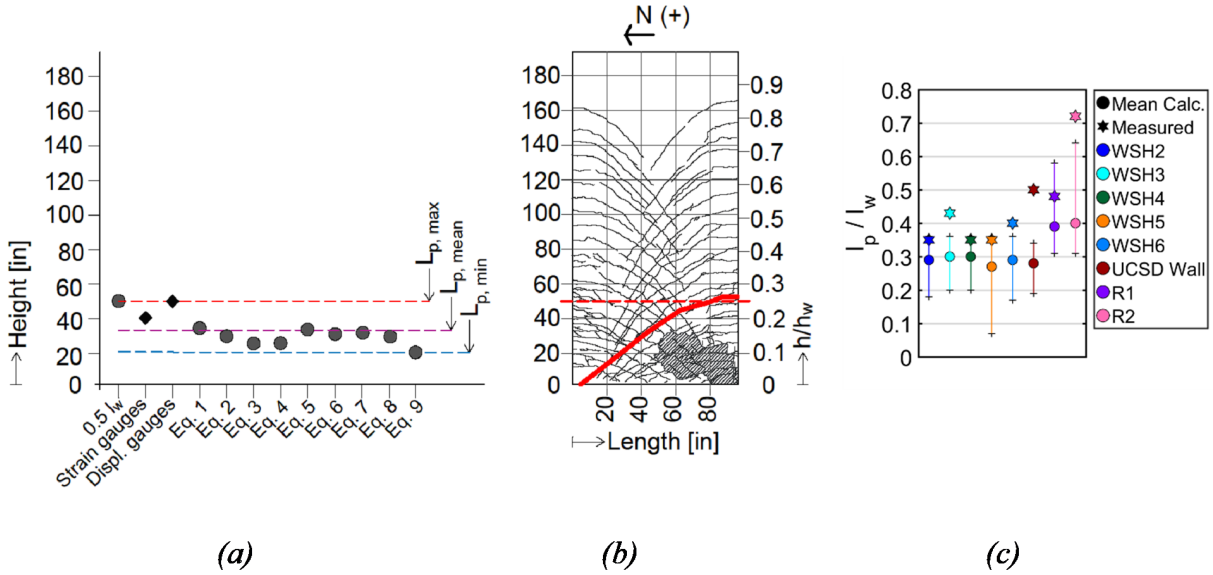


Figure 2.15: Estimated plastic hinge length values. (a) Measured test values compared to analytical predictions, from the equations in Table 2.2. (b) Graphical representation of the maximum value of the plastic hinge length on top of the damage pattern at the end of the full-scale wall test. The steepest inclined crack extending from the base compression zone to the centroid of the tension boundary element is highlighted. The height at which this crack intercepts the centroid of the boundary element is a rough estimation of the plastic hinge length in the presence of diagonal cracking (see Oesterle et al. 1976).(c) Comparison of the analytical predictions versus measured values of the plastic hinge length for the full-scale wall and for half-scale WSH2-WSH6 wall specimens (tested by Dazio et al. 2009) and 1/3 scale R1 and R2 wall specimens (tested by Oesterle et al. 1976)

Table 2.2: Empirical equations adopted to estimate the plastic hinge length in rectangular walls

	Reference	Equation	L_p/L_w
L_{p1}	Paulay and Priestley (1992)[1]	$0.2L_w + 0.07M/V$	0.34
L_{p2}	Paulay and Priestley (1993) [2]	$0.2L_w + 0.044H_w$	0.29
L_{p3}	Priestley et al. (1996)	$0.08H_w + 0.15f_y\Phi$	0.25
L_{p4}	Panagiotakos and Fardis (2001)	$0.12H_w + 0.014f_y\Phi$	0.25
L_{p5}	Thomsen and Wallace (2004)	$0.33L_w$	0.33
L_{p6}	Bohl and Adebar (2011)[3]	$(0.2L_w + 0.05M/V)(1 - 1.5P/f'_cA_g)$	0.27
L_{p7}	Kazaz (2013) [4]	$(0.27L_w)(1 - P/f'_cA_g)(1 - f_y\rho_h/f'_c)(M/VL_w)^{0.45}$	0.32
L_{p8}	Kazaz (2013)[4]	$0.143L_w + 0.072M/V$	0.29
L_{p9}	Aaleti et al. (2014)	$0.07H_w(1 - 10e^{-0.6\rho_t}P/f'_cA_g) + 0.15f_y\phi$	0.19

Note: Axial load ratio P/f'_cA_g at the time of testing was 7.5% for wall SQ7.5
[1] : Based on research specifically applicable to walls
[2] : Lower bound estimate
[3] : Lower bound estimate for isolated high-rise shear walls
[4] : Derived using the results of comprehensive nonlinear finite element analyses within a parametric study and verified against available shear wall tests results

2.4 Summary Remarks

Reinforced concrete shear walls are common structural components utilized in building systems. Structural and nonstructural components are often attached to concrete walls using metal anchors. These anchors can be significantly affected by the development of cracks and damage in the concrete wall. Previous investigations into the performance of anchor in cracks has been limited to anchorage in flexure-dominated concrete beams, with little focus on the impact of the broader types of cracking patterns expected in other types of structural components. In the present study, a slender full-scale reinforced concrete shear wall, designed to be a ductile specimen in accordance with current US practice, was constructed and tested under combined constant axial compression and reversed cyclic quasi-static displacement loading. Post-installed anchors were installed on one face of the wall and maintained under constant tension load during the axial and lateral loading to the wall. The experimental observations of this unique full-scale wall behavior as well as comparison with predictions provided via finite element modeling are of focus in the present Chapter, while Chapter 4 presents the findings related to the performance of the anchors installed within the wall. Coupled shear and flexure behavior dominated the response of the full-scale wall, which developed the design flexural strength and well distributed tension and shear cracks during the application of the increasing amplitude displacement protocol. Boundary

longitudinal reinforcing bars buckled and fractured at a target drift amplitude of 3%, resulting in about a 20% load capacity reduction. The wall failed in flexure, with concrete crushing and fractured reinforcing bars in the boundaries. The evolution of the crack pattern and the crack characteristics, namely the width and spacing, demonstrate the positive response of this flexural specimen. Furthermore, the measured flexural deformation was considerably larger than the shear deformation, the latter contribution to the total lateral displacement was on average less than about 20%. Shear contributions to the lateral displacement were estimated to be roughly constant for the duration of the cyclic displacement history applied to the wall, as expected for flexure dominated RC shear walls. A non-negligible wall vertical growth was measured at the end of the test, attributed to ten of the eighteen longitudinal boundary reinforcing bars fracturing. The plastification at the base of the wall was measured by the sensors installed in the wall, and the estimated measured plastic hinge length compared favorably with empirical relations available in the literature.

2.5 Acknowledgment of Publications

Chapter 2 contains material published in the following journal paper: Faraone, G., Hutchinson, T. C., Piccinin, R., and Silva, J., 2019, "Cyclic Lateral Load Response of a Full-Scale Flexure-Dominated Shear Wall" *ACI Structural Journal*. V. 116, No. 6, pp. 281-292. The dissertation author was the primary author on this paper. Chapter 2 also contains material published in the following report: Faraone, G. and Hutchinson, T. C., 2018, "Behavior of post-installed anchors in reinforced concrete shear walls subjected to cyclic lateral loading. Part I: slender wall test program" *Structural Systems Research Project Report SSRP- 2018/05*, UC San Diego. The dissertation author was the primary author on this report.

Chapter 3

Squat Wall Test Program

It is well known that crack patterns (types and extent of cracking) will vary depending primarily on the wall geometric characteristics, imposed axial load and detailing. While the aforementioned investigation in Chapter 2 focused on a slender wall, the present Chapter expands the experimental study to understand such crack pattern characteristics and anchor performance in squat walls under varying axial loads. To this end, two identical full-scale reinforced concrete shear walls with low aspect ratios were tested under equivalent seismic loads. One of the walls was tested absent axial load to investigate the effect of compression on wall damage. Both walls exhibited appreciable deformation capacity and significant energy dissipation. Buckling and rupture of the longitudinal reinforcing bars after diagonal cracking and concrete crushing resulted in mixed shear-flexure failure modes. Analysis of the results from these tests and from prior test on the flexure-dominated wall, described in Chapter 2, focus on the damage evolution. This is then compared to the performance limit states from current U.S. codes. Crack trajectories appeared to be slightly influenced by anchors installed in the wall face, but this did not negatively affect wall strength. To complement this effort, the response of anchors installed in these walls during the ensued damage evolution is reported in Chapter 4, where global cross-comparison of anchor behavior is presented.

3.1 Motivation

Reinforced concrete (RC) shear walls provide lateral strength and stiffness against wind and/or earthquake loading. Their global behavior is typically characterized by a combination of flexural and shear responses, with varying extent of each, dependent on the walls' geometric characteristics and reinforcement detailing. Properly reinforced walls with low aspect ratio (AR= wall height / length $\leq$ 1), exhibit a significant shear component in the total lateral displacement. Slender walls (AR $\geq$ 2) are typically dominated by flexural behavior. To this end, in this Chapter, the experimental campaign of this dissertation is expanded to address squat wall behavior.

3.2 Relating Design to Damage

To characterize the response of walls with varying aspect ratio and reinforcement detailing, focus is placed on wall ductility as represented by the response modification (R) factor (ASCE/SEI 7-16 2016) and by the displacement ductility ratio μ_Δ defined as the displacement associated with a 20% reduction in strength within the post-strength region of response divided by the displacement at yield. These key displacement values are obtained from experimental lateral load response curves. A consistent definition of yield displacement is particularly important for concrete shear walls with uniform reinforcing density over the wall length since the longitudinal reinforcing steel will yield at different locations along the wall cross-section, leading to an ill-defined yield point. A consistent definition of effective yield displacement in RC shear walls can be obtained using the drift at the intersection of the secant stiffness through first yield with the lateral strength (Faraone et al. 2019). The relationship of the displacement ductility ratio μ_Δ to the response modification factor R for RC walls is often taken as μ_Δ = R (equal displacement approach in Veletsos and Newmark 1960). Design lateral forces associated with elastic response are reduced directly by the R factor to account for inelastic deformations and energy dissipation, in accordance with common design methods (ASCE/SEI 7-16 2016). To characterize the damage response of walls of different ARs focus is placed on damage and crack evolution as the lateral demand increases. Wall damage relevant for structural stability is related to energy dissipation and displacement ductility. U.S. codes and guidelines categorize visual damage of concrete walls in terms of crack width and degree of concrete spalling to establish post-event immediate occupancy or to assess the

need for repair before re-opening the structure to public (e.g., ASCE 356 2000). In addition, specific acceptance limits representing levels of performance expected for structural components under seismic loading are defined on the basis of cracking and other signs of damage. In line with this concept, alternative design methods based on targeting specific structural performance states have been developed (e.g., Moehle 1992). These performance-based design approaches posit three performance levels, namely, Immediate Occupancy (IO), Life Safety (LS) and Collapse Prevention (CP), (SEOAC 1999). These states define post-earthquake damage levels of different intensities, varying from very limited damage requiring minimal repair and not affecting strength and stiffness properties (IO), to partial or total collapse with significant strength and stiffness degradation and large permanent lateral deformations (CP). The intermediate LS level, instead, is a residual post-earthquake state where some margin against partial or total structural collapse is preserved, despite significant damage to the structure (ASCE 356 2000). The prevention of global collapse under an extremely strong earthquake associated with the 2% chance of exceedance in 50 years, i.e., the "Maximum Considered Earthquake" (MCE), can be approximately represented by the CP performance level, where the gravity load resisting system carries the gravity load demands regardless of the severe damage to the lateral force resisting components.

In the context of performance-based design, it is useful to directly express damage related acceptance limits in terms of story drift ratios. This concept is adopted for the three full-scale RC shear wall tested within the research project presented herein, see Table 3.1. It is notable that a definition of representative drift ratio limits is essential to prevent damage to nonstructural components, to avoid structural instabilities and to avert human discomfort during low-level excitation (ASCE 356 2000). In ASCE 41 (2014) limiting values are given as a function of the relative amount of shear stresses and axial load acting on the structural component. For this reason, limits for flexural walls in ASCE 41 (2014) are expressed in terms of rotation of the section at the plastic hinge level. However, in Table 3.1 they were converted to drift ratio values, considering the idealized curvature distribution at the ultimate moment defined in Paulay and Priestley (1992), to allow consistent comparison amongst data. Interestingly, a large spread is observed in the drift ratio limits representative of IO and LS (Table 3.1). Values suggested in the literature (e.g., Ghobarah 2004 and Carrillo and Alcocer 2012) are on average about half of the corresponding codified drift ratio values. Although improved agreement in the drift ratio at the limit state CP is noted, the variation may still be significant. For the purpose of the analysis presented in this

dissertation, the values suggested by ASCE 356 (2000) are adopted as baseline, since, while they roughly agree with ASCE 41 (2014), they also allow a consistent comparison across all specimens.

Table 3.1: Drift ratio δ (%) corresponding to performance limit states for RC shear walls adopted by various codes and in the literature

Performance State [1]	Reference								
	ASCE 41 (2014)			ASCE 356 (2000)	Ghobarah (2004)		Carrillo and Alcocer (2012)		
	SL7.5[2]	SQ0[3]	SQ7.5[4]	All	SL7.5[2]	SQ0[3];SQ7.5[4]	SL7.5[2]	SQ0[3]	SQ7.5[4]
IO	0.4	0.4	0.4	0.5	0.2	0.1	0.1	0.05	0.07
LS	1.0	1.5	0.75	1.5	1.5	0.7	0.4	0.31	0.27
CP	1.5	2.0	1.0	2.0	>2.5	>0.8	2.0	1.5	0.84

[1] : **IO**: Immediate Occupancy; **LS**: Life Safety; **CP**: Collapse Prevention

[2] : *SL*7.5: Slender wall axially loaded to 7.5% of its section capacity

[3] : *SQ*0: Squat wall tested without axial load

[2] : *SQ*7.5: Squat wall axially loaded to 7.5% of its section capacity

3.2.1 Scope of this Test Program

As noted, the pair of test programs conducted in this dissertation is part of a broader effort to advance accuracy of evaluating the performance of concrete anchorage in a wide variety of realistic crack scenarios. An underlying outcome of which will be the assessment of the validity of current anchor qualification guidelines. Such guidelines require anchor tests in tension-flexural cracks only, as information regarding the anchorage behavior in other types of cracks, such as shear and crossing cracks, is lacking. Moreover, there is limited data regarding the width of cracks that develop within low AR RC walls subject to seismic loading. Currently available data have been conducted on small scale walls with wall thicknesses smaller than that possible in realistic anchor installations. In addition, the effect of axial load on the wall performance has yet to be evaluated in relation to anchor performance, though it is evident that the presence of additional compression across a concrete section will affect the embedded anchors boundary condition. To this end, the work presented in this Chapter intends to evaluate the global and local responses of two full-scale RC walls with post-installed anchors installed in each wall, while the walls are subjected to simulated seismic loads and varying axial loads. Comparison with the prior flexural wall tested under a similar protocol (see Chapter 2) is also conducted. Focus is given to crack assessment and damage characterization of the walls, with particular reference to existing code damage classifications and performance limit states. The availability of the walls experimental response also

offers an opportunity to evaluate the robustness of shear wall strength prediction models in the literature. Chapter 4 focuses on characterizing the performance of the tension loaded anchors which were installed in the progressively damaged walls.

3.2.2 Research Significance

Two identical RC shear walls with post-installed anchors subject to sustained tension were tested as cantilevers under reversed cyclic lateral load and varying amplitudes of constant axial compression. Combined with results of a prior flexural wall test program, these unique walls offer experimental data to enrich the literature on the seismic performance of full-scale RC shear walls. Moreover, the squat wall tests offer insight regarding the damage evolution and crack propagation due to lateral cyclic loads and therefore are used to compare with design guidance performance limit states, strength prediction formulations and damage estimations existing in the literature.

3.3 Experimental Investigation

3.3.1 Program Overview

Two identical AR=1 RC shear walls provided anchorage material for post-installed anchors, which were continuously loaded in tension. The full-scale walls were tested as cantilevers under reversed cyclic lateral displacement. Constant axial compression was applied to one low-aspect ratio wall, denoted wall SQ7.5, in the amount of about 7.5% of its section capacity and the second wall, called wall SQ0, was tested in the absence of axial load to elicit lower bound behavior. The design of walls SQ0 and SQ7.5 and analysis of these test results are summarized herein. Partial results of the slender wall test (Chapter 2), denoted here as wall SL7.5, are also reproduced in this Chapter to globally compare the response of different aspect ratio walls. The results of the performance of the anchors installed in these walls are cross-compared and used to elicit insight into the implications of the presence of progressively developing seismic-induced cracks on anchor load capacity in Chapter 4. The next sections describe the squat walls test program, providing information on the wall design and instrumentation. Additional information on the walls' design calculations and material tests are summarized in Appendix A and Appendix B, respectively, while other information on the preparation, setup and discussion of the results

of the two squat wall tests is described in detail in Faraone and Hutchinson (2021).

3.3.2 Design and Description of Test Walls

Walls SQ7.5 and SQ0 were identically designed according to ASCE/SEI 7-16 (2016) and ACI 318 (2019) design codes and constructed simultaneously to assure similar material batches and consistent construction methods. Their design-basis was derived using a reference prototype one-story building with concrete shear walls serving as the sole lateral resisting system. The prototypical building was assumed to be in the high seismic region of downtown Los Angeles, Site Class D, S_1=0.819g and S_s=2.330g. A response modification factor R for bearing wall systems with special reinforced concrete shear walls is taken as R = 5 per Table 12.2-1 Design Coefficients and Factors for Seismic Force-Resisting Systems, ASCE/SEI 7-16 (2016). The height of the physical walls was reduced according to the resultant of the triangular lateral load distribution applied at 2/3 of the total height. For consistency with the previous slender wall test, the walls length was assumed like the slender wall SL7.5, at L_w = 8 ft. However, the squat walls adopted an aspect ratio of AR = 1, therefore the wall height resulted in H_w = 8 ft. A stiff RC foundation and load stub were constructed with the RC walls. Ordinary normal-weight concrete with specified compressive strength of 5 ksi and deformed reinforcing bars ASTM A615, grade 60 (414 MPa), satisfying the requirements of ACI 318 (2019), were used in concert with conventional practice. The average material characteristics were calculated using a minimum of three samples of reinforcing steel and concrete from the batch of material used to construct the walls, tested under uniaxial tension and compression, respectively. The average uniaxial concrete compressive strength at the time of cyclic testing of the walls, was f'_c = 7 ksi and f'_c = 8 ksi for wall SQ7.5 and wall SQ0, respectively. The average yield and tensile strength of the longitudinal and horizontal reinforcing bars were measured to be 67 ksi and 71 ksi, respectively. The governing shear V_u= 45 kip was used to determine the minimum thickness of the wall by limiting the average shear stress in the wall to $3\sqrt{f'_c}$. However, to better accommodate the anchor embedment depth and limit the average shear stress to less than $\sqrt{f'_c}$ a wall thickness of t_w=10 inches was selected. The governing axial load demand P_u = 480 kip and governing moment demand at the base of the wall M_u = 534 kip-ft were considered to determine the layout of the vertical reinforcement, as shown in Fig. 3.1. Fig. 3.1(a)-(b) provides a photograph and annotated drawing of the typical reinforcement cage. The longitudinal reinforcement was distributed in two layers of 6-# 5 reinforcing

bars in each boundary element (ρ_{BE}=1%) and 14-# 5 reinforcing bars in the web (ρ_v=0.7%) of the walls.

The flexural strength of the walls was estimated to be M_n = 3259 kip-ft and the top shear at the flexural strength resulted in V at M_n = 407 kip. Design for shear resistance for the two walls considered the shear demand V_u=445 kip calculated considering the probable flexural strength, M_{pr} = 3559 kip-ft, which accounts for amplified reinforcement strength of 1.25 f_y = 75 ksi. Refer to the axial force moment interaction diagram in Fig. 3.2 for each wall. The required amount of horizontal reinforcement to satisfy the shear demand V_u was about ρ_h=0.35% according to the shear strength equation for special structural walls in Section 18.10.4.1 of ACI 318-19 (2019). However, since the intent of the experimental program was to develop a mixed shear-flexure failure, the web horizontal reinforcement was reduced to anticipate the fulfillment of the shear capacity of the wall with respect to the flexural strength. Thus, #4 reinforcing bars placed at 15 inches (ρ_h=0.27%) satisfied the minimum transverse reinforcement allowed by Section 18.10.2.1 ACI 318 (2019), with resulting shear strength of 357 kip. Sliding shear resistance was verified according to ACI 318 (2019), Section 22.9.4.2, under the undesirable assumptions of absence of axial load and smooth surface, although the wall-footing interface was roughened. Finally, to provide sufficient strength and ductility under reversed cyclic loading, boundary elements were detailed according to Section 18.10.6 ACI 318 (2019), as it is represented in Fig. 3.1(c). Within these boundary elements, transverse confinement was provided with #4 ties placed at 4 inches on center, and horizontal reinforcement anchored inside the confined core, see Fig. 3.1(c). This detailing was similar to wall SL7.5. The confined boundaries were detailed to extend 17 inches horizontally (l_{be}/t_w = 1.7) and to vertically extend along the entire wall height, as shown in Fig. 3.1(b).

3.3.3 Test Setup and Instrumentation

The annotated photograph in Fig. 3.3 shows the setup of the full-scale low-aspect ratio walls prior to testing. The walls were post-tensioned to the laboratory strong floor through an RC footing. The footing was designed with ample margin of safety against tension splitting induced by the post-tensioning system and to counteract sliding and uplift during the wall lateral loading. Cyclic lateral displacement was applied to the walls using a 500-kip hydraulic actuator attached to the strong wall on one end and to the RC post-tensioned load stub at the top of the walls on the other end, see Fig. 3.3(a). Out-of-plane guides provided lateral support to the walls during lateral loading. The setup amongst the pair of

walls differed only in that an axial load application transverse beam, thread rod, and jack assembly were utilized to impose constant axial load to wall SQ7.5 during imposition of lateral displacement. In this regard, four post-tensioned thread rods transferred 125 kip of axial load from the top of the load stub to the wall through two steel spreader beams mounted transversely on top of the load stub, see Fig. 3.3(a). Instrumentation installed on the walls included twenty-four linear potentiometers arrayed to measure displacements, uplift, and sliding during the wall cyclic tests (see Faraone and Hutchinson 2021). Two regions with at least one pair of vertical and diagonal potentiometers each were selected in the test walls, as shown in Fig. 3.4. Three pairs of vertical sensors were provided in the region nearest the base of the walls, to better capture the anticipated nonlinear strain profile within the most damaged region. In addition to external displacement sensors, strain gauges were installed on the reinforcing steel to measure strain at forty-eight locations extending up to about 0.5 L_w from the wall-footing interface. Finally, to aid in quantifying the evolution of concrete damage, crack width was measured at discrete locations during each test. These measurements involved installation of high-precision linear potentiometer at select locations close to anchors to monitor crack width history as well as a dozen manual crack width sensors. In the case of manual sensors, crack width values were only attainable with visual inspection at peak drift amplitudes.

3.3.4 Test Procedure

The adopted displacement protocol, shown in Fig. 3.5, nominally incorporated ACI 374 (2013) recommendations. Namely, imposition of three cycles per amplitude (multiples of the predicted yield drift, as determined from preliminary numerical models) performed within the linear, quasi-linear, expected yield and up to significant load degradation levels. Two cycles per amplitude were performed when severe damage was evident, and the drift ratio was incremented by twice the predicted yield drift. The displacement-controlled protocol was intended to continue up to about a 20% reduction in strength. As a result of this general guidance, the final protocol for wall SQ0 involved three cycles at 0.05, 0.1, 0.2, 0.3, 0.4% drift and two cycles at subsequent increments of 0.2% drift ratio up to 2.2% drift ratio (thick gray line in Fig. 3.5). After the 2.6% drift ratio cycle grouping, three cycles were again imposed at 2.9% drift ratio, to accelerate degradation prior to imposition of the final monotonic push to 4% drift ratio. The cyclic protocol for wall SQ7.5 replicated that utilized for wall SQ0 up to 1.4% drift ratio (thin black line

in Fig. 3.5). Then two cycles at 1.8% were imposed, resulting in about a nominal 20% drop in strength and the wall slightly tilted out of plane. The test was ended for safety reasons; however, it was notable that substantial strength degradation was still attainable prior to test conclusion as will be discussed in later sections. Visual inspection was performed at the first cycle of each drift amplitude while holding at peak push (+) and pull (-) directions, and at zero load, following completion of a cycle amplitude group. Open cracks were marked during the (+) and (-) directions of the first cycle of each new amplitude, while axial loads on the anchors were assessed, as explained in Chapter 4.

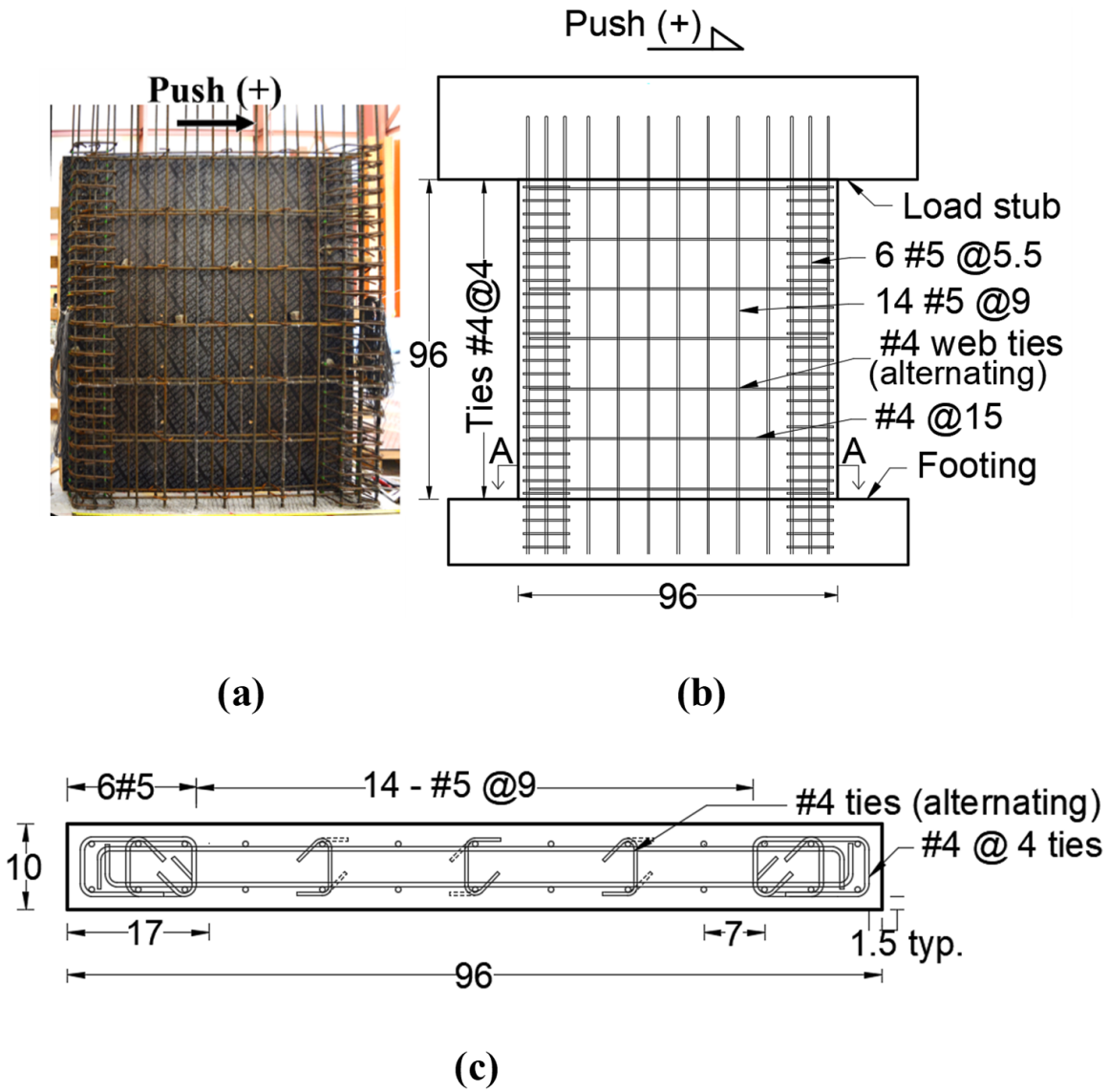


Figure 3.1: AR=1 walls. (a) Photograph of reinforcement cage during construction (elevation view), and schematics: (b) elevation and (c) cross section reinforcement details. All units in inches. [1 in = 25.4 mm]

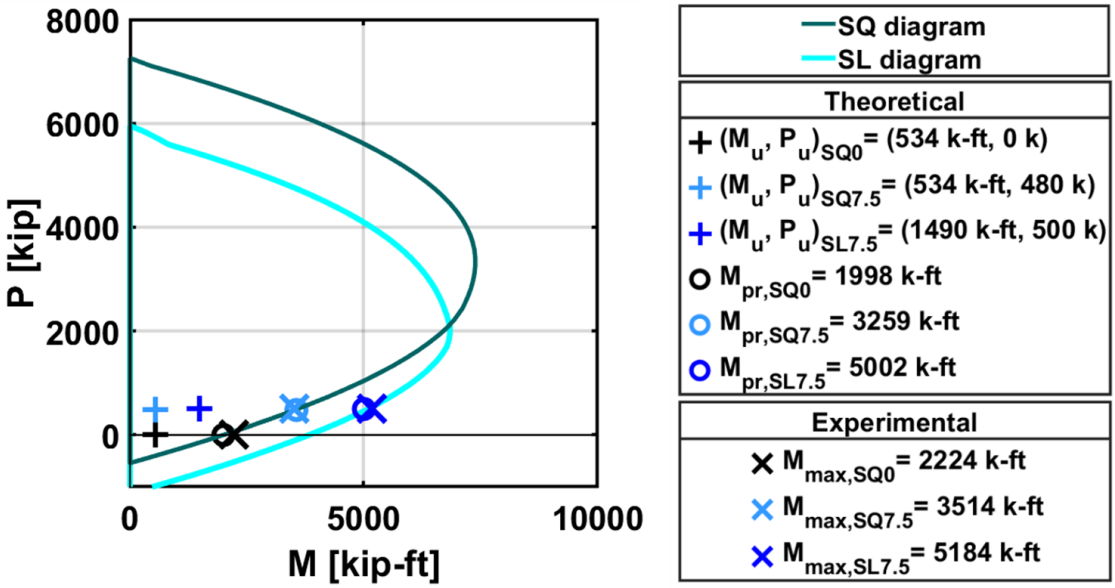


Figure 3.2: Moment-axial force interaction diagram. M_u= required moment; P_u= factored axial force; M_{pr}= probable flexural strength; M_{max} = maximum moment measured during the test. Subscript SQ0, SQ7.5 and SL7.5 denote the test wall. [1 in = 25.4 mm; 1 kip =4.45 kN]

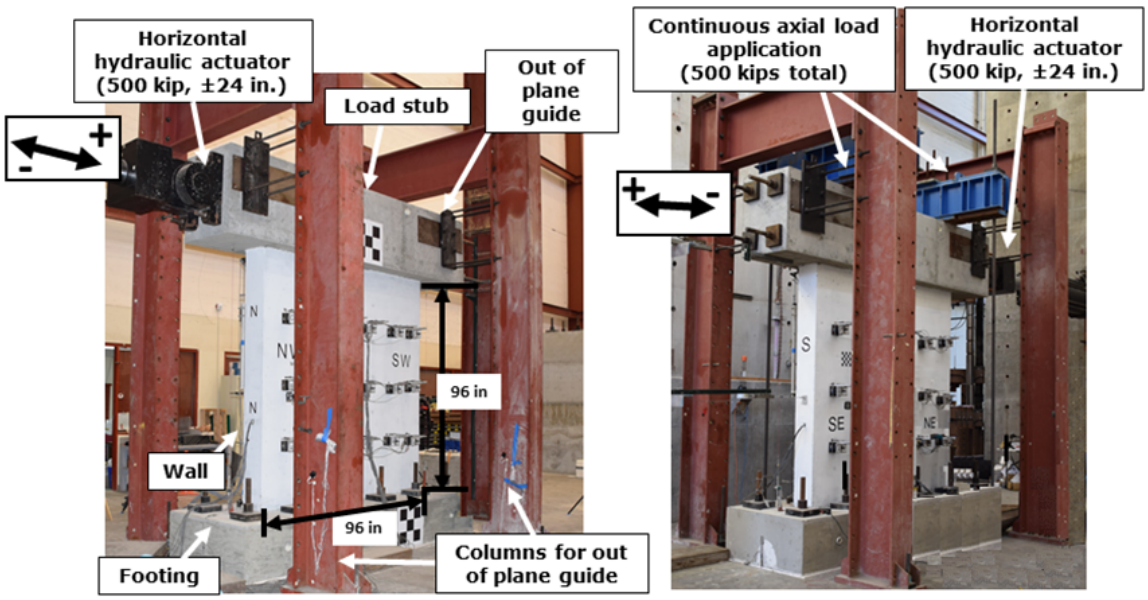


Figure 3.3: Annotated photographs of test setup: anchor face of a) wall SQ0 and b) wall SQ7.5 [1 in = 25.4 mm; 1 kip =4.45 kN]

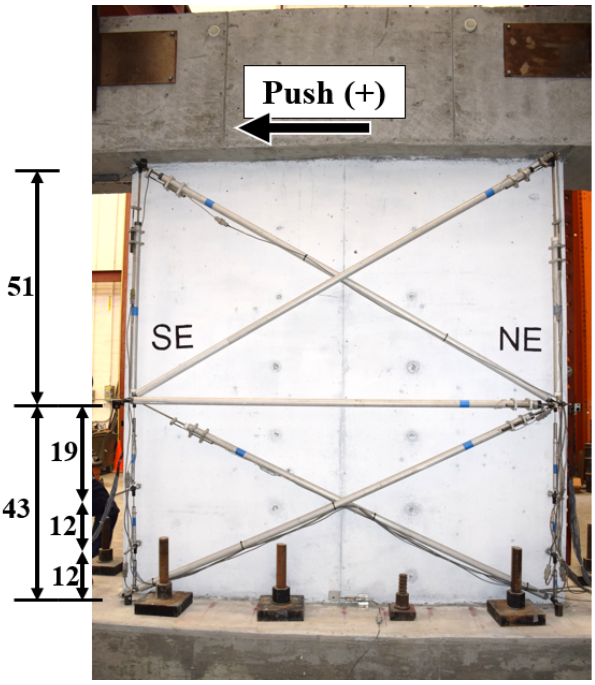


Figure 3.4: Layout of linear variable displacement transducers used to capture distortion of walls (typical both specimens). All dimensions in inches. [1 in =25.4 mm]

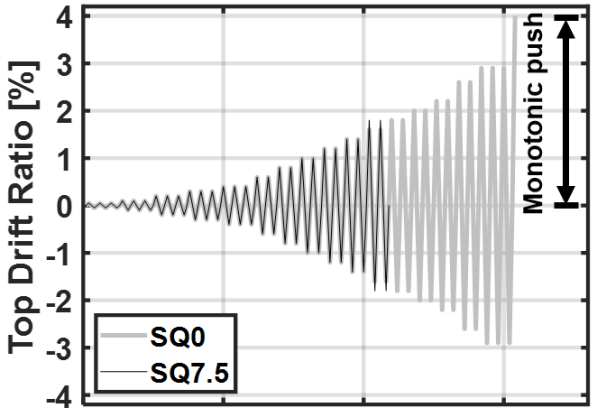


Figure 3.5: Displacement protocol utilized in the tests, adapted from ACI 374 (2013)

3.4 Experimental Results

In this section the experimental results of the wall tests are illustrated. It is reminded that constant axial compression was applied to one low-aspect ratio wall, denoted wall SQ7.5, in the amount of about 7.5% of its section capacity and the second wall, called wall SQ0, was tested in the absence of axial load to elicit lower bound behavior. Partial results of the slender wall test (Chapter 2), denoted as wall SL7.5, are reproduced in this section to globally compare the response of different aspect ratio walls. Additional information on crack width values measured during the tests is summarized in Appendix C, while other information on test results is exhaustively reported in Faraone and Hutchinson (2021).

3.4.1 Global Response

The global response of the low-aspect ratio walls is summarized in Fig. 3.6, where the lateral load versus drift ratio response is plotted for wall SQ7.5 and wall SQ0, respectively. Hysteresis loops in Fig. 3.6 are wide and stable for the two walls, demonstrating only a minor strength and stiffness degradation. Pinching of the load-displacement response is observed in the response shown in Fig. 3.6(b) where the absence of axial load softens the wall upon unloading. This observation agrees with prior tests observations, e.g., those by Lefas et al. (1990) and Li et al. (2015). Instances of first yield, attainment of strength and reinforcement fracture are also noted in Fig. 3.6. Table 3.2 reports important response parameters identified in both lateral strength and displacement at the first observed crack, at the first measured yield of the longitudinal bars in the boundary elements, at strength and at the strength reduction. It is notable to mention that the yield drift ratio predicted by pre-test numerical models was 0.1%, while the first yield was measured at 0.2% drift ratio during both tests. Moreover, the lateral strength, average in push and pull directions, was 0.62 V_n and 1.03 V_n for wall SQ0 and wall SQ7.5, respectively, where V_n is the expected shear strength of the cross section calculated with material properties at the day of test, according to Section 18.10.4.1 of ACI 318 (2019). Finally, approximately 1.06 V @ M_{pr} and 1.05 V @ M_{pr} were measured for wall SQ0 and wall SQ7.5, respectively, values in good agreement with design predictions.

The experimental displacement ductility was estimated considering the effective yield displacement, identified at the intersection of the secant stiffness through the measured first yield with the

Table 3.2: Summary of experimental results. [1 kip= 4.45 kN; 1 in= 25.4 mm]

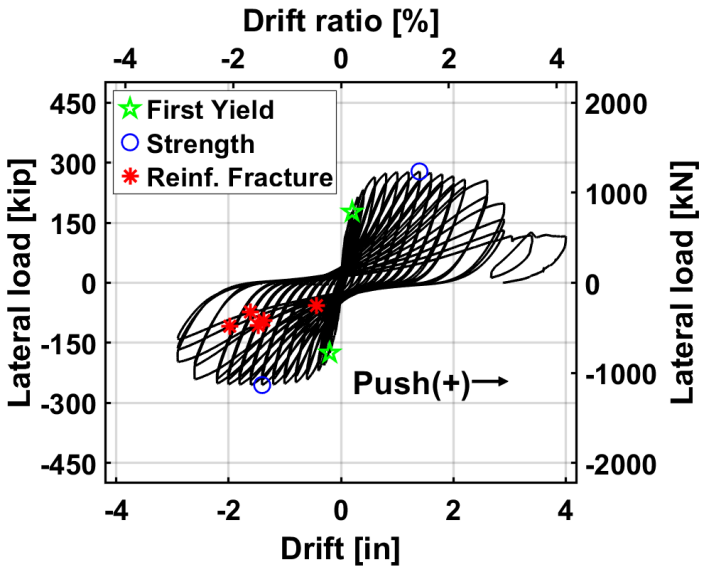
Wall	Loading Direction	First crack[1]		Yield[2]		Strength		Strength Reduction[3]	
		V [kip]	Δ [in]	V [kip]	Δ [in]	V [kip]	Δ [in]	V [kip]	Δ [in]
SQ0	**Push (+)**	88	0.05	177	0.2	278	1.4	198	2.9
	Pull (-)	83	0.05	175	0.2	255	1.4	197	3.0
SQ7.5	**Push (+)**	139	0.07	311	0.2	434	0.8	216	1.8
	Pull (-)	101	0.03	276	0.2	423	0.8	241	1.8
SL7.5	**Push (+)**	145	0.21	257	0.82	324	3.84	252	5.73
	Pull (-)	167	0.24	292	0.98	326	3.84	123	5.76

[1] : Instance of first observable crack

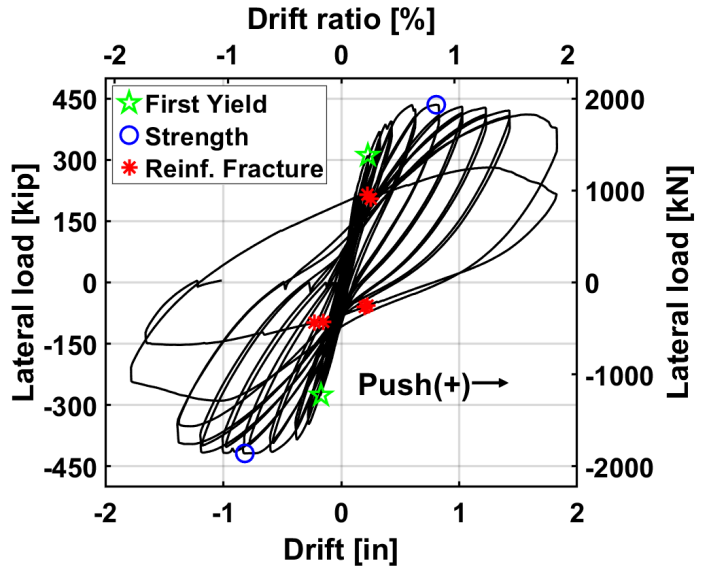
[2] : First yield as measured strain in reinforcing bars

[3] : Load at the first cycle attaining a minimum of a 20% load reduction

strength, and the ultimate displacement at about 20% reduction in strength. Utilizing these metrics, the displacement ductility values of μ_{Δ}=6, 6 and 8 were estimated for walls SL7.5, SQ7.5 and SQ0, respectively. These results show that properly detailed low-aspect ratio walls can undergo large displacement cycles without significant strength degradation, while also demonstrating appreciable energy dissipation. It is believed that the significant level of hoop stress exerted by the closely spaced transverse reinforcement in the boundary elements enhanced the drift capacity of the tested low-aspect ratio walls and ultimately their displacement ductility, which is comparable to that obtained by more slender counterparts presented in Chapter 2.



(a) Squat wall tested without axial load



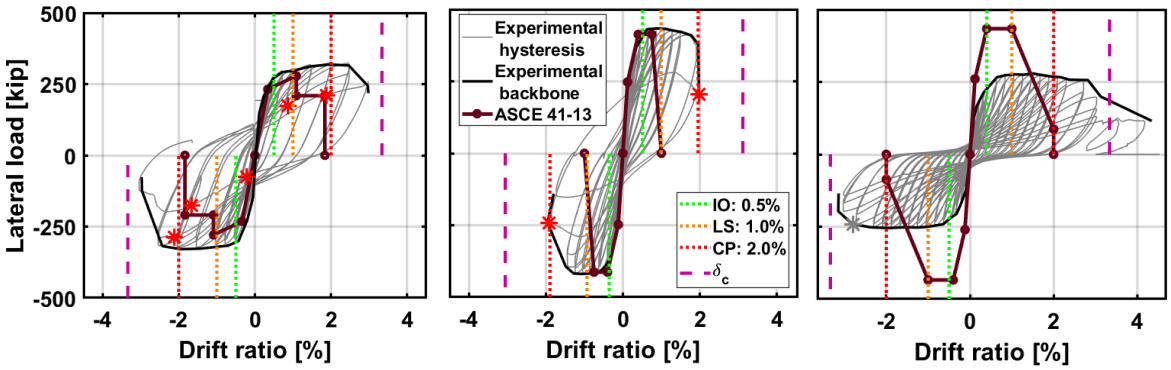
(b) Squat wall tested with axial load

Figure 3.6: Lateral load versus top wall displacement (and drift ratio): a) wall SQ0 and b) wall SQ7.5 Note: the amplitude of the x-axis varies for clarity. [1 in =25.4 mm; 1 kip =4.45 kN]

3.4.2 Drift Ratios at Performance Limits

The three full-scale walls tested within this program provide an opportunity to compare with the backbone curves defined in design guidance, such as ASCE 41 (2014) and drift values at performance limits, such as those suggested by ASCE 356 (2000). To this end, three sets of key parameters are specified in ASCE 41 (2014) to construct backbone envelopes of structural components, as shown in Fig. 3.7. These allow account for the different levels of applied axial load and geometry of the walls. Comparison of these design backbone curves with the experimental hysteresis indicate that the drift capacity is underestimated by the piece-wise envelope for each of the tested full-scale walls. In addition, the lateral strength of wall SQ0 is significantly overestimated (Fig. 3.7(c)), due to the absence of axial load information in the coded shear strength equation (ACI 318 2019). Fig. 3.7 incorporates computations of the lateral drift capacity δ_c for walls with special boundary elements using the equation suggested by Abdullah and Wallace (2019), denoted by the dashed vertical lines in Fig. 3.7. The approximation of the neutral axis depth, which is involved in the calculation of δ_c, is a likely reason for the 15% and 78% overestimation of the lateral drift capacity of wall SL7.5 and wall SQ7.5, respectively. In like fashion, the dotted vertical lines at 0.5%, 1.0% and 2.0% drift ratios refer to the Immediate Occupancy (IO), Life Safety (LS) and Collapse Prevention (CP) limit states as defined in ASCE 356 (2000). The IO, LS and CP limit states may be nominally associated with three notable performance states of the response of the walls during the test, which are first yield, effective yield (defined at the intersection of the secant stiffness through the measured first experimental yield with the lateral strength), lateral strength and incipient failure (taken as the drift at 20% reduction post-strength). These performance limit states are denoted on the envelope curve in Fig. 3.8(a). The displacement and load values measured at the key states as characterized in Fig. 3.8(a) are reported in Table 3.2. Notably, the three cyclic experimental curves show a large plateau around the lateral strength, thus a range of drift ratios may be associated with the lateral strength, and as a result, the region where V_{max} varies by +/- 5% of the lateral strength has been denoted in Fig. 3.8(a). Fig. 3.8(b) directly compares the performance drift limits by ASCE 356 (2000) to the range of experimental drift values measured at the key states in Fig. 3.8(a). The 1:1 line overlaid on this plot indicates that the limiting drift ratios suggested by ASCE 356 (2000) generally underestimate the drift capacity of the three full-scale walls, especially at LS and CP states.

To further analyze the walls' behavior, important response characteristics such as the secant



(a) Slender wall tested with axial load (b) Squat wall tested with axial load (c) Squat wall tested without axial load

Figure 3.7: ASCE 41 (2014) envelope compared to experimental backbone: a) wall SL7.5 b) wall SQ7.5 and c) wall SQ0. IO LS and CP performance limit states from ASCE 356 (2000). δ_c = drift capacity estimated according to Abdullah and Wallace (2019). Asterisks identify instances of fracture of the boundary reinforcing bars

stiffness, the displacement ductility and the dissipated energy occurring at the experimental performance drift, δ_{exp}, are computed and reported in Table 3.3. It is observed that the gradual reduction in secant stiffness with increasing drift limit values is approximately constant for all the three walls. Average 71% and 90% reductions from IO to LS and from IO to CP states, respectively, are observed to have 6% and 3% coefficient of variation, respectively. In particular, it is noted that the axial compression has a minor effect on the rate of degradation of secant stiffness, when comparing wall SQ7.5 and wall SQ0. This is consistent with observations of Li et al. (2015). Conversely, the application of the axial load affects the calculated displacement ductility at the experimental performance drift δ_{exp}. Despite the relatively large ductile behavior exhibited by all three full-scale walls, the displacement ductility at the LS state of wall SQ0 is estimated to be 30% larger than that of the nominally identical wall with axial load (SQ7.5). Table 3.3 summarizes the dissipated energy at the experimental performance drift δ_{exp}, however presented as a ratio. Herein this value is calculated as the energy dissipated at the end of a cycle grouping to the target performance normalized by the total cumulative energy dissipated by the wall at the experimental CP. These values represent an energy-based definition of the performance limit states. Namely IO is attained when the dissipated energy ratio is approximately less than 2% and LS when on average about 40% of the total energy is dissipated. Finally, Table 3.3 summarizes code limit margin values, defined as the ratio between the experimental performance drift δ_{exp} to δ_{FEMA}. In this definition, a ratio larger than unity

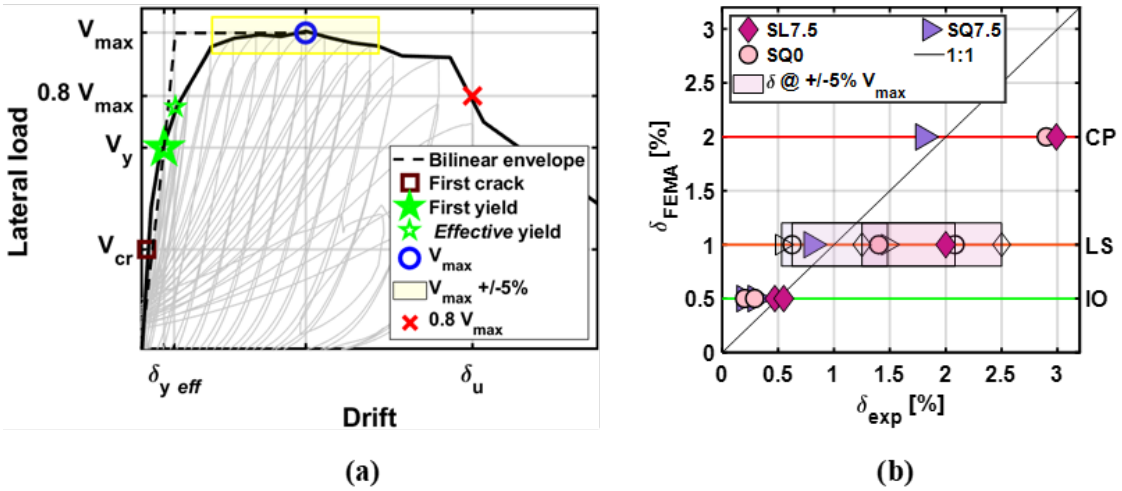


Figure 3.8: a) Characterization of lateral load and drift ratio at performance limit states (only positive quadrant shown for clarity). b) Comparison between experimental performance drift, denoted as δ_{exp}, versus ASCE 356 (2000) drift, denoted as δ_{FEMA}. Average of positive and negative values are considered. IO: Immediate Occupancy; LS: Life Safety; CP: Collapse Prevention. The shaded area at LS represents the +/- 5% strength interval

denotes an underestimation of the drift capacity at a performance state utilizing the FEMA drift limit states, whereas values less than one imply an unconservative drift capacity estimate at key performance limit states. Results utilizing the experiments presented herein indicate that at the IO limit state, FEMA drift limit values are generally unconservative, whereas at the LS and CP limit states, the FEMA drift limit values are generally over-conservative, in some cases two-fold. The latter observation is a useful outcome emphasizing that an ample reserve drift capacity may be realized during design and more severe earthquakes in modern detailed walls.

Table 3.3: Summary of experimental results. [1 kip= 4.45 kN; 1 in= 25.4 mm]

	Wall								
	SL7.5			**SQ7.5**			**SQ0**		
Performance State	**IO**	**LS**	**CP**	**IO**	**LS**	**CP**	**IO**	**LS**	**CP**
δ_{FEMA}	**0.5%**	**1%**	**2%**	**0.5%**	**1%**	**2%**	**0.5%**	**1%**	**2%**
Experimental Performance State	**First Yield**	**Strength**	**0.8 Strength (post-peak)**	**First Yield**	**Strength**	**0.8 Strength (post-peak)**	**First Yield**	**Strength**	**0.8 Strength (post-peak)**
δ_{exp}[1]	**0.5%**	**1%**	**2%**	**0.5%**	**1%**	**2%**	**0.5%**	**1%**	**2%**
Secant stiffness [kip/in] through δ_{exp}	**306**	**85**	**46**	**1468**	**536**	**127**	**880**	**191**	**67**
Displacement ductility[2] at δ_{exp}	**0.9**	**3.6**	**6**	**0.7**	**2.7**	**6**	**0.7**	**4.8**	**8**
Energy ratio[3] [%] at δ_{exp}	**5**	**67**	**100**	**1**	**20**	**100**	**1**	**31**	**100**
Code limit margin[4]	**1**	**2**	**1.5**	**0.4**	**0.8**	**0.9**	**0.4**	**1.4**	**1.5**

[1] : Average of negative and positive envelope
[2] : $\delta_{exp}/\delta_{y,eff}$
[3] : Cumulative dissipated energy ratio E/E_{CP} [%], where
E = cumulative energy at test performance drift ratio
E_{CP} = total cumulative dissipated energy at 0.8 strength = 1002 k-ft, 430 k-ft and 543 k-ft, for walls SL7.5, SQ7.5 and SQ0, respectively
[4] : Code limit margin values $\delta_{exp}/\delta_{y,eff}$ defined as the ratio of test to FEMA drift limit at the performance limit states

3.4.3 Damage Evolution

The damage evolution of the low-aspect ratio walls is analyzed by evaluating the pattern and width of the cracks developed during the test. To this end, digital sketches of the crack pattern of the walls were created using high resolution photographs obtained whereby crack patterns were manually tracked during the tests. Figs. 3.9 and 3.10 show photographs and crack pattern sketches at the 0.4%, 1.0% and 2.0% (1.8% for the wall SQ7.5) drift ratio values, since these were the instances closest to the target drift amplitudes of ASCE 356 (2000). This imagery demonstrates that in both walls, cracks initiated from the wall toe regions and propagated towards the interior of the wall faces, where diagonal cracks are evident from the mid-web region. The presence of strong reinforced columns at the wall boundaries (i.e., the boundary elements) reorient the web diagonal cracks to horizontal at the web-boundary element interface. Figs. 3.9 and 3.10 also demonstrates that at the CP limit state, the wall without axial load does not display as localized of a spalled region at its toe regions, but rather articulates a tighter and shallower extent of distributed cracks up the height of the wall, when compared with its axially loaded counterpart.

Data from strain gauges installed on boundary longitudinal reinforcement show that first yielding in tension occurred within the lower 7 inches from the wall-footing interface at 0.2% drift ratio for both the squat walls, see Table 3.2. At this drift ratio the first few diagonal cracks crossed the mid region of the walls, at about mid-height of the wall. Following identified reinforcing steel first yield, the evolution of cracking in the wall pairs varied due to the presence of the axial compression. This was noted not only in terms of the pattern of cracking, but also in the measured crack width. For example, at 0.4% drift ratio, maximum crack widths on the wall face were measured at 0.8 mm and 1.25 mm in wall SQ7.5 and wall SQ0, respectively. The walls' response to increasing drift demands is summarized as follows:

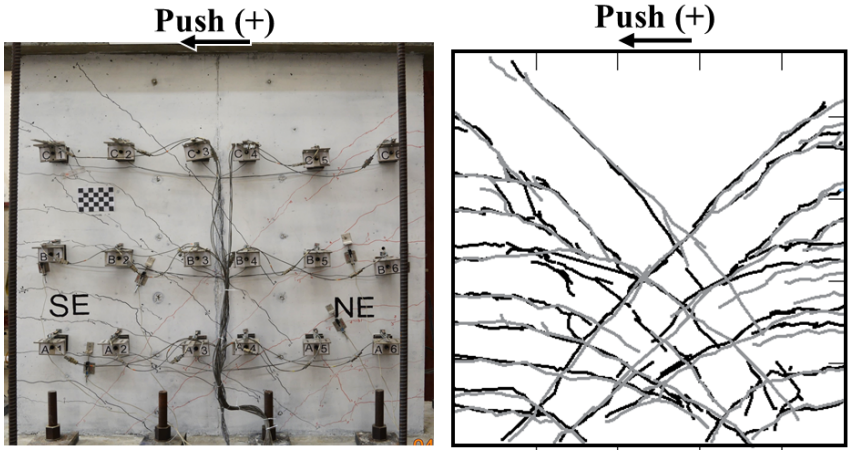
- **Wall SQ7.5**: the crack pattern stabilized at 0.6% drift ratio, with cracks distributed readily at about $s_{r,av}$ = 9 inches on center. Initial concrete spalling occurred in the (+) toe at 0.8% drift ratio, when the stabilized cracks in the wall faces significantly widened up. Exposed boundary longitudinal reinforcement showed first signs of buckling. At 1.0% drift ratio superficial concrete spalling occurred also in the (-) toe (see Fig. 3.9(a)) and the horizontal cracks in the boundary elements measured 3 mm maximum crack width. Two large diagonal struts on the wall face were identified and delimited by three main diagonal cracks, spanning from the top to opposite bottom

corner of the wall faces. Crack widths increased and spalled concrete regions expanded at 1.4% drift ratio, however no significant strength degradation was measured yet. Finally, at 1.8% drift ratio a total of eight longitudinal bars fractured after buckling and severe concrete crushing was observed not only in the wall toes, as is typical of flexure-dominated walls, but also in the lower compression regions of main diagonal struts. This damage was well distributed, extending up to about mid-height of the wall. It is also noted that the elevation of buckling and fracture of the longitudinal reinforcement occurred on the diagonal plane identified by concrete crushing on the main diagonal strut. The test ended at 1.8% drift ratio with about δ_r = 1% residual drift ratio in the pull (-) direction, and approximately 50% reduction in lateral strength. Although out of plane tilting of the wall precluded safe continuation of the test, a well-defined combined shear-flexure mode was observed as denoted by severe diagonal compression and buckling and fracture of the reinforcement along the diagonal strut. At its final damage state, the total area of crushed concrete on the wall faces was estimated to be 2891 in^2, about 16% of the total surface area.

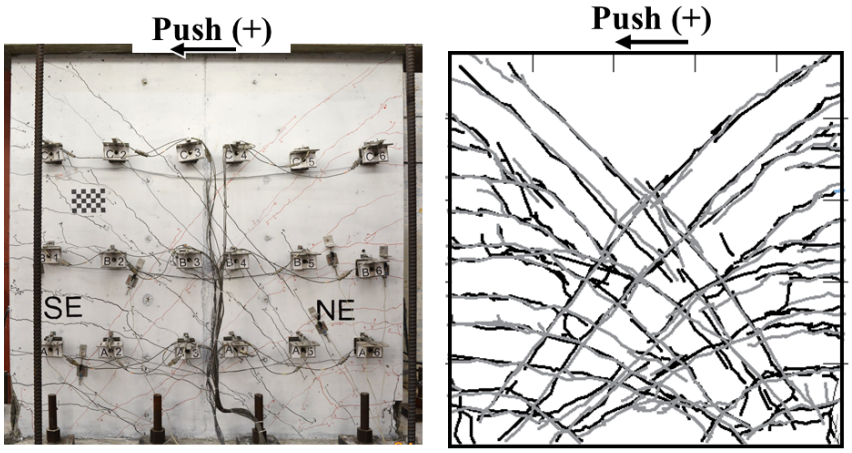
- **Wall SQ0**: the crack pattern stabilized at 1.0% drift ratio, with cracks distributed readily at about $s_{r,av}$ = 8 inches on center. At this drift amplitude, three main diagonal cracks characterized well-defined diagonal struts extending from top to bottom opposing corners, see Fig. 3.10(b). In addition, vertical splitting cracks appeared in the wall toes. Strength was reached at 1.4% drift ratio without signs of localized damage. However, diagonal crack widths increased significantly, measuring 5 mm at 1.8% drift ratio. At 2.0% drift ratio, the damage spread across the entire wall height and concrete spalling was only foreseen by a large crack width in the (+) wall toe. Reinforcing bars were visible at 2.2% drift ratio, when concrete cover spalled in the (+) end of the wall. Buckling occurred at 2.6% drift ratio and finally reinforcing bars ruptured at 2.9% drift ratio, when lateral strength dropped by 29%. A monotonic pushover was also performed to further characterize the post-strength response of the wall. About 60% lateral strength reduction was measured in the final push to 4% drift ratio. The test ended with a residual drift ratio δ_r=3% in the push (+) direction. Wall SQ0 failed with combined shear-flexure mode, as denoted by reinforcement buckling and diagonal compression concrete crushing. Residual crack widths were significantly large in the lower half of the wall and spalling of the concrete along the diagonal cracks was observed. Total area of crushed concrete in the wall faces is estimated to be about 1446 in^2, about 8% of the total surface

area.

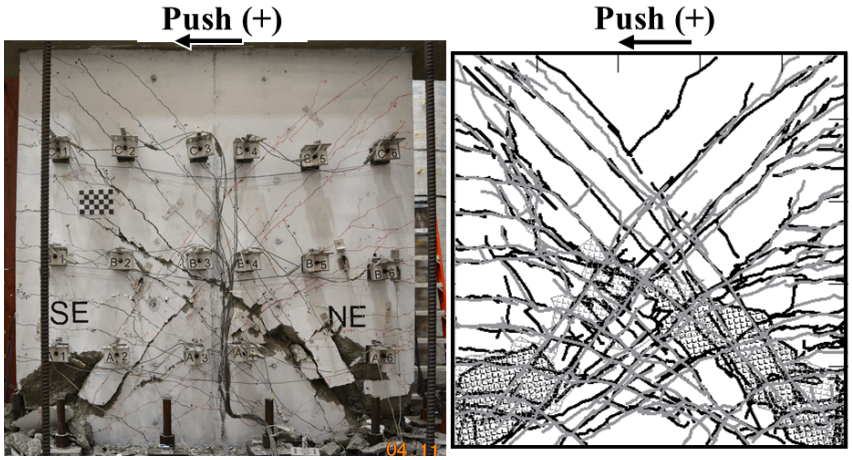
A comparison of the final residual damage state of the two walls is provided in Fig. 3.11. This side-by-side comparison demonstrates that wall SQ7.5 developed fewer cracks during the cyclic test than wall SQ0, however the final concrete spalled region of SQ7.5 resulted in wider and more equally distributed cracks along the main diagonal struts. The total spalled concrete region in wall SQ7.5 is estimated to be about twice the spalled area in wall SQ0. A steep angle of network of web cracks in wall SQ7.5 is observed, whereas the SQ0 wall developed a dense network and shallow (more horizontal) crack array. Notably, the boundary elements provide frame action when the wall is axially loaded. The stabilized cracks in the walls' toe regions were almost horizontal and the crack pattern in the two faces resulted in approximately symmetric patterns with respect to the walls' long axis, see Fig. 3.11. In addition, many small cracks, primarily extension from main diagonal cracks, occurred in wall SQ0 due to the absence of compression loading, which promoted the vertical spread of damage.



(a) Squat wall tested with axial load SQ7.5- 0.4% drift ratio

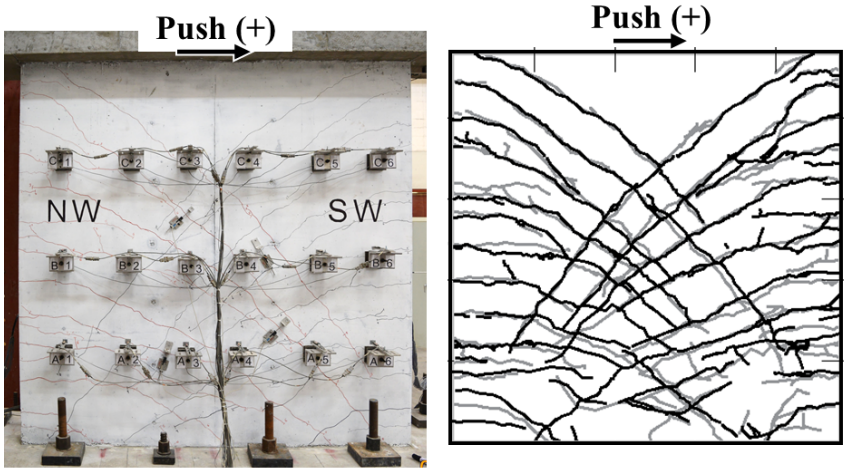


(b) Squat wall tested with axial load SQ7.5- 1.0% drift ratio

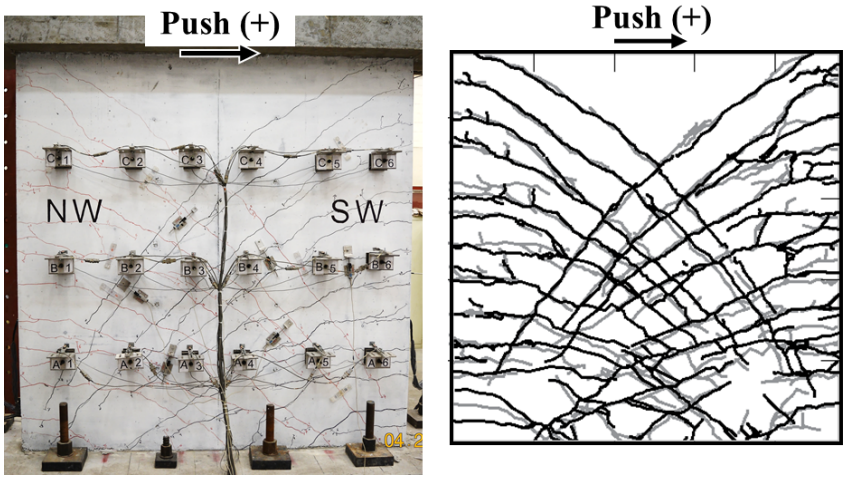


(c) Squat wall tested with axial load SQ7.5- 1.8% drift ratio

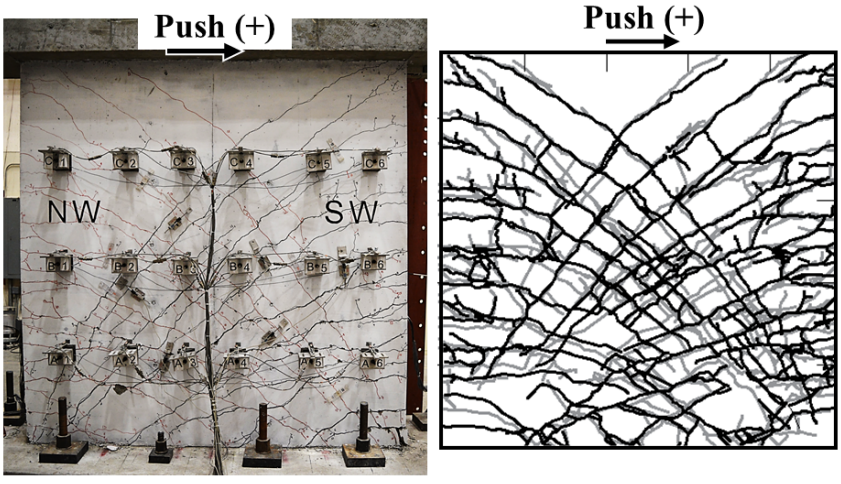
Figure 3.9: Photographs and sketches of the crack pattern of wall SQ7.5. Dark and light gray lines show cracks on the face with and without anchors, respectively



(a) Squat wall tested without axial load SQ0- 0.4% drift ratio

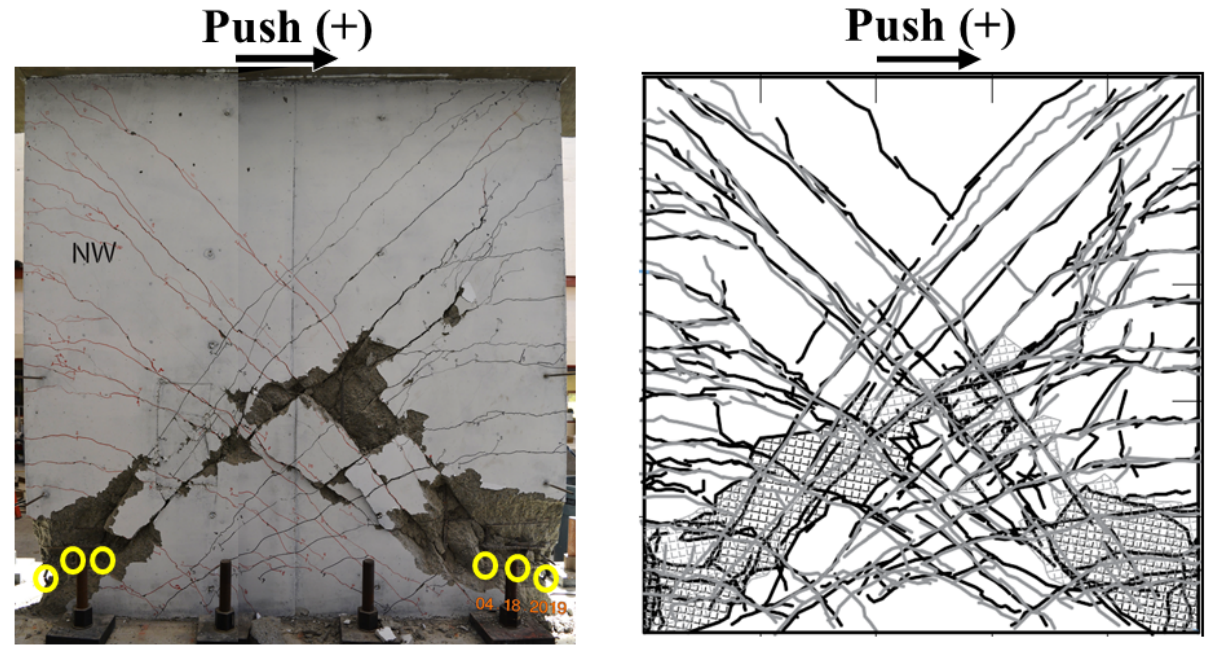


(b) Squat wall tested without axial load SQ0- 1.0% drift ratio

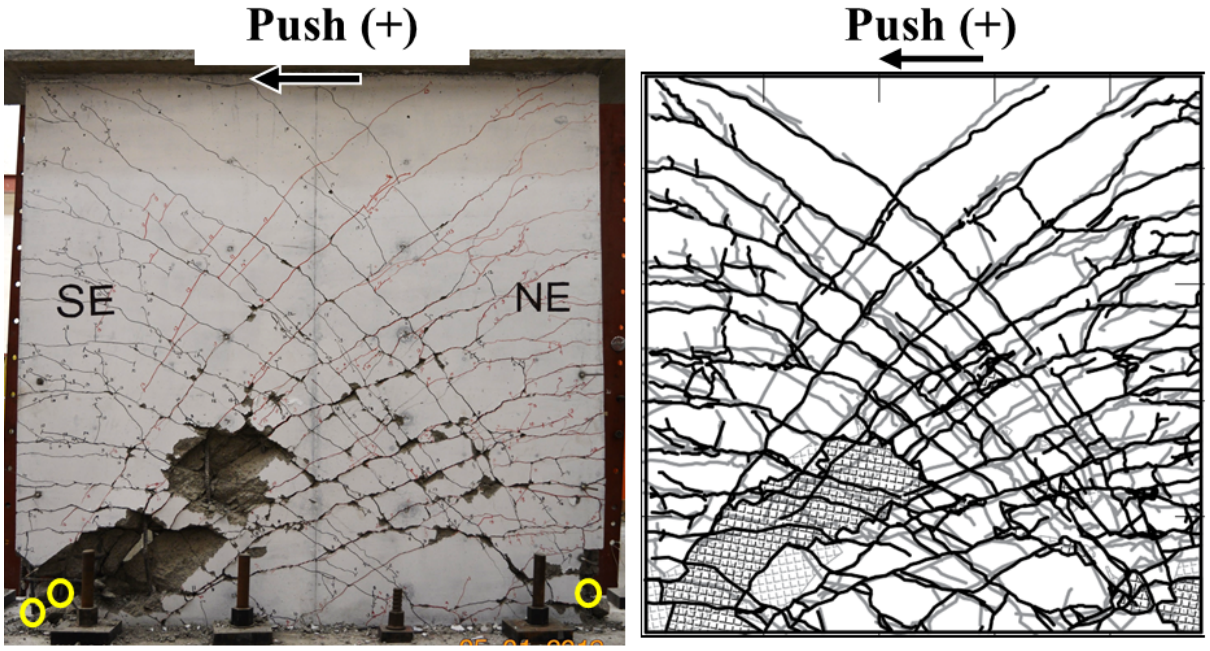


(c) Squat wall tested without axial load SQ0- 2.0% drift ratio

Figure 3.10: Photographs and sketches of the crack pattern of wall SQ0. Dark and light gray lines show cracks on the face with and without anchors, respectively



(a)



(b)

Figure 3.11: Photographs (with fractured longitudinal boundary bars identified with circles) and sketches of the crack pattern at the end of the wall test. Dark and light gray lines show cracks on the face with and without anchors, respectively. Hatched regions represented spalled concrete. a) Wall SQ7.5 and b) wall SQ0

3.4.4 Estimated Crack Spacing

The crack spacing in the two tested walls are measured with the help of the crack pattern sketches in Figs. 3.9 and 3.10, and for the symmetry of the crack pattern only the anchors face is here considered in the estimations of the crack spacing. The measured stabilized crack spacing, averaged on the two wall faces, was about 9 inches and 8 inches for the shear diagonal cracks in the SQ.5 and SQ0 walls, respectively. Flexural horizontal cracks within the boundary elements of the wall specimens are spaced on average 6 inches and 5 inches in the SQ.5 and SQ0 walls, respectively.

3.4.5 Base Curvature and Estimation of Plastic Hinge Length

The base curvature is estimated from the strain measurements obtained above the wall base. Figs. 3.12 and 3.13 show the estimated curvature profile for the SQ7.5 and SQ0 walls, respectively obtained from the deformation panel measurements. For the larger amplitude of drift demands, the curvature plot for the SQ0 wall is also zoomed in the first drift values to better capture the first yield drift demand (see Fig. 3.13). The theoretical value of the yield curvature as empirically estimated by Priestley et al. 2007 Priestley et al. (2007),

$$\chi_y = 2\frac{\varepsilon_y}{L_w} = 6.25 \cdot 10^{-05} 1/in, \tag{3.1}$$

is also represented in Figs. 3.12 and 3.13 with a red solid line. In Equation (3.1) the yield strain of the reinforcement ε_y is 0.3% in/in from material tests. It is noted that the base curvature experienced by the wall tested without axial load is about half of the base curvature of the wall tested with axial load at the same 1.8% drift ratio. The base curvature measured for the SQ0 wall almost doubled the ultimate curvature of the SQ7.5 wall, highlighting the large drift and deformation capacity reached by the wall absent axial compression load.

This observation is also confirmed in Fig. 3.14, which compares the curvature values measured at the base of wall SQ7.5 and wall SQ0 normalized by the yield curvature χ_y calculated according to Equation (3.1) by Priestley et al. (2007). This analysis indicates that beyond about 1% drift ratio, the linear relation between the two normalized curvature values deviates from the 1:1 line, since the absence of axial compression on wall SQ0 facilitates the strain and hence damage distribution. Conversely, the presence of axial load accelerated the degradation of wall SQ7.5 particularly in its lower region. It is

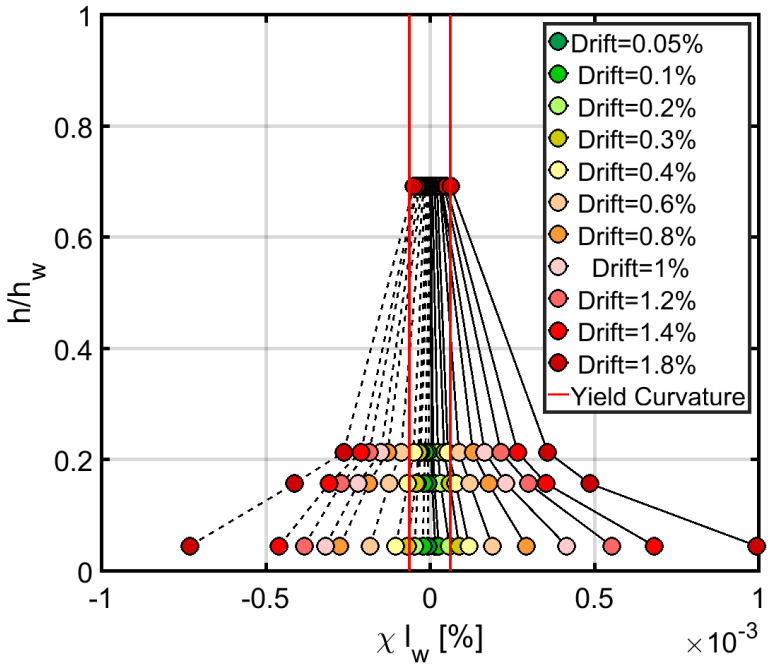


Figure 3.12: Curvature diagram estimated from gauges measurements in the wall tested with axial load

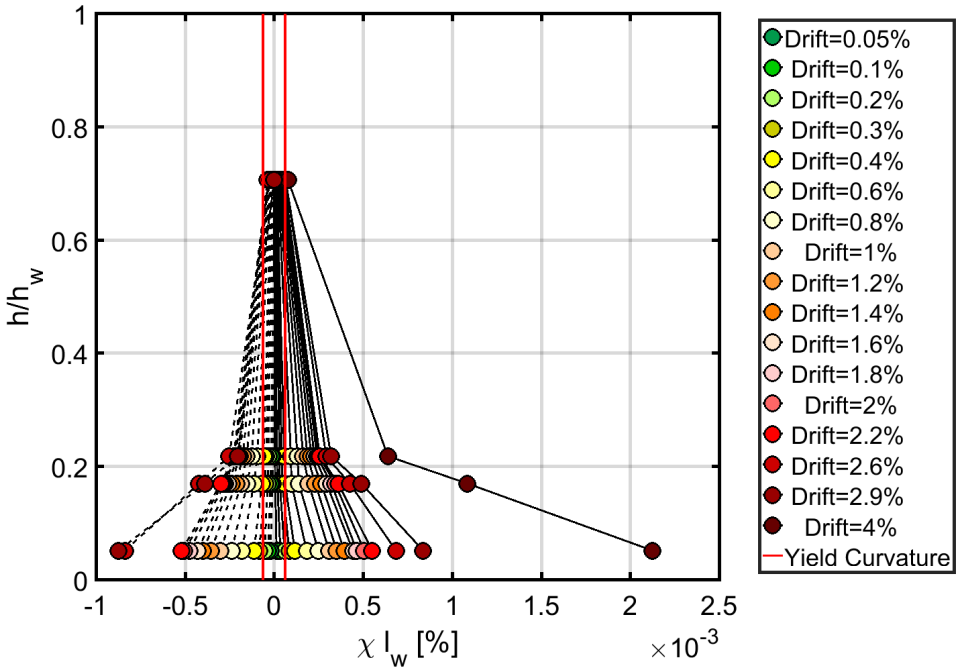
indeed noticed that many small cracks, primarily extension from main diagonal cracks, occurred in wall SQ0 due to the absence of compression loading, which promoted the vertical spread of damage.

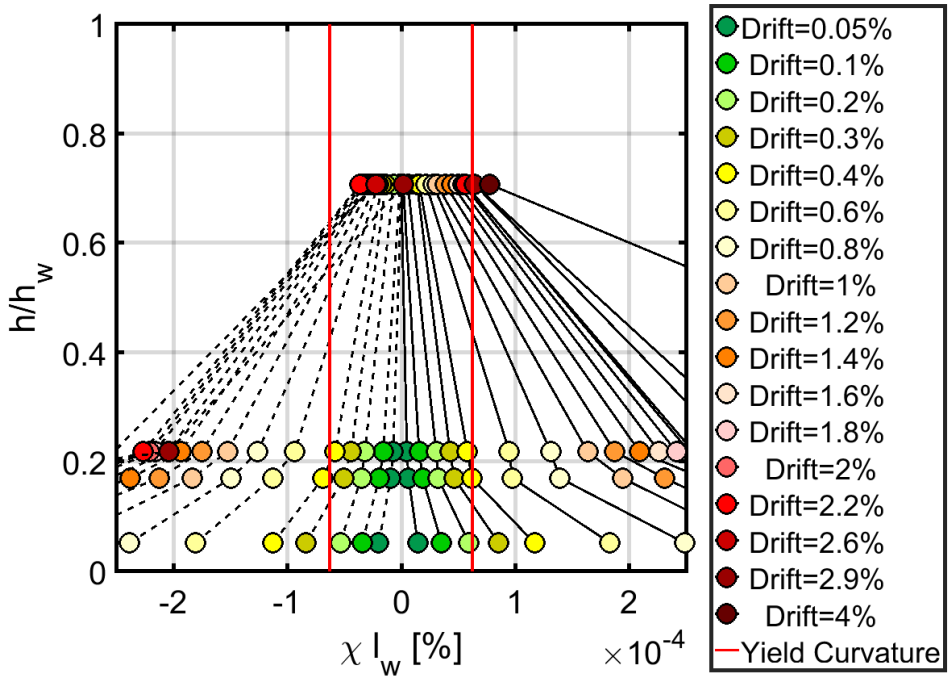
The plastic hinge length is not as well defined for squat walls as it is for flexure dominated walls. The length of the plastic hinge can be only estimated from the displacements measured during the test. The length of the plastic zone, L_{pz}, was estimated as the height above the footing for which the curvature was equal to the yield curvature. From Figs. 3.12 and 3.13 the estimated L_{pz} was about 0.66 L_w for both the SQ7.5 and the SQ0 walls, and consequently

$$L_p = 0.5L_{pz} \approx 0.3L_w \approx 2.4ft. \tag{3.2}$$

From the literature, typical values of the plastic hinge length of flexural shear walls reside in the range:

$$0.3L_w < L_p < 0.8L_w, \tag{3.3}$$





(b) Zoom in the small drift ratio amplitudes

Figure 3.13: Curvature diagram estimated from gauges measurements in the wall tested without axial load

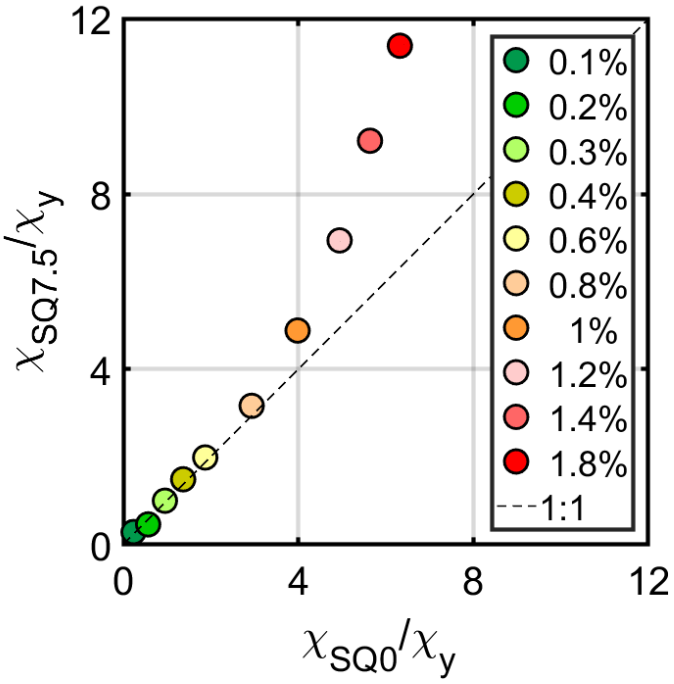


Figure 3.14: Comparison of curvature values measured during the wall tests at achieved drift amplitudes (average of push and pull) normalized by yield curvature X_y. Subscript SQ0 and SQ7.5 refer to the wall tested absent and with axial load, respectively

and for the full-scale walls considered here:

$$2.4ft < L_p < 6.4ft \tag{3.4}$$

hence the measured plastic hinge length resides in the lower bound of this range. However, it is notes again that no specific indications exist for squat walls, since they are supposed to show a mixed shear-flexure response with extended damage not limited to the wall base. Some of the equations described in Chapter 1 are here considered, despite their common application to slender walls, to better investigate the plastic hinge length for the two tested squat walls:

- Equation (1.3) in Chapter 1 formulated by Paulay and Priestley (1993):

$$L_p = \alpha \cdot 0.8 \cdot L_w + \beta \cdot H_w = 0.2 \cdot 96 + 0.044 \cdot 96 = 23 inches \approx 0.2 L_w, \tag{3.5}$$

  where wall dimensions are in inches (H_w=96 inches, L_w = 96 inches);

- Equation (1.4) in Chapter 1 formulated by Paulay and Priestley (1992):

$$L_p = 0.2 \cdot L_w + 0.07 \cdot (M/V) = 0.2 \cdot 96 + 0.07 \cdot 96 = 26 inches \approx 0.3 L_w, \tag{3.6}$$

where wall dimensions are in inches (M/V=96 inches, L_w = 96 inches);

- Equation (1.5) in Chapter 1 formulated by Bohl and Adebar (2011):

$$L_p = (0.2 \cdot L_w + 0.05 \cdot (M/V))(1 - 1.5P/f'_c A_g). \tag{3.7}$$

SQ7.5 wall:

$$L_p = (0.2 \cdot L_w + 0.05 \cdot (M/V))(1 - 1.5P/f'_c A_g) = (0.2 \cdot 96 + 0.05 \cdot 96)(1 - 0.07) \tag{3.8}$$
$$= 22 inches \approx 0.2 L_w$$

where the axial load ratio at the time of testing was $P/f'_c A_g \approx 7.5\%$ and wall dimensions are in inches (M/V= 98 inches, L_w= 96 inches).

SQ0 Wall:

$$L_p = (0.2 \cdot L_w + 0.05 \cdot (M/V))(1 - 1.5P/f'_c A_g) = (0.2 \cdot 96 + 0.05 \cdot 96)(1 - 0.0) \tag{3.9}$$
$$= 24 inches \approx 0.25 L_w,$$

where no axial load ratio was applied and wall dimensions are in inches (M/V=96 inches, L_w = 96 inches);

- Equation (1.6) in Chapter 1 formulated by Kazaz (2013):

$$L_p = 0.27 \cdot L_w \left(1 - \frac{P}{A_w \cdot f'_c}\right) \left(1 - \frac{f_y \cdot \rho_{sh}}{f'_c}\right) \left(\frac{M/V}{L_w}\right)^{0.45} \tag{3.10}$$

SQ7.5 wall:

$$L_p = 0.27 \cdot L_w \left(1 - \frac{P}{A_w \cdot f'_c}\right)\left(1 - \frac{f_y \cdot \rho_{sh}}{f'_c}\right)\left(\frac{M/V}{L_w}\right)^{0.45} \tag{3.11}$$
$$= 0.27 \cdot 96(1-0.07)(1 - \frac{67 \cdot 0.00267}{7})(1)^{0.45} = 23.5 inches = 0.2 L_w,$$

with the material properties at the day of test.

SQ0 wall:

$$L_p = 0.27 \cdot L_w \left(1 - \frac{P}{A_w \cdot f'_c}\right)\left(1 - \frac{f_y \cdot \rho_{sh}}{f'_c}\right)\left(\frac{M/V}{L_w}\right)^{0.45} \tag{3.12}$$
$$= 0.27 \cdot 96(1-0)(1 - \frac{67 \cdot 0.00267}{8.3})(1)^{0.45} = 25 inches = 0.3 L_w,$$

with the material properties at the day of test.

- Equation (1.7) in Chapter 1 formulated by Kazaz (2013):

$$L_p = 0.143 \cdot L_w + 0.072(M/V) = 0.143 \cdot 96 + 0.072 \cdot 96 = 21 inches \approx 0.2 L_w. \tag{3.13}$$

It is noted that the so calculated plastic hinge length values vary between 0.2 L_w and 0.3 L_w regardless the axial load applied to the wall and hence they lie in the lower limit of the common range represented in Equation (3.3), as observed from tests measurements, despite cracks and damage extended through the whole height of the tested walls.

The plastic hinge length expressions from the American, Canadian and European design codes are also considered here to estimate the plastic hinge length of the tested walls:

- **ASCE/SEI 41**, Elwood et al. (2007) (see Chapter 1):

$$L_p = 0.5 \cdot L_w = 48 inches; \tag{3.14}$$

- **NZ 3101.1.2006**, NZS 3101 (2006) (see Chapter 1):

$$0.15 \cdot M/V = 14.4 inches \approx 0.15 L_w; \tag{3.15}$$

- **Eurocode 8**, CEN (2004), (Equation (1.12) in Chapter 1):

  SQ7.5 wall:

$$L_p = 1/30 \cdot M/V + 0.2 \cdot L_w + 0.11 \cdot \frac{f_y(MPa) \cdot d_b}{\sqrt{f_c(MPa)}} \tag{3.16}$$
$$= 1/30 \cdot 2438.4 + 0.2 \cdot 2438.4 + 0.11 \cdot \frac{464 \cdot 15.9}{\sqrt{48}}$$
$$= 686mm(27in.) \approx 0.3L_w.$$

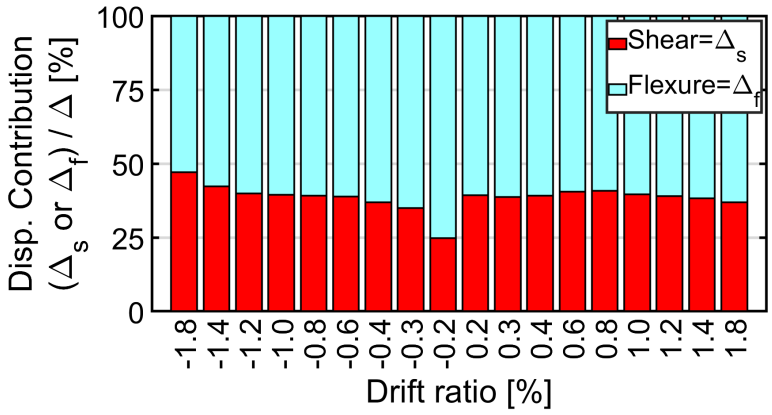
  SQ0 wall:

$$L_p = 1/30 \cdot M/V + 0.2 \cdot L_w + 0.11 \cdot \frac{f_y(MPa) \cdot d_b}{\sqrt{f_c(MPa)}} \tag{3.17}$$
$$= 1/30 \cdot 2438.4 + 0.2 \cdot 2438.4 + 0.11 \cdot \frac{464 \cdot 15.9}{\sqrt{57}}$$
$$= 676mm(27in.) \approx 0.3L_w.$$

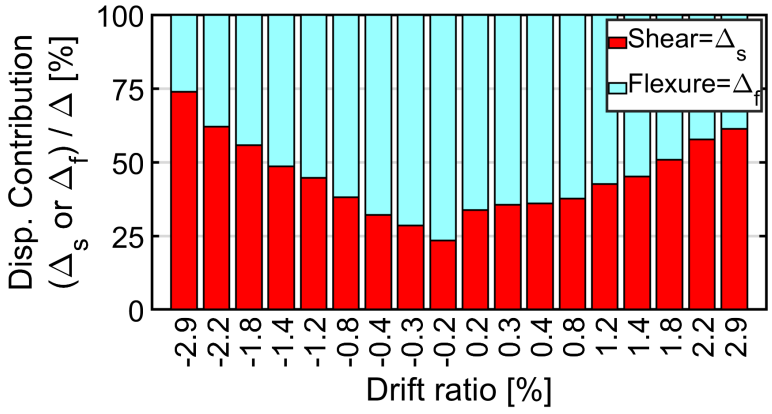
The experimental plastic hinge length value (same for both the tested walls, thus independent of the applied axial load ratio) is better predicted by the Eurocode 8, CEN (2004) formulation among the other here considered. However, the theoretic plastic hinge length $L_p = 0.5 \cdot L_w$ = 48 inches will be considered in the following analysis of the results to be able to trace more general conclusions on the anchors performance in concrete shear walls.

3.4.6 Components of Lateral Displacement

The relative contributions of flexural, shear and sliding displacement components to the total lateral displacement of the walls are estimated using the displacement sensors installed on the walls, see Fig. 3.4, and using the methods detailed in Massone and Wallace (2004). As expected, the major contribution to the total displacement is attributed to flexure and shear distortions, whereas sliding between the wall and the footing during both tests are observed to be negligible. Fig. 3.15 shows the shear and flexure contribution to the lateral displacement calculated at positive and negative peaks of the first cycle at each new drift amplitude of the imposed displacement protocol. Although the average shear contribution is about 40% for both the walls throughout the entire protocol, the effect of the axial load on wall SQ7.5 is visible in that the shear contribution remains nominally constant across all drift levels. This trend is indicative of a slowly degrading shear transfer mechanism. Conversely, analysis of wall SQ0 displacement contributions as shown in Fig. 3.15(b), indicate an increasing shear contribution with drift demand due to the absence of the restraining effect of axial load in wall SQ0. The shear displacement participation to the total displacement at the top of the wall achieved a maximum value of about 74% during the final cycle of the test of the wall SQ0, when significant strength degradation occurred, and reinforcing bars fractured. The average shear to flexure displacement components ratio, Δ_s/Δ_f, was about 60% for both tested walls, however, significant variation was measured at large wall drifts in wall SQ0. This observation concurs with prior studies. For example, Beyer et al. (2011) showed that large values of shear to flexure deformation ratio occur in laterally cycled walls with increasing intensity of deformation due to the degradation of the shear-transfer mechanism. Wall SQ0 experienced abrasive rubbing and spalling of the concrete along diagonal cracks through the web, aggravated by the absence of axial compression force in the wall. As a result, cracks did not properly close upon load reversal, causing additional deterioration and an increase in the measured shear deformation. Notably, Fig. 3.11 shows the exaggerated density of the cracks not only in the web region but also at the base of wall SQ0. The frame action developed in wall SQ7.5 is, on the contrary, evident in the absence of cracks in the web section extending about 20 inches from the wall base.



(a)



(b)

Figure 3.15: Flexural and shear displacement contributions to total lateral displacement at top of wall Δ. Values computed at both positive and negative peaks of the first cycle at each wall drift amplitude. a) wall SQ7.5 and b) wall SQ0

3.5 Comparison of Strength Predictions with Available Analytical Models

The availability of full-scale experimental data provides a unique opportunity to compare results with expressions in the literature. To this end, the shear strength of the low-aspect ratio walls may be estimated using the widely available strut-and-tie approach (e.g., Hwang et al. 2001) and the shear strength model (Krolicki et al. 2011).

3.5.1 Strut-and-Tie Model

Two main analytical models describe the shear strength of walls, namely the truss-based model and the strut-and-tie model. The shear strength of low-aspect ratio shear walls is, however, better estimated by the latter, for which compressive stress is concentrated along the paths of concrete struts, rather than uniformly distributed (Schlaich et al. 1987 and Yanez et al. 1989). Hwang et al. (2001) developed a modified strut-and-tie model, which considers the typical failure modes of squat walls to identify the three main load paths shown in Fig. 3.16. The main strut in the diagonal mechanism is oriented at an angle θ_d = 55 degrees from the horizontal, and the two couples which comprise flat and steep struts are θ_f = 35 and θ_s = 70 degrees relative to the horizontal base plane, respectively. Diagonal strut area is computed considering the wall thickness t_w multiplied by the projection of the compression length along the diagonal direction. The compression length, estimated as suggested by Park and Paulay (1975), is determined to be 30 inches and 24 inches for wall SQ7.5 and wall SQ0, respectively. It is noted that the effect of the axial compression on the wall SQ7.5 is included in the increased depth of the strut in the wall. In addition, the area of the ties is computed considering the reinforcement distribution in the wall. The horizontal ties include 14-#4 of horizontal shear reinforcement and the vertical ties considered the contribution of the 14-#5 of web vertical reinforcement. Accordingly, the strength of the struts and ties are calculated per Sections 23.4.1(a) and Section 23.7.2 in ACI 318 (2019), respectively. The effective compressive strength of concrete in a strut is then calculated per Equation 23.4.3 (ACI 318 2019) to be 4.7 ksi and 5.3 ksi for wall SQ7.5 and wall SQ0, respectively. The steel yield strength obtained from material tests is subsequently considered in the estimation of the ties' strength. By applying the equilibrium of the forces at the node, according to the free body diagram in Fig. 3.16, the lateral capacity of the walls is estimated to be about 507 kips and 424 kips for wall SQ7.5 and wall SQ0, respectively.

These analyses indicate that the strut and tie model developed by Hwang et al. (2001) overestimates the wall lateral strength by 15% and 37% for wall SQ7.5 and wall SQ0, respectively. It is noted that this overestimation is in line with expectations for walls tested under repeated cyclic loading, as they are known to suffer from cumulative damage not observed in monotonically loaded walls (Kassem 2014).

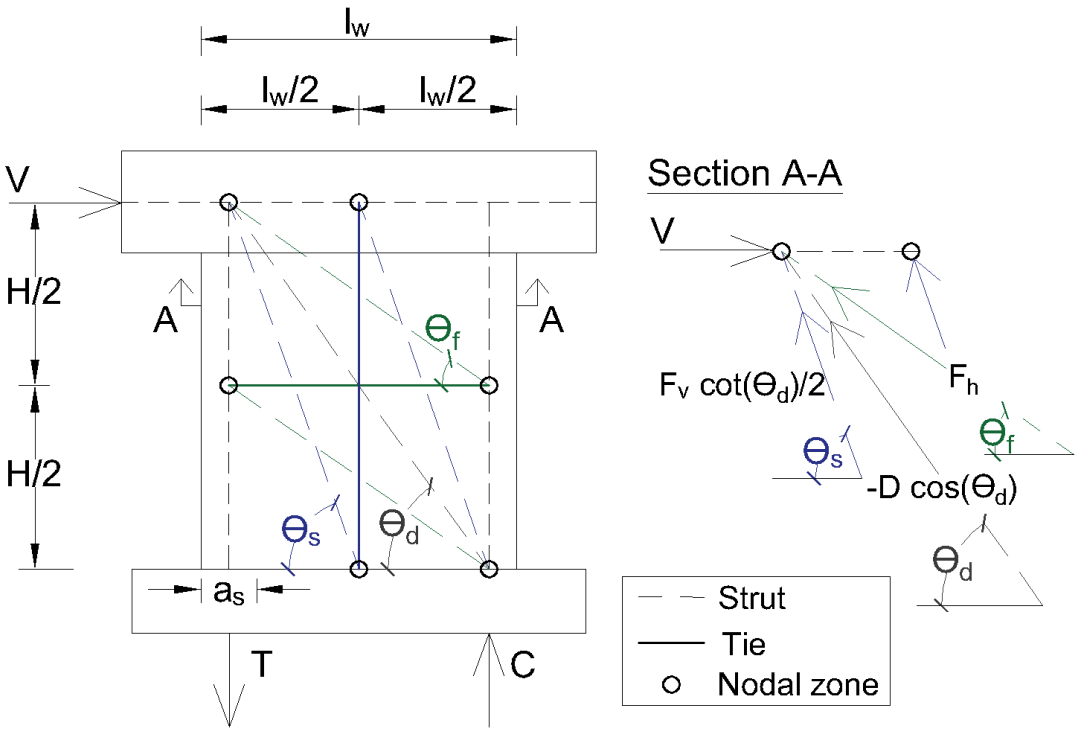


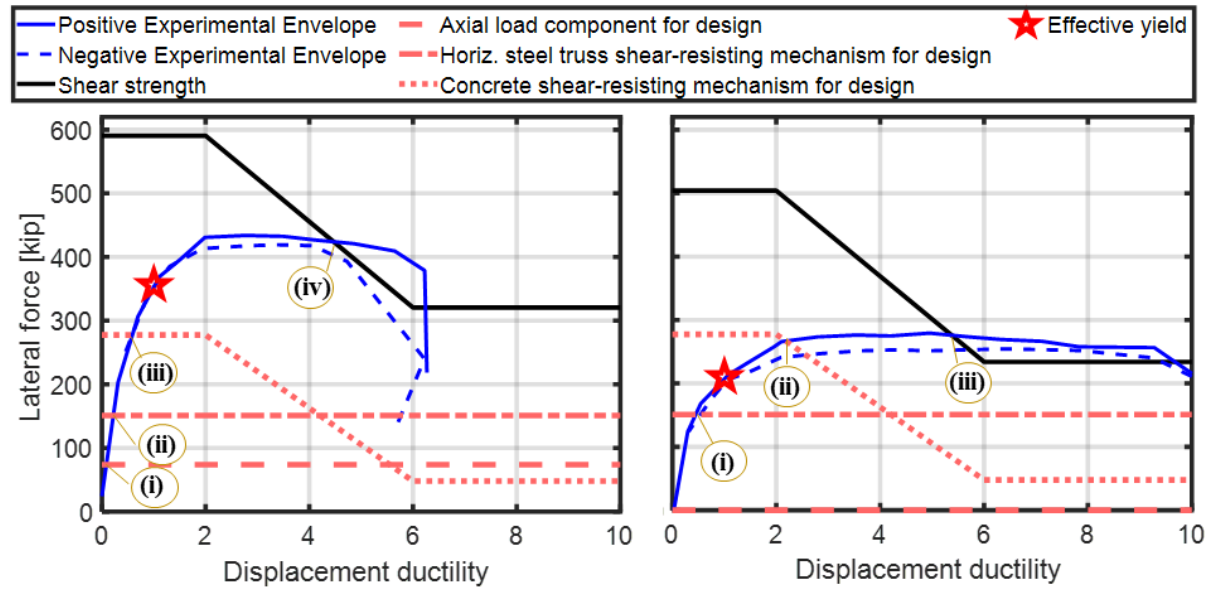
Figure 3.16: Strut and tie model (adapted from Hwang et al. 2001). V = lateral load at top of wall; T, C = tension and compression forces at the wall base, respectively; θ_d, θ_s and θ_f = main, steep and flat strut orientations with respect to the horizontal plane, respectively

3.5.2 Shear Strength Prediction

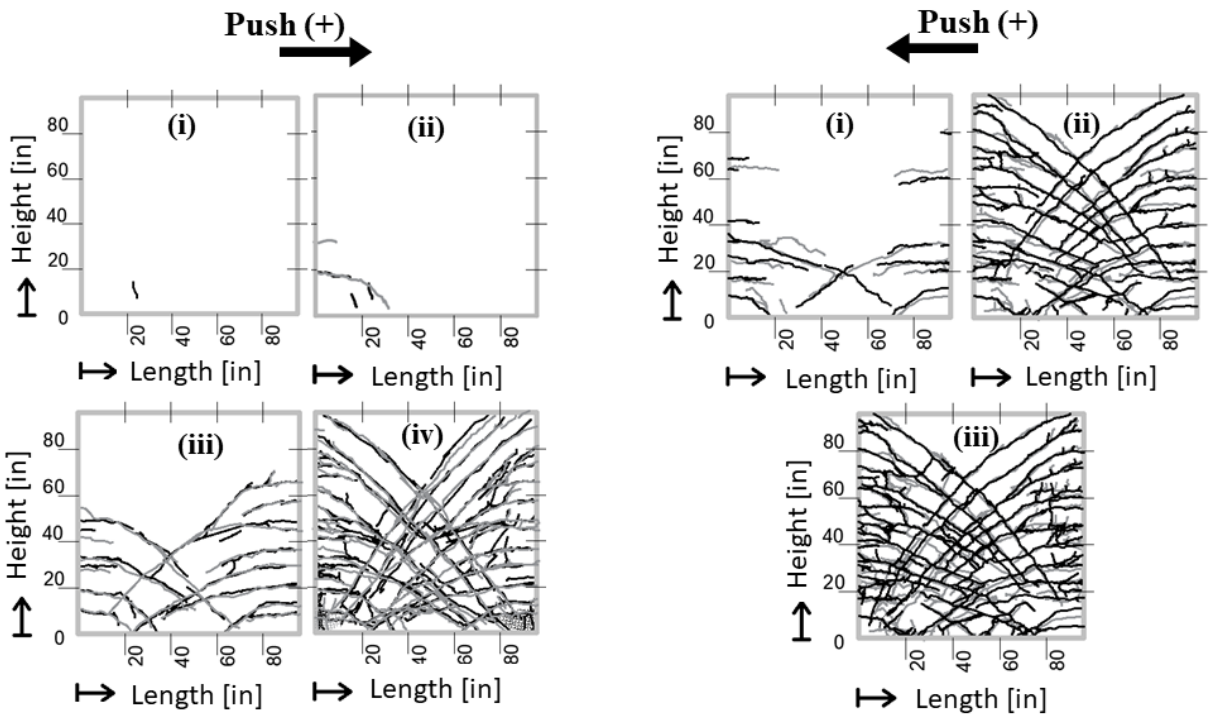
To offer an additional point of comparison, the measured shear strength was compared to estimates according to the shear model proposed by Krolicki et al. (2011). In this model, the shear capacity is estimated to be the summation of three components, namely a concrete shear-resisting mechanism, a horizontal reinforcement truss shear-resisting mechanism and an axial load component. To this end, Fig. 3.17 shows the experimental positive and negative envelopes overlaid with the predicted shear strength capacity versus the experimental displacement ductility exhibited by the walls. In this analysis, the experimental effective yield, taken as the drift at the intersection of the secant stiffness through

measured first yield, is considered to estimate the experimental displacement ductility. Individual components of the shear strength, calculated per Krolicki et al. (2011), are also shown in Fig. 3.17 with varied line types. Note that the concrete shear strength resisting mechanism varies with the displacement ductility, whereas the other two components are constant across all levels of displacement ductility. The resulting shear strength envelope is characterized by a linearly decreasing value between displacement ductility values from 2 to 6. To facilitate visual damage assessment, the crack pattern at the saturation of each shear resistance component is also represented in the subfigures below each of parts a and b. Notably, when the axial load component of the shear resistance is attained (Fig. 3.17(a),(i)) only small shear cracks developed in the base region of wall SQ7.5. When the horizontal reinforcement and concrete shear-resisting mechanisms are attained, the crack pattern in wall SQ0 is well distributed, see Fig. 3.17(b),(i)-(ii), whereas it is confined to about 2/3 of the wall height, due to the restraining effect of the axial load in wall SQ7.5, see Fig. 3.17(a),(ii)-(iii). It is also interesting to observe that in wall SQ7.5 the effective yield occurs after the concrete shear resisting mechanism is realized, whereas in wall SQ0 it occurs before this mechanism is attained. This appears to be due to the presence of the axial load, which globally increases the concrete strength of the wall. The shear envelope and the experimental envelope meet at displacement ductility of 4.5 and 5.4 for wall SQ7.5 and wall SQ0. Analysis of Fig. 3.17 indicates that in essence a mixed shear-flexure failure is thus reached (Krolicki et al. 2011), which corroborates visual observations. At this stage, the crack pattern of the two walls similarly shows an intensely distributed damage with diagonal cracks extending from lower to upper opposing corners of the walls. Minor concrete crushing/spalling at the bottom corner region of wall SQ7.5 is also visible, see Fig. 3.17(a),(iv)-(b),(iii). The effect of the axial load on the damage distribution is particularly evident in the limited number of vertical splitting cracks in wall SQ7.5 (Fig. 3.17(a),(iv)). Fig. 3.17 conveys important considerations regarding the response modification coefficient factor R, which is related to the displacement ductility according to the equal displacement approach (i.e., μ_Δ = R). In principle the current value of R = 5 adopted in ASCE/SEI 7-16 (2016) for specially reinforced shear walls is intended to correspond to the saturation of shear strength of the wall. Failure can be expected after the attainment of the shear strength of the wall. In the present walls, attainment of shear strength is nominally in agreement with an assumed average of the specimen pair of about μ_Δ = 5.0. However, it is notable that the wall with axial loading reveals a slightly lower value of μ_Δ = 4.5 at attainment of shear strength, as estimated per

the Krolicki et al. (2011) model.



(a)



(b)

Figure 3.17: Experimental envelope curve compared to shear strength predicted by the Krolicki et al. (2011) model. a) Wall SQ7.5 and b) wall SQ0, (i)-(iv): sketches of crack pattern at attainment of components and total shear strength. [1 kip =4.45 kN; 1 in =25.4 mm]

3.6 Summary Remarks

Reinforced concrete shear walls are commonly used to provide lateral strength and stiffness to building systems. Nonstructural components are often attached to these concrete walls via metal anchors, thus their functionality is affected by the integrity of the concrete. The distribution of damage in shear walls is therefore important to assess anchorage performance, particularly under earthquake loading when progression of cracking and spalling of the concrete is inevitable (for more on this refer to Chapter 4). To link physical damage with component performance, U.S. design codes correlate levels of seismic performance with damage states of increasing intensity. In this regard, seismic performance-based design guidelines typically include three important limit states, namely: Immediate Occupancy (IO), Life Safety (LS) and Collapse Prevention (CP), each associated with certain drift ratio values. In the present dissertation, a unique full-scale experimental program intends to provide data to assess damage in reinforced concrete shear walls and thus offers an opportunity to evaluate the robustness of these drift limit values. To this end, a pair of reinforced concrete low-aspect ratio walls were designed with AR = 1 and subjected to cyclic displacement of increasing amplitude to simulate seismic-induced damage. Two levels of constant axial loads were applied to the walls, namely 7.5% and 0% of their section capacity (wall SQ7.5 and wall SQ0, respectively). Boundary elements were implemented in the walls design to engage the flexural response and increase the displacement capacity of the walls. Results indicate that the displacement ductility capacity of these low-aspect ratio walls is comparable to the experimentally determined ductility capacity measured for a related, but slender wall previously tested within this research program (see Chapter 2).

ASCE 41 (2014) is adopted herein to construct envelope curves for the three walls tested. Analysis of these curves indicates that drift capacity is consistently underestimated for all three walls. In particular, it is noted that the shear strength of wall SQ0 (wall tested without axial load) is significantly overestimated. The walls performance at first yield, effective yield, lateral strength and 80% post-strength is also evaluated and compared to drift limits proposed in design and rehabilitation guidelines (ASCE 356 2000). It is noted that drift limit values associated with the LS and CP performance limit states in (ASCE 356 2000) underestimate the actual drift capacity of the tested full-scale walls, leading to conservative estimations. Physical damage at the IO, LS and CP limit states was carefully documented in the

test program to elicit the effect of axial load on reinforced concrete shear walls and facilitate assessment of the progression of damage. Analysis of this photographic and other documentation taken during testing indicates that axial compression facilitated crack closure and therefore enhanced strain localization and local damage within the lower half of the wall's height, as also reflected in the measured curvature profile.

To complement this effort, shear and flexural components of total displacement are estimated from the displacement sensors installed on the wall faces. The average shear contribution is determined to be about 40% for both walls. However, the shear displacements increased significantly with the drift demand in the squat wall without axial load, whereas it remained approximately constant in the comparable squat wall with axial load imposed. The degradation of the shear-transfer mechanism is, indeed, enhanced by unrestrained shear sliding in walls absent superimposed axial load.

Finally, the experimental results are compared to shear strength values predicted using two well-known methods available in the literature, namely: 1) the strut-and-tie model and 2) a shear strength model. To this end, the strut-and-tie model proposed by Hwang et al. (2001) overestimated the wall lateral strength by 15% and 37% for the wall with and without axial load, respectively. However, this is in line with expectations for walls tested under repeated cyclic loading, which will realize more significant damage prior to strength attainment when compared with walls loaded monotonically. The shear model proposed by Krolicki et al. (2011) on the other hand correctly predicts a mixed shear-flexure failure at a displacement ductility of about 5, which reflects the response modification factor R = 5 currently attributed to RC specially reinforced shear walls in ASCE/SEI 7-16 (2016).

3.7 Acknowledgment of Publications

Chapter 3 contains material submitted for publication in the following journal paper: Faraone, G., Hutchinson, T. C., Piccinin, R., and Silva, J. (2021). "Seismic Performance of Varying Aspect Ratio Full-Scale Concrete Walls," ACI Structural Journal (under review). The dissertation author was the primary author on this paper. Chapter 3 also contains material published in the following report: Faraone, G. and Hutchinson, T. C., 2021, "Behavior of post-installed anchors in reinforced concrete shear walls subjected to cyclic lateral loading. Part II: squat walls test program," *Structural Systems*

Research Project Report SSRP- 2021/01, UC San Diego. The dissertation author was the primary author on this report.

Chapter 4

Response of Anchors in Cracked Concrete

Post-installed anchors connect various components to concrete members, which undergo cyclic cracking during a seismic event. Cracks and damage occurring in concrete members as a result of earthquake-induced ground motion may impact the performance of anchors installed in those members. In recognition of this, current guidelines to qualify anchors for seismic applications require adequate performance in cracked concrete without substantial load loss. The interaction between anchors and pure flexural cracks has been studied for decades (Eligehausen et al. 2006); however, the response of anchors to shear and x-type (crossing) cracks—that is, the complex situation realized in shear-flexure structural components—has been neglected thus far. Hence, the behavior of expansion and bonded anchors installed horizontally in full-scale reinforced concrete shear walls was investigated, while the walls were subjected to cyclic lateral loading. Experimental results on the behavior of the post-installed anchors are presented in this Chapter. The test walls, described in Chapters 2 and 3, were detailed with boundary elements to ensure a range of crack types with appreciable distribution throughout the wall. The load and displacement histories of the anchors are analyzed to characterize their performance under a variety of concrete damage states. Anchor axial strength reduction is estimated at key performance limit states typical of concrete shear walls in an effort to link the structural components performance with the anchor response. Results confirm the sensitivity of the performance of expansion anchors amidst the presence of a variety of cracked concrete conditions. Finally, the residual tension capacity of the anchors is assessed in contrast with the concrete damage distribution in the wall. Anchors in the slender wall test

demonstrate sufficient residual axial load capacity and post-peak strength during pullout tests to failure, as opposed to anchors in the squat wall tests, which showed limitations in their residual pullout capacity, due to the extensive damage developed throughout the whole wall faces.

4.1 Introduction

In reinforced concrete (RC) members, ductility predictably comes with cracking because it is associated with displacement and deformations. Moreover, the performance of fasteners embedded in concrete is inevitably affected by the occurrence of cracks. The likelihood of the presence and extent of such cracks will be greater for RC members subjected to earthquake demands when these members are stressed beyond their elastic limit.

In Europe, current anchor qualification guidelines EOTA TR 045 (2013) subdivide the anchors into two seismic performance categories, defined by the seismicity of the site and the importance class of the building. In the United States, qualification procedures provide only requirements for one seismic performance category for anchors to be used in both cracked and uncracked concrete (ACI 355 2019). However, anchor performance categories and the expected inelastic behavior of the building structure are not explicitly related in any anchor qualification guidelines because different structural systems located at the same site may undergo varying types and degrees of damage.

Anchor performance is not only influenced by the load transfer mechanism and anchors characteristics, but also by the direction of load application, amplitude, rate, and number of cycles of the imposed action. For example, during a seismic event, anchors may be subjected to a combination of cyclic tension (direction of action along long axis of anchor body) and shear (direction of action orthogonal to long axis of the anchor body) forces while also carrying their service load. Affecting their boundary conditions, i.e., the material surrounding the anchor and the interface between this material and the anchor itself, anchors may also reside in cracks, which can open and close several times during the earthquake, while the structure is deforming. The state of the surrounding concrete is, therefore, of primary importance, as cracks may perturb the hole and the stress distribution and thus compromise the anchor's behavior. It is well known, for example, that the axial stiffness and strength are significantly reduced if anchors are located in flexural cracks (Eligehausen et al. 2006). The behavior of anchors in

cracks has been studied since the 1980s; however, these studies primarily focused on the performance of anchors under service conditions with an assumed maximum crack width of 0.3 mm, whereas fastener qualification under a wider range of performance states is desirable. Furthermore, in current design, to reliably bound the expected crack width for the purpose of assuring adequate behavior, the location of the fasteners is required to be outside of the plastic hinge zone (ACI 355 2019). This was supported by the evidence that large crack widths inside of the plastic hinge length make fastening impractical by reducing the embedment depth after concrete spalling (Eligehausen et al. 2006). Eligehausen and Hoehler (2003) performed a parametric study on RC flexural members to determine the maximum crack width expected outside of plastic hinge regions. This maximum crack width offers guidance for qualification testing of anchorage in the presence of cracks. In other words, outside of the zone of plastic deformation, the maximum crack opening width, for which fastenings should be qualified, is that closest to the attainment of the sectional yield curvature. In this sense, it is independent of the performance state (that is, service or seismic level). Results of the parametric study showed that in flexure, the crack width at yield varied between 0.3 and 0.9 mm. To assess the impact of such crack widths on anchor performance, Mahrenholtz et al. (2016) tested a variety of anchor types under conditions they were not qualified for, imposing a maximum crack width of 0.8 mm, which was significantly larger than the 0.5 mm specified in the guidelines evolving at the time—that is, ETAG version of 2006 and ACI 355.2-07 (Mahrenholtz et al. 2016). Mahrenholtz performed simultaneous load and crack cycling tests for the first time, adopting a unified test protocol that was developed to combine different demand levels. The maximum crack width of 0.8 mm was generally accepted to occur before yielding of the reinforcement, just outside of the plastic hinge zone, and it was assumed to represent extreme conditions (95% fractile). The unified protocol with a maximum crack width of 0.8 mm was adopted in the 2012 version of ETAG 001- Annex E (refer to Mahrenholtz et al. 2017).

Absent from investigations thus far, however, has been the effect of multiple intersecting cracks at the anchor location on the anchor performance. It is hypothesized that this more complex crack boundary condition may severely undermine the behavior of certain anchor types. Bonded anchors, for example, may suffer a reduced bonded area if multiple cracks cross the adhesive that fills the hole, and they may fail by pullout (that is, bond failure). Bond loss may also bring about the generation of tensile stresses perpendicular to the bond interface required to balance the secondary moment given

by the eccentricity between the tension load and the resultant of the bond stresses (Eligehausen et al. 2006). Similarly, multiple cracks widening with time and passing through the anchor's location will likely reduce the expansion force developed by expansion anchors. Even small crack openings may reduce the otherwise reliable expansion stress by unloading the concrete, while multiple crossing cracks at the anchor may unevenly modify the expansion capacity, compromising the overall performance of these types of anchors (Eligehausen et al. 2006).

Advance understanding of the impact of these issues on the performance of anchors in cracked concrete, the full-scale laterally loaded RC shear walls test programs, described in Chapters 2 and 3, were used to investigate and cross-compare the behavior of bonded and torque-controlled expansion anchors in the presence of a wide range of crack types evolving during the wall cyclic load application. The details of the RC shear walls and synthesis of their performance are described in Chapters 2 and 3 of this dissertation. The performance of the seventy-two anchors in terms of axial load, displacement, residual capacity and physical observations related to failure characteristics are discussed herein with additional data from the anchor observations are reported in Appendix C and Appendix E.

4.1.1 Research Significance

Current anchor qualification procedures are premised on crack width values expected in flexure-dominated RC members. However, anchors are more often installed in walls and slabs than in beams. In the former, the crack distribution manifests in shear-flexure combinations. The impact of such crack patterns on the performance of post-installed anchors has yet to be investigated experimentally. Moreover, prior experimental studies on anchor seismic performance have thus far been conducted with anchors installed vertically. The present investigation offers important insight into the behavior of post-installed anchors placed horizontally in cracks naturally evolving in full-scale modern designed RC shear walls subjected to simulated earthquake loading.

4.2 Experimental Investigation

4.2.1 Description of the Post-Installed Anchors

Two types of post-installed metal anchors were selected among the fasteners of interest in most practical shear wall applications—namely, bonded and torque-controlled expansion anchors. These two types of anchor bolts are expected to have very different behavior in even single tension cracks, thus offering an important opportunity for cross-comparison. Bonded anchors are conventionally not ideal for resisting tension loads in cracked concrete because tensile stresses are transmitted to the concrete via bond stress, which can partially be destroyed by cracks (Eligehausen 1992). An adhesive material (mortar) typically bonds the threaded rod of the anchors to the sides of the drilled hole. When continuity of the adhesive material around the anchor is disrupted by one or multiple crossing cracks, the ensuing unbalanced stresses affect the anchors capacity, see Fig. 4.1. In this study, an ultimate performance hybrid mortar was selected for its suitability in cracked applications. In contrast, the torque-controlled expansion anchors selected in this study transfer tensile forces by means of friction between an expanded sleeve and the concrete and partly via mechanical interlock. In these anchors, the installation torque moves the cone at the embedded end of the anchor up into the expansion sleeve (e.g., refer to Eligehausen et al. 2006). Thus, the anchor develops tension and mobilizes frictional resistance between the expanded element and the sides of the drilled hole and, in turn, generates expansion forces—that is, compression forces acting on the concrete due to the dilation of the expansion sleeve, see Fig. 4.1. If the concrete surrounding the sleeve is overall continuous and undamaged, the stresses are ideally symmetrically distributed around the anchor. When external load is applied to the anchor, tensile stresses are gradually relieved until residual stress is completely balanced by the external load. The immediate outcome is the further expansion of the anchor, generated by the additional movement of the cone into the expansion sleeve. Additional friction is developed to resist the increasing external load only if the friction between the cone and the sleeve of the expansion anchor is lower than the friction forces generated between the sleeve and the concrete. Otherwise, the anchor is pulled out of the concrete hole. Torque-controlled expansion anchors were typically designed to respond to widening cracks by expanding further into the concrete. This mechanism, termed “follow-up expansion,” reestablishes the expansion forces up to a certain limit. However, the described mechanism may be compromised by the presence of defects in the

concrete. In the absence of substantial expansion forces, the anchor may not attain strength from the very beginning, but rather could spin when the installation torque is applied.

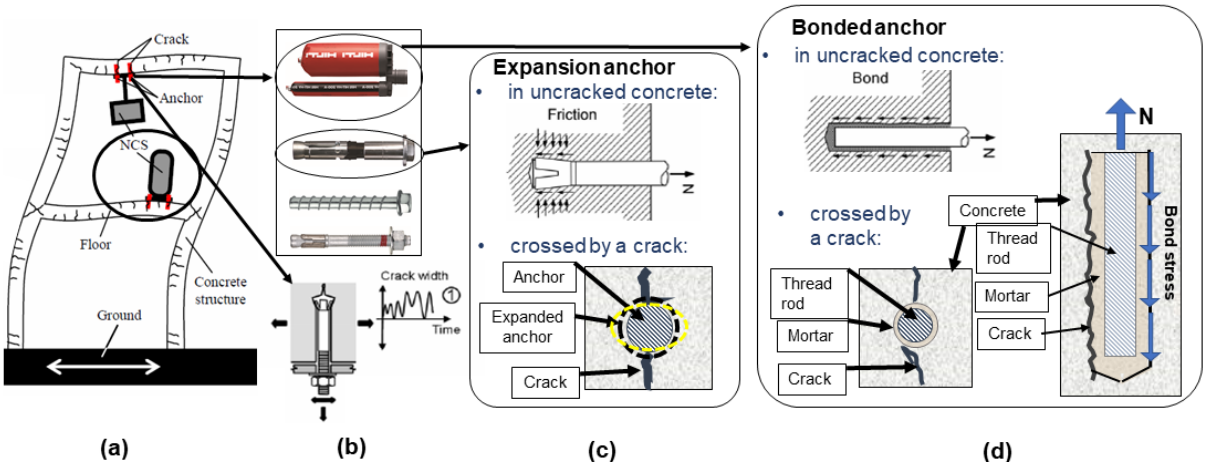
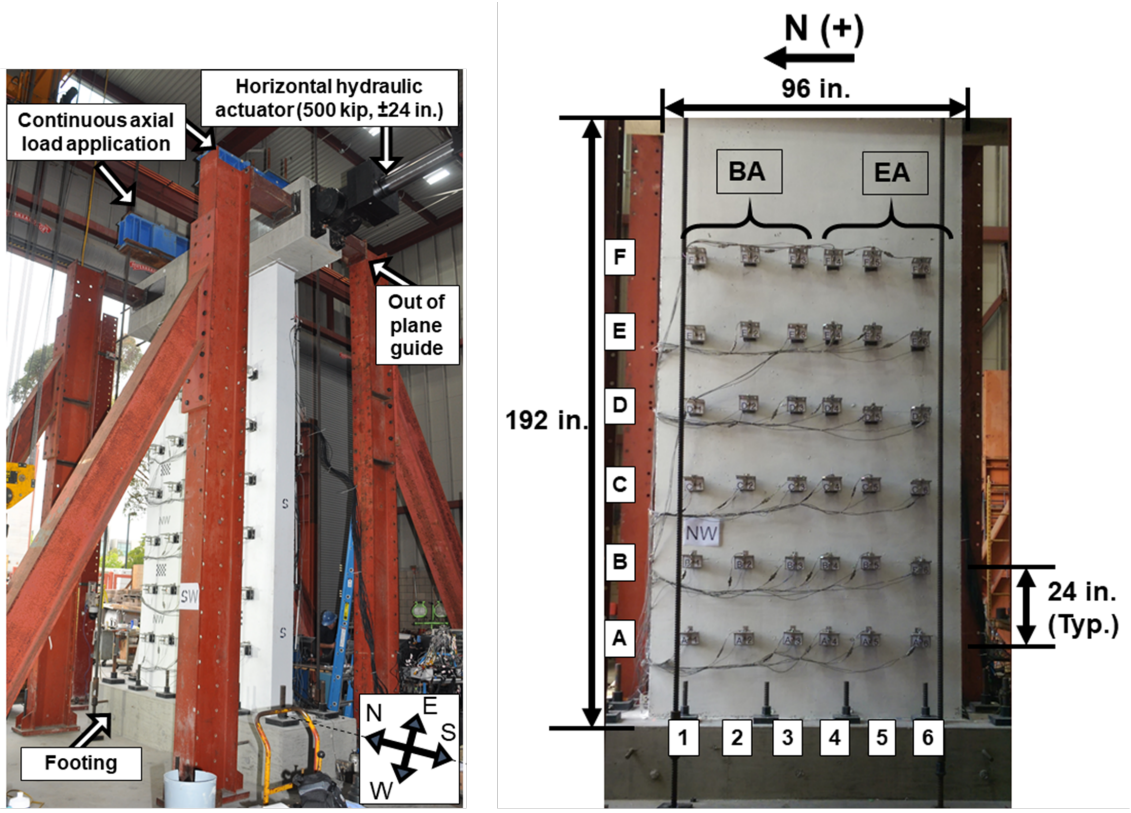


Figure 4.1: Schematic showing the effect of cracks on anchors: (a): seismic action on a concrete frame induces cracking. (b) Post-installed anchors connecting nonstructural components are in crack cycling boundary conditions. Effect of crack crossing on (c) expansion anchors and (d) bonded anchors

In these tests, a total of eighteen 0.5 inches diameter bonded anchors and fifty-four 0.47 inches diameter torque-controlled expansion anchors were installed in the faces of the three full-scale walls, discussed in Chapters 2 and 3. The anchors were installed prior to application of any gravity or lateral load to the wall. Of these anchors, eighteen bonded and eighteen expansion anchors were installed in the slender wall and distributed in six rows (denoted rows A to F) with six anchors each row, thus approximately equally spaced in Columns 1 to 6; refer to Fig. 4.2. Anchors in columns 1-3 were bonded anchors (BA) and anchors in columns 4-6 were expansion anchors (EA) as reported in Fig. 4.2. Similarly, the remainder torque-controlled expansion anchors were installed in each face of the two full-scale squat walls (eighteen anchors per face), as it was evident from the slender wall-anchor test program that further study on expansion anchors was warranted. As the full-scale squat walls are half the height of the slender wall, the anchors were distributed over three rows only (denoted rows A to C) with six anchors in each row, thus approximately equally spaced in Columns 1 to 6; refer to Figs. 4.3 and 4.4.

The distance between each anchor was equal to or greater than 1.5 h_{ef} to avoid anchor interference during the wall cyclic tests. Values of the embedment depth h_{ef} are reported in Table 4.1, along with other anchor installation and design parameters. Commonly available bonded and expansion anchors were slightly modified to accommodate the tension load application setup, which is illustrated in



(a) **(b)**

Figure 4.2: Slender wall SL7.5 tested with axial load: (a) annotated photograph of test setup (b) photograph of wall and anchors prior to testing [1 in = 25.4 mm; 1 kip = 4.45 kN] BA= bonded anchors and EA= torque-controlled expansion anchors

the next section. The anchors were formed of high-strength (12.9 grade steel) thread rods approximately 11.5 inches long, high-strength nuts, and spherical washers were used. To achieve the required installation torque, the axial load on the expansion anchors was T_{inst} = 6 kip, whereas the conventional pre-load on the bonded anchor was selected to be 1 kip. The seismic design axial load $T_{seismic}$ was calculated considering the concrete strength of each wall at the day of testing (see Appendix D for more information). However, a target value T_{design} (see Table 4.1) about 20% greater than the seismic design axial load was applied to the anchors to account for load relaxation expected in the loading setup, as explained in the next section.

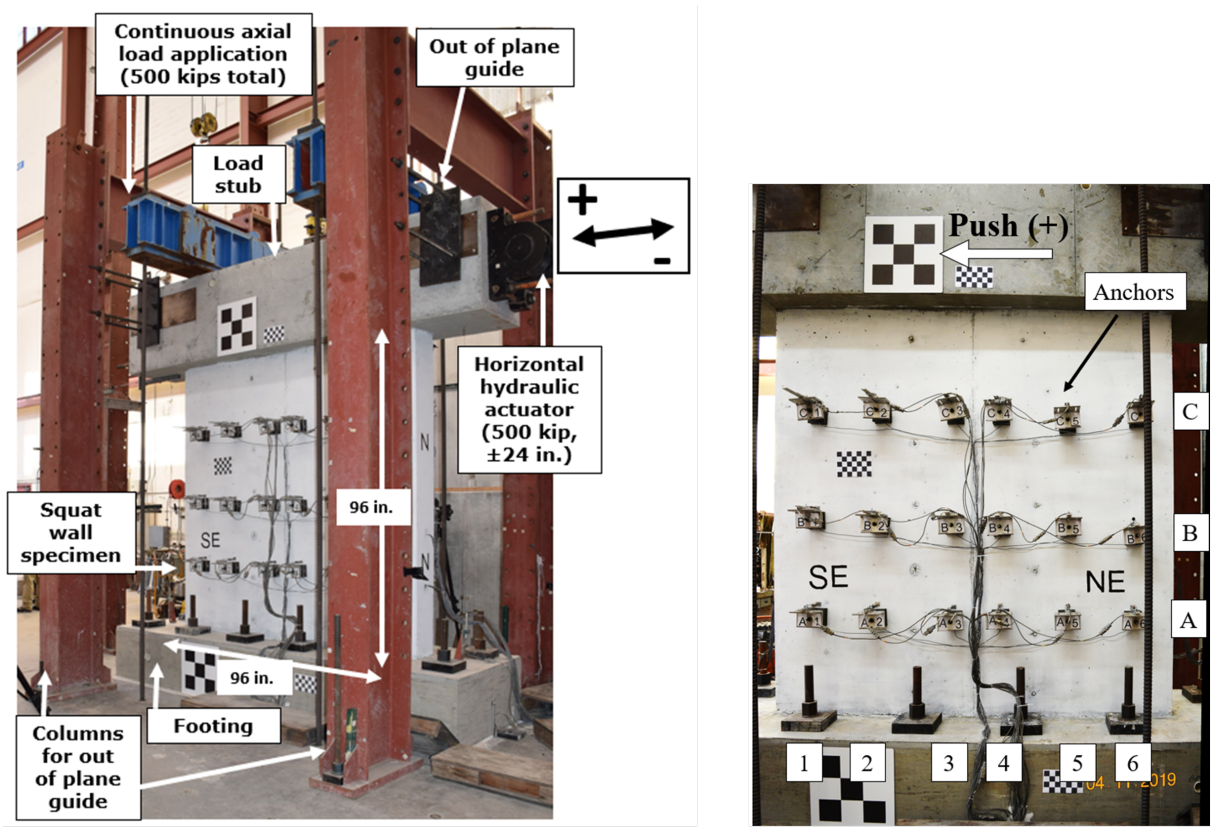
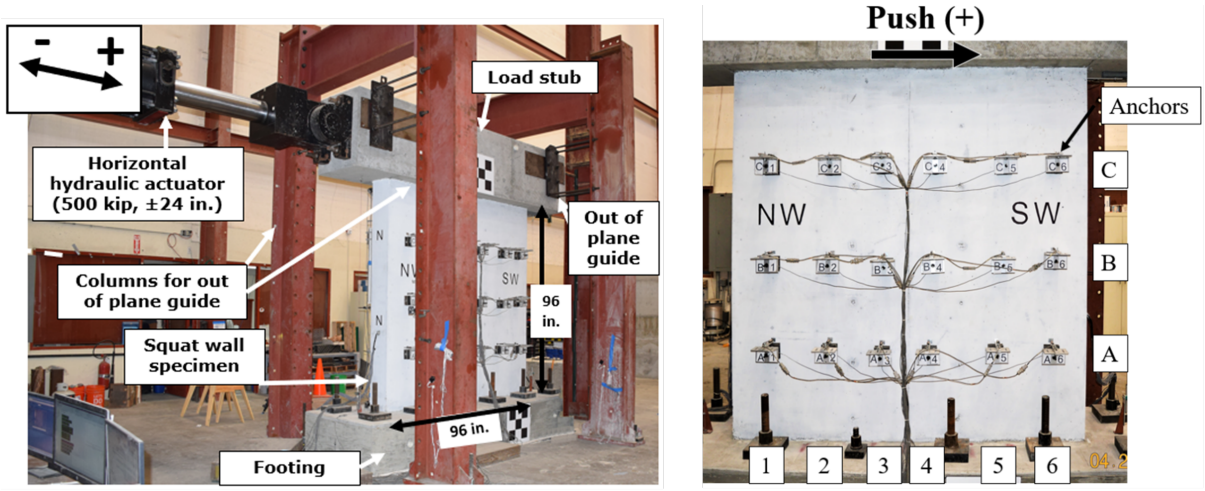


Figure 4.3: Squat wall SQ7.5 tested with axial load: (a) annotated photograph of test setup (b) photograph of wall and anchors prior to testing. Note all anchors are EA. [1 in = 25.4 mm; 1 kip = 4.45 kN]

4.2.2 Anchor Axial Loading Setup

To create a realistic application of constant axial load and replicate as near as possible field conditions, anchors were loaded in tension by means of a self-reacting loading assembly. This setup was designed to induce minimal out of plane loading on the wall. Namely, the loading assembly was targeted to hold the anchor load constant for the duration of the wall lateral load test through a spring mechanism mechanized by hardened rubber bumpers. These bumpers were able, when compressed, to sustain a large load and to transmit it to the anchor. The advantage of using these types of springs, as opposed to typical steel springs, resided in the softness of the material, which allowed the anchors to slightly adjust without losing a large amount of the applied design load. Moreover, the bumpers are compact and offer a natural through-hole compatibility for the anchor rod extension outside of its embedded region. For



(a) **(b)**

Figure 4.4: Squat wall SQ0 tested without axial load: (a) annotated photograph of test setup (b) photograph of wall and anchors prior to testing. Note all anchors are EA. [1 in = 25.4 mm; 1 kip = 4.45 kN]

the anchors located in the full-scale slender wall in rows A to E (from 2 to 10 ft above the wall-footing interface) and for all the anchors installed in the squat walls the loading assemblies were equipped with one compression-only load cell. Fig. 4.5 shows the typical load and measurement setup for the installed anchors. The bonded and expansion anchor setups differed slightly to accommodate the varied fastening thicknesses needed for the expansion anchor to properly be installed, as well as the bumper size, for the different levels of applied design load. Regardless of the anchor type, the load cell was placed between two cold-rolled steel plates at the interface between the bumper and the face of concrete to accurately measure the global tension applied to the anchor. Anchors were loaded to the design tension T_{design} reported in Table 4.1 by compressing the bumper, which was placed in series with the anchor and first nut. The bumper was compressed with an aluminum angle that served both as reaction surface and as attachment for a displacement gauge. It is noted that the global displacement of the system (anchor plus bumper) was measured; thus, system displacements were only cross-compared among anchors in the interpretation of the results. All the elements of the loading setup were placed concentric with the anchor rod to minimize inaccurate readings due to eccentricities. Tests were performed on the assemblies shown in Fig. 4.5 to assess the potential for relaxation of the rubber bumper. Pilot tests conducted prior to the shear wall tests, with only the anchor bolts and loading assembly, indicate that an approximate

Table 4.1: Anchor installation and design parameters

Parameter	Symbol	Units	Anchor Type (ID)			
			Bonded (BA)	Expansion (EA)		
			SL7.5	SL7.5	SQ7.5	SQ0
Thread rod diameter	d	in. (mm)	0.5 (13)	0.47 (12)		
Thread rod type			Gr. 12.9	Gr. 12.9		
Effective depth of embedment	h_{ef}	in. (mm)	4 (102)	3.2 (81)		
Selected pre-load (axial)	T_{inst}	kip (kN)	1 (4)	6 (27)		
Seismic design axial load [1]	$N_{ba,seismic}$	kip (kN)	2.8 (13)	5.1 (23)	5.6 (25)	6 (27)
1.2 x Seismic design axial load (applied)[2]	T_{design}	kip (kN)	3.5 (16)	6.3 (28)	6.7 (30)	7.2 (32)

[1]: Calculated considering the concrete strength at the day of testing (6 ksi, 7.4 ksi and 8.3 ksi for SL7.5, SQ7.5 and SQ0 walls, respectively);
[2]: Target applied axial load on the anchors was 20% greater than the seismic design axial load to account for load relaxation expected in the loading setup.

20% relaxation in load may be realized; therefore, the design loads, $T_{seismic}$ in Table 4.1, were increased to account for this effect during the slow cyclic lateral load application to the full-scale shear walls. In addition, Table 4.1 shows that design loads for expansion anchors slightly differed, as they are a function of the concrete strength at the day of testing.

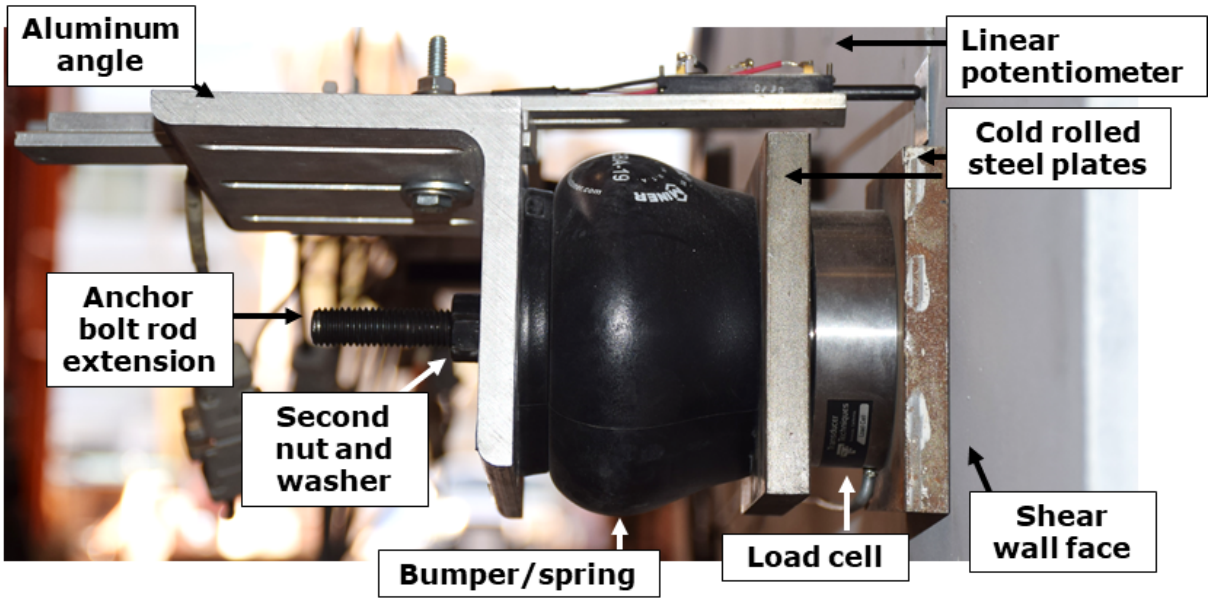
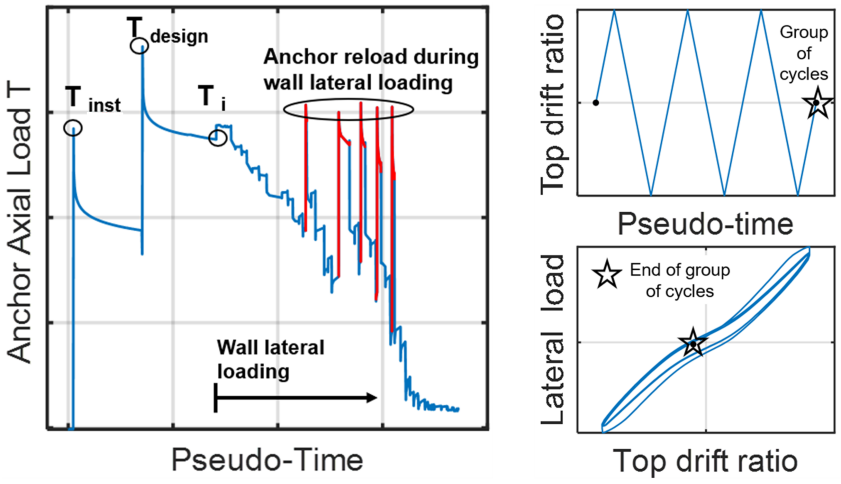


Figure 4.5: Annotated photograph of the anchor load setup (typical)

4.2.3 Anchor Load History

Anchors were installed in one face of the walls and pre-loaded prior to the application of load to the walls themselves. Central to these tests is understanding the anchor history of tension load. Prior to summarizing this information for various anchors during the shear wall test program the anchors load history is conceptually presented in this section. The anchors experienced variation in axial load from the point in time when the bumpers were initially compressed until the end of the wall tests (Fig. 4.6(a)). Initially, an installation load T_{inst} = 1 kip was applied to the bonded anchors. For the torque-controlled expansion anchors T_{inst} was the axial load corresponding to the installation torque required to activate the anchoring mechanism in the anchor (also called preload). From the reference tests, the preload was found to be approximately 5500 lb, as indicated by the change in slope of the curves in Figs. 4.8(b) and 4.9(a). In some instances, T_{inst} decreased slightly due to relaxation of the bumper. To compensate for this, the bumper compression was increased to the design load T_{design}. Similarly, a minor relaxation of the bumper results in a reduction of the actual load on the anchor. Consequently, the tension in the anchor T_i is realized prior to the start of the wall tests, when the initial lateral displacement was imposed at the top of the walls. In other terms, when the axial and lateral loads were applied to the walls, the load on the anchor was T_i — namely, the initial load measured at the beginning of the wall cyclic tests. For estimations of fluctuations in anchor capacity over the course of the tests, the initial load T_i was used as a baseline.

Application of the axial load to the wall may further influence the tension in the anchors. During imposition of lateral cyclic loading, it is natural for the axial load in the anchors to fluctuate in time, resulting in the variable amplitude grouped under the wall loading label in Fig. 4.6. During the wall testing, anchors were re-tensioned by re-compressing the bumpers as they experienced load losses, to assess if the load loss was comparable in subsequent cycles. In particular, anchors experiencing about 30% reduction in load were re-tensioned before each new wall drift amplitude. This is indicated in Fig. 4.6(a). All anchors that survived the wall cyclic lateral tests (i.e., that did not come loose) were tension tested to failure to measure their residual strength. Fig. 4.6(b) graphically depicts the end of a set of cycles, grouped by amplitude, applied to the walls. By tracking this response, information on the wall damage state can be related to the anchor performance. In the next section, the anchor load and global displacement histories measured during the wall lateral cyclic tests are presented.



(a) **(b)**

Figure 4.6: (a) Typical anchor axial load history, from installation to application of the target load. T_{inst} = installation load; T_{design} = applied target load and T_i = measured load at the beginning of the wall test, prior to the imposition of the lateral displacement to the walls. (b) Representation of a set of cycles at constant amplitude drift applied to the top of the walls

4.2.4 Reference Tests and Characterization of Anchor Behavior

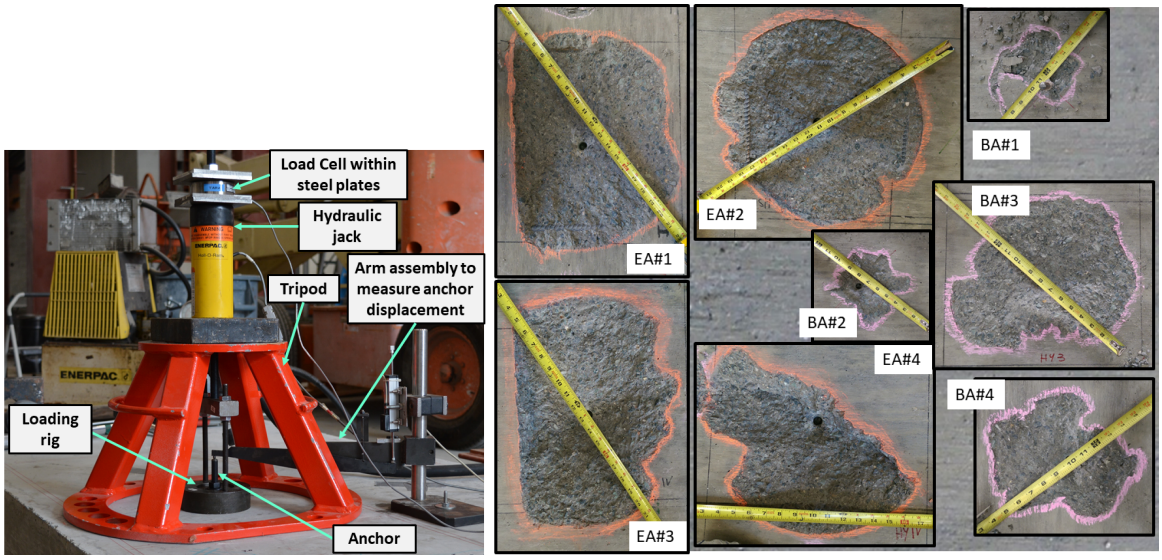
Anchor behavior is characterized by load-displacement curves measured from tension tests on the anchor size and type used for the wall tests. Anchors used in the walls were installed per the manufacturer instructions in 12-inch thick normal-weight concrete slabs and loaded monotonically in tension to failure. The slabs were cast from the same concrete batch used for the wall pours. The slabs were lightly reinforced to permit handling and avoid splitting failures during anchor loading. The test setup is represented in Fig. 4.7, and the resulting tension load-displacement curves and the reference slab surface at the end of the reference tests are shown in Figs. 4.7, 4.8 and 4.9.

Bonded anchors consistently displayed a concrete cone breakout failure mode combined with pullout of the embedded end of the anchors, i.e., a combined cone-bond failure as described in Cook (1993) and Cook and Konz (2001). The shallow concrete cones (approximately 2 inches deep) developed an average radius of about 5 inches, as shown in Fig. 4.7. The ultimate loads and the displacements at peak load were repeatable with low variability, as seen in Fig. 4.8(a). The torque-controlled expansion anchors presented more variability in the displacement at peak load, in comparison with the bonded anchors; refer to Fig. 4.8(b). However, the load-displacement curves repeatedly demonstrated the mech-

anism of anchoring of this type of anchor - namely, via large displacement capacity post-peak strength. A concrete cone breakout failure mechanism was consistently observed having an average radius of 7 inches and extending approximately 3 inches deep into the reference slab, as shown in Fig. 4.7. Reference tests in uncracked concrete of the anchors installed in the two squat walls show similar results (see Fig. 4.9). The re-expansion mechanism characteristic of torque-controlled expansion anchors is identifiable in the curves in Fig. 4.9(a) as the change in slope at roughly 5500 lb, which marks the exceedance of the anchor bolt prestress. The tested anchors also show a relatively large displacement at peak load and significant softening in the post-peak range. The recorded mean ultimate load for this anchor in the reference slab was approximately 16000 lb with 13% coefficient of variation and a mean displacement at ultimate load of 0.3 inches with 16% coefficient of variation. This anchor demonstrated concrete breakout failure in the majority of the tests, while in a few other tests the failure mode was pull-through of the expansion cone, as depicted in Fig. 4.9(b). However, the measured average failure load agrees well with the mean predictor for tension breakout failure, which is determined as:

$$N_{u,m} = 35\sqrt{(f'_c)} \cdot h_{ef}^{1.5} = 35\sqrt{6900} \cdot 3.2^{1.5} \approx 16\,kips \tag{4.1}$$

(Fuchs et al. 1995). From this it may be concluded that in all cases the anchor had mobilized most, if not all, of the concrete breakout capacity for the given effective embedment depth h_{ef} = 3.2 inches $\approx$ 7d. More information on the estimation of the theoretical anchor capacity at different failure modes is reported in Appendix D.



(a) Annotated photograph of the loading assembly (b) Photograph of cone of rupture produced by anchors loaded in tension to failure. EA= expansion anchor and BA= bonded anchor

Figure 4.7: Reference test setup and failure cones of anchors tested in uncracked concrete within the slender wall-anchor test program

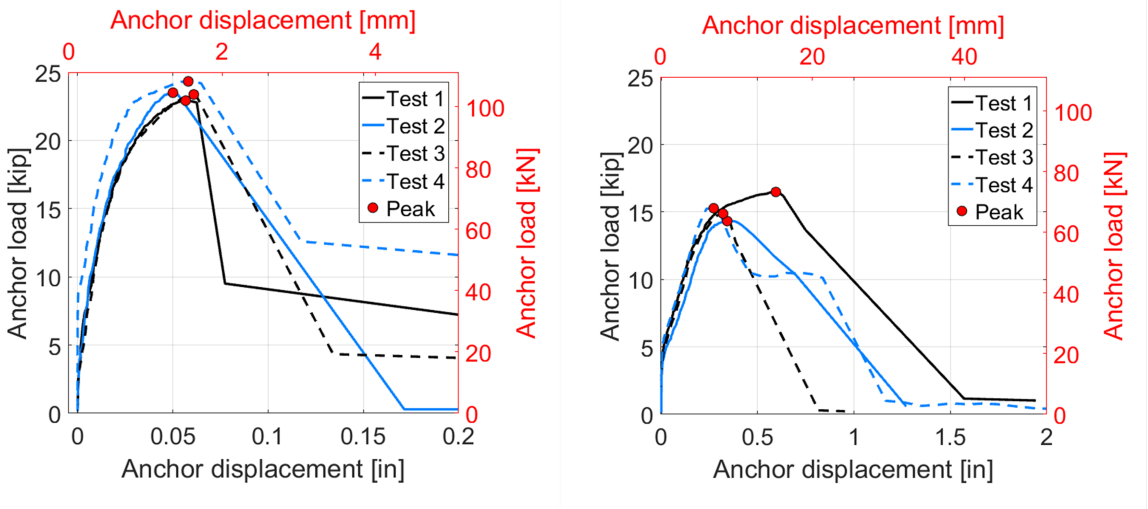
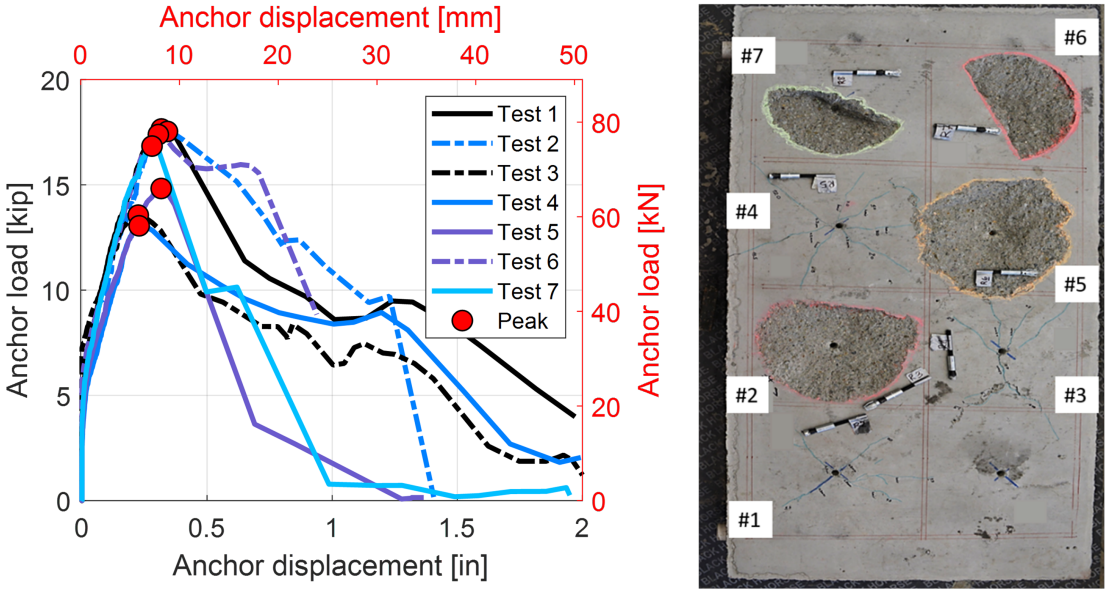


Figure 4.8: Slender wall test: tension load versus displacement curves from reference tests in uncracked concrete (anchors vertically installed): (a) bonded anchors and (b) torque-controlled expansion anchors



(a) Load-slip curves **(b) Plan view**

Figure 4.9: Squat wall tests: reference anchor tension tests to failure in uncracked concrete (torque-controlled expansion anchors vertically installed). (a) Tension load versus axial displacement curves (b) photograph of reference slab after anchors loaded in tension to failure tests (plan view)

4.3 Experimental Results and Discussion

Results of the anchor response during the lateral wall cycling are described here. It is noted that the results of all three wall tests are cross compared in the following section. Anchor load and displacement histories measured during the wall tests are reported in Appendix E. Additional details are in Faraone and Hutchinson (2018) and Faraone and Hutchinson (2021).

4.3.1 Crack Pattern and Anchor Behavior

Damage accumulated as the drift amplitude and number of cycles applied to the top of the walls was increased and a complex crack pattern developed on the wall faces. The residual crack pattern and damage distribution at the end of the three wall tests are reproduced in Figs. 4.10 and 4.11. Herein, the influence of the anchors on the propagation of the cracks is evaluated by comparing the crack pattern on the two faces—that is, the face where anchors are installed to the free face—from its initial formation to the end of the cyclic wall tests. Figs. 4.10 and 4.11 are developed using photographs of the walls taken at the end of each test.

Overlay of the two slender wall SL7.5 face crack patterns in Fig. 4.10 confirms that cracks were running through the thickness of the wall in the plane orthogonal to the loading direction. Moreover, because the crack pattern evolved almost in parallel on the two faces of the slender wall SL7.5, one may deduce that the anchors' presence had little impact on the resulting pattern of damage. Most of the cracks on the lower portion of the wall, within the theoretical plastic hinge length ($L_{p,th}$ = 4 ft), developed during the drift cycles leading up to yield, while the regions above $L_{p,th}$ developed cracks mostly during cycles with an amplitude two times the yield drift. Fig. 4.10 also shows that the two crack patterns overlaid almost everywhere, with the exception of a few cracks, which slightly modified their path to intersect a nearby anchor. This was particularly notable with the torque-controlled expansion anchors (south side of the west face in Fig. 4.10), which were more likely to act as stress concentrators in the concrete due to their inherent mechanism of anchorage. This aspect is revisited in a later discussion.

In both of the two squat wall specimens the crack pattern is dominated by cracks extending from the top corner of the wall to the opposite bottom corner in response to the compression struts developed during wall loading. The progression of the damage and its characteristics are described in

detail in Chapter 3, while salient features affecting the anchors are highlighted herein. The crack patterns developed on the two wall faces, one with and one without anchors, are overlain in Fig. 4.11 to query the potential influence of the anchors on the propagation of the cracks. Similar damage patterns developed in the two walls, and the crack patterns tracked consistently on both wall faces. However, as observed in the slender wall test, crack trajectories deviated to intersect nearby anchor locations in some instances. This effect seems to be more pronounced in the SQ7.5 wall, than in the SQ0 wall; however, no clear trend could be discerned.

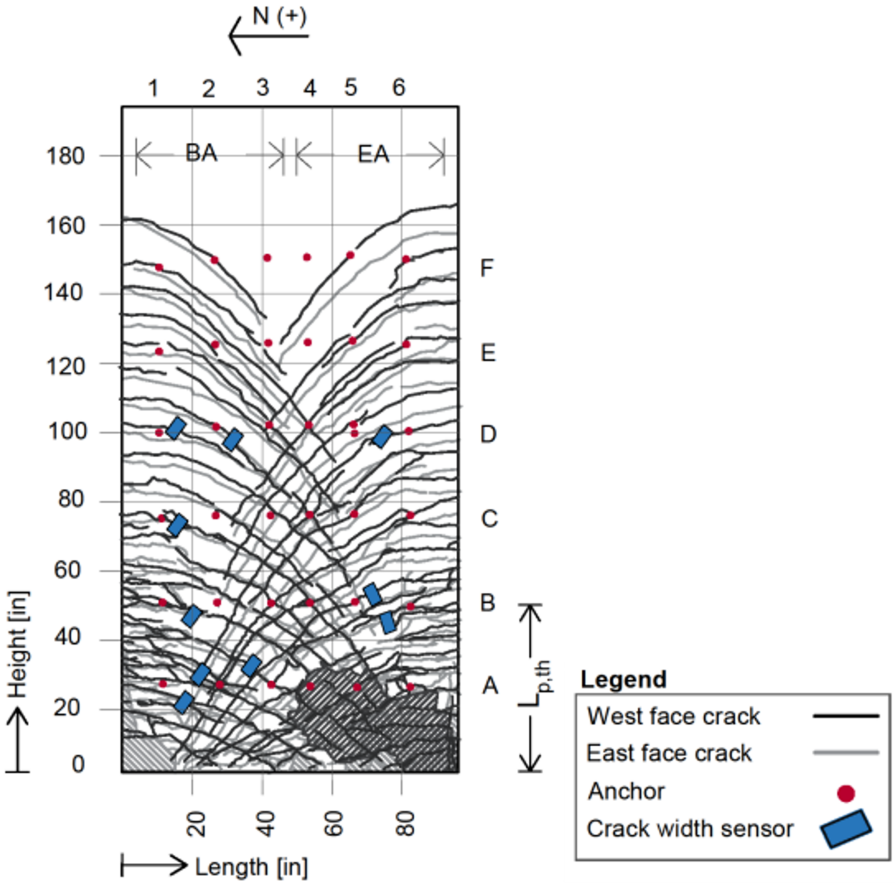


Figure 4.10: Crack pattern on the East (gray lines) and West (black lines) wall faces at the end of the slender wall SL7.5 test. Hatching represents regions of spalled concrete. The locations of anchors and crack width instruments (all installed on the West face) are also included. Bonded anchors (BA): columns 1 to 3. Expansion anchors (EA): columns 4 to 6

It is noted that the presence of the cold-rolled steel plate placed against the concrete surface to assure reliable readings of the load cell (see Fig. 4.5) prevented crack inspection within a radius of 2 inches from the anchor axis during the conduct of the wall tests. The anchor loading setup was removed

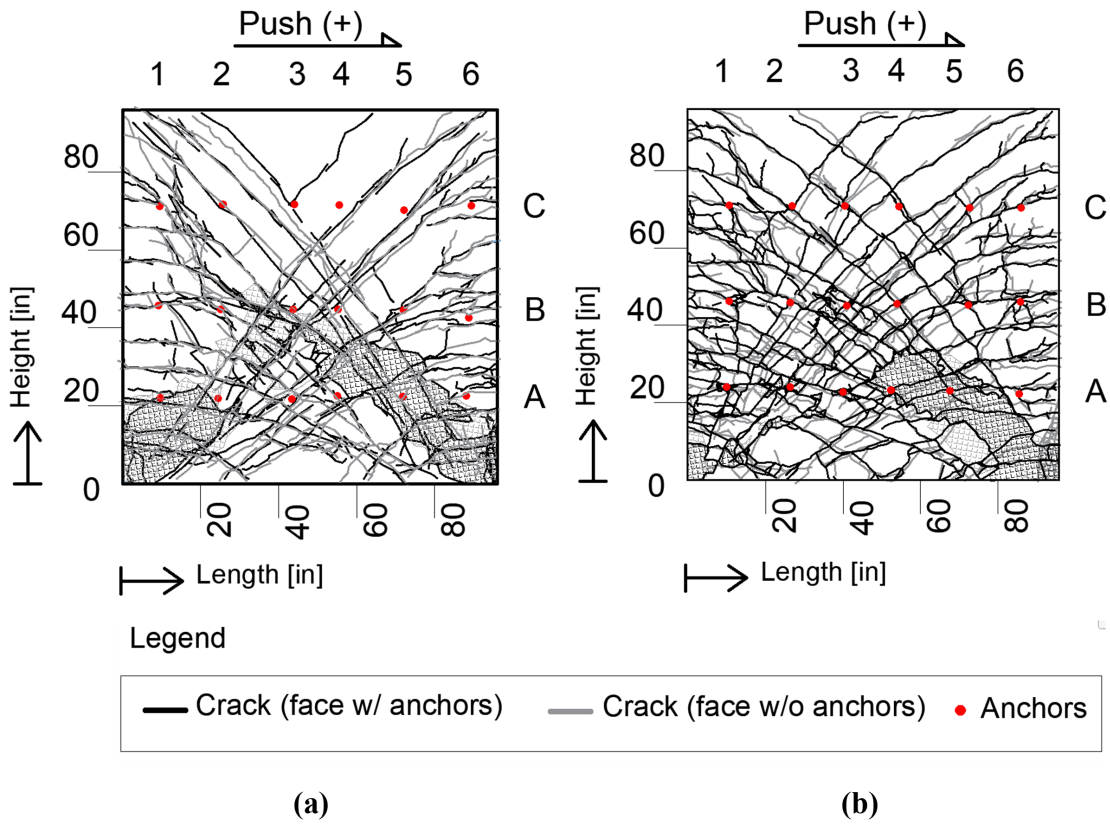


Figure 4.11: Crack pattern at the end of squat wall tests. Hatching represents regions of spalled concrete. (a) Wall SQ7.5 (residual drift = -1%), and (b) wall SQ0 (residual drift = 3%). Push (+) load direction shown

to reveal the crack pattern in the immediate vicinity of the anchors at the end of the wall cyclic tests, thus facilitating inspection of the cracking damage of the residual state of the walls (summarized in Fig. 4.15). It is observed that the tensile stress field generated around the anchor increases the likelihood that cracks will pass through the anchor location. At the end of each wall cyclic test, the anchor loading assemblies were carefully removed and the crack pattern in the immediate vicinity of the anchors was revealed. Figs. 4.12, 4.13 and 4.14 show photographs taken on the anchor face of the residual crack pattern after removal of the anchor load assemblies on the SL7.5, SQ7.5 and SQ0 walls, respectively. The observed crack geometry around the perimeter of the hole of the anchors varied considerably from anchor to anchor in terms of distribution, crack width and trajectory, with each crack path presumably diversified along the embedment depth of the anchor. In Fig. 4.15, anchors are classified according to the residual width of cracks intersecting the anchor location. For example, Anchor Class 3 is defined

by large residual crack widths equal to or exceeding 0.8 mm, whereby 0.8 mm is the threshold crack width adopted for level C2 anchor seismic qualification in Europe (EOTA TR 045 2013, see Chapter 1). A notable observation is that cracks crossed a strong majority (80%) of the expansion anchors installed in columns 4-6 of the wall SL7.5, whereas most of the bonded anchors (installed in columns 1-3 of the wall SL7.5) had no adjacent visible cracks at the end of the wall test. One may therefore conclude that, since the bonded anchors had little impact on the development of the crack pattern, bonded anchors were less prone to attract developing cracks as compared with expansion anchors. This is likely due to the more uniform bond stress distribution engaged between the adhesive material and the concrete. In contrast, torque-controlled expansion anchors develop localized expansion forces fundamentally relying upon outward pressure within the concrete to develop the anchor tensile capacity. Approximately 95% of bonded anchors were classified as Anchor Class 1, being only bonded anchor B1 found in residual cracks larger than $w_r = 0.3$ mm. About one third of the expansion anchors, instead, were crossed by large cracks, as defined by Anchor Classes 2 and 3. In wall SQ7.5, 28% of the anchors were classified as Anchor Class 3. In contrast, more than 60% of the anchors installed in wall SQ0 belonged in this category at the end of wall cycling. This is likely due to the absence of compression load on the wall which resulted in a larger total drift imposed on wall SQ0 and in more distributed cracking and greater residual crack widths. Roughly less than half of the anchors in wall SQ7.5 were assigned to Anchor Class 2, defined as anchors crossing crack with widths of 0.3 – 0.8 mm, while under a third of the anchors in wall SQ0 belonged to this category. The w_r = 0.3 mm lower bound was selected to represent the performance of anchors under service conditions (ACI 355 2019). Anchor Class 1 includes both anchors crossed by hairline cracks (with a residual crack width $w_r \leq 0.3$ mm) and anchors with no visible cracks crossing the anchor location within a unit inch radius. Wall SQ0 had no anchors that were not crossed by at least one crack, while three anchors (18% of the total) in wall SQ7.5 were adjacent to cracks not crossing the anchor. This continues to demonstrate the influence of the wall axial load on crack distribution and is evident by contrasting Fig. 4.13 with Fig. 4.14.

To better understand the influence of the crack trajectories passing through or near anchors representative examples are provided. In the first example, bonded anchor B1 and expansion anchor B6 installed in wall SL7.5 are compared. These anchors were located at the edges of the theoretical plastic hinge length of the slender wall SL7.5, and linear potentiometers continuously measured one intersect-

ing crack close to each anchor. Both anchors were crossed by one or more tension cracks, as shown in Fig. 4.16(a) and (b), because they were installed inside the boundary elements of the wall SL7.5. These regions, extending approximately 18 inches from the full-scale slender wall edges, were confined and thus characterized by a dense crack pattern with closely spaced (2 inches) cracks. Two tension cracks passed around the perimeter of bonded anchor B1, which was installed within the northwest boundary element of the wall SL7.5, and an additional pair of tension cracks crossed the anchor. The maximum crack width measured by the adjacent sensor *cw1* was 3.0 mm at 2.5% drift ratio. Expansion anchor B6, located within the southwest boundary element region of wall SL7.5, was crossed by two tension and one shear crack and it was framed by two tension cracks a few inches above and below it; refer to Fig. 4.16(b). The maximum crack width recorded by the sensor *cw2* closest to anchor B6 was 2.2 mm at 2.5% drift ratio. In contrast, bonded anchor D3 and expansion anchor D4, which were about 2 $L_{p,th}$ above the base of the wall SL7.5 yet in the web region of the wall, were both crossed by multiple cracks (X-cracking pattern), as is shown in Fig. 4.16(c) and (d). Intersecting crack widths were not continuously measured adjacent to these anchors, however visual sensors installed in row D showed crack widths not exceeding 1.00 mm during the entirety of the wall SL7.5 cyclic test. In later sections, the influence of the crack pattern that evolved around these anchors will be assessed relative to their load capacity.

Crack pattern development around anchors B2 and B6, installed in the SQ7.5 and SQ0 walls, respectively, are presented in Fig. 4.17 and Fig. 4.18. Both anchors were located at approximately wall mid-height. Linear potentiometers continuously tracked crack widths close to each anchor. In addition, static gauges were employed at other locations on the wall face. Anchor B2 was located outside of the boundary region of wall SQ7.5, the squat wall tested with axial load (see Fig. 4.17(b)). After the conclusion of wall cycling, this anchor was found to have been intersected by one large diagonal crack with a residual width w_r= 0.75 mm. Several other diagonal cracks paralled this through-anchor crack, traversing the region around the anchor, including one very significant crack (w_r > 10 mm) that widened considerably during the last lateral displacement increment, as illustrated in the annotated photograph taken after removal of the anchor load setup (in Fig. 4.17(c)). As annotated in Fig. 4.17(a), the maximum crack width measured by the digital sensor adjacent to the anchor was w= 1.6 mm at a drift ratio of approximately 1.5%. The largest increase in width of this through-anchor crack was observed during the final displacement increment, which resulted in loss of wall strength, when this crack width reached

w= 2.4 mm. However, the residual crack width following unloading of the wall was w_r= 0.75 mm. Therefore, anchor B2 in wall SQ7.5 was grouped in Anchor Class 2 (see Fig. 4.15). In contrast, anchor B6, installed within the boundary element in wall SQ0 (the full-scale wall tested absent axial load), was intersected by a number of tension (horizontal) and shear (diagonal) cracks, as depicted in Fig. 4.18(c)). The width of the diagonal crack running between anchors B5 and B6 was continuously recorded by a digital sensor during the wall cycling. This crack reached a maximum width of w_{max}= 1.6 mm at about 2.0% drift ratio. As the damage evolved and stress redistributed through the wall section, this measured crack width did not increase, as annotated in Fig. 4.18(a). However, a tension crack, extending from the end of the wall, also transected the anchor location and attained a residual maximum width of w_r= 1.8 mm, as annotated in the photograph in Fig. 4.18(c), as a result of the final displacement demand imposed on the wall. Anchor B6 in wall SQ0 was indeed assigned to Anchor Class 3 (see Fig. 4.15). Finally, Fig. 4.17(a) and Fig. 4.18(a) illustrate the crack evolution in the vicinity of the two selected anchors and maximum measured crack width at each drift demand. This extensive photographic documentation together with anchor load and global wall displacement histories as measured during the tests provides correlation of anchor behavior with wall component damage states in accordance with current structure performance expectations. Engineers performing post-earthquake assessments of structures may also find this documentation useful as a guide to determining the residual connection capacities based on observed crack widths.

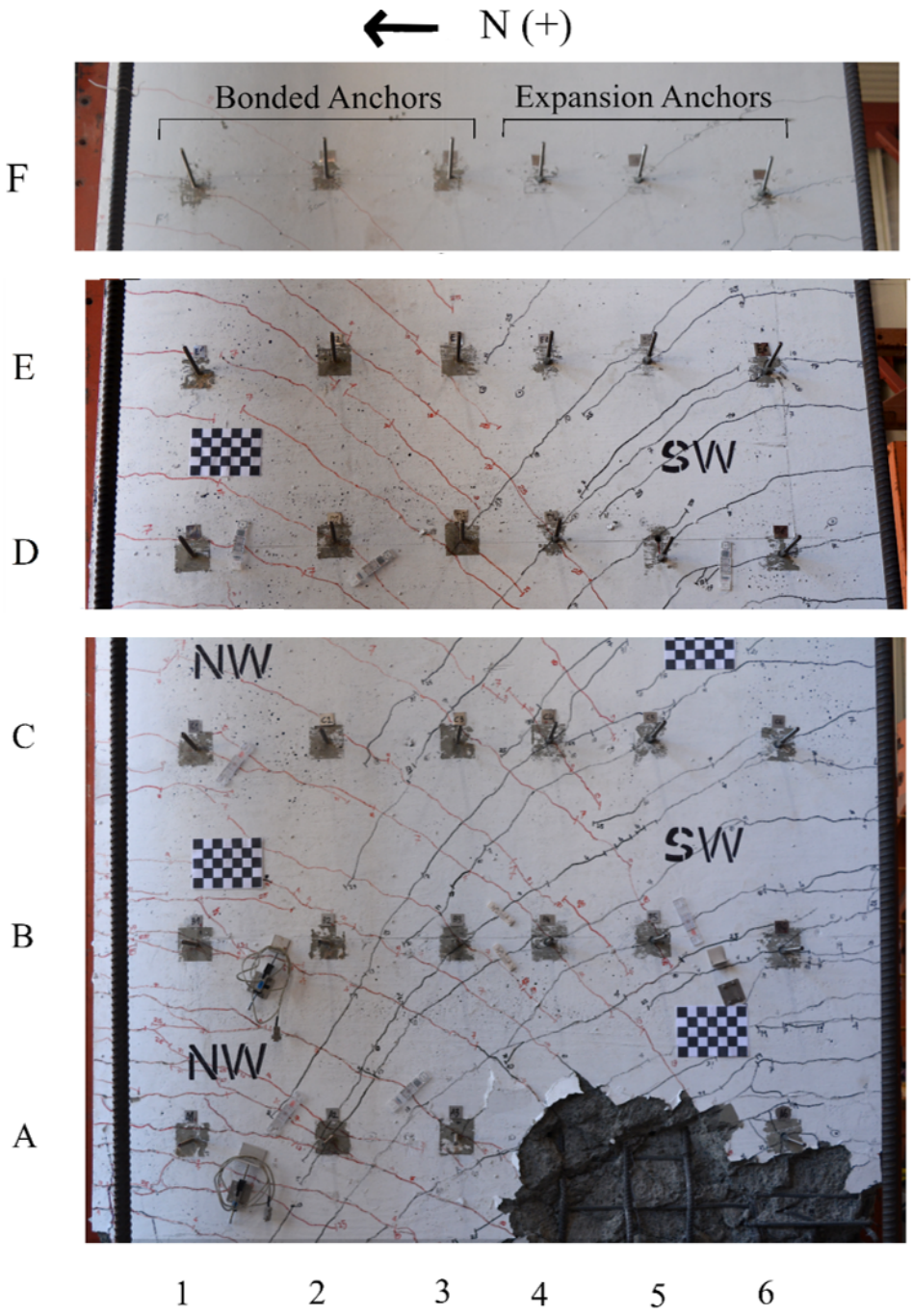


Figure 4.12: Photograph of the final crack pattern and anchors at the end of the SL7.5 wall cyclic test (after removal of the anchor axial load assemblies). Torque-controlled expansion anchors A4 and A5 failed due to the surrounding spalled concrete. Black/red pen denotes cracks that developed during the load cycle in the North (+)/South (-) direction. Note that NW = northwest and SW = southwest

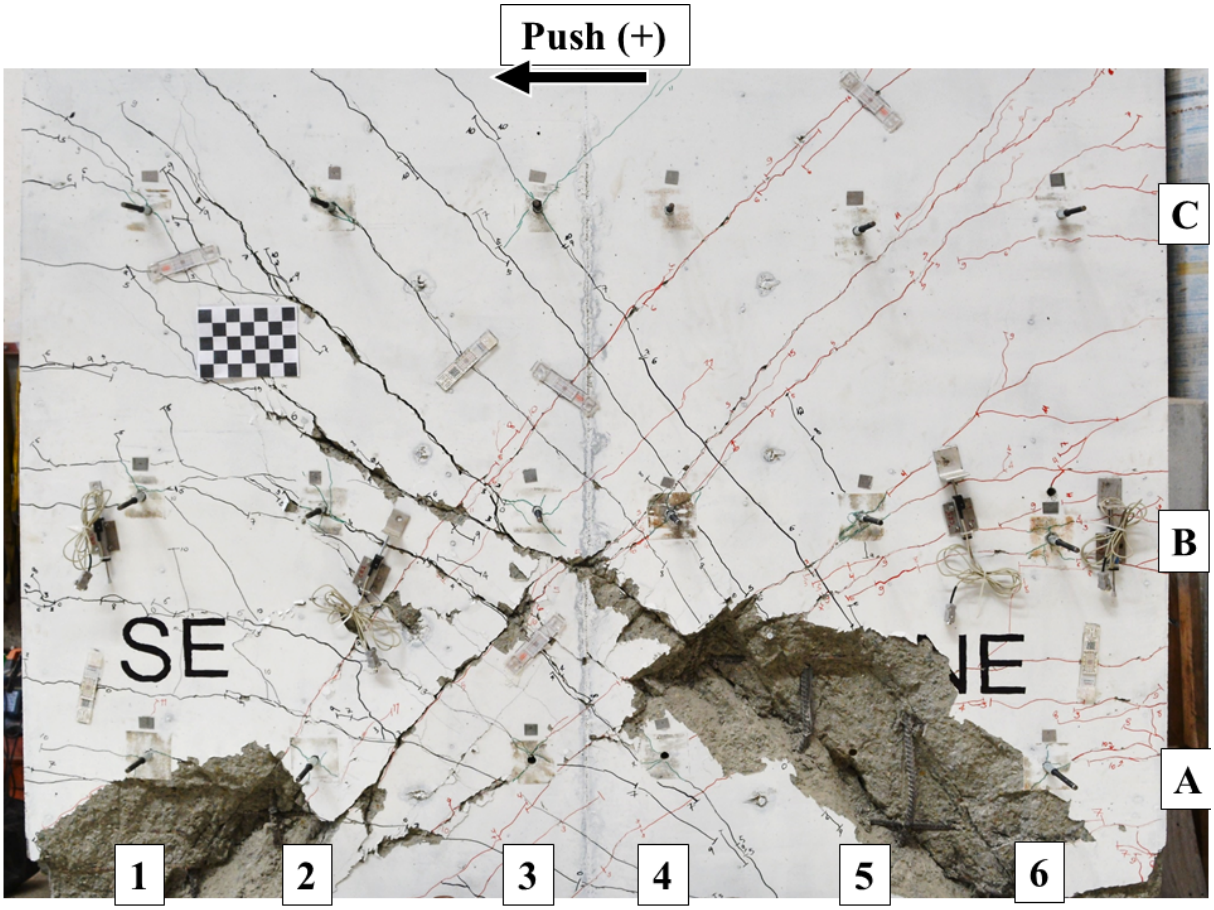


Figure 4.13: Photograph of the residual crack pattern in wall SQ7.5 (anchor axial load assemblies removed; wall subjected to maximum drift of 1.8%). Concrete spalling caused complete loss of anchor A5. Anchors A3 and A4 were loose and could be removed by hand at the end of the wall cycling. Red and black crack trajectories: cracks noted in successive push (+) and pull (-) cycles, respectively. Note that SE = southeast and NE =northeast

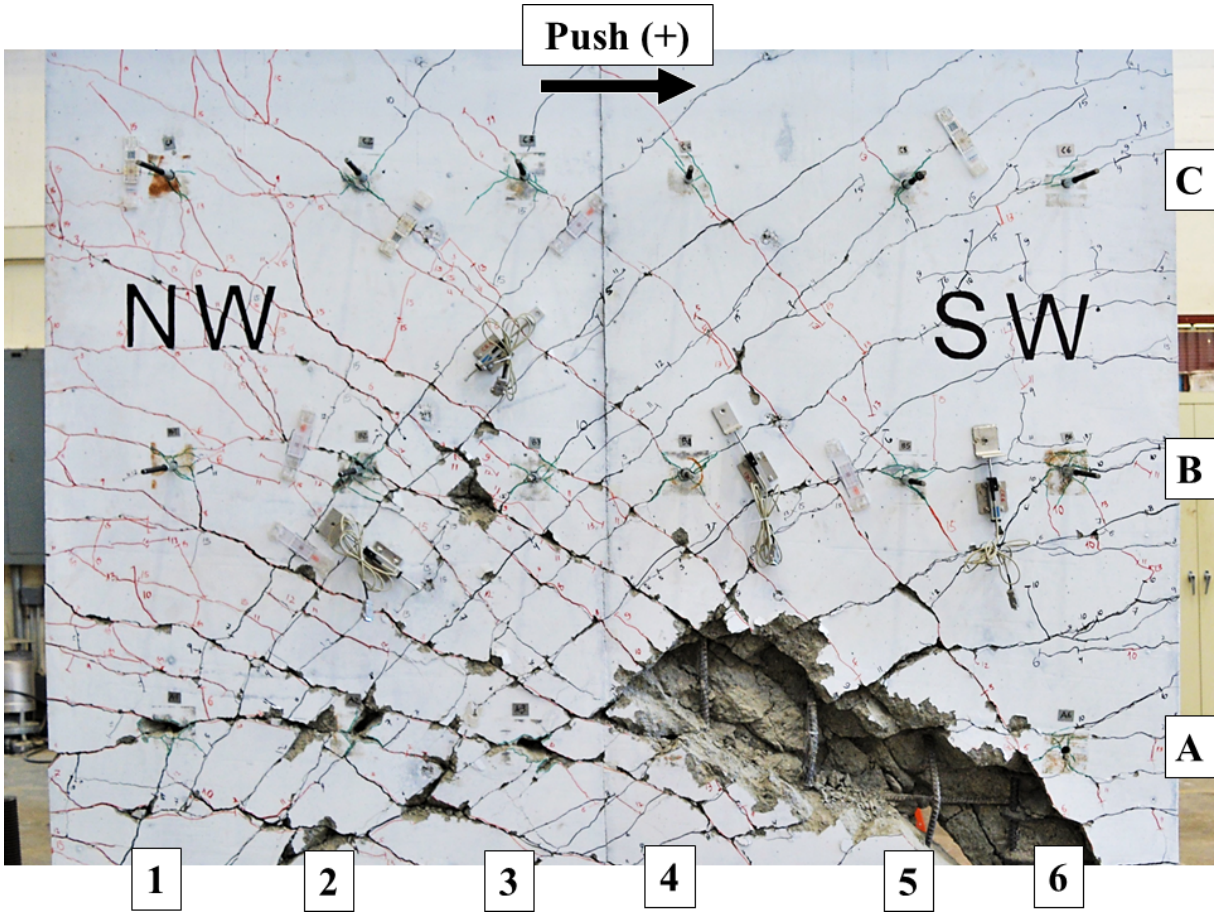
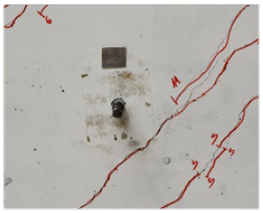
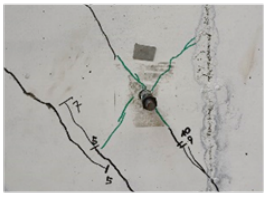
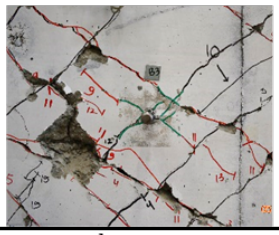
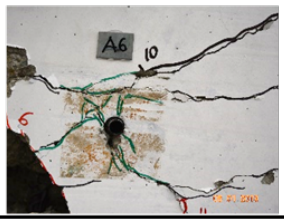


Figure 4.14: Photograph of the residual crack pattern in wall SQ0 (anchor axial load assemblies removed; wall subjected to maximum drift of 4%). Spalling caused complete loss of anchor A5. Anchors in row A were loose and were removed prior to the imposition of the final displacement cycle to avoid damage to load sensors. Red and black crack trajectories: cracks noted in successive push (+) and pull (-) cycles, respectively. Note that NW = northwest and SW = southwest

	Residual crack widths after completion of wall cycling	Anchor[3]	% of anchors
ANCHOR CLASS 1	**No cracks through the anchor outside 25 mm radius[2]** 	A1, B3, C2, C3, D1, D5, E1, E2, E3, E4, F3, F4, F6 ***(SL7.5 wall)***	36% ***(SL7.5 wall)***
		C4, C5, C6 ***(SQ7.5 wall)***	16% ***(SQ7.5 wall)***
		- ***(SQ0 wall)***	0% ***(SQ0 wall)***
	w_r [1] ≤ 0.3 mm 	A2, A3, B2, C1, C4, C5, C6, D2, D3, D4, D6, E5, E6, F1, F2, F5 ***(SL7.5 wall)***	45% ***(SL7.5 wall)***
		A4, B1, C3 ***(SQ7.5 wall)***	16% ***(SQ7.5 wall)***
		C4, C6 ***(SQ0 wall)***	11% ***(SQ0 wall)***
ANCHOR CLASS 2	**0.3 mm < w_r [1] < 0.8 mm** 	B1, B4, B5, B6 ***(SL7.5 wall)***	11% ***(SL7.5 wall)***
		A1, A3, A6, B2, B3, B6, C1 ***(SQ7.5 wall)***	40% ***(SQ7.5 wall)***
		B3, B5, C1, C3, C5 ***(SQ0 wall)***	28% ***(SQ0 wall)***
ANCHOR CLASS 3	**w_r [1] ≥ 0.8 mm** 	A4, A5, A6 ***(SL7.5 wall)***	8% ***(SL7.5 wall)***
		A2, A5, B4, B5, C2 ***(SQ7.5 wall)***	28% ***(SQ7.5 wall)***
		A1, A2, A3, A4, A5, A6, B1, B2, B4, B6, C2 ***(SQ0 wall)***	61% ***(SQ0 wall)***

[1] w_r : residual crack width;
[2] 1 in = 25.4 mm;
[3] Anchor letter- number refers to the location by row and column, e.g., A1=anchor in row A, column 1
Note: Data collection occurred at the residual state of walls *SL7.5*, *SQ7.5* and *SQ0*, which experienced maximum 3%, 1.8% and 4% drift ratio, respectively.

Figure 4.15: Categorization of residual cracking around anchor locations (evaluated at end of wall cyclic testing)

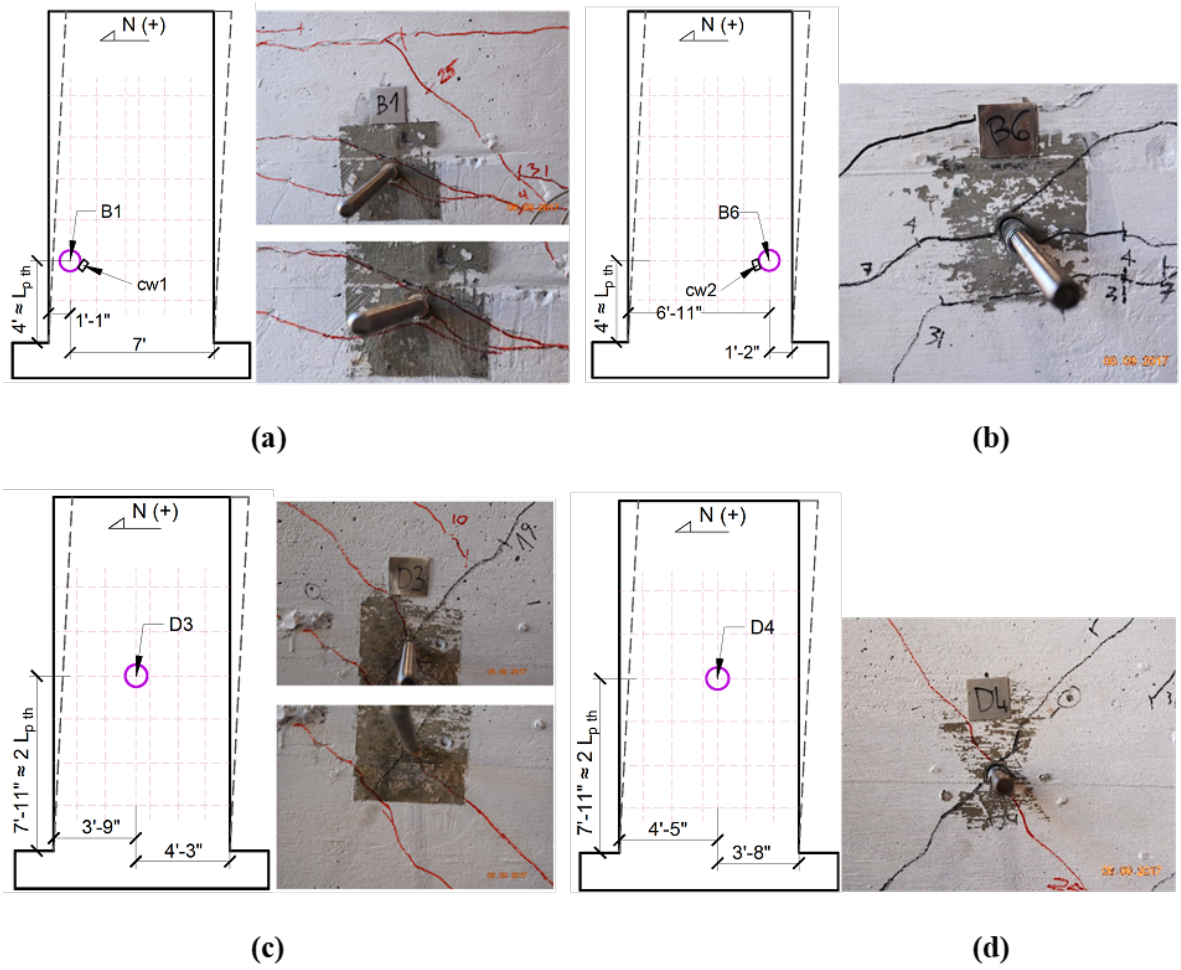
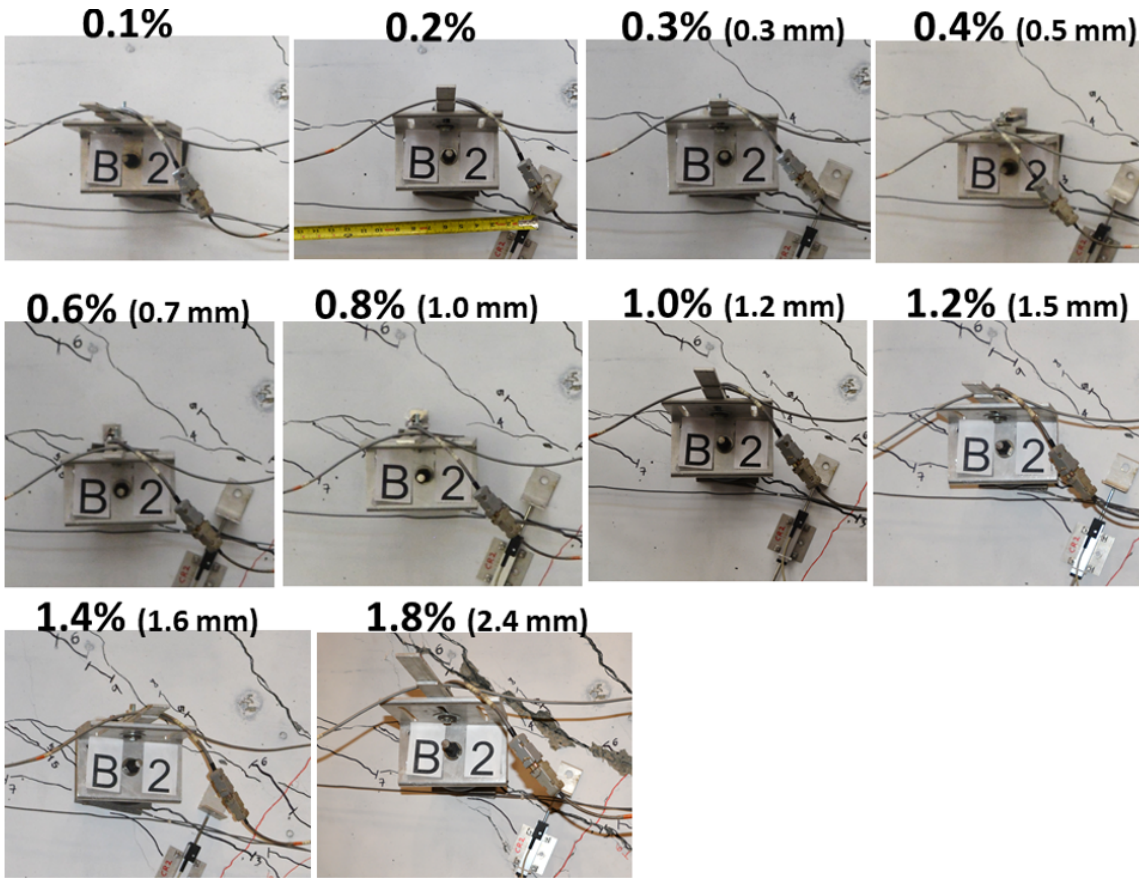
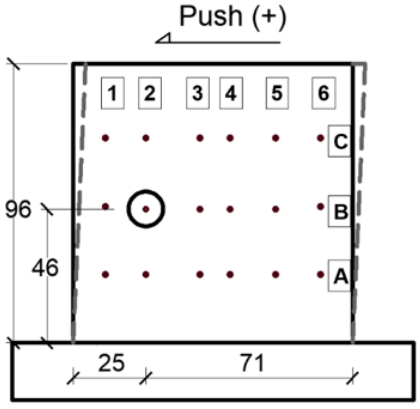


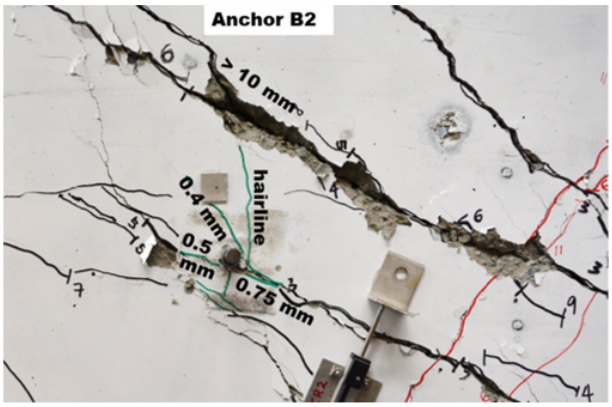
Figure 4.16: Select anchor locations and intersecting crack pattern at the end of the wall SL7.5 cyclic test: (a) bonded anchor B1, (b) expansion anchor B6, (c) bonded anchor D3 and (d) expansion anchor D4. Note the dashed line in the wall elevation depicts a larger than true scale final wall position for visual purposes. *cw1* and *cw2* denote continuously measuring crack width sensors. [1 in. = 25.4 mm]



(a)

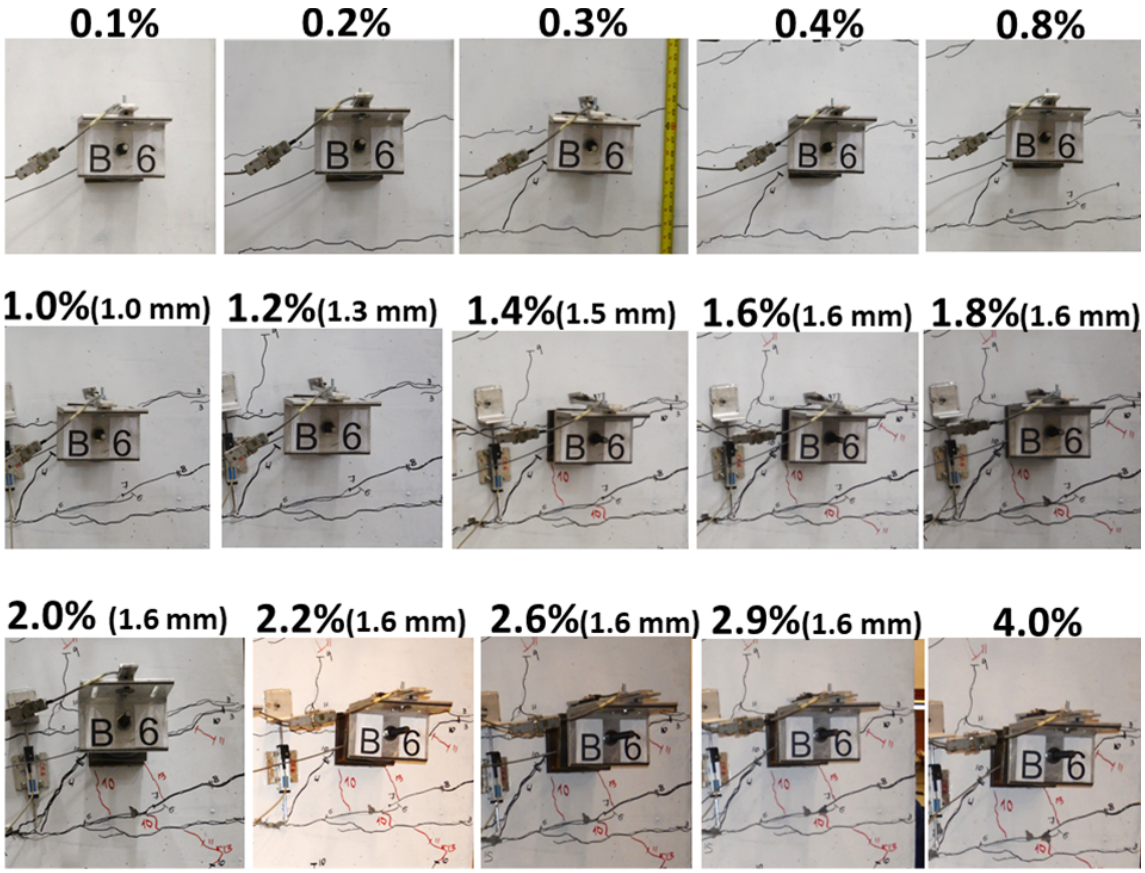


(b)

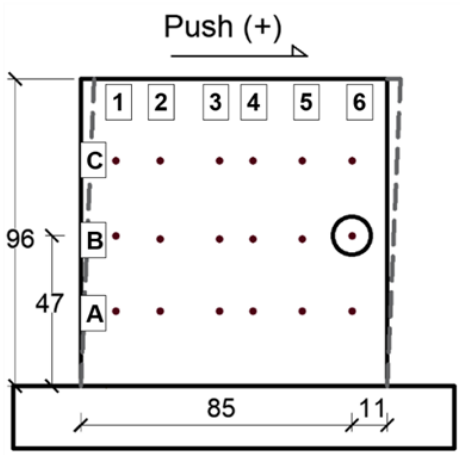


(c)

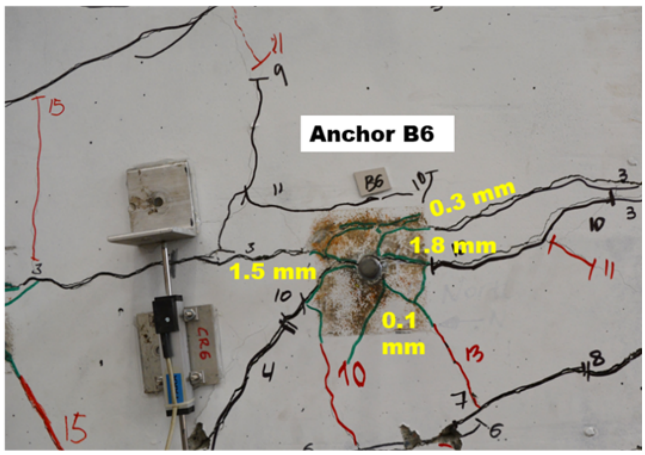
Figure 4.17: Anchor B2 in wall SQ7.5: (a) Photographs indicating crack geometry and maximum measured crack width around B2 at each drift amplitude in the testing of the wall. (b) Sketch of location of B2 in the wall. Final wall residual offset also shown (not to scale). Dimensions in inches. [1 in = 25.4 mm] (c) Photograph of residual cracks around B2 following removal of loading apparatus



(a)



(b)



(c)

Figure 4.18: Anchor B6 in wall SQ0: (a) Photographs indicating crack geometry and maximum measured crack width around B6 at each drift amplitude in the testing of the wall. (b) Sketch of location of B6 in the wall. Final wall residual offset also shown (not to scale). Dimensions in inches. [1 in = 25.4 mm] (c) Photograph of residual cracks around B6 following removal of loading apparatus

4.3.2 Anchor Load and Displacement Histories

The development of cracks in the walls affected the performance of the anchors quite differently from location to location, as also measured by their residual tension load capacity. Consistent with anchors carrying a constant dead load, the anchor loading devices were re-tensioned several times during the wall cycling tests to re-establish the initial design load. Similarly to all the performed wall tests, anchor load loss and global displacement increase occurred upon opening of one or more cracks in the anchor vicinity. Anchor load and displacement histories therefore reflect the presence of cracks, both at the concrete surface (as marked during the test) and below the concrete surface where the anchor transfers load. Anchor tension load loss as measured at the end of the wall cycling and maximum measured displacement during the wall tests are summarized in Fig. 4.19 to evaluate the effect of cyclic opening cracks on the anchor performance. Note that anchors are categorized according to the severity of the crack environment as per Fig. 4.15.

The global load loss values are the summation of the individual load losses recorded just prior to each re-tensioning of the anchors, which occurred when the anchor load dropped by more than 30%. Therefore, the total losses numerically exceeded 100% of the initial value T_i in most cases for the way they are defined, see Fig. 4.6. Generally, bonded anchor displacements were small (on the order of a thousandth of an inch [a hundredth of a millimeter]), and the load was sustained within 10% of its initial value until the end of the test, with the exception of anchor A2, which was at 2 ft (0.61 m) from the wall-footing interface, located inside the severely damaged region of the theoretical plastic hinge ($L_p = 0.5L_w$). No reload application during the slender wall SL7.5 cyclic test was required for the bonded anchors and the local load and measured displacement variations when cracks crossed these anchors were hardly recognizable. Conversely, expansion anchors in the slender SL7.5 wall were reloaded three times during the wall cycling history to reestablish the initial design load. The global load reduction reported in Fig. 4.19 is the summation of the reduction experienced between each of the reloads. The anchors installed in the plastic hinge region (anchor rows A and B) experienced as high as nearly 300% global load reduction, as large as twice the value experienced by the anchors installed outside of the theoretical plastic hinge length (anchor rows C to E). Similarly, the measured axial displacements were larger for anchors installed inside the plastic hinge length with respect to the other expansion anchors (anchor rows C to E). Measured displacements were also considerably larger for expansion anchors with respect to

bonded anchors, as the comparison of maximum measured values in Fig. 4.19 shows. This difference in response reflects the varied anchor mechanisms for the two anchor types selected in this study.

Data from the two squat wall tests are also reported in Fig. 4.19. Anchors C4 to C6 in wall SQ7.5 were used to characterize baseline performance since no visible cracks intersected their location for the duration of the wall test. The average maximum measured displacement for these two anchors was 0.02 inches and the average global load loss was 10%, attributable to normal relaxation of the loading apparatus. The balance of Anchor Class 1 exhibited an average maximum measured global displacement for both the squat wall tests of 0.17 inches and average global load loss of 123%. Anchor Class 2 is associated on average with a 20% greater global load loss - 150% on average for walls SQ7.5 and SQ0. The average maximum global displacement associated with Anchor Class 2 was 0.25 inches – significant but still tolerable. However, Anchor Class 3 is associated with a 0.48 inches average global displacement. The effect of the axial compression load applied to the wall on the anchor displacements appears to be significant. The average of the maximum measured global displacements associated with Anchor Class 3 in wall SQ0 is 0.56 inches and 0.26 inches in wall SQ7.5. This is likely attributable to the large residual crack widths in wall SQ0 at larger drift levels and it is also reflected in the average global anchor load losses associated with Anchor Class 3 of 234% for wall SQ0 and 162% for wall SQ7.5. The large values of load loss may at first imply that the anchors could offer little sustainable load carrying capacity. However, noting that the anchors were reloaded to replicate true sustained service load conditions, an alternative definition to characterize load loss is used.

To better understand the relation between measured load and displacement of the anchor when crossing cracks cycled, normalized plots were produced. The normalized load T^* was calculated as

$$T^* = \frac{T - T_i}{T_i} \cdot 100[\%] \tag{4.2}$$

where T_i is the load on the anchor at the beginning of the cyclic test; refer to Fig. 4.6. Similarly, the measured displacement was biased at the beginning of the cyclic test (initial measured displacement Δ_i) and subsequently normalized by the maximum measured displacement Δ_{max}

$$\Delta^* = \frac{\Delta - \Delta_i}{\Delta_{max} - \Delta_i} \tag{4.3}$$

and the crack width history was normalized by the maximum crack width experienced during the test, w_{max}, as

$$w^* = \frac{w}{w_{max}} \tag{4.4}$$

The applied wall drift history is reported in the x-axis of the plots to keep track of the applied top wall drift demand, related to the damage history of the wall. Since each group of cycles consists of at least 2 push/pull cycles, the end of each group at constant amplitude is reported in the x-axis of the plots, see Fig. 4.6.

Using the aforementioned parameters, Fig. 4.20 shows the normalized measured load and displacement histories for bonded anchor D3, installed in the slender wall SL7.5 as described in Fig. 4.16(c). The effects of the cycling cracks on the anchor were sought by inspecting these and other similar histories. Fig. 4.20 shows that bonded anchor D3 experienced approximately 7.5% load reduction with respect to the initial load T_i. The normalized measured displacement history (pink and black curve) was globally increasing; however, the maximum measured displacement Δ_{max} was on the order of a thousandth of an inch (a hundredth of a millimeter) toward the end of the test. The measured displacement was, therefore, negligible. The micro-trend of small load and displacement oscillations within each wall drift cycle, noticeable in Fig. 4.20, was attributed to small unequal distributions of stresses within the anchor loading system. The appearance of shear cracks crossing the anchor is denoted by the arrows $c_{s,1}$ and $c_{s,2}$ in Fig. 4.20. Small load reductions and measured displacement increments were observed at crack crossing, as the zoomed-in region of the first crossing crack in Fig. 4.20 highlights. When a crack disturbed the concrete region involved in the anchor mechanism, torque-controlled expansion anchors behaved similar to the bonded anchors; however, the magnitude of load reduction and displacement increment was larger. For example, Fig. 4.21 shows the normalized load, displacement, and crack histories during the wall cycling of anchor B6. The anchor was reloaded three times, at the end of 0.25%, 0.5%, and 1.5% drift ratios. During the wall cyclic test, between each time the load was reapplied, the anchor experienced approximately 57% reduction of the initial load and the displacement increased an average of 0.09 inches. Noteworthy, every time the continuously monitored crossing crack opened, the measured displacement in the anchor increased and the load decreased. The appearance of the tension cracks crossing the anchor (annotated during the wall test) was denoted by the arrows $c_{t,1}$ and $c_{t,2}$ in Fig. 4.21. The

opening of other smaller cracks across the anchor was instead inferred from the typical load drops and measured displacement increments, which are highlighted in the closeup in Fig. 4.21.

The instance when cracks crossed the anchors was estimated by the marks on the wall. Moreover, expansion anchors typically showed a clear load drop and a corresponding axial displacement increment when a crack initially crossed the anchor. The presence of non-visible, smaller cracks within the embedded portion of the anchors was deduced by the sudden load drop and simultaneous displacement increase.

Fig. 4.22 indicates that anchor B2, installed in wall SQ7.5, was re-loaded four times during the wall test, at the end of the 0.4%, 0.8%, 1.2% and 1.4% drift cycles. The average increment in measured global axial displacement within each reapplication of the load is about 0.12 inches, consistent with the results of the slender SL7.5 wall test. It is observed that every time the intersecting crack opened at the anchor location, the measured displacement in the anchor increased and the load decreased (see zoomed region in Fig. 4.22). Fig. 4.17(a) shows that the monitored shear crack crossing the anchor formed at the 0.2% drift amplitude, when the first load drop and displacement increase were measured. Fig. 4.17(a) does not show any other crack intersecting the location of anchor B2, as is also reflected in the measured load and global displacement histories, see Fig. 4.22. Anchor B6 installed in wall SQ0 shows a more pronounced response to increasing wall damage, see Fig. 4.23. Similar to anchor B2, anchor B6 was re-loaded four times during the wall test, at the end of the 0.6%, 1.0%, 1.2% and 1.4% drift amplitude cycles. The average increment in measured global displacement within each reapplication of the load was about 0.12 in (3 mm), in line with the other tests. The trend observed in previous tests at the opening of an intersecting crack is also visible in Fig. 4.23, especially in the zoomed region. Fig. 4.18(a) indicates that the instrumented crack and a second horizontal crack on the opposite side of the anchor formed at the 0.2% drift ratio amplitude. Fig. 4.18(a) also shows that anchor B6 was affected by several other crossing cracks, which were marked at 1.6% and 2.0% drift ratio amplitudes, when wall SQ0 was at approximately 5% post- lateral strength. The effect of these crossing cracks is confirmed by the load drop and displacement increments at end of the 1.6% and 2.0% drift cycles, respectively, in Fig. 4.23.

Comparison of the global load reduction is presented in Fig. 4.24, where the results of the three full-scale walls are also included to facilitate observations regarding the performance of anchors installed in progressively damaged reinforced concrete shear walls of varying aspect ratio. Please note

that, as described in Chapter 2, anchors were installed in the slender wall SL7.5 and distributed in six rows, denoted as A through F, with six approximately equally spaced anchors in each row, similarly to the squat walls. However, anchor load was monitored during the slender wall test only for anchors in rows A-E. These data are represented in Fig. 4.24 to better analyze the load reduction trend observed during the tests. The drift ratios corresponding to structure performance levels Immediate Occupancy (IO), Life Safety (LS) and Collapse Prevention (CP) as suggested by ASCE 356 (2000), i.e., 0.5%, 1% and 2% respectively, are also provided for reference to the walls' global performance state (see also Chapter 3). Theoretically, shear wall in-plane strength is unaffected at IO, peaks at LS and declines in a stable fashion at CP. Anchors installed in the face of shear walls will exhibit correspondingly reduced capacity as the wall drift demand and associated damage increases. The trend of mean normalized loads shown in Fig. 4.24 demonstrates this capacity reduction, with the severity of the reduction dependent on the anchor location and also on the magnitude of applied compression load on the wall. Notably, the uppermost row of anchors in walls SL7.5 (rows C-E) and SQ7.5 (row C) showed fairly constant load as the wall drift demand increased, unlike the anchors in the top row of wall SQ0 (row C), which experienced more damage in the absence of compression load applied to the wall.

Globally, average load reductions at IO, LS and CP wall performance levels, measured at all locations in all three walls, were 25%, 30% and 52%, respectively. Considering that the damage in reinforced concrete shear walls typically concentrates along the wall height, extending from its base to approximately 50% of the wall length (ACI 318 2019), it is useful to compare the load capacity of the anchors installed in the A and B rows only. Mean load reductions across these two rows in all the three walls were 26%, 33%, 65% at IO, LS and CP, respectively. These numbers suggest that the performance of the anchors located within the region extending approximately 50% of the wall length from the wall base may be severely compromised.

	SL7.5		*SQ7.5*		*SQ0*	
Anchor	**Load loss[2]**	**Max Disp[3] [in]**	**Load loss[2]**	**Max Disp[3] [in]**	**Load loss [2]**	**Max Disp[3] [in]**
A1	*- 4%**	*~ 0**	- 157%	0.17	**- 347%**	**0.58**
A2	*- 74%**	*0.1**	**- 76%**	**0.28**	**-286%**	**0.66**
A3	*-3%**	*~ 0**	- 191%	0.30	**-243%**	**0.71**
A4	**-159%**	**0.3**	*- 195%*	*0.17*	**-248%**	**0.20**
A5	**-291%**	**0.4**	**- 203%**	**0.30**	**-195%**	**0.77**
A6	**-171%**	**0.2**	- 139%	0.17	**-178%**	**0.73**
B1	~ 0%*	~ 0*	*- 122%*	*0.24*	**-122%**	**0.54**
B2	*-11%**	*~ 0**	- 239%	0.14	**-183%**	**0.69**
B3	*-4%**	*~ 0**	- 63%	0.14	-100%	0.35
B4	-182%	0.03	**- 206%**	**0.40**	**-182%**	**0.17**
B5	-194%	0.1	**- 290%**	**0.27**	-176%	0.47
B6	-177%	0.04	- 160%	0.21	**-290%**	**0.63**
C1	*30%**	*~ 0**	- 75%	0.12	-144%	0.13
C2	*-3%**	*~ 0**	**- 194%**	**0.29**	**-303%**	**0.52**
C3	*-5%**	*~ 0**	*- 64%*	*0.09*	-264%	0.42
C4	*-108%*	*0.03*	*- 8%*	*0.01*	*-126%*	*0.20*
C5	*-92%*	*0.06*	*- 8%*	*0.01*	-114%	0.42
C6	*-39%*	*~ 0*	*- 14%*	*0.03*	*-112%*	*0.14*
D1	*-7%**	*~ 0**				
D2	*-7%**	*~ 0**				
D3	*-7%**	*~ 0**				
D4	*-113%*	*0.03*				
D5	*-52%*	*~ 0*				
D6	*-113%*	*0.03*				
E1	*2%**	*~ 0**				
E2	*-7%**	*~ 0**				
E3	*-6%**	*~ 0**				
E4	*-32%*	*~ 0*				
E5	*-61%*	*~ 0*				
E6	*-49%*	*0.02*				

* *Bonded Anchors installed in SL7.5*

[1] Anchor Class 1 – green shading and italic font
Anchor Class 2 – yellow shading and normal font
Anchor Class 3 – red shading and bold font

[2] Cumulative load loss from the initial tension load T_i

[3] Maximum measured displacement; 1 in = 25.4 mm

Figure 4.19: Summary of anchor response during wall cyclic tests

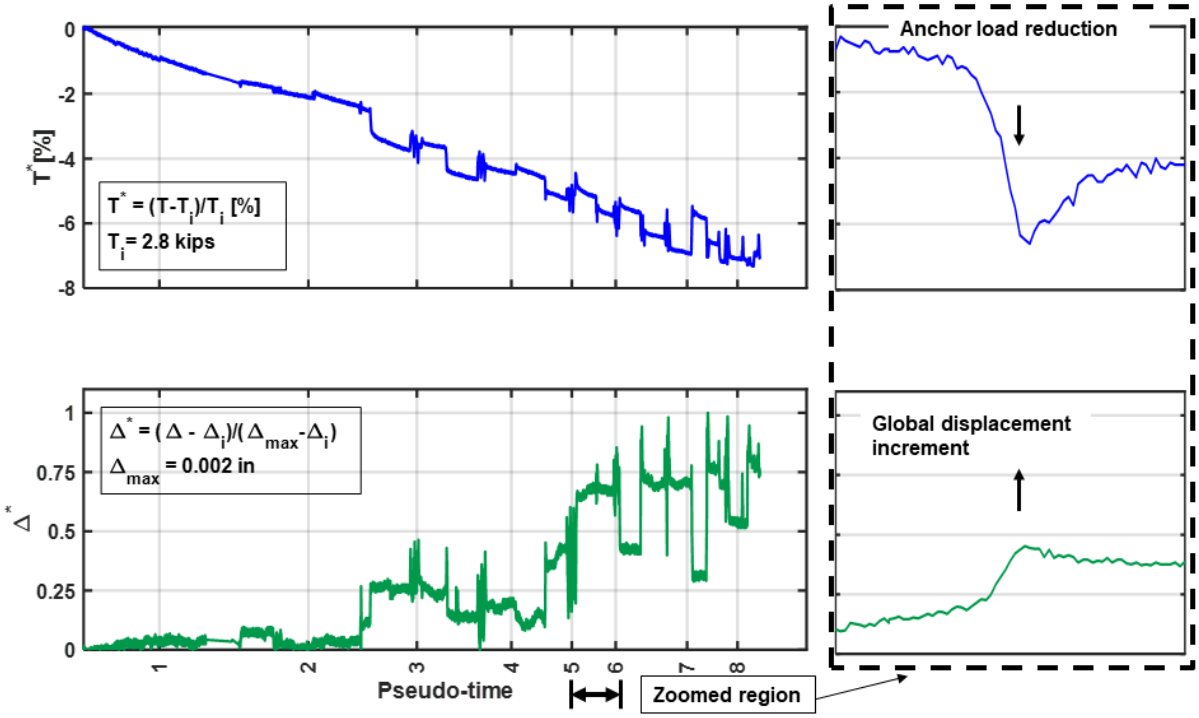


Figure 4.20: Bonded anchor D3 in wall SL7.5: normalized load (T^*) and normalized measured displacement (Δ^*) histories and zoom at crack opening. Initial load (T_i) and maximum measured displacement (Δ_{max}) are reported in the legend. Maximum estimated crack width during the wall test w = 0.1 mm [1 in = 25.4 mm; 1 kip = 4.45 kN]

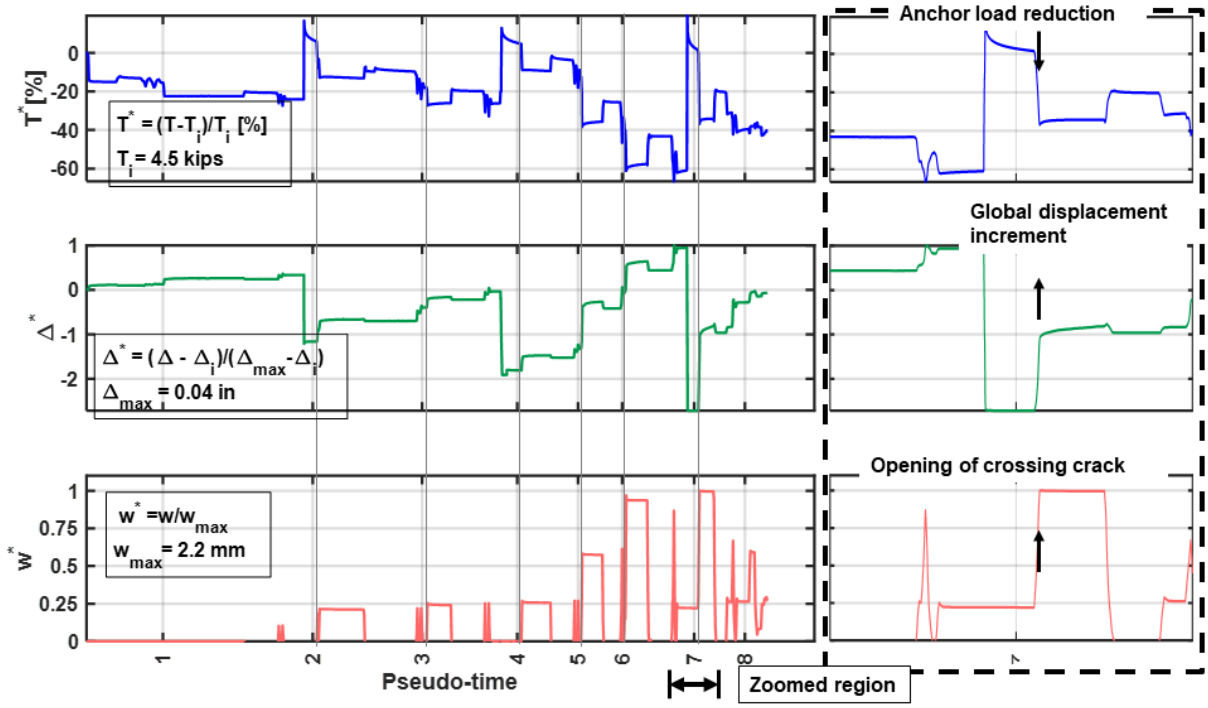


Figure 4.21: Torque-controlled expansion anchor B6 in wall SL7.5: normalized load (T^*), normalized measured displacement (Δ^*), and normalized crack width (w^*) histories. Zoom at crack opening shows load drop and displacement increase. Initial load (T_i), maximum measured displacement (Δ_{max}) and maximum crack width (w_{max}) are reported in the legend. [1 in = 25.4 mm; 1 kip = 4.45 kN]

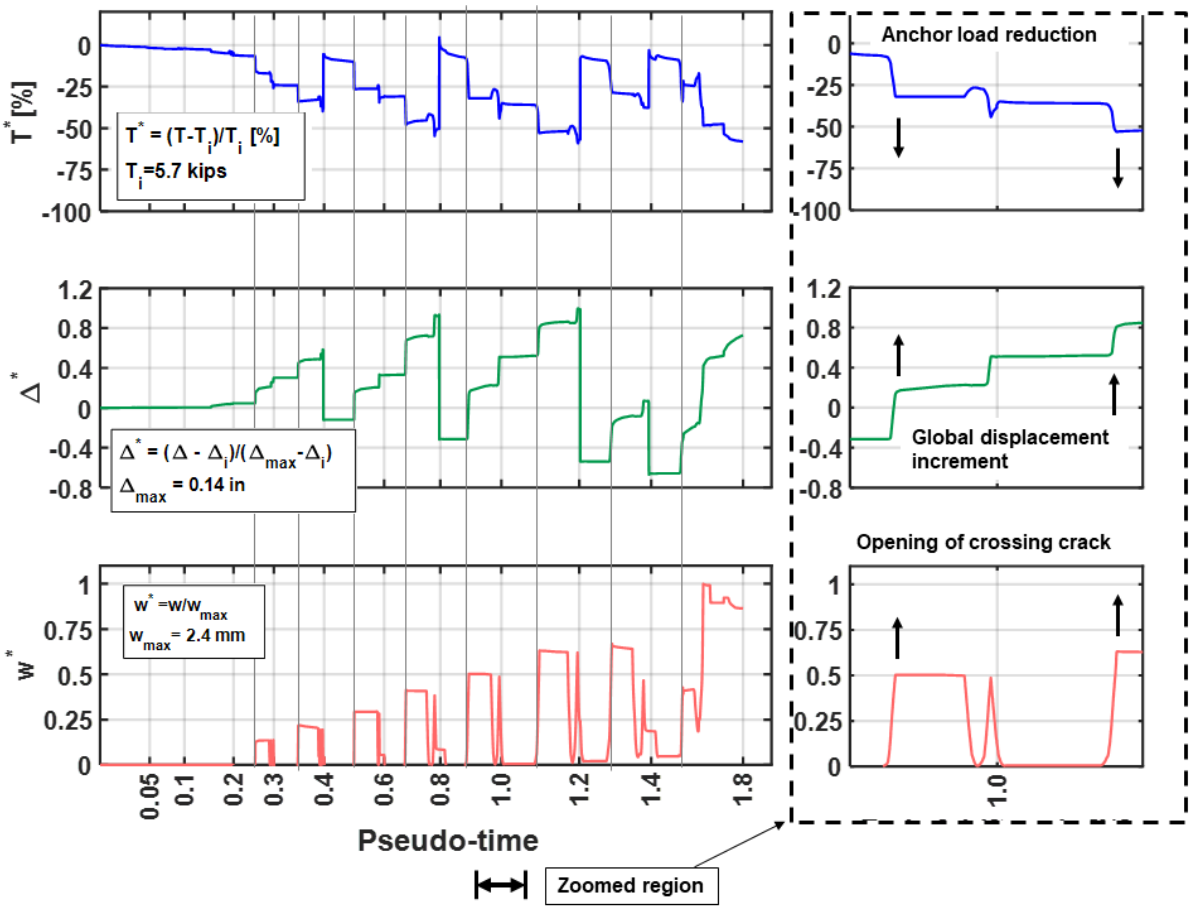


Figure 4.22: Torque-controlled expansion anchor B2 in wall SQ7.5: normalized load T^*, normalized measured displacement Δ^*, and normalized crack width w^* histories. Initial load T_i, maximum measured displacement Δ_{max} and maximum crack width w_{max} are reported in the legend. Zoom at crack opening shows load drop and increase in measured global displacement. [1 in = 25.4 mm; 1 kip = 4.45 kN]

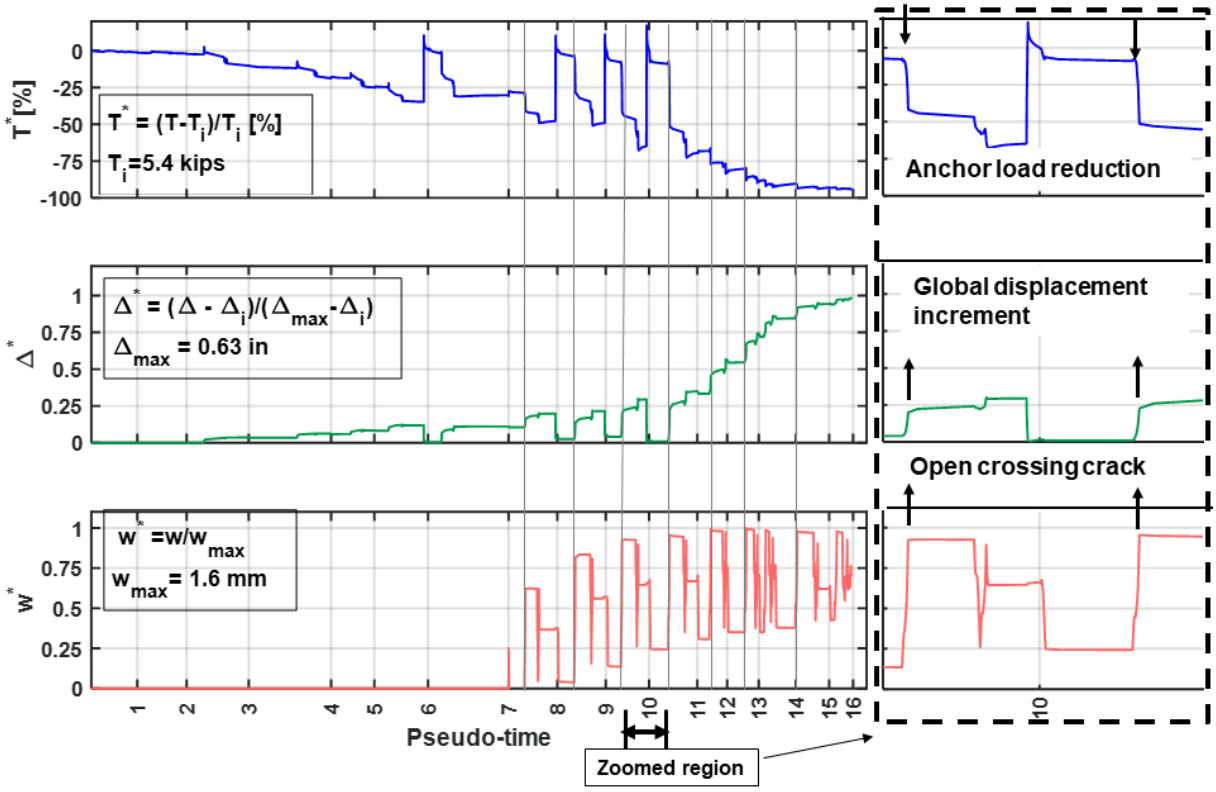


Figure 4.23: Torque-controlled expansion anchor B6 in wall SQ0: normalized load T^*, normalized measured displacement Δ^*, and normalized crack width w^* histories. Initial load T_i, maximum measured displacement Δ_{max} and maximum crack width w_{max} are reported in the legend. Zoom at crack opening shows load drop and increase in measured global displacement. [1 in = 25.4 mm; 1 kip = 4.45 kN]

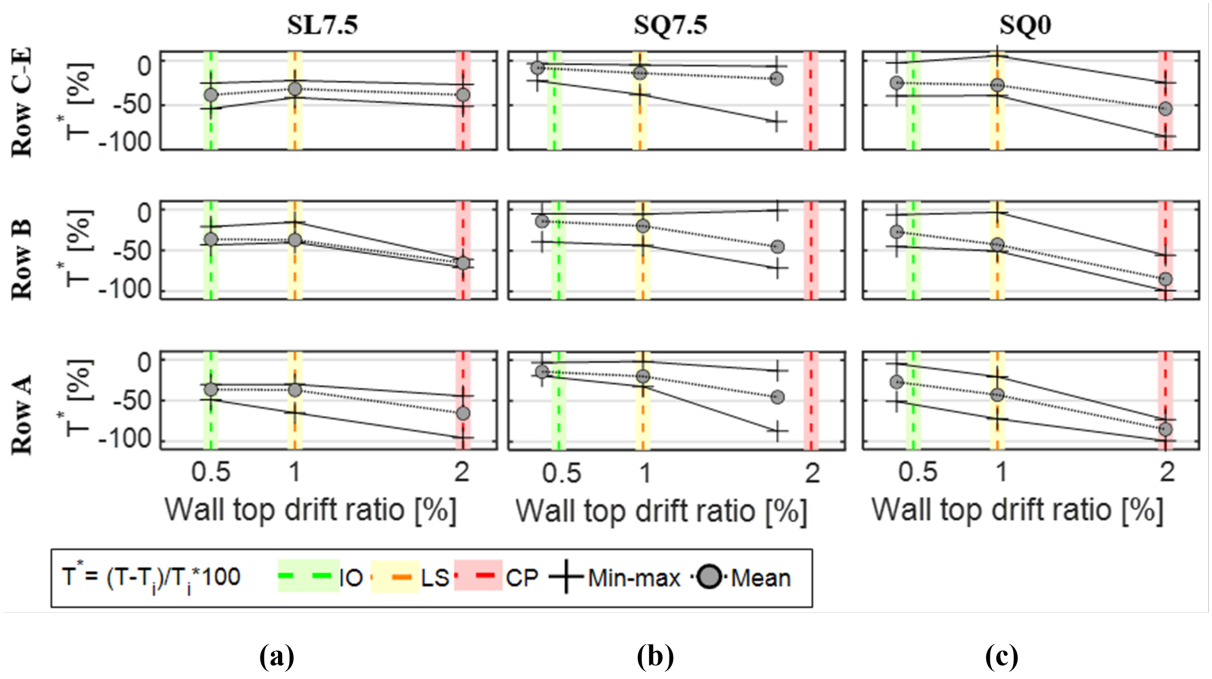


Figure 4.24: Comparison of anchor load reduction at key performance drift levels for the (a) flexure-dominated wall SL7.5 (b) squat wall SQ7.5 and (c) squat wall SQ0. Anchors grouped by row location. IO: Immediate Occupancy, LS: Life Safety and CP: Collapse Prevention limit states from ASCE 356 (2000)

4.3.3 Anchor Residual Capacity Following Wall Cyclic Test

While the ability of the anchors to maintain a consistent load during wall cycling is an important metric for determining anchor performance, measurement of the anchor tension strength following the wall lateral load testing, i.e., the residual capacity, in a direct tension test to failure provides a conclusive understanding of the remaining safety margin. As such, tension tests were performed on the anchors at the conclusion of the cyclic wall tests. Tests were performed with the same loading assembly used in the reference tests (Fig. 4.25) to minimize variability in the results due to testing conditions. However, tests were performed with the loading apparatus rotated by 90 degrees to accommodate pullout of the anchors while in the wall. Tension load was applied monotonically to the anchor through a loading tripod connected to a hydraulic ram and a load cell. Three steel blocks elevated the tripod to leave enough room to pull the anchor out. The displacement assembly, which hosted the high-precision linear displacement potentiometer, was fixed to the tripod to allow the test assembly to be hang on the crane, all as in one assembly as represented in Fig. 4.25.

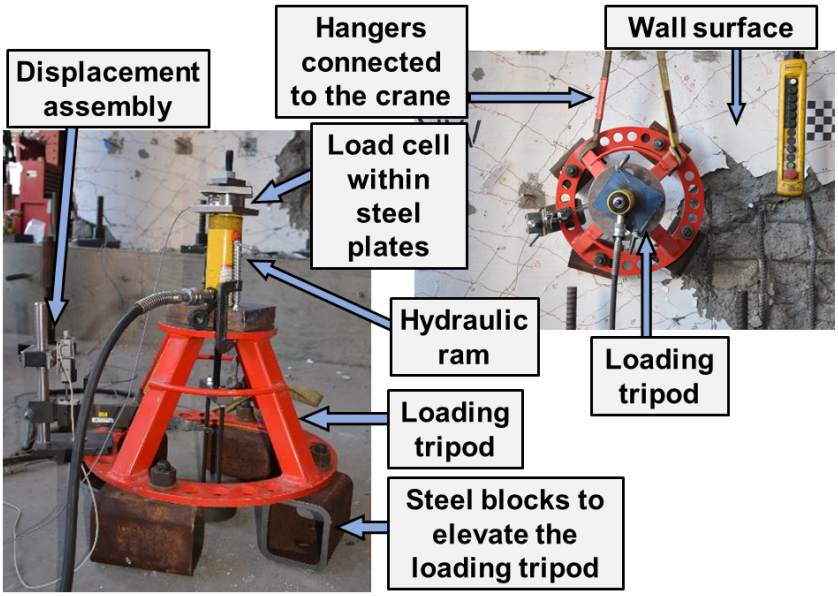


Figure 4.25: Annotated photograph of the tension to failure test assembly

It is noted that not all anchors could safely be tested to failure due to damage to the wall or to the thread rod of the anchor. A total of forty-seven anchors, twenty-two in wall SL7.5, fourteen in wall SQ7.5 and eleven in wall SQ0 were viable for testing to failure to measure their residual axial load capacities

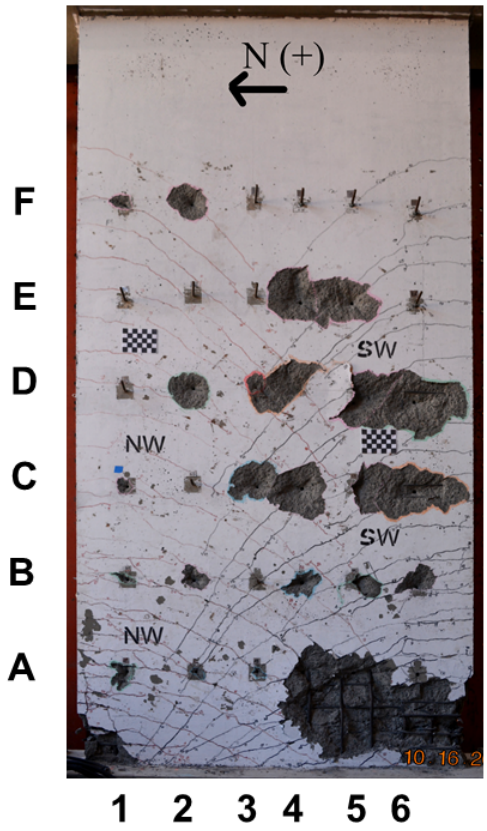


Figure 4.26: Photograph of the West face of the SL7.5 wall following tension to failure tests on twenty-two bonded and torque-controlled expansion anchors

after wall cycling. Residual load-displacement curves are reported in Appendix E. It is important to note that the concrete strength at the time of the residual capacity tests differed from the concrete strength at the day of reference testing. Therefore, the measured peak loads are normalized to the concrete strength measured at the time of the reference tests using the square root of the ratio of the compressive strengths. For the slender SL7.5 wall, tension to failure tests were conducted during a span of 12 weeks, during which the wall strength increased from f'_c = 6 ksi to f'_c = 7.4 ksi. For the two squat walls (poured out of the same concrete batch) the concrete strength at the day of reference tests and at the day of residual tension testing are f'_c = 6.9 ksi and f'_c = 8.3 ksi, respectively. In addition, it is noted that after the wall tests were concluded and the full-scale walls unloaded a residual drift was observed to affect the results of the tension to failure tests.

In the slender wall SL7.5, the residual 0.4% drift ratio (corresponding to a displacement of 0.7 inches) in the negative direction triggered the cracks in the north side of the wall to be slightly open

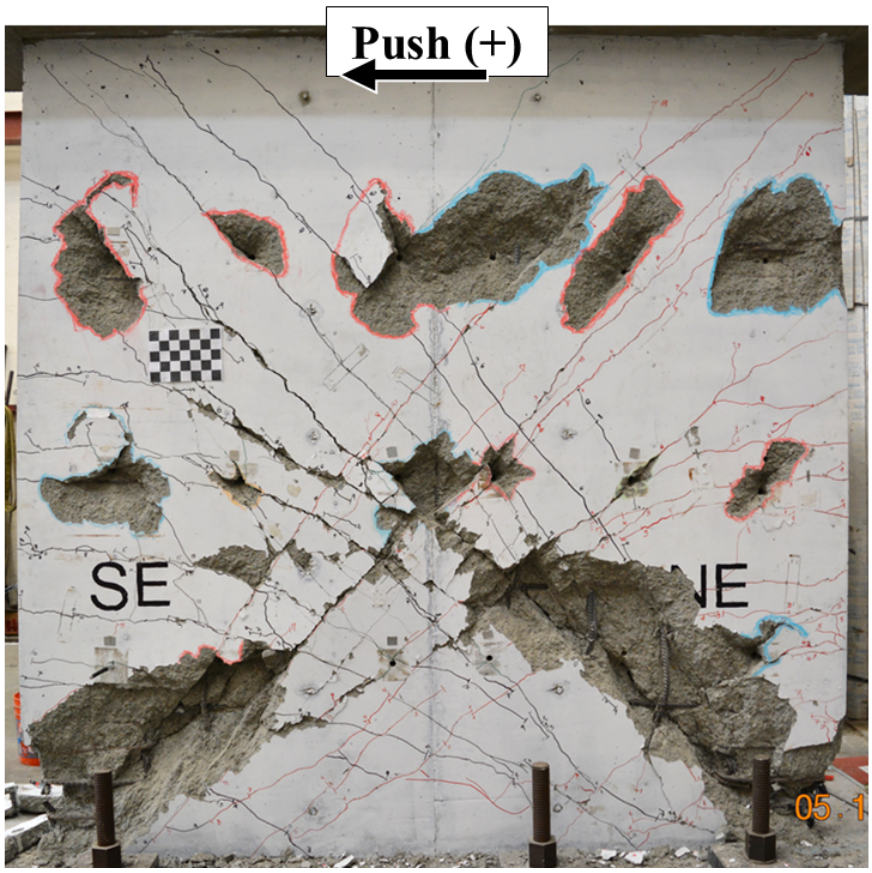


Figure 4.27: Photograph of the East face of the SQ7.5 wall following tension to failure tests on fourteen torque-controlled expansion anchors

when pullout tests were executed. At the completion of the tests, the west face of the wall (where anchors were installed) was severely damaged by the failure cones produced by bonded and, above all, expansion anchors (see Fig. 4.26). The residual capacities of eleven of the installed bonded anchors were determined through tension to failure tests conducted following the wall cyclic test. All these tension tests showed a combined concrete breakout-pullout type of failure, where the concrete cone depth did not exceed 2 inches. The average dimensions of the concrete surfaces of rupture varied from 2 inches (anchors A1, A2, and A3) to 10 inches (anchors C3, D2, and F2). In addition, the pullout tests conducted following the wall cyclic test on the torque-controlled expansion anchors showed a combined concrete breakout-pullout type of failure, where the concrete cone depth did not exceed 3 inches. The average dimensions of the concrete surfaces of rupture varied from 6 inches minimum (anchors B4, B5, and B6) to 22 inches maximum (anchor D5). It is noted that the concrete surface of rupture for anchors C4, C5, D4, D5, and E4 was significantly affected by the previous failure of the adjacent anchors, as demonstrated

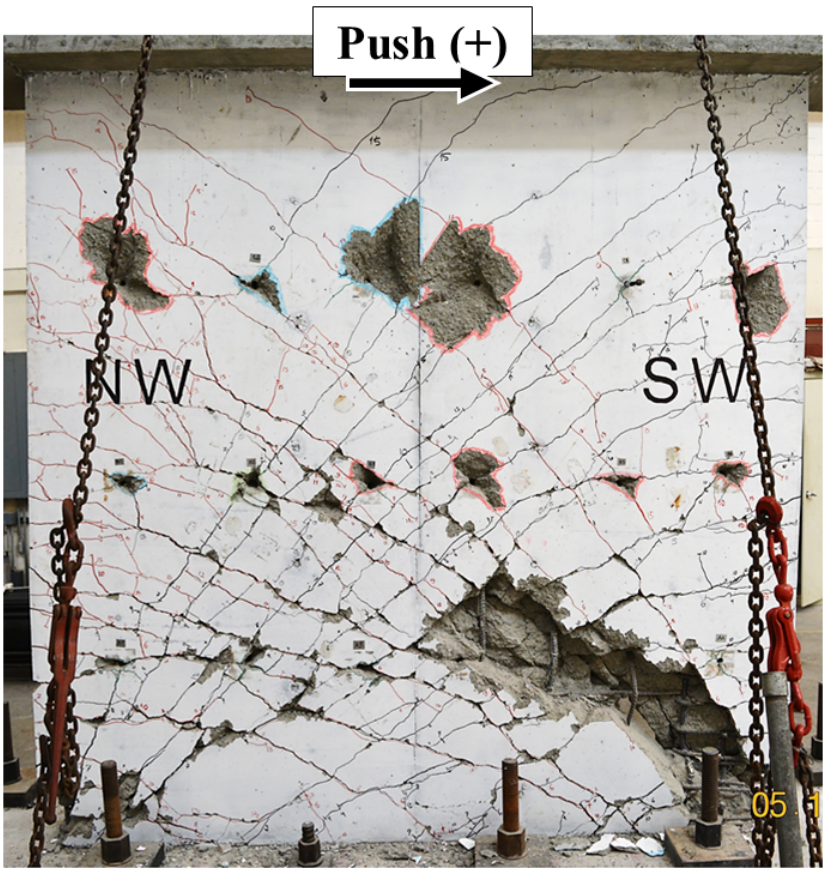


Figure 4.28: Photograph of the West face of the SQ0 wall following tension to failure tests on eleven torque-controlled expansion anchors

by merging and overlapping of the surfaces of rupture in Fig. 4.26. For most of the anchors tested, the surface of rupture initiated from the existing crossing cracks developed during the wall cyclic test.

In the squat wall tests all the anchors exhibited concrete failure modes (breakout/pull-through) with the exception of anchor B1 in wall SQ0, which pulled out. For most of the anchors tested the surface of rupture initiated from the existing crossing cracks developed during the wall cyclic test and eventually produced new cracks and fractures. Similarly to the slender wall test, the faces of the squat walls where anchors were installed (East face and West face for wall SQ7.5 and wall SQ0, respectively) were severely damaged by the failure breakout cones, as in Figs. 4.27 and 4.28. All of the anchors tested in wall SQ7.5 showed a combined concrete breakout-pullout type of failure, where the concrete cone depth did not exceed 3 inches. The average dimensions of the concrete surfaces of rupture varied from 3 inches minimum (i.e., anchors A2, B2 and B4) to 20 inches maximum (i.e., anchor C6). It is noted that the concrete surface of rupture for anchor C4 was significantly affected by the previous failure

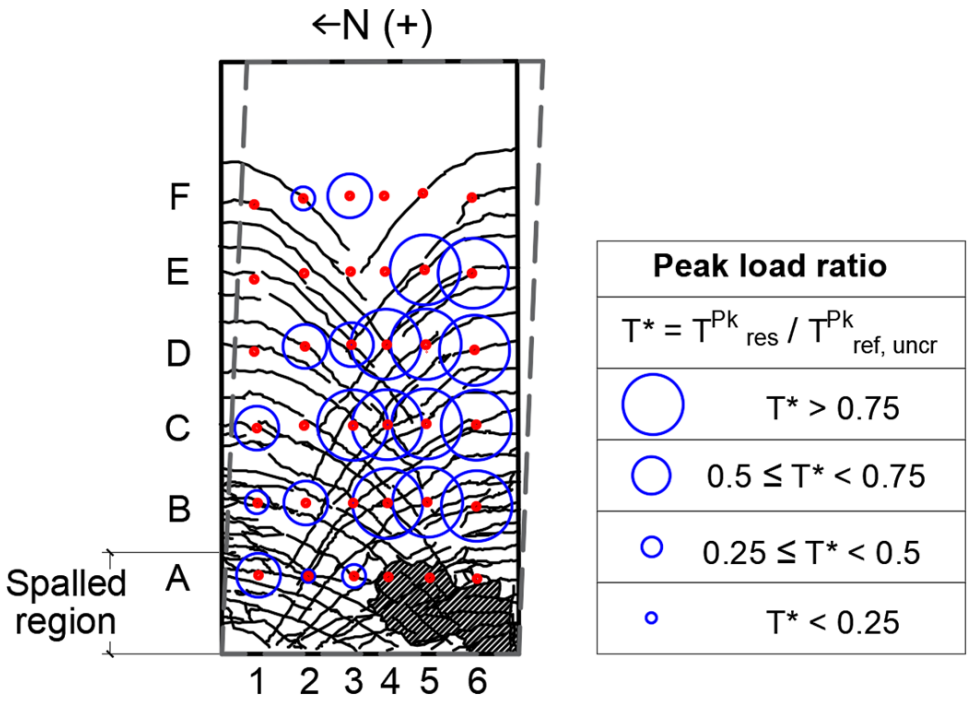


Figure 4.29: Anchor tension to failure test results of slender wall SL7.5. Circles size provides a proxy for the magnitude of the peak residual load ratio T^*_{res}, where smaller circles denote larger loss in peak residual load capacity relative to the reference uncracked concrete strengths. Note the dashed lines in the wall elevations depict larger than true scale final wall positions for visual purposes. T^*_{res} = ratio of peak residual load from tension to failure tests after wall cycling T^{Pk}_{res} to the average peak load from reference tests in uncracked concrete $T^{Pk}_{ref,uncr}$

of the adjacent anchor C3, as demonstrated by merging and overlapping of the surfaces of rupture. As observed in the slender wall tests, breakout cones of adjacent anchors in wall SQ7.5 were influenced by the previous failure of the adjacent anchors, as demonstrated by merging and overlapping of the surfaces of rupture in Fig. 4.26. This phenomenon is less pronounced in wall SQ0, being the concrete damage well distributed in a dense net of cracks. Concrete cone depth did not exceed 3 inches and the average dimensions of the concrete surfaces of rupture varied from 2.5 inches minimum (i.e., anchor B3) to 15 inches maximum (i.e., anchor C4).

Global results are reported in terms of peak residual load ratio T^*_{ref} defined as the value from tension to failure tests after wall cycling T^{Pk}_{res} normalized to the average peak load from reference tests $T^{Pk}_{ref,uncr}$. Figs. 4.29 and 4.30 articulate using circle size as proxy for the relative magnitude of the residual load capacity normalized by the reference anchor load capacity in uncracked concrete, overlaid with the sketches of the crack pattern at the end of the wall tests. Inspection of these figures show that the residual

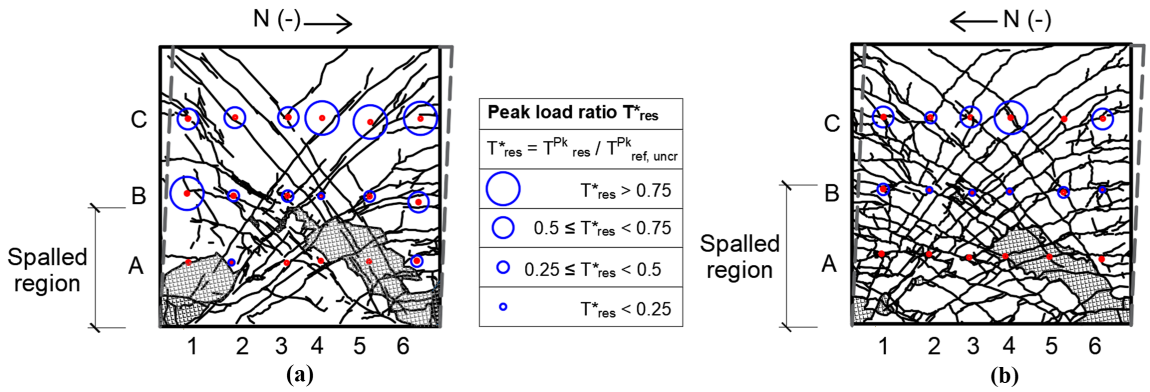


Figure 4.30: Anchor tension to failure test results of squat walls SQ7.5 and SQ0. Circles size provides a proxy for the magnitude of the peak residual load ratio T^*_{res}, where smaller circles denote larger loss in peak residual load capacity relative to the reference uncracked concrete strengths. Note the dashed lines in the wall elevations depict larger than true scale final wall positions for visual purposes. (a) Wall SQ7.5 (b) wall SQ0. T^*_{res}= ratio of peak load from tension to failure tests after wall cycling T^{Pk}_{res} to the average peak load from reference tests in uncracked concrete $T^{Pk}_{ref,uncr}$

load capacity of the anchors was reduced in the region where the concrete experienced severe cracking and damage. Notably, in the slender wall SL7.5 anchor rows A and B residing within the theoretical plastic hinge length ($L_p = 0.5L_w$ for ACI 318 2019) in residual crossing cracks as large as 0.4 mm, the residual peak load value from pullout tests after wall cycling was less than 0.5 $T^{Pk}_{res,uncr}$. Because the wall cyclic test ended with a residual drift ratio of 0.4% (0.7 inches) in the negative direction, the reduced residual capacity of the bonded anchors, which remained in slightly opened cracks, is justified. In addition, the increased residual capacity of the expansion anchors is also expected, as they not only were in closed cracks but were also experiencing increased compression due to the wall tilted state. Fig. 4.29 also shows that no significant difference in terms of peak load ratio was observed between bonded anchors, even if located in different types of cracks at the end of the wall cyclic test. The peak load ratio of bonded anchors was typically in the range of 0.6. In contrast, peak load ratio of expansion anchors was always greater than 1.0 but less than 1.2, regardless the anchor location. The maximum peak load ratio of 1.17 was measured in anchor D6, which was crossed by tension cracks during the wall cycling test and located at the corner of the tilted shear wall, therefore it had the greatest residual load capacity, presumably for the maximum compression coming from the residual wall drift.

Similarly to the anchors in the slender wall SL7.5, concrete crushing (showed by hatched regions in Figs. 4.29 and 4.30) in the lower 1/3 of the wall height compromised anchor performance and often

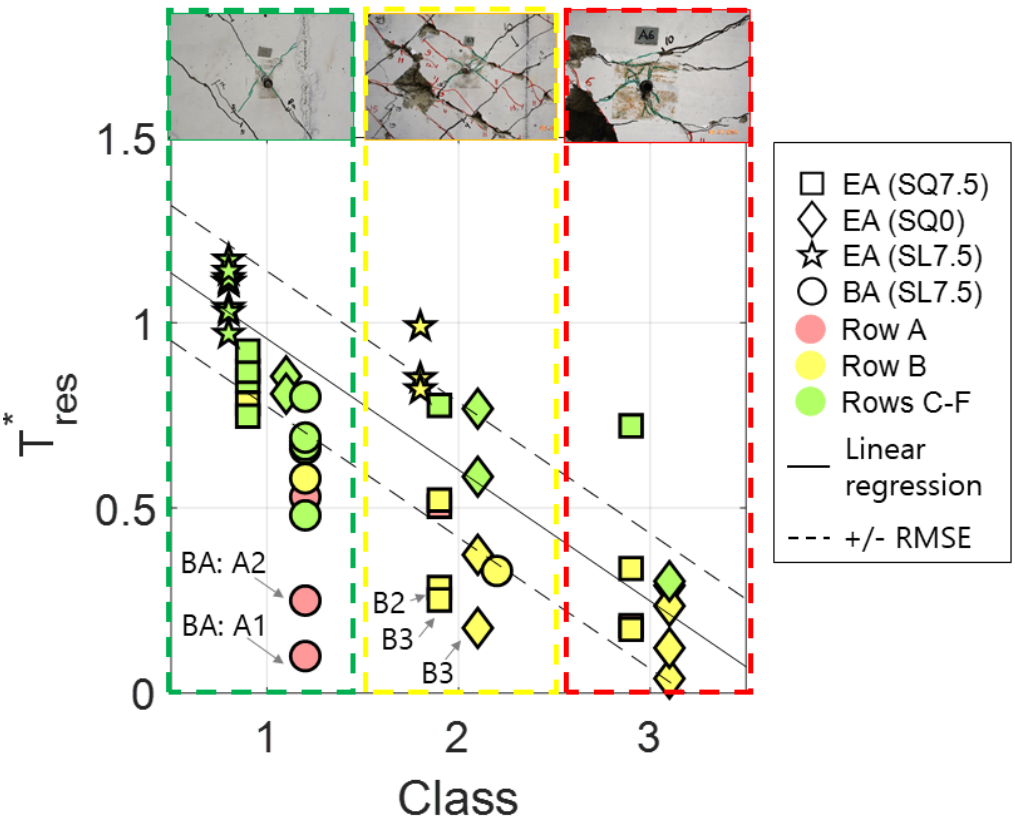


Figure 4.31: Tension to failure test results of anchors grouped by Class, see Table Fig. 4.15. T^{*}_{res} = ratio of peak residual load from tension to failure tests after wall cycling T^{Pk}_{res} to the average peak load from reference tests in uncracked concrete $T^{Pk}_{ref,uncr}$; RMSE: Root Mean Square Error; EA = expansion anchors; BA = bonded anchors

necessitated the removal of the majority of the anchors installed in row A. Indeed, only two anchors in wall SQ7.5 were suitable for tension to failure testing, namely A2 and A6. The residual load capacity of A2 and A6 measured 17% and 46% of $T^{Pk}_{ref,uncr}$, respectively, falling within the projected trend for Anchor Class 3 and 2, respectively, as explained in the following section (see Fig. 4.31). Similarly, small peak residual load ratios were observed for anchors B2, B3, B4 and B5, located in the web region of wall SQ7.5, at about mid-wall height. Anchors in the confined boundary regions of the wall and in C row reported a residual load capacity at least greater than 0.5 $T^{Pk}_{ref,uncr}$, see Fig. 4.30(a), due to the limited damage and small crack widths in the surrounding region. These results reflect the effect of the stress distribution in squat walls, where web diagonal damage may be predominant. Conversely, only four of the eleven anchors tested to pullout failure in wall SQ0 achieved 0.5 $T^{Pk}_{ref,uncr}$, reflecting the dense network of relatively larger crack widths and damage pattern experienced by this wall with respect to the

companion wall. The largest peak residual load ratios of 0.84 and 0.78 were measured for anchors C6 and C4, installed in walls SQ7.5 and SQ0, respectively. As expected, the lowest residual load capacity values were measured in anchors located inside the most significantly damaged regions of the walls, such as along the main diagonal strut or within the bottom half of the wall height, see Fig. 4.30. The average peak residual load ratios, 0.78, 0.53 and 0.38 for the wall SL7.5, SQ7.5 (tested with axial load) and SQ0 (tested without axial load), respectively, indicate the beneficial effect on anchor performance of the compression axial load on the wall, which promoted crack closure and limited the propagation of the concrete damage. It is noted, however, that the difference in average peak load ratios may also be sensitive to the larger drift demand imposed to wall SQ0 with respect to the other two walls, as documented in previous Chapters. Nevertheless, the loss of anchor load capacity is directly attributable to the presence of cyclic cracks intersecting the anchors during the wall test.

Results of the tension to failure tests performed on all anchors installed in the three full-scale walls tested within this research program are globally compared in Fig. 4.31, in terms of the peak load ratio versus Anchor Class (described in Fig. 4.15). It is noted that bonded anchors were tested in wall SL7.5 and are included to facilitate additional comparison. It is also important to note that the majority of the anchors tested in the full-scale slender wall SL7.5 fall in Anchor Class 1 or 2, due to the moderate damage experienced by this wall, and they are all approximately within the +/- RMSE (Root Mean Square Error) of the linear regression. Moreover, the relatively high self-weight of the wall, combined with the applied axial load and its predominantly flexural response to lateral load, were identified as the principal beneficial determinants, as also observed in Piccinin et al. (2010).

Only two significant outliers in Anchor Class 1 are identified within the bonded anchors as annotated in Fig. 4.31 (BA: A1, A2). These anchors were installed at about 1/8 H_w, where the wall experienced accumulation of significant internal stresses and growth of cracks. Similar to the bonded anchors in wall SL7.5, expansion anchors B2 and B3 in wall SQ7.5 and anchor B3 in wall SQ0 fell below the lower bound of the projected trend, represented in Fig. 4.31 by the black dashed line. These anchors showed residual crack widths within the Anchor Class 2 limits (see Fig. 4.15), but they all presented large residual not-through-cracks or crushed concrete in the surrounding region. Absent these outliers, the linear regression line (+/- RMSE) in Fig. 4.31 shows that increased wall damage surrounding the anchor significantly affects its residual load capacity, which may eventually reduce on average as low

as 0.15 $T^{Pk}_{ref,uncr}$ when the anchors are crossed by large residual crack widths (Anchor Class 3). In the presence of intermediate damage (Anchor Class 2), an average $T^{Pk}_{res} = 0.5T^{Pk}_{ref,uncr}$ is expected by the anchors. It is noted that globally more than 60% of the anchors tested to failure showed residual load capacity larger than 50% of the average capacity measured in reference uncracked concrete tests.

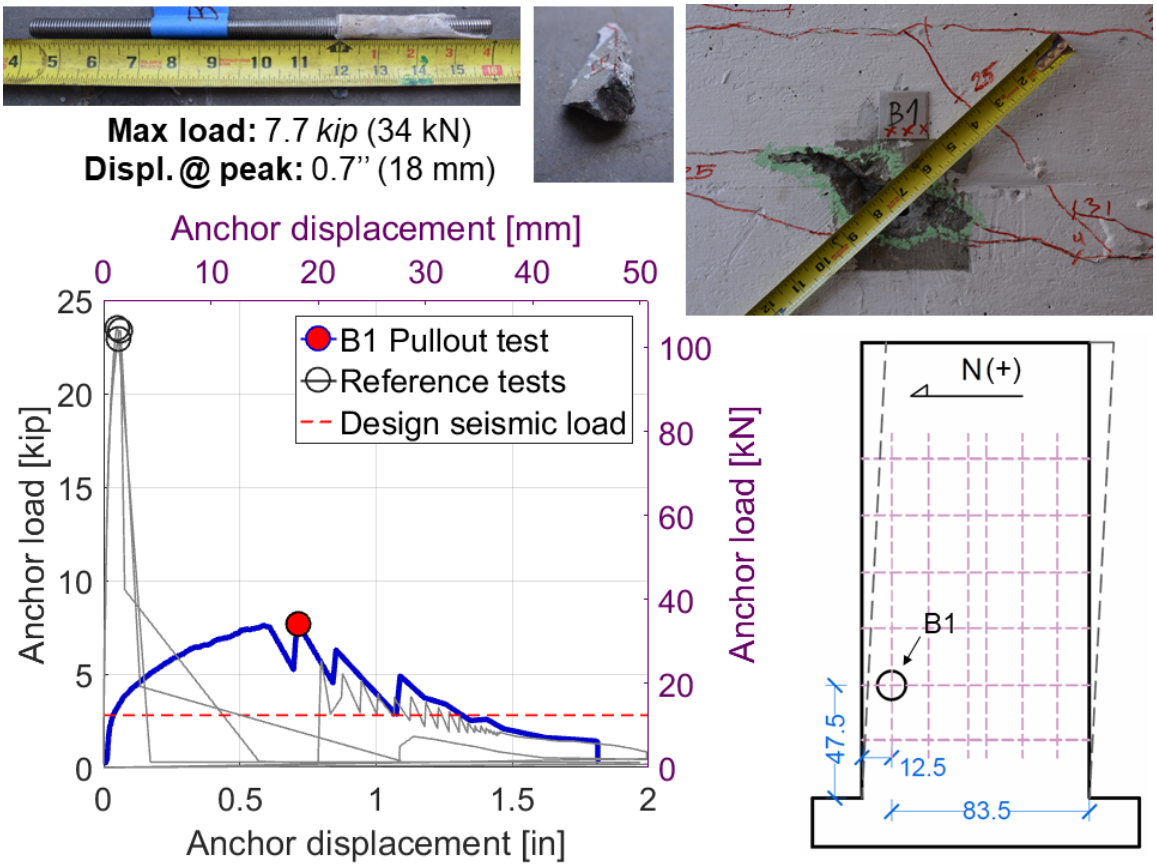


Figure 4.32: Anchor residual load-displacement curve of bonded anchor B1 in slender wall SL7.5 compared to reference test curves in uncracked concrete (circles refer to peak load values). Sketch of anchor location with residual wall drift. Photographs of the extracted anchor, of the cone of rupture, and of the surface of rupture in the wall. Note the dashed line in the wall elevation depicts a larger than true scale final wall position for visual purposes. [1 in = 25.4 mm; 1 kip = 4.45 kN]

Figs. 4.32 and 4.33 present select load-displacement curves measured during the tension to failure tests of anchors B1 and D4 from the slender wall SL7.5, respectively, together with photographs of the anchors following the test and of the surfaces of rupture. The residual capacity of bonded anchor B1 was considerably low, as the anchor experienced severe and multiple cracking during the cyclic test, being installed within the plastic hinge region. Moreover, its final position was within the tension region of the wall as the permanent (residual) drift was toward the south, while B1 was along the north end. In

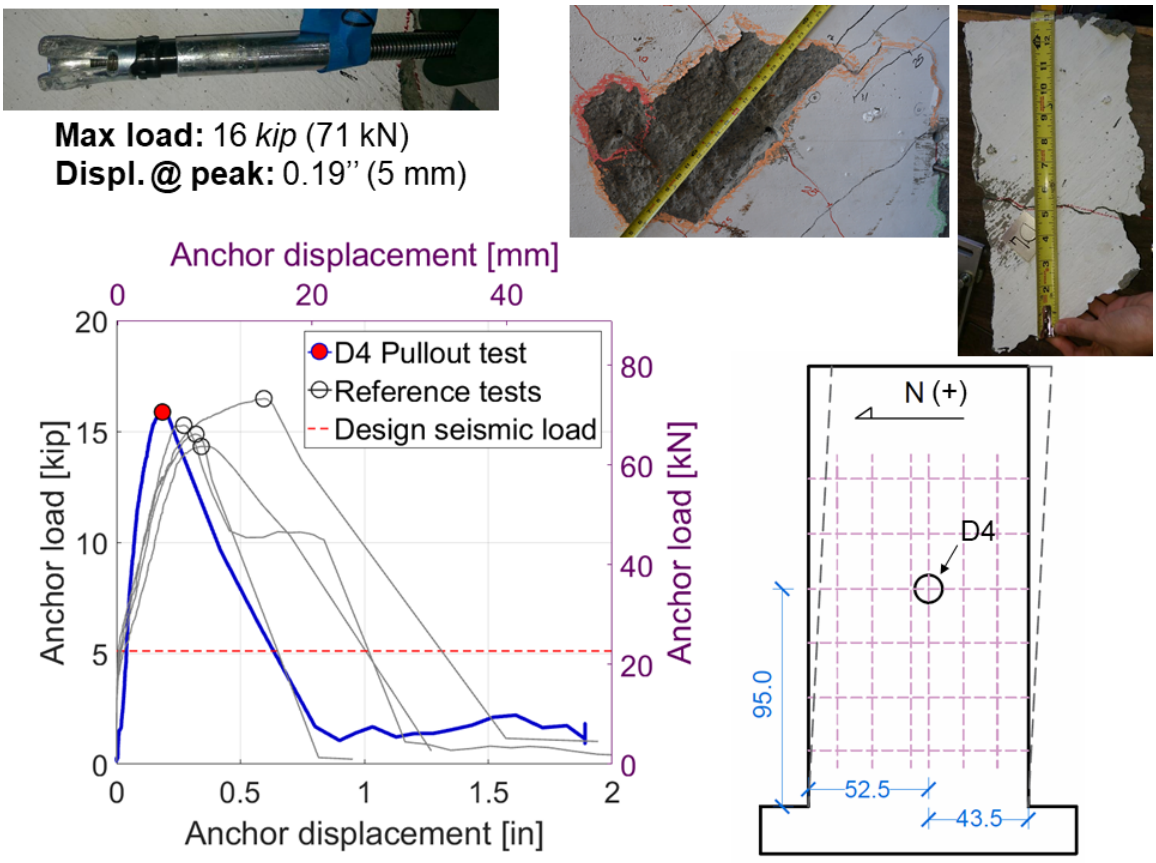


Figure 4.33: Anchor residual load-displacement curve of torque-controlled expansion anchor D4 in slender wall SL7.5 compared to reference test curves in uncracked concrete (circles refer to peak load values). Sketch of anchor location with residual wall drift. Photographs of the extracted anchor, of the surface of rupture in the wall, and of the cone of rupture. Note the dashed line in the wall elevation depicts a larger than true scale final wall position for visual purposes. [1 in = 25.4 mm; 1 kip = 4.45 kN]

contrast, the surface of rupture of anchor D4, in Fig. 4.33, shows the asymmetry of the stress distribution generated by multiple cracks intersecting as an X at the anchor location and the overlay of anchor load-displacement between the residual pullout and reference tests in uncracked concrete compares more favorably.

To further demonstrate that the compression load applied to the wall affects the performance of the anchors, the load-displacement curves from tension to failure testing of anchor B6 installed in SQ7.5 and SQ0 walls at the same location with respect to the Push (+) direction are analyzed and compared to the reference tests curves in uncracked concrete and to the design seismic loads range, see Fig. 4.34. This and the analysis of other anchors show that in general the compression load on wall SQ7.5 resulted in a greater retention of anchor tension capacity. Notably, a larger surface of rupture was produced during

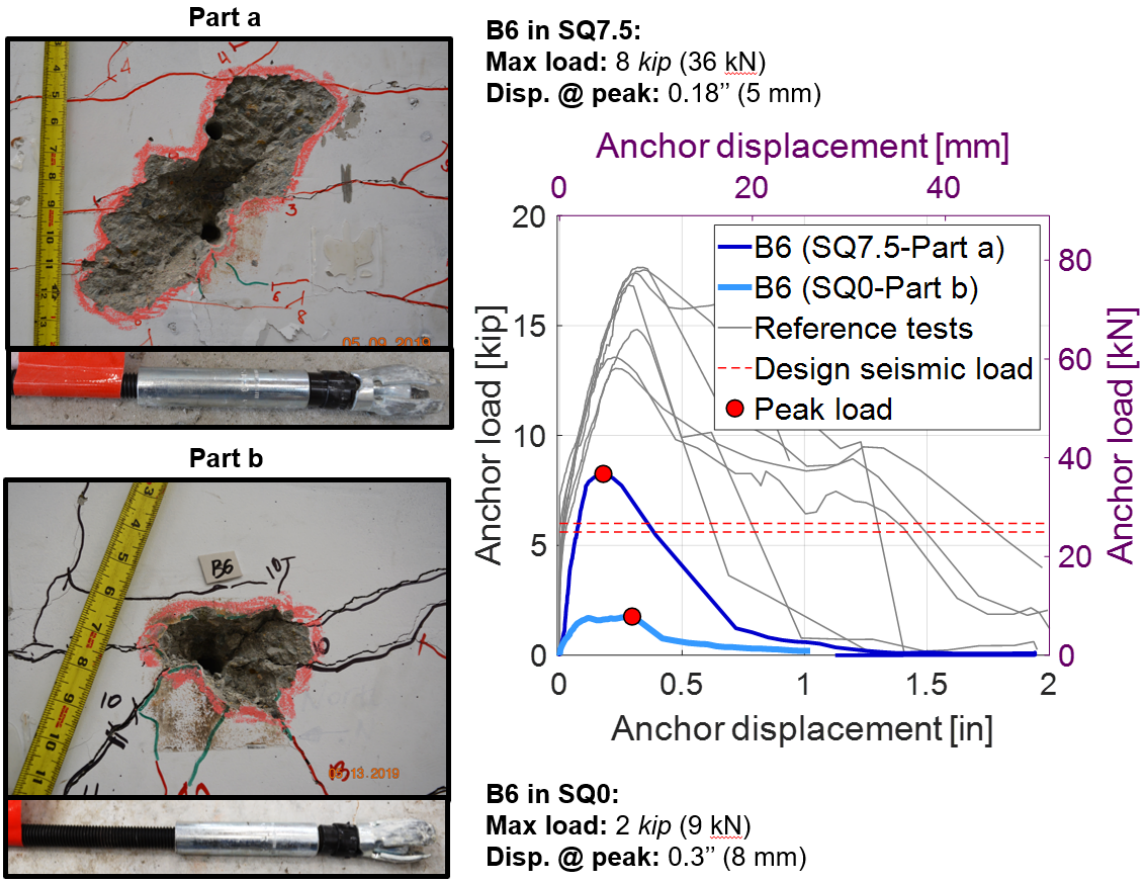


Figure 4.34: Comparison of results of anchor B6 tested to failure in wall SQ7.5 and wall SQ0. Photographs of the extracted anchor and of the surface of rupture in the walls and residual load-displacement curves compared to reference test curves in uncracked concrete. [1 in = 25.4 mm; 1 kip = 4.45 kN]

the tension to failure test of anchor B6 in wall SQ7.5, as compared to the rupture cone in wall SQ0, see Fig. 4.34. In fact, the peak load measured during tension to failure testing of anchor B6 in wall SQ0 did not reach the calculated design seismic load level. Finally, it is noted that anchor B6 in wall SQ0 was critically grouped in Anchor Class 3, due to the severe residual damage state in its surrounding concrete, as opposed to the mild damage observed in wall SQ7.5 (see Fig. 4.15).

4.4 Summary Remarks

Three full-scale reinforced concrete walls were tested under reversed cyclic lateral loads to replicate anticipated boundary conditions for tension-loaded anchors installed in the face of structural walls. This data set included one slender, flexure dominated full-scale shear wall, denoted SL7.5 wall, and two

squat shear-dominated, each full-scale wall (see Chapters 2 and 3). One of the two squat walls, denoted SQ7.5, was axially loaded with about 7.5% of its section capacity to investigate the effect of compression load on both the wall and anchor performance. The second squat wall was tested absent axial compression load, and denoted wall SQ0. The slender wall SL7.5 was designed to maximize flexural cracks, whereas the two squat walls were designed with the minimum horizontal reinforcement required by current U.S. design codes to enhance their shear response. Comparatively robust boundary detailing at the ends of all of the three walls offered sufficient strength to undergo several load reversals and manifest in ductile flexural behavior for each. A well distributed crack pattern developed in all the three walls, with a mixed shear-flexure mode in the squat walls, rendering a variety of crack scenarios unique to each of the installed anchors. Following wall cyclic tests, the anchors were tension loaded to failure, and their residual capacity was compared to the reference capacity in uncracked concrete. The behavior of the primary lateral force resisting wall element in which anchors are installed is important for assessing the anchor response in cracked conditions, as the comparison of the anchor performance in the three considered full-scale walls shows. To facilitate comparison across anchors installed in all walls, the state of damage at the residual state of the wall in the proximity of the anchors was classified as minor, moderate and severe. The most notable conclusions from this unique test series include the following:

- The shear dominated walls observed a shear displacement component that reached and exceeded, in wall SQ0, 50% of the total lateral displacement. This particular stress distribution manifested concrete struts along with ample damage to the concrete in the form of a dense network of cracks. The load capacity of anchors installed in these struts was progressively affected during the wall test and severely reduced by the end of the test, as shown by the residual direct tension tests to failure.

  In contrast, in slender walls, the damage is localized within a plastic hinge region, nominally considered as extending from the base of the wall to a distance 50% of the wall length and in the boundary elements, as reflected by the stress distribution in these types of walls. Moreover, the relatively high self-weight of the full-scale slender wall in addition to the applied axial load coupled with its predominantly flexural response to lateral load resulted in a limited effect on overall anchor performance, as reflected by the residual anchor capacity from tension to failure tests.

- Comparing the pair of squat walls considered herein, it is notable that the axial load applied to wall SQ7.5 limited the concrete damage and thus beneficially impacted anchor performance. In particular, the only three anchors which retained their design load within an average 10% variation during the entire wall cyclic test were installed in wall SQ7.5. These three baseline anchors were not crossed by cracks. Anchors installed in the wall without axial load SQ0, instead, experienced about a 20% larger load reduction on average compared with anchors installed in the most damaged regions of wall SQ7.5.

- The maximum global axial displacement of the anchors ranged on average from 0.02 inches for baseline anchors (not in the proximity of cracks) to average 0.52 inches for anchors in the region generally extending from the wall base up to 50% of the wall length and along the main strut directions (in low aspect ratio walls only). The relatively large anchor displacement in the most severely damaged regions coupled with their significant load loss emphasizes the need to avoid anchor installations in such regions of wall components.

- It is concluded that in slender ductile walls, designed with boundary elements eliciting a flexural failure, the damage is anticipated to extend from the toe of the wall vertically up to about 50% of the wall length from the wall base, and in the confined end regions of the wall. In low-aspect ratio walls designed as ductile specimens, instead, the main diagonal struts are the high stress zones where severe damage occurs, followed by the zone extending vertically up to 50% of the wall length from the wall base and the boundary elements. The intensity of damage in the three regions depends on different factors affecting the stress distribution within the wall, such as the reinforcement layout and the amount of axial load applied to the wall, as these also control the type of failure of the wall. Limited experimental data is presented in this study on ductile walls of different aspect ratios. It is noted, however, that brittle shear failure, e.g., sliding shear failure, generally results in less damage over the wall height, minimizing the effect of wall damage on the performance of anchors placed outside of the failure zone. It is clear, however, that sliding shear failure is not a desirable failure mode for concrete structures, causing potentially more severe safety and global stability issues for the structure.

Overall, anchor performance was affected by the width of the cracks and the amount of con-

crete spalling in the anchor vicinity, being less sensitive to the type of cracks. It is also noted that the anchors considered in this study represent a superior post-installed expansion anchor for use in cracked concrete conditions. Since damage accumulates in specific regions of RC walls, as described above, anchors should be avoided in these locations, where assuring that acceptable anchors capacity is preserved would be problematic. Indeed, improved anchor performance was observed outside of these regions, as confirmed by the tension tests to failure results.

4.5 Acknowledgment of Publications

Chapter 4 in part contains material published in the following journal paper: Faraone, G., Hutchinson, T. C., Piccinin, R., and Silva, J., 2019, "Performance of Post-Installed Anchors in a Progressively Damaged Concrete Shear Wall," *ACI Structural Journal*. V. 116, No. 6, pp. 293-306. In part contains material submitted for publication in the following journal paper: Faraone, G., Hutchinson, T. C., Piccinin, R., and Silva, J. (2021). "Anchor Performance in Cyclically Loaded Shear Walls," ACI Structural Journal (under review). The dissertation author was the primary author on these papers.

Chapter 5

Numerical Analysis of Reinforced Concrete Shear Wall Test Specimens

This Chapter describes the numerical model used to perform pre- and post-test analysis of the tested walls. In the present Chapter, the model robustness is evaluated against the experimental results of the three full-scale shear walls, described in Chapters 2 and 3, before carrying out a parametric study described in Chapter 6.

5.1 Scope

The numerical representation of the behavior of reinforced concrete shear walls of different geometry under simulated earthquake action is significantly important to evaluate the performance of concrete buildings. Reliable damage predictions of concrete shear walls are also essential to understand the response of components attached to wall's surface area. Indeed, the research presented in Chapter 4 showed that anchor load capacity suffers in the presence of concrete damage. Amongst the available finite element models, a macro-model able to couple shear and flexure interaction is selected for this numerical study to identify regions of severe damage. The multiple-vertical line element model presented in this Chapter was validated against the three full-scale reinforced concrete walls with varying geometric characteristics tested within this research study. A parametric study is then conducted considering varying wall height to length ratios, detailing properties and amount of applied constant compression

load, in an effort to explore the walls response (Chapter 6). Results of the considered wall models are compared at key performance states, which are commonly used in performance-based design to estimate the expected damage. In the analysis of the numerical model results, particular focus is given to the distribution of the predicted crack pattern to provide insight on the likelihood of the impact of concrete damage on the performance of components which may require attachment with concrete anchorage. Results of the validation study show good prediction capabilities in terms of global and local responses. Despite the limitations of the model, e.g., lack of specific modeling of reinforcement debonding and out of plane deformations, overall reasonable estimation of cracks and damage is observed. This study enriches research efforts towards more reliable seismic design and performance assessment of reinforced concrete buildings.

5.2 Introduction

Reinforced concrete (RC) structural walls are used in concrete buildings to provide lateral stiffness and lateral load capacity, as well as ductility of a building in the event of moderate to severe earthquakes. Current U.S. design codes and guidelines recommend specific design and reinforcement detailing to enhance ductile flexural behavior of the wall and to avoid brittle failures, usually related to shear mechanisms (ASCE/SEI 7-16 2016, ACI 318 2019). In particular, the presence of well confined boundary elements at the wall ends is desirable to increase the flexural strength of the structural element, as this leads to well distributed concrete damage and limits shear stress.

In general, RC walls exhibit predominantly flexural or shear responses when subjected to lateral loads, as a result of their geometry and reinforcement detailing. Concrete walls are commonly classified in terms of their aspect ratio (AR = wall height / wall length), with low AR values (AR $\leq$ 1.5) associated with predominantly shear response, and large AR values (AR $\geq$ 2) related to predominantly flexural behavior. Walls with ARs in the intermediate range usually show a coupled shear-flexure response which may compromise the desired flexural failure mode in the event of lateral excitation.

Proper characterization and analytical prediction of the behavior of concrete walls is a research topic of interest in the performance assessment of concrete buildings. In addition, understanding damage distribution within RC walls is useful to predict the response of structural and nonstructural components

and system, which are often attached to these walls via various types of anchors. Indeed, anchors rely on the integrity of the surrounding concrete to transmit their bond stress and properly serve their function. Unfortunately, as illustrated in Chapter 4, certain types of anchors may be severely affected by cracks and concrete crushing. The experimental effort illustrated in this dissertation and in Faraone et al. (view) showed indeed that load capacity of post-installed anchors in RC shear walls is compromised by the concrete damage developing in shear walls. Therefore, being able to predict concrete damage in laterally loaded RC walls provides insight not only on the walls structural response, but also on the likelihood of attachment components failure. The latter is known to contribute in large part to the total downtime related to seismic events and it is often the main cause of injuries and loss of life in modern earthquakes.

Extensive studies on the analytical modeling of the inelastic shear and flexural response of structural wall systems have advanced in recent years, based on the evidence that previous models, which uncouple flexure and shear responses tend to result in low accuracy estimations of their lateral load capacity (Orakcal and Wallace 2006). Robust models capable of coupling shear and flexure response, as typically observed in concrete shear walls, were subsequently developed (Massone et al. 2006, Xu and Zhang 2010, Panagiotou et al. 2012). Amongst these models, many are semi-empirical or capable of simulating only monotonic response. While others present instead limited success when compared with experimental data or have yet to be studied for their sensitivity considering varied numerical and material parameters. On the other end, an attractive strategy for predicting the coupled shear-flexure response in RC structural walls under reversed-cyclic loading conditions involves the use of RC panels in a two-dimensional fiber-based macroscopic formulation. Macro-models are effective computational tools as they are relatively easy to implement and efficient. They reasonably predict important hysteretic response characteristics of those RC walls which satisfy the main assumptions of the model formulation (e.g., plane sections remain plane, uncoupling of flexural and shear responses, assumption of uniformly distributed shear strains along the wall cross sections, and similar) (Gullu and Orakcal 2019). An example of these models can be found in Massone et al. (2009), Vulcano et al. (1988) and Orakcal et al. (2004). This modeling strategy, referred to as Shear-Flexure Interaction-Multiple Vertical Line Element Model (SFI-MVLEM), represented in Fig. 5.1, is selected amongst these models for its simple formulation, numerical stability and efficiency. The behavioral characteristics of the constitutive panel elements incorporated in the SFI-MVLEM model formulation are based on a fixed-crack-angle method-

ology. Panel stress and strain are evaluated in the principal directions using equilibrium and kinematic considerations and principal stress is calculated from principal strain based on pertinent material constitutive relations, developed from standard uniaxial compression tests of concrete. The SFI-MVLEM also simulates behavioral features observed in the shear stress transfer mechanism across concrete cracks, like the shear-aggregate interlock in concrete and the dowel action mechanisms.

The SFI-MVLEM model was validated against small-scale tests aimed to understand the response of different structural walls available in literature in Tran and Wallace (2015). However, the soundness of small-scale test validation may be compromised by concrete scale effects showed by RC structures subjected to lateral loads, as observed in Rasoolinejad and Bazant (2019). True comparison to the analytical predictions may therefore be offered by utilizing the three-full scale walls with rectangular section considered in the experimental program described in Chapters 2 and 3. In this study, the SFI-MVLEM model is used to simulate the hysteretic lateral load behavior of RC structural walls with varying levels of flexural and shear deformation contributions on wall response. First, evaluation of the models robustness when compared with the experimental response of the three full-scale reinforced concrete shear walls is performed. Subsequently, geometry, detailing and amount of applied compression load are varied to generate a parametric study utilizing different wall models. The response of these wall models is analyzed in terms of global and local behavior, with particular attention given to the evolution of damage characteristics in Chapter 6.

To demonstrate the suitability of the model to predict the evolution of the damage, attention is given to the damage pattern response at three performance limit states commonly considered in a performance based approach (ASCE 356 2000), namely Immediate Occupancy, Life Safety and Collapse Prevention. These three performance states are usually identified by key structural conditions typical of structures subjected to lateral loads. In the context of performance-based design, it is useful to directly express these damage acceptance limits in terms of story drift ratio to prevent damage to nonstructural components, avoid structural instabilities and avert human discomfort during low-level excitation. To this end, the drift values suggested by ASCE 356 (2000) are adopted as baseline for this study, since they allow a consistent comparison across walls of different geometry. These performance limit states and the associated drift limit values are described as follows:

- Immediate Occupancy (IO) is reached when structural walls remain elastic after an earthquake and

buildings with these walls can be immediately occupied afterwards. This level is usually reached at 0.5% drift ratio.

- Life Safety (LS) occurs when the building structure undergoes extensive damage after an earthquake event, but structural walls remain stable, and it is possible to access the building. This state is usually reached at 1.0% drift ratio.

- Collapse Prevention (CP) is the critical limit state, reached when the building structure is standing, but substantial damage prevents access. The gravity load resisting system still carries the gravity load demands, regardless of the severe damage to the lateral force resisting components. This state is usually reached at 2.0% drift ratio. It is noted that this performance level approximately represents the prevention of global collapse under an extremely strong earthquake associated with the 2.0% chance of exceedance in 50 years, i.e., the "Maximum Considered Earthquake" (MCE).

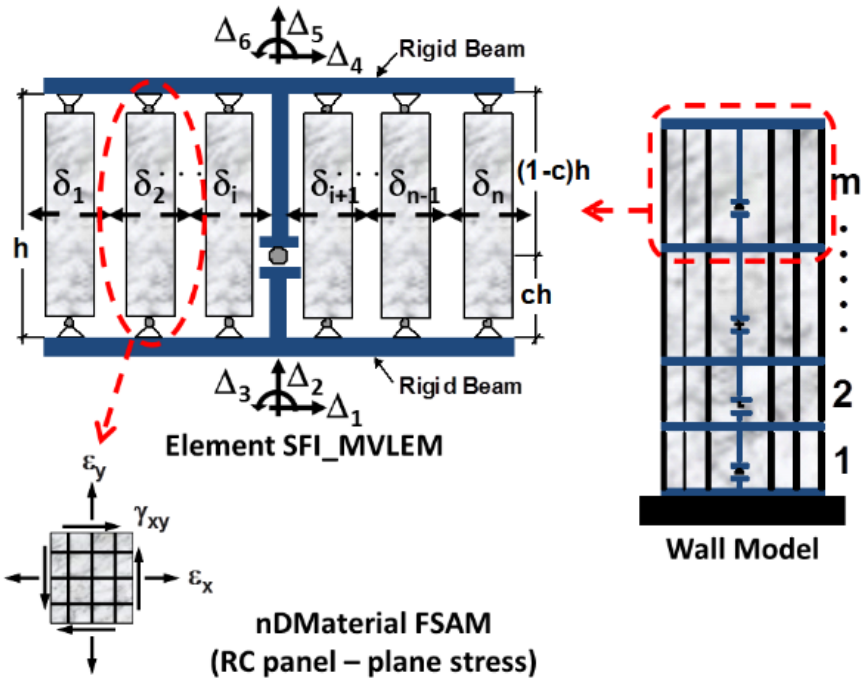


Figure 5.1: Representation of the SFI-MVLEM model. Element and RC panel element exploded for details. Figure by Kolozvari et al. (2015) from *opensees.berkeley.edu*

5.2.1 Description of the Numerical Model

The nonlinear SFI-MVLEM model considered in this study was developed by Kolozvari et al. (2015) and geared towards prediction of the nonlinear response of RC shear walls subjected to lateral loading. The SFI-MVLEM analytical model consists of reinforced concrete panels subjected to in-plane actions inserted into a two-dimensional macroscopic fiber model, previously formulated by Orakcal et al. (2004), as represented in Fig. 5.1. The coupling of axial and shear responses is achieved at the macro-fiber level and it is converted at the element-level in shear and flexural-axial interaction.

The model formulation assumes that 1) plane-sections-remain-plane, 2) shear strains are uniformly distributed along the wall section and 3) the horizontal axial stresses assigned to each reinforced concrete panel have a null resultant. Panels are connected at top and bottom by rigid beams for assumption 1), as represented in Fig. 5.1. Assumption 2) is deemed acceptable as long as lateral displacement is primarily due to flexural deformation. This condition may not be satisfied by low-aspect ratio walls, which may show varied deformation modes and load transfer mechanisms, such as strut-and-tie, or significant contributions of shear deformations. In addition to these phenomena, the relatively small

height of low-aspect ratio walls may limit redistribution of stresses, which tend to concentrate around the support and around the point of application, according to the Saint Venant's principle, introducing non-uniformity in stress and strains. Therefore, low-aspect ratio wall models may result in a considerably ill-conditioned wall response. Indeed, Massone et al. (2006) showed that the assumptions 1-3 are reasonable for RC walls with aspect ratio greater than 1.0. Thus, conservatism is observed when the described model is used to capture the response of low-rise RC walls with AR $\leq$ 1 (Kolozvari 2013). However, it is noted that recent studies showed promising results also for shorter walls with AR $\leq$ 1 (Gullu and Orakcal 2019). Therefore, the SFI-MVLEM model is used to predict the response of all the full-scale tested walls herein.

Analytical Model Formulation

The finite element model of a wall is constructed with a series of elements stacked one over the other to cover the height of the wall. Within each element, a customized number of panels connected in series describe the wall length. Each panel is a bi-dimensional element, which couples the concrete and steel material properties to predict the nonlinear response of the wall under cyclic lateral load. A single two-dimensional element of the FE model has three degrees of freedom per node, which is assumed at the center of the top and bottom rigid beams Orakcal et al. (2004), see Fig. 5.1. The relative rotation between the top and bottom rigid beams (curvature) occurs around a point, the center of rotation of the element, placed on the central axis of the element at height c·h, with a recommended value c = 0.4 from comparison with experimental results Kolozvari et al. (2015). The distribution of wall curvature over the vertical extension of each wall element is assumed to be uniform. Similar to the curvature, the shear deformation of an element occurs at height c·h within the element and it is computed from the shear deformations of each individual panel. The strain components of concrete and reinforcing steel of a RC panel element are considered to be equal to each other, implying the assumption of a perfect bond between concrete and reinforcing steel bars.

The constitutive RC panel behavior under generalized reversed-cyclic in-plane membrane action is modeled with the Fixed-Strut-Angle-Model (FSAM). The main assumption of this formulation is that the directions of the cracks do not rotate with subsequent loading, once the concrete is cracked. The first crack is formed when the principal tensile strain in concrete exceeds a specified cracking strain of

concrete. The principal strain direction at this instance is the "fixed strut" direction of the panel, which remains unchanged for all the subsequent loading stages. As the loading proceeds, the model tracks the concrete stress-strain response along the first strut direction, and the second crack is formed when the strain exceeds the specified cracking strain of concrete. The direction of the second fixed-strut is assumed to be perpendicular to the first crack. Although this second crack direction could deviate from the perpendicular for the presence of shear aggregate interlock, experimental results of concrete panels show that the deviation from the direction perpendicular to the first fixed-strut is small. The model formulation is hence deemed acceptable.

The FSAM was modified by Kolozvari et al. (2015) to include shear resistance along the cracks (shear aggregate interlock) and dowel action of reinforcement, as shown in Fig. 5.2. The two effects are modeled to be independent, to provide more flexibility in calibrating results with experimentally observed behavior. The shear aggregate interlock is modeled with a simple friction-based constitutive relationship, in which the amount of shear resistance across crack surfaces when the crack is closed is described by a coefficient of friction ranging from 0.6 to 1.4. The dowel resisting action is described instead by a linear-elastic relation. When the crack across the panel is open the shear resistance given by the dowel resistance of the vertical reinforcement is modeled as a fraction α of the steel elastic modulus E_s. This shear contribution prevents an excessive pinching of force-deformation response and a negative stiffness in the unloading branch around zero lateral deformation.

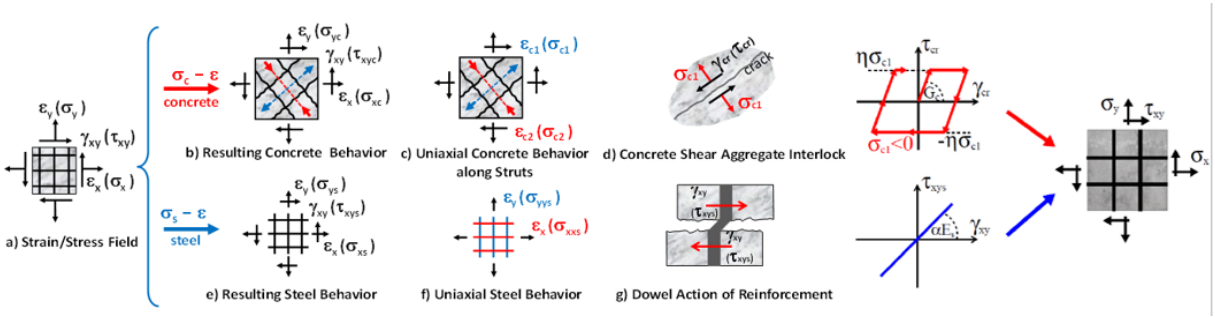


Figure 5.2: Stress-strain field in each panel. Concrete aggregate interlock and dowel action shear resisting components are also graphically represented. Figure by Kolozvari et al. (2015) from *opensees.berkeley.edu*

Constitutive Relationships

Responses obtained with the SFI-MVLEM model are governed by the properties and parameters defining material constitutive relationships (stress-strain material behavior) which define the panel stiffness. The material models used in these analyses are briefly described here. Further information on the analytical formulation of the SFI-MVLEM is in Kolozvari et al. (2015).

The concrete behavior under biaxial loading along fixed struts is modeled with the simple *Concrete02* material implemented in OpenSees, which considers linear tension softening and linear concrete degradation in compression. Alternatively, an advanced material model, the *ConcreteCM*, may be used. The *ConcreteCM* model is based on the hysteretic constitutive relation developed by Chang and Mander (1994) to describe the uni-axial hysteretic constitutive model of confined and unconfined concrete in both cyclic compression and tension, with progressive stiffness degradation associated with smooth unloading and reloading curves at increasing strain values. Empirical equations for key hysteretic parameters are used to estimate the secant stiffness and the plastic stiffness upon unloading from the envelope and stress and strain offsets upon returning to the compression envelope (see Fig. 5.3). It is noted that the models response is studied using both material models, as discussed later in Section 5.4.

The nonlinear hysteretic model of Menegotto and Pinto (1973) extended by Filippou et al. (1983) to include isotropic strain hardening is used to represent the uniaxial stress-strain relationship for the reinforcing steel. As shown in Fig. 5.3, the hysteretic stress-strain relationship follows curved transitions, defined by the cyclic curvature parameter R, to account for Bauschinger's effect. The initial slope of the stress-strain line, the Young Modulus E_0, is reduced by the strain hardening coefficient b, which defines the slope of the straight-line asymptote in the bi-linear model. This material model is widely implemented in numerical models and is able to accurately reproduce test results on individual reinforcing bar specimens, despite its simple formulation. It is noted, however, that this model does not incorporate certain degradation and failure mechanisms of the reinforcement typically observed in reality, such as out of plane buckling and fracture of the reinforcement. Low-cycle fatigue also is not incorporated in this material model formulation.

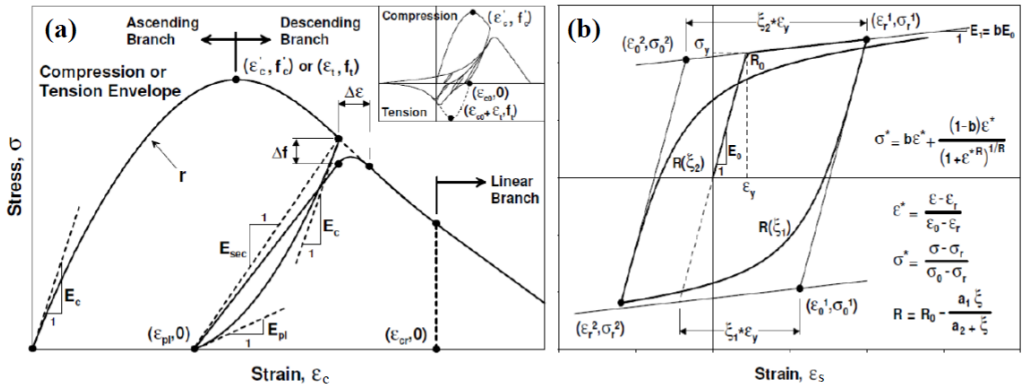


Figure 5.3: Material constitutive models (a) hysteretic constitutive behavior by Chang and Mander 1994 and (b) steel model Menegotto-Pinto-Filippou. Figures from Orakcal and Wallace 2006 Orakcal and Wallace (2006).

5.3 Model Validation

Validation of the commonly used nonlinear numerical SFI-MVLE model against three full-scale reinforced concrete shear walls previously tested within this dissertation is conducted. Results are presented in the following sections in terms of global and local response and damage evolution.

5.3.1 Description of the Wall Models

Three full-scale reinforced concrete shear walls with rectangular cross-section described in Chapters 2 and 3 were considered to validate the numerical model. Key characteristics of these walls are briefly summarized in the following paragraphs for the reader's convenience.

One slender wall with AR=2 was 8 ft by 16 ft high and 12 inches thick and was designed to exhibit ductile flexural behavior according to the capacity design approach. Strong boundary elements properly confined with closely spaced hoops and horizontal reinforcement distributed over the wall height satisfied the shear demand corresponding to the flexural capacity. The slender wall, here referred to as AR2-8-BE in harmony with the parametric study presented in Chapter 6, was laterally cycled at increased drift amplitude up to 3% drift ratio, when about 20% in strength was observed. A consistent axial load ratio of about 8% of its section capacity was applied during the wall test.

Two AR=1, 8 ft long by 8 ft high and 10 inches thick full-scale identical shear walls were also tested by imposing cyclic increasing lateral displacement to the walls' top. These two squat walls were designed to elicit their shear response during the cyclic loading, to get a combined shear-flexure failure which could show significant spread of damage along diagonal planes. This objective was reached by designing strong and well-confined boundary elements and concurrently placing the minimum amount of horizontal shear reinforcement allowed by code ACI 318 (2011). Axial load was constantly applied in the amount of 0% and about 8% of the walls' section capacity to investigate the effect of axial compression on the wall response. These two walls are herein referred to as AR1-0-BE and AR1-8-BE, respectively, in harmony with the parametric study presented in Chapter 6.

Final detailing of the three full-scale walls is reported in Figs. 5.4 and 5.5. Reinforcement ratios and material properties determined from material tests on the day of wall testing are summarized in Table 5.1, along with geometric properties of the walls, as implemented in the numerical models. The

lateral cyclic displacement history was imposed at the top of the wall through the top beam attached to an actuator as shown in Fig. 5.6. Axial compression load was imposed on the AR=2 and one AR=1 wall through four post-tensioned high strength cables acting on two spreader beams transversely placed on top of the wall top beam, see Fig. 5.6. It is noted that the axial load is imposed in the numerical representation as a constant load along the stiff top beam.

The presence of the two strong flexural end boundaries increased the flexural strength and lateral load capacity of the walls and intensified the damage distribution through the wall height. Failure of wall AR2-8-BE was initiated by longitudinal reinforcement buckling and concrete spalling at the wall toes and was followed by concrete crushing in the wall faces and longitudinal reinforcement rupture. Similarly, failure of the two squat walls ultimately occurred for concrete crushing and longitudinal reinforcement rupture. However, since shear deformations contributed significantly to the wall lateral displacement, strength degradation was initiated by significant concrete deterioration along the two major diagonal struts. The shear component to the total displacement measured in these squat walls affects the global response of the walls to lateral forces and the prediction potential of the numerical model, as it will be discussed later in Section 5.4.

Table 5.1: Geometric and material properties of the tested full-scale walls: AR=aspect ratio= wall height/ wall length; ALR= axial load ratio = $\frac{N}{A \cdot f'_c}$, where N=applied axial load, A= cross section area and f'_c = concrete compressive strength at the day of the test; $\frac{\mathbf{L_{BE}}}{\mathbf{L_w}}$= boundary element to wall length ratio; $\rho_{\mathbf{v,web}}$ = vertical reinforcement ratio in the web; $\rho_{\mathbf{v,BE}}$ = vertical reinforcement ratio in the boundary elements; $\rho_{\mathbf{h,web}}$ = horizontal reinforcement ratio in the web; $\rho_{\mathbf{h,BE}}$ = horizontal reinforcement ratio in the boundary elements; $\mathbf{f'_c}$ = concrete compressive strength determined on day of test; $\mathbf{f_{y,v}}$ = average yield strength of the vertical reinforcement steel

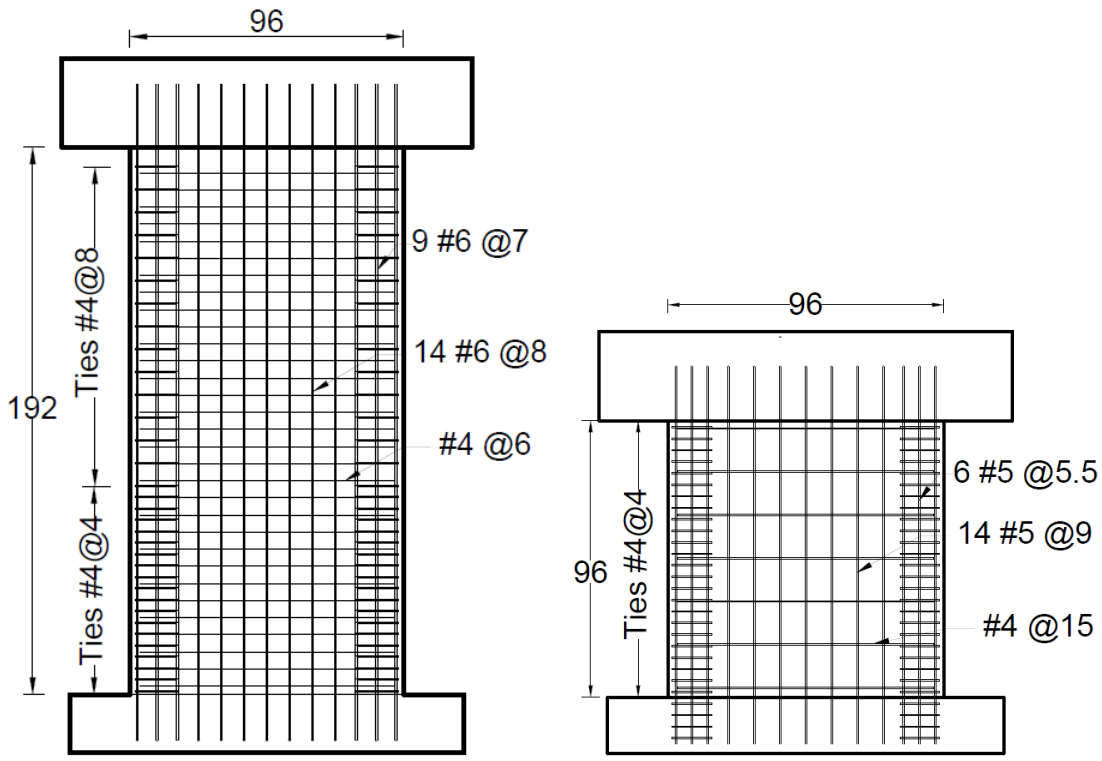
Wall	AR	ALR [%]	$\frac{\mathbf{L_{BE}}}{\mathbf{L_w}}$	$\rho_{\mathbf{v,web}}$ [%]	$\rho_{\mathbf{v,BE}}$ [%]	$\rho_{\mathbf{h,web}}$ [%]	$\rho_{\mathbf{h,BE}}$ [%]	$\mathbf{f'_c}$ [ksi]	$\mathbf{f_{y,v}}$ [ksi]
AR2-8-BE†	2	8	0.2	1.0	2.2	0.6	1.25	6	73
AR1-8-BE$^{\mp}$	1	8	0.2	0.7	1.0	0.35	1.5	7	67
AR1-0-BE$^{\vee}$	1	0	0.2	0.7	1.0	0.35	1.5	8	67

†: slender wall axially loaded to about 8% of its section capacity

$^{\mp}$: squat wall axially loaded to about 8% of its section capacity

$^{\vee}$: squat wall tested without axial load

To perform the numerical analysis of the tested full-scale walls, the geometry of the mesh is defined in terms of panels, i.e., the elements along the wall length, and of nodes, which define the number of elements along the wall height. The number of nodes and panels is varied accordingly to the desired

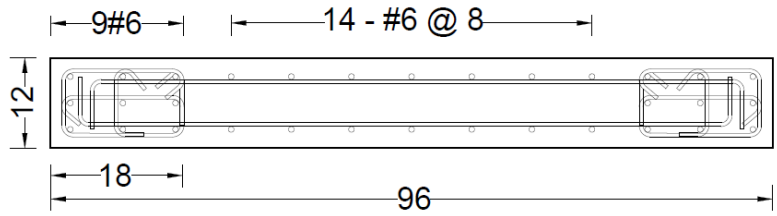


(a) Slender wall AR2-8-BE

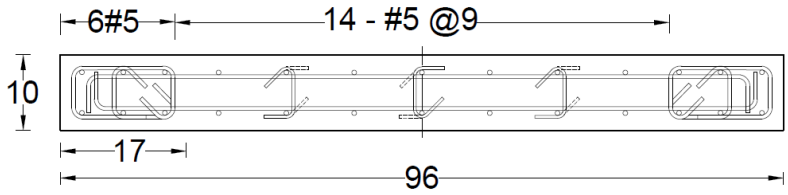
(b) Squat wall (typical)

Figure 5.4: Elevation view. Note these are (a) SL7.5 and (b) SQ7.5 and SQ0 walls described in Chapters 2 and 3. Units in inches [1 in =25.4 mm; 1 kip =4.45 kN]

level of description of the local response of the wall models. To explore the mesh effect on the model response, two discretizations are considered, namely a 12x12 inches and a 6x6 inches square elements meshes. In particular, the large meshes of the AR=1 and AR=2 models were obtained considering eight and sixteen SFI-MVLEM elements along the height of the wall, respectively, and eight panels (macro-fibers) along the wall length, as shown in Fig. 5.7. Similarly, the dense meshes of the AR=1 and AR=2 models were obtained considering sixteen and thirty-two SFI-MVLEM elements along the height of the wall, respectively, and sixteen panels along the wall length. All models are fixed-supported at the base to simulate the fixed connection at the wall-footing interface of the tested walls (see Figs. 5.6 and 5.7). The cyclic displacement protocol and constant axial load (if present) are applied to the top node of the numerical model, i.e., the control node in Fig. 5.7, and thus result in uniform distribution between the concrete panels. The difference in global response and damage characteristic predicted by the two meshes is analyzed in the following sections. It is noted that boundary elements are modeled by assigning confined concrete properties to the finite elements located within the design boundary element length.



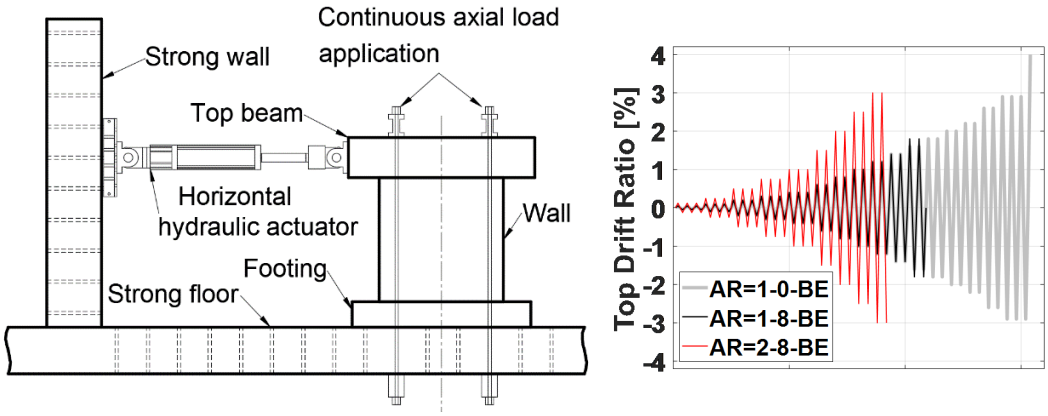
(a) Slender wall AR2-8-BE



(b) Squat wall AR1-BE (typical)

Figure 5.5: Cross section view. Note these are (a) SL7.5 and (b) SQ7.5 and SQ0 walls described in Chapters 2 and 3. Units in inches [1 in =25.4 mm; 1 kip =4.45 kN]

The constitutive material parameters used in the numerical models reflect the as-tested material properties on the day of the test if available, or are calculated with well-established empirical relationships from the measured material properties, see Table 5.1. In the definition of the *ConcreteCM* material model, a value of 0.00008 was selected for the tensile strain at strength, as suggested for RC panels by Belarbi and Hsu (1994). The parameters describing the cyclic stiffness degradation of the reinforcing steel, instead, are assumed as originally proposed by Menegotto and Pinto (1973). It is worth noting that the material parameters are not finely tuned to fit the experimental responses of the tested walls with the model predictions to provide a general validation of the numerical model. Displacement-controlled analyses were carried out in OpenSees adopting multiple solution algorithms to solve any convergence issues. In particular, the modified Newton-Raphson approach, which computes the tangent stiffness matrix at the beginning of each load step, and the Krylov-Newton algorithm, which uses a Krylov subspace accelerator to accelerate the convergence of the modified Newton method, were adopted in these analyses. For more information on the solution algorithms see Gil et al. (2007) and Scott and Fenves (2010).



(a) Test setup (typical)

(b) Displacement protocol

Figure 5.6: Test setup and displacement protocol. Additional details in in Chapters 2 and 3

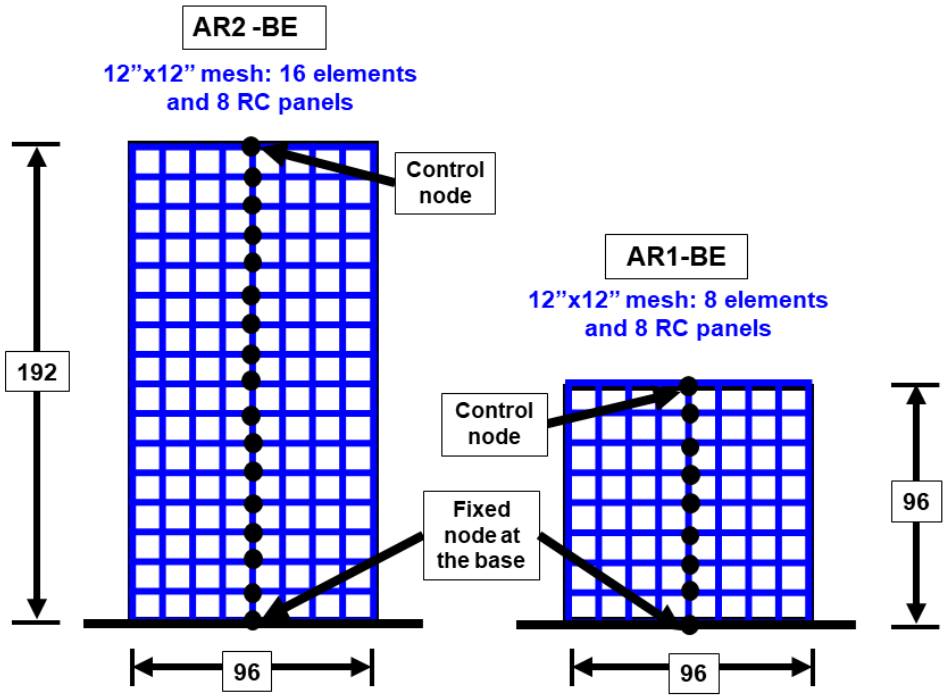


Figure 5.7: Schematic representation of the dense meshes of walls AR2-8-BE and AR1-BE (typical). Note these are SL7.5 and SQ7.5 and SQ0 walls described in Chapters 2 and 3. Units in inches [1 in =25.4 mm; 1 kip =4.45 kN]

5.4 Analysis of the Results

The numerical predictions are herein compared to the test results in terms of lateral load versus lateral displacement at the top, shear and flexure contributions to total displacement and concrete crack pattern at the end of the test. In addition, maximum crack widths were estimated within each RC panel element and compared with the crack widths measured during the test. Such comparisons are referred to as global and local response, respectively.

5.4.1 Global Response

The models replicated the experimental load-displacement curves of the three full-scale walls with a reasonable level of accuracy, see Fig. 5.8. It is noted that two numerical models with different geometric discretization were considered to evaluate the effect of the mesh on the results. It is observed that using a larger number of finite elements does not alter the global response prediction of the walls. Both numerical models, with dense and sparse meshes, predicted the wall strength within the average $\pm 10\%$ range of the experimentally measured capacities. It is concluded that finite elements measuring about $\frac{L_w}{8}$ are sufficient to get an accurate prediction of the hysteresis curve. In general, model response predictions agree with test results in terms of lateral load capacity and lateral stiffness of the tested walls. However, the drift value associated to wall collapse is hardly predicted by the numerical models, for the poor degradation modeling capability.

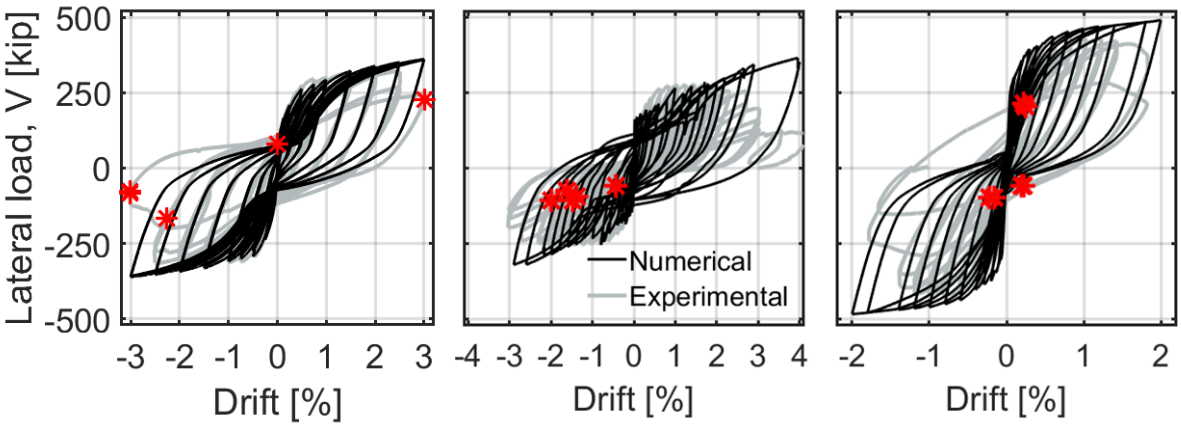


Figure 5.8: Numerical and experimental lateral load vs. drift ratio. Asterisks show estimated instances of fracture of the longitudinal reinforcing bars during wall tests. Left: wall AR2-8-BE, center: wall AR1-0-BE and right: wall AR1-8-BE. Note x-axis varies for clarity

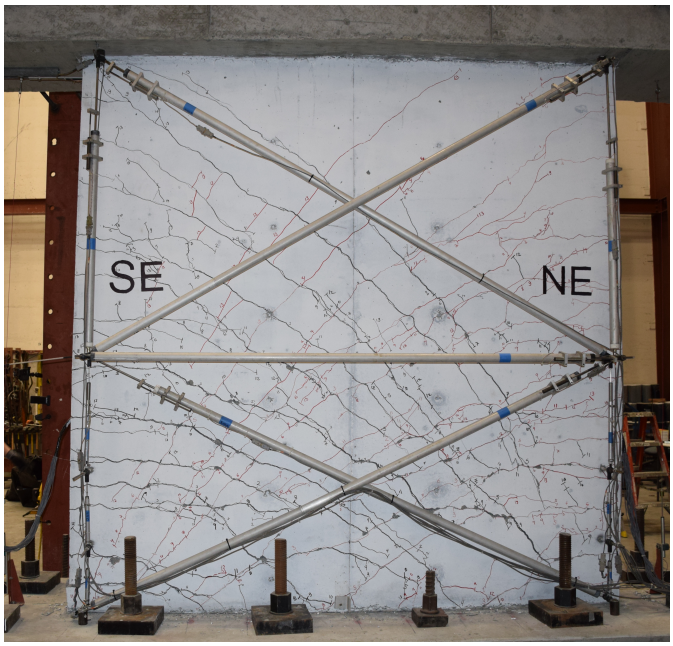


Figure 5.9: Crack pattern at 2% drift ratio in wall AR1-0-BE

The least robust numerical prediction amongst the three test walls modeled is observed for the squat wall tested absent axial load in the post-experimental strength for the reasons provided above. The strength of the wall tested in the absence of axial load, wall AR1-0-BE, is underestimated by the numerical model in the region after yielding and before the attainment of strength. Predicted wall strength is within the $\pm$12% range of the experimentally measured capacities in these regions, but the few cycles at strength level are captured with good agreement by the numerical model. Hence the experimental strength would be well predicted if the numerical model offered nominal degradation. Degradation of the experimental response is observed between 2 and 2.2% drift ratio strength due to buckling and associated out of plane deformation of the reinforcement and damage accumulation. The experiential hysteresis curve therefore shows progressive strength reduction, as opposed to the numerically predicted curve, which gains additional strength. A significant overprediction of about 200% of the lateral capacity at 4% drift ratio is observed during the final monotonic push of the full-scale wall. The deviation of the numerically predicted hysteresis in comparison with the experimental curve of wall AR1-0-BE is observed to occur at about 2% drift ratio, when the damage spread across the entire wall and concrete spalling was evident, as well as large crack widths at the wall toes, as in Figs. 5.9 and 5.10. These conditions indicate initiation of reinforcing bars debonding in the wall toes and highlight the limitations

of the numerical model. It is noted that the asymmetry of the hysteresis in Fig. 5.8 is due to the monotonic push to 4%.



Figure 5.10: Detail of the damage in the toe of wall AR1-0-BE at 2% drift ratio



(a) (b)

Figure 5.11: Detail of the damage in the toes of wall AR2-8-BE at 2% drift ratio: (a) North toe on the push side and (b) South toe on the pull side

Similar to the wall tested absent axial load, the other two models overpredicted the lateral load capacity of the axially loaded test walls after attainment of the experimental strength, for the limitation of the model in simulating reinforcement buckling and rupture. Failure of the tested walls was anticipated instead by local buckling and rupture of the reinforcement, as in Figs. 5.11 and 5.12. These figures show the typical damage of wall toes after reinforcement buckling and concrete spalling observed in the slender and squat wall tests with applied axial load, respectively. Estimated instances of rupture of select longitudinal boundary bars are also indicated by the red marks in Fig. 5.8 for comparison. Indeed, the model utilized in this study can only capture wall failure modes associated with concrete stress-strain behavior and is incapable of capturing lateral instability due to the severe limit state of

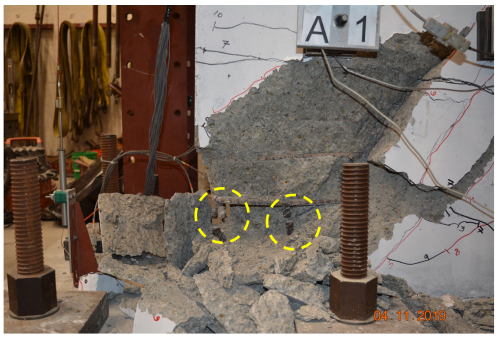


Figure 5.12: Detail of the toe on the push side of wall AR1-8-BE at 1.2% drift ratio. Circles highlight the ruptured longitudinal reinforcing bars

bar buckling. The model provides reasonable load versus displacement response predictions as long as buckling and lateral instability do not occur. These figures indicate that the most appreciable divergence between the numerical and experimental results occurred upon rupture of the longitudinal reinforcement, when the lateral strength of the walls drops drastically. The global response of the walls is predicted with a high level of accuracy prior to significant development of inelastic response and failure of the reinforcing bars. It is also observed that other important cyclic response characteristics, such as the plastic residual displacements upon unloading to zero load and the pinching behavior of the hysteresis curves are estimated with sufficient accuracy up to experimental strength for each of the three considered wall models, see Fig. 5.8.

Fig. 5.13 shows the cumulative dissipated energy versus the cumulative top displacement for the three tested walls. The energy dissipated is calculated as the area under the hysteresis curves, to evaluate the capability of the model in capturing the salient hysteresis and dissipated energy. Good agreement of the numerical and experimental results is observed for the two axially loaded walls, thus suggesting the model robustly captured the relevant hysteresis of the wall prior to failure. However, the hysteresis loops predicted by the numerical model of the low-aspect ratio wall tested absent axial load are larger and wider with respect to the experimental results, as shown in the hysteresis in Fig. 5.8. An approximately 60% over-prediction of the numerical cumulative dissipated energy with respect to that of the experiment for the low-aspect ratio wall tested without axial load, is observed.

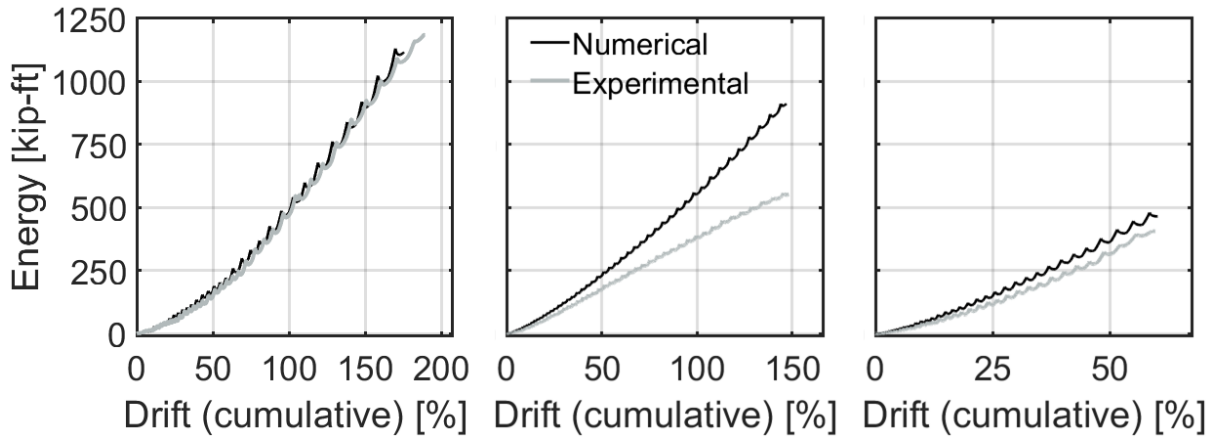


Figure 5.13: Cumulative hysteretic energy vs. absolute value of cumulative drift [%]. Left: wall AR2-8-BE, center: wall AR1-0-BE and right: wall AR1-8-BE. Note: x-axis range varies for clarity

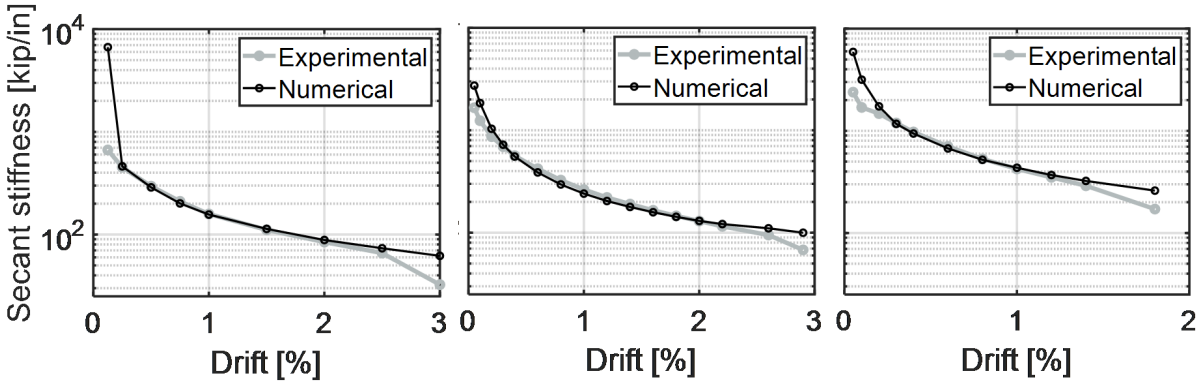


Figure 5.14: Secant stiffness degradation (log scale) vs drift imposed at the top. Left: wall AR2-8-BE, center: wall AR1-0-BE and right: wall AR1-8-BE. Note: x-axis range varies for clarity

Fig. 5.14 shows the secant stiffness degradation (in logarithmic scale) versus the imposed drift.

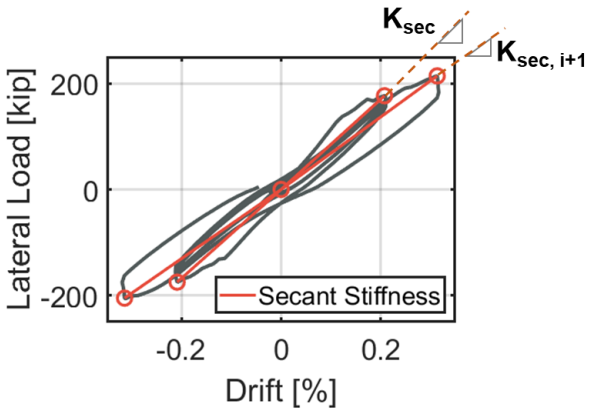


Figure 5.15: Example calculation of secant stiffness

The secant stiffness values are calculated as the slope of the line going through each peak load value per drift amplitude, as represented in Fig. 5.15. Positive and negative peaks are considered individually, and the values represented in Fig. 5.14 are the average of positive and negative slopes. The predicted secant stiffness is remarkably larger than the experimental one at the first and last applied drift amplitudes. This observation reflects the large initial stiffness of the models and the unsuccessful failure prediction.

Cyclic Degradation

The displacement protocol applied to the test walls involved at least two cycles at each drift amplitude to elicit cyclic degradation effects, see Fig. 5.6 and Chapters 2 and 3 for additional details. To investigate the effect of the application of multiple cycles at the same drift amplitude, numerical models considering one and two cycles per drift amplitude are compared in Fig. 5.16. The numerical models of the three tested walls show that the effect of repeated cycles does not affect the predicted lateral load- drift ratio curves presented in Fig. 5.16. In addition, no significant differences were observed in the damage distribution and crack width estimation. The inaccuracy of the model in capturing the rate of degradation in the lateral load is probably attributed to the fact that reinforcement bar-concrete debonding and local bar buckling behavior is not considered in the present model formulation.

It can be therefore concluded that the cyclic degradation predicted by the model is negligible. In light of this consideration, the displacement protocol adopted in the parametric study prescribes only one cycle per drift amplitude to the considered numerical models for sake of time and computational efficiency.

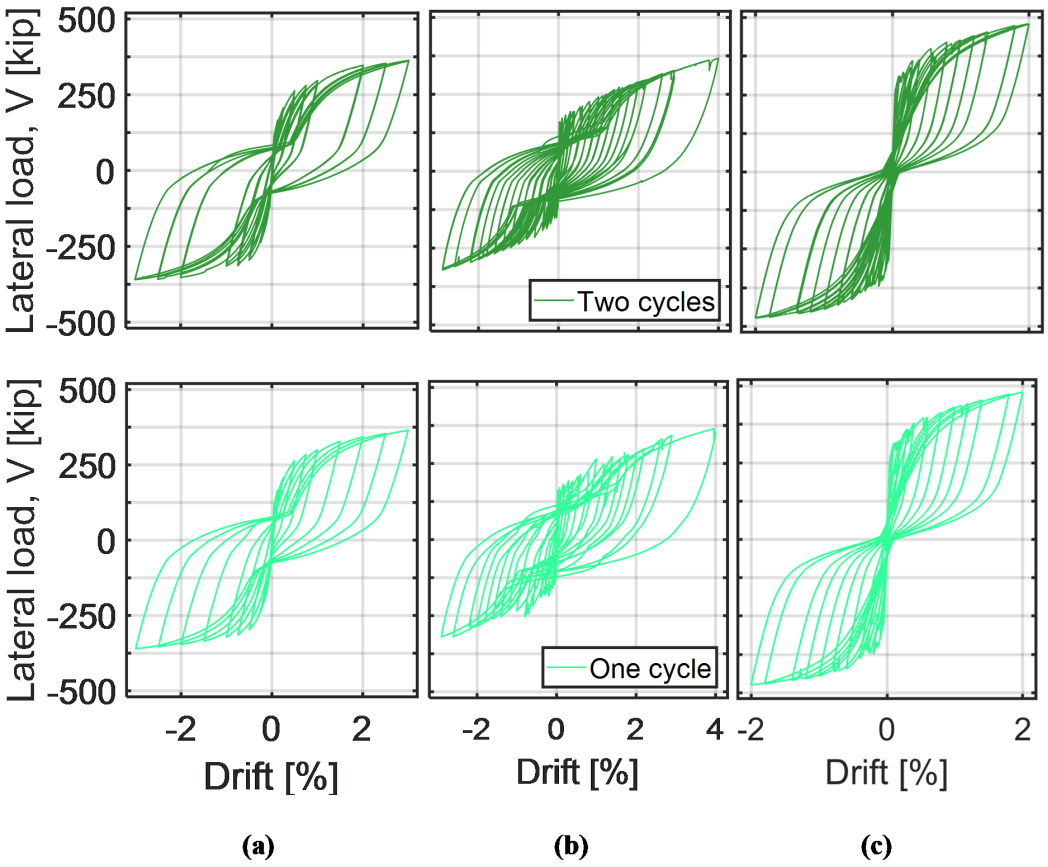


Figure 5.16: Comparison of numerical hysteresis curves when one or two cycles are applied at the same drift amplitude. (a) AR2-8-BE, (b) AR1-0-BE and (c) AR1-8-BE. Note x-axis varies for clarity

5.4.2 Local Response

Local response is evaluated in this section by analyzing the contribution to total displacement due to shear and flexural components. In addition, the damage of walls is inferred by strain and crack profiles and discussed in this section.

Deformation Contributions

One of the main features of the model is the ability to predict the amount of shear contribution to total displacement. The bar charts in Fig. 5.17 compare the predicted (bars) and measured (dots) shear and flexural contributions to the total displacement applied to the wall top. This analysis indicates that:

- Before significant nonlinearity is observed in the test wall, at about 0.5% drift, predictions agree with the slender wall tests results. After yielding, the measured shear contribution slowly ramps up to 25% at 3% drift in the pull direction. Conversely, the numerical shear contribution upholds stable at approximately 10% of the total displacement at top (Fig. 5.17). Therefore, the model slightly underestimates the shear displacements, in agreement with the results presented in Gullu and Orakcal (2019). However, it is noted that the shear displacement contribution is small in magnitude for this slender wall and the underestimation is considered acceptable because small. It is indeed remarkable that the model is able to capture the nonlinear shear-flexure interaction behavior in walls with predominant flexure behavior.

- The main assumptions behind the formulation of the considered numerical model are expected to be not satisfied for large drifts experienced by walls with aspect ratio AR $\leq$ 1 as undeformed plane wall sections will probably show out of plane deformation with increasing shear participation to lateral loads response. Also, shear strains will probably be unevenly distributed along the wall section, due to the formation of strut-and-tie loading mechanisms. The two full-scale walls considered in this study are therefore interesting samples of the lower range of applicability of the numerical FE model. Results in terms of local response overall confirm the considerations already presented in the global analysis of the wall hysteresis curves. In particular, it is noted that in the axially loaded wall AR1-8-BE the shear component to top displacement measured during the test is well predicted by the model, since the model is successful in capturing the influence of the axial

load on the response characteristics of shear-controlled walls. Conversely, absence of axial compression load has some effects on the experimentally observed response of wall AR1-0-BE, not well-estimated by the numerical model. The measured shear contribution to the total displacement at the top increases with larger drift demands, as opposed to an approximately constant numerical prediction. Analysis of the test results shows, indeed, that the severity of the damage on wall AR1-0-BE increased with larger drift demand, forming a dense network of large cracks, complemented by severe concrete crushing at cracks interface. The increasing severity of the damage affects the distribution of stresses and, therefore, the amount of shear component to the total displacement, which is estimated to increase up to 75% of the top displacement at 2.9% drift.

- Consistently for all the three experimental investigated walls, the numerical models predicted an overall constant component of shear displacement, even at large drifts. This behavior is observed to be acceptable for flexural dominated walls but is not realistic in the case of walls with significant concrete degradation, for which the shear component may overcome the flexural counterpart at large drift amplitudes. The shear displacement in the full-scale walls is indeed measured to increase with the drift demand on the walls, as crack widths enlarge and concrete deteriorates.

- Even if the previous observation underlines the poor degradation features and failure predicted by the SFI-MVLEM, it is significantly noted that the average predicted shear contribution to total displacement is well captured for the AR=1 full-scale shear walls, despite all the implications presented by low-aspect ratio walls with regards to the applicability of the numerical model. The model is apparently successful in capturing the influence of the axial load on the response characteristics of shear-controlled walls. Also, acceptable average results ($\Delta_s \approx 10\%$) are predicted for the slender AR=2 wall, for which the shear contribution to total displacement at top is not predominant, consistently with measured values.

Damage Prediction

The SFI-MVLEM model predicts the angles of inclination of the main concrete struts and the angles of the cracks opening when the concrete tensile strength is reached. Two orthogonal cracks per finite element are considered in the model formulation to preserve their orientation as the applied cyclic

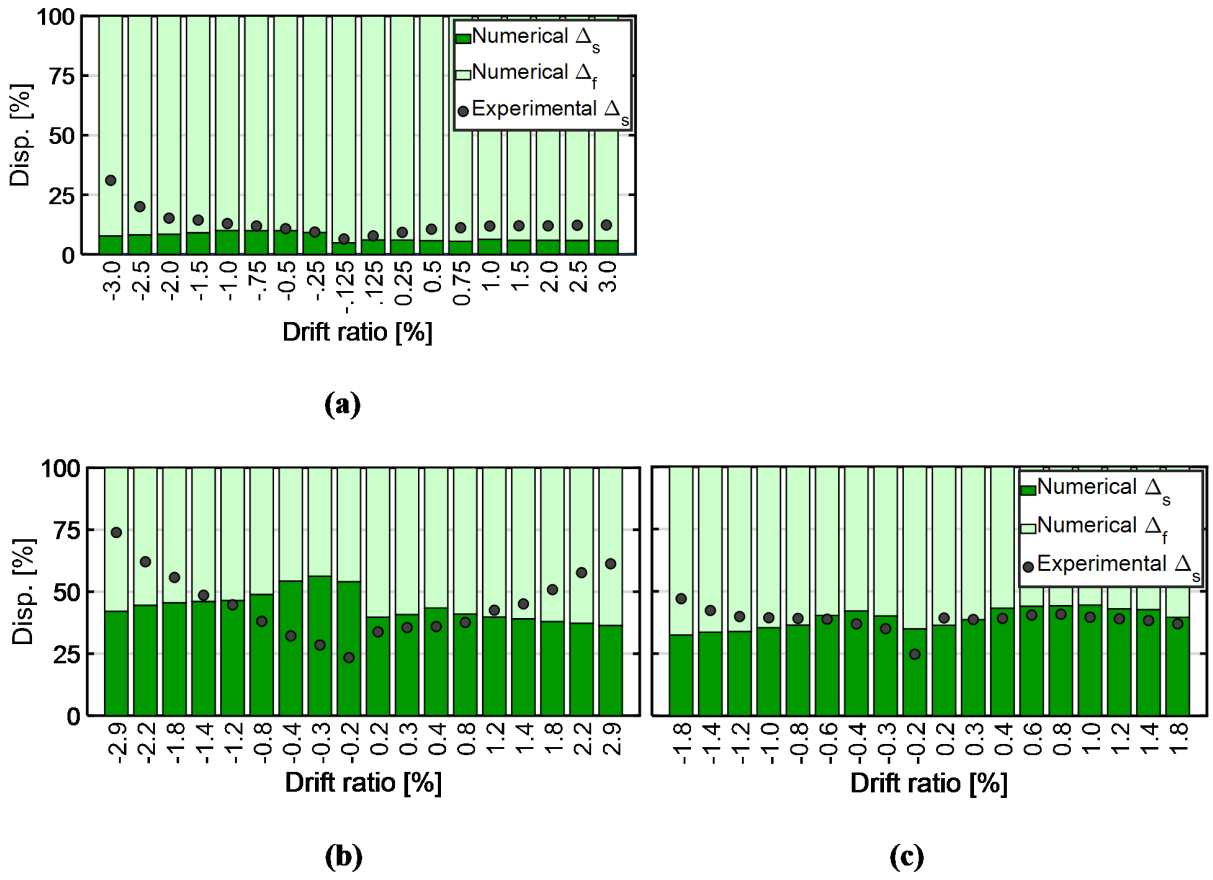


Figure 5.17: Shear and flexural components to top lateral displacement predicted by the FEMs and measured during the tests. (a) AR2-8-BE, (b) AR1-0-BE and (c) AR1-8-BE

displacement at top of the wall ramps up in amplitude and the wall damage evolves Kolozvari et al. (2015). In this study, the steel strain output data are considered to estimate the maximum average crack width in each finite element, according to a smeared crack approach Hutchinson and Wang (2009). The crack forming in each finite element was considered to be a segment passing through the center of the panel, with orientation perpendicular to the first principal strut direction. To estimate the maximum average crack width per each finite element of the model, an equivalent element with the same area is idealized. The sides of this equivalent element are defined by the crack segment (*side one* in Fig. 5.18) and by the perpendicular segment, also parallel to the first principal strut direction (*side two* in Fig. 5.18). The maximum average crack width per finite element is calculated as the product between *side two* of the equivalent element and the maximum principal strain registered by the numerical model for the finite element under consideration.

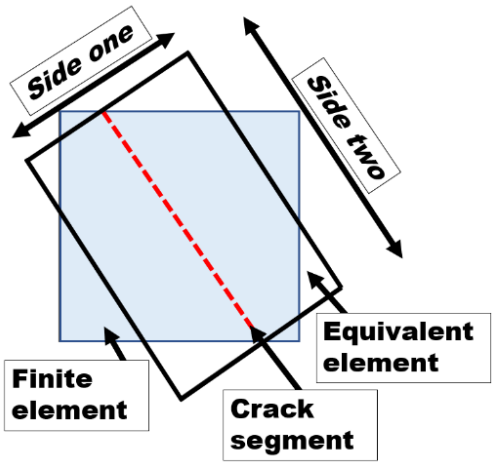


Figure 5.18: Representation of an equivalent element

Mesh Size Effects on Crack Pattern

The three tested walls are modeled with 12x12 inches and 6x6 inches element size meshes to evaluate the effect of the mesh on the crack pattern prediction. Crack angles are combined with the maximum smeared crack width estimations into sketches of the damage and cracks distribution. Results show limited influence on the crack distribution at different mesh sizes. For both the numerical models, the crack pattern does not vary significantly with the mesh size. The crack angle orientation is consistent in the two considered numerical models, as it is presented in Figs. 5.19 - 5.21.

The estimated crack width values are anticipated to be sensitive to the size of the finite element, i.e., the panel, on which the average stress and strain are calculated. This is also observed in Fig. 5.25, where different colors are used to group the predicted crack width values in different bins. The small element size mesh gives a refined strain distribution and therefore a refined identification of the low, medium and high intensity cracked damage regions. Since this study focuses on concrete damage and crack characteristics, such as orientation and width, the 6x6 inches element mesh is considered in the following parametric study, as this element size is deemed sufficient to represent the experimental characteristics of the crack pattern. As a result, the slender full-scale wall is numerically discretized into 32 vertical elements, each of which includes 16 panels, for a total of 512 6x6 inches elements about 1/32 and 1/16 of the wall height and length, respectively. The two full-scale squat walls are numerically represented by 16 vertical elements, each of which includes 16 panels, for a total of 256 6x6 inches elements about 1/16

of both the wall height and length. This element size is deemed capable to provide sufficiently detailed estimations of the crack pattern at each drift amplitude.

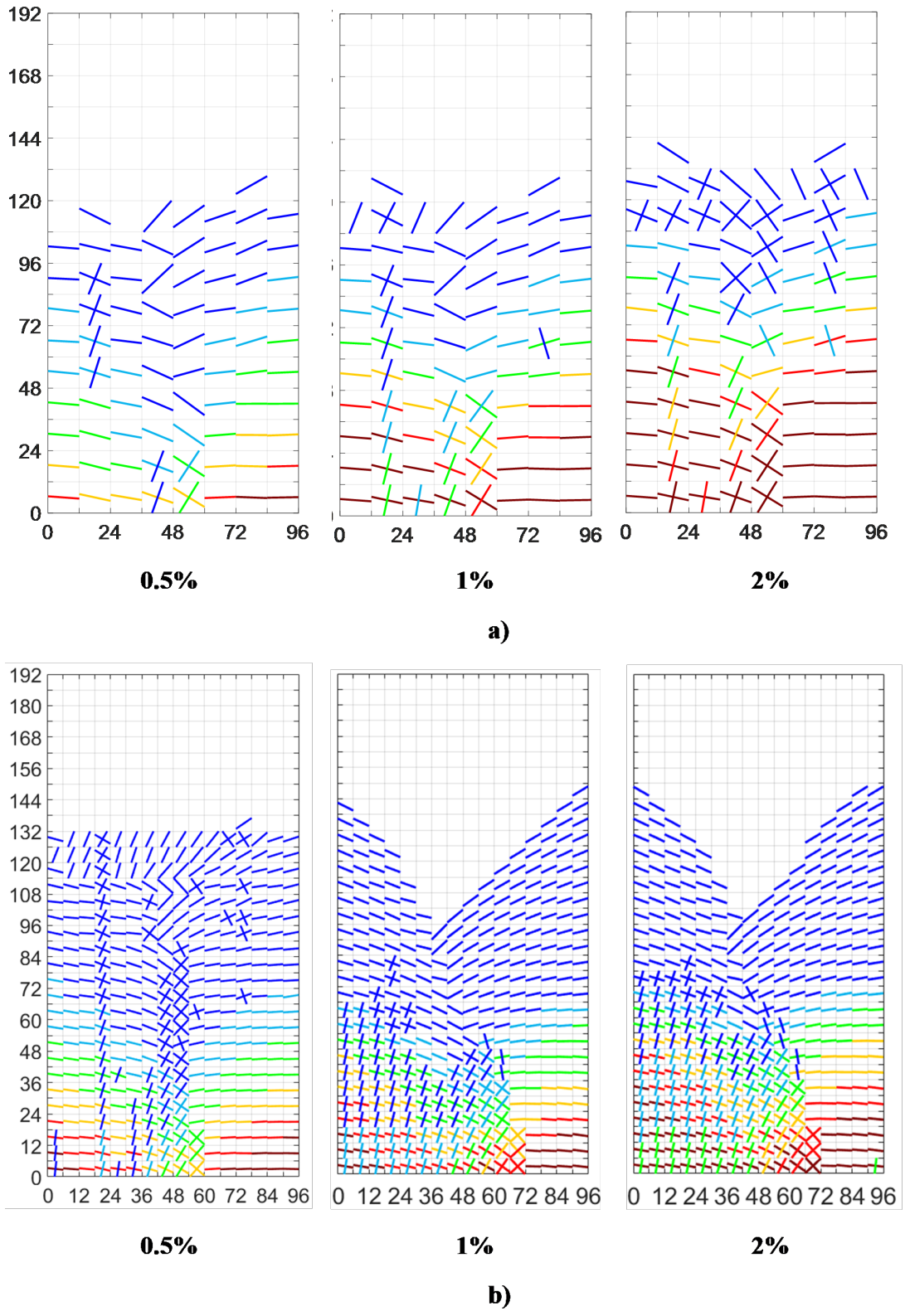


Figure 5.19: Effect of mesh size on crack pattern for the slender wall model AR2-8-BE at key performance drift ratios. a) 12 x 12 inches and b) 6 x 6 inches mesh. Wall dimensions in inches

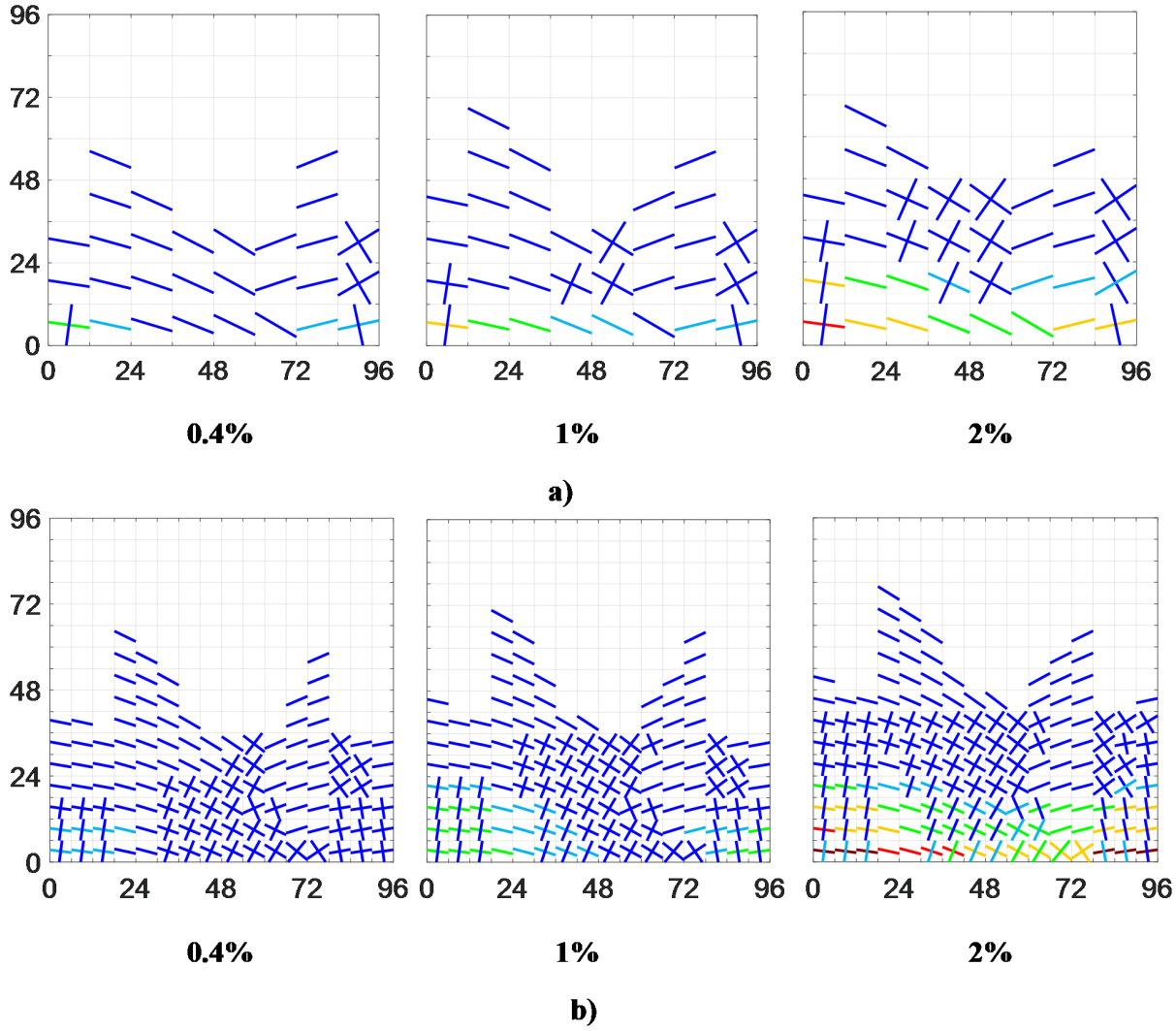


Figure 5.20: Effect of mesh size on crack pattern for the squat wall model without applied axial load AR1-0-BE at key performance drift ratios. a) 12 x 12 inches and b) 6 x 6 inches mesh. Wall dimensions in inches

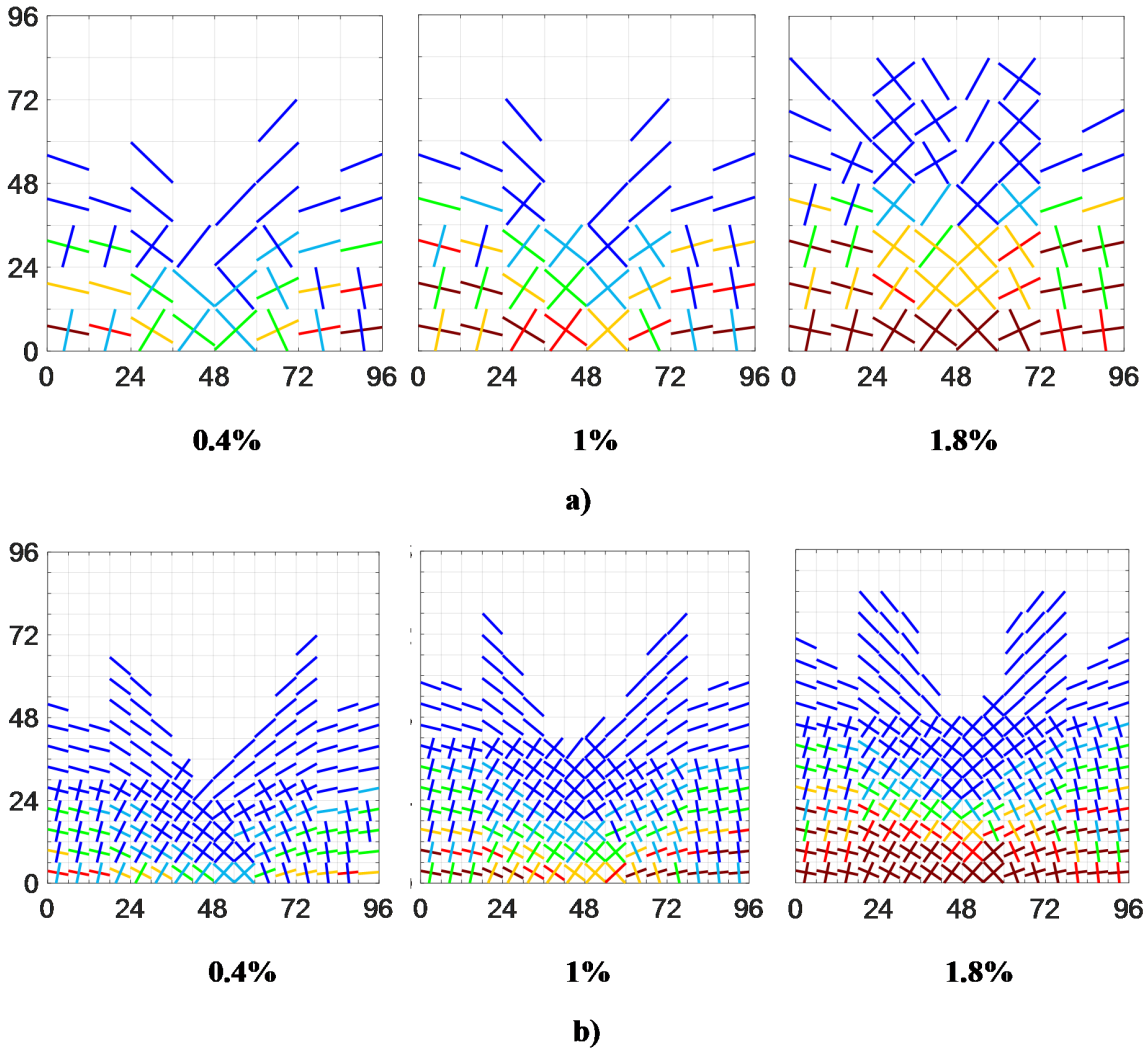


Figure 5.21: Effect of mesh size on crack pattern for the squat wall model with applied axial load AR1-8-BE at key performance drift ratios. a) 12 x 12 inches and b) 6 x 6 inches mesh. Wall dimensions in inches

Crack Pattern at Key Performance Limit States

Previous studies using the SFI-MVLEM formulation to model various RC walls in the literature indicate that vertical elements as large as one fifth of the wall height are sufficient to reasonably capture the global response of concrete shear walls (Faraone and Hutchinson 2018). Smaller elements are necessary, however, for a more precise prediction of the crack pattern. Several FEMs of the specimen were developed and analyzed to investigate various mesh sizes and constitutive material models. Upon analyses of all models, the 6x6 inches element size was selected. Reinforcement steel element strains are used to estimate maximum crack width within each panel. Crack angles are combined with the maximum smeared crack width estimations into sketches of the damage and cracks distribution, reproduced after photographs taken during the tests of the three full-scale walls. In particular, the drift values of 0.5%, 1.0% and 2.0% associated with the IO, LS and CP performance limits suggested by ASCE 356 (2000) are considered herein as checkpoints to evaluate the damage evolution in the walls. It is noted, however, that the 0.4%, 1% and 2% drift ratios, which are the test drift amplitudes closest to drift values at the target performance limit states, are utilized for the two squat wall models. In addition, test wall AR1-8-BE failed before reaching the 2% drift ratio, hence the crack pattern at 1.8% is shown in the following Figures.

Digital sketches of the crack pattern of the walls were created using high resolution photographs obtained whereby crack patterns were manually tracked during the tests and compared to the crack pattern predicted by two numerical models, which included the *Concrete02* and the *ConcreteCM* material models, respectively. Figs. 5.22 - 5.24 compare the crack pattern observed in the slender wall test to the AR2-8-BE wall models prediction, and the crack patterns obtained in the squat wall tests to the AR1-0-BE and AR1-8-BE wall models predictions, respectively. Estimated and measured crack widths are color coded according to the bin subdivision represented in each Figure. In particular, crack width binning was performed considering the crack width values deemed critical for anchor performance, as related to the anchor classification (seismic performance category according to EOTA TR 045 2013) and performance limit state of the wall, as reported in Table 5.2. These values are also supported in the literature presented in Chapter 1. Notably, anchor qualification testing (EOTA TR 045 2013) requires that concrete anchors remain in service (i.e., carry their service load) while embedded in a crack of width w = 0.5 mm and previous studies, e.g., Eligehausen and Hoehler (2003), Mahrenholtz et al. (2016) and

Mahrenholtz et al. (2017), showed that w = 0.8 mm may be assumed as the crack width limit representing extreme conditions on the anchors.

Table 5.2: Crack width ranges related to shear wall and anchor performance

Performance Limit State	Anchor class	Crack Width Range
IO	**C1**	0 to 0.3 mm
	C2	0.3 to 0.5 mm
LS	**C1**	0.3 to 0.8 mm
	C2	0.5 to 1.2 mm
CP	**C1**	0.8 to 1.2 mm
	C2	1.2 to 1.8 mm

The main observations noted by considering Figs. 5.22 -5.24 are as follows:

- Qualitatively, the orientation and vertical extension of the numerical and experimental damage patterns do not differ significantly for all the considered drift ratios and wall models. Comparing the predictions with the measured results shown in Figs. 5.22 -5.24 indicates that the crack pattern during each key drift cycle was quite reasonably predicted using the FE model.

- The estimated crack widths are in good agreement with the measured values during the tests. The width of several cracks was continuously measured by crack width sensors installed during the tests at discrete locations (see Chapters 2-3). In Figs. 5.22 - 5.24 the measured cracks at the drift demand under consideration are color coded according to the crack width bins in the legend, also used to represent the numerical crack width predictions. It is noted that the measured crack widths, as directly measured with high precision crack width sensors, nominally are in the same range as the average estimated crack widths from the numerical simulations. The numerical model combined with the smeared crack approach is hence a reasonable tool to predict the crack widths of shear walls of different aspect ratios.

- It is observed that the number of cracked elements may vary significantly with the concrete material model implemented in the numerical analysis. As opposed to the *Concrete02*, where linear behavior of the concrete in tension is defined by the linear Young Modulus, the *ConcreteCM* material model defines a nonlinear behavior of the concrete in tension, allowing the user to set the concrete strain at cracking ε_{cr}. The value ε_{cr} =0.00008 is suggested by Kolozvari et al. (2015) as

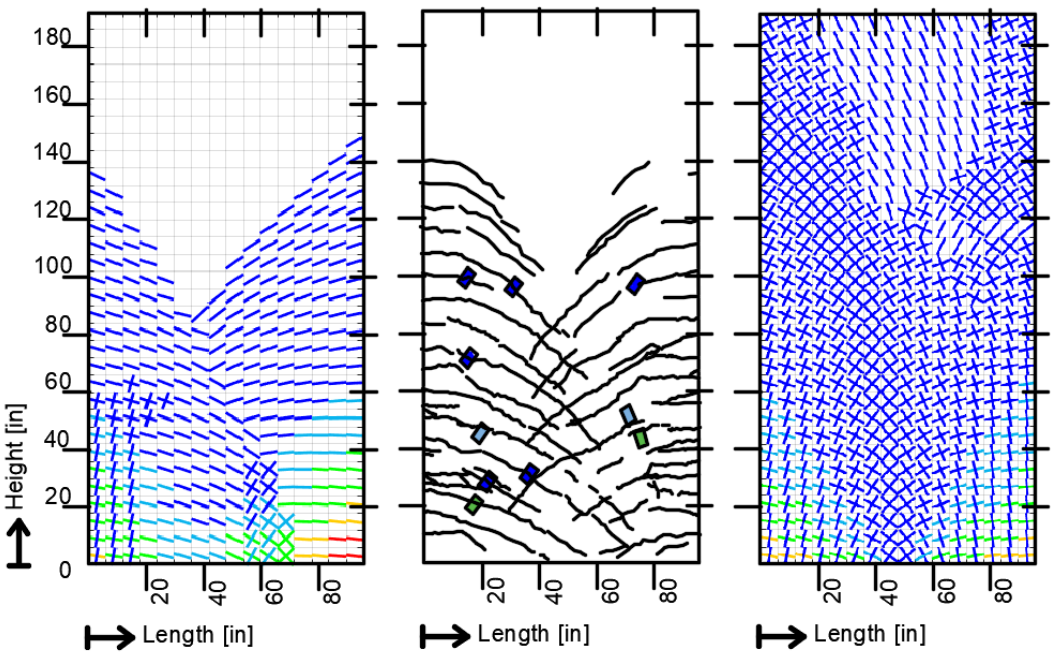
appropriate to represent evolving damage in concrete shear walls. Results presented in Fig. 5.22 to Fig. 5.24 show that for the slender shear wall more realistic crack pattern is predicted when the *Concrete02* material model is adopted in the analysis with respect to the other material model considered in this study. On the contrary, adopting the *ConcreteCM* material model yields to a better distributed crack pattern similar to the crack pattern observed in the squat wall tests.

For this reason, models implementing the advanced *ConcreteCM* material model are considered in the rest of this study. Fig. 5.25 offers a clean comparison of the numerical prediction with the experimental damage observed during the full-scale wall tests. Estimated and measured crack widths are color coded according to the bin subdivision represented in Fig. 5.25. It is noted that only cracks with estimated width w $>$ 0.1 mm are included in the numerical crack prediction sketch in Fig. 5.25. The following observations are made:

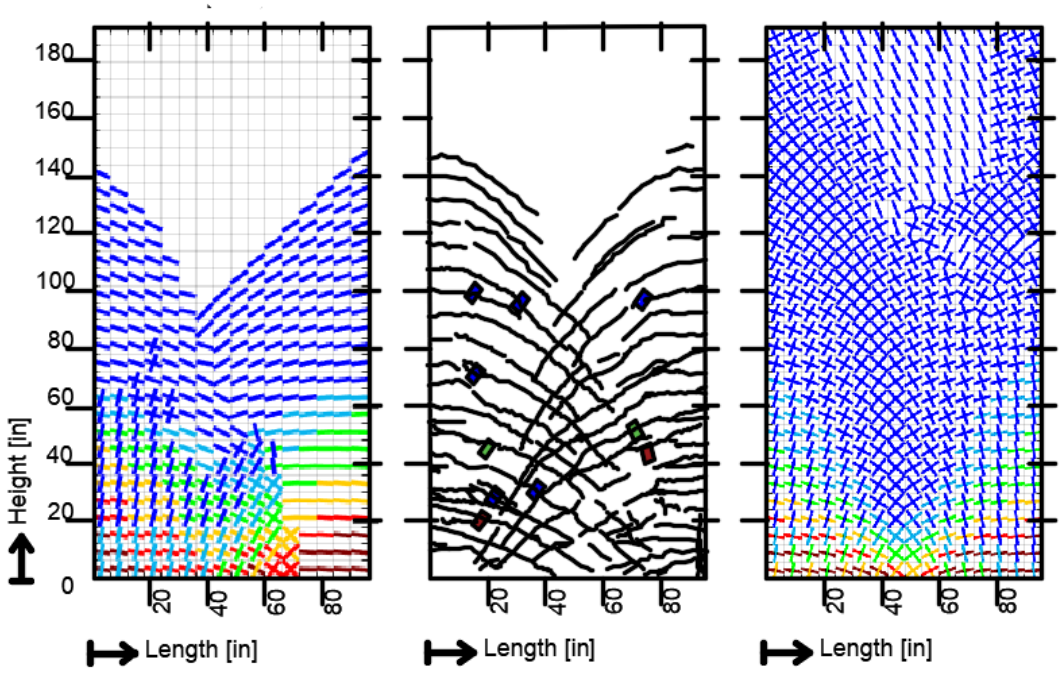
- It is observed that the cracks propagate from the boundary elements of the wall, where flexural strains are predominant, to the web of the wall, where shear strain become larger. This mechanism of stress distribution, also observed during wall testing, is well represented by the numerical model.

- The predicted crack angles provide reasonable estimations of crack orientations observed during the tests. Particularly, it is noted the change in slope of the cracks, which start as tension cracks (horizontal cracks) close to the wall, i.e., within the boundary elements where flexural strains predominate, and progressively propagate with a steeper angle toward the web of the wall, where the crack angle is close to 45 degrees (shear cracks). This trend suggests a continuous propagation of the cracks in the wall as the drift demand is applied. However, it is significantly noted that cracks in the model are inherently discontinuous and crack directions in each finite element differ. Therefore, the resulting crack pattern predicted by the numerical model should be carefully interpreted by visual extrapolation. Nonetheless, the model is an excellent predictor of crack orientation for shear walls of different aspect ratios.

- Regions of the full-scale walls where concrete crushing was observed are also well captured by the numerical models. Crack widths as large as 10 mm at the wall toes were predicted where concrete spalling and crushing occurred during the last cycles of the wall tests, as in Fig. 5.25.

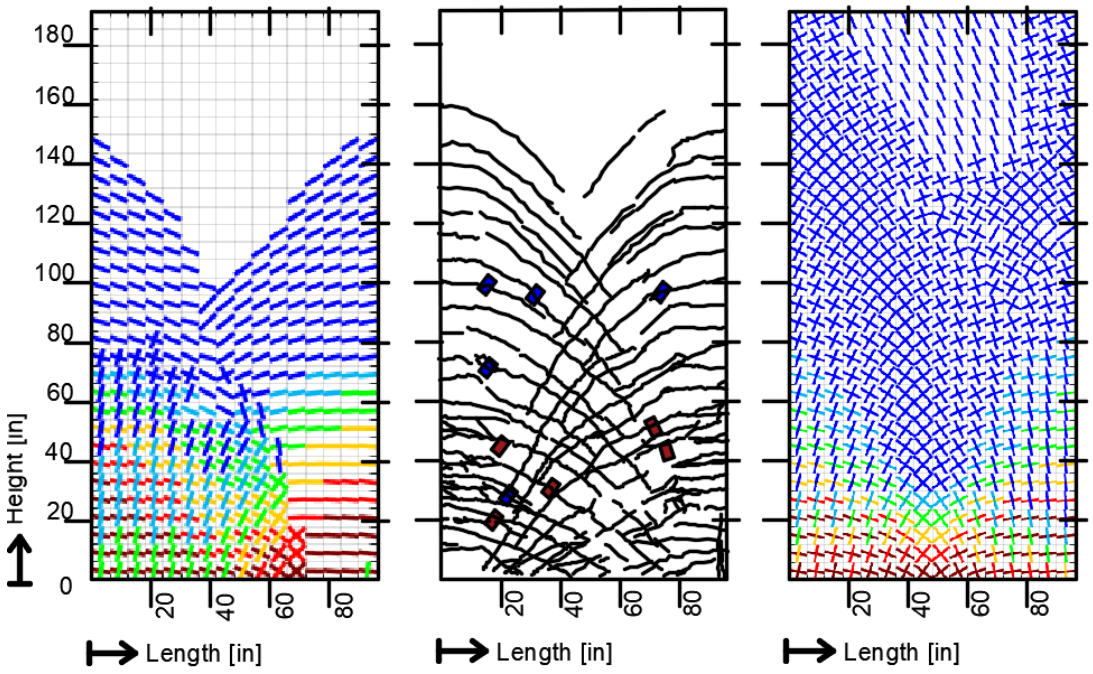


(a) 0.5% drift



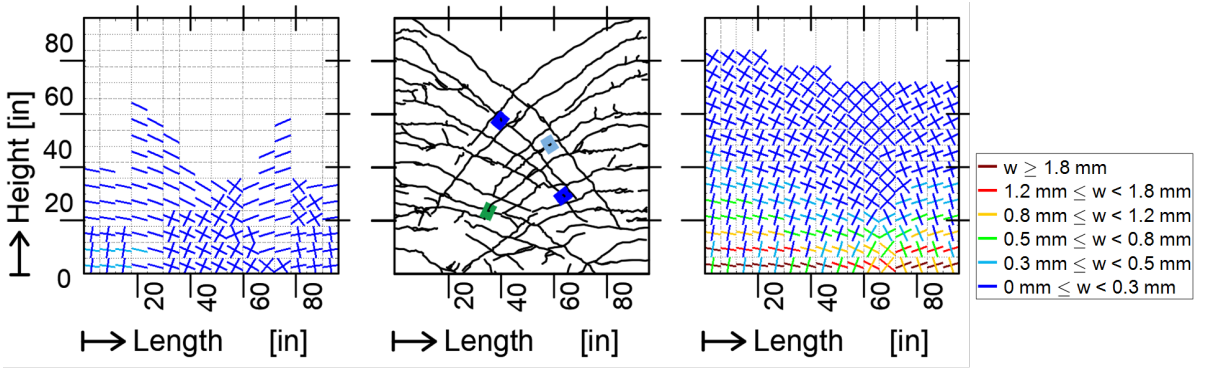
(b) 1% drift

Figure 5.22: Numerical crack pattern obtained using the *Concrete02* material model (left); experimental crack pattern (center); numerical crack pattern obtained using the *ConcreteCM* material model (right) for wall AR2-8-BE

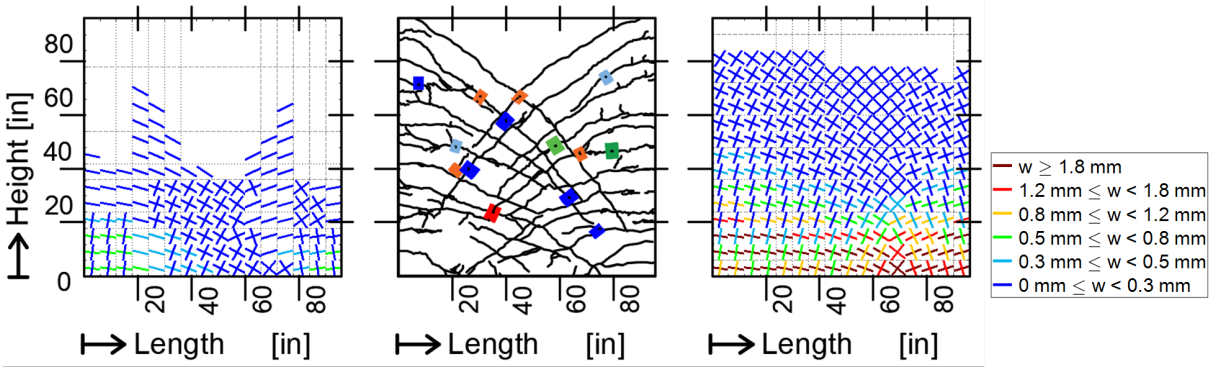


(c) 2% drift

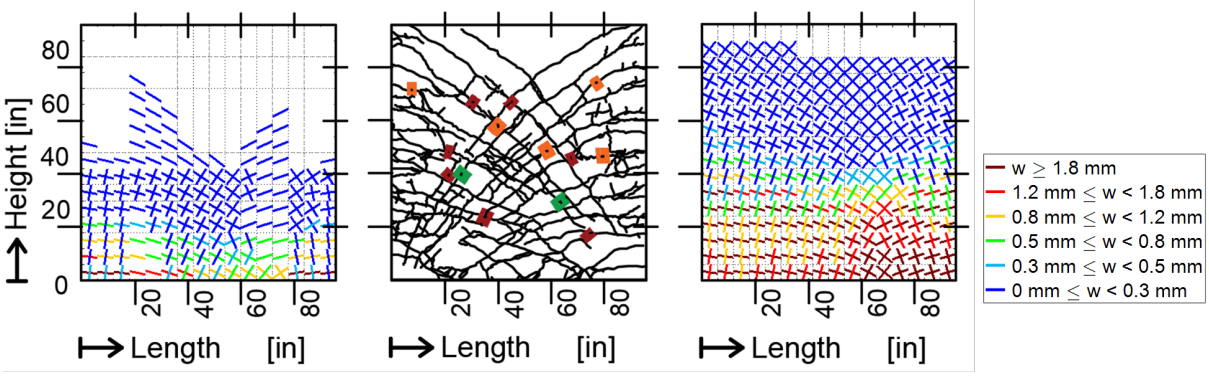
Figure 5.22: (Continued) Numerical crack pattern obtained using the *Concrete02* material model (left); experimental crack pattern (center); numerical crack pattern obtained using the *ConcreteCM* material model (right) for wall AR2-8-BE



(a) 0.4% drift



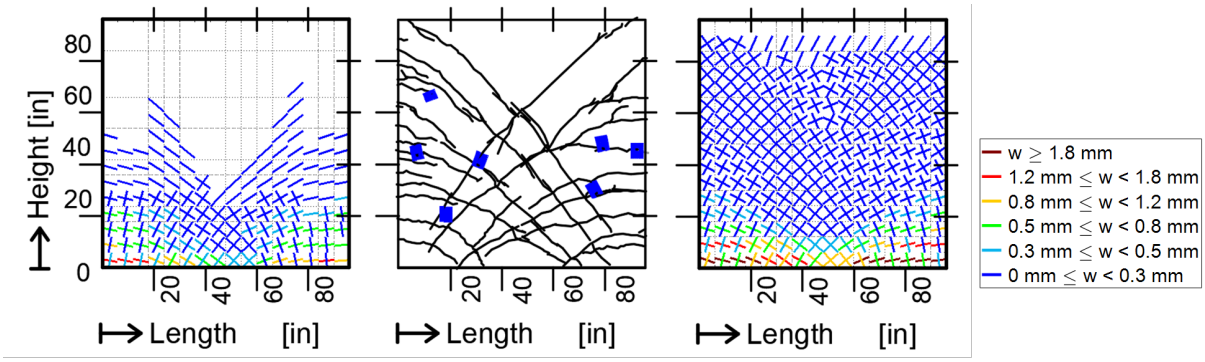
(b) 1% drift



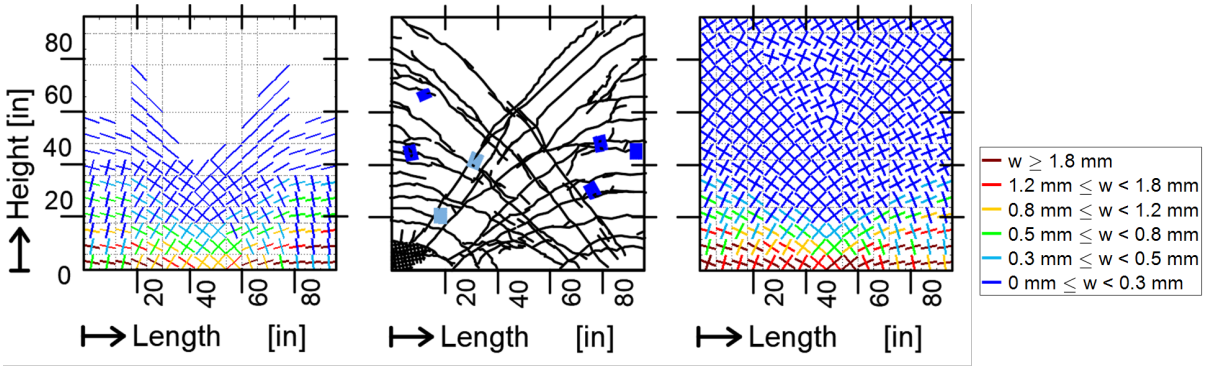
(c) 2% drift

Figure 5.23: Numerical crack pattern obtained using the *Concrete02* material model (left); experimental crack pattern (center); numerical crack pattern obtained using the *ConcreteCM* material model (right) for wall AR1-0-BE

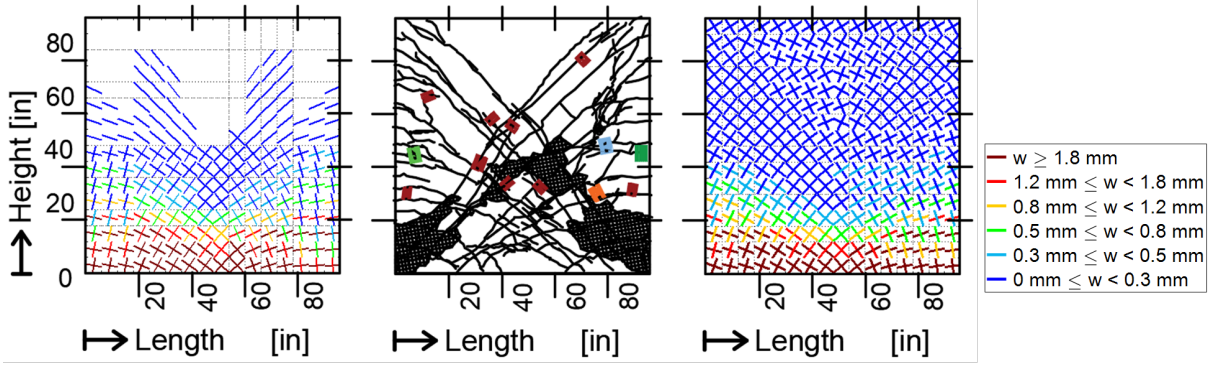
- Lastly, it has to be acknowledged that significant cracking is predicted in the low-aspect ratio walls in the elements at the top row, whereas no visible cracking was registered during the wall tests. This crack concentration can be explained considering not only the model limitations for low aspect ratio walls, but also the relatively small wall height of the models, which may limit redistribution of stress and invalidate the Saint Venant's principle at the base of the model formulation.



(a) 0.4% drift

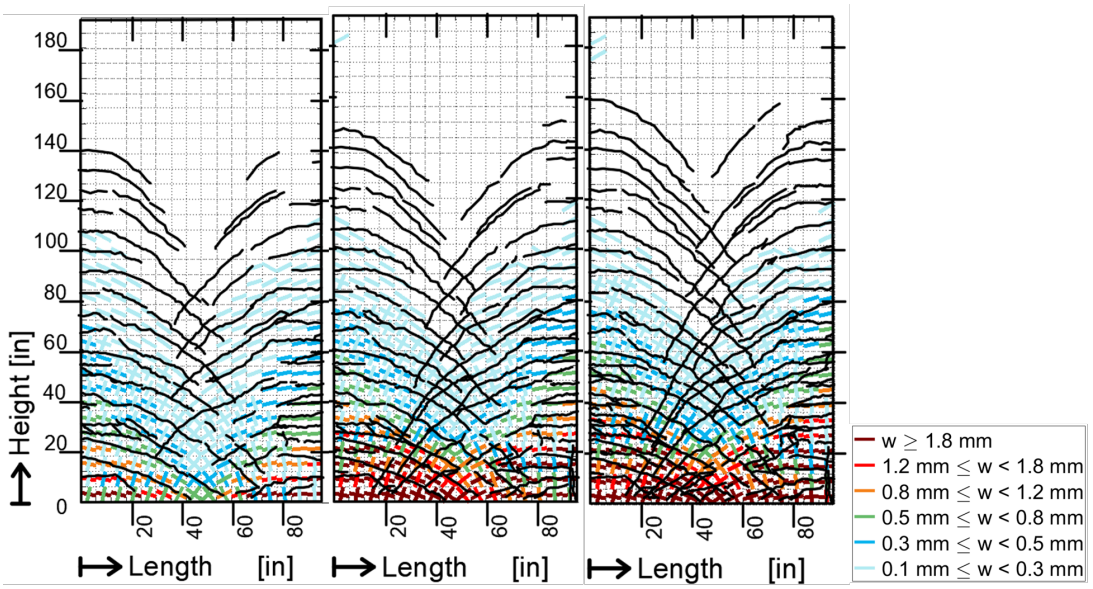


(b) 1% drift

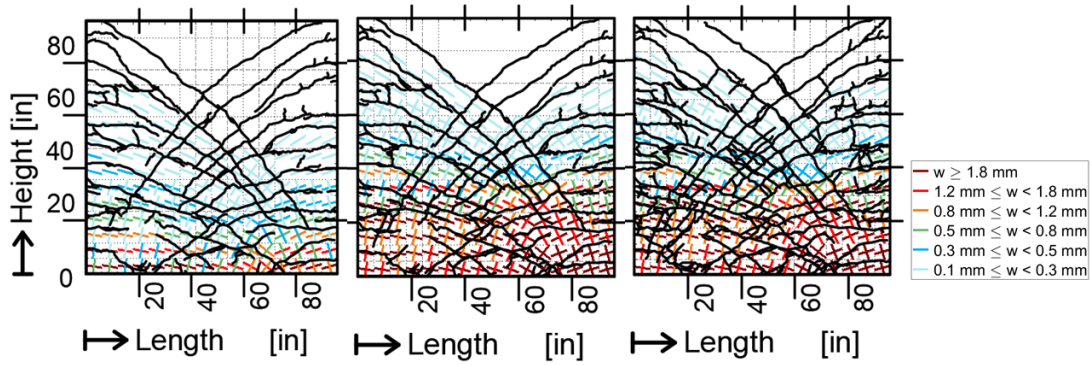


(c) 1.8% drift

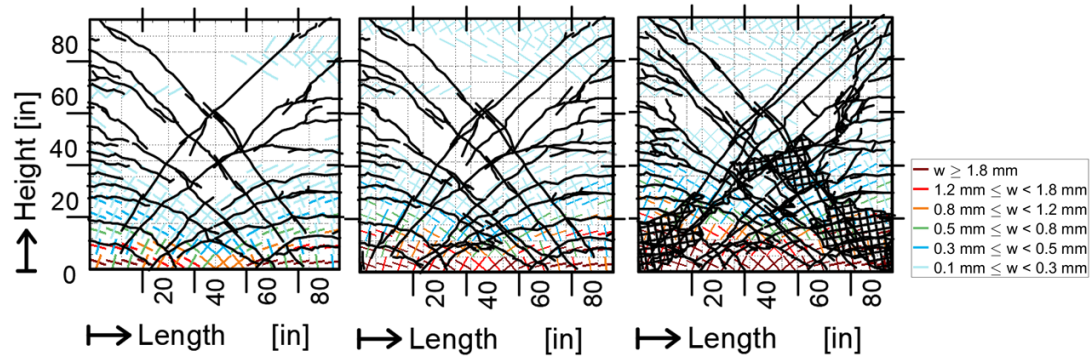
Figure 5.24: Numerical crack pattern obtained using the *Concrete02* material model (left); experimental crack pattern (center); numerical crack pattern obtained using the *ConcreteCM* material model (right) for wall AR1-8-BE



(a) AR2-8-BE



(b) AR1-0-BE



(c) AR1-8-BE

Figure 5.25: Comparison of numerical and experimental crack patterns at 0.5% (left), 1.0% (center) and 2.0% (right)

5.5 Summary Remarks

Results of the validation study presented in this Chapter show that the SFI-MVLEM model is able to reasonably predict the experimentally observed response of laterally cycled shear walls. Two numerical models, with different geometric discretization were considered to evaluate the effect of the mesh on the results. Both numerical models, with dense and sparse meshes, predicted the wall strength within the average $\pm 10\%$ range of the experimentally measured capacities. Global and local response of shear walls subjected to equivalent seismic loads are also captured with good confidence. In particular, the salient features of the measured load-displacement response characteristics of the three tested full-scale walls are estimated with accuracy, namely the lateral stiffness, lateral load capacity and pinching behavior. In contrast, drift and lateral load capacity and hysteretic degradation in lateral capacity after strength is reached are less reliable, as the model lacks the ability to replicate reinforcement bar-concrete debonding, local buckling and out of plane instability, each of which was observed at the end of the wall tests. Nonetheless, successful representation of the shear-flexure interaction behavior is observed for both the slender and squat walls designed to fail in flexure. The model accurately captures the average shear contribution to the total displacement measured throughout the tests. The damage characterization of walls subjected to equivalent lateral loads is also sufficiently well represented. The FEM estimates the angle of orientation of the cracks in each element, under the assumption that cracks remain orthogonal to the main concrete struts. The orientation of the cracks is in good agreement with the majority of the experimental cracks annotated during the test. In addition, crack width values were approximated by processing the numerical data according to the smeared crack approach. Predicted crack width values are nominally within the amplitude range of the discrete crack widths measured during the tests. It is noted that all predictions are accurate with some overall acceptable margin of error considering the relatively simple model formulation, which idealizes the mechanical behavior of concrete walls and offers an appreciable efficient analysis.

5.6 Acknowledgment of Publications

Chapter 5 contains material published in the following conference papers: Faraone, G., Moschetti L., and Hutchinson T. C., 2018, “Numerical Prediction of the In-Plane Cyclic Behavior

of Reinforced Concrete Shear Walls," Proceedings of the 11th National Conference on Earthquake Engineering, Los Angeles, CA and Faraone, G., and Hutchinson T. C., 2018, "Numerical Prediction of the Behavior of Reinforced Concrete Shear Walls under In-Plane Cyclic Loading, with Particular Focus on Assessing Local Cracking Response," Proceedings of the 2018 ASCE Structures Congress, Fort Worth, Texas. In addition, Chapter 5, in part is currently being prepared for submission for publication of the material: Faraone, G., Hutchinson, T. C., Piccinin, R., and Silva, J., "Numerical Prediction of the Response of Full-Scale Laterally Loaded Concrete Shear Walls." The dissertation author was the primary investigator and author of this material.

Chapter 6

Numerical Parametric Study

This chapter describes a parametric study performed using the SFI-MVLEM numerical model, validated in Chapter 5 against the full-scale shear wall tests specimens described in Chapters 2 and 3. To investigate the variation of damage in walls of different characteristics, this parametric study is conducted by extending the geometry and design properties beyond that of the validation walls in this dissertation. In addition to assessing the influence of typical geometric and design variables on the response of reinforced concrete shear walls subjected to simulated earthquake loads, this Chapter concludes by drawing general conclusions regarding the anticipated behavior of anchors in such wall models.

6.1 Introduction

After confidence in the model is gained through validation against full-scale experimental results in Chapter 5, the reinforcement layout, applied compression load and height of the wall models are systematically varied. Each parametrically different model is then subjected to the same seismic loading simulated history and the global and local response of each cross compared. This parametric numerical study intends to provide insight regarding the viability of anchorage attachment on a wide range of geometric and detailed RC shear walls. To offer this important link, the results of the crack pattern predictions are systematically compared.

6.2 Description of the Numerical Wall Models

Twenty-four walls are modeled with the SFI-MVLEM model described in Chapter 5. These wall models are designed by varying the applied axial load ratio, the confinement of the concrete in the boundary elements and the wall height, in an effort to systematically explore the effects of each, while also expanding beyond the experimental parameter range of the walls tested herein. The wall models are short named as listed in Table 6.1 to easily identify the aspect ratio (AR=1, 2, 4), the applied axial load ratio (ALR $=\frac{N}{f'_c A_g}=$ 0%, 4%, 8% and 15%) and the presence of confinement in the boundary elements (special, none). The applied axial load ratio is varied over the common design range, i.e., self-weight (zero) to about 20% of the section capacity (Birely 2012). With regards to the wall reinforcement detailing, the reinforcement ratios used in the full-scale wall specimens are also implemented in the wall models with boundary elements. Note that special boundary elements were designed in the full-scale wall specimens according to ACI 318 (2019). Special boundary elements have increased confinement capacity than ordinary boundary elements, thanks to reduced horizontal and vertical spacing of the hoop sets and cross ties. In terms of modeling, wall models with ordinary boundary elements do not give significantly different results than walls with special boundary elements, therefore ordinary wall models are not included in this study, as explained in the following section. The wall models without boundary elements are, instead, designed with the same amount of longitudinal reinforcement as the models with special boundary elements, but the reinforcing bars are considered to be uniformly distributed along the cross section, and no transverse reinforcement is provided at the wall ends, see Table 5.1. The same material properties of the full-scale walls are considered in the wall models developed for the parametric study, see Table 5.1. Additional information on material properties is reported in Appendix B.

Although a large design space potentially exists for shear wall components, a subset of cantilever walls with rectangular cross section and a fixed base condition were considered in this parametric study with the goal of extending the experimental dataset of the three full-scale walls. As reported in Chapters 2 and 3, the tested AR=2 and AR=1 full-scale shear walls are designed considering a simple two-story and a one-story prototype building, respectively, with an assumed floor height of 12 ft. The height of the test specimens was therefore reduced to 2/3 of the prototype height, assuming a triangular lateral seismic load distribution, as adopted in current design codes ASCE/SEI 7-16 (2016). Similarly, the AR=4

walls modeled within this parametric study may represent the test specimen of rectangular bearing walls of a four-story commercial building, with an assumed floor height of 12 ft and an assumed triangular lateral seismic load distribution. The walls length L_w = 8 ft is kept unchanged in the models considered in this parametric study, as for the full-scale wall specimens. Regarding the wall thickness, the same values of the full-scale walls are considered in this parametric study, namely: $t_w = 12in$ for the slender flexure-dominated walls and $t_w = 10in$ for the AR =1 wall models. These values reside, respectively, in the lower bound of the typical thickness of slender walls of modern mid-rise buildings presented in the inventory by Brown et al. (2006), and in the upper bound of the typical low-aspect ratio walls (Carrillo and Alcocer 2012). It is finally noted that in general AR=1 rectangular walls can commonly be found in low-rise buildings (1-2 story), such as a precast warehouse building, and walls with AR=2 and AR=4 may also be found in mid and high-rise, including four-story and twelve-story tall buildings, such as office and apartment buildings. Fig. 6.1 shows a sketch of the three different archetype buildings configurations adopted, namely involving bearing shear walls with AR=1, AR=2 and AR=4. While plan geometry of each is preserved, the design detailing required to sustain loads for the taller archetype models naturally would require special consideration. In addition, taller structures would lead to larger axial loads imposed. These attributes are the focus of this parametric study.

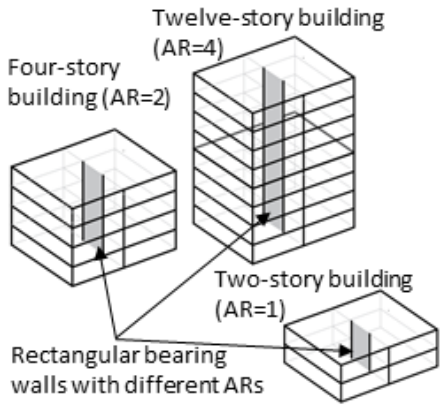


Figure 6.1: Buildings configurations with bearing walls of different aspect ratios (ARs)

To model each of these parametrically varied walls, observations from the validation study of Chapter 5 are considered. For example, the geometry of the mesh is defined using the improved mesh size of 6x6 inches, as this was observed to improve the damage and crack width estimation. In addition, boundary elements are modeled by assigning confined concrete properties to the finite elements located

Table 6.1: Matrix of wall models considered in the numerical parametric study

Model Name	AR[1]	BE[2]	ALR[3] [%]
AR1-0-BE *	1.0	special	0
AR1-4-BE	1.0	special	4
AR1-8-BE *	1.0	special	8
AR1-15-BE	1.0	special	15
AR1-0-noBE	1.0	none	0
AR1-4-noBE	1.0	none	4
AR1-8-noBE	1.0	none	8
AR1-15-noBE	1.0	none	15
AR2-0-BE	2.0	special	0
AR2-4-BE	2.0	special	4
AR2-8-BE *	2.0	special	8
AR2-15-BE	2.0	special	15
AR2-0-noBE	2.0	none	0
AR2-4-noBE	2.0	none	4
AR2-8-noBE	2.0	none	8
AR2-15-noBE	2.0	none	15
AR4-0-BE	4.0	special	0
AR4-4-BE	4.0	special	4
AR4-8-BE	4.0	special	8
AR4-15-BE	4.0	special	15
AR4-0-noBE	4.0	none	0
AR4-4-noBE	4.0	none	4
AR4-8-noBE	4.0	none	8
AR4-15-noBE	4.0	none	15

* *:wall model of the full-scale tested wall. Experimental data available*

[1] *:Aspect Ratio: wall height / length* = $\frac{H_w}{L_w}$

[2] *:Boundary elements*

[3] *:Axial Load Ratio* = $\frac{N}{A_g f'_c}$ *where N= applied axial load;* f'_c *= concrete compressive strength;* A_g *= cross section gross area*

within the design boundary element length. In terms of the boundary conditions, all numerical wall models are fixed-supported at their base and loaded at their control node, i.e, the top node. A cyclic displacement protocol and constant axial load are uniformly distributed between the wall concrete panels. The constitutive material parameters used in the parametric study are kept constant and equal to that used in the validation study presented in Chapter 5. Note that this reflects the as-tested material properties on the day of the tests of the reference full-scale walls. *ConcreteCM* material model with 0.00008 tensile strain at strength is adopted in the wall models considered in this parametric study, as the validation study in Chapter 5 showed superior results in terms of crack distribution obtained with the *ConcreteCM*, compared with the *Concrete*02 material model. The parameters describing cyclic stiffness degradation

of the reinforcing steel are also left unchanged with respect to the reference full-scale models in Chapter 5, in line with what suggestions of Menegotto and Pinto (1973). Displacement controlled analyses were carried out in OpenSees, adopting multiple solution algorithms to solve any convergence issues. In particular, the modified Newton-Raphson approach, which computes the tangent stiffness matrix at the beginning of each load step, and the Krylov-Newton algorithm, which uses a Krylov subspace accelerator to accelerate the convergence of the modified Newton method, were adopted in these analyses. For more information on the solution algorithms see Gil et al. (2007) and Scott and Fenves (2010).

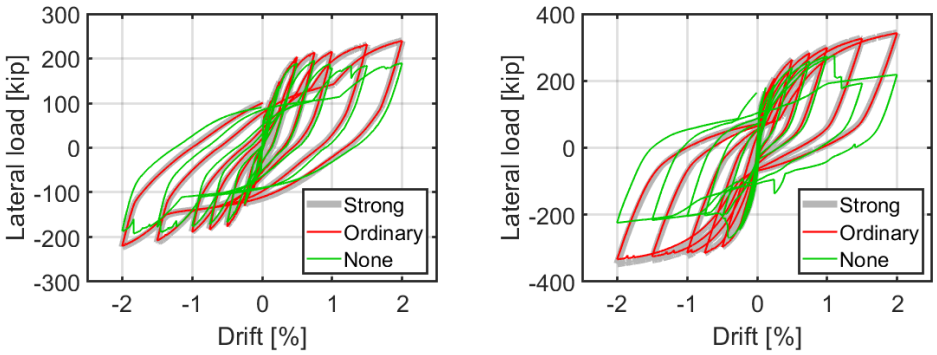
6.2.1 Load Protocol

The adopted displacement protocol applied to the wall models considered in this parametric study consisted of single full cycles with increasing amplitude. One cycle per amplitude was imposed at 0.125%, 0.25%, 0.5%, 0.75%, 1.0%, 1.5% and 2.0% drift ratios. The displacement protocol was defined to capture the wall response at the drift ratios associated with key wall response by ASCE 356 (2000).

6.2.2 Justification for the Parametric Wall Models

Before choosing the final wall models listed in Table 6.1, various types of reinforcement distribution were considered as follows:

- Wall models with a reduced amount of confinement in the boundary elements ("ordinary boundary elements" in ACI 318 2019) were examined as representative of an intermediate case between wall models with special and without boundary elements. Note that special boundary elements were designed according to ACI 318 (2019) in the full-scale wall specimens described in Chapters 2 and 3. Special boundary elements have increased confinement capacity than ordinary boundary elements, thanks to reduced horizontal and vertical spacing of the hoop sets and cross ties. ACI 318 (2019) specifications for special boundary elements applied to the full-scale walls resulted in transverse reinforcement ratio in the boundary elements $\rho_{h,web}$ = 1.25 and $\rho_{h,web}$ = 1.5 for the slender and squat walls, respectively. To model "ordinary boundary elements" the transverse reinforcement ratio $\rho_{h,web}$ was reduced by about 50% in the intermediate wall models (denoted as "ordinary transverse reinforcement" wall models in Figs. 6.2 to 6.4).



(a) AR= 2, Axial Load Ratio = 0%

(b) AR= 2, Axial Load Ratio = 8%

Figure 6.2: Lateral load versus drift ratio curves of AR=2 wall models with different levels of transverse confinement in the boundary elements

Analysis of these wall models resulted in similar damage predictions for both the levels of confinement in the boundary elements, therefore further variation of the geometry or details, using an ordinary detailing in the boundary region was not explored. The limited sensitivity of the model to changes in the transverse reinforcement ratio in the boundary elements of the walls is shown

in Fig. 6.2 in terms of global lateral load versus drift ratio. Results of wall models with strong, ordinary and no transverse boundary reinforcement are considered. In addition, Figs. 6.3 and 6.4 show the limited effect of a reduced confinement case in the model prediction of the damage. The damage predicted by the models with strong boundary elements does not appreciably differ from the models with about 50% reduction in transverse reinforcement.

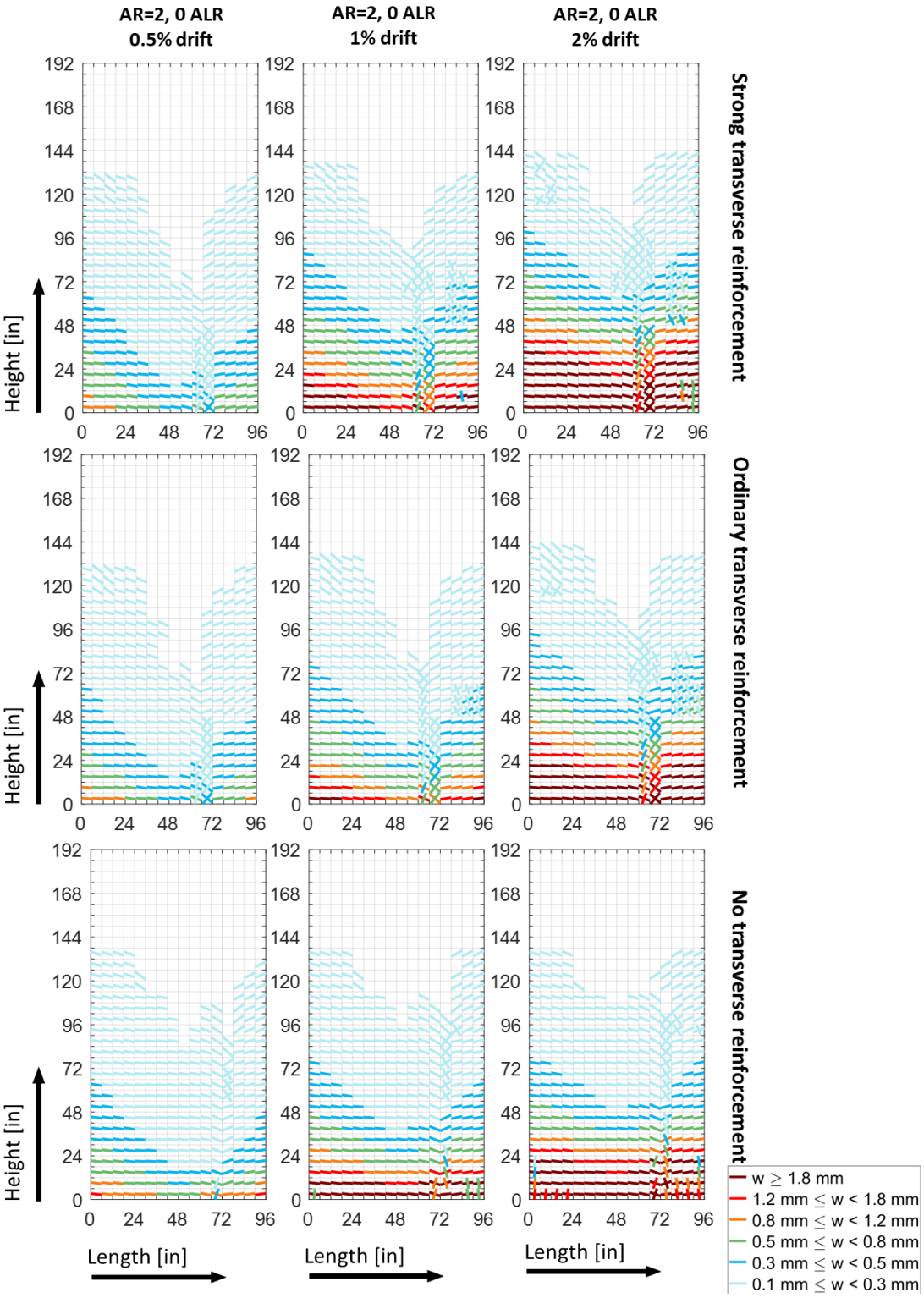


Figure 6.3: AR= 2, Axial Load Ratio = 0% wall models with different levels of transverse confinement in the boundary elements. Estimated damage prediction at 0.5%, 1% and 2% drift ratios

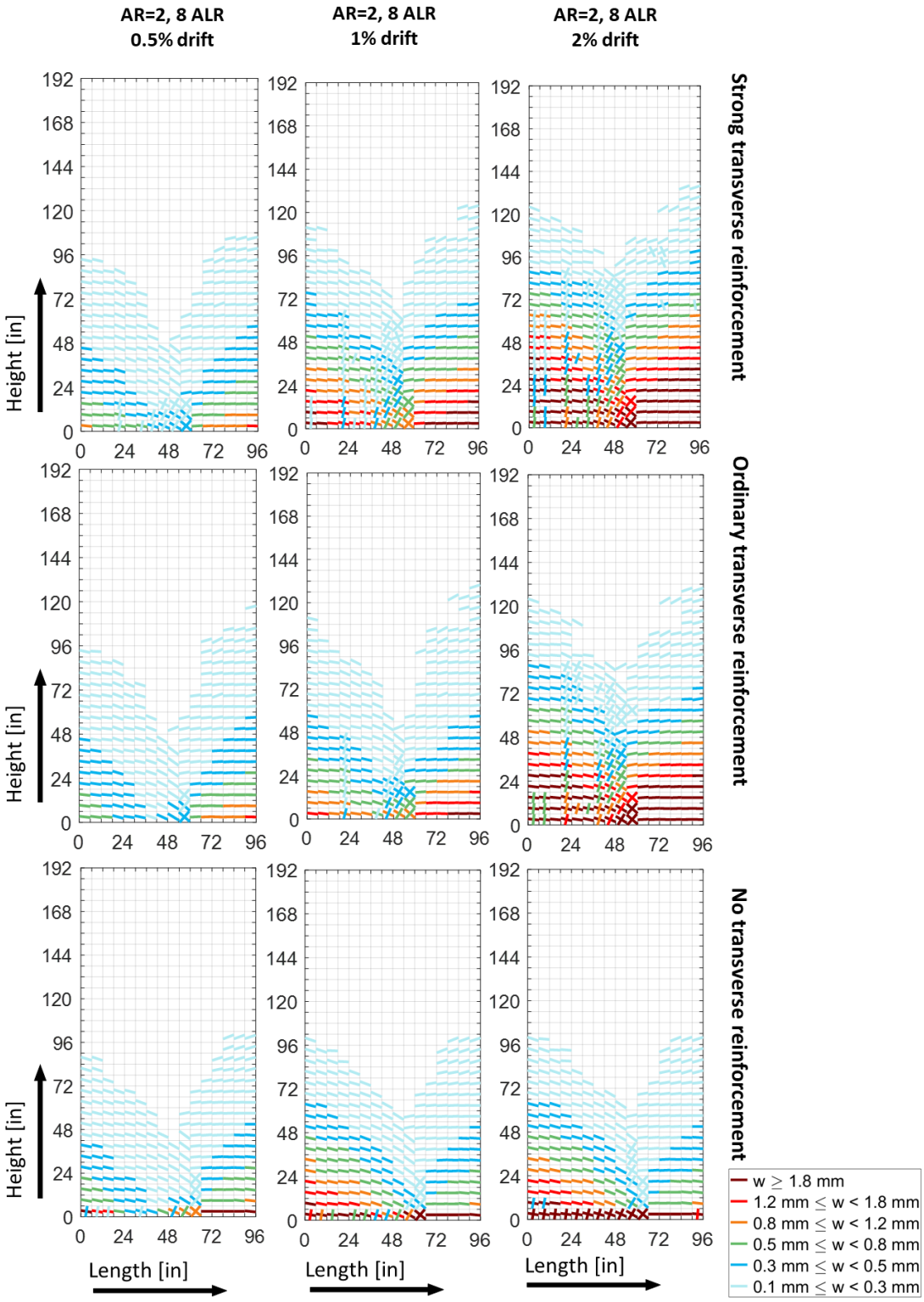


Figure 6.4: AR= 2, Axial Load Ratio = 8% wall models with different levels of transverse confinement in the boundary elements. Estimated damage prediction at 0.5%, 1% and 2% drift ratios

- Wall models with minimum horizontal and vertical reinforcement ratios of 0.25% (as for code ACI 318 2019) are also explored within this parametric study to provide insight on the performance of some old existing concrete shear walls, designed according to non-seismic codes, potentially not satisfying current seismic requirements. Extensive literature on the response of the Chilean walls design, which were subject to the 2010 Maule Earthquake shows poor performance of typical walls with small thickness, light reinforcement and inadequate confinement (Saatcioglu et al. 2013, Alarcon et al. 2014 ,Jünemann et al. 2015). The response of these walls can be represented with good accuracy by the wall models without boundary elements analyzed in this parametric study. In addition, wall models with the minimum reinforcement ratio per code ACI 318 (2019), i.e., 0.25%, in both the longitudinal and transverse directions were examined herein to offer an understanding of these low bounds. The limited detailing resulted in poor performance of these models, the majority of which failed before reaching 2% drift ratio. Fig. 6.5 shows that significant pinching of the hysteresis curves of the slender wall models is also observed, as an expected consequence of the inadequate shear strength, which is severely limited by the low transverse reinforcement ratio. Since numerical data at the Collapse Prevention limit state (2% drift ratio) of these wall models are not consistently available, results are not included in the presented numerical study and will not be considered in the comparison of the predicted response of varied concrete shear walls.

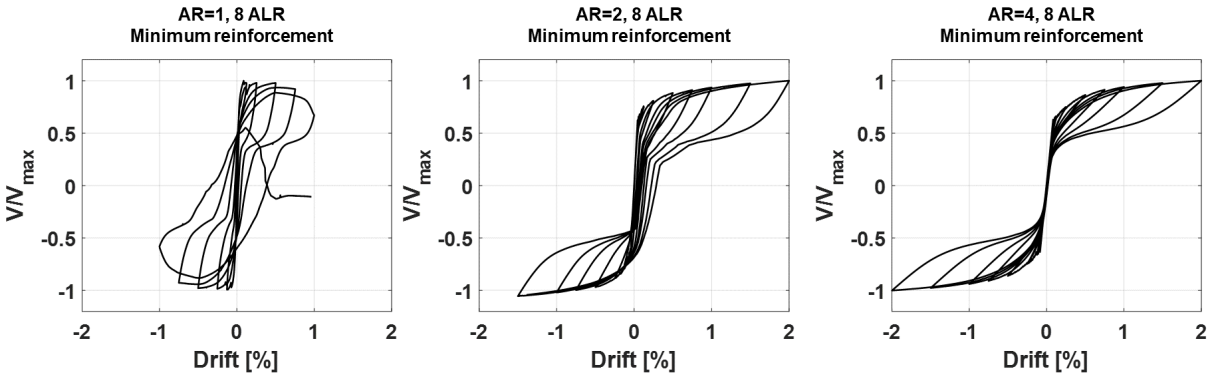


Figure 6.5: Hysteresis curves predicted by numerical models with minimum amount of horizontal and vertical reinforcement by code (0.25% in ACI 318 2019)

6.3 Results of the Parametric Study

Results of the numerical wall models are analyzed in terms of global and local response to understand the behavior of the various shear wall models to simulated earthquake loads, with particular focus on characterizing expected damage. Consideration of the predicted cracks and damage distributions is adopted to advise on the design locations of anchors, which commonly connect nonstructural components and systems to concrete buildings.

6.3.1 Hysteresis Curves

The lateral load versus drift ratio curves of the wall models considered in this study are presented in Figs. 6.6-6.8. In these plots, the lateral load V is normalized by the load V_{CP} predicted by the numerical model at the collapse prevention performance limit state, associated with a 2% drift ratio by FEMA 356 (ASCE 356 2000). It is noted that some walls may still have significant strength and stiffness at this drift ratio, as was observed in the full-scale wall tests. However, 2% drift ratio is a reasonable drift value limit from a performance-based perspective and adopted in a number of design guidelines, thus it is hence adopted in this study. It is also noted that the actual strength reduction of each wall model is not feasible to adopt as a consistent incipient failure criterion, due to the inability of the numerical model to robustly simulate significant wall degradation.

The hysteresis curves in Figs. 6.6-6.8 show that the lateral load in the elastic range is larger than V_{CP}, the load at 2% drift ratio as for FEMA 356 (ASCE 356 2000) for the majority of the wall models considered. This observation is also discussed in Fig. 5.14 within the validation study in Chapter 5, where it is shown that the secant stiffness of the experimental walls is significantly smaller than the numerical prediction in the elastic range.

To assess the effect of varying reinforcement layouts, the hysteretic response of wall models with and without boundary elements may be cross-compared in Figs. 6.6-6.8. One notes the beneficial effect of confined wall ends on the stability of the models, regardless of the slenderness of the walls. Similarly, it is observed that larger values of applied compression load in the low aspect ratio (AR=1) wall models have a negative effect on the stability of the numerical model, as is demonstrated by the irregular hysteresis cycles in Fig. 6.6, less stable at larger drift ratios. The hysteresis curves of the

slender wall models with AR=4 and boundary elements trend from full to narrow loops as the applied axial load increases, indicating that high axial loads reduce the energy dissipation capacity of the wall models, as further discussed in the following paragraphs.

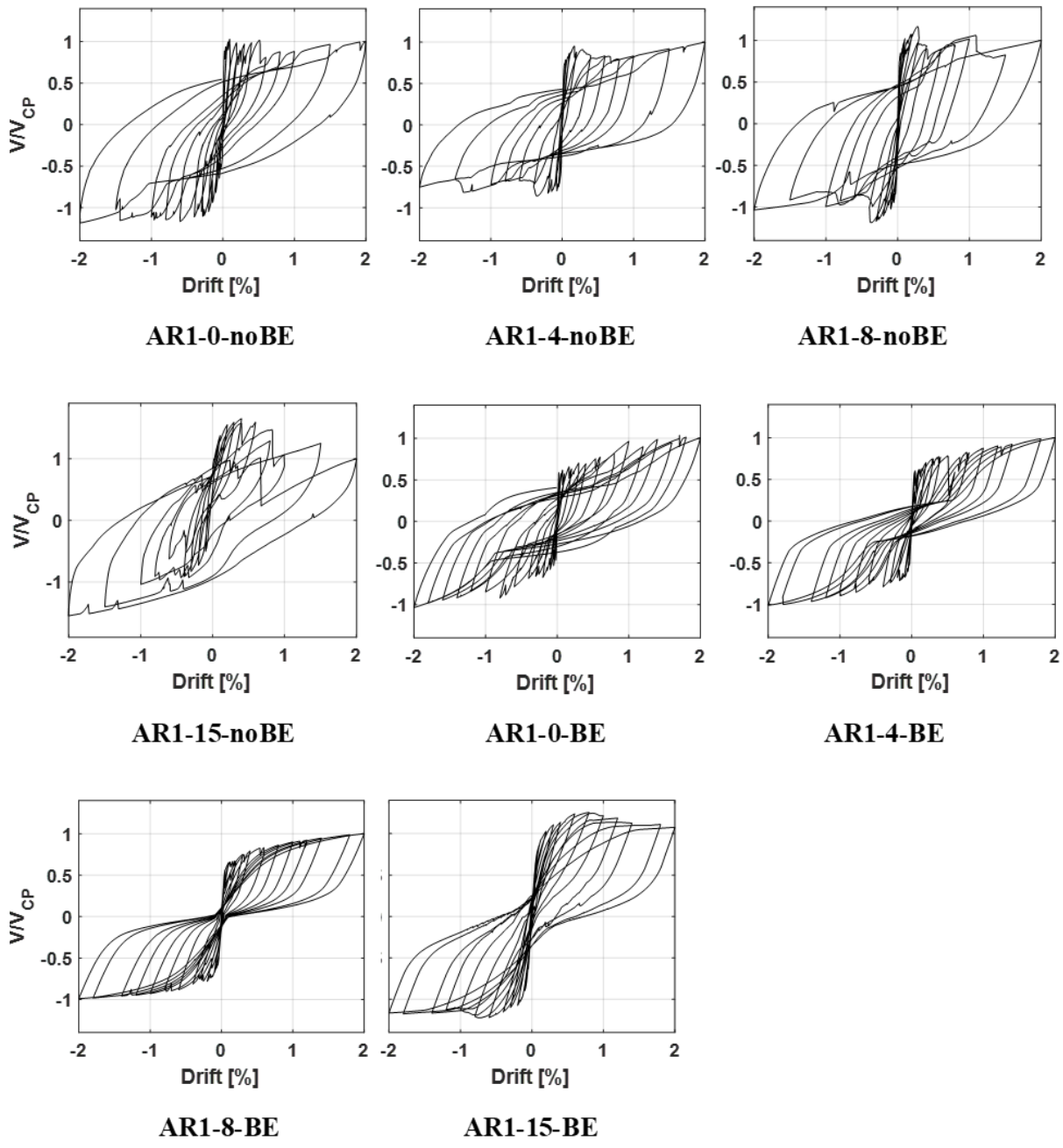


Figure 6.6: Lateral load versus drift hysteresis curves of AR=1 wall models. For model short name see Table 6.1

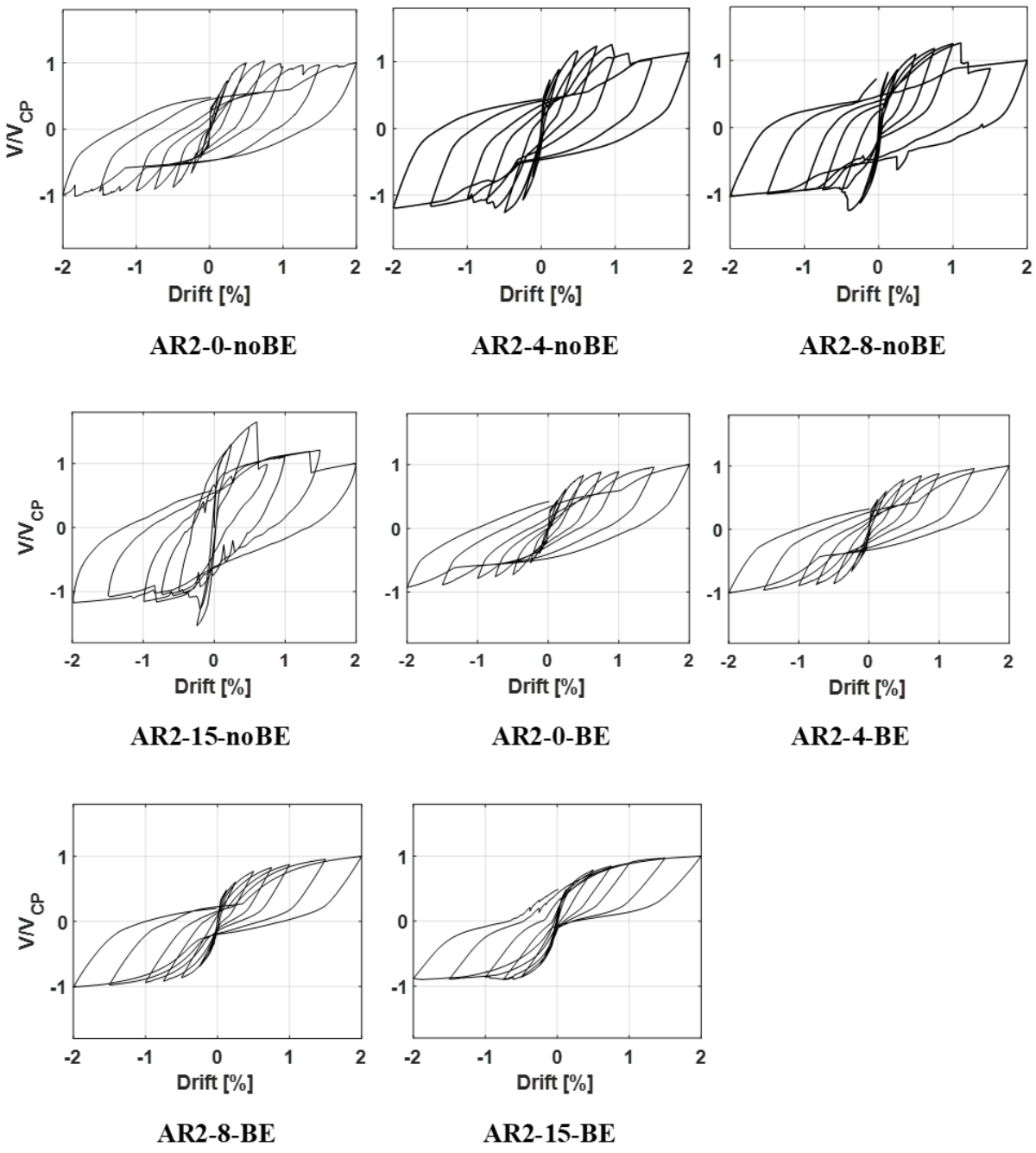


Figure 6.7: Lateral load versus drift hysteresis curves of AR=2 wall models. For model short name see Table 6.1

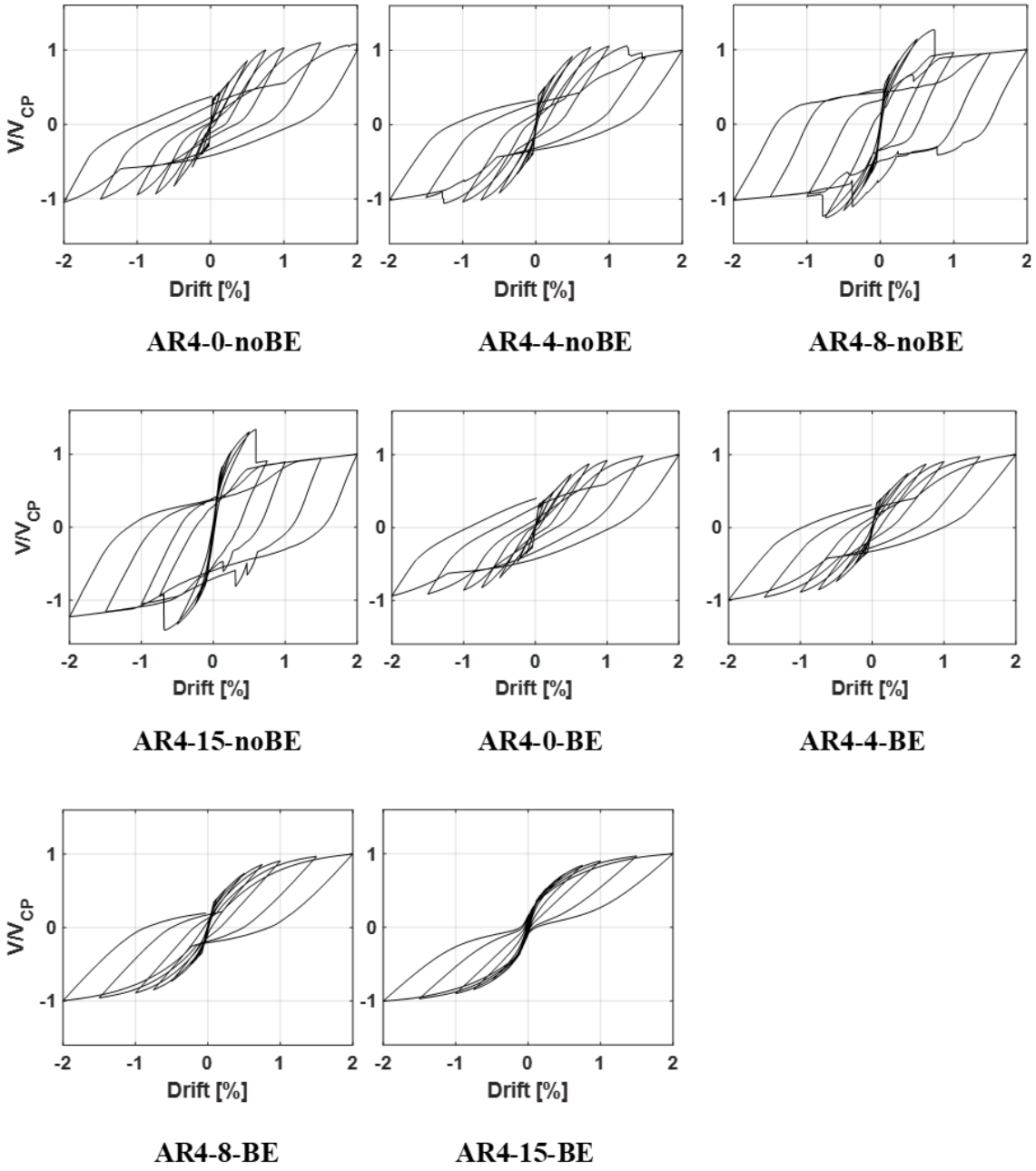


Figure 6.8: Lateral load versus drift hysteresis curves of AR=4 wall models. For model short name see Table 6.1

To further study the effect of the applied axial load on wall response, Fig. 6.9 shows the normalized lateral strength of the wall models versus the applied compression load. The y-axis shows the lateral wall strength at the 0.5%, 1% and 2% key drift ratios, which are associated with the Immediate Occupancy (IO), Life Safety (LS) and Collapse Prevention (CP) performance limit states, normalized by the values predicted for the correspondent model (same geometry, same reinforcement distribution) but without applied axial load. Results show that:

- Wall lateral strength increases as axial compression load is applied to the wall models, irrespective of the presence of boundary elements.

- For all aspect ratio walls considered in this study, confined boundary elements ("+" symbol in Fig. 6.9) provide additional lateral strength to the wall. Wall models with distributed reinforcement predict a lower lateral strength increment with respect to wall models with boundary elements, especially at large drift ratios (about 2%) and large axial compression load ($\geq$ 15%).

- In slender wall models (AR=2 and AR=4) the lateral strength is approximately doubled when the axial load is large, i.e., 15% of the section capacity, especially if confined boundary elements are incorporated in the design. However, wall models with distributed reinforcement predicted a drop in strength at the LS and CP limit states, suggesting the incipient failure of the wall, when such large axial load is applied.

- In squat wall models (AR=1) the rate of increase in lateral capacity with applied axial load is larger than that of the slender walls, with a 60% average increment in strength gain estimated for AR=1 walls at the applied compression load of 8% of the section capacity, versus approximate a 40% average increment in AR=2 and AR=4 wall models at the same applied compression load. However, similar to the slender walls, the AR=1 wall models with distributed reinforcement ("noBE" models) predict a lateral strength drop when axial load is applied in the amount of 15% of the section capacity, highlighting the insufficiency of such design to carry large load demands.

- Experimental data for the AR=1 shear walls are also presented in Fig. 6.9 with a thick black "+" symbol. These data points agree with the numerical prediction with good confidence at the IO and LS performance limit states. However, at the CP drift ratio the experimental full-scale wall

exhibited strength reduction, as opposed to the numerical model. This data point falls out of the predicted range for walls with boundary elements and agrees with the IO prediction for walls with distributed reinforcement (see Fig. 6.9).

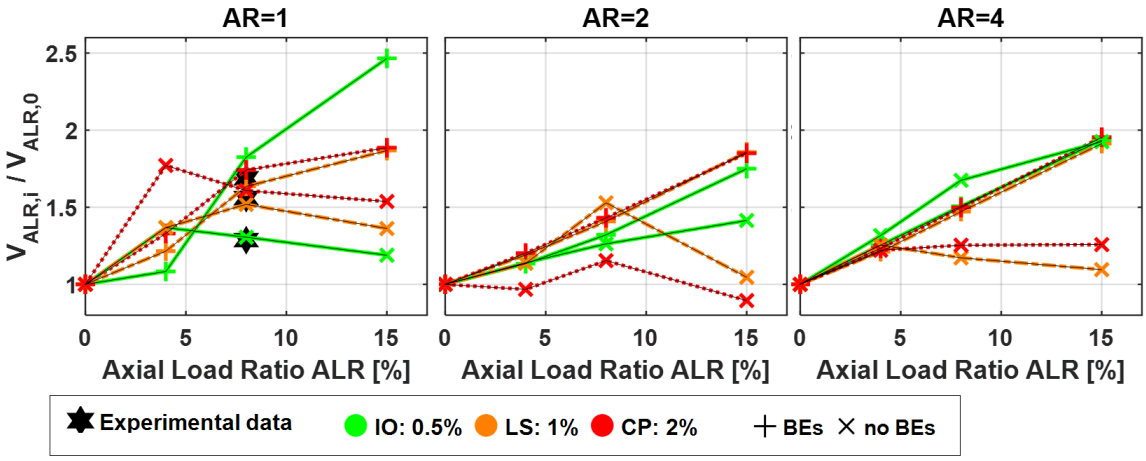


Figure 6.9: Normalized lateral strength of the wall models as a function of axial load ratio. Wall strength is normalized to strength predicted by wall models without axial load: AR=1 (left), AR=2 (center) and AR=4 (right)

The hysteresis loops presented in Figs. 6.6-6.8 also may be used to calculate the energy dissipation, the amount of which is essential to offering ample resistance to seismic demands. Ductile RC structures are typically designed to accommodate damage without collapse and in the event of an earthquake they are able to preserve substantial strength while also dissipating the input energy via mechanical hysteretic response of their structural elements. Nonlinear static design methods use parameters related to the energy dissipation capacity to evaluate the inelastic seismic response of structures and to describe the strength and stiffness degradation of RC elements subjected to cyclic loading. For example, viscous damping is used to characterize the energy dissipation capacity of RC elements and is one of the key parameters for the application of displacement-based design methods (Moehle 1992, Wallace and Moehle 1992, Paulay 2002, Chopra 2017 and ACI 318 2019). In addition, equivalent viscous damping can be related to the displacement ductility of the RC element, which is another way to characterize the performance of structural elements subjected to lateral seismic loads. The equivalent damping is generally interpreted as the superposition of the elastic and hysteretic damping, where the elastic damping is often assumed as 5% of the critical damping (Chopra 2017) and computed proportionally either to the

initial stiffness, or to the mass, or both. The hysteretic damping, instead, depends essentially on the post-yielding characteristics of the structural element and thus can be estimated from its hysteretic response. Therefore, to further characterize the influence of compression axial load, geometry and detailing of the wall models on their response to lateral loads, the equivalent hysteretic damping is estimated from the hysteresis curves of the wall models using Equation (6.1).

$$\xi = \frac{A_{loop}}{(2\pi V_{max} D_{max})} \tag{6.1}$$

A_{loop} is the area of closed loop in the force-displacement response delimited by the maximum force V_{max} and maximum displacement D_{max}. Results from these analyses are reported in Fig. 6.10. The y-axis of the plots represents the equivalent damping of the i-th wall model normalized by the equivalent damping of the same wall model (same geometry, same aspect ratio) but modeled without axial load, see values in Table 6.2. In general, it is observed that the normalized equivalent damping ratio varies as a function of the applied axial compression load, with the following specific conclusions observed:

- Large applied axial compression load to the wall models generally has a detrimental effect on the energy dissipation behavior of the wall models. Physically, the axial load assists with crack closing upon reversal, and reduces residual displacement and plastic deformations. This phenomenon is expressed in the numerical models by the shape of the hysteresis curves in Figs. 6.6-6.8. The estimated equivalent damping is therefore reduced by the stabilizing effect of the axial load combined with the frame action induced by the confined ends of the wall models with boundary elements.

- Wall models with distributed reinforcement generally observe increasing energy dissipation when larger axial compression loads are applied. In the real world, this behavior may reflect partial concrete failure and large residual displacements. This behavior is numerically justified by the wide hysteresis loops in Figs. 6.6-6.8.

- Experimental values fall in the upper bound of the range of normalized hysteretic damping ratios predicted by the numerical models with AR=1, see Fig. 6.10. For this reason, sufficient confidence is attributed to the results obtained with this model.

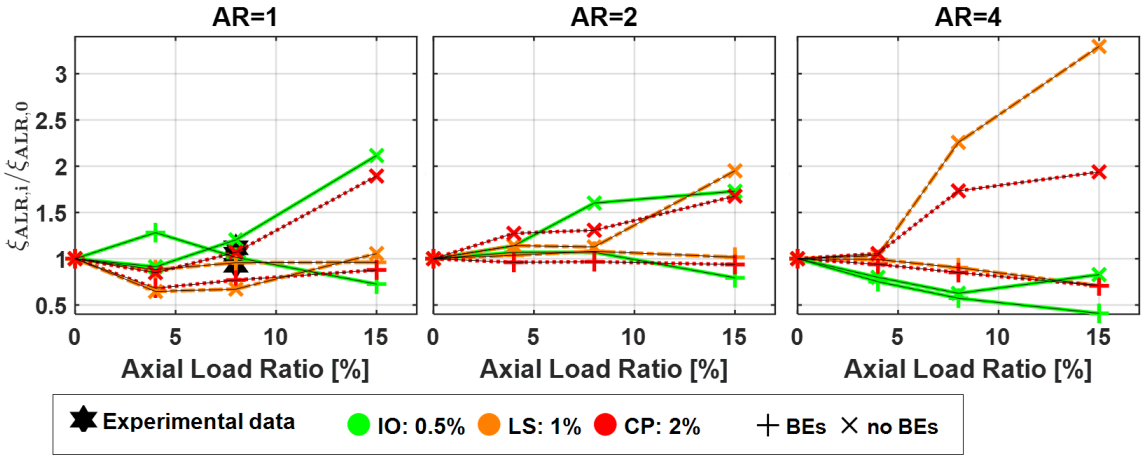


Figure 6.10: Normalized equivalent damping of wall models as a function of the applied axial load for different aspect ratios: AR=1 (left), AR=2 (center) and AR=4 (right)

Table 6.2: Equivalent hysteretic damping values predicted by wall models absent axial load

Wall model	$\xi_{ALR,0}$ [%] at Limit State:		
	IO	**LS**	**CP**
AR1-0-BE	34	41	89
AR1-0-noBE	50	56	71
AR2-0-BE	11	26	44
AR2-0-noBE	11	31	55
AR4-0-BE	7	16	37
AR4-0-noBE	6	16	38

Consideration of Material Model Parameters

Analyses results from this parametric study demonstrate significant load drop following the elastic cycles at low drift amplitudes in walls with distributed reinforcement, especially in the models with medium to large values of applied axial load. This observation revealed the importance of accurately selecting adequate material modeling parameters for shear stiffness and strength, especially for low-aspect ratio walls (AR=1) whose behavior is dominated by nonlinear shear response. In this regard, the relevance of the parameter regulating the dowel action α_{dow} is observed to have a significant impact on the predicted shear wall response. Within the SFI-MVLEM numerical model, the dowel force is computed as the dowel displacement Δ_d multiplied by the stiffness coefficient k_d which is a fraction α_{dow} of the initial elastic modulus of the reinforcement steel E_{s0} with α_{dow} ranging from 0 to 0.05 (Kolozvari et al. 2015). While conducting this parametric study additional insight regarding the impact of the α_{dow} pa-

rameter was obtained. In particular, it is found that for the $AR = 1$ shear wall models with distributed reinforcement and a relatively large amount of applied axial load, values of α_{dow} closer to the upper bound of that suggested resulted in a more realistic prediction of the global response of walls to lateral loads, see Fig. 6.11. In addition, the estimation of the lateral capacity improves when a large amount of dowel force is considered, since open crack widths grow and complement wall shear strength. This evidence is also supported in the literature. Experimental studies on test beams without web reinforcement showed that 50%-70% of the total shear is resisted by aggregate interlock mechanism (Ince et al. 2007). It is also well-known that the larger the beam depth, the smaller the contribution of aggregate interlock since cracks near the main reinforcement are significantly wide. In this situation, the dowel effect is quite important. Nevertheless, the contribution of dowel action to shear capacity is either ignored or limited to 15%-25% of the shear stiffness for design purposes (Ince et al. 2007). Therefore, the range of α_{dow} values suggested to model reinforced concrete shear walls is deemed reasonable.

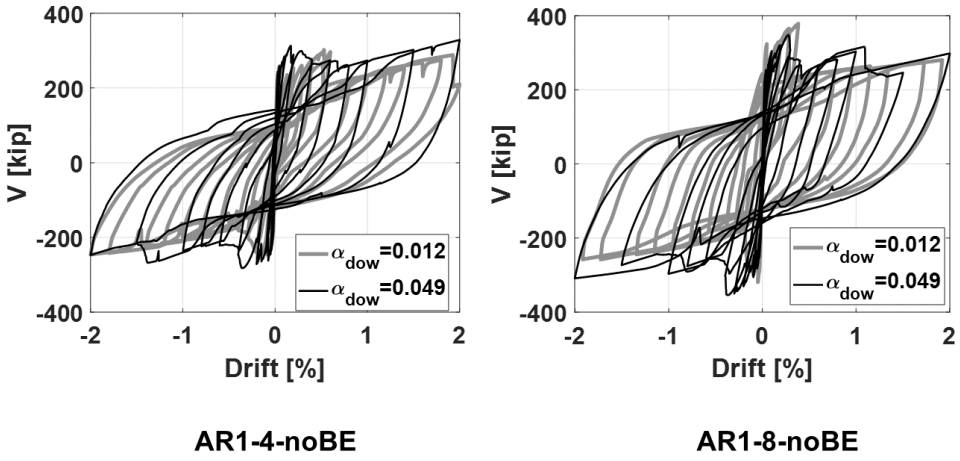


Figure 6.11: Effect of α_{dow} parameter on wall hysteresis curve of AR=1 wall models

6.3.2 Damage Characterization of Walls with Different AR

The evolution of damage during the loading history for the various wall models is presented in this section. To this end, the crack distribution at the key drift ratios of 0.5%, 1% and 2% is associated with the damage typical of the Immediate Occupancy (IO), Life Safety (LS) and Collapse Prevention (CP) limit states, respectively, as for FEMA 356 ASCE 356 (2000), is reproduced for each wall model. Crack width values are estimated according to the smeared crack approach described in Chapter 5 and color coded according to the bin legend in Figs. 6.12 to 6.30. It is noted that cracks whose estimated width is w $<$ 0.1 mm are not included in these plots, similarly to Chapter 5.

Squat Wall Models (AR=1)

The crack pattern predicted at IO, LS and CP for the AR=1 wall models are represented in Figs. 6.12 to 6.17. The following observations are made from these figures:

- As observed during the full-scale squat wall tests, the axial compression load on the wall suppresses the vertical crack propagation. It is further observed in the parametric study that this evidence is irrespective of the presence of boundary elements. Large axial load levels of 8%, however, tend to create a localization effect on the models, producing cracks in the top elements where the load is applied, see for example AR1-8-BE for the most severe demonstration of this effect.

- Wall models with confined boundary elements predict crack patterns which extend further in elevation at the wall ends with respect to the wall web. This effect may be explained considering the frame action of the reinforced boundary ends of the wall. Wall models with distributed reinforcement, on the other hand, predict a uniform crack distribution over the wall length.

- Estimated crack widths transition gradually to lower values away from the base of walls modeled with boundary elements with respect to walls modeled with distributed reinforcement. This is mainly due to the different failure mode observed by wall models without boundary elements, which have a tendency towards a sliding shear failure. This failure mode is characterized by sliding of the wall on significantly large cracks, opening almost horizontally near the base of the wall. This mechanism prevents a well-distributed spread of damage. Possible representation of sliding failure mode is observed in Fig. 6.17 for the AR1-8-noBE and AR1-15-noBE wall models

at the Collapse Prevention performance state (2% drift ratio). These two models predict crack widths $w \geq 1.8mm$ up to 20% of the wall height, measured from the wall base.

- Irrespective of the reinforcement distribution, the majority of the predicted cracks is oriented in the 40° - 50 ° range, remarking the strong presence of shear stresses in these low-aspect ratio shear walls. This crack pattern orientation also suggests the strut-and-tie type of response of these walls, and anticipates severe damage along the main diagonal struts.

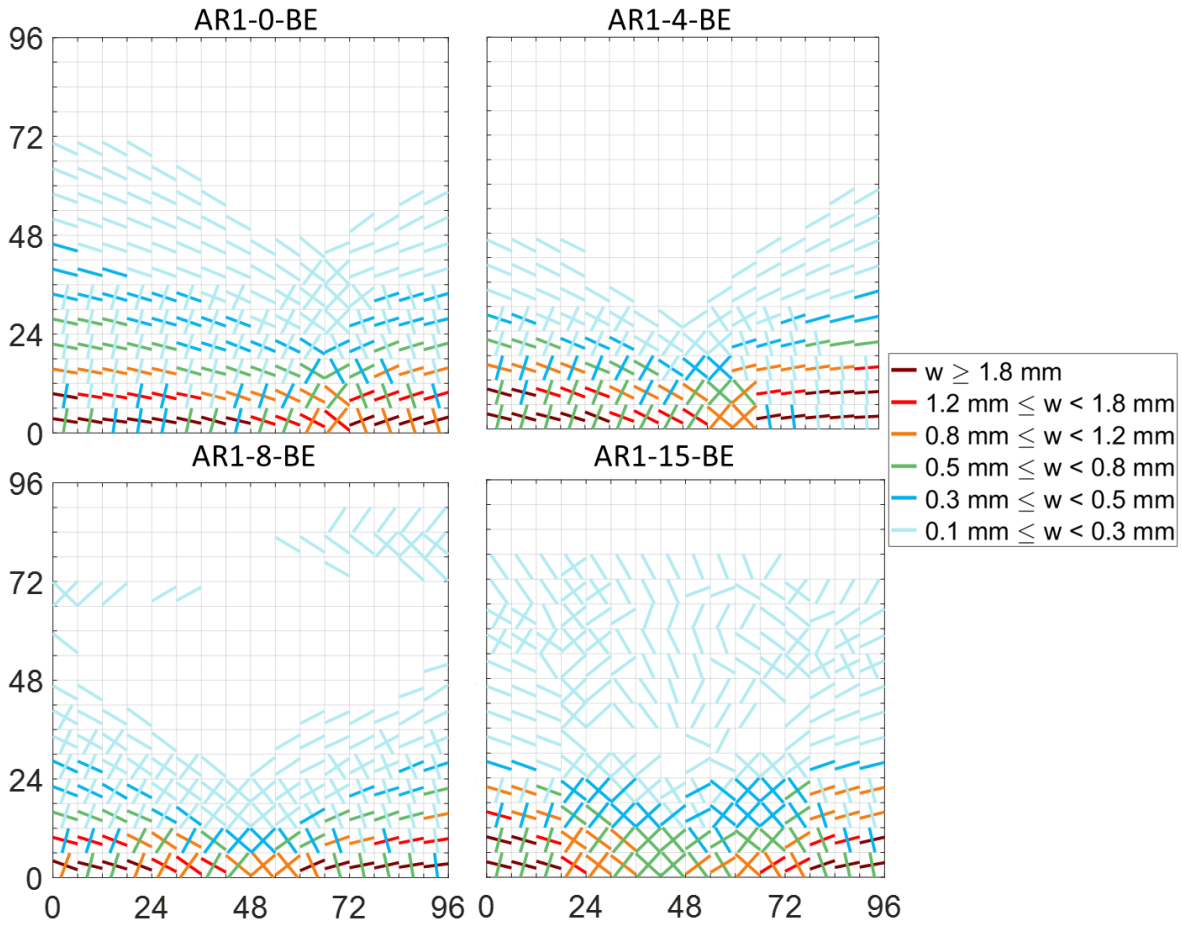


Figure 6.12: Crack pattern at **0.5% drift ratio** predicted by the **AR=1** wall models with **boundary elements** and different axial load ratios. AR: Aspect Ratio; ALR: Axial Load Ratio and BE: Boundary Elements. Wall dimensions in inches

Fig. 6.18 combines the crack pattern at 2% predicted by the AR=1 wall models to highlight the regions where the majority of the damage is expected to develop. The important geometric locations of the elevation from the wall base to $L_w/2$ and the longitudinal extension of the boundary elements, L_{be}

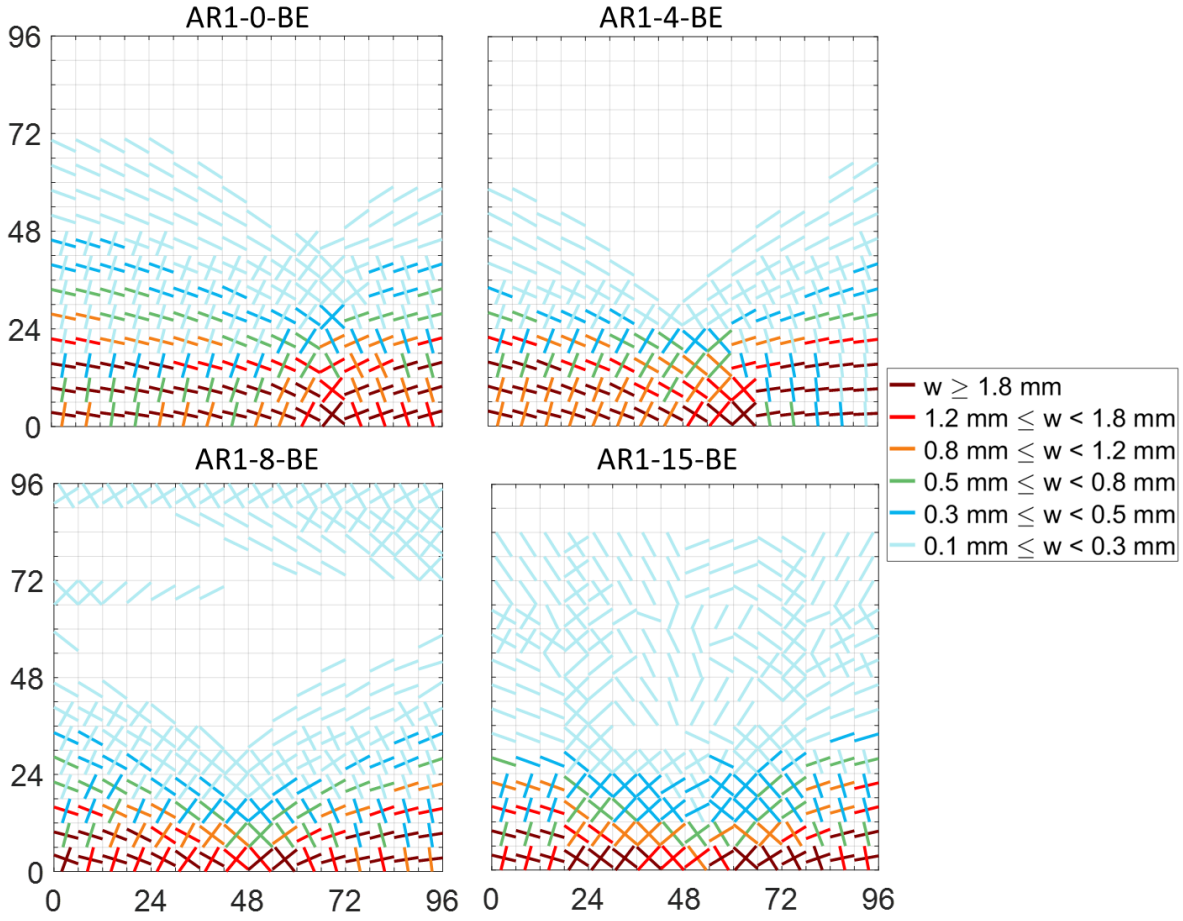


Figure 6.13: Crack pattern at **1% drift ratio** predicted by the **AR=1** wall models with **boundary elements** and different axial load ratios. AR: Aspect Ratio; ALR: Axial Load Ratio and BE: Boundary Elements. Wall dimensions in inches

= 0.2 L_w as considered in this study, are also drawn on the crack pattern sketches of the wall models with and without boundary elements. Fig. 6.18 shows that large cracks are predicted to occur up to $L_w/2$ from the wall base irrespective of the chosen design. It is also noted, however, that wall models with confined boundary elements present larger cracks along the boundary ends and a larger number of cracked elements in the upper corners with respect to walls without boundary elements. This observation suggests that in these types of ductile AR=1 shear walls, significant concrete damage can be expected in three regions, namely i) within $L_w/2$ from the wall base, ii) in the boundary elements (extending longitudinally up to L_{be} = 0.2 L_w), and iii) along the diagonal struts crossing the wall face from bottom corner to top opposite corner.

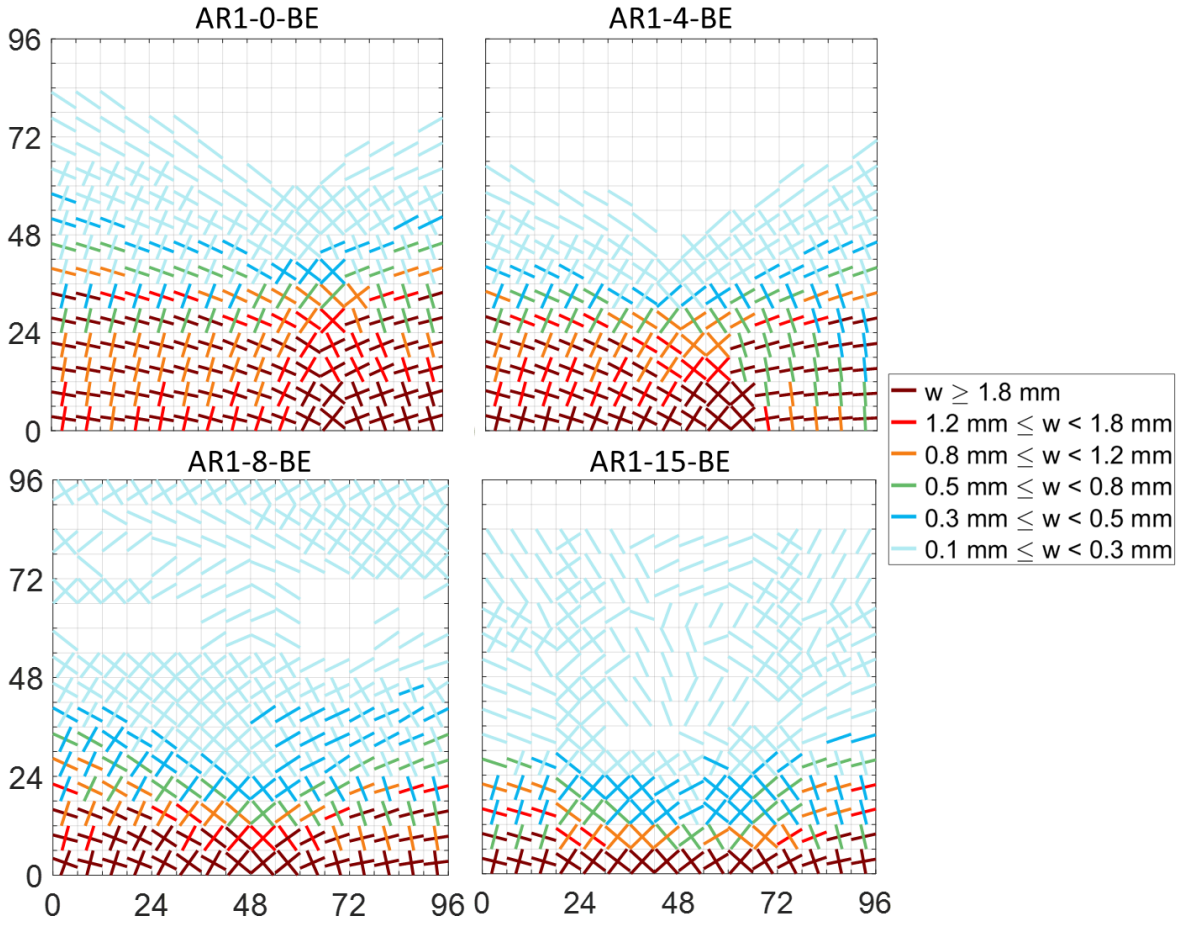


Figure 6.14: Crack pattern at **2% drift ratio** predicted by the **AR=1** wall models with **boundary elements** and different axial load ratios. AR: Aspect Ratio; ALR: Axial Load Ratio and BE: Boundary Elements. Wall dimensions in inches

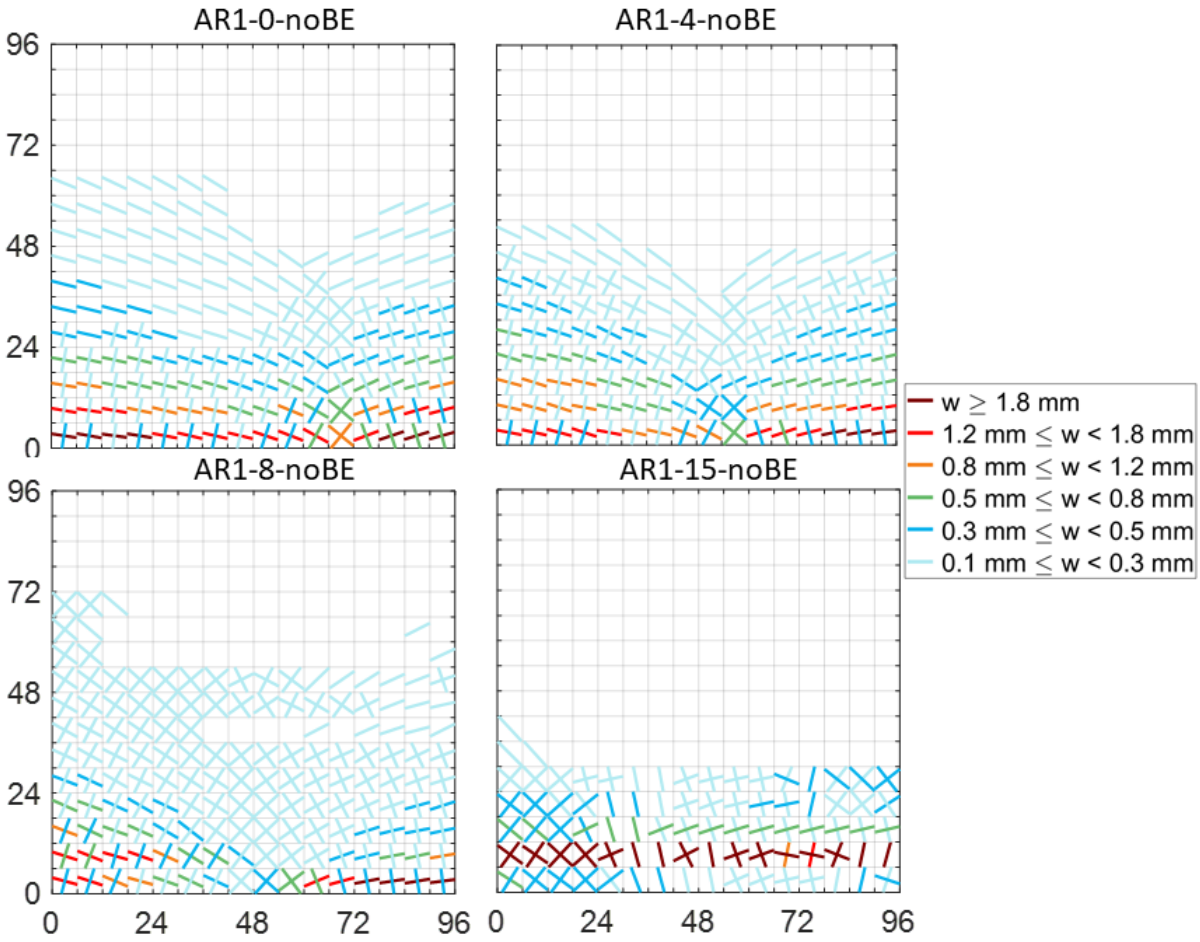


Figure 6.15: Crack pattern at **0.5% drift ratio** predicted by the **AR=1** wall models with distributed reinforcement, i.e., "**noBE**", and different axial load ratios. AR: Aspect Ratio; ALR: Axial Load Ratio and BE: Boundary Elements. Wall dimensions in inches

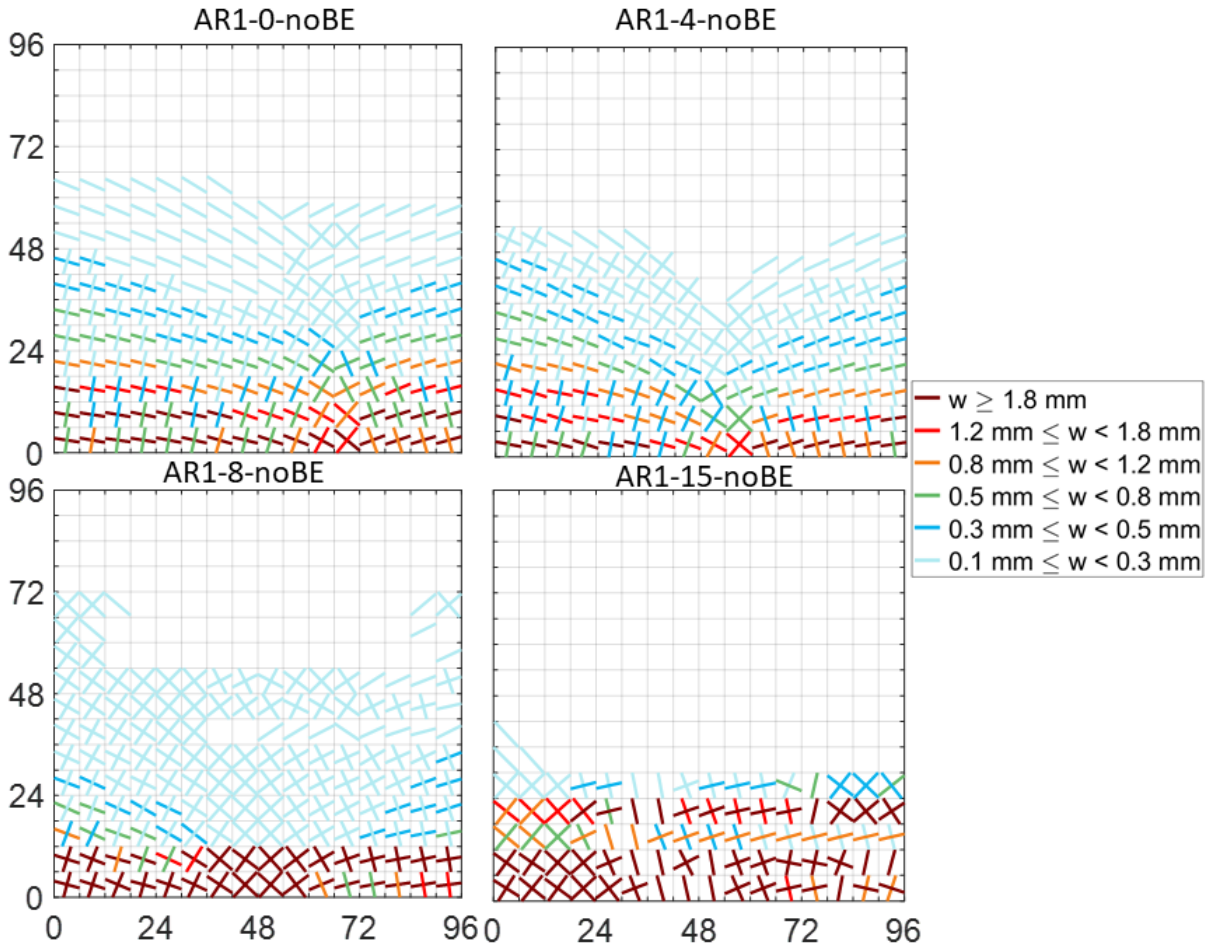


Figure 6.16: Crack pattern at **1% drift ratio** predicted by the **AR=1** wall models with distributed reinforcement, i.e., "**noBE**", and different axial load ratios. AR: Aspect Ratio; ALR: Axial Load Ratio and BE: Boundary Elements. Wall dimensions in inches

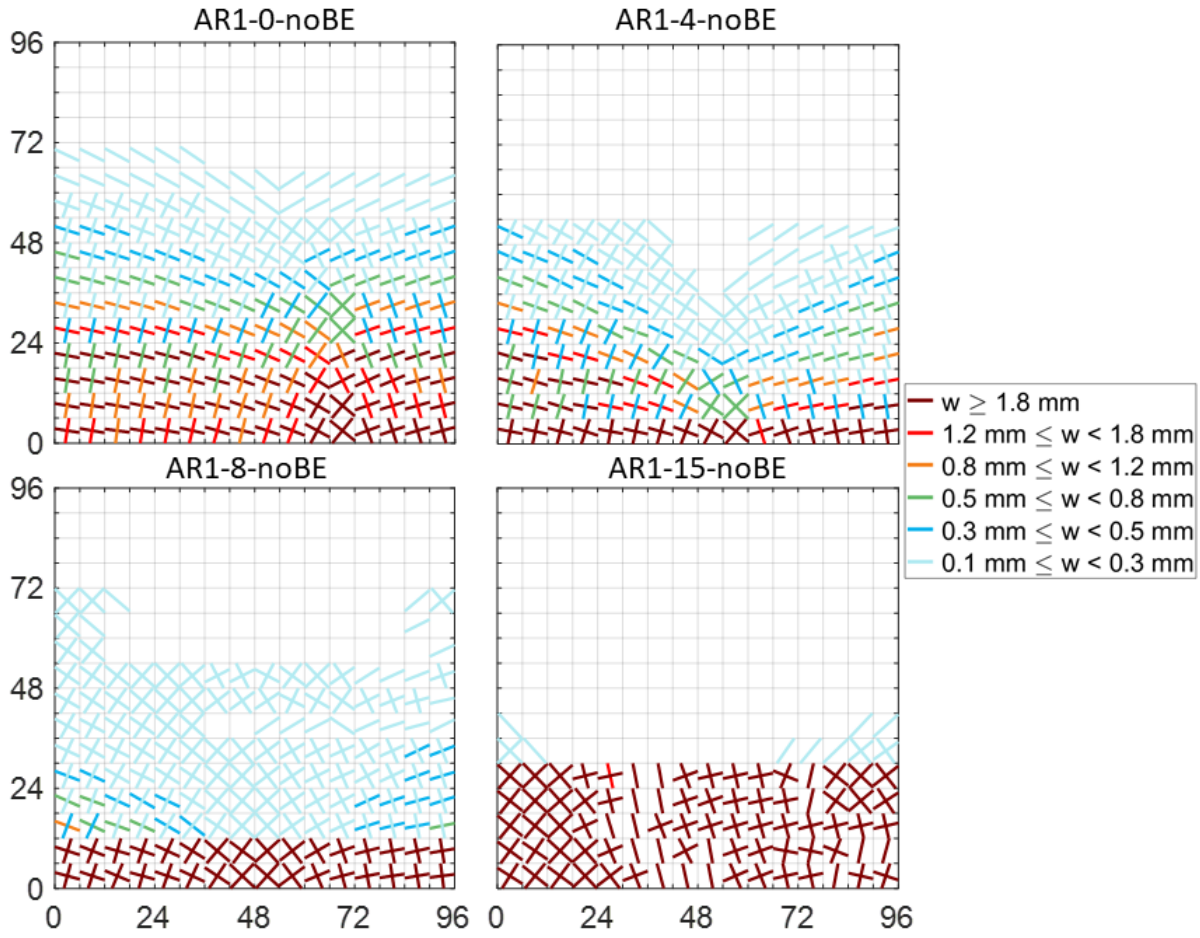


Figure 6.17: Crack pattern at **2% drift ratio** predicted by the **AR=1** wall models with distributed reinforcement, i.e., "**noBE**", and different axial load ratios. AR: Aspect Ratio; ALR: Axial Load Ratio and BE: Boundary Elements. Wall dimensions in inches

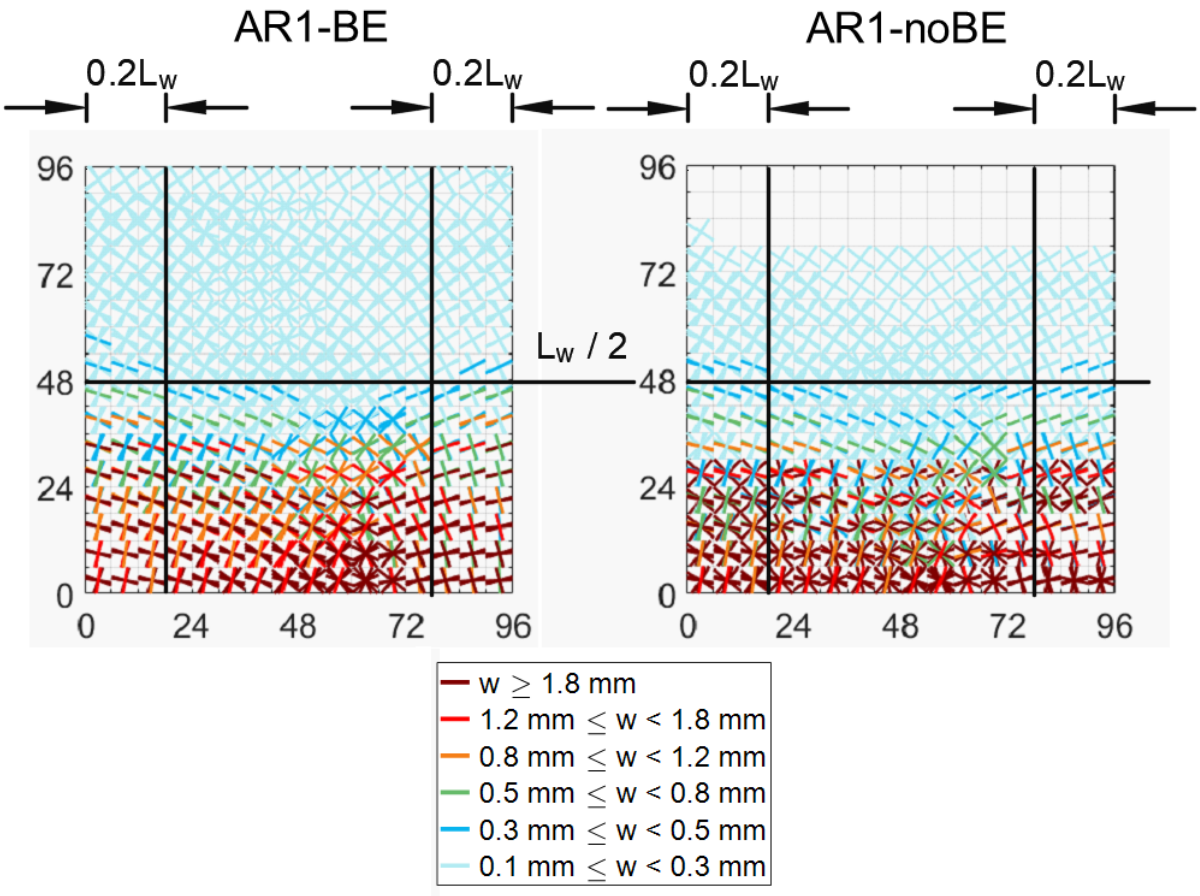


Figure 6.18: Summary of predicted crack pattern for **AR=1** wall models at **2% drift ratio**. Wall dimensions in inches

Slender Wall Models (AR= 2 and AR= 4)

In this section, the evolution of the damage in the slender wall models with AR=2 and AR=4 is analyzed. Slender walls with AR $\geq$ 2 are expected to respond largely with flexural deformations to lateral loads. Small angles of orientation of the predicted cracks are anticipated to develop in these wall models, as opposed to the predominant 45° cracks developed in low-aspect ratio walls.

The crack pattern predicted at Immediate Occupancy, Life Safety and Collapse Prevention for the AR=2 and AR=4 wall models are combined with the smeared crack width estimations and represented in Figs. 6.19 to 6.30. From these figures, the following observations are made:

- The vertical extension of the cracks is reduced for larger applied compression loads, irrespective of the reinforcement distribution and of the aspect ratios.

- The wall models with distributed reinforcement resulted in inadequate carrying capacity for large axial compression loads, as expressed by the limited cracks distributed along the wall height. The damage in the AR2-15-noBE and AR4-15-noBE wall models concentrates in the two rows of elements close to the fixed base of the wall, where estimated crack widths exceed 1.8 mm.

- Even if the vertical extension of the cracks is predicted to vary according to the amount of compression load, there is a fairly constant region where cracks larger than 1.2 mm are estimated to occur. For both AR=2 and AR=4 wall models, this region extends up the height for about 50% of the wall length at the Collapse Prevention (CP) limit states, when the imposed drift ratio is 2%. This average result agrees with the theoretical plastic hinge length, defined as $0.5L_w$ by Park and Paulay (1975).

- There is little difference in the predicted damage distribution observed in the AR=4 wall models with and without boundary elements at low levels of applied compression load. This is due to the large reserve of strength of the taller walls. However, when 15% axial load ratio is applied to the wall models, the absence of properly confined boundary elements is visible in the reduced damage spread and crack width variation. Namely, wall model AR4-15-noBE predicts crack widths $w \geq$ 1.8 mm in the first row of elements only, near the fixed base of the wall model, at 2% drift ratio. Above this row of elements, the predicted crack widths abruptly reduce to relatively low values,

at the expense of a reduced region of intermediate intensity damage, which is instead predicted in the AR4-15-BE wall model.

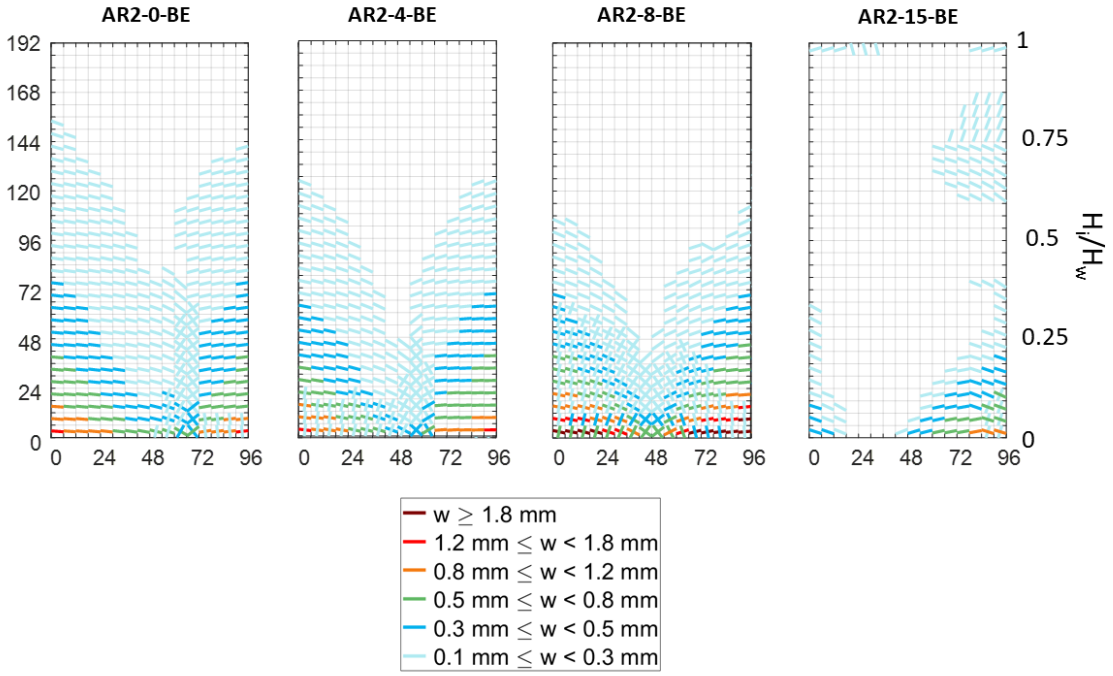


Figure 6.19: Crack pattern at **0.5% drift ratio** predicted by the **AR=2** wall models with **boundary elements** and different axial load ratios. AR: Aspect Ratio; ALR: Axial Load Ratio and BE: Boundary Elements. Wall dimensions in inches

Figs. 6.31 and 6.32 combine the crack pattern at 2% drift ratio predicted by the AR=2 and AR=4 wall models, respectively, to highlight the regions where the majority of the damage is expected to develop. To help in this damage assessment, the elevation from the wall base to $L_w/2$, L_w, and $2L_w$ and the longitudinal extension of the boundary elements, L_{be} = 0.2 L_w, are also drawn on the crack pattern plots of the wall models with and without boundary elements. Similar to the AR=1 wall models represented in Fig. 6.18, Figs. 6.31 and 6.32 show that large cracks are predicted to occur in the first $L_w/2$ region from the wall base, irrespective of the design. It is also noted in Fig. 6.31 that the AR=2 wall models with confined boundary elements present larger cracks along the boundary ends and a larger number of cracked elements in the upper corners with respect to walls without boundary elements. On the contrary, in Fig. 6.32 no significant difference in terms of cracks distribution is observed in the AR=4 wall models with and without boundary elements, as also noted in the previous paragraph. These

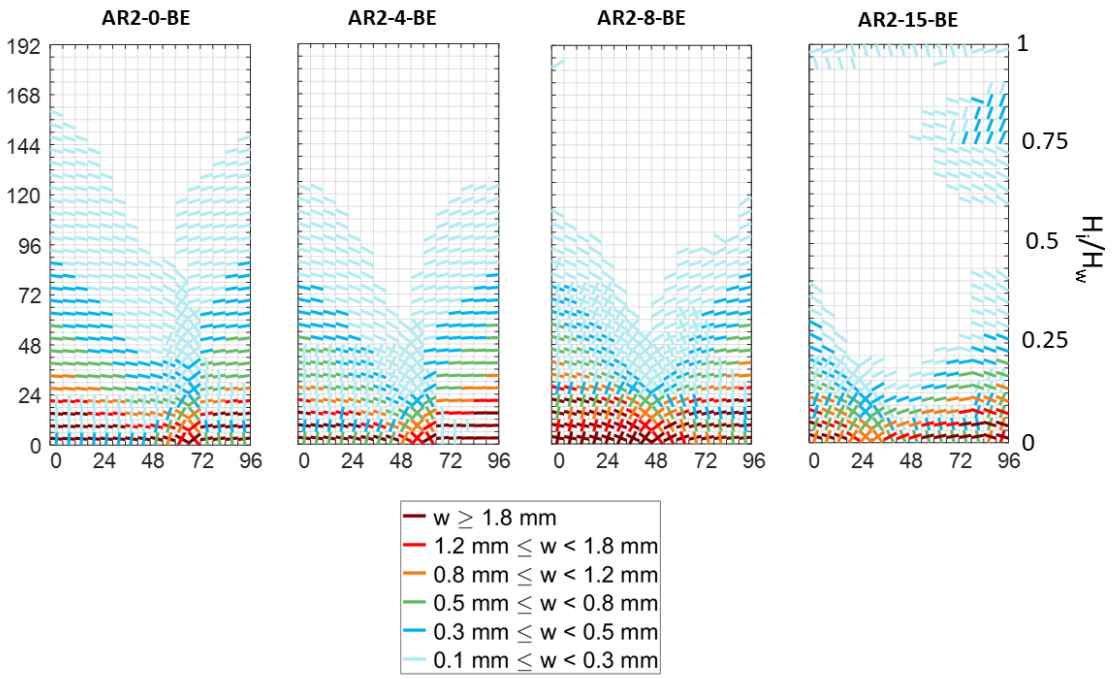


Figure 6.20: Crack pattern at **1% drift ratio** predicted by the **AR=2** wall models with **boundary elements** and different axial load ratios. AR: Aspect Ratio; ALR: Axial Load Ratio and BE: Boundary Elements. Wall dimensions in inches

conclusions suggest that in these types of slender, ductile shear walls, significant concrete damage can be expected within $L_w/2$ from the wall base and in the boundary elements, which in this study extend longitudinally up to $L_{be} = 0.2\ L_w$.

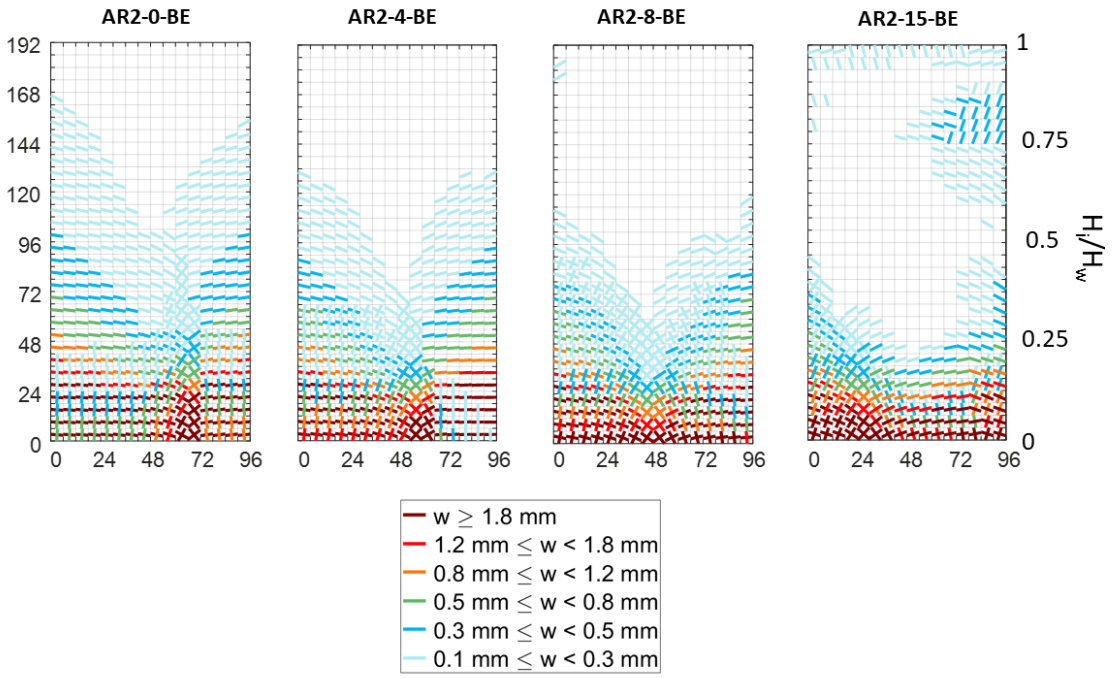


Figure 6.21: Crack pattern at **2% drift ratio** predicted by the **AR=2** wall models with **boundary elements** and different axial load ratios. AR: Aspect Ratio; ALR: Axial Load Ratio and BE: Boundary Elements. Wall dimensions in inches

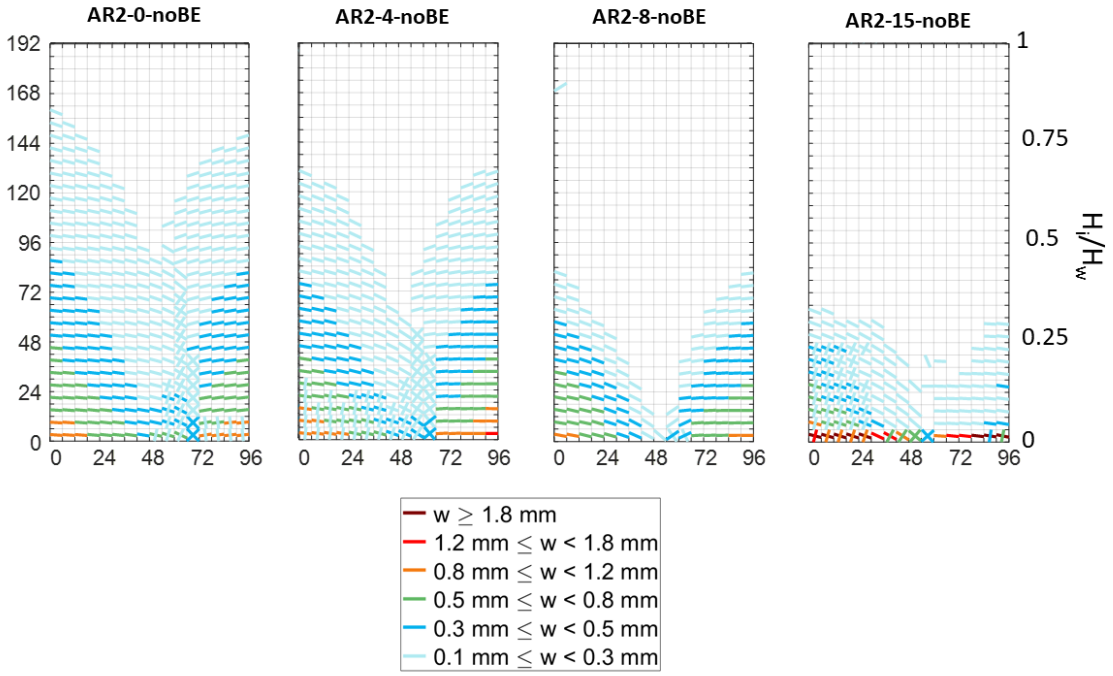


Figure 6.22: Crack pattern at **0.5% drift ratio** predicted by the **AR=2** wall models with distributed reinforcement, i.e., "**noBE**", and different axial load ratios. AR: Aspect Ratio; ALR: Axial Load Ratio and BE: Boundary Elements. Wall dimensions in inches

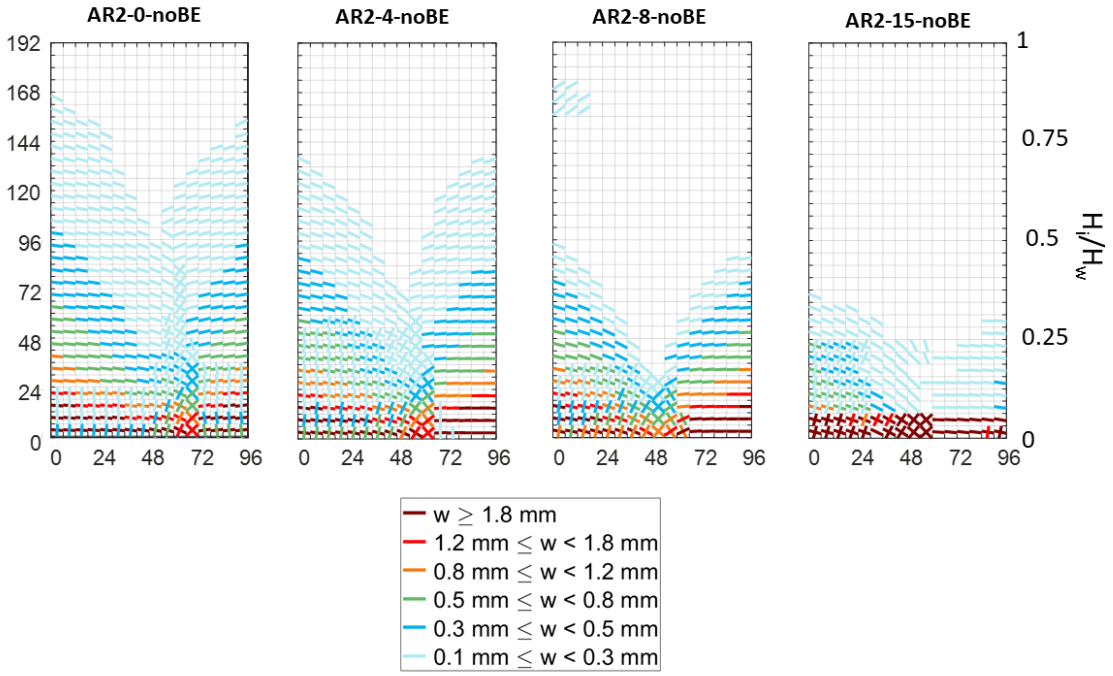


Figure 6.23: Crack pattern at **1% drift ratio** predicted by the **AR=2** wall models with distributed reinforcement, i.e., "**noBE**", and different axial load ratios. AR: Aspect Ratio; ALR: Axial Load Ratio and BE: Boundary Elements. Wall dimensions in inches

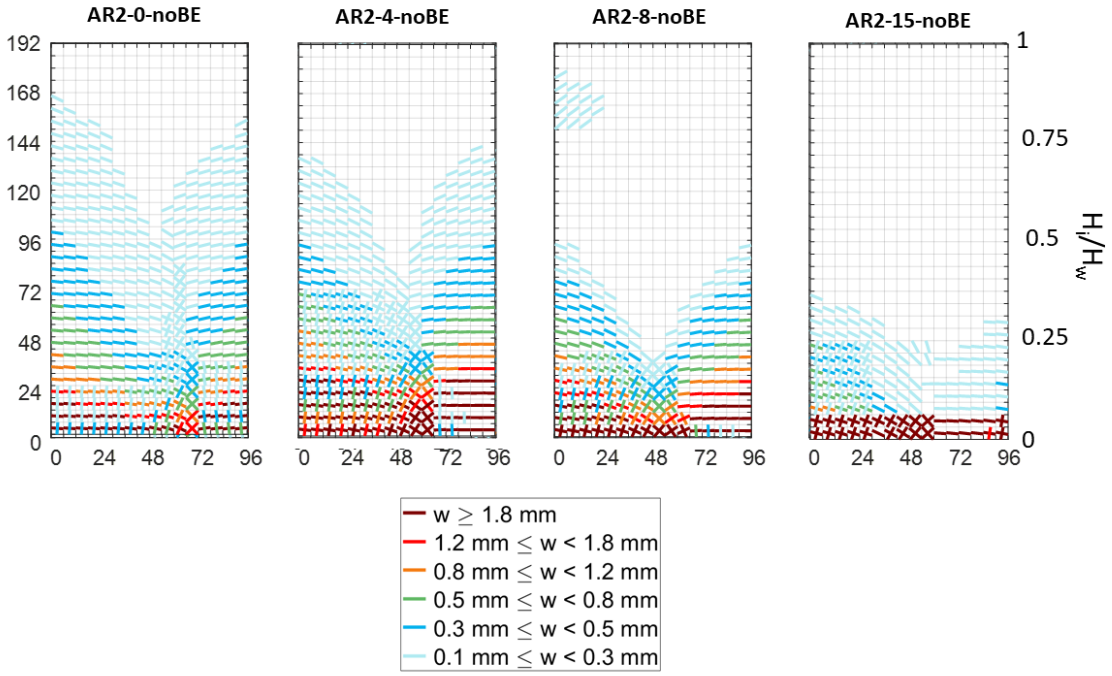


Figure 6.24: Crack pattern at **2% drift ratio** predicted by the **AR=2** wall models with distributed reinforcement, i.e., "**noBE**", and different axial load ratios. AR: Aspect Ratio; ALR: Axial Load Ratio and BE: Boundary Elements. Wall dimensions in inches

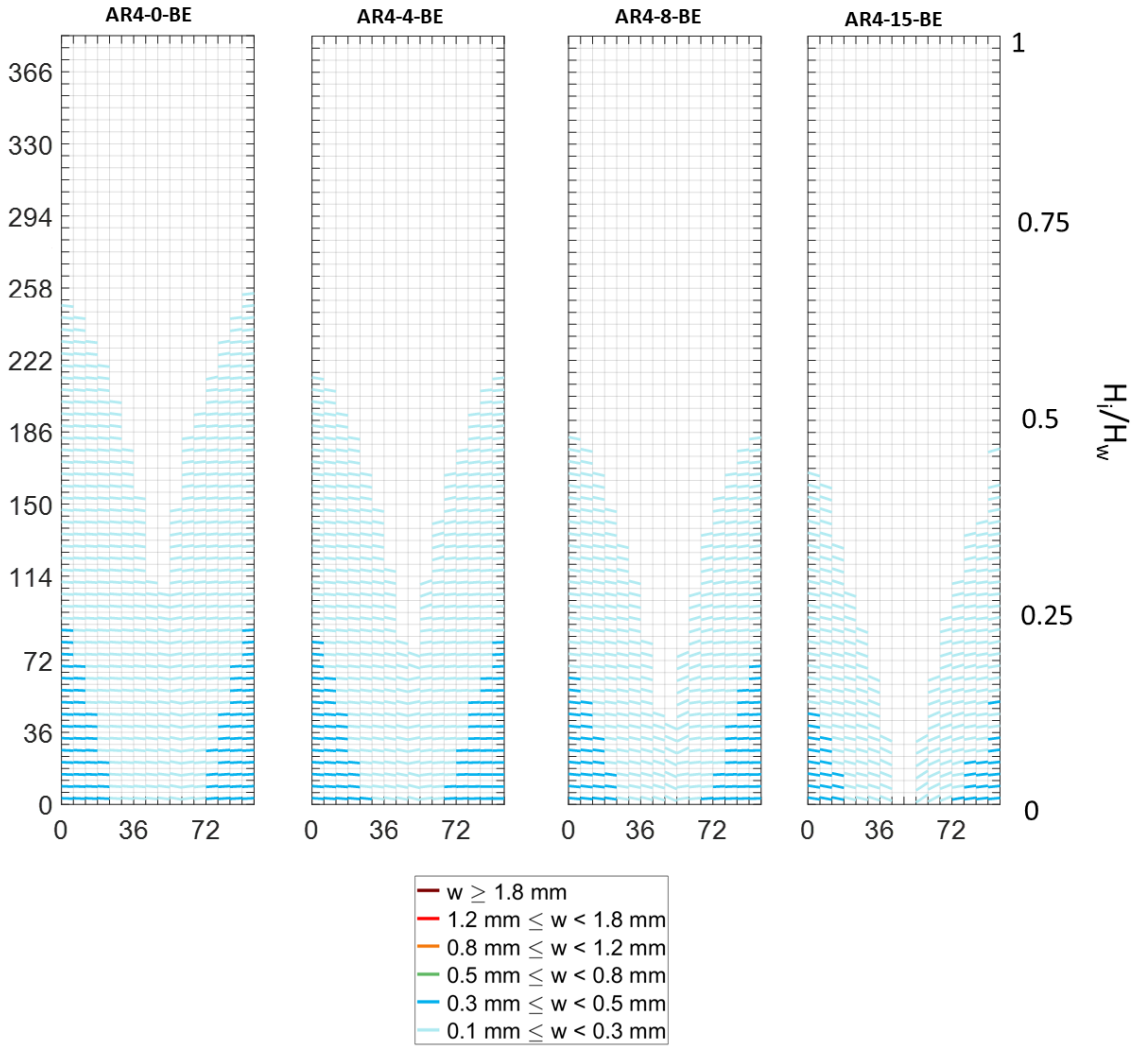


Figure 6.25: Crack pattern at **0.5% drift ratio** predicted by the **AR=4** wall models with **boundary elements** and different axial load ratios. AR: Aspect Ratio; ALR: Axial Load Ratio and BE: Boundary Elements. Wall dimensions in inches

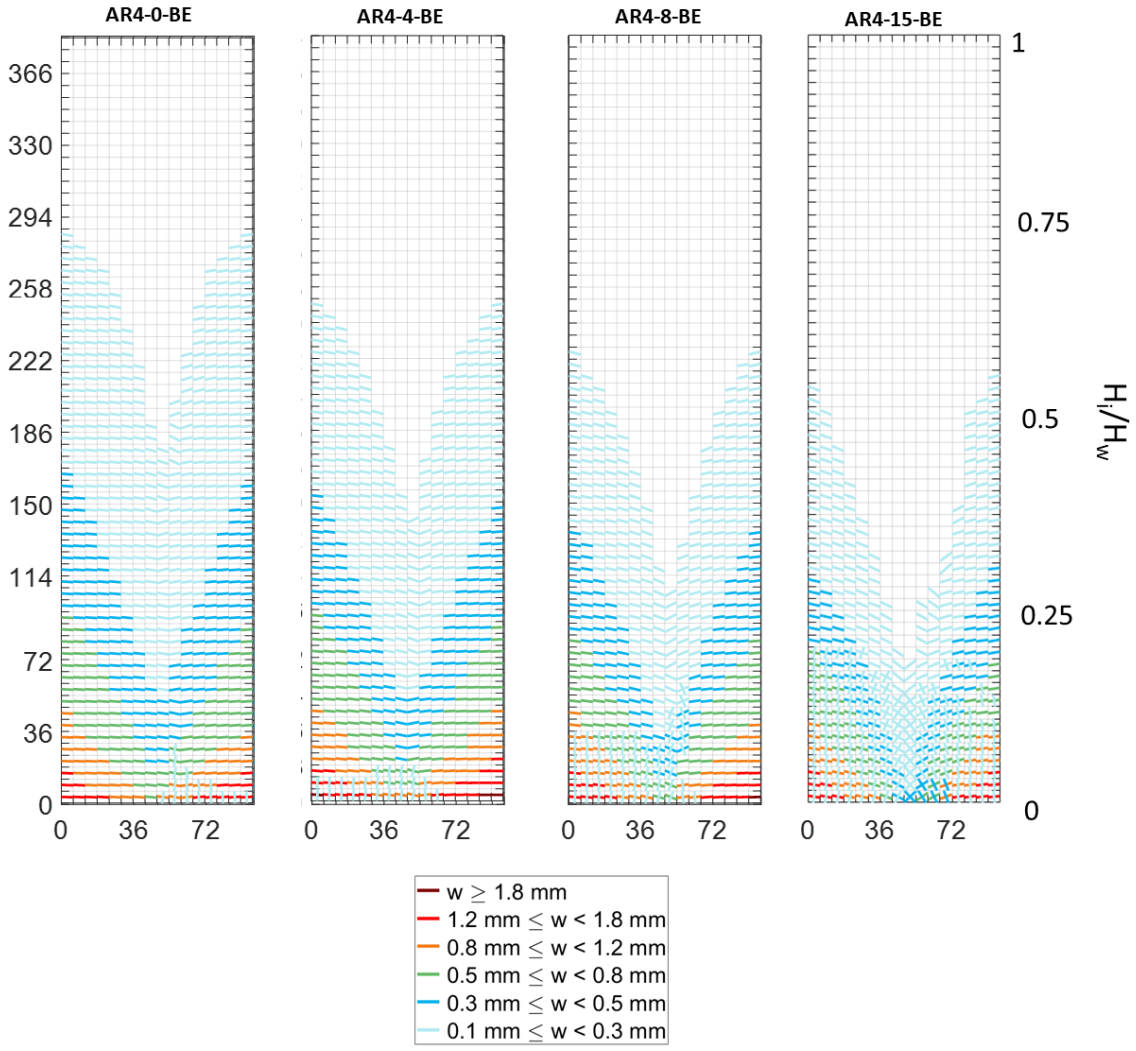


Figure 6.26: Crack pattern at **1% drift ratio** predicted by the **AR=4** wall models with **boundary elements** and different axial load ratios. AR: Aspect Ratio; ALR: Axial Load Ratio and BE: Boundary Elements. Wall dimensions in inches

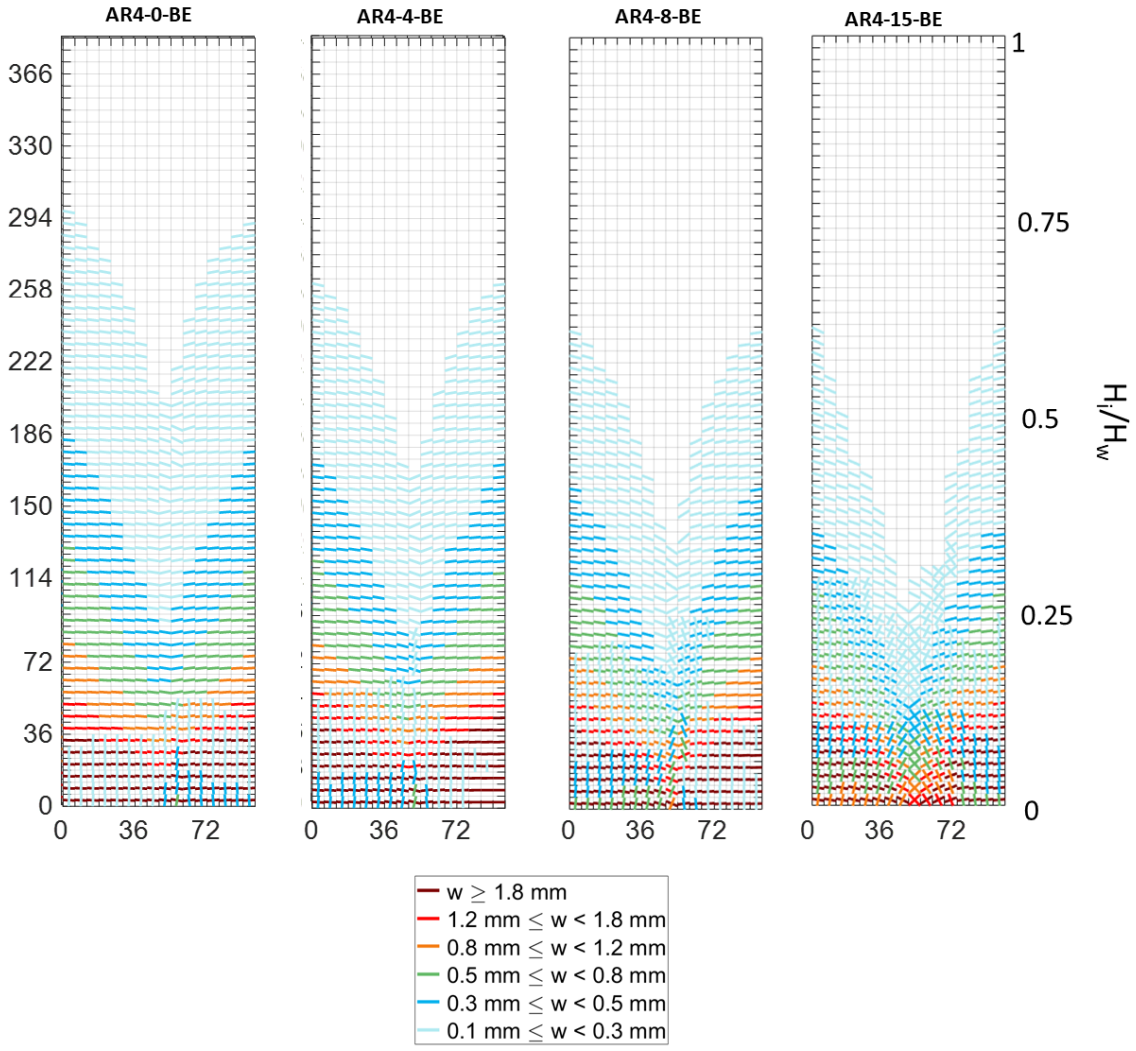


Figure 6.27: Crack pattern at **2% drift ratio** predicted by the **AR=4** wall models with **boundary elements** and different axial load ratios. AR: Aspect Ratio; ALR: Axial Load Ratio and BE: Boundary Elements. Wall dimensions in inches

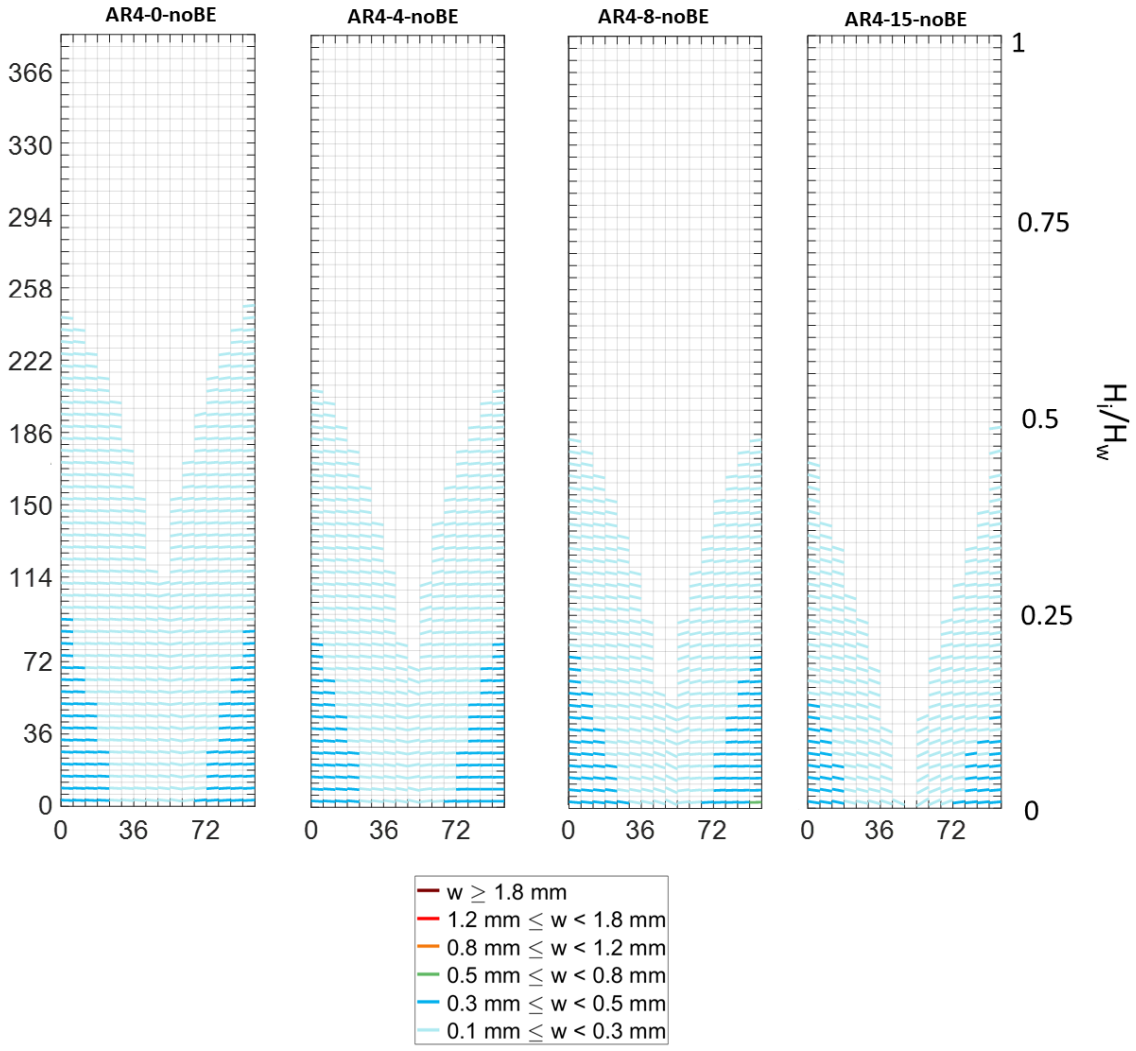


Figure 6.28: Crack pattern at **0.5% drift ratio** predicted by the **AR=4** wall models with distributed reinforcement, i.e., "**noBE**", and different axial load ratios. AR: Aspect Ratio; ALR: Axial Load Ratio and BE: Boundary Elements. Wall dimensions in inches

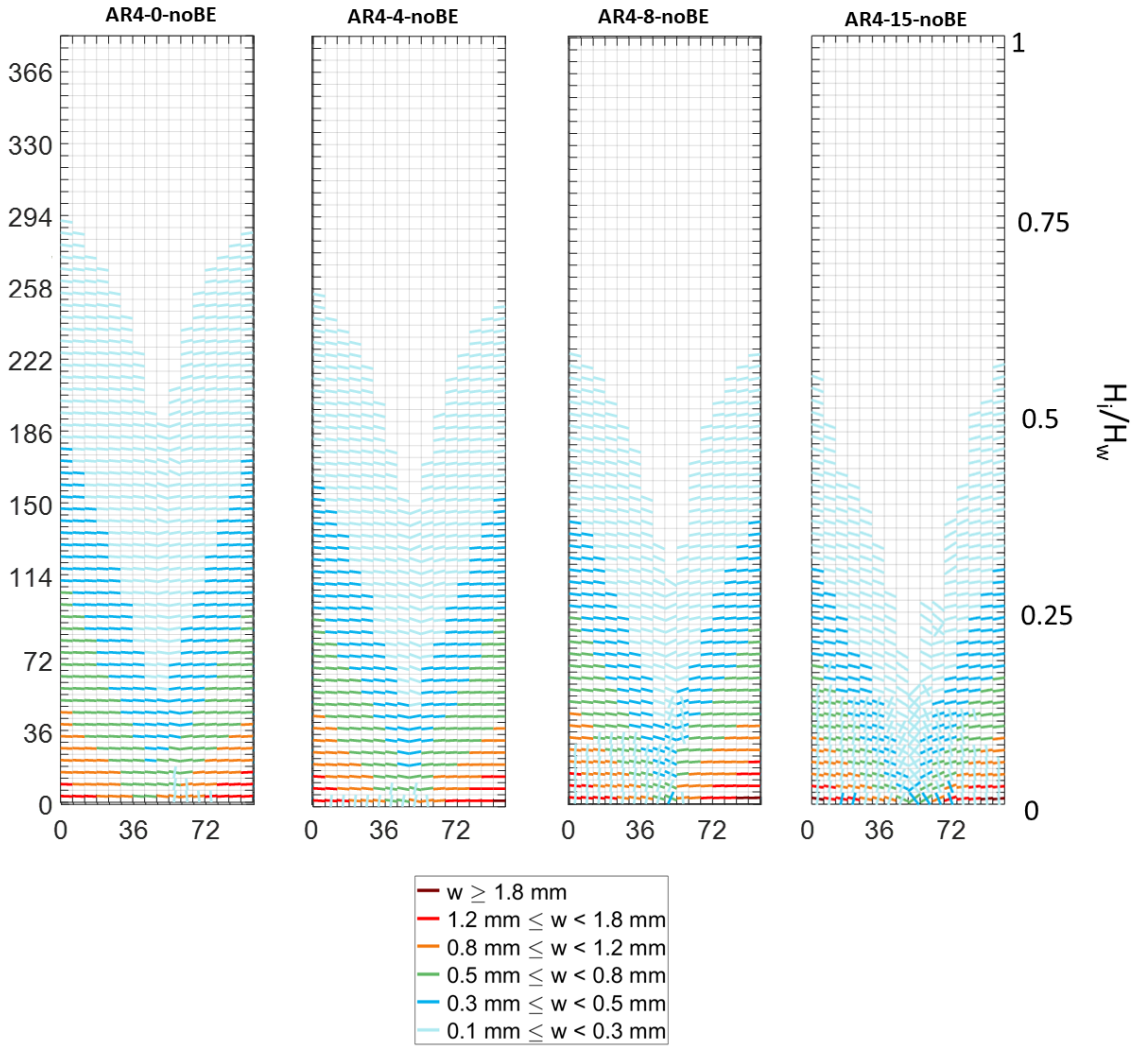


Figure 6.29: Crack pattern at **1% drift ratio** predicted by the **AR=4** wall models with distributed reinforcement, i.e., "**noBE**", and different axial load ratios. AR: Aspect Ratio; ALR: Axial Load Ratio and BE: Boundary Elements. Wall dimensions in inches

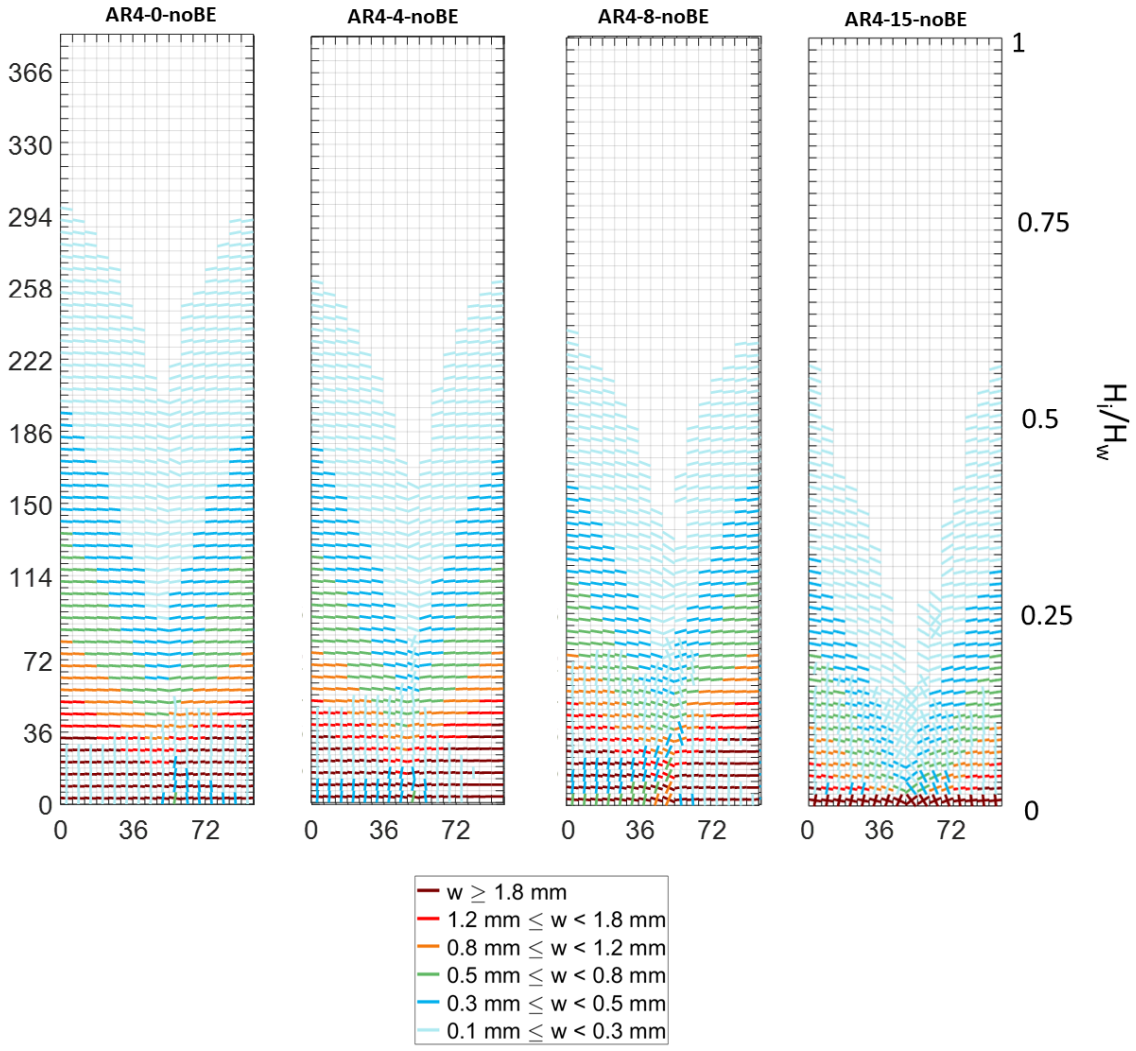


Figure 6.30: Crack pattern at **2% drift ratio** predicted by the **AR=4** wall models with distributed reinforcement, i.e., "**noBE**", and different axial load ratios. AR: Aspect Ratio; ALR: Axial Load Ratio and BE: Boundary Elements. Wall dimensions in inches

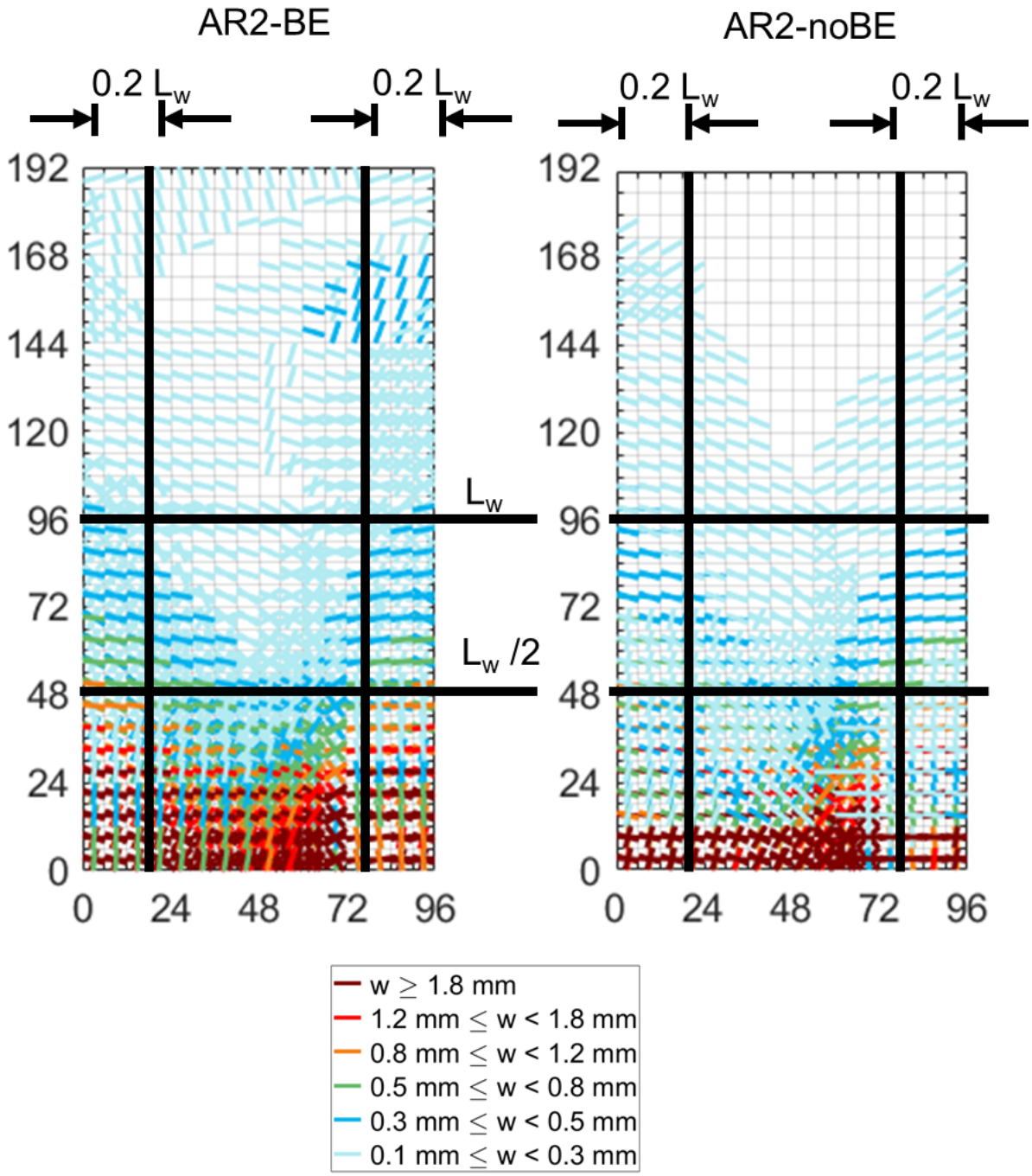


Figure 6.31: Summary of predicted crack pattern for **AR=2** wall models at **2% drift ratio**. Wall dimensions in inches

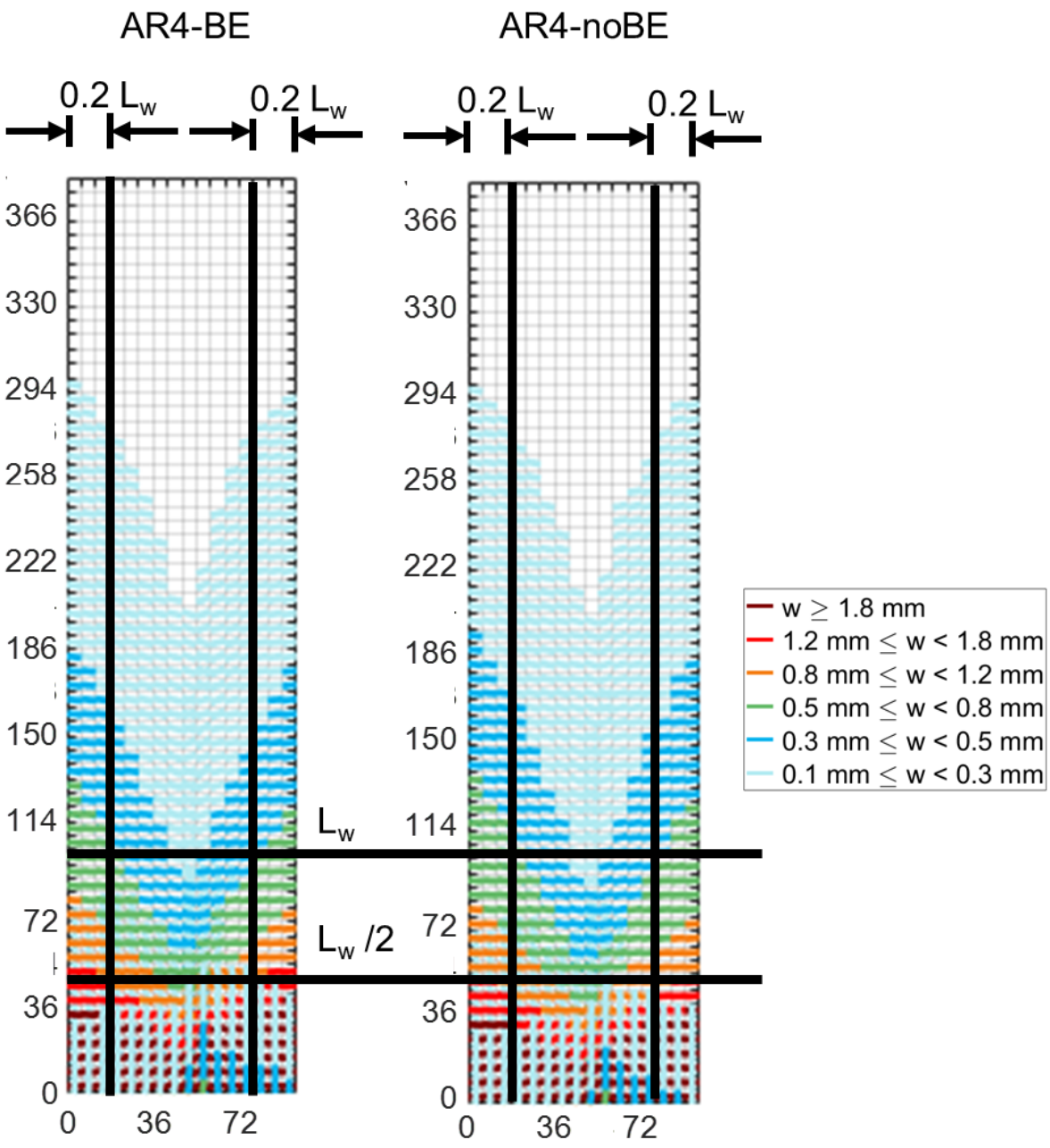


Figure 6.32: Summary of predicted crack pattern for **AR=4** wall models at **2% drift ratio**. Wall dimensions in inches

6.3.3 Consideration of Estimated Crack Widths

In Chapter 5, it was observed that crack angles are well captured by the numerical model (see Fig. 5.25) and that reasonable estimates of the crack width values can be predicted assuming a smeared crack model utilizing the element strains within the 6x6 inches mesh size model. Figs. 5.22 - 5.24 show that the maximum measured crack width at key drift ratios walls fall in the same crack width bins of the numerical estimations modeling the full-scale tested walls. Central to the study presented in this dissertation is the crack width at yield, which can be expected in reinforced concrete shear walls. This information is important for anchor performance, recalling that the maximum estimated crack width at yield of the reinforcement in concrete beams and frame elements was chosen as the reference value to qualify anchors for seismic conditions in EOTA TR 045 (2013). To assess the applicability of this standard to concrete shear walls, the crack width estimations at yield predicted within the parametric study are collected in Fig. 6.33 and overlaid to the literature data presented in Chapter 1 and to the results of the full-scale walls tested within the experimental program presented in this dissertation. Two separate trend lines delineate the crack width at yield progression as the aspect ratio and the axial load ratio of the wall specimens are varied in Fig. 6.33. It is observed that the slopes of these two lines similarly predict an increase in the maximum crack width at yield as the wall slenderness increases. On the other hand, the maximum crack width at yield is predicted to remain overall constant or to slightly decrease as the compression load applied to the wall is increased. It is noted that the numerical model predictions tend to differ from the experimental data measured during small scale shear wall tests, but the difference is on average within about 0.2 mm, which is the amplitude variation included in a crack width bin. Therefore, this difference in crack width may be considered acceptable, especially as it may be attributed to the nature of the data here compared, namely, discrete manual measurements performed during small-scale shear wall tests and numerical crack widths smeared over the panel size and calculated considering reinforcement strains averaged over each finite panel element.

Information regarding the spread of damage along the wall height can be obtained by the estimated crack pattern sketches presented in the previous sections. In particular, Fig. 6.34 shows the maximum elevation of cracked elements with crack width values included in the bin of interest, calculated as for Fig. 6.35, normalized by the wall height versus the amount of applied compression load at 2% drift ratio (Collapse Prevention performance limit state). Crack width values considered in this

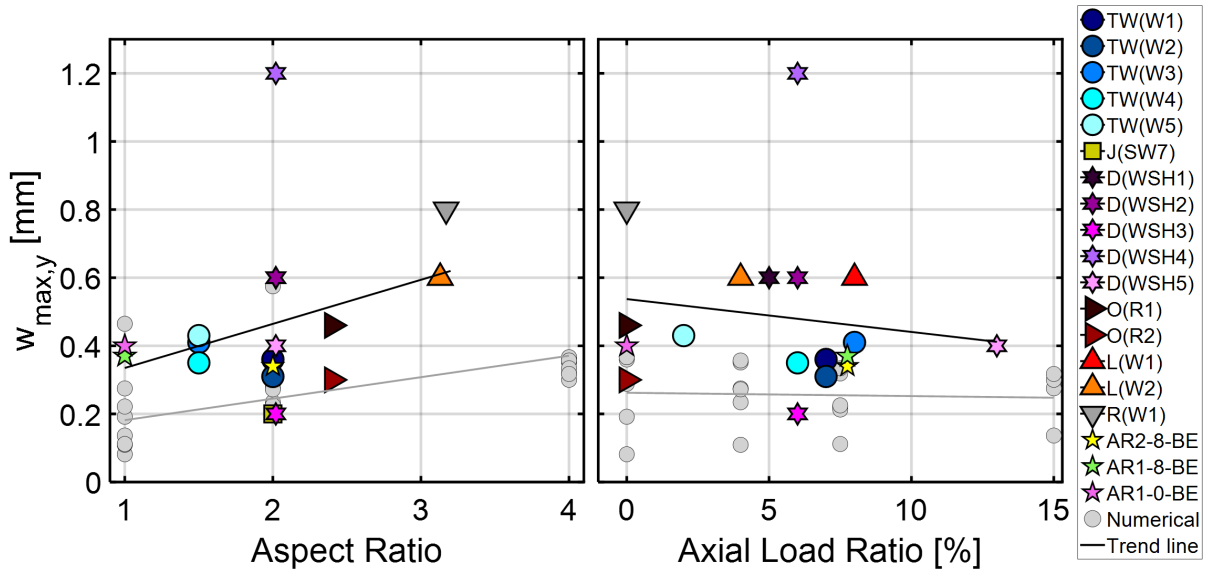


Figure 6.33: Maximum crack width at yield of the reinforcement in rectangular shear walls versus (a) aspect ratio AR and (b) Axial load ratio [%]. Experimental values from literature and numerical from the parametric study are presented for comparison. Note that the experiments in this dissertation are shown with the star symbol; all others are from available literature (see Table 1.4)

Figure cover the minor, moderate, and severe crack width bins, i.e., 0.1 $\leq$ w$\leq$0.3 mm, 0.3 $\leq$ w$\leq$0.5 mm and 0.5 $\leq$ w$\leq$0.8 mm bins. Walls with boundary elements are represented with solid markers, and wall models without end confinement are represented by the open markers. Irrespective of the reinforcement detailing, a clear descending trend is observed in Fig. 6.34, as also highlighted by the linear regression lines. The numerical model predicts crack widths of small amplitude to reduce their maximum elevation in walls with large compression loads with a faster rate than cracks of medium to large amplitude. This observation demonstrates the restraining effect of the compressing axial load applied to the wall on cracks formation, and at the same time shows that walls with large compression may develop severe damage concentrated near the wall base and below 0.4 H_w.

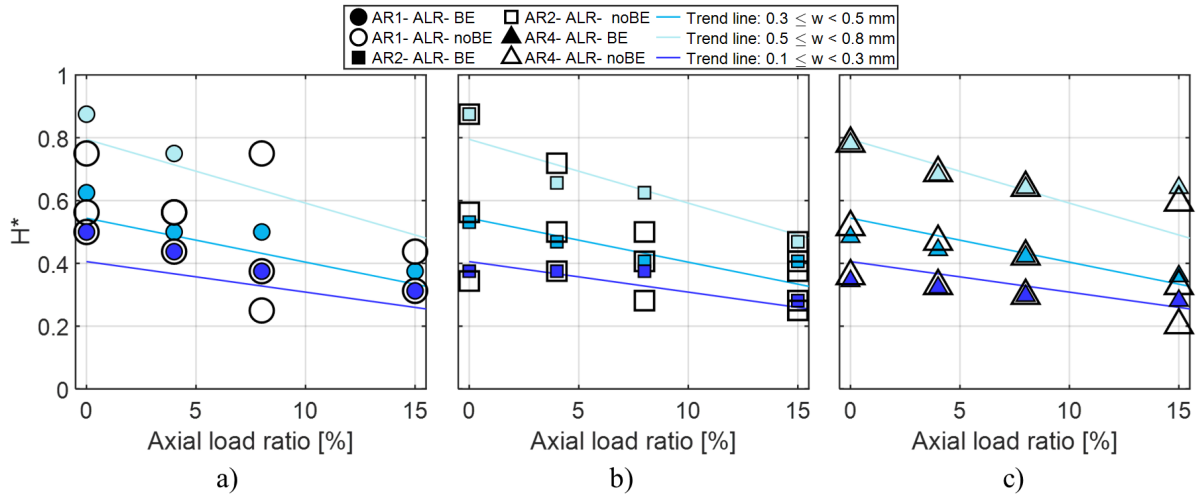


Figure 6.34: Maximum elevation normalized by the wall height of elements in the minor, moderate, and severe crack width bins, i.e., 0.1-0.3 mm, 0.3-0.5 and 0.5-0.8 mm estimated bins, versus applied axial load ratio at the Collapse Prevention limit state (2% drift ratio) for a) AR=1, b) AR=2 and c) AR=4 wall models

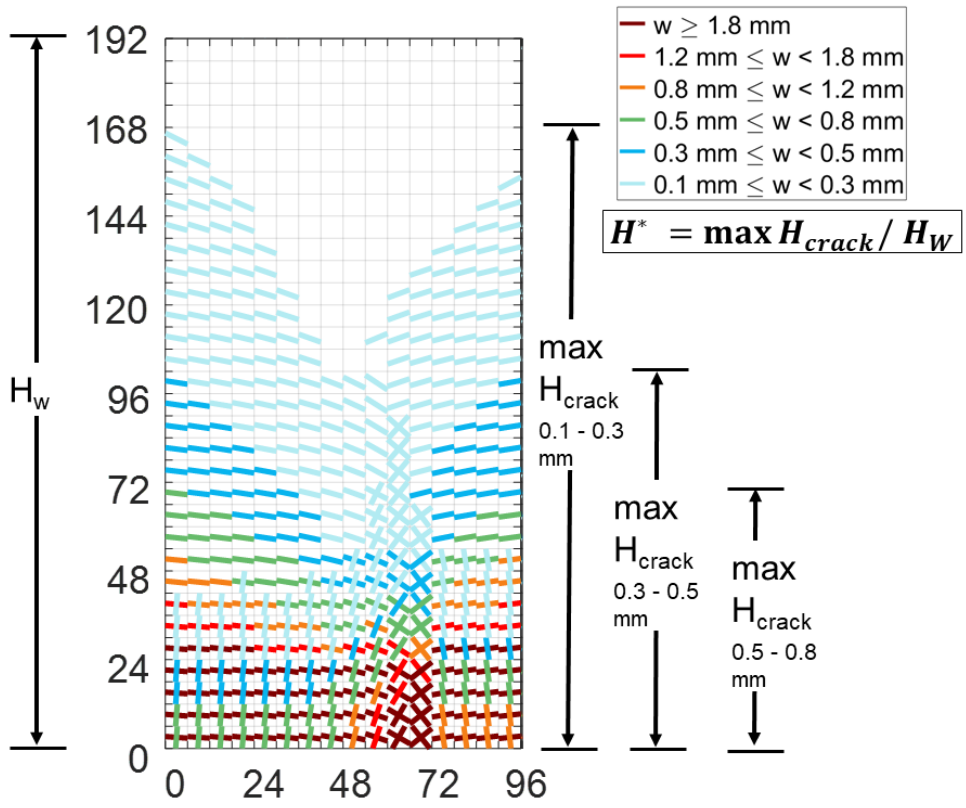


Figure 6.35: Graphic representation of maximum elevation of cracked elements as predicted by the wall model

6.3.4 Damage Distribution as a Function of Building Height

The observations presented in the previous sections are in this section generalized to the buildings height shown in Fig.6.1. In this context, special attention is given to the installation of nonstructural components attached to reinforced concrete shear walls via metal anchors. Notably, current qualification guidelines (i.e., EOTA TR 045 2013, ACI 355 2019) prohibit anchor installation within the plastic hinge region of flexural reinforced concrete frame elements. In a similar manner, the location of anchorage in concrete shear walls should be designed considering the expected damage on the wall produced by lateral forces. Experimental data collected within this study on the response of full-scale reinforced concrete shear walls to lateral loads showed, however, that the plastic hinge length is not as well defined in walls as in frame elements (see Chapters 2 and 3). Moreover, severe damage may develop in other regions of the wall, as a function of its geometry. This parametric study demonstrated that damage distribution is certainly affected by the walls height, axial load and detailing, each of which may be delineated due to a building configuration. Notable observations include the following:

- Low-rise buildings, in this study assumed to be two-story buildings, with bearing walls of AR=1 are expected to carry limited amounts of axial load and therefore well-spread damage is anticipated, especially when the walls are designed as ductile walls with confined boundary elements. Moreover, it is observed that designing low-aspect ratio walls to behave as ductile specimens promotes the damage distribution along the confined boundary elements. This numerical observation is confirmed by the results of the full-scale wall tests presented in the previous Chapters. Finally, it is noted that ductile low-aspect ratio walls are expected to develop significant nonlinear damage on average extending within the first 0.30 L_w from the fixed wall end at the onset of 2% drift ratio. Anchors should, therefore, be avoided in these regions, where significant damage is anticipated.

- Mid-rise buildings, in this study with an assumed four-story configuration, with bearing walls of AR=2 and high-rise buildings, with an assumed twelve-story configuration and with bearing walls of AR=4, usually carry intermediate-large levels of axial load, therefore the damage distribution is expected to be limited by the restraining compression effect to the first 0.5 L_w from the fixed wall end at the onset of 2% drift ratio. This condition may benefit the anchorage of nonstructural components to the wall.

- It is noted that irrespective of the amount of axial load and wall aspect ratio, anchors should be avoided in the region extending up to about 0.3-0.5 L_w from the base of the wall, since large crack widths and severe concentration of damage is here predicted by the numerical model and confirmed by the full-scale wall tests conducted within this research. Alternatively, the wall region within 0.2 H_w is predicted to experience severe damage by the onset of 2% drift ratio, often associated with concrete crushing and out of plane deformation of the reinforcing bars.

- Small-hairline cracks are expected to appear throughout the whole wall face at large wall drift demands. However, small hairline cracks are well tolerated by anchors, as observed in the full-scale tests presented in this dissertation, see Chapter 5.

6.4 Summary Remarks

Nonlinear finite element analyses of twenty-four wall models with different geometric and material properties are conducted in OpenSees to predict the damage response of reinforced concrete shear walls subjected to simulated lateral seismic loads. Smeared crack width values are estimated from the numerical element strains and results are presented in the form of sketches of crack pattern at key drift levels. Performance limit states of Immediate Occupancy, Life Safety and Collapse Prevention are associated with 0.5%, 1% and 2% drift levels in FEMA 356 ASCE 356 (2000) and therefore snapshots of the damage at these drift ratios are considered. The main observations and conclusions reported here highlight the importance of the designed wall, its axial load ratio and geometry:

- Predicted wall lateral strength increases with the amount of applied compression load to the wall models if the provided reinforcement detailing is adequate to carry the lateral and axial load demand. Conversely, wall models with large axial load and distributed reinforcement show strength reduction before or at 2% drift ratio. This observation indicates that a uniform distribution of the reinforcement without confined boundary elements may result inadequate to carry axial load.

- The axial load is predicted to limit the vertical extension of the cracks, as also observed during the full-scale wall tests. Irrespective of the reinforcement detailing, a clear descending trend of the crack width elevation as a function of the compression applied to the wall is observed in Fig. 6.34.

- The presence of confined boundary elements (i.e., the confined wall ends) increases the wall models lateral capacity and promotes the distribution of the damage, especially along the confined boundary elements. This is especially observed in AR=1 and AR=2 wall models. It is noted, however, that large shear stress will have a tendency to modify the failure mode of the shear wall, affecting the stress and strain (and thus the crack) distribution within the wall face.

- Common damage features are observed in all wall models, independently of the applied axial load ratio and reinforcement distribution. The wall region extending 0.2 H_w from the wall base is predicted to experience severe damage by the onset of 2% drift ratio, when concrete crushing and out of plane deformation of the reinforcing bars are expected. It is noted, however, that phenomena of debonding and buckling of the reinforcement are not included in the numerical model formulation.

- The numerical models show that most of the moderate intensity damage develops up to 0.6 H_w from the wall base at Collapse Prevention limit state (2% drift ratio). Small-hairline cracks within the "uncracked elements" of the numerical models, however, are expected to happen at larger wall drift demands.

6.5 Acknowledgment of Publications

Chapter 6, in part is currently being prepared for submission for publication of the material: Faraone, G., Hutchinson, T. C., Piccinin, R., and Silva, J., "Evolution of Simulated Seismic Damage in Concrete Shear Walls of Varying Aspect Ratios." The dissertation author was the primary investigator and author of this material.

Chapter 7

Conclusions and Future Work

A brief summary of each Chapter is described and concluding remarks are discussed in this Chapter. The most relevant general outcomes are presented, and concluding observations on the behavior of post-installed anchors in progressively damaged structural walls are summarized. Future work important to strengthening the body of knowledge gained herein is suggested.

7.1 Motivation for this Research

The research presented in this dissertation was motivated by the essential role that anchors play in the performance of structures during seismic events. Observed performance in recent earthquakes indicates that poor behavior of nonstructural components, equipment, and systems is the greatest contributor to damage, losses, and business interruption for most facilities after a seismic event. Notably, in many situations, the cost of loss of operations can exceed the value of the building itself. These nonstructural components, such as those typically provided for equipment, facade, or other connections, are anchored to the main structural elements through anchors. It is hence important to understand the behavior of anchors in the event of concrete damage associated to an earthquake. Past studies of anchor performance in cracked concrete focused on anchors installed in concrete frame elements, but anchors are often installed in shear walls and diaphragms, which develop a different type of damage profile than the flexure dominated elements utilized in concrete frames.

7.2 Adopted Approach

This dissertation focuses on the behavior of anchors installed in reinforced concrete shear walls subjected to lateral loads. As the concrete damage evolves during increased displacement demand imposed on a shear wall, the load carrying capacity of anchors, which are installed in the wall, is compromised. To evaluate this issue and offer guidance to design practice, this study involved both full-scale experiments and complementary numerical simulations. The test specimens include three full-scale reinforced concrete shear walls with different aspect ratios (AR) anticipated to develop varying lateral load resisting mechanisms, which result in different cracking conditions to the anchors installed on the face of the wall specimens. In particular, wall specimens with AR= 2 and AR= 1 are of focus in these tests due to their prevalence in practice and for the anticipation of flexure and mixed shear-flexure (or near fully shear) dominated response. These wall specimens, being referred to as slender and squat, respectively, provided anchorage material for a total of seventy-two post-installed anchors, representative of two anchoring mechanisms commonly used in practice, namely, bonded and expansion anchors. As the most pronounced effect on anchor performance due to cracks is expected to occur when the anchors are loaded in tension, approximately constant design tension load was applied to the anchors while the wall was laterally cycled. In particular, the expansion anchor type tested in this study relies on expansion forces to generate its tensile resistance, and is the most susceptible to cracks when loaded in tension. These tests showed that the amount of concrete damage exhibited by the walls may severely impact anchor behavior, especially when crack propagation is not restrained by the axial compression applied to the wall. In addition, numerical predictions of reinforced concrete shear walls response to lateral loads are used in this dissertation to support the investigation on anchor behavior in concrete shear walls during seismic events. After validation against the experimental wall data, a finite element model capable of coupling shear and flexure stress components is used in this dissertation to estimate the seismic response of walls with different geometric characteristics and detailing. Results from the parametric study highlight the existence of wall regions where severe damage accumulates, and where anchor installation should be avoided.

7.3 Research Significance

The scope of the experimental and numerical programs performed within this research study is unique. Amongst the most significant contribution of this dissertation is the collection of carefully documented experimental data on the behavior of post-installed anchors in full-scale reinforced concrete shear walls subjected to evolving simulated seismic-induced damage. To the author's knowledge, thus for post-installed tension loaded anchors, horizontally installed in full-scale concrete shear walls have yet to be tested under the scenario of free-evolving cracks. For the first time, these unique tests replicate realistic cracking scenarios occurring in full-scale concrete walls, exposing post-installed anchors to field crack and concrete damage conditions. Crack trajectory and width developed around each of the seventy-two tested anchors, installed in three different full-scale shear walls, afforded a unique opportunity to evaluate the anchors load and displacement. In addition to the anchor data, this research resulted in a large experimental database demonstrating the response to lateral loads of full-scale reinforced concrete shear walls of different aspect ratios. Literature on concrete shear walls is often limited to small scale specimens, which may be affected by scale effects. On the contrary, these experiments offer information representative of the response of full-scale concrete shear walls to assess damage and to evaluate the robustness of the drift limit values commonly used in design practice. In addition, the experimental load-displacement response of these full-scale walls are used to evaluate the robustness of a nonlinear finite element model to simulate shear wall response to simulated seismic loading. In particular, the validation against the two full-scale squat walls is an important contribution expanding the applicability of the adopted numerical model to low aspect ratio walls. Finally, the numerical parametric study performed with this validated model provides original analysis regarding the predicted crack pattern and damage in different reinforced concrete shear walls, highlighting the anticipated damaged regions where anchor installation should be avoided.

7.4 Primary Conclusions

7.4.1 Experimental Program: Wall Tests and Anchor Tests

The most significant conclusions obtained from the full-scale experiments pertained to the walls response and the behavior of anchors in uncracked concrete. These are summarized as follows:

1. Coupled shear-flexure behavior dominated the response of the full-scale walls, which developed the design flexural strength and well distributed tension and shear cracks during the application of simulated earthquake loads. Wall response to lateral load was not affected by the presence of the tension loaded anchors installed in the wall faces. In particular the following was observed:

    - The slender wall failed in flexure, with concrete crushing at the wall end boundaries, where longitudinal reinforcing bars buckled and fractured at a drift amplitude of 3%, leading to an approximately 20% lateral load reduction. The evolution of the crack pattern and the crack characteristics, namely the width and spacing, demonstrate the specimens' dominant response was a mode consistent with flexure, as anticipated for a slender wall. Consistent with this physical observation, the measured flexural deformation was considerably larger than the shear deformation, with the shear contribution to the total lateral displacement on average less than about 20%. Shear contributions to the lateral displacement were estimated to be roughly constant for the duration of the cyclic displacement history applied to the wall, as expected for flexure dominated RC shear walls. A non-negligible wall vertical extension was measured at the end of the test, attributed to the fracture of ten of the eighteen longitudinal boundary reinforcing bars.
    - The two squat walls exhibited a mixed shear-flexure failure, physically manifested by reinforcing bar buckling and concrete crushing, regardless of the levels of constant axial loads applied to the walls (namely 7.5% and 0% of their section capacity). The average contribution of shear deformation to the total wall lateral deformation was determined to be about 40% for both walls. However, the shear displacements increased significantly with the drift demand in the squat wall absent supplementary axial load, whereas it remained approximately constant in the comparable squat wall with axial load imposed. The degradation of the shear-transfer

mechanism is, indeed, enhanced by unrestrained shear sliding in walls absent superimposed axial load. Nonetheless, boundary elements were implemented in the walls and demonstrated the engagement of the flexural component of response and consequently an increase in the displacement capacity of the walls. Results indicate that the displacement ductility capacity of these low-aspect ratio walls is comparable to the experimentally determined ductility capacity measured for the related, but slender wall previously tested within this research program. Moreover, the experimental results of the squat wall tests herein offered favorable comparison to shear strength values predicted using a shear strength model proposed by Krolicki et al. (2011). Results predict a mixed shear-flexure failure at a displacement ductility of about 5, reflecting the response modification factor R = 5 currently attributed to RC specially reinforced shear walls in ASCE/SEI 7-16 (2016).

- Each of the three full-scale walls developed well defined zones of significant damage closer to the base of the wall. These zones of plastification could be characterized via a measurable plastic hinge length. The measured plastic hinge length at the base of each wall compared favorably with empirical relations available in the literature.

2. ASCE 41 (2014) is adopted herein to construct envelope of the experimental hysteresis curves for the three tested walls. Analysis of these load-displacement envelopes indicates that drift capacity is consistently underestimated for all three walls. In particular, it is noted that the shear strength of the squat wall tested without axial load is significantly overestimated. The walls performance at first yield, effective yield, lateral strength and 80% post-strength is also evaluated and compared to drift limits proposed in design and rehabilitation guidelines (ASCE 356 2000), namely, Immediate Occupancy, Life Safety and Collapse Prevention performance limit states. It is observed that drift limit values associated with the latter underestimate the actual drift capacity of the tested full-scale walls, leading to conservative estimations. Physical damage at these performance limit states was carefully documented in the test program to elicit the effect of axial load on reinforced concrete shear walls and facilitate assessment of the progression of damage. Analysis of this photographic and other documentation taken during testing indicates that the presence of axial compression facilitated crack closure and therefore enhanced strain localization and local damage within the

lower half of the wall's height, as also reflected in the measured curvature profile.

3. The slender wall was designed to maximize flexural cracks, whereas the two squat walls were designed with nominally minimum horizontal reinforcement required by current U.S. design codes to enhance their shear response. Comparatively robust boundary elements at the ends of all three walls offered sufficient strength to assure the walls would undergo several cyclic load reversals prior to strength deterioration. A well distributed crack pattern developed in all three walls, with mixed shear-flexure components in the squat walls, rendering a variety of crack scenarios unique to each of the installed anchors. The response of the primary lateral force resisting wall element in which anchors are installed is important for assessing the anchor performance in cracked conditions, as the comparison of the anchors response in the three considered full-scale walls demonstrated. To facilitate comparison across anchors installed in all walls, the state of damage at the residual state of the wall in the proximity of the anchors was classified as minor, moderate and severe. The most notable conclusions regarding the walls damage distribution and its impact on anchor performance include the following:

    - The stress distribution in the squat walls manifested in the form of concrete diagonal struts along with ample damage to the concrete in the form of a dense network of cracks. The load capacity of anchors installed in these struts was progressively affected during the wall lateral test and severely reduced by the end of the test, as shown by the residual direct tension tests to failure.
    - In contrast, in the slender walls, the damage was largely localized within a plastic hinge region, nominally considered to extend from the base of the wall to a distance 50% of the wall length and in the boundary elements. Moreover, the relatively high self-weight of the full-scale slender wall in addition to the applied axial load coupled with its predominantly flexural response to lateral load resulted in a limited effect on overall anchor performance, as reflected by the residual anchor capacity from tension to failure tests.
    - Comparing the pair of squat walls considered herein, it is notable that the axial load applied to one of the squat walls limited the concrete damage and thus beneficially impacted anchor performance. In particular, the only three anchors which retained their design load within

an average 10% variation during the entire wall cyclic test were installed in the wall with imposed axial load. These three baseline anchors were not crossed by cracks. Anchors installed in the wall without axial load, instead, experienced more significant load reduction, on average about 20% more compared with anchors installed in the most damaged regions of the comparable wall tested with supplemental axial load.

- The maximum global axial displacement of the anchors ranged on average from 0.02 inches for baseline anchors (not in the proximity of cracks) to an average 0.52 inches for anchors in the region generally extending from the wall base up to 50% of the wall length and along the main strut directions (in low aspect ratio walls only). The relatively large anchor axial displacements in the most severely damaged regions coupled with their significant load loss emphasizes the need to avoid anchor installations in such heavenly damaged regions of wall components.
- It is concluded that in slender, ductile walls, designed with boundary elements eliciting a flexural failure, the damage is anticipated to extend from the wall toe over the wall height to 50% of the wall length, and in the confined end regions of the wall. In low-aspect ratio walls designed as ductile specimens, instead, the main diagonal struts are the high stress zones where severe damage occurs, followed by the zone extending over the wall height to 50% of the wall length and the boundary elements. The intensity of damage in the three regions depends on different factors affecting the stress distribution within the wall, such as the reinforcement layout and the amount of axial load applied to the wall, as these also control the type of failure of the wall. It is noted, however, that brittle shear failure, e.g., sliding shear failure, is anticipated to generally result in less damage along the wall height, thus minimizing the effect of wall damage on the performance of anchors placed outside of the failure zone. It is clear, however, that sliding shear failure is not a desirable failure mode for concrete structures, causing potentially more severe safety and global stability issues for the structure.

Overall, anchor performance was affected by the width of the cracks and the amount of concrete spalling in the anchor vicinity, being less sensitive to the type of cracks. It is also noted that the

anchors considered in this study represent a high performance post-installed expansion anchor for use in cracked concrete conditions. Since damage accumulates in specific regions of a RC wall, as described above, anchors should be avoided in these locations, to assure that acceptable anchor load capacity is preserved and excessive anchor displacement is not realized. Indeed, improved anchor performance was observed outside of these regions, as confirmed by the tension to failure test results.

7.4.2 Numerical Program: Validation and Parametric Study

The primary conclusions regarding the finite element validation effort and subsequent parametric study are summarized as follows:

1. Results of the validation study show that the Shear-Flexure Interaction - Multiple Vertical Line Element Model (SFI-MVLEM) model is able to predict the experimentally observed response of laterally cycled shear walls with a high degree of accuracy. Two numerical models, with different geometric discretizations were constructed to evaluate the effect of the mesh on the results. Both numerical models, with dense and sparse meshes, predicted the wall strength within on average 10% that measured during the tests. Moreover, the local response of each of the tested shear walls subjected to simulated seismic loads are captured with a high level of confidence. In particular, the numerical models reasonably predicted the measured load-displacement response characteristics of the three tested full-scale walls including their lateral stiffness, lateral load capacity and salient hysteretic pinching behavior. On the contrary, ultimate drift, wall lateral strength and degradation in lateral load after strength is reached are less accurate when predicted with the proposed numerical model. Capturing these limit states is likely limited by the models inability to explicitly consider reinforcement bar-concrete debonding, local bar buckling and concrete spalling, each of which were observed at the end of the wall tests. Successful representation of the shear-flexure interaction behavior is observed for both the slender and squat walls designed to fail in flexure. The model accurately captures the average shear contribution to the total displacement measured throughout the tests. The damage characterization of walls subjected to equivalent lateral loads is also sufficiently well represented. The finite element model estimates the angle of orientation of the cracks in each element, under the assumption that cracks remain orthogonal to the main concrete

struts. The orientation of the cracks is in good agreement with the majority of the experimental cracks annotated during the test program. In addition, crack width values were approximated by processing the numerical data according to the smeared crack approach. Predicted crack width values fall in the same amplitude range as those of the discrete crack widths measured during the tests.

2. Nonlinear finite element analysis of twenty-four wall models with different geometric and material properties are conducted using the aforementioned numerical modeling approach. Each of the models are subjected to the same simulated seismic load history with the goal of predicting their global hysteresis and inferring their local damage. To evaluate the later, smeared crack width values are estimated from the element strain values and results are presented in the form of sketches of predicted crack patterns at key drift levels. Performance limit states of Immediate Occupancy, Life Safety and Collapse Prevention are associated with 0.5%, 1% and 2% drift levels in accordance with ASCE 356 (2000). As a result, the damage at these drift ratios is presented and cross-compared for the different wall geometries and detailing scenarios. The key conclusions from this numerical parametric study are as follows:

    - Predicted wall lateral strength increases with the amount of applied compression load to the wall if the provided reinforcement detailing is adequate to carry the lateral and axial load demand. Conversely, wall models with large axial load and distributed reinforcement demonstrate an appreciable strength reduction prior to or at about 2% drift ratio. This observation indicates that a uniform distribution of the reinforcement without confined boundary elements may result in inadequate axial load carrying capacity.

    - The axial load is predicted to limit the vertical extension of the cracks, as also observed during the full-scale wall tests. Irrespective of the reinforcement detailing, a clear descending trend of the crack width extension along the wall height as a function of the compression applied to the wall is observed.

    - The presence of confined boundary elements (i.e., the confined region at the wall ends) increases the wall models lateral capacity and promotes the distribution of damage, especially along the confined boundary elements. This is especially observed in AR=1 and AR=2 wall

models. It is noted, however, that large shear stress will have a tendency to modify the failure mode of the shear wall, affecting the stress and strain and thus the crack distribution within the wall face.

- Common damage features are observed in all wall models, independent of the applied axial load ratio and reinforcement distribution. Notably, the wall region extending 0.2 H_w (where H_w = wall height) from the wall base is predicted to experience severe damage by the onset of the collapse prevention limit state (2% drift ratio), when concrete crushing and out of plane deformation of the reinforcing bars are expected. It is noted, however, that the phenomena of debonding and buckling of the reinforcement are not explicitly considered in the numerical model formulation.
- The numerical models show that most of the moderate intensity damage develops up to 0.6 H_w from the wall base at the Collapse Prevention limit state (2% drift ratio). Small-hairline cracks within the "uncracked elements" of the numerical models, however, are expected to happen at larger wall drift demands.

7.5 Recommendations for Future Research

The current work aims to evaluate for the first time the behavior of post-installed anchors in reinforced concrete shear walls to assess their performance under different cracking conditions, typical of reinforced concrete walls. The experimental portion of this work only sheds light on the problem of anchor installation in concrete shear walls, hence additional research should address more consistently the following issues:

- These experimental efforts only considered two types of post-installed anchors loaded under constant tension. However, nominal amounts of shear load may be anticipated for most the horizontally places anchors, as the gravity loads provided by the attached component is always present when anchors are placed horizontally. Shear demand may reduce the final capacity of the anchors, therefore some testing involving mixed loading conditions should be carried out. In addition, different types of post-installed anchors as well as cast-in anchors may be tested to extend this investigation to assess if additional negative effects are imposed on other types of anchors in the

presence of wall damage.

- In the full-scale tests presented herein, a global displacement including the anchor displacement was measured for each anchor. Quantifying anchor displacement is important, particularly in the optic of defining the serviceability limit state of the anchor. The author suggests that future experimental efforts should seek to isolate the different components of anchor displacement during wall cycling. This is a challenging task due to the surrounding damaged surface of concrete and the desire to preserve a sustained axial (and possibly shear) load on the anchor.

- The relation between the response modification R factor assumed in the wall design phase and the amount of damage and displacement tolerated by the wall should be assessed systematically for various wall types as a way to predict concrete damage related to anchor performance. Hence, reliable anchor qualification testing can be defined to avoid failure of anchorage attached nonstructural components. To expand the work presented herein, investigation of the performance of anchors in other structural elements defined by different response modification R factors could be carried out, similarly at full-scale. Additional study of the following key reinforced concrete components is needed:

  - Reinforced concrete wall piers and spandrels, i.e., vertical and horizontal wall segments between window openings in buildings with reinforced perimeter walls. These wall segments often comprise the primary lateral load-resisting elements of existing and new buildings, and are subjected to high shear stresses and shear-controlled damage. These regions may pose detrimental to anchor performance.
  - Reinforced concrete floor diaphragms with focus on corner regions and openings. These components show a mixed shear-flexure response to lateral loads and their deformation may be controlled by stress concentration at corner regions and by shear lag effects. In addition to the large component of shear deformations, these stiff concrete floors diaphragms may interfere with the flexural deformations typical of reinforced concrete moment frames. In particular, the development of the plastic hinge region may be compromised and anchor installation may also be affected by this change in plastic hinge length.

  Understanding the damage in these important reinforced concrete components would allow a pre-

cise mapping of concrete damage and anchor performance used to classify different types of anchors. However, it is noted that the failure mode is the main factor affecting anchor performance, as the damage distribution is characterized by the failure mode and thus critical to anchor response. Within the same suggested R factor value, i.e., within the same category of lateral resisting structural component varied failure modes may develop, triggered by varied geometric and detailing characteristics. Therefore, the author believes that seismic anchor performance classification should focus more on the expected damage failure mode, rather than on the R factor value associated with the different structural components.

The numerical portion of this works underlines the importance and potential of finite element modeling to predict the response of reinforced concrete shear walls to lateral loads. Efficient models allow a reasonable understanding of the behavior of new and existing walls, and can be used to design for reduced seismic damage and ultimately improved performance of anchorage. Nonetheless, the validation study presented in this dissertation highlights the need for additional studies to address the following key points:

- The effect of bond between concrete and reinforcing steel bars on the wall response and on the crack pattern. The finite element model used in this dissertation does not consider the effect of bond-slip deformations and bond stress on the predicted wall response.

- The extent of crack evolution and crack width intensity due to the severe limit state of bar buckling was not incorporated herein. High fidelity finite element modeling tools are available for such assessment and would be of value to utilize them in modeling the experimental walls presented herein. The author recognizes however that such numerical tools are not mainstream and readily available. An additional challenge is to facilitate a link between numerical models for buckling with a realistic crack width estimation and quantification of concrete crushing.

Appendix A

Slender and Squat Wall Test Specimens: Design Calculations

The design process of the wall test specimens presented in Chapters 2 and 3 is reported here. The calculations are illustrated in English units, according to the U.S. design building codes adopted in the design process (ACI 318 2011, ASCE/SEI 7-16 2016, ACI 318 2019). Note that 1 kip = 4.45 kN and 1 in = 25.4 mm.

A.1 Slender Wall Design

The slender wall was designed in accordance with the most recent design codes at the time of construction (ASCE/SEI 7-16 2016, ACI 318 2019) and assuming a 2-story office prototype building with load bearing reinforced concrete shear walls as lateral force resisting system. The baseline size of the prototypical load bearing RC wall was 24 ft tall by 8 ft long, having a design tributary area of 35 ft x 35 ft. Considering the resultant lateral load applied at 2/3 of the total height, the physical specimen was constructed with a height of 16 ft. In the design process it is assumed that the foundation system is rigid and the wall is considered to have a fixed base.

The prototype structure was assumed located in downtown Los Angeles (34.040° N, 118.247 ° W), at a site class D, with mapped spectral response acceleration values, $S_{DS} = 1.555g$ and $S_{D1} = 0.819g$, taken from the USGS website (USGS, 2018). The design was based on the response modification factor

R=5, assigned to bearing wall systems with special reinforced concrete shear walls (ASCE/SEI 7-16 2016). The Risk Category is assumed to be I or II (buildings of minor importance/ordinary bullrings), with Seismic Importance Factor I = 1.0. The material properties considered in the design phase are:

- Concrete strength $f'_c = 5000psi$
- Steel yield strength $f_y = 60ksi$

A.1.1 Load Combinations

Load combinations for the seismic design of concrete are given in ASCE/SEI 7-16 (2016) §2.3.2:

$1.2D + 1.0E + L$

$0.9D + 1.0E$

where D stands for dead load, L for live load and E for earthquake load. E includes both horizontal and vertical components (ASCE/SEI 7-16 2016 §12.4-1:4):

$$E = \rho Q_E \pm 0.2 S_{DS} D. \tag{A.1}$$

Since

$$S_{MS} = F_a S_s = 2.333, \tag{A.2}$$

$$S_{DS} = 2/3 S_{MS} = 1.555 \tag{A.3}$$

(ASCE 7-10 §11.4-1 & 11.4-3) and the redundancy factor ρ is assumed to be equal to unity, the governing load combinations are:

$$1.51D + 1.0L \pm 1.0Q_E \tag{A.4}$$

$$0.589D \pm 1.0Q_E. \tag{A.5}$$

A.1.2 Design Loads

Structural dead loads include the self-weight of the wall and the self-weight of 6 inches concrete slab (concrete unit weight γ, is 150 pcf). Superimposed dead and live loads assume the design of the 2 story building, as reported in Tables A.1 and A.2. Gravity loads per each floor are obtained considering the tributary area $A_i = 1225 ft^2$, as reported in Table A.3.

Table A.1: Summary of the Dead Loads assumed in the design of the slender wall

Superimposed Floor Dead Load (Uniformly distributed) [psf]	
Covering	1
Mechanical electrical	3
Ceiling	3
Misc.	3
	Total 10
Superimposed Roof Dead Load (Uniformly distributed) [psf]	
Roofing	5
Ceiling	3
Insulation	3
Mechanical electrical	3
Misc.	1
	Total 15

Table A.2: Superimposed Live Loads on the slender wall*

Live loads for Office Building [psf]	
Floor 2	50
Roof	20
Partition walls	15

Note: partition walls weight for floor area needs to be considered in the superimposed live loads on the second floor.
*: from Table- Minimum Uniformly Distributed Live Loads, in ASCE 7-16 ASCE/SEI 7-16 (2016).

The effective seismic weight for each floor, which includes 15 psf partition weight per floor area, is reported in Table A.4. The effective seismic weight at the base of the wall is $W = 30 + 217 = 247 kips$ (ASCE/SEI 7-16 2016). Known the effective seismic weight, the base shear and the vertical distribution of seismic forces are calculated according to ASCE/SEI 7-16 (2016) §12.8 (Equivalent lateral load

Table A.3: Gravity load on the slender wall specimen

Gravity load per floor						
Floor	**Dead Load**		**Structural Self-Weight**		**Live Load**	
	kips	*psf*	*kips*	*psf*	*kips*	*psf*
Roof	18	15	92	75	25	20
Floor 2	12	10	106	87	80	65

Note: structural self-weight at the "roof" level is the slab weight.
Structural self-weight at the "floor 2" level is the slab weight + half of the wall self-weight.

procedure).

$$T = 0.02h_n^{0.75} = 0.2sec \tag{A.6}$$

$$C_s = \frac{S_{DS}}{R} \cdot I_e = 0.31 \tag{A.7}$$

$$C_s(Upperlimit) = \frac{S_{D1}}{T \cdot \frac{R}{I_e}} = 1.3 \tag{A.8}$$

$$C_s(Lowerlimit,1) = 0.044 \cdot S_{Ds} \cdot I_e = 0.07 \geqslant 0.01 \tag{A.9}$$

$$C_s(Lowerlimit,2) = 0.5 \cdot \frac{S_1}{R} \cdot I_e = 0.08 \tag{A.10}$$

$$V = C_s \cdot W = 77kips \tag{A.11}$$

$$F_x = C_{vx} \cdot V \tag{A.12}$$

$$C_{vx} = \frac{w_x h_x^k}{[\sum_{i=1}^{n} w_i h_i^k]} \tag{A.13}$$

where k = 1 for structures having a period less than 0.5 sec.

The seismic design story shear ASCE/SEI 7-16 (2016) §12.8.4 is therefore calculated as

$$V_x = [\sum_{i=x}^{n} F_i] \tag{A.14}$$

and results are reported in Table A.5.

Table A.4: Effective seismic weight per floor of the slender wall specimen

Seismic load on the wall [kips]		
Floor	**Superimposed Dead Load**	**Structural self-weight + Partition walls**
Roof	18	92
2	12	125
Total	30	217

Table A.5: Seismic design story shear of the slender wall specimen

Floor	**Height** *[ft]*	**Weight per floor** *[kips]*	**Vertical distribution factor**		**Vertical force distribution** *[kips]*	**Design lateral force** *[kips]*	**Design moment** *[kips - ft]*
	h_x	w_x	$w_x h_x^k$	C_{vx}	F_x	V_E	M_E
Roof	24	110	2646	0.62	47	47	0
2	12	137	1643	0.38	29	77	568
1	0	0	0	0	0.00	0.00	1490

A.1.3 Actions at the Base of the Slender Wall

The dead and live load cause axial load only and the earthquake forces produce shear and moment only. Since the axial load is less than the axial load that causes the balanced strain condition, the combination that gives the lower bound axial load is more critical for the moment strength of the wall. The governing axial load, moment and shear at the base of the wall are:

$$P_u = 0.589D = 154kips \tag{A.15}$$

$$M_u = 1490kips - ft \tag{A.16}$$

$$V_u = 77kips \tag{A.17}$$

A.2 Squat Walls Design

Similarly to the slender wall design, the squat walls were designed in accordance with the most recent design codes at the time of construction (ASCE/SEI 7-16 2016; ACI 318 2019) and assuming a single story prototype building with load bearing reinforced concrete shear walls as lateral force resisting system. The baseline size of the prototypical load bearing RC wall was 12 ft tall by 8 ft long, having a design tributary area of 35 ft x 35 ft. Considering the resultant lateral load applied at 2/3 of the total height, the physical specimen was constructed with a height of 8 ft. In the design process it is assumed that the foundation system is rigid and the wall is considered to have a fixed base.

The prototype structure was assumed located in downtown Los Angeles (34.040° N, 118.247 ° W), at a site class D, with mapped spectral response acceleration values, $S_{DS} = 1.555g$ and $S_{D1} = 0.819g$, taken from the USGS website (USGS, 2018). The design was based on the response modification factor R=5, assigned to bearing wall systems with special reinforced concrete shear walls (ASCE/SEI 7-16 2016). The Risk Category is assumed to be I or II (buildings of minor importance/ordinary buildings), with Seismic Importance Factor I = 1.0. The material properties considered in the design phase are:

- Concrete strength $f'_c = 5000psi$
- Steel yield strength $f_y = 60ksi$

A.2.1 Design Loads

Load combinations presented in Section A.1.1 for the slender wall design are also assumed in the design process of the two squat walls. It is noted that the two squat walls utilized the same design procedure. Structural dead load is the self-weight of the wall (concrete unit weight γ, is 150 pcf). Tables A.6 and A.7 shows the superimposed dead and live loads assumed in the design phase of the prototype structure. Gravity loads per each floor are obtained considering the tributary area $A_i = 1225ft^2$, as for Table A.8. The effective seismic weight at the base of the wall is $W = 110$ kips (ASCE/SEI 7-16 2016). Known the effective seismic weight, the base shear and the vertical distribution of seismic forces are calculated according to ASCE/SEI 7-16 (2016) §12.8 (Equivalent lateral load procedure) with the equations reported in the previous section on the slender wall (see Section A.1.2).

Table A.6: Summary of the Dead Loads assumed in the design of the squat walls

Superimposed Roof Dead Load (Uniformly distributed) [psf]	
Roofing	5
Ceiling	3
Insulation	3
Mechanical electrical	3
Misc.	1
	Total 15

Table A.7: Superimposed Live Loads on the squat wall*

Live loads for file and computer rooms [psf]	
Floor	100
Roof	20
Partition walls	15

*: from Table- Minimum Uniformly Distributed Live Loads, in ASCE/SEI 7-16 (2016).

The seismic design story shear ASCE/SEI 7-16 (2016) §12.8.4 is therefore calculated as for Equation (A.14) and results are reported in Table A.9. Final design actions are obtained by multiplying the seismic design story shear by the redundancy factor ρ=1.3.

A.2.2 Actions at the Base of the Squat Wall

The dead and live load cause axial load only and the earthquake forces produce shear and moment only. Since the axial load is less than the axial load that causes the balanced strain condition, the combination that gives the lower bound axial load is more critical for the moment strength of the wall. The governing axial load, moment and shear at the base of the wall are:

$$P_u = 0.589D = 10kips \tag{A.18}$$

$$M_u = 534kips - ft \tag{A.19}$$

$$V_u = 45kips \tag{A.20}$$

Table A.8: Gravity loads on the squat wall specimen

Gravity load on the wall						
Floor	**Dead Load**		**Structural Self-Weight**		**Live Load**	
	kips	*psf*	*kips*	*psf*	*kips*	*psf*
Roof	18	15	92	75	25	20

Note: structural self-weight at the "roof" level is the slab weight.

Table A.9: Seismic design story shear of the squat wall specimen

Floor	**Height** *[ft]*	**Weight per floor** *[kips]*	**Vertical distribution factor**		**Vertical force distribution** *[kips]*	**Design lateral force** *[kips]*	**Design moment** *[kips - ft]*
	h_x	w_x	$w_x h_x^k$	C_{vx}	F_x	V_E	M_E
Roof	12	110	1323	1	34	34	0
1	0	0	0	0	0	0	411

Appendix B

Materials Related Data: Wall Test Specimens

The material tests performed to characterize the material properties of both the concrete and the reinforcing steel used in the walls construction are summarized in this Appendix. Testing on the concrete were performed every week after pouring to ensure that the design strength of the concrete was achieved. The results are illustrated in English units, according to the U.S. design building codes adopted in the design process (ACI 318 2011, ASCE/SEI 7-16 2016, ACI 318 2019). Note that 1 kip = 4.45 kN and 1 in = 25.4 mm.

B.1 Slender Wall

Concrete placement for the foundation block took place on April 3^{rd}, 2017, while concrete for the wall section was poured on April 12^{th}, 2017. The concrete mix for the wall is in Fig. B.1.

B.1.1 Tests on Concrete

Unconfined Compression Tests

Three 6 x 12 in concrete cylinders were tested in compression at 28 days and at or close to the test day in the Satec machine with an MTS controller available in the Powell Structural Laboratories at UC San

Concrete Mix Design Submittal

Customer: UCSD POWELL STRUCTURES
Project: MATTHEWS & VOIGT, LA JOLLA
Usage:
Plant: L82 - MISSION VALLEY R/M

Mix Number: **1578336** **856LB SW PG FA HR HS**

Material Type	Description	Standard	Design Quantity	Specific Gravity	Volume (ft3)
Cement	Type II/V Cement	C150	685 lb	3.15	3.48
Fly Ash	Class F Fly Ash	C618	171 lb	2.20	1.25
Coarse Aggregate	3/8" X#8	C33	1575 lb	2.73	9.25
Fine Aggregate	Con Sand	C33	1181 lb	2.65	7.14
Admixture	HRWR / Type A & F	C494	8.0 dose	-	-
Admixture	Retarding Admxiture / Type D	C494	1.0 dose	-	-
Water	Water	C1602	40.0 gal	1.00	5.34
		Air Content	**2 %**	**–**	**0.54**
		Yield	**3950 lb**	**–**	**27.00**

Specified F'c:	5000 psi	Designed Unit Weight:	146.3 lb/ft3
Target Slump:	7 "	Designed W/C + P Ratio:	0.39
Air Content:	2 %	Designed Volume:	27.00 cu.ft.

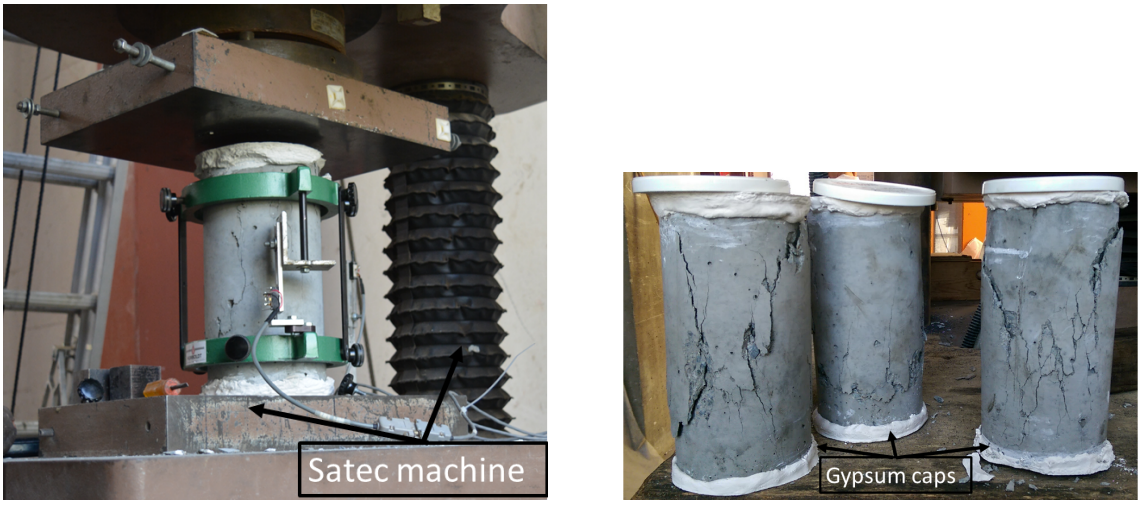
Figure B.1: Design concrete mix

Diego. The Satec machine has a capacity of 600 kips and a stroke of 12 inches and can operate in static tension or compression modes only. Fig. B.2 shows the test setup and the three tested cylinders. Note that cylinders were prepared at top and bottom ends before testing with gypsum caps, to ensure that test cylinders had smooth, parallel, uniform bearing surfaces, perpendicular to the applied axial load during compressive strength testing. Stress-strain relations are presented in Fig.B.3. The compressive strength and strain at peak stress, together with their average values are summarized in Table B.1.

Table B.1: Compressive strength and strain at peak stress at 28 days

Day of test: 28		
Cylinder [#]	**Compressive Strength [ksi]**	**Strain at Peak Stress**
1	5.698	0.0024
2	5.763	0.0025
3	5.426	0.0022
Average	5.629	0.0024

Note: 1 kip = 4.45 kN and 1 in = 25.4 mm



(a) Cylinder in the compression machine

(b) Cylinders at the end of the test

Figure B.2: Unconfined Compression Tests

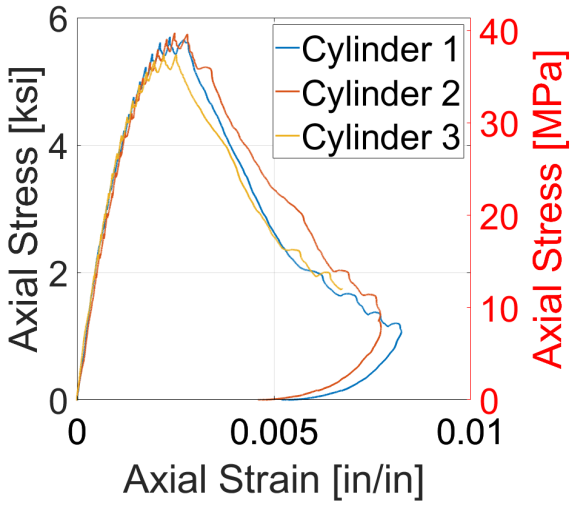


Figure B.3: Strain Stress relationship at 28 days



Figure B.4: Split test

Split Cylinder Tension Tests

In a splitting tension test (or Brazilian test), a standard cylinder is tested on its side, as illustrated in Fig. B.4. Methods for determining the splitting tensile strength of concrete are given in ASTM C496/C496M-04, Standard Test Method for Splitting Tensile Strength of Cylindrical Concrete Specimens (ASTM 2004). The compression force applied from a testing machine along the diameter of the specimen introduces very high lateral load compressive stresses near the points of load application and a nearly uniform lateral tensile stress over approximately two-thirds of the specimen. Because the concrete is stronger in compression than in tension, the specimen will split along the diameter of the specimen before it crushes at its ends. The stress at which splitting occurs is defined as the splitting tensile strength of concrete T , that can be calculated as for Equation 1 in (ASTM 2004):

$$T = 2P/(\pi \cdot l \cdot d) \tag{B.1}$$

P = maximum applied load indicated by testing machine;

l = length of the specimen;

d = diameter of the specimen.

The value of the tensile strength obtained from split cylinder tests is generally observed to be approximately 15% greater than that from direct tension test. The length and the diameter of the cylinders were taken at two different locations and averaged. Results for the three 6 x 12 in tested concrete cylinders are reported in Table B.2.

Table B.2: Split test results at 28 days

Day of test: 28								
Specimen #	**L1** [in]	**L2** [in]	**Average L** [in]	**D1** [in]	**D2** [in]	**Average D** [in]	**P** [kips]	**T** [ksi]
1	12.00	12.00	12.00	5.99	5.99	5.99	55.53	0.49
2	12.00	12.06	12.03	6.02	6.02	6.02	59.38	0.52
3	12.00	12.00	12.00	5.98	5.98	5.98	49.3	0.44
							Average T	0.48

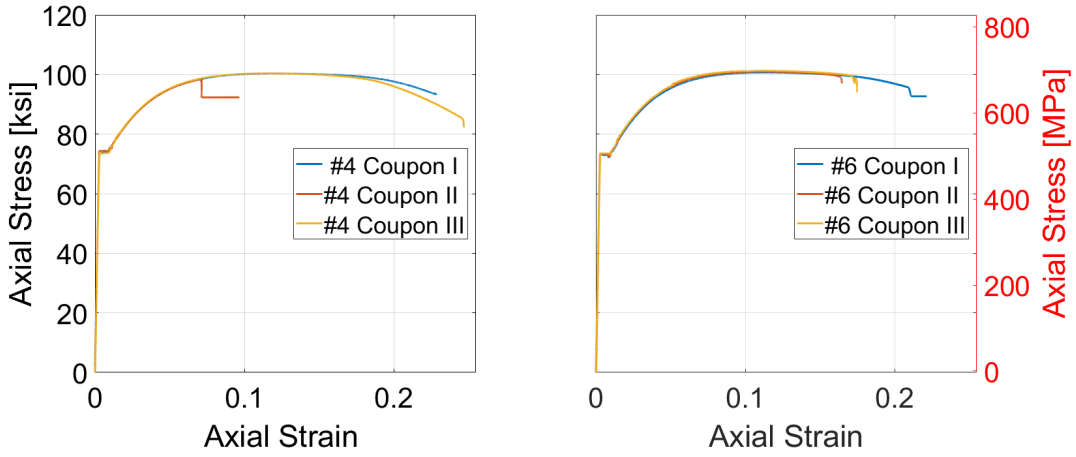


Figure B.5: Strain Stress relationship

B.1.2 Tests on reinforcing bars

Tensile Test

Three samples of both the longitudinal and transverse reinforcing bars used in the wall specimen were obtained and tested under uni-direction tension in the hydraulic Universal Test System at the UC San Diego laboratory. Notably, these reinforcing bars were Gr. 60 #6 and Gr. 60 #4 respectively. The obtained stress-strain relationships are represented in Fig. B.5. Average yield and ultimate strengths from three tests per bar, together with diameter and cross sectional area of the tested reinforcement bars are summarized in Table B.3.

Table B.3: Average yield and ultimate strengths of reinforcement from tension test

Bar	Diameter $[in]$	Cross-sectional area $[in^2]$	Yield strength $[ksi]$	Ultimate strength $[ksi]$
#4	0.5	0.2	73.99	99.73
#6	0.75	0.44	73.25	101.01

B.2 Squat Walls

Concrete for the wall specimens and slab for reference tests was poured on March 4^{th}, 2019. The material tests performed to characterize the concrete and reinforcing bars properties are here reported.



(a) Cylinder #1 (b) Cylinder #2 (c) Cylinder #3

Figure B.6: Three tested cylinders at the end of the test

B.2.1 Tests on concrete

Unconfined Compression Tests

Three 6 x 12 in concrete cylinders were tested in compression at 28 days and at day of tests in the compression machine. The three cylinders at the end of the test are shown in Fig. B.6. Stress-strain relations are presented in Fig.B.7. The compressive strength and strain at peak stress, together with their average values are summarized in Table B.4.

The concrete tensile strength is also evaluated with common equations available in literature (ACI 1992, Belarbi and Hsu 1994 and CEN 2008, respectively) as a comparison with the real strength:

$$f_t = 7.4\sqrt{f'_c} = 619ksi \tag{B.2}$$

$$f_t = 3.75\sqrt{f'_c} = 314ksi \tag{B.3}$$

$$f_t = 1.5f_c^{'0.67} = 565ksi \tag{B.4}$$

(B.5)

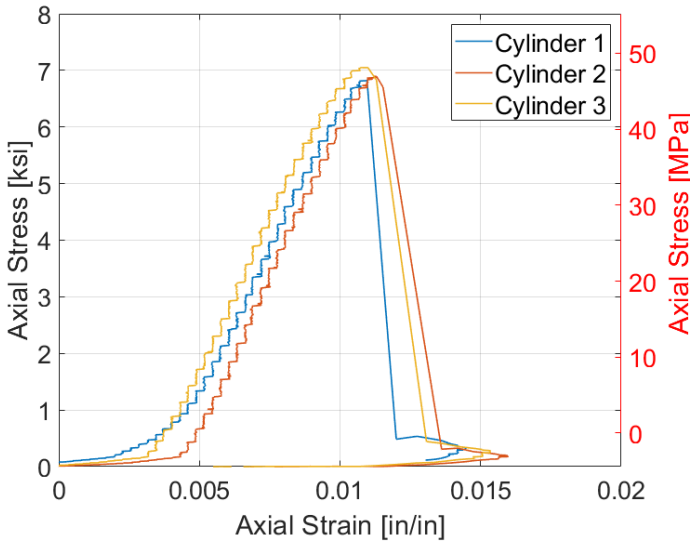


Figure B.7: Strain Stress relationship for the three cylinders at 28 days. Note: displacement slip occurred at the beginning of the tests, which affected strain measurement

Table B.4: Compressive strength and strain at peak stress at 28 days

Day of test: 28		
Cylinder [#]	**Compressive Strength [ksi]**	**Strain at Peak Stress**
1	6.8	0.011*
2	6.9	0.011*
3	7.0	0.011*
Average	6.9	0.216*

*: note displacement slip occurred at the beginning of the compression tests.

Split Cylinder Tension Tests

Results for the three 6 x 12 in tested concrete cylinders are reported in Table B.5. Average measured splitting tensile strength of concrete at day of test is $T = 0.568ksi$.

B.2.2 Tests on reinforcing bars

Tensile Test

Three coupons of both the longitudinal and transverse reinforcing bars of the wall specimens, Gr. 60 #5 and Gr. 60 #4 respectively, were tested in tension in the hydraulic Universal Test System at the University

Table B.5: Split test results at 28 days

Day of test: 28								
Specimen #	**L1** [in]	**L2** [in]	**Average L** [in]	**D1** [in]	**D2** [in]	**Average D** [in]	**P** [kips]	**T** [ksi]
1	12.00	12.00	12.00	6.00	5.99	5.99	57.0	0.504
2	12.10	12.00	12.05	6.02	5.97	5.99	71.3	0.628
3	12.00	12.00	12.00	5.98	6.02	6.00	64.5	0.571
							Average T	0.568

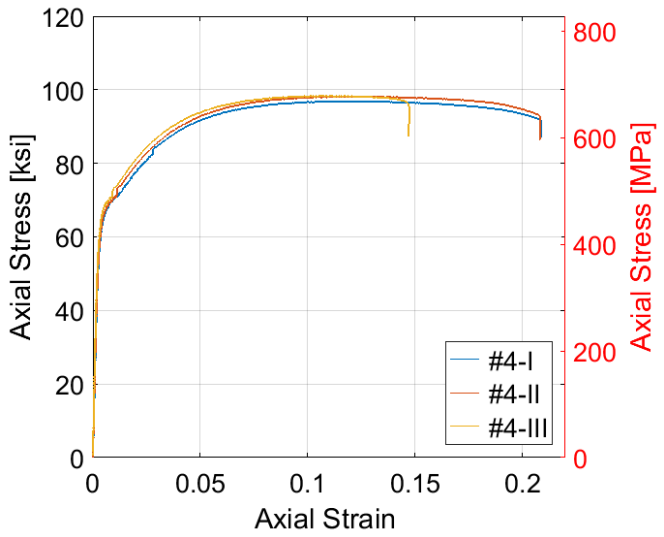


Figure B.8: # 4 Transverse reinforcing bars: Strain Stress relationship

of California San Diego laboratory. The obtained stress-strain relationships are represented in Figs. B.8 and B.9. Average yield and ultimate strengths from three tests per bar, together with diameter and cross sectional area of the tested reinforcement bars are summarized in Table B.6.

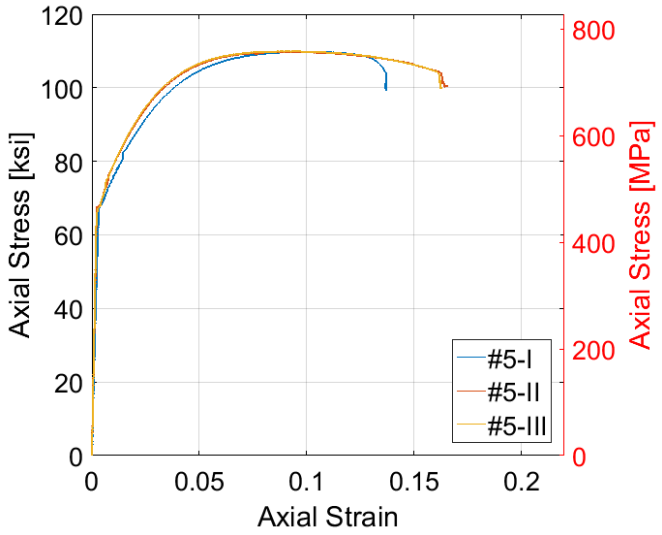


Figure B.9: # 5 Longitudinal reinforcing bars: Strain Stress relationship

Table B.6: Average yield and ultimate strengths of reinforcement from tension test

Bar	Diameter	Cross-sectional area	Yield strength	Ultimate strength
	$[in]$	$[in^2]$	$[ksi]$	$[ksi]$
#4	0.5	0.2	71	97
#5	0.625	0.31	67	110

Appendix C

Crack Width Histories: Wall Test Specimens

Crack width values were measured in the locations indicated in Figs.C.1, C.2 and C.3 for walls SL7.5, SQ7.5 and SQ0, respectively, by linear position transducers TR/TRS-50 mm with return spring by Novotechnik. Four crack width sensors measured the crack width histories in wall SL7.5, as reported in Figs. C.4-C.7. Six crack width sensors measured the crack width histories reported in Figs.C.8-C.13 and Figs.C.14-C.19 for wall SQ7.5 and SQ0, respectively. Maximum measured crack width is reported in the caption of Figs.C.8-C.13 and Figs.C.14-C.19. Additional standard manual crack width sensors were added to monitor crack widths at other important locations, close to anchors of interest. These readings were taken by photographs at the end of each wall load cycle.

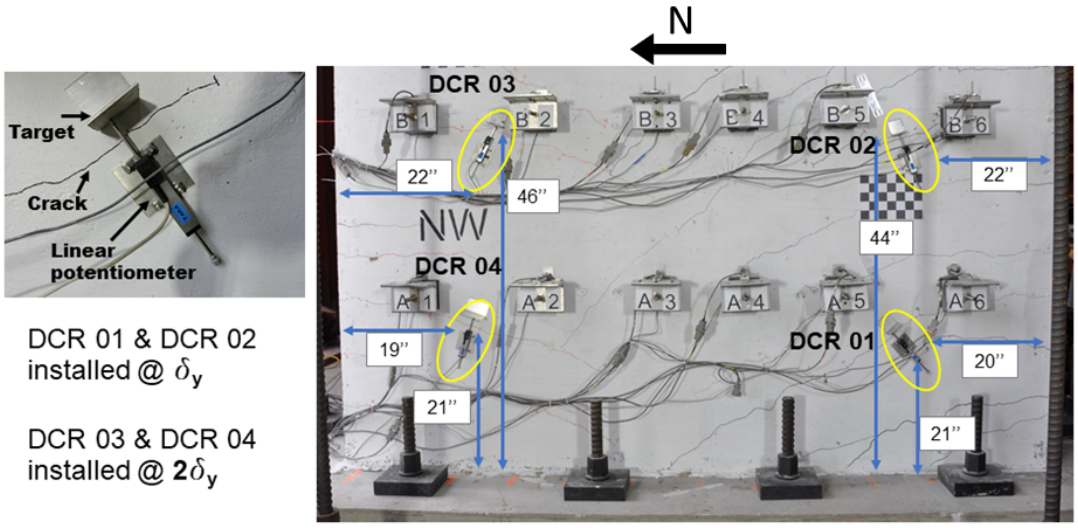


Figure C.1: Wall SL7.5. Location of crack width sensors

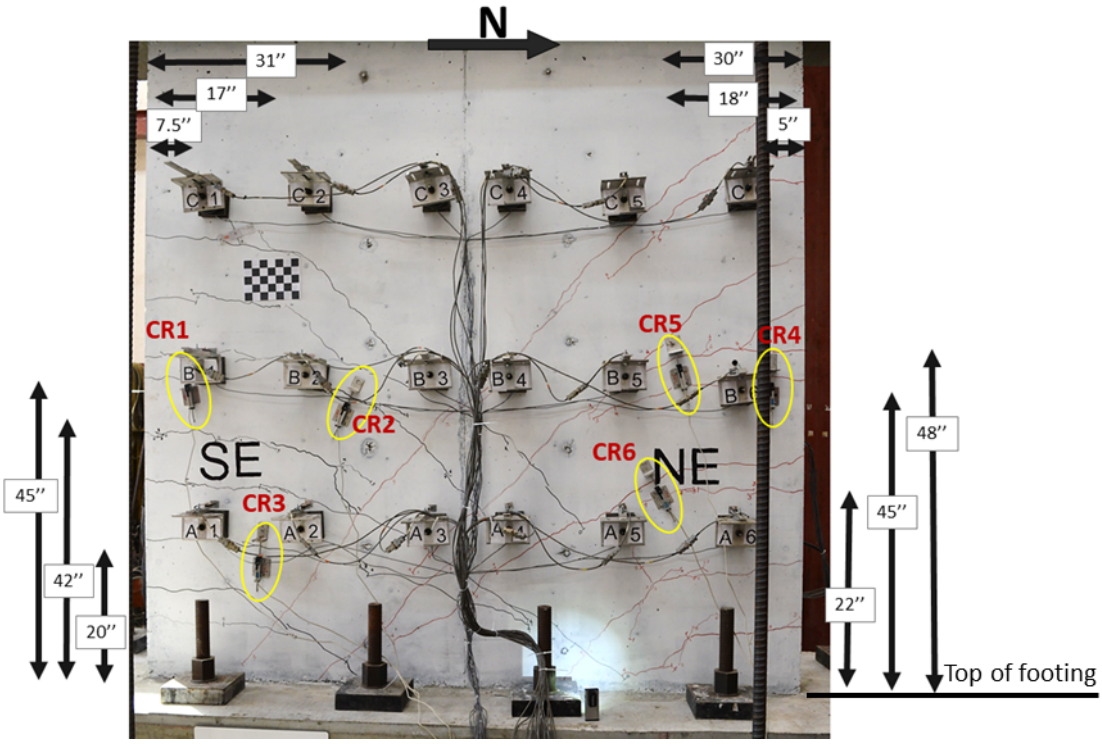


Figure C.2: Wall SQ7.5. Location of crack width sensors

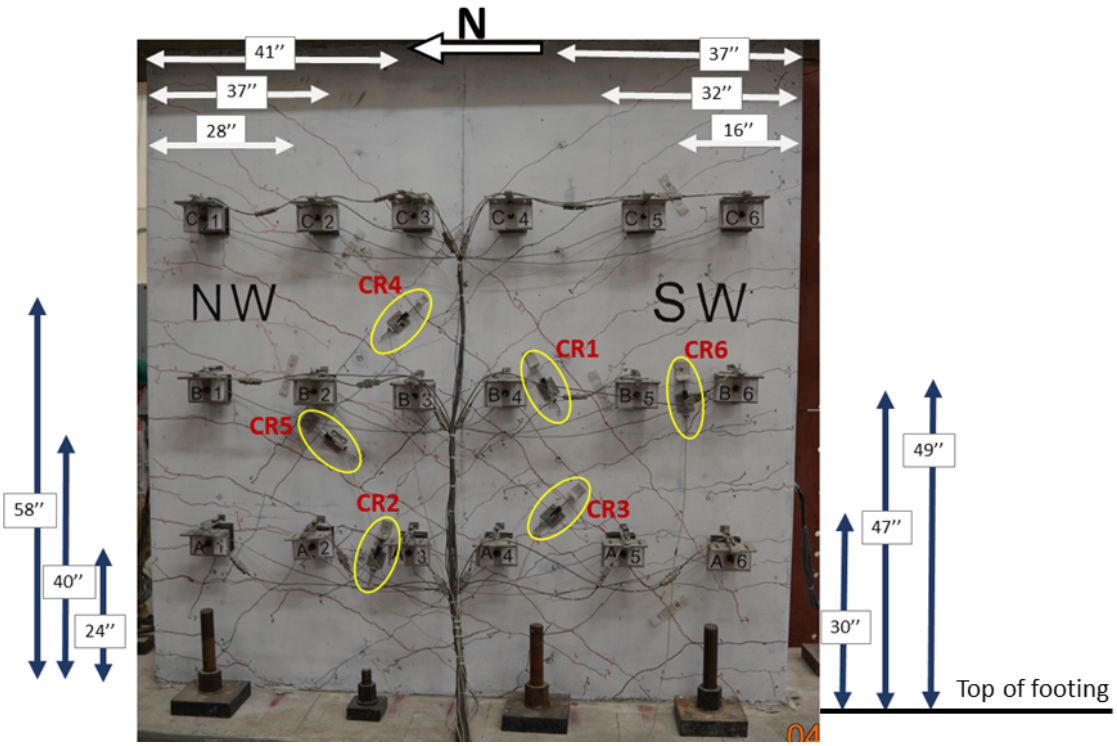
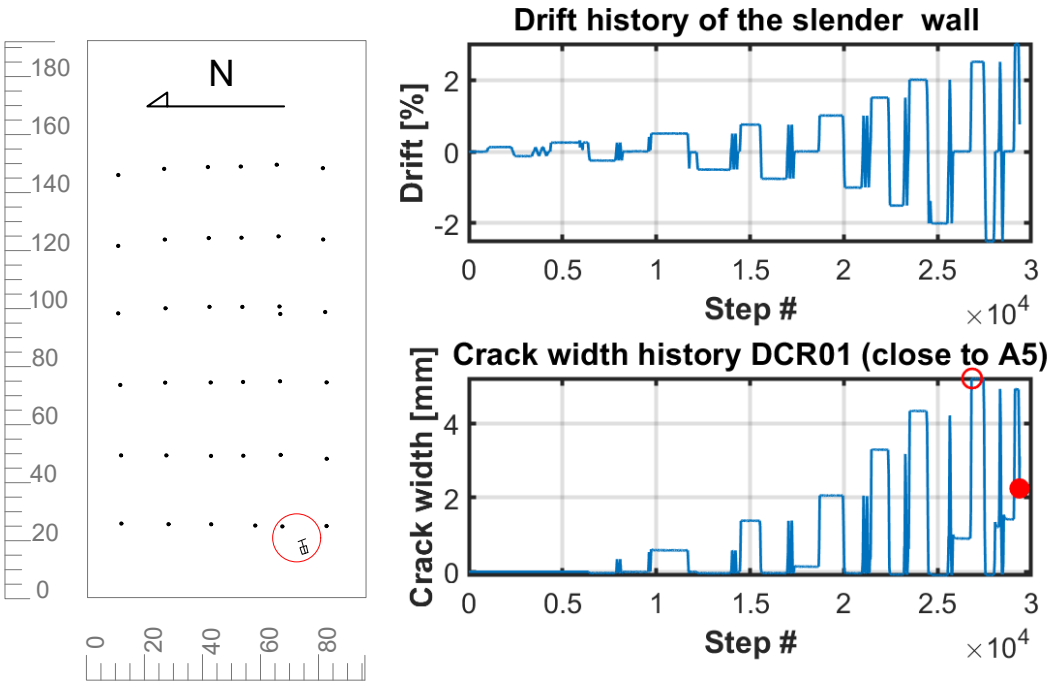


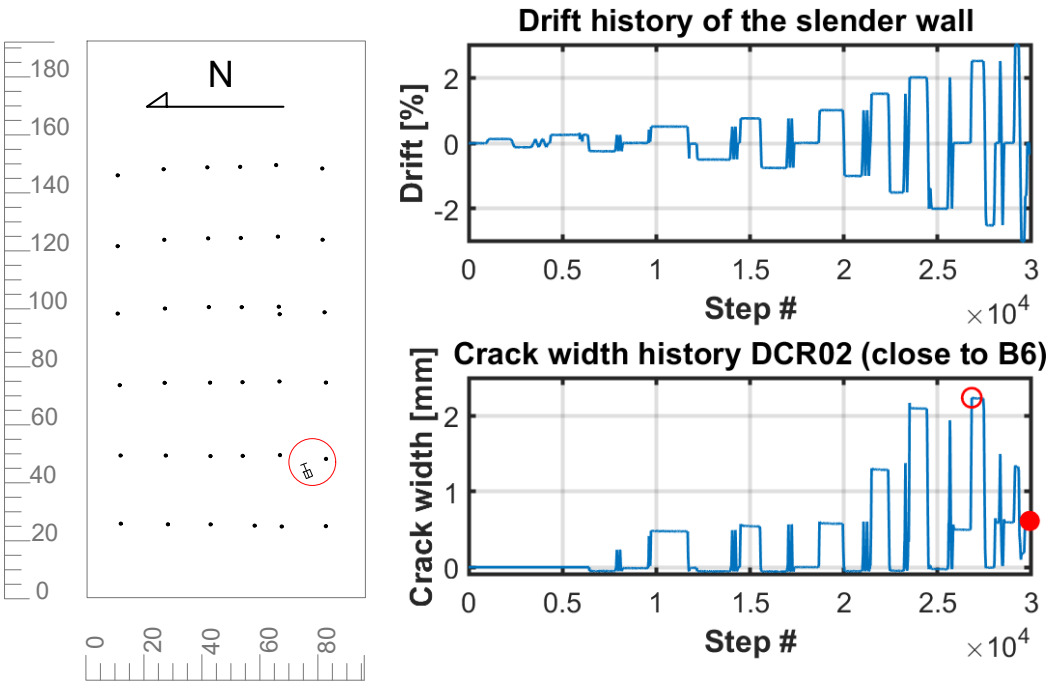
Figure C.3: Wall SQ0. Location of crack width sensors



(a) Location of the sensor. Units in inches

(b) Crack width history

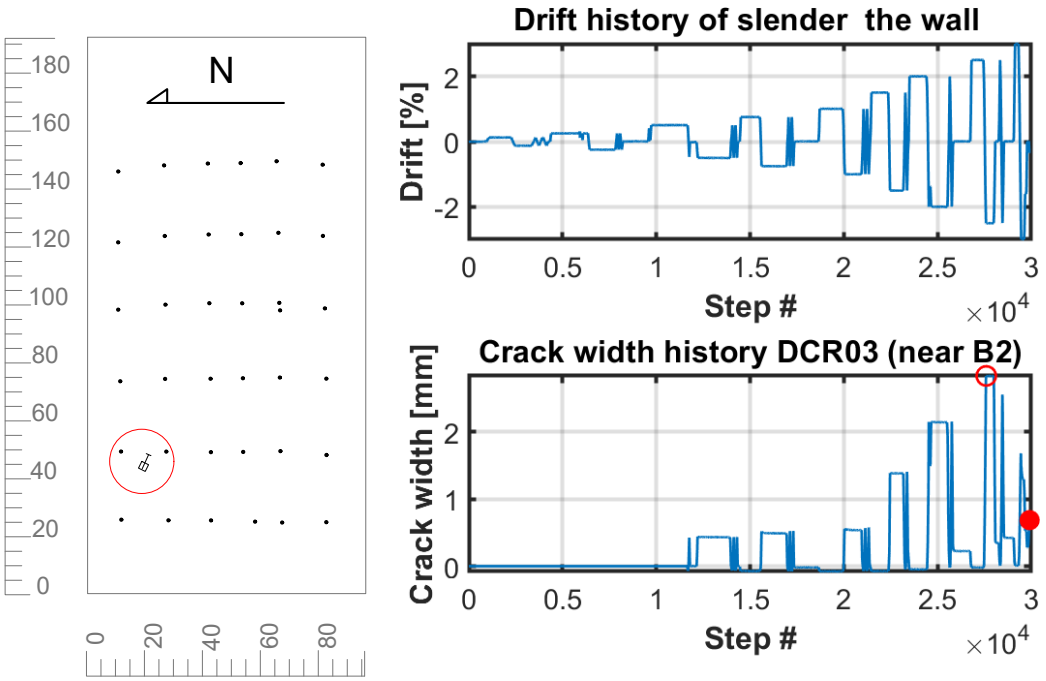
Figure C.4: Crack width history of sensor DCR01 in the slender wall SL7.5. Maximum measured crack width = 5.2 mm and residual measured crack width = 2.3 mm



(a) Location of the sensor. Units in inches

(b) Crack width history

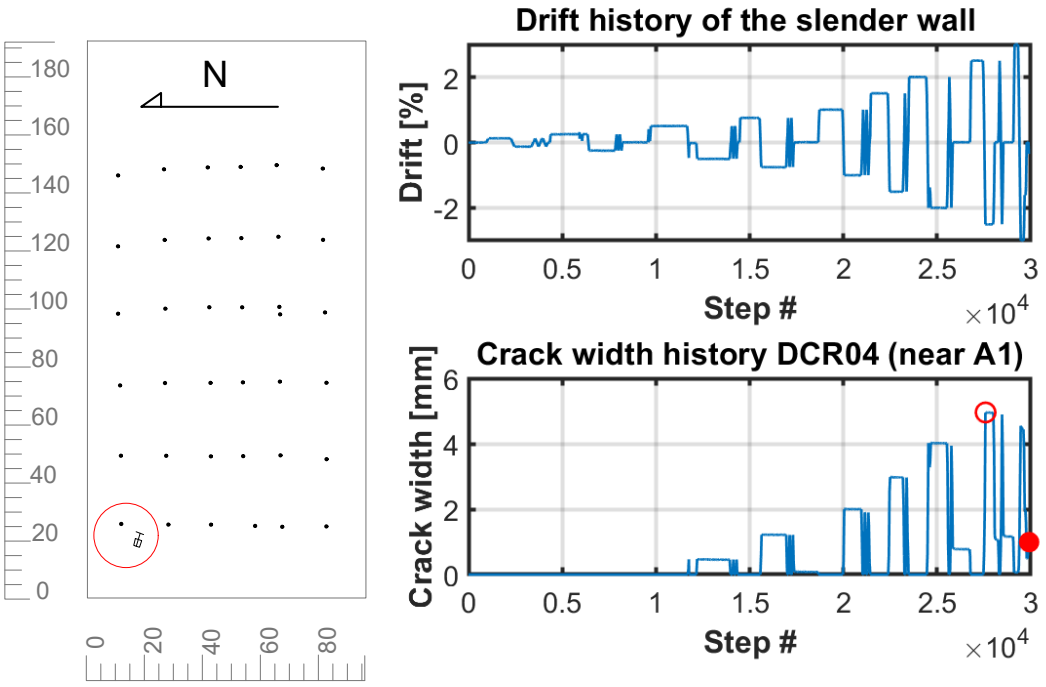
Figure C.5: Crack width history of sensor DCR02 installed in slender wall SL7.5. Maximum measured crack width = 2.2 mm and residual measured crack width = 0.61 mm



(a) Location of the sensor. Units in inches

(b) Crack width history

Figure C.6: Crack width history of sensor DCR03 installed in slender wall SL7.5. Maximum measured crack width = 2.8 mm and residual measured crack width = 0.68 mm



(a) Location of the sensor. Units in inches

(b) Crack width history.

Figure C.7: Crack width history of sensor DCR04 installed in slender wall SL7.5. Maximum measured crack width = 5.0 mm and residual measured crack width = 1.0 mm

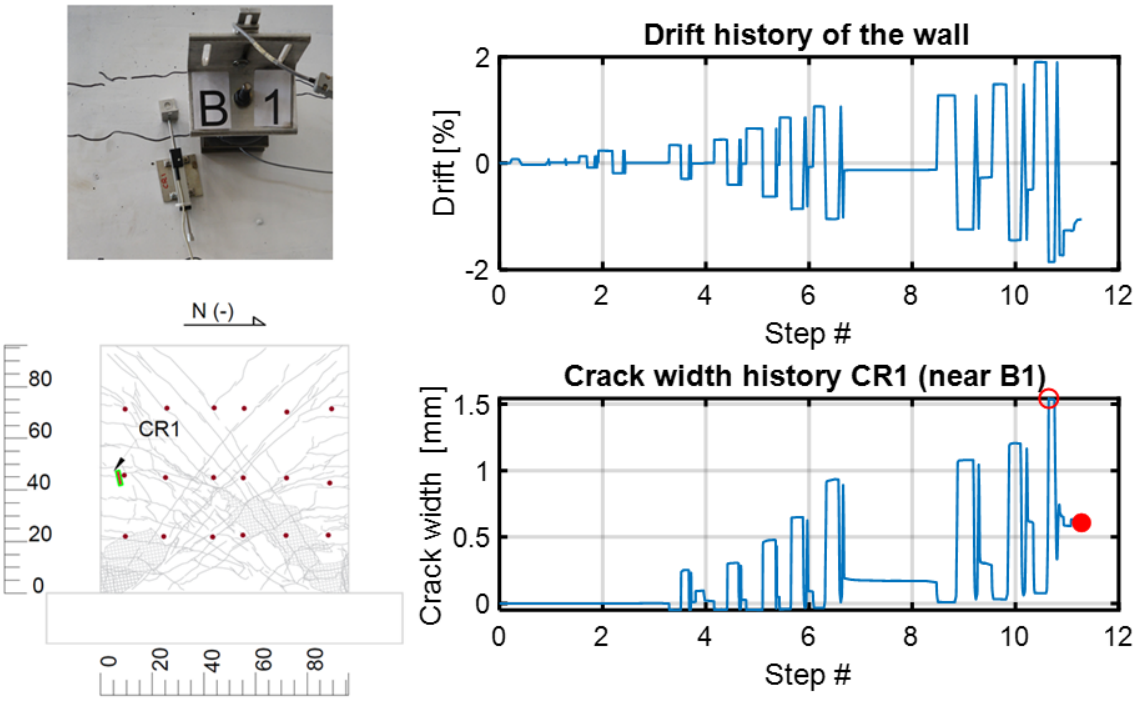


Figure C.8: Crack width history, photograph and location (units in inches) of sensor CR1 installed in wall SQ7.5. Maximum measured crack width = 1.5 mm and residual crack width = 0.6 mm

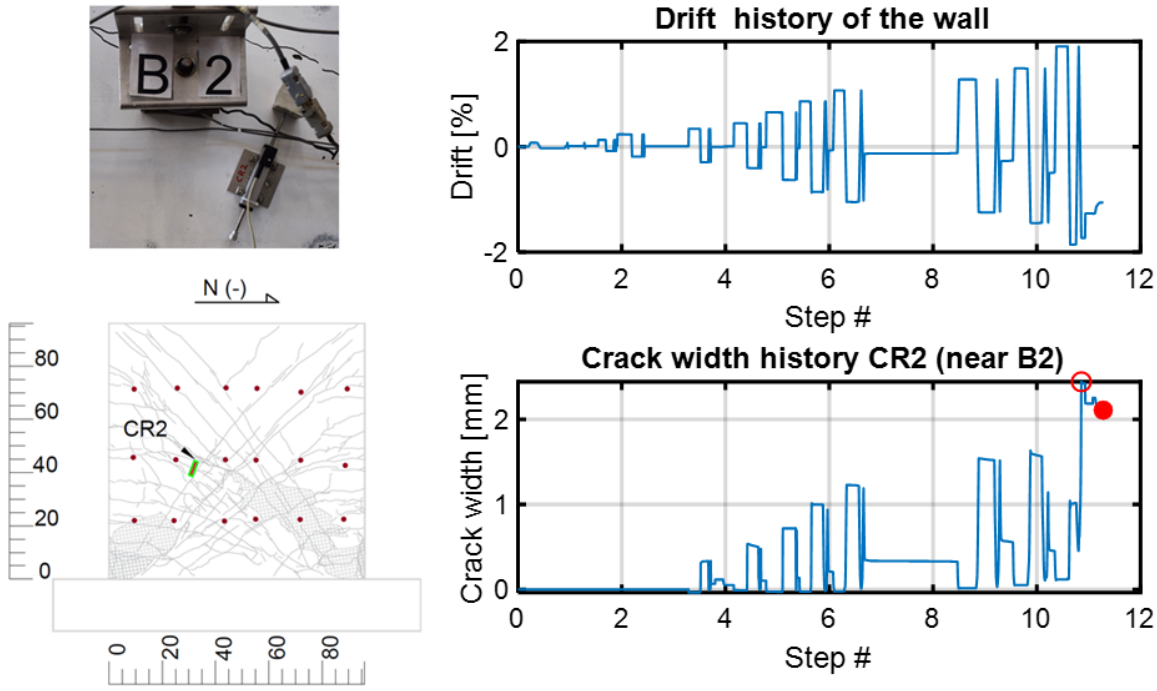


Figure C.9: Crack width history, photograph and location (units in inches) of sensor CR2 installed in wall SQ7.5. Maximum measured crack width = 2.4 mm and residual crack width = 2.1 mm

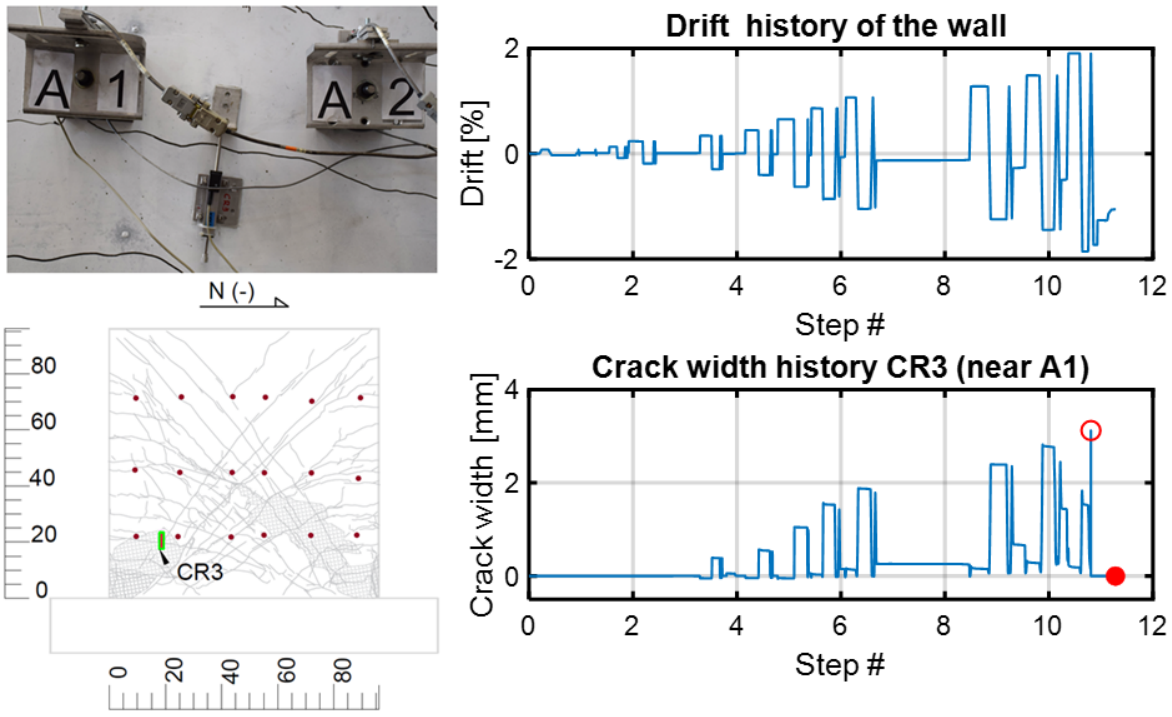


Figure C.10: Crack width history, photograph and location (units in inches) of sensor CR3 installed in wall SQ7.5. Maximum measured crack width = 3.1 mm and residual crack width = 0 mm

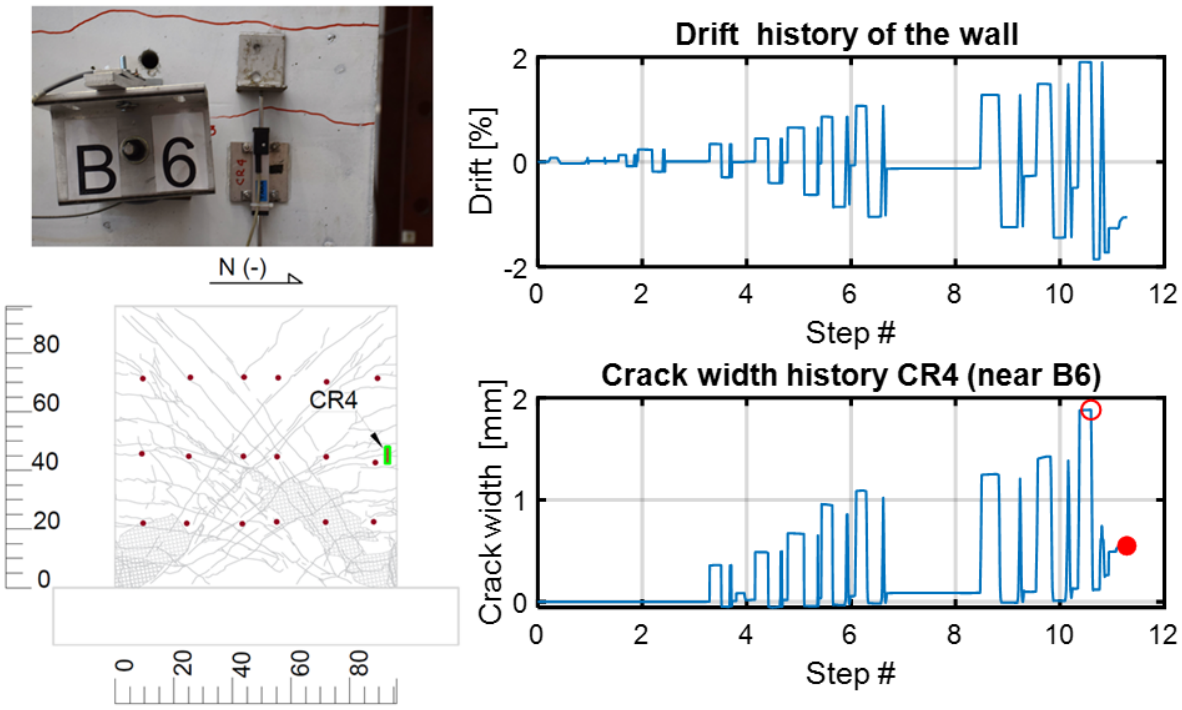


Figure C.11: Crack width history, photograph and location (units in inches) of sensor CR4 installed in wall SQ7.5. Maximum measured crack width = 1.9 mm and residual crack width = 0.5 mm

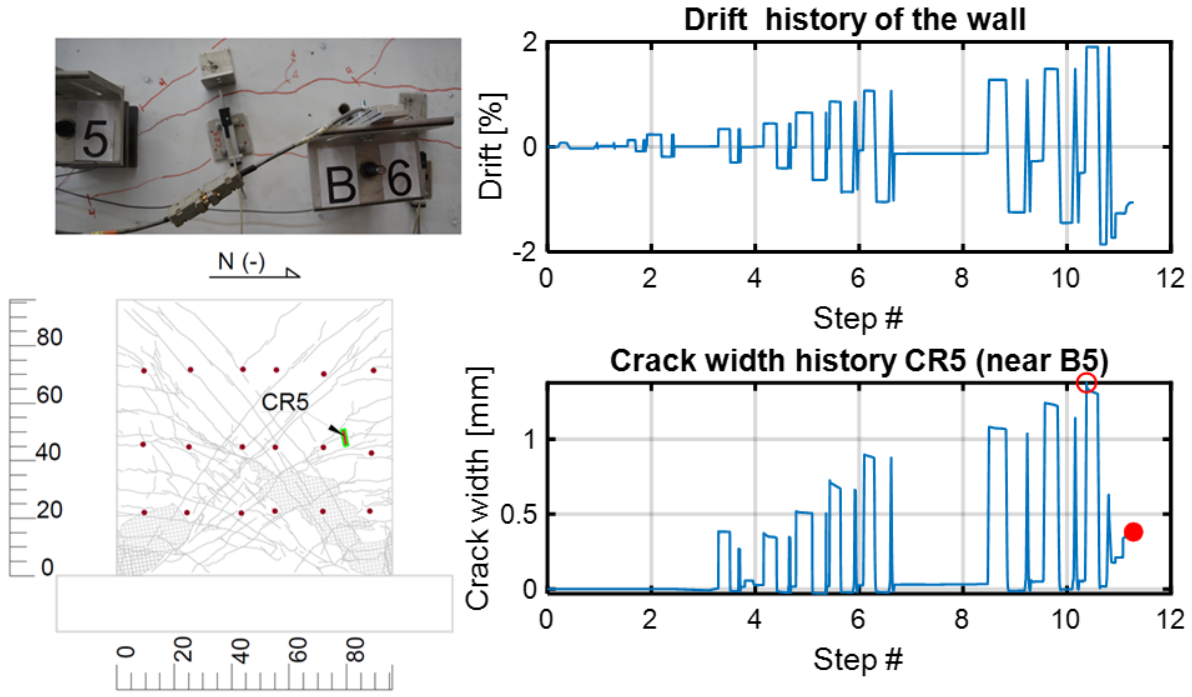


Figure C.12: Crack width history, photograph and location (units in inches) of sensor CR5 installed in wall SQ7.5. Maximum measured crack width = 1.4 mm and residual crack width = 0.4 mm

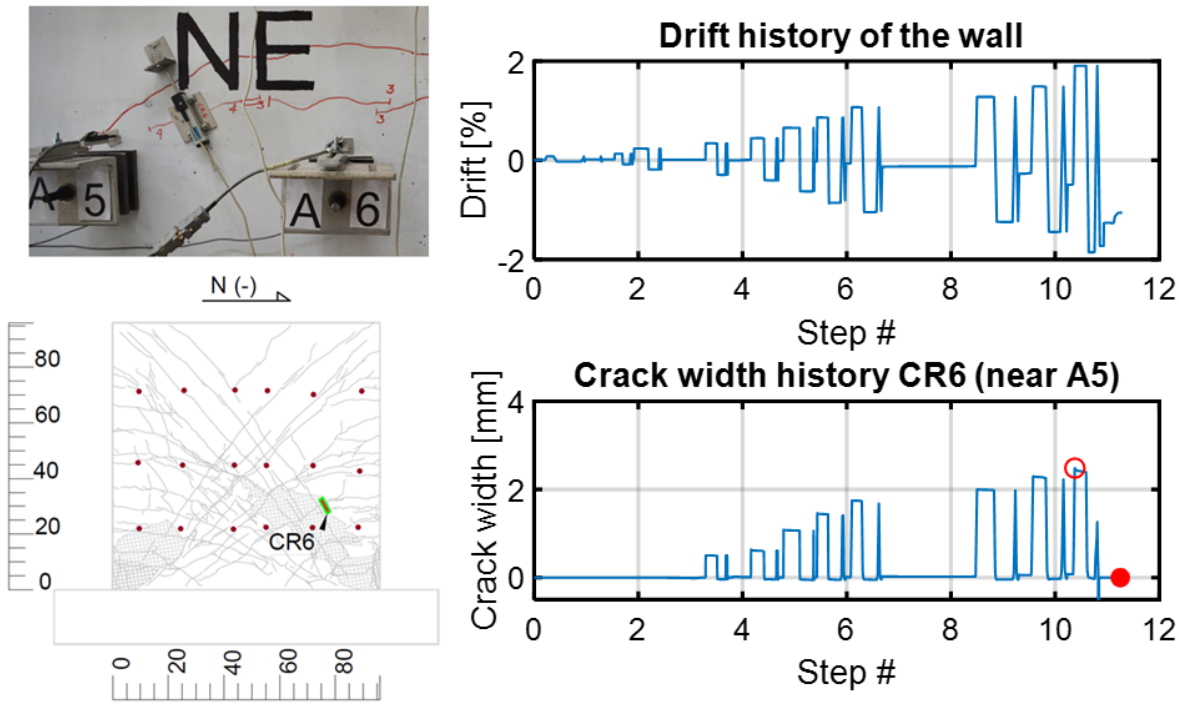


Figure C.13: Crack width history, photograph and location (units in inches) of sensor CR6 installed in wall SQ7.5. Maximum measured crack width = 2.5 mm and residual crack width = 0 mm

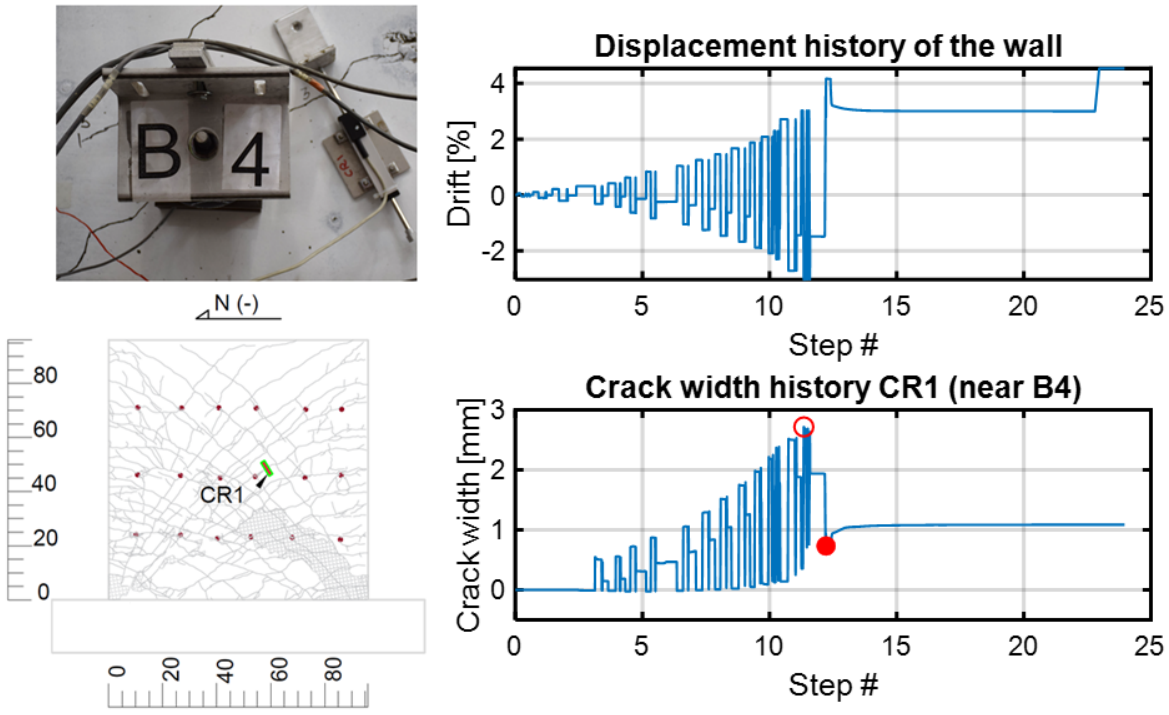


Figure C.14: Crack width history, photograph and location (units in inches) of sensor CR1 installed in wall SQ0. Maximum measured crack width = 2.7 mm and residual crack width = 0.7 mm

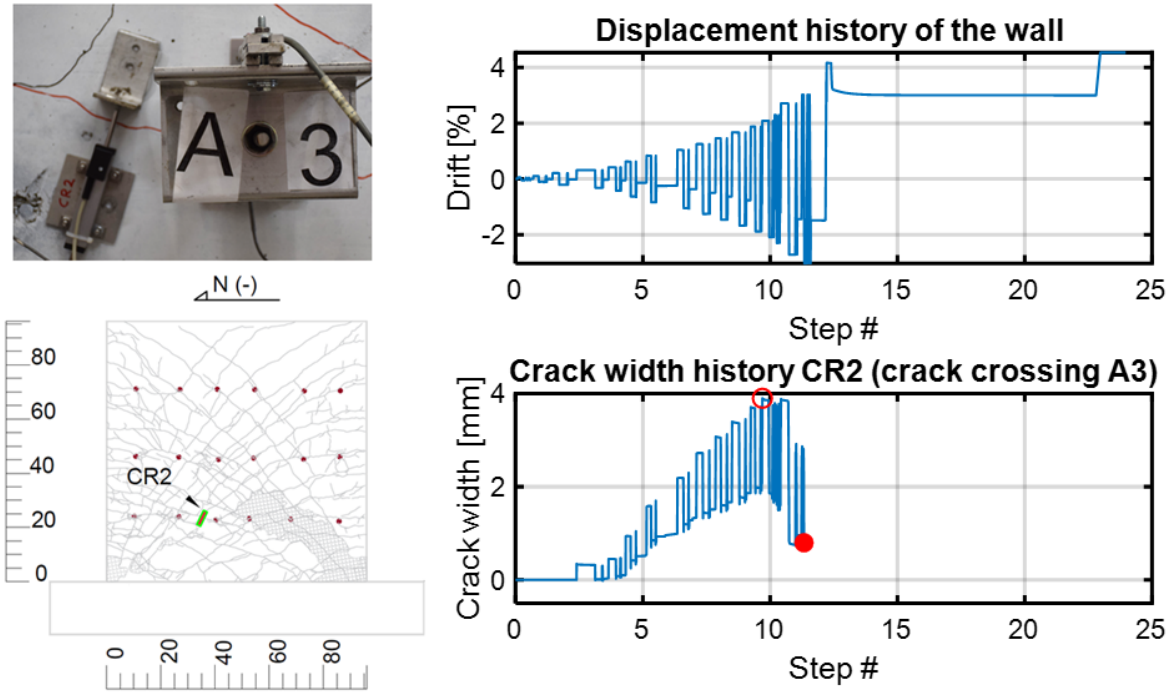


Figure C.15: Crack width history, photograph and location (units in inches) of sensor CR2 installed in wall SQ0. Maximum measured crack width = 3.9 mm and residual crack width = 0.8 mm

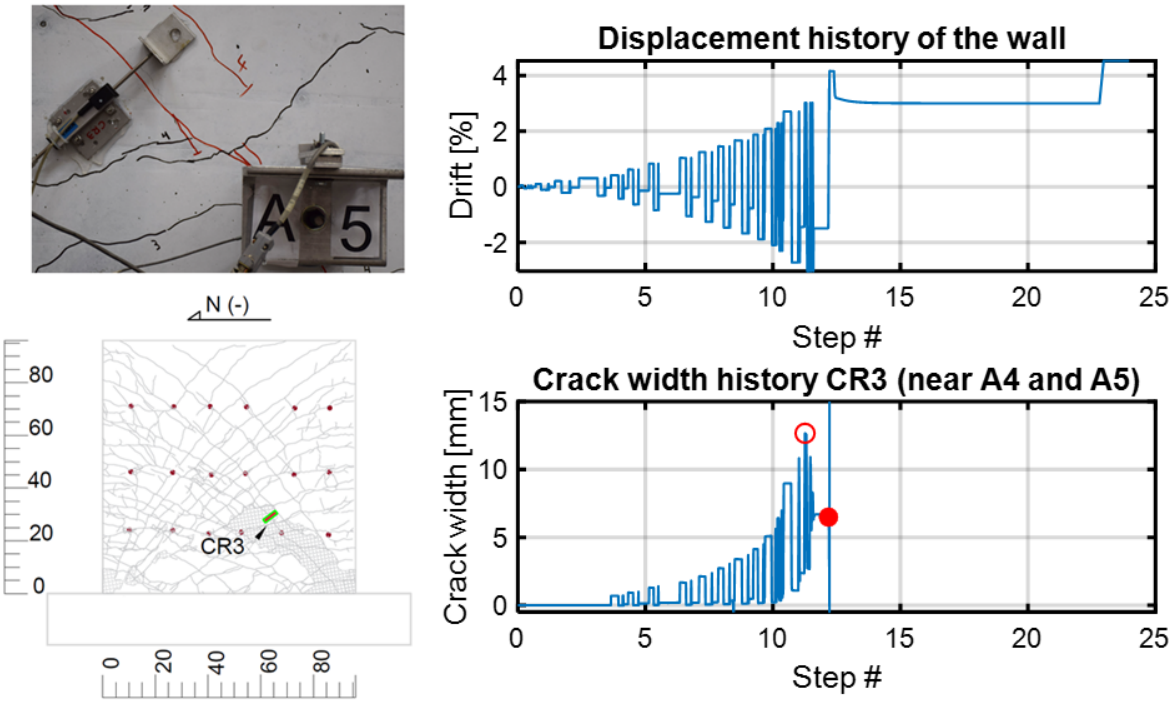


Figure C.16: Crack width history, photograph and location (units in inches) of sensor CR3 installed in wall SQ0. Maximum measured crack width = 12.7 mm and residual crack width = 6.5 mm

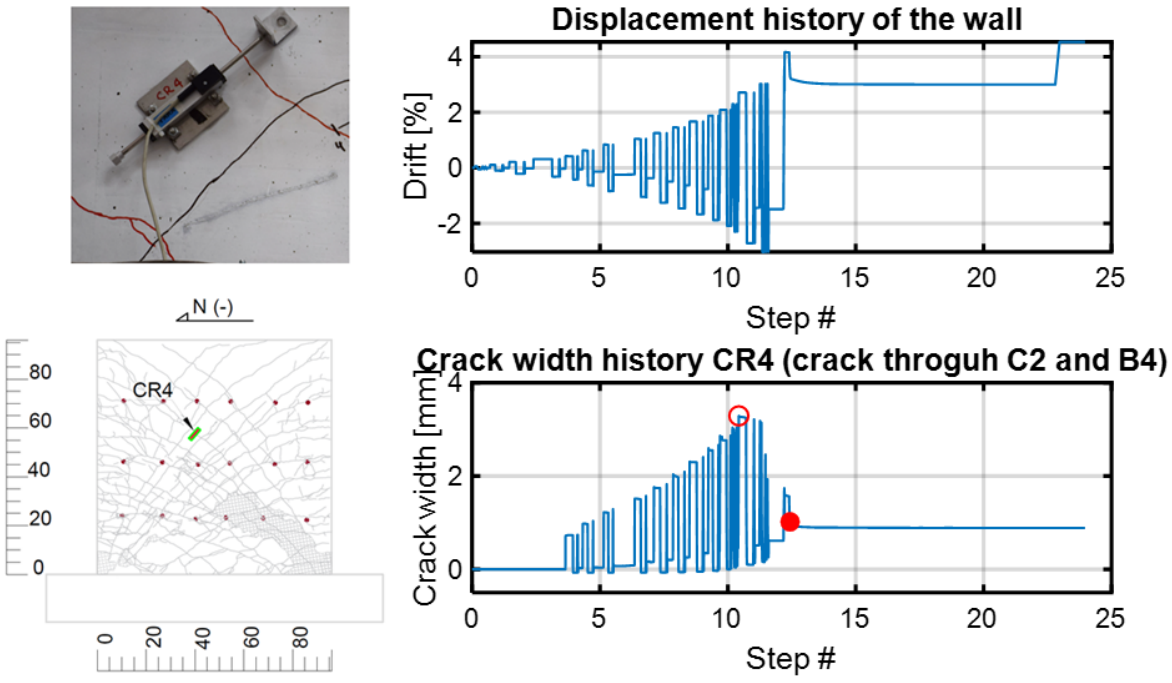


Figure C.17: Crack width history, photograph and location (units in inches) of sensor CR4 installed in wall SQ0. Maximum measured crack width = 3.3 mm and residual crack width = 1.0 mm

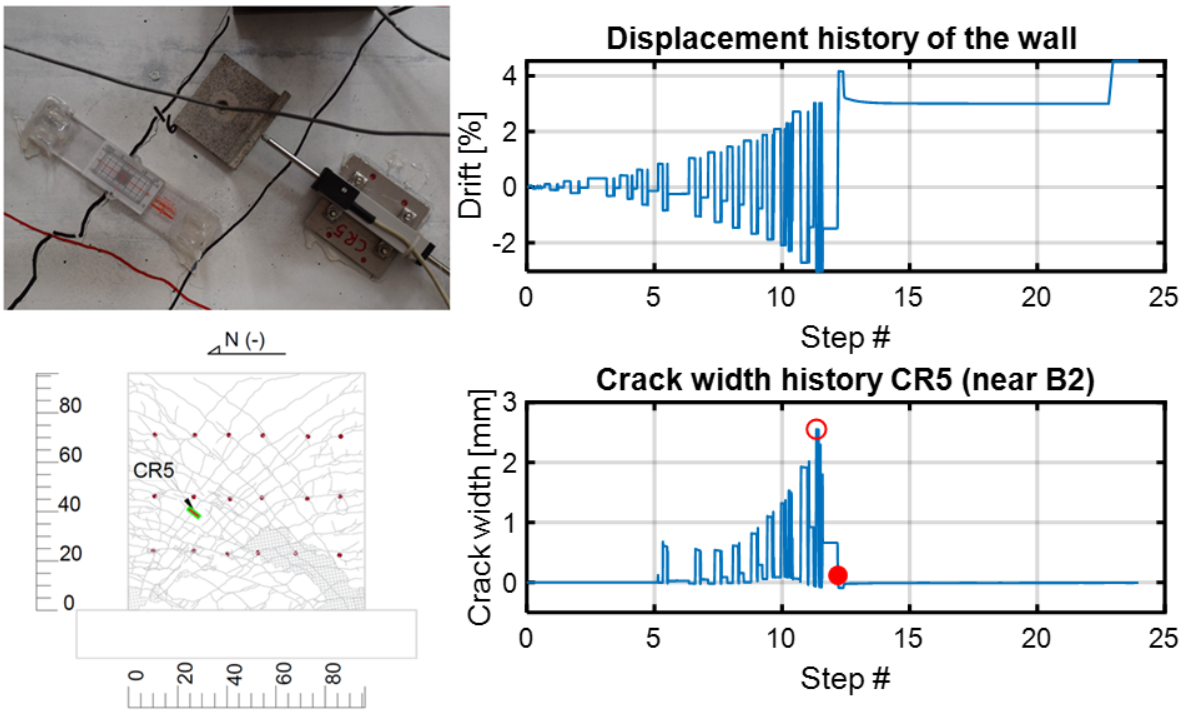


Figure C.18: Crack width history, photograph and location (units in inches) of sensor CR5 installed in wall SQ0. Maximum measured crack width = 2.6 mm and residual crack width = 0.1 mm

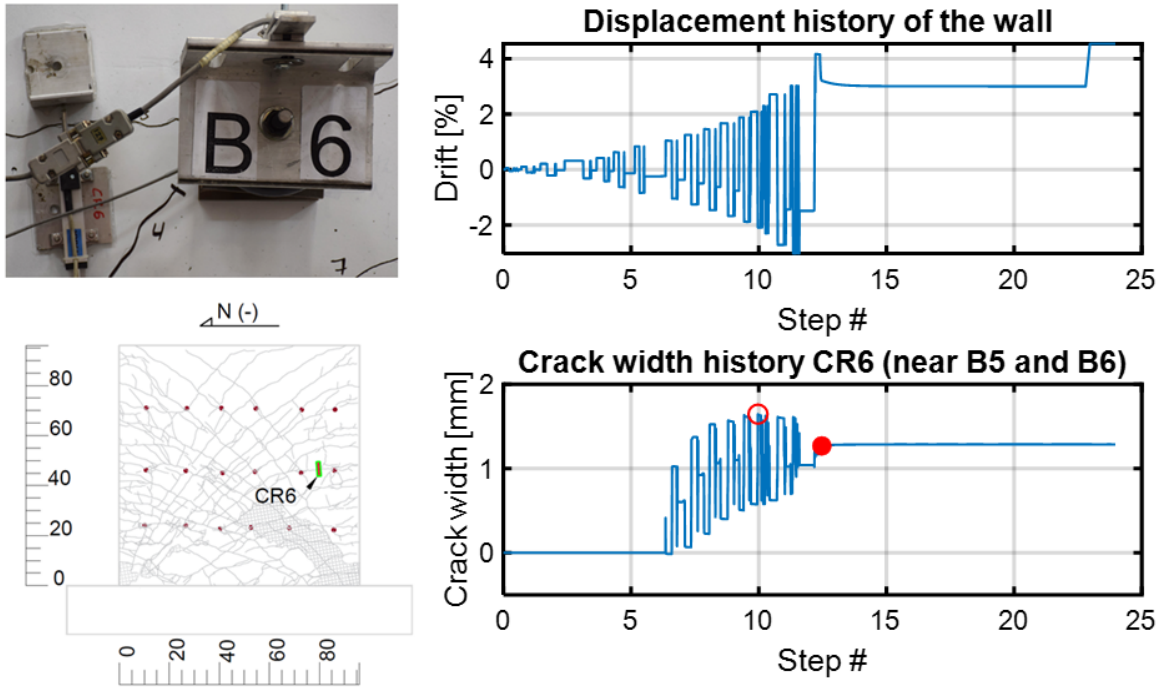


Figure C.19: Crack width history, photograph and location (units in inches) of sensor CR6 installed in wall SQ0. Maximum measured crack width = 1.6 mm and residual crack width = 1.3 mm

Appendix D

Anchor Seismic Demand and Capacity

Calculation of the anchor design loads and theoretical estimates of anchor capacity is reported in this Appendix. Equations reported in Chapter 17 of ACI 318 (2019) are adopted in the estimation of the tension capacity of the anchors.

The lowest design strength is associated to concrete cone breakout failure mode for both the post-installed anchors considered in this study. To account for the brittle type of this failure mode, strength reduction coefficient is considered as for ACI 318 (2019). The so reduced anchor nominal tensile strength associated to concrete cone breakout failure accounts for increased concrete cracking and spalling in the concrete, as a result of seismic action. The seismic design tension load is computed as

$$N_{ba,seismic} = \alpha_{seism} \Phi k_{cr} h_{ef}^{1.5} \sqrt{f_c'} \tag{D.1}$$

where α_{seism} = 0.75, Φ = 0.65, and k_{cr} = 24 for torque-controlled expansion anchors and k_{cr} = 17 for bonded anchors. The concrete strength at the day of test was f_c' = 6000 psi, 7360 psi and 8317 psi for the slender wall, squat wall with and squat wall without axial load specimens, respectively.

The anchor load capacity associated with steel failure of the threaded rod is estimated as

$$N_{sa,seismic} = A_{se} f_{uta} \tag{D.2}$$

where A_{se} is the tensile stress area of the anchor and f_{uta} = 174 ksi is the ultimate strength of Grade 12.9

anchor steel. The expansion anchors have A_{se} = 0.131 in^2 and the bonded anchors have A_{se} = 0.1419 in^2 , hence $N_{sa,seismic}$ = 10644 lb and 11529 psi for expansion and bonded anchors, respectively.

The equation by Fuchs et al. (1995) is used to estimate the mean concrete breakout capacity in uncracked concrete of the two types of post-installed anchors considered in this study, as follows:

- expansion anchors installed in the slender wall reference test slab:

$$N_b = 35\sqrt{5951}(3.2)^{1.5} \approx 15.5\text{kips} \tag{D.3}$$

- expansion anchors installed in the squat wall reference test slab:

$$N_b = 35\sqrt{6900}(3.2)^{1.5} \approx 16\text{kips} \tag{D.4}$$

- bonded anchors installed in the slender wall reference slab:

$$N_b = 35\sqrt{5951}(4.0)^{1.5} \approx 21.6\text{kips} \tag{D.5}$$

Eligehausen et al. (2006) shows that for crack width w = 0.3 mm to 0.4 mm, the capacity is about 0.4 to 0.85, on average 0.7 of that in uncracked concrete. In particular, expansion anchors display a marked sensitivity to crack width, hence when two crossing cracks intersect anchor location an additional 20% reduction beyond the 0.7 average reduction should be considered.

Appendix E

Anchor Response Data: Wall Test Specimens

E.1 Anchor Response during Wall Cyclic Tests

Anchor loading and displacement histories, and crack information, when available, are presented in this Appendix. Table E.1 complements the crack progression pictures, presented in Chapter 4 for each anchor, with the measured crack width values at each wall drift demand. Note that these crack widths values were taken manually during the test, at least 2 in afar from each anchor (due to the presence of the anchor setup plates). Hence, the crack width values reported in this Appendix represent a qualitative indication of the damage progression and these values can be assumed to be similar to those of the cracks crossing the anchors, if developed at the same stage. No additional information was available at the time of these measurements about whether or not the crack actually crossed the anchor. These crack width measurements are reported in this Appendix to give a general order of magnitude of the damage likely to interfere with the anchor functionality. Note that crack widths values were not collected during the wall drift at the final drift demands, since the damage was largely spread over the whole walls.

Table E.1: Crack width measured around the anchor plates during the cyclic test of wall SQ7.5. Note that these are local measurements collected during the wall test. Crack width values were measured more than 2 in away from the anchors

Anchor	Wall drift [%]								
	0.1	**0.2**	**0.3**	**0.4**	**0.6**	**0.8**	**1.0**	**1.2**	**1.4**
Within $L_w/2$ from the wall base									
A1*	0.10	0.40	0.55	0.75	0.85	1.00	2.00	2.00	2.00
A2	-	-	-	-	-	-	-	-	-
A3	0.10	0.35	0.40	0.75	0.85	1.00	2.00	2.00	2.50
A4	-	-	0.40	0.50	x	x	x	x	x
A5*	-	-	-	x	x	1.00	x	x	x
A6	-	-	-	-	-	-	-	-	1.50
B1*	0.10	0.20	x	x	x	x	x	x	x
B2*	-	0.20	-	0.20	x	x	x	x	x
B3	-	-	-	-	-	-	-	-	-
B4	-	-	-	0.50	x	1.00	1.00	1.00	x
B5*	-	0.35	0.60	x	0.85	1.00	x	x	2.50
B6*	-	x	x	x	x	x	x	x	1.00
Outside $L_w/2$ from the wall base									
C1	-	-	-	0.10	0.20	x	x	x	x
C2	-	-	-	-	-	-	1.00	x	x
C3	-	-	-	-	-	-	-	-	0.30
C4	-	-	-	-	-	-	-	-	-
C5	-	-	-	-	-	-	-	-	-
C6	-	-	-	-	-	-	-	-	-

**: refer to correspondent crack width sensor for crack width measurement*
-: no cracks crossing the anchors plate
x:measurement not available

Table E.2: Crack width measured around the anchor plates during the cyclic test of wall SQ0. Note that these are local measurements collected during the wall test. Crack width values were measured more than 2 in away from the anchors

Anchor	Wall drift amplitude [%]										
	0.1	**0.2**	**0.3**	**0.4**	**0.6**	**0.8**	**1.0**	**1.2**	**1.4**	**1.6**	**1.8**
Within $L_w/2$ from the wall base											
A1	0.30	x	x	0.35/hairline	x	1.5	2.00	2.50/1.25	2.00/1.5	5.00	5.00/2.5
A2	0.30	x	x	x	x	1.25	0.80	2.50	2.50	5.00	4.00
A3*	x	x	x	x	x	x	x	1.50	2.00	3.00	3.00
A4	0.2	x	x	x	0.75	0.80	1.50	1.50	1.50	3.00	2.00
A5*	x	0.33	0.33	x	0.50	1.50	1.00	1.25	2.00	3.00	2.50
A6	0.25	x	x	x	0.50	1.80	1.50	2.50	2.50	x	2.50
B1	-	x	x	x	x	x	0.80	1.00	1.00	1.25	2.00
B2	-	x	0.50	x	0.33/0.75	0.80	x	1.50	2.00	3.00	2.00
B3	-	x	x	x	x	x	x	1.25	1.50	x	2.00
B4*	-	-	x	x	x	x	1.00	1.25	2.00	2.00	2.50
B5	-	x	0.40	x	0.30	1.25	0.75	1.25	2.00	x	x
B6*	-	0.40	x	x	0.60	1.00	1.00	1.50	2.00	x	1.50
Outside $L_w/2$ from the wall base											
C1	-	x	0.40	x	x	x	x	x	x	0.40	0.30
C2	-	x	x	x	x	1.00	x	x	x	1.00	1.50
C3	-	-	x	x	x	x	x	x	x	x	x
C4	-	-	-	-	-	-	-	-	-	-	-
C5	-	-	0.50	x	x	x	0.40	0.50	0.50	x	x
C6	-	0.40	x	x	x	x	0.50	0.40	0.50	0.50	0.40

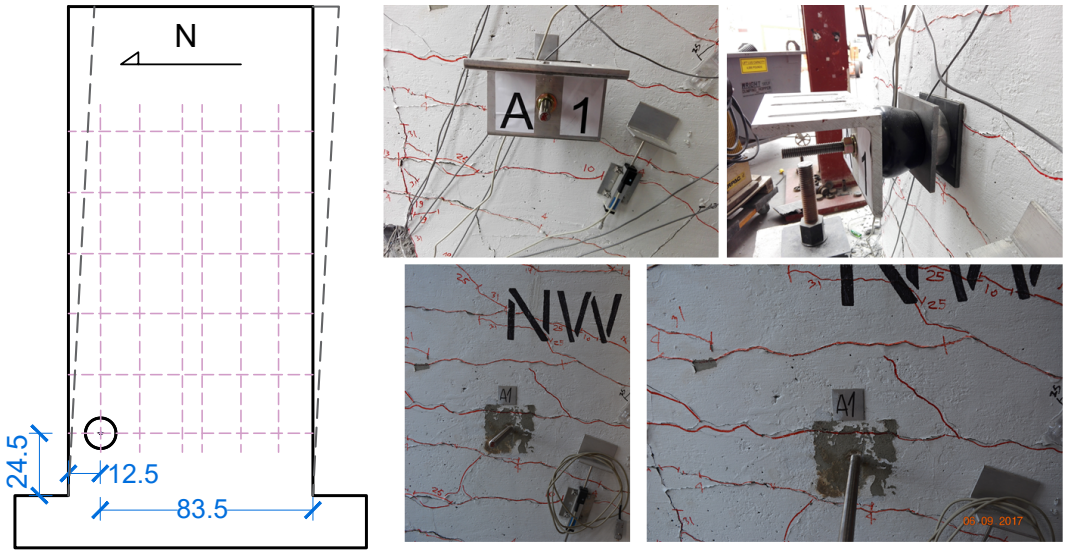
**: refer to correspondent crack width sensors for crack width measurement*

-: no cracks crossing the anchor plate

x:measurement not available

E.1.1 Anchors in Wall SL7.5

Figures presented in this section show the load and displacement histories measured during wall cycling for each anchor installed in slender wall SL7.5. Photographs of the residual concrete damage in the vicinity of each anchor are also included to show the unique crack pattern developed around each anchor. Anchor row A was located inside the plastic hinge length of wall SL7.5 at about 0.125 h_w, 2 ft from the wall-footing interface, and anchors A1 and A6 were located within the North and South end boundary elements of the wall, respectively. Similarly, anchor row B was located inside the plastic hinge length of slender wall SL7.5 at 0.25 $h_w \approx 4$ ft from the wall-footing interface, and anchors B1 and B6 were located within North and South end boundary elements of the wall, respectively. Anchor row C was located outside the plastic hinge length of slender wall SL7.5 at 0.375 $h_w \approx 6$ ft from the wall-footing interface, and anchors C1 and C6 were located within North and South end boundary elements of the wall, respectively. Anchor row D was located outside the plastic hinge length of slender wall SL7.5 at 0.5 $h_w \approx 8$ ft from the wall-footing interface, and anchors D1 and D6 were located within North and South end boundary elements of the wall, respectively. Anchor row E was located outside the plastic hinge length of slender wall SL7.5 at 0.625 $h_w \approx 10$ ft from the wall-footing interface, and anchors E1 and E6 were located within North and South end boundary elements of the wall, respectively. Anchor row F was located outside the plastic hinge length of slender wall SL7.5 at 0.75 $h_w \approx 12$ ft from the wall-footing interface, and anchors F1 and F6 were located within North and South end boundary elements of the wall, respectively. It is noted that anchor row F was instrumented with displacement sensors only.



(a) Anchor location. Units in inches

(b) Photograph of anchor and cracks at end of test

Figure E.1: Bonded anchor A1 in wall SL7.5: location and photographs. Wall residual drift is diagrammatically shown exaggerated for the purpose of illustrating the final context around the anchor

A1

Two horizontal cracks framed bonded anchor A1, as photographs in Fig.E.1 show, but no visible cracks crossed the anchor. Anchor load slightly decreased and displacement was almost constant during test. A significant load drop occurred at 2.5% drift ratio, without significant related variations in the displacement. The maximum measured displacement was about zero.

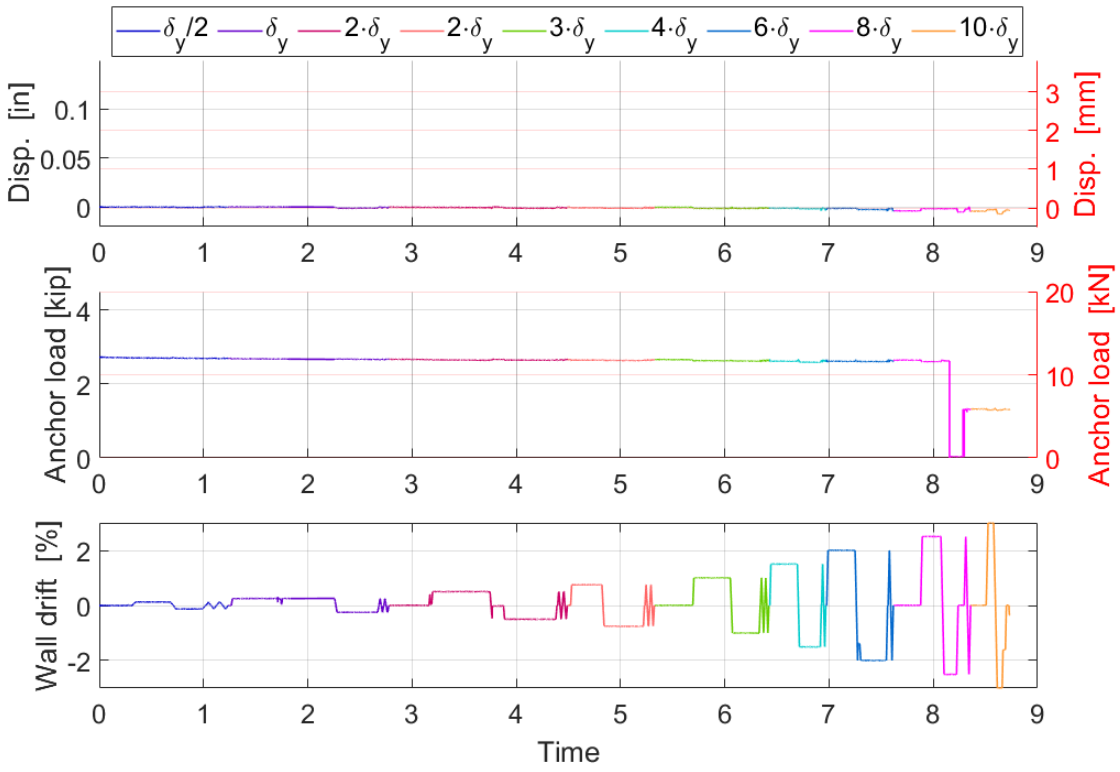
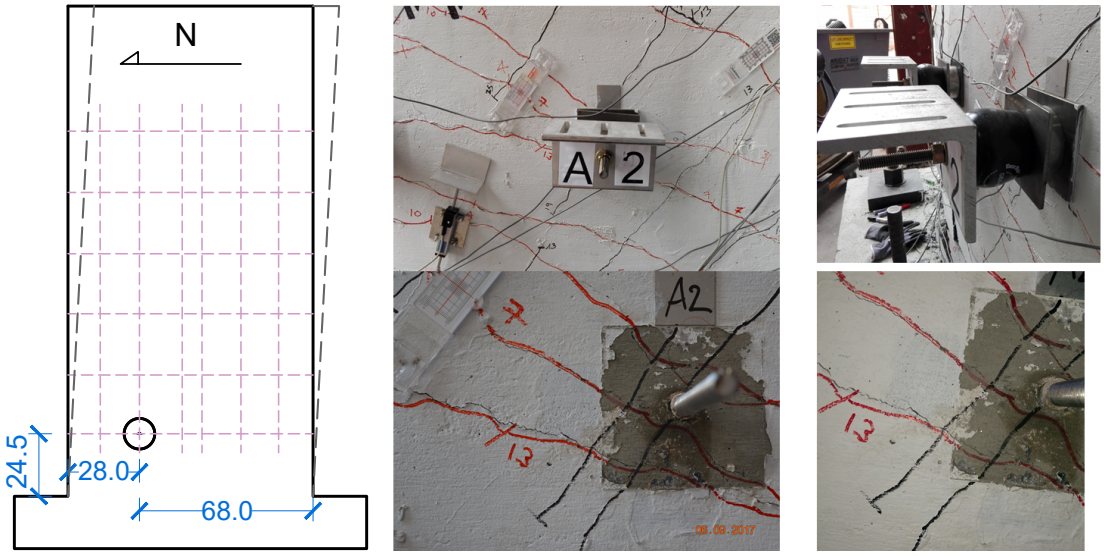


Figure E.2: Bonded anchor A1 in wall SL7.5: measured load and displacement histories and wall drift ratio history



(a) Anchor location. Units in inches

(b) Photograph of anchor and cracks at end of test

Figure E.3: Bonded anchor A2 in wall SL7.5: location and photographs. Wall residual drift is diagrammatically shown exaggerated for the purpose of illustrating the final context around the anchor

A2

A couple of shear cracks crossed bonded anchor A2, as represented in Fig.E.3. Load significantly decreased after the second shear crack crossed the anchor at 2% drift ratio. As a consequence of the load drop, the anchor was reloaded during the 2% drift ratio stop at zero wall displacement. Displacement was small during wall cycling, and it increased significantly in correspondence of the big load drop at 2.5% drift ratio. The maximum measured displacement was 0.15 in.

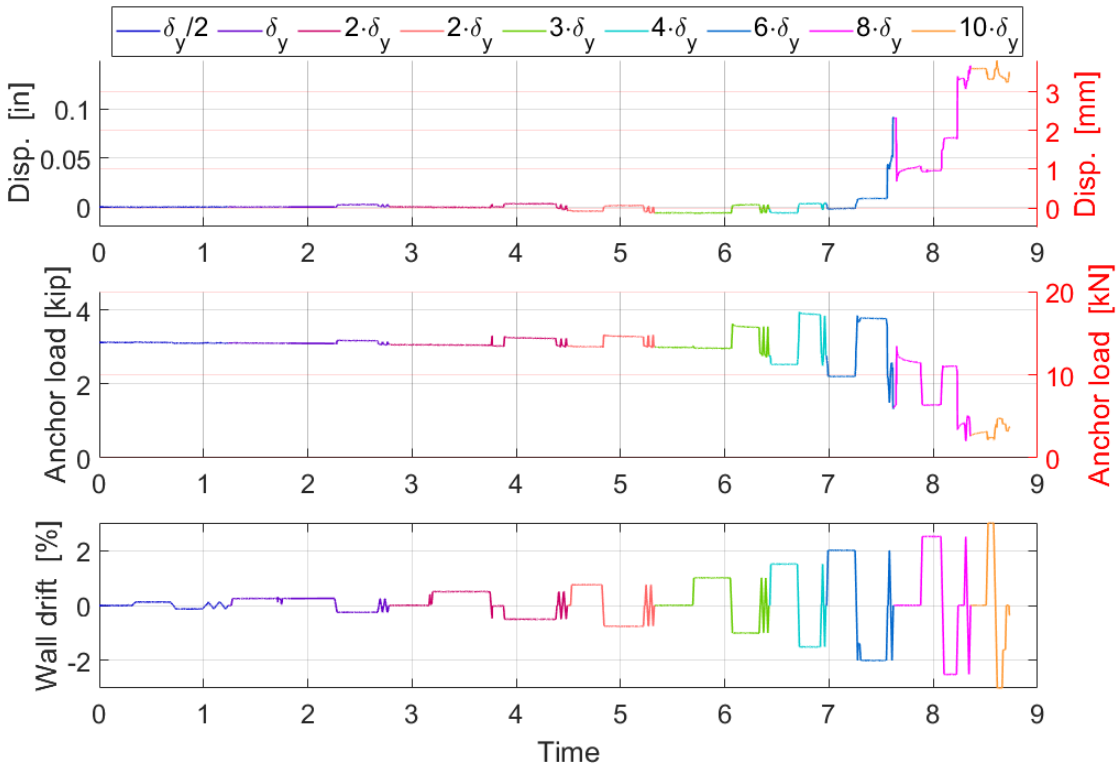
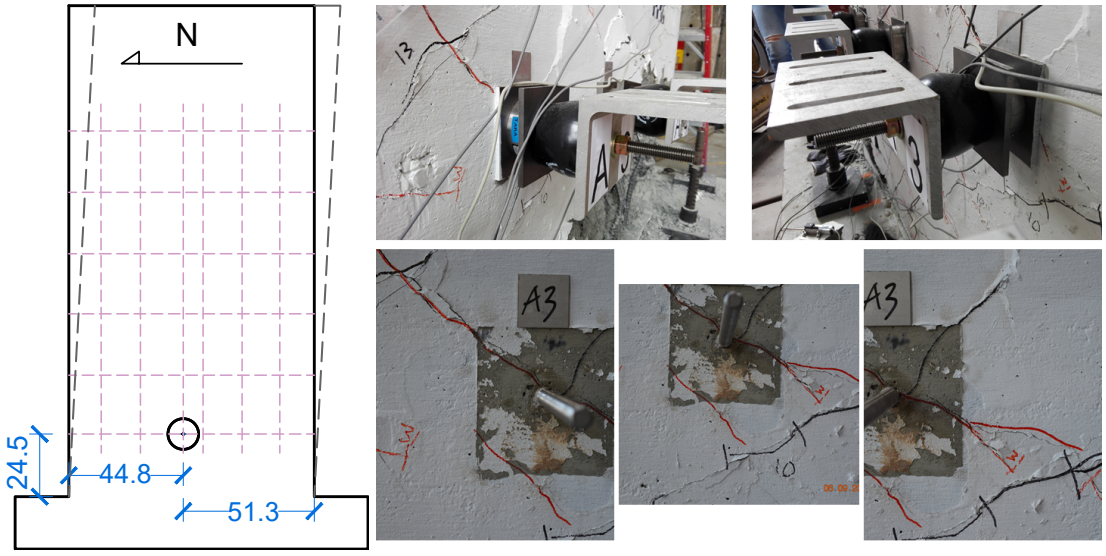


Figure E.4: Bonded anchor A2 in wall SL7.5: measured load and displacement histories and wall drift ratio history



(a) Anchor location. Units in inches (b) Photograph of anchor and cracks at end of test

Figure E.5: Bonded anchor A3 in wall SL7.5: location and photographs. Wall residual drift is diagrammatically shown exaggerated for the purpose of illustrating the final context around the anchor

A3

A couple of shear cracks crossed bonded anchor A3, forming the pattern shown in Fig.E.5. Load decreased up to 10% and measured displacement was small. At the end of the test (3% drift ratio) load increased up to 25% of initial load due to the increased curvature of the wall surface at the end of the test. The maximum measured displacement was close to zero.

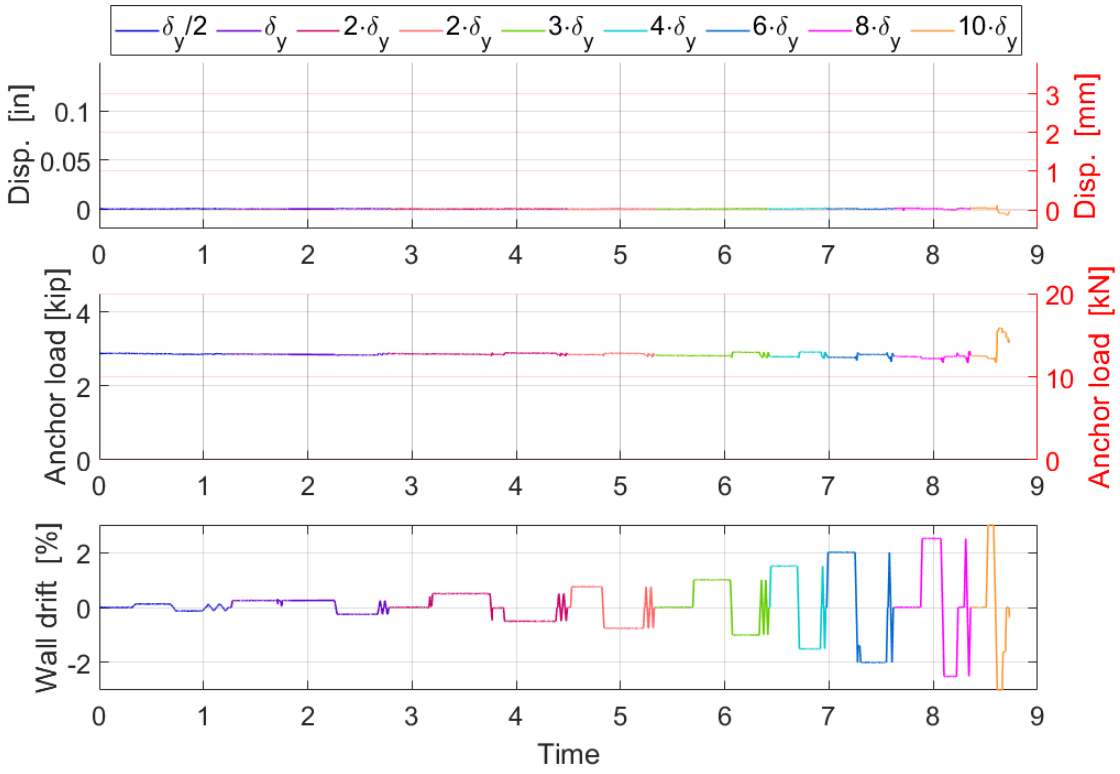
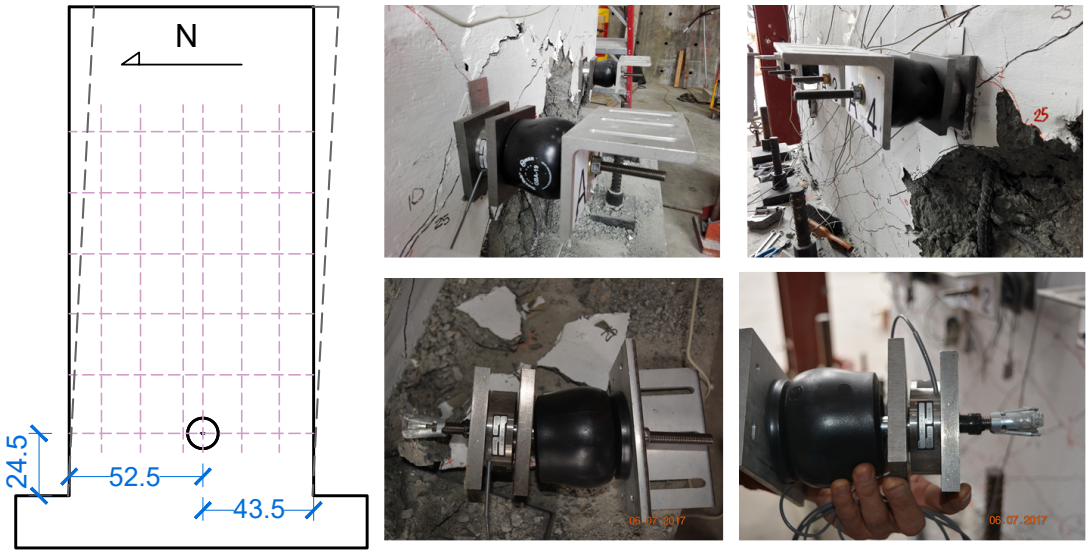


Figure E.6: Bonded anchor A3 in wall SL7.5: measured load and displacement histories and wall drift ratio history.



(a) Anchor location. Units in inches

(b) Photograph of anchor and cracks at end of test

Figure E.7: Expansion anchor A4 in wall SL7.5: location and photographs. Wall residual drift is diagrammatically shown exaggerated for the purpose of illustrating the final context around the anchor

A4

Several shear cracks opened in the vicinity of torque-controlled expansion anchor A4 during the wall cyclic test, as photographs in Fig.E.7 show. Visual assessment of the cracks crossing the anchor was prohibited by concrete crushing before the end of the test. However, load decreased and displacement overall increased. Significant load drop and simultaneous increase in displacement occurred at the end of the test, reflecting the cyclic opening of cracks throughout the anchor embedded length. As a consequence of the load drop, the anchor was reloaded three times. The maximum measured displacement away from the wall was about 0.31 in and the total displacement at the end of test, calculated neglecting the displacement due the compression of the spring, was 0.41 in.

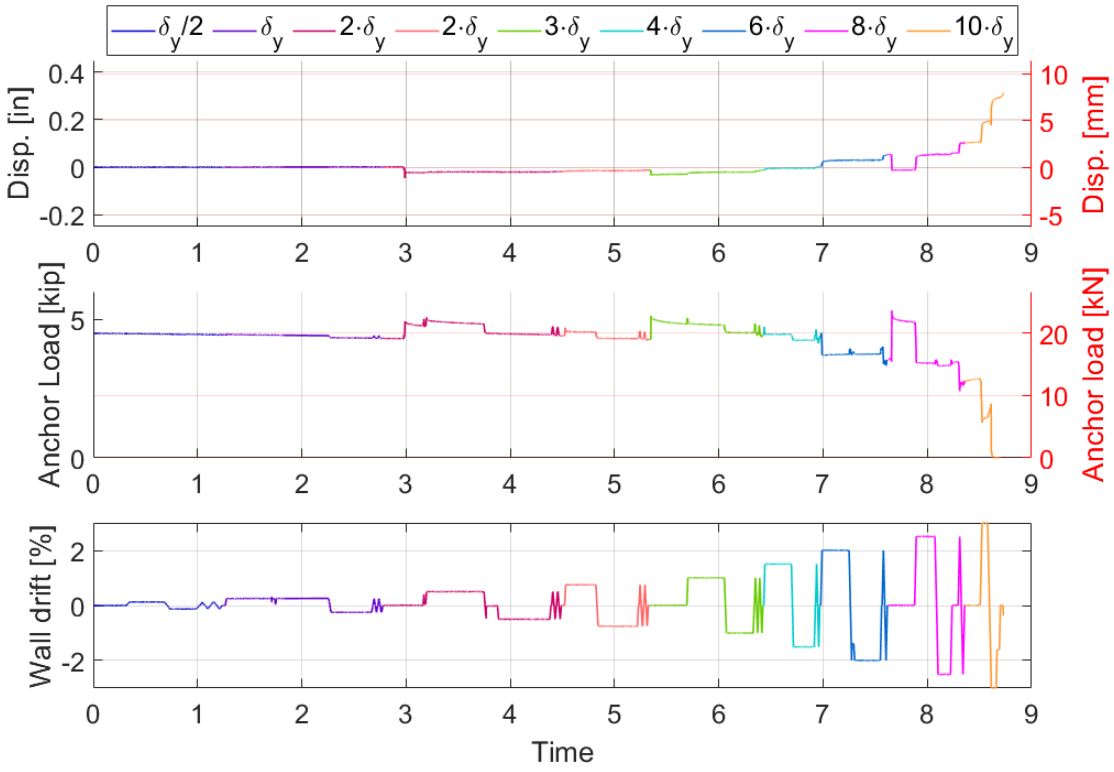
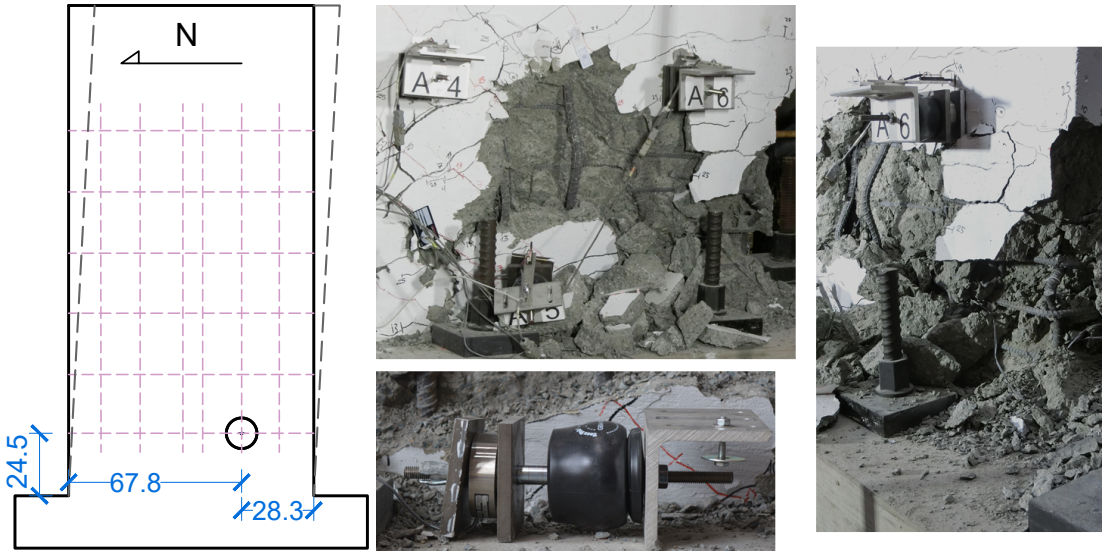


Figure E.8: Expansion anchor A4 in wall SL7.5: measured load and displacement histories and wall drift ratio history



(a) Anchor location. Units in inches (b) Photograph of anchor and cracks at end of test

Figure E.9: Expansion anchor A5 in wall SL7.5: location and photographs. Wall residual drift is diagrammatically shown exaggerated for the purpose of illustrating the final context around the anchor

A5

Several shear cracks opened in the vicinity of torque-controlled expansion anchor A5 during the wall cyclic test, with a dense crack pattern developed in this plastic hinge region. Visual assessment of the cracks crossing the anchor was prohibited by concrete crushing before the end of the test and consequent anchor failure (see Fig.E.9). However, load decreased and displacement overall increased. Significant load drop and simultaneous increase in displacement occurred at the end of the test, reflecting the cyclic opening of cracks throughout the anchor embedded length. As a consequence of the load drop, the anchor was reloaded three times. The maximum measured displacement was about 0.4 in and the total displacement at the end of test, calculated neglecting the displacement due the compression of the spring, was 1.11 in.

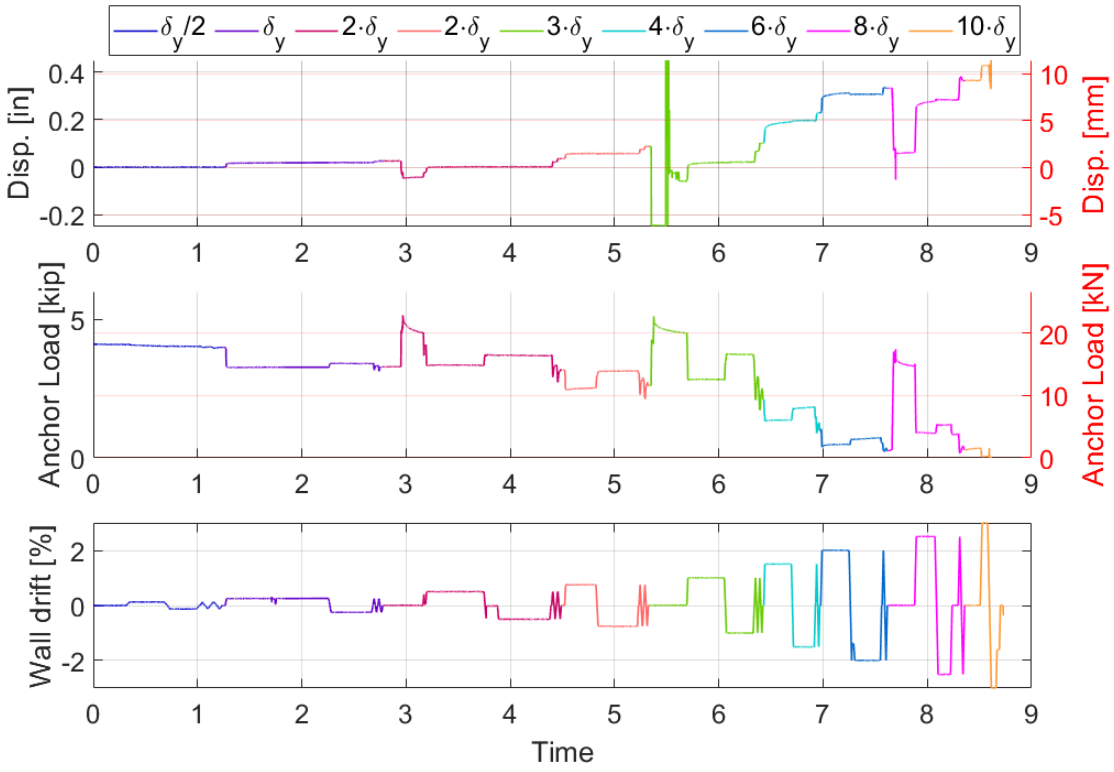


Figure E.10: Expansion anchor A5 in wall SL7.5: measured load and displacement histories and wall drift ratio history



(a) Anchor location. Units in inches

(b) Photograph of anchor and cracks at end of test

Figure E.11: Expansion anchor A6 in wall SL7.5: location and photographs. Wall residual drift is diagrammatically shown exaggerated for the purpose of illustrating the final context around the anchor

A6

Two tension and one shear cracks crossed torque-controlled expansion anchor A6, as the photographs in Fig.E.11 show. The crack width history of one tension crack crossing the anchor was recorded by sensor DCR01, installed at 0.25% drift ratio. Load and displacement were almost constant for great part of the test. During the last drift ratio applied to the wall, the anchor displacement increased and the load decreased. The maximum crack width recorded at 2.5% drift ratio was w_{max} = 5.2 mm. During the last cycles, severe spalling occurred around the anchor, affecting anchor load measurements. Since the anchor held almost a constant load through large part of the wall displacement history, anchor A6 was reloaded only two times, at the 0.5% and 2.0% drift ratios. The maximum measured displacement was 0.2 in and the total displacement at the end of test, calculated neglecting the displacement due the compression of the spring, was 0.35 in.

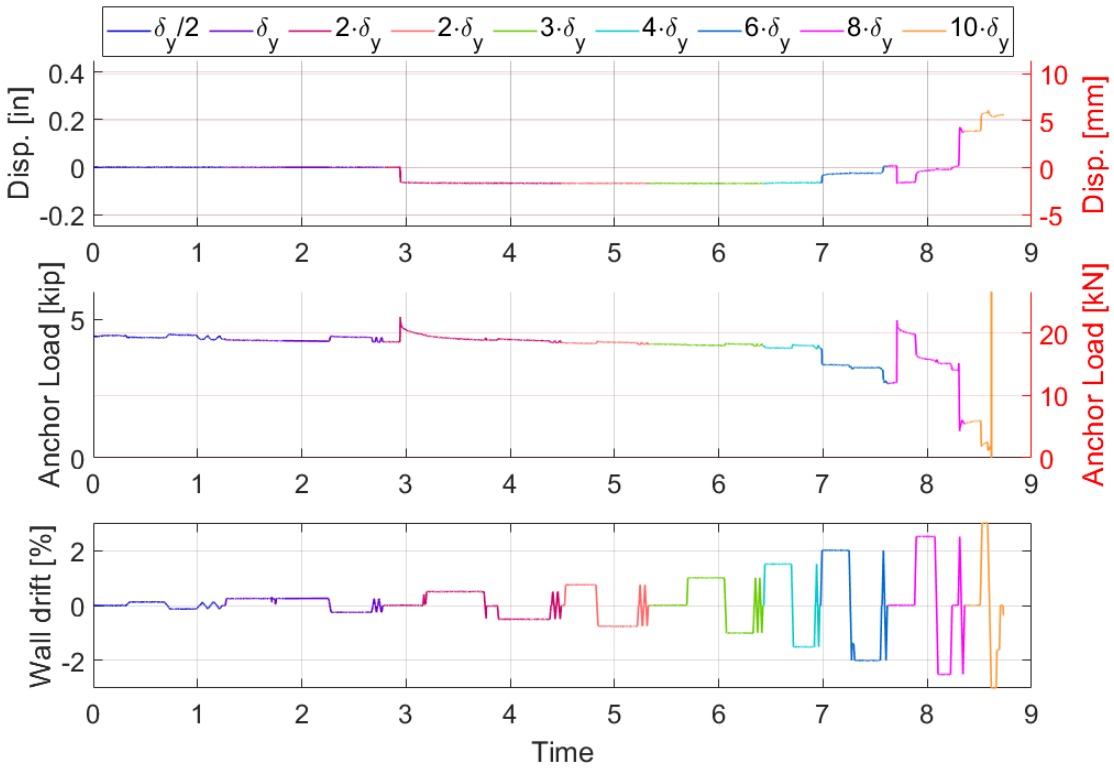
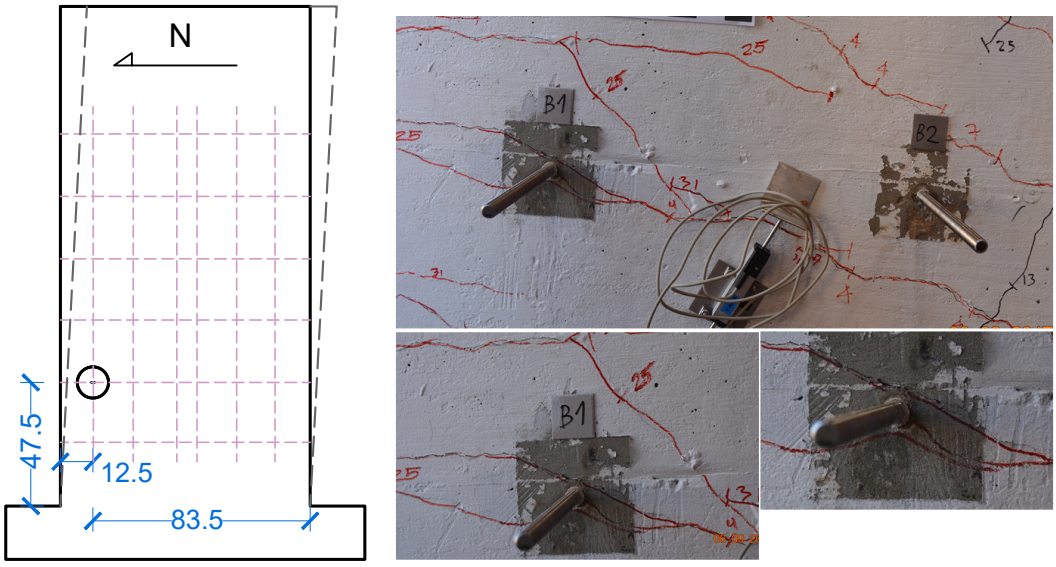


Figure E.12: Expansion anchor A6 in wall SL7.5: measured load and displacement histories and wall drift ratio history



(a) Anchor location. Units in inches

(b) Photograph of anchor and cracks at end of test

Figure E.13: Bonded anchor B1 in wall SL7.5: location and photographs. Wall residual drift is diagrammatically shown exaggerated for the purpose of illustrating the final context around the anchor

B1

A dense crack pattern developed around bonded anchor B1, as shown in Fig.E.13. Two tension cracks opened around the anchor and another couple of tension cracks framed anchor location. The crack width history of one tension crack crossing the anchor was measured by sensor DCR04, installed at 0.5% drift ratio. The maximum crack width measured at 2.5% drift ratio was w_{max} = 2.99 mm. Load increased up to 60% before dropping at the end of the test. Displacement was constant through big part of the test and reached its maximum value at the end of the test. The maximum measured displacement was estimated to be 0.03 in, neglecting the final instrumental spike.

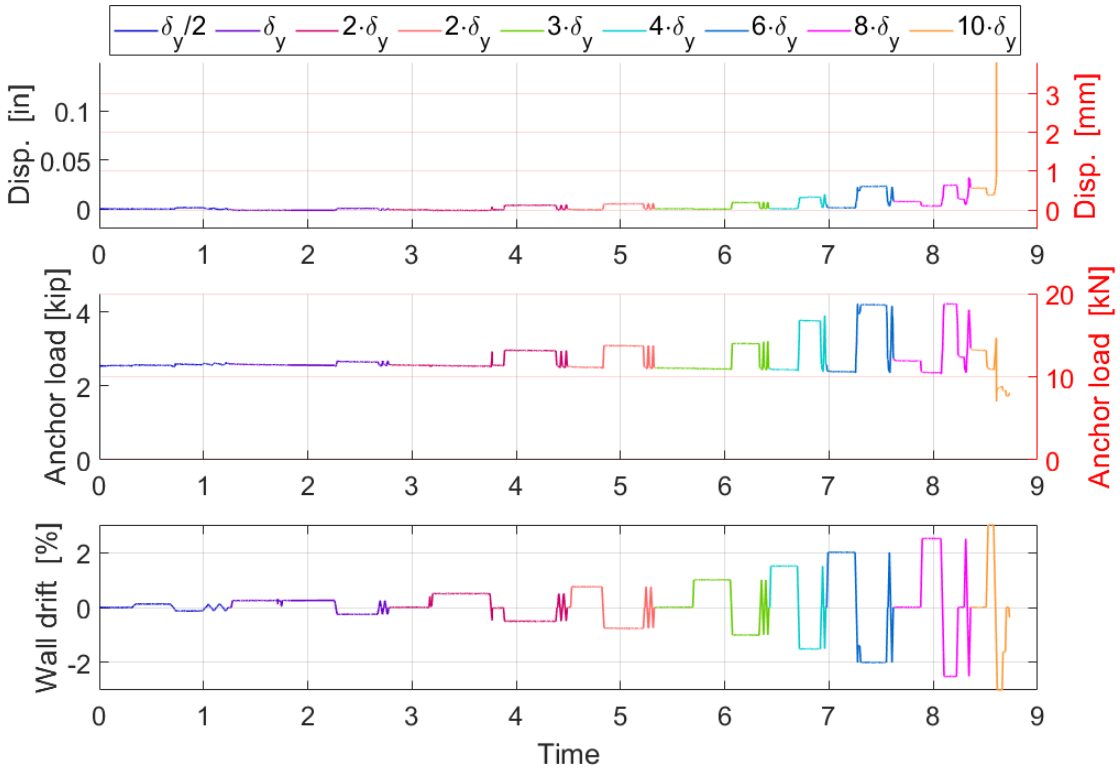
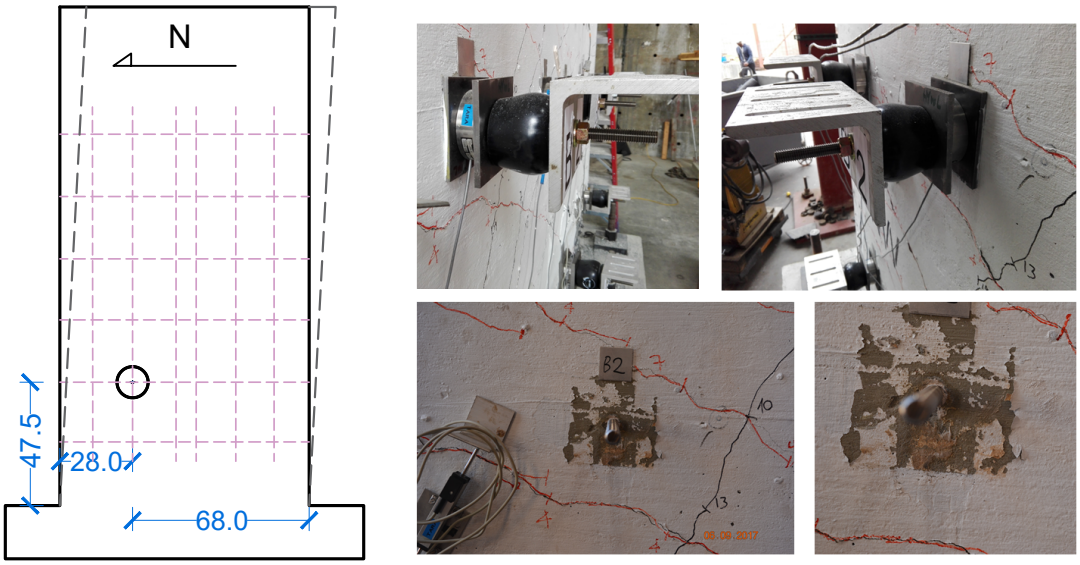


Figure E.14: Bonded anchor B1 in wall SL7.5: measured load and displacement histories and wall drift ratio history



(a) Anchor location. Units in inches

(b) Photograph of anchor and cracks at end of test

Figure E.15: Bonded anchor B2 in wall SL7.5: location and photographs. Wall residual drift is diagrammatically shown exaggerated for the purpose of illustrating the final context around the anchor

B2

Two approximately horizontal cracks surrounded bonded anchor B2 without crossing the anchor location, as shown in Fig.E.15. Load progressively decreased up to 10% of the initial load, but displacement was small and almost constant. The maximum measured displacement was close to zero.

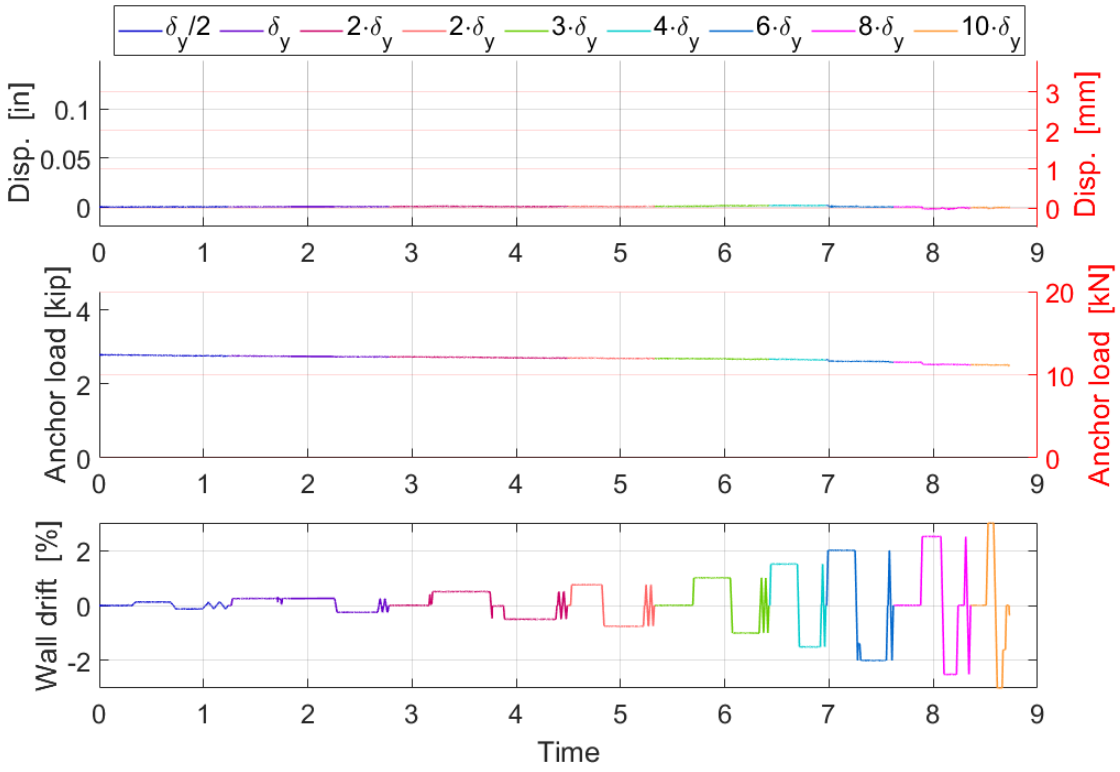
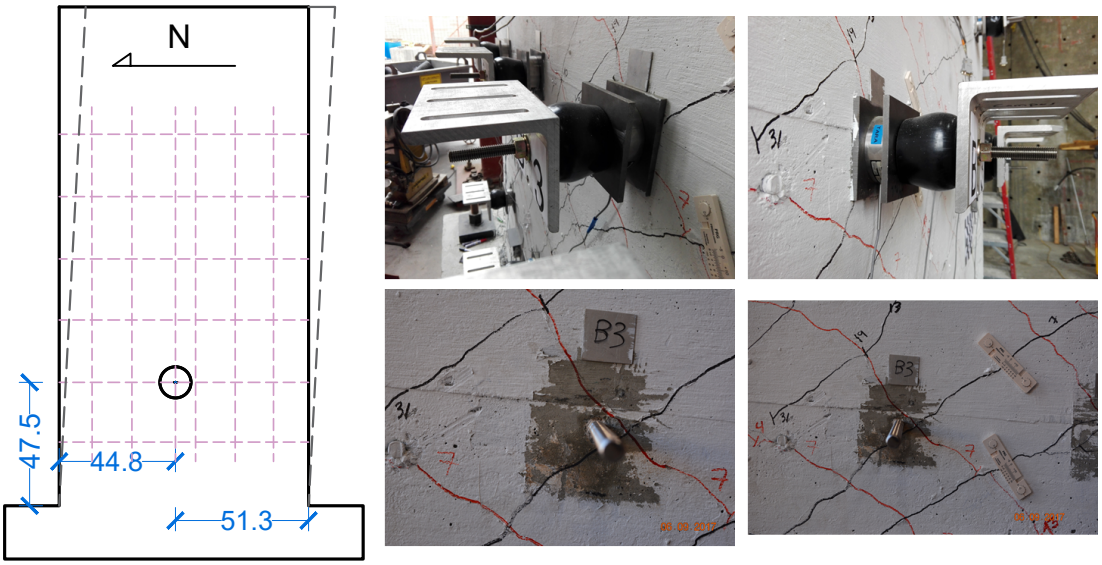


Figure E.16: Bonded anchor B2 in wall SL7.5: measured load and displacement histories and wall drift ratio history



(a) Anchor location. Units in inches

(b) Photograph of anchor and cracks at end of test

Figure E.17: Bonded anchor B3 in wall SL7.5: location and photographs. Wall residual drift is diagrammatically shown exaggerated for the purpose of illustrating the final context around the anchor

B3

Two shear cracks developed around bonded anchor B3, as shown in Fig.E.17. Anchor load progressively decreased up to 5% of the initial load, while global displacement was small and almost constant. The maximum measured displacement was about zero.

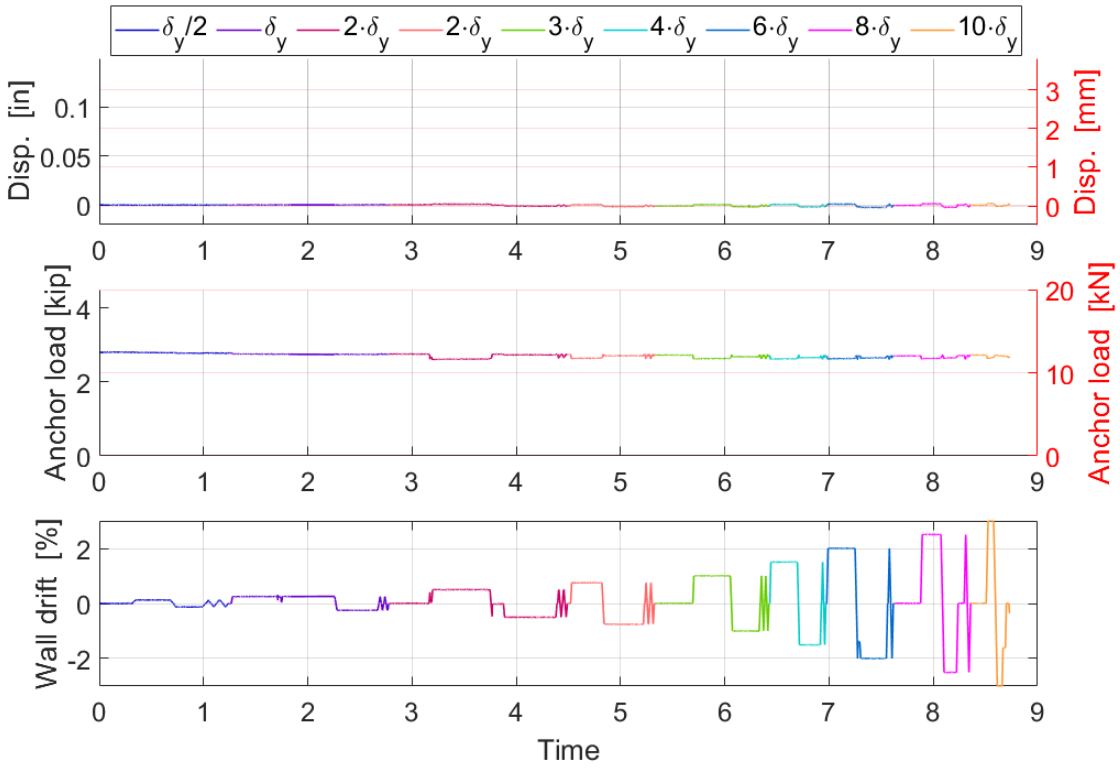
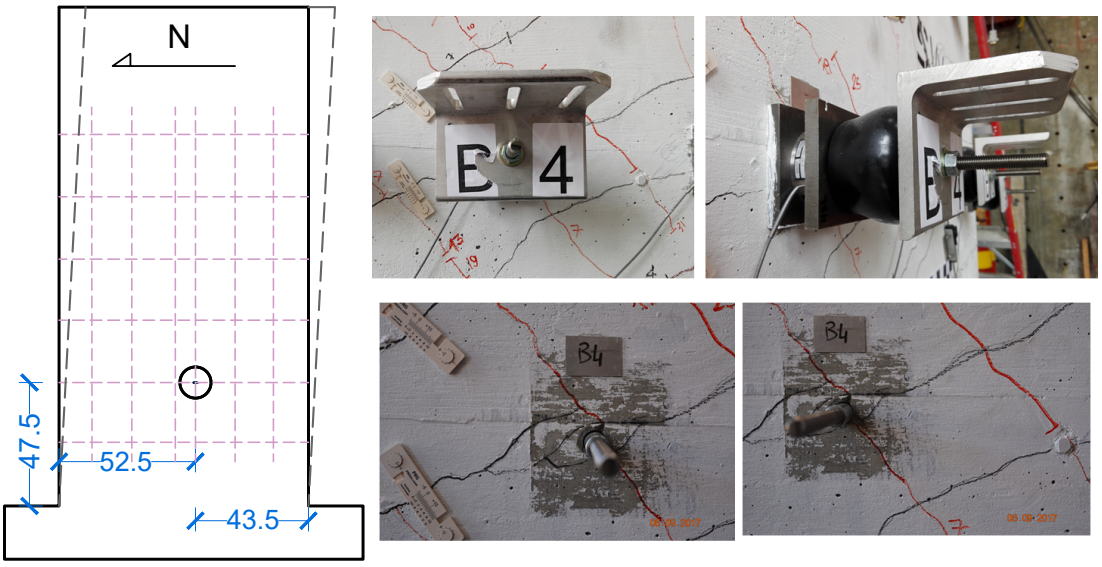


Figure E.18: Bonded anchor B3 in wall SL7.5: measured load and displacement histories and wall drift ratio history



(a) Anchor location. Units in inches

(b) Photograph of anchor and cracks at end of test

Figure E.19: Expansion anchor B4 in wall SL7.5: location and photographs. Wall residual drift is diagrammatically shown exaggerated for the purpose of illustrating the final context around the anchor

B4

Several shear cracks formed in the vicinity of torque-controlled expansion anchor B4 during the wall cyclic test, as in Fig.E.19. Anchor load and global displacement reflected cracks crossing the anchor. As a consequence of anchor load loss, the anchor was reloaded three times. The maximum measured displacement was about 0.03 in, and the total displacement at the end of test, calculated neglecting the displacement due the compression of the spring, was 0.31 in.

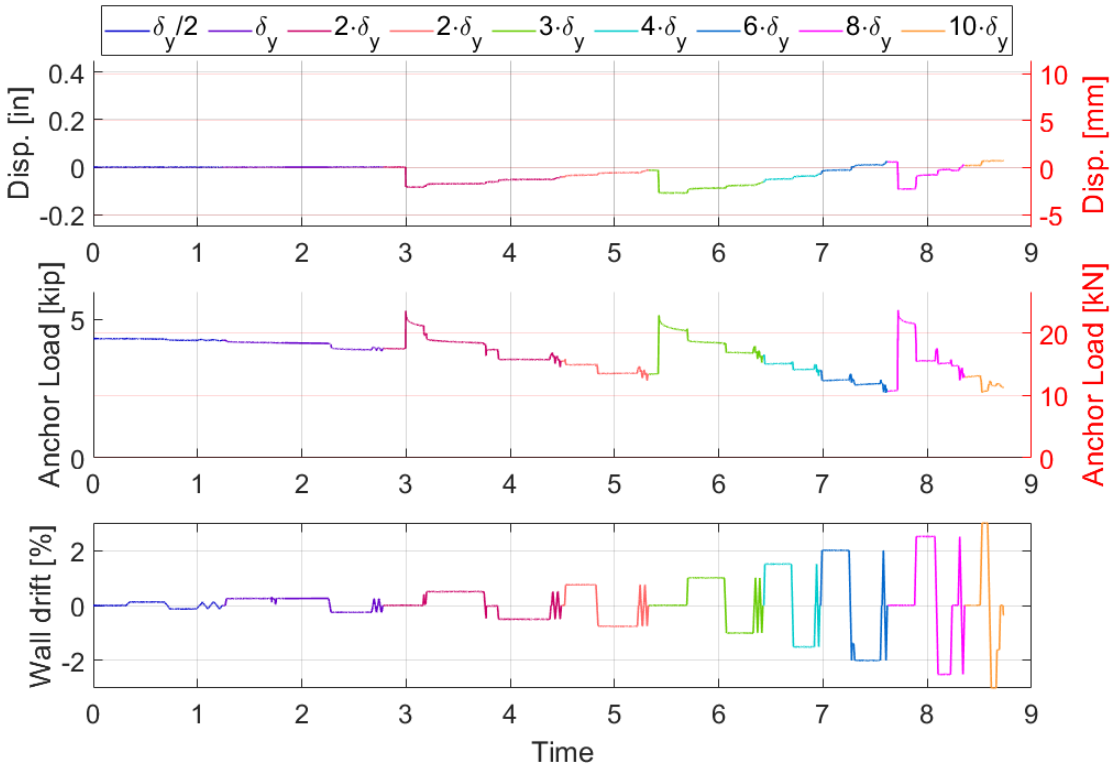
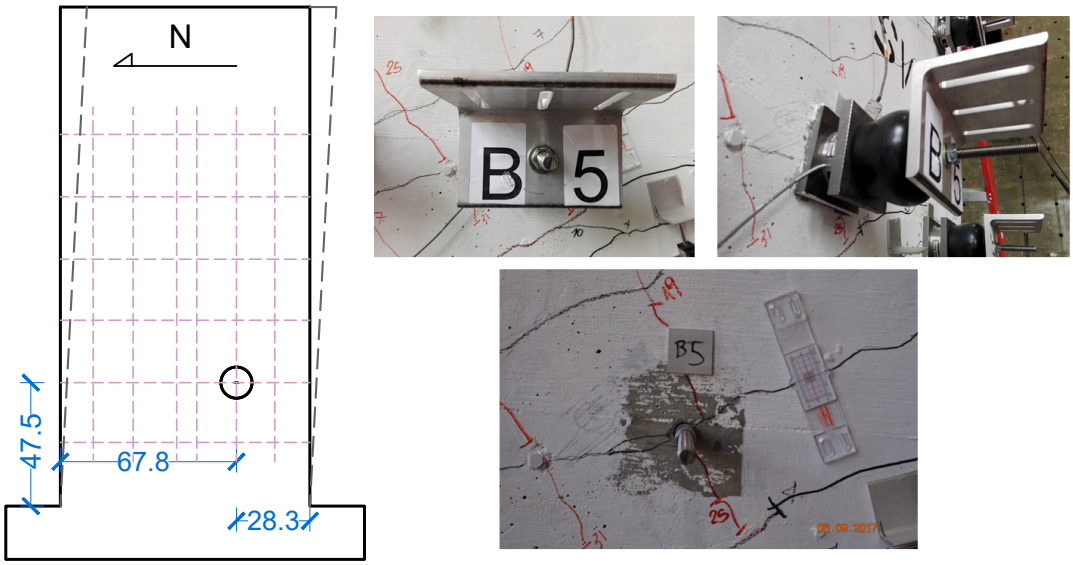


Figure E.20: Expansion anchor B4 in wall SL7.5: measured load and displacement histories and wall drift ratio history



(a) Anchor location. Units in inches

(b) Photograph of anchor and cracks at end of test

Figure E.21: Expansion anchor B5 in wall SL7.5: location and photographs. Wall residual drift is diagrammatically shown exaggerated for the purpose of illustrating the final context around the anchor

B5

Several shear cracks formed in the vicinity of torque-controlled expansion anchor B5 during the wall cyclic test, as in Fig.E.21. Anchor load and global displacement reflected cracks crossing the anchor. As a consequence of anchor load loss, the anchor was reloaded three times. The maximum measured displacement was about 0.13 in and the total displacement at the end of test, calculated neglecting the displacement due the compression of the spring, was 0.47 in.

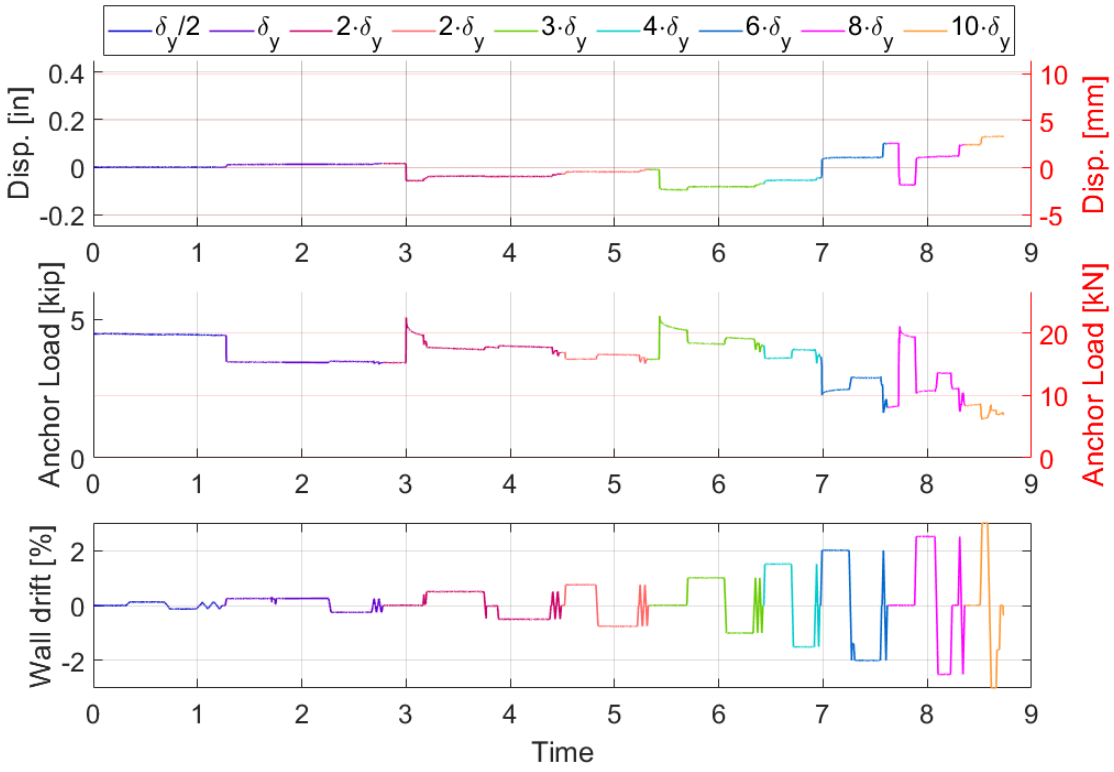
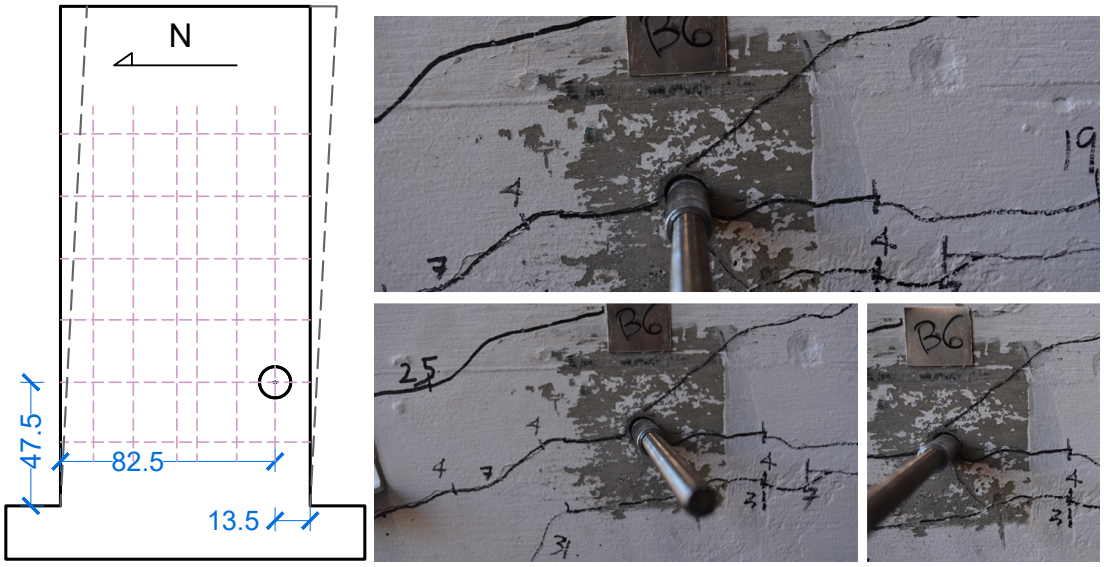


Figure E.22: Expansion anchor B5 in wall SL7.5: measured load and displacement histories and wall drift ratio history



(a) Anchor location. Units in inches (b) Photograph of anchor and cracks at end of test

Figure E.23: Expansion anchor B6 in wall SL7.5: location and photographs. Wall residual drift is diagrammatically shown exaggerated for the purpose of illustrating the final context around the anchor

B6

A dense crack pattern surrounded torque-controlled expansion anchor B6: two tension and one shear cracks crossed the anchor and two tension cracks framed anchor location, as in Fig.E.23. The crack width history of one tension crack crossing the anchors was recorded by sensor DCR02, installed at 0.25% drift ratio. Load and displacement were almost constant for great part of the test. The anchor was reloaded three times, and small increase in the displacement and small load reductions were measured after each reloading instant. The maximum crack width recorded at 2.5% drift ratio was w_{max}= 2.2 mm. The maximum displacement measured about 0.04 in and the total displacement at the end of test, calculated neglecting the displacement due the compression of the spring, was 0.27 in.

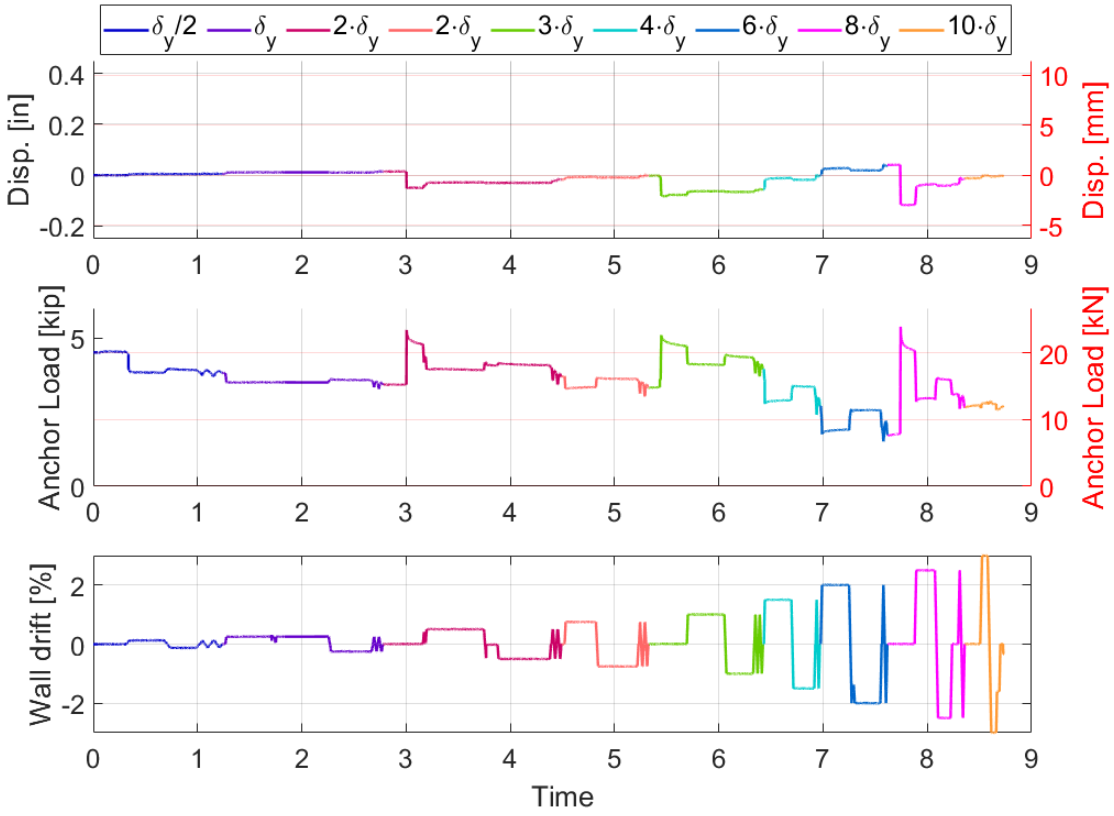
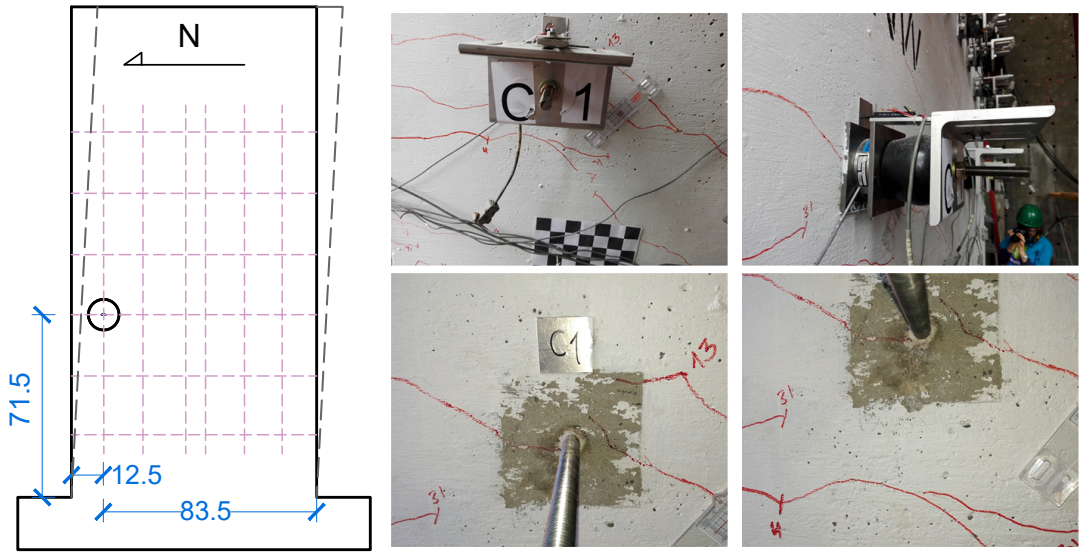


Figure E.24: Expansion anchor B6 in wall SL7.5: measured load and displacement histories and wall drift ratio history



(a) Anchor location. Units in inches

(b) Photograph of anchor and cracks at end of test

Figure E.25: Bonded anchor C1 in wall SL7.5: location and photographs. Wall residual drift is diagrammatically shown exaggerated for the purpose of illustrating the final context around the anchor

C1

One tension crack crossed bonded anchor C1, while other tension cracks developed in this region of the wall, as shown in Fig.E.25. Measured anchor load progressively increased up to 30% of the initial load, denoting increasing eccentricity in the anchor loading setup. However, global displacement was small and almost constant, with about zero maximum measured displacement.

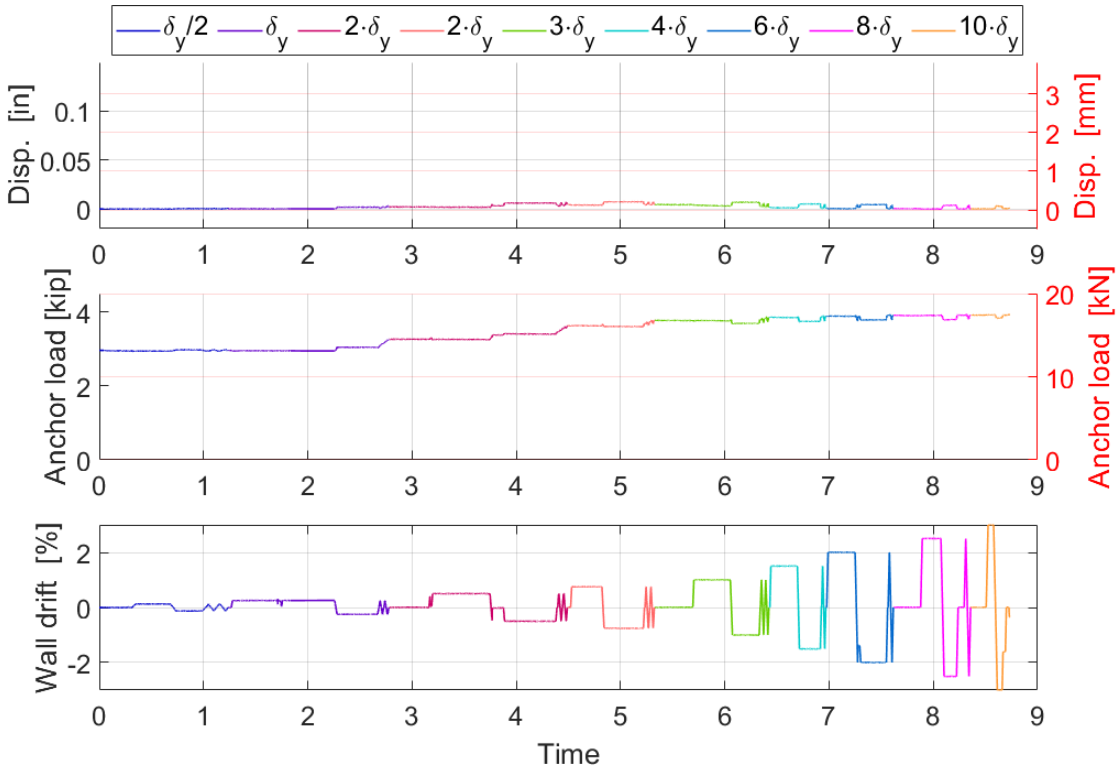
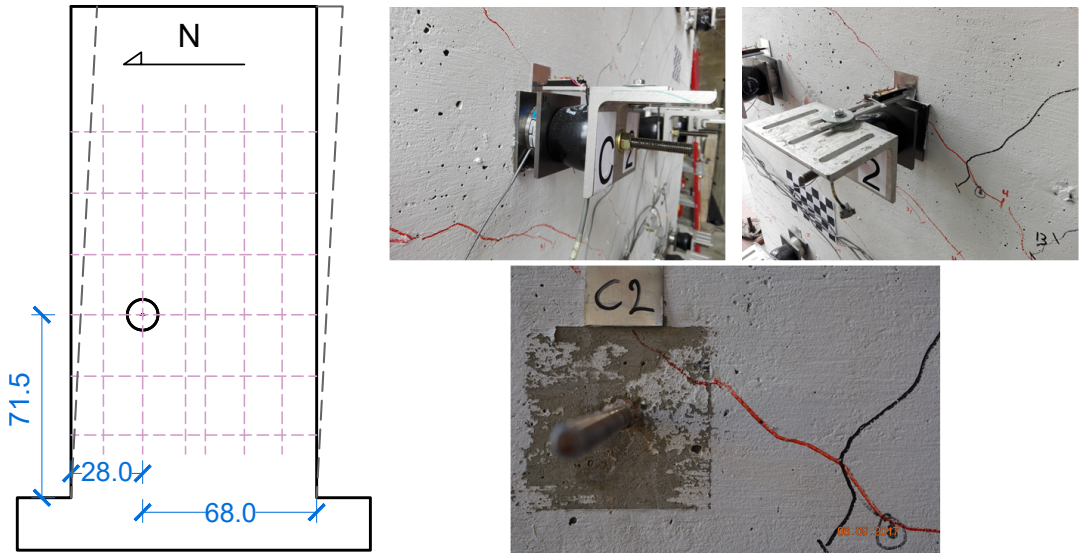


Figure E.26: Bonded anchor C1 in wall SL7.5: measured load and displacement histories and wall drift ratio history



(a) Anchor location. Units in inches

(b) Photograph of anchor and cracks at end of test

Figure E.27: Bonded anchor C2 in wall SL7.5:location and photographs. Wall residual drift is diagrammatically shown exaggerated for the purpose of illustrating the final context around the anchor

C2

No visible cracks intersected the location of bonded anchor C2, as shown in Fig.E.27. Measured anchor load progressively decreased up to 5% of the initial load, while measured global displacement was small and almost constant.

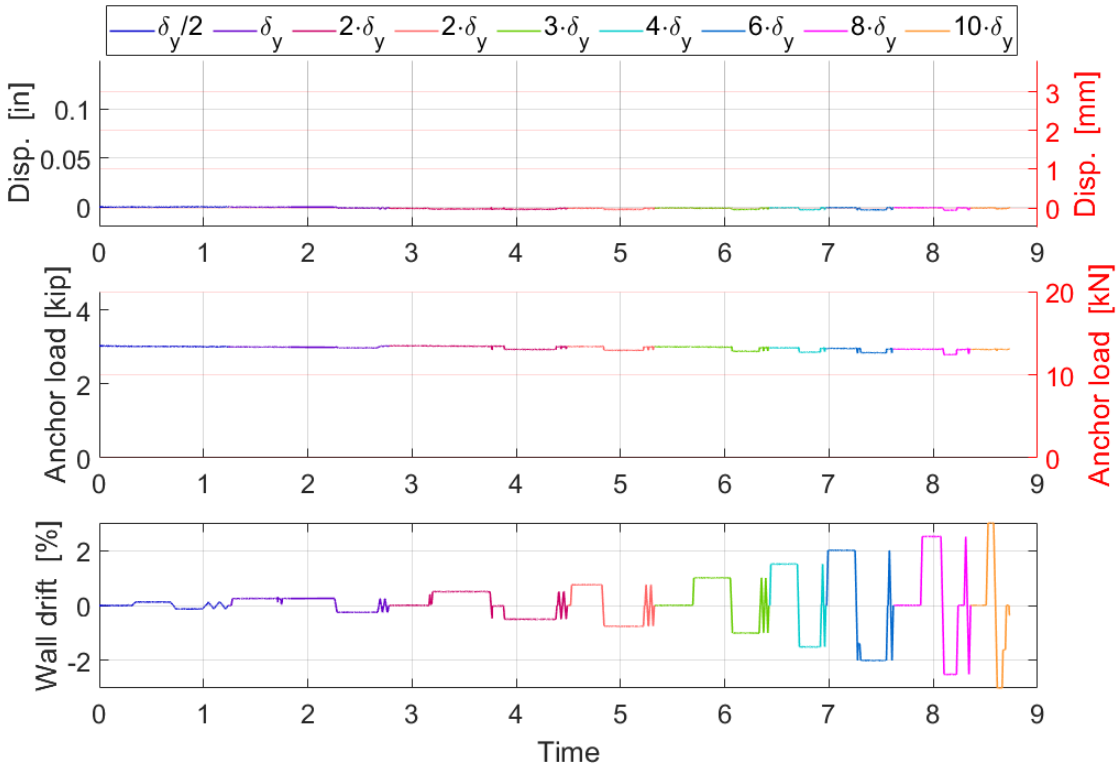
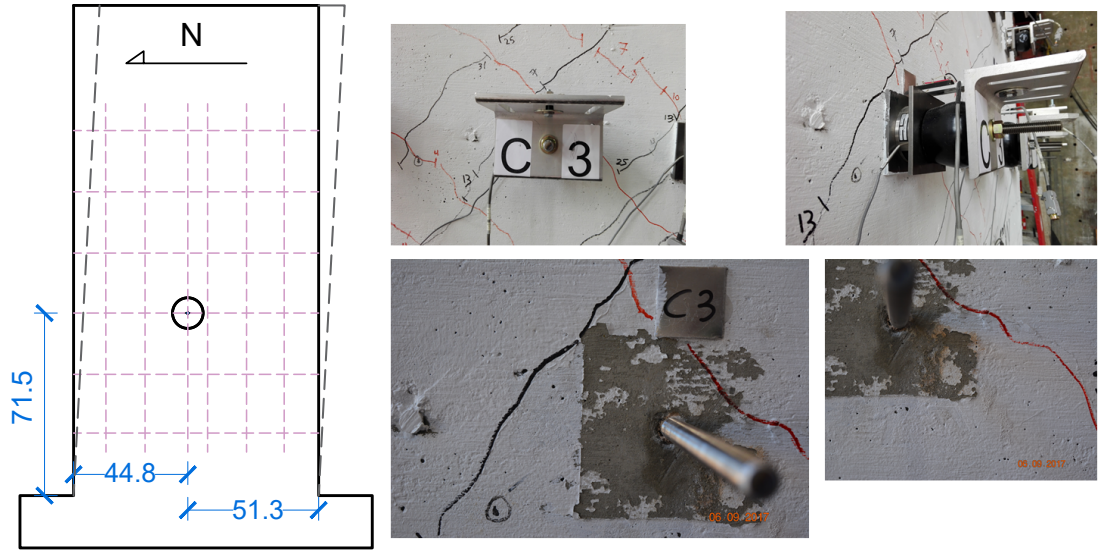


Figure E.28: Bonded anchor C2 in wall SL7.5: measured load and displacement histories and wall drift ratio history



(a) Anchor location. Units in inches

(b) Photograph of anchor and cracks at end of test

Figure E.29: Bonded anchor C3 in wall SL7.5: location and photographs. Wall residual drift is diagrammatically shown exaggerated for the purpose of illustrating the final context around the anchor

C3

No visible cracks intersected the location of bonded anchor C3, as shown in Fig.E.29. Measured anchor load progressively decreased up to 5% of the initial load, while global displacement was small and almost constant. Consistently, maximum measured displacement was about zero.

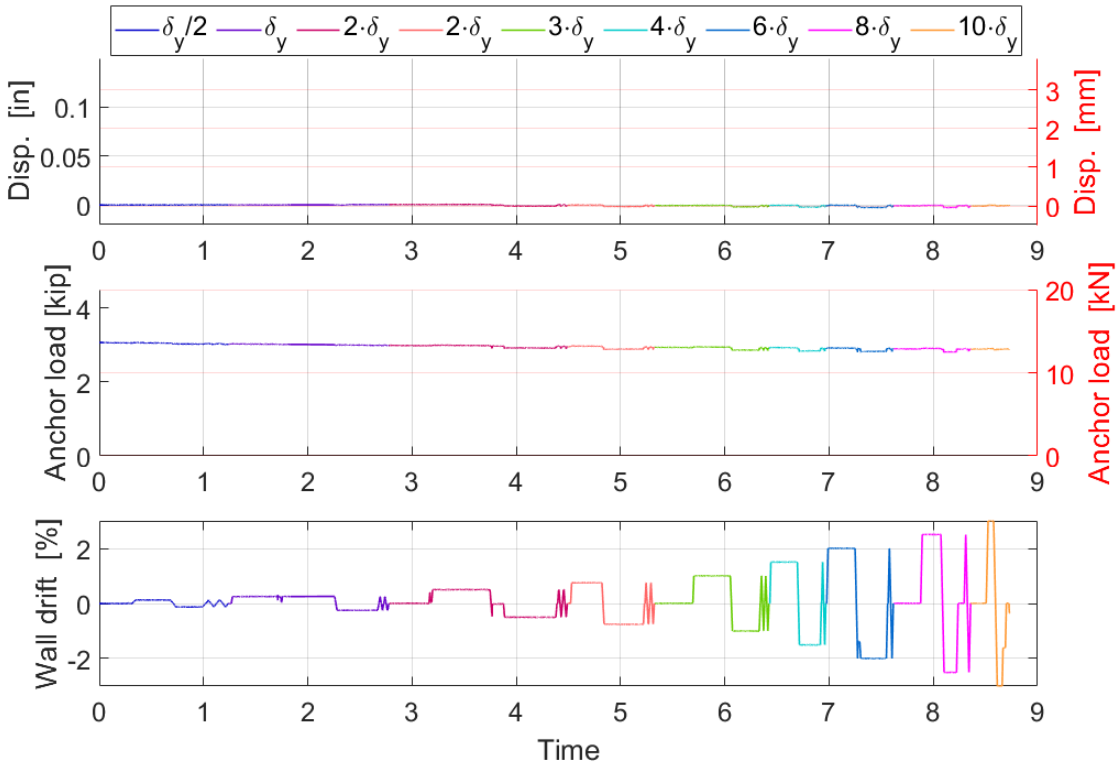
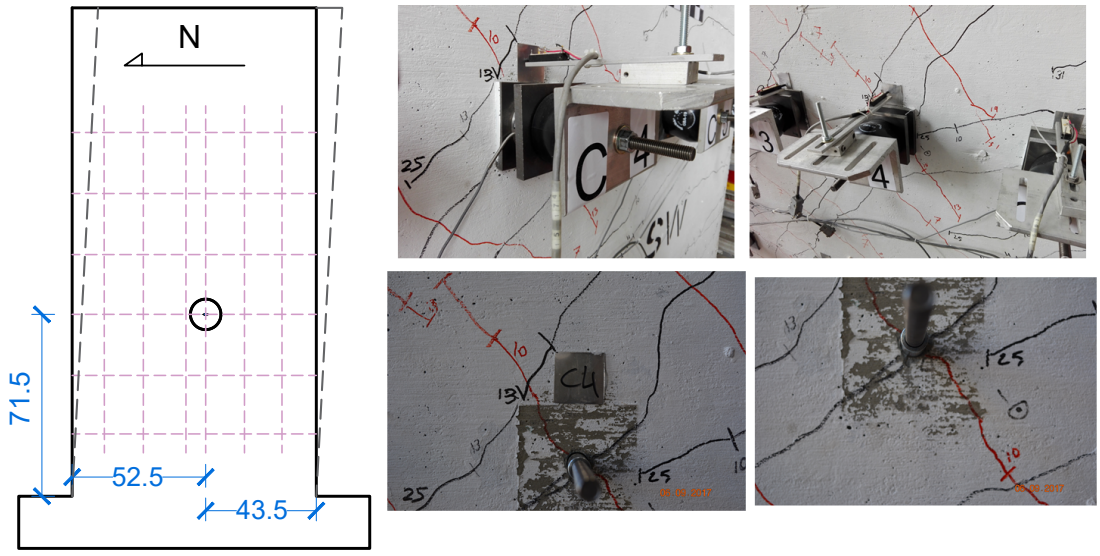


Figure E.30: Bonded anchor C3 in wall SL7.5: measured load and displacement histories and wall drift ratio history



(a) Anchor location. Units in inches

(b) Photograph of anchor and cracks at end of test

Figure E.31: Expansion anchor C4 in wall SL7.5: location and photographs. Wall residual drift is diagrammatically shown exaggerated for the purpose of illustrating the final context around the anchor

C4

Two shear cracks crossed torque-controlled expansion anchor C4, as shown in Fig.E.31. Measured anchor load and displacement overall decreased and increased, respectively. To maintain constant tension, the anchor was reloaded three times. The maximum displacement measured 0.03 in and the total displacement at the end of test, calculated neglecting the displacement due the compression of the spring, was 0.16 in.

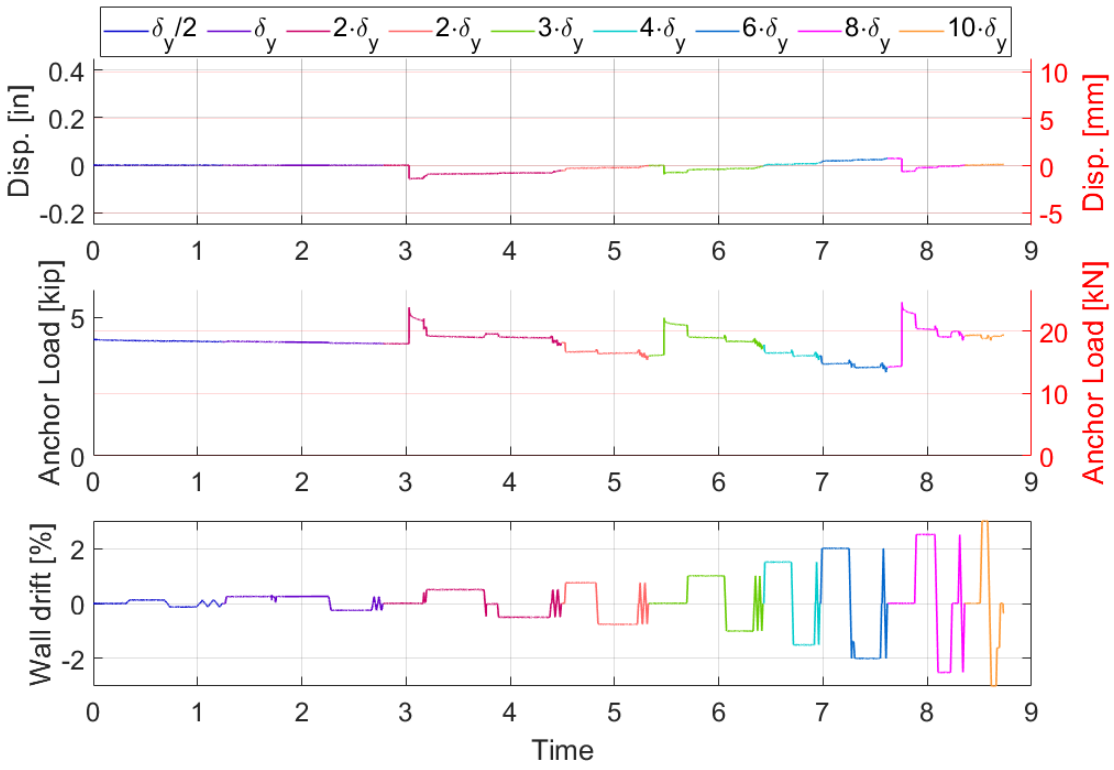
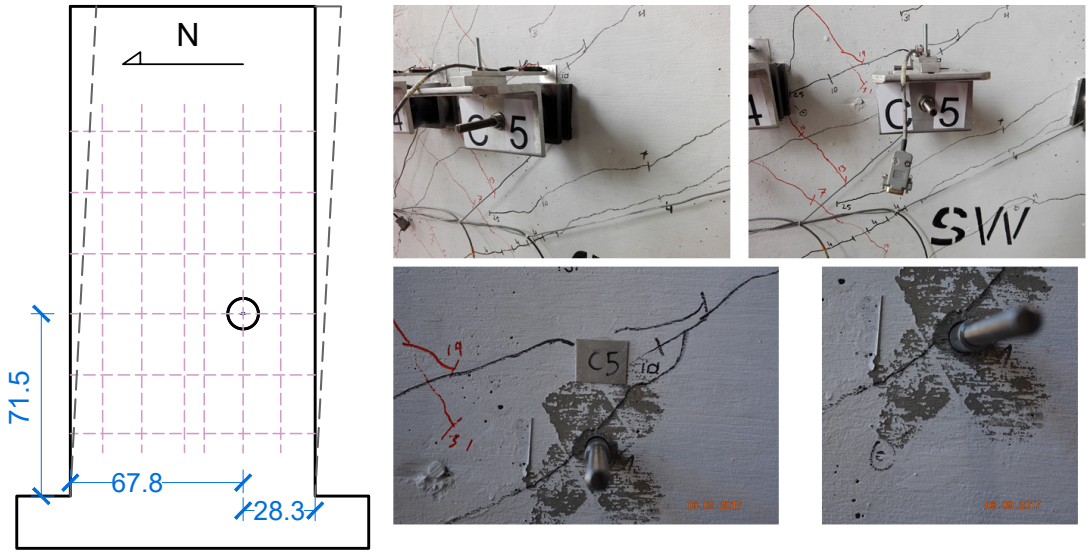


Figure E.32: Expansion anchor C4 in wall SL7.5: measured load and displacement histories and wall drift ratio history



(a) Anchor location. Units in inches

(b) Photograph of anchor and cracks at end of test

Figure E.33: Expansion anchor C5 in wall SL7.5: location and photographs. Wall residual drift is diagrammatically shown exaggerated for the purpose of illustrating the final context around the anchor

C5

One shear crack crossed torque-controlled expansion anchor C5, as shown in Fig.E.33. Measured anchor load and displacement were almost constant for great part of the test. Small increase in the displacement and load reduction were measured after each of the three reloadings. The maximum displacement measured 0.06 in. It is noted that the total displacement was not calculated, since the sensors significantly displaced during the first anchor reloading.

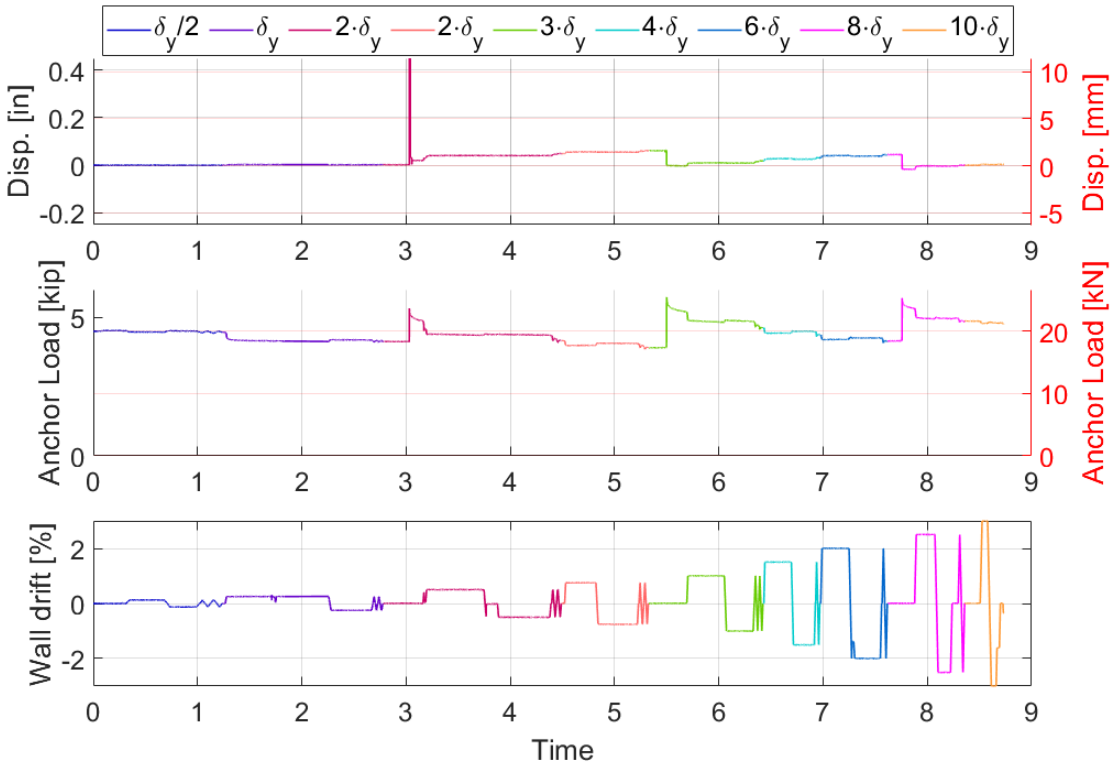
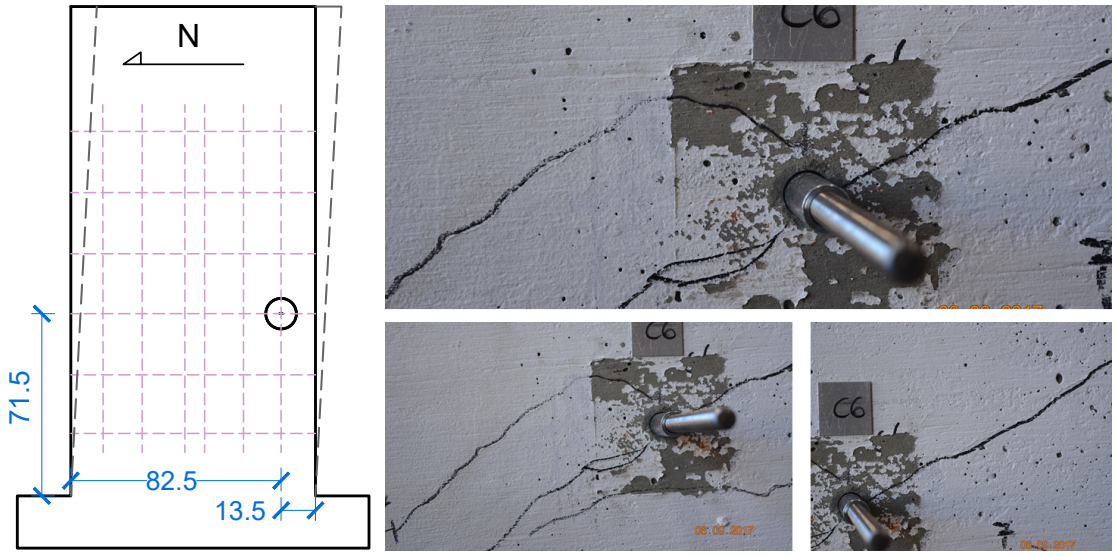


Figure E.34: Expansion anchor C5 in wall SL7.5: measured load and displacement histories and wall drift ratio history



(a) Anchor location. Units in inches

(b) Photograph of anchor and cracks at end of test

Figure E.35: Expansion anchor C6 in wall SL7.5: location and photographs. Wall residual drift is diagrammatically shown exaggerated for the purpose of illustrating the final context around the anchor

C6

One tension crack intersected the location of torque-controlled expansion anchor C6, as shown in Fig.E.35. Measured load and displacement were almost constant for great part of the test. The displacement sensor was compromised by the first reloading of the anchor at 0.25% drift ratio, therefore subsequent displacement readings are not considered reliable. To maintain constant tension on the anchor, the load was reapplied two times at 0.5% and 0.75% drift ratios. The maximum displacement of 0.18 in is not considered reliable due to the displacement sensor movement in the first reloading stage.

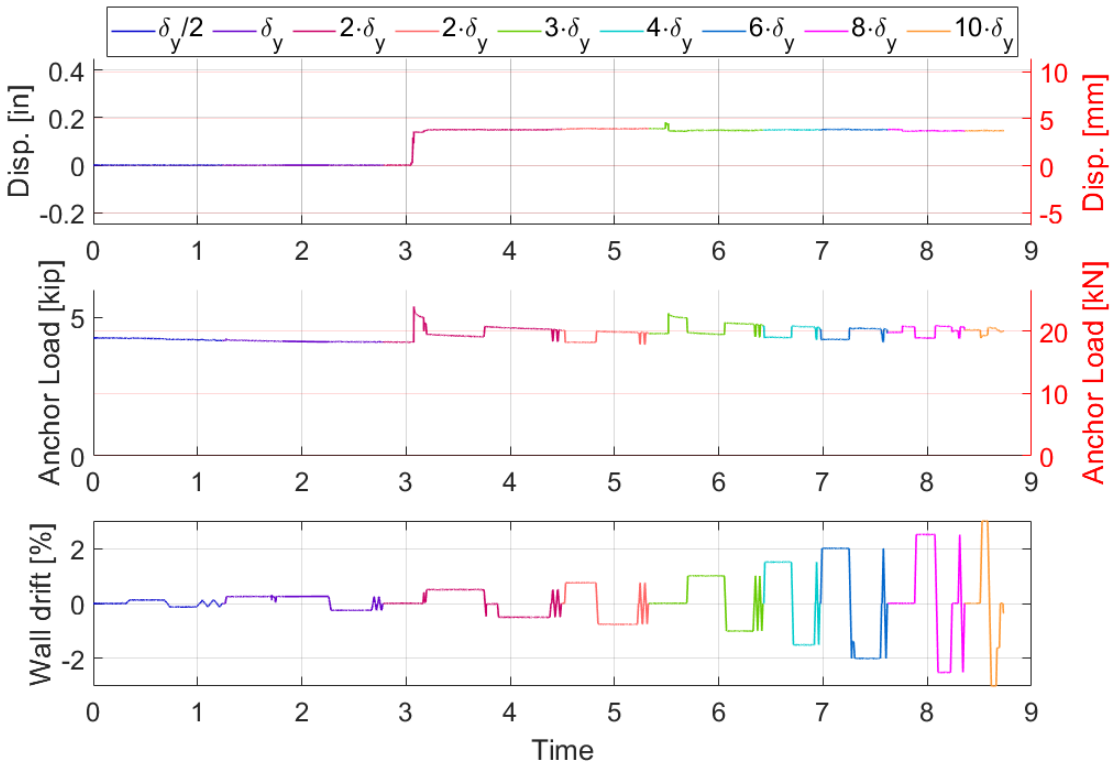
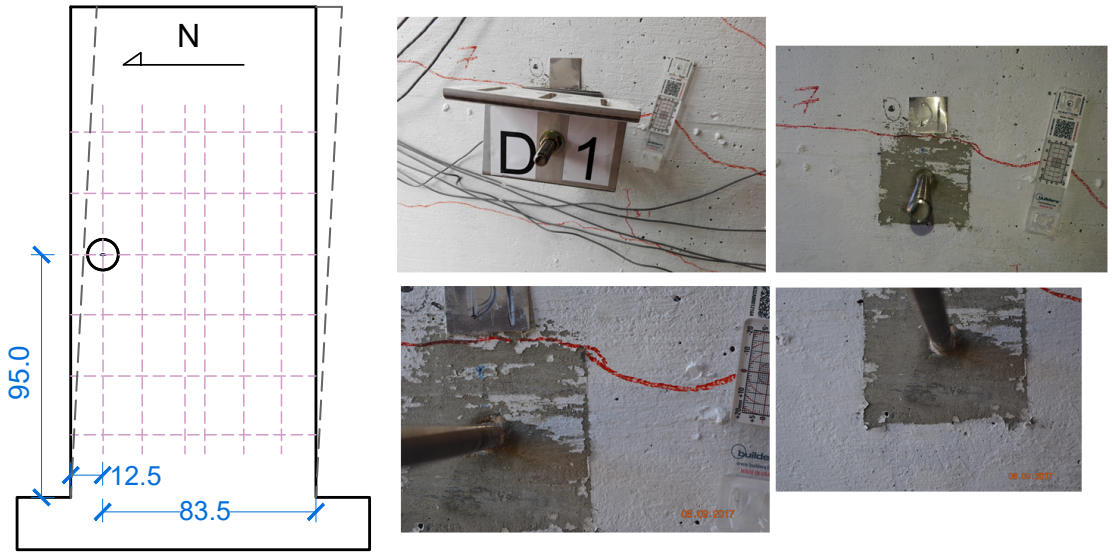


Figure E.36: Expansion anchor C6 in wall SL7.5: measured load and displacement histories and wall drift ratio history



(a) Anchor location. Units in inches

(b) Photograph of anchor and cracks at end of test

Figure E.37: Bonded anchor D1 in wall SL7.5: location and photographs. Wall residual drift is diagrammatically shown exaggerated for the purpose of illustrating the final context around the anchor

D1

No visible cracks crossed bonded anchor D1, as shown in Fig.E.37. Load progressively decreased up to 6% of the initial applied load, while global displacement was small and almost constant. The maximum measured displacement was about zero.

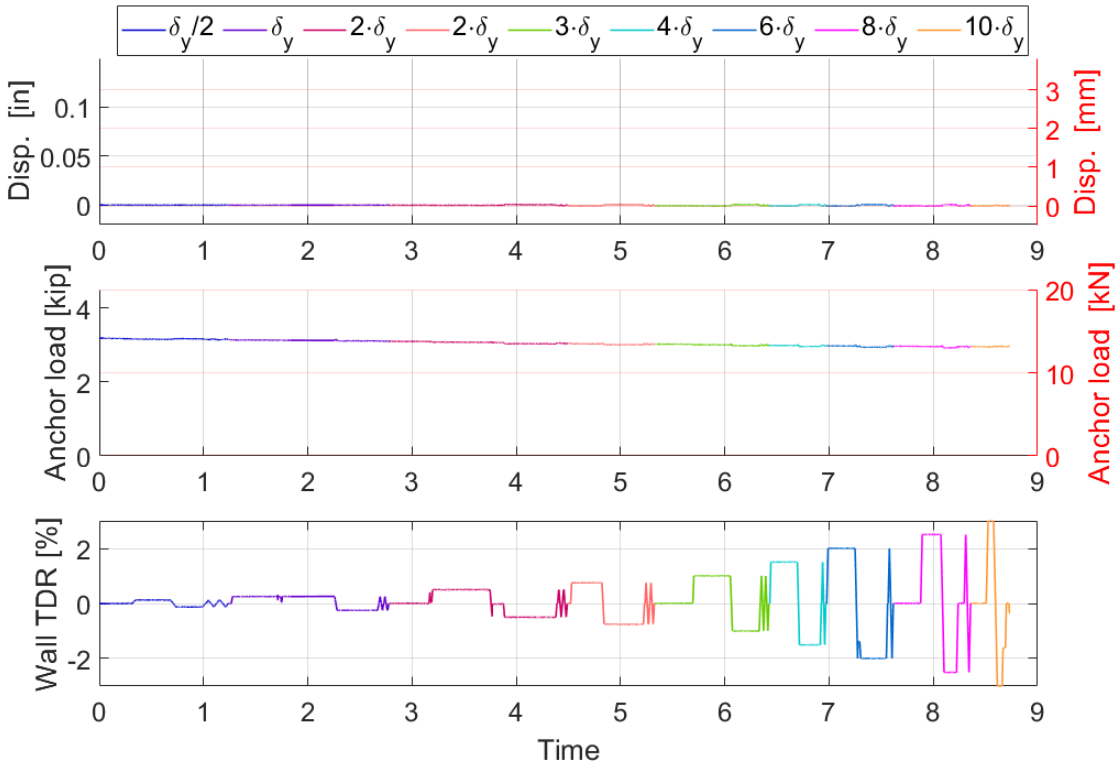
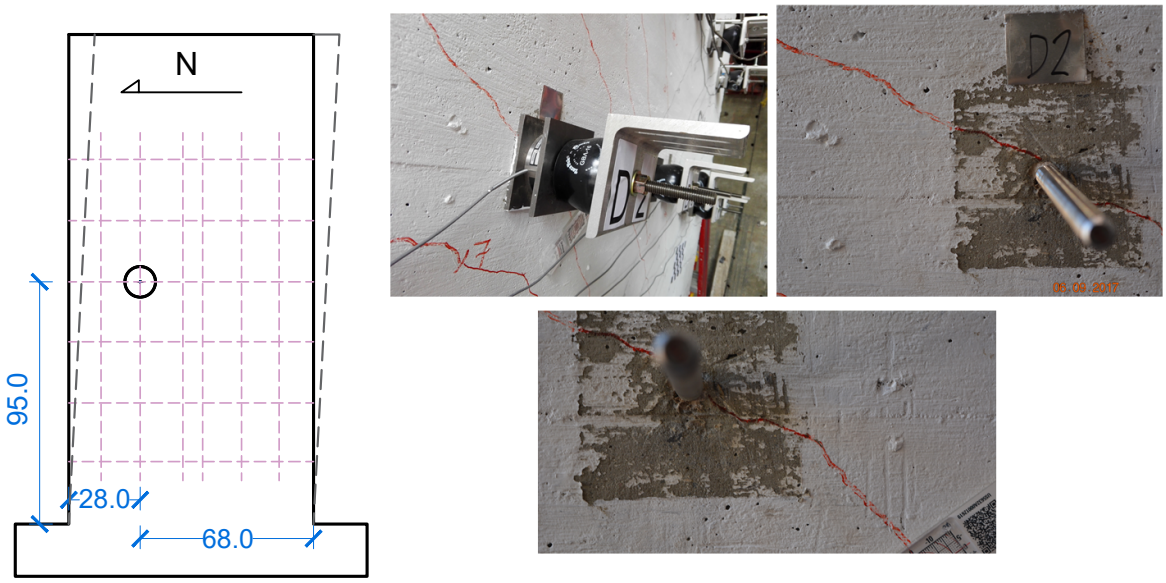


Figure E.38: Bonded anchor D1 in wall SL7.5: measured load and displacement histories and wall drift ratio history



(a) Anchor location. Units in inches

(b) Photograph of anchor and cracks at end of test

Figure E.39: Bonded anchor D2 in wall SL7.5: location and photographs. Wall residual drift is diagrammatically shown exaggerated for the purpose of illustrating the final context around the anchor

D2

One tension crack crossed bonded anchor D2, as shown in Fig.E.39. Measured anchor load progressively decreased up to 7% of the initial load, while displacement was small and almost constant. The maximum measured displacement was about zero.

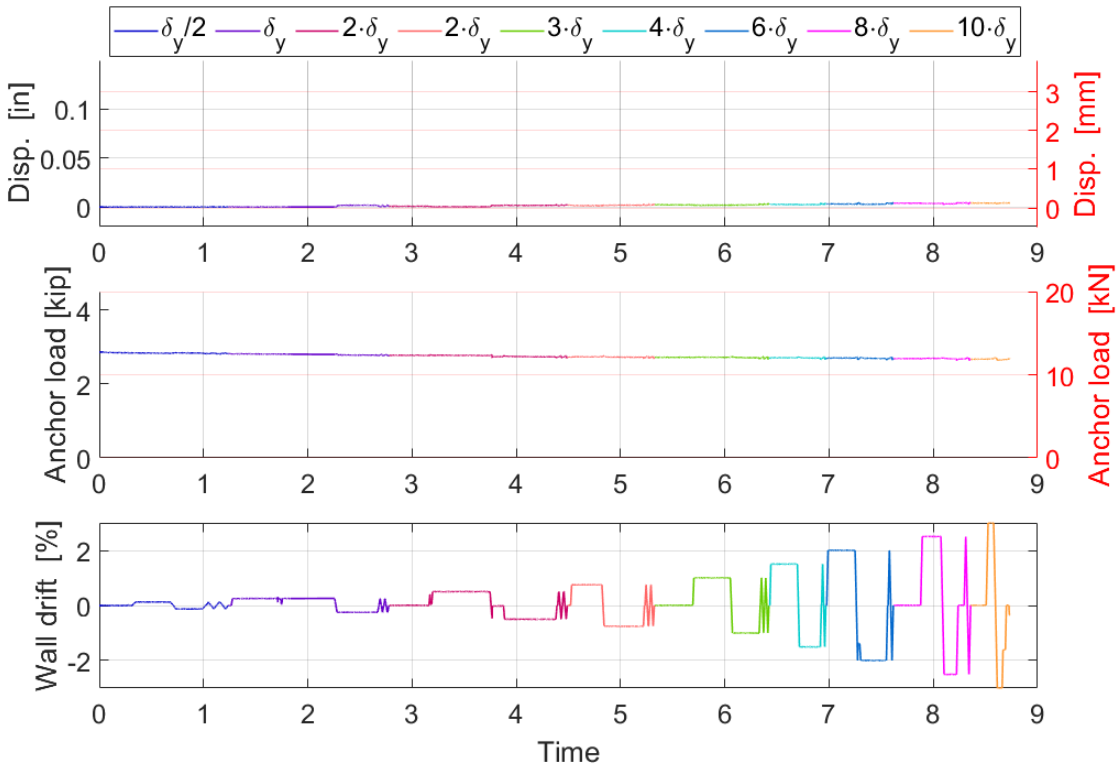
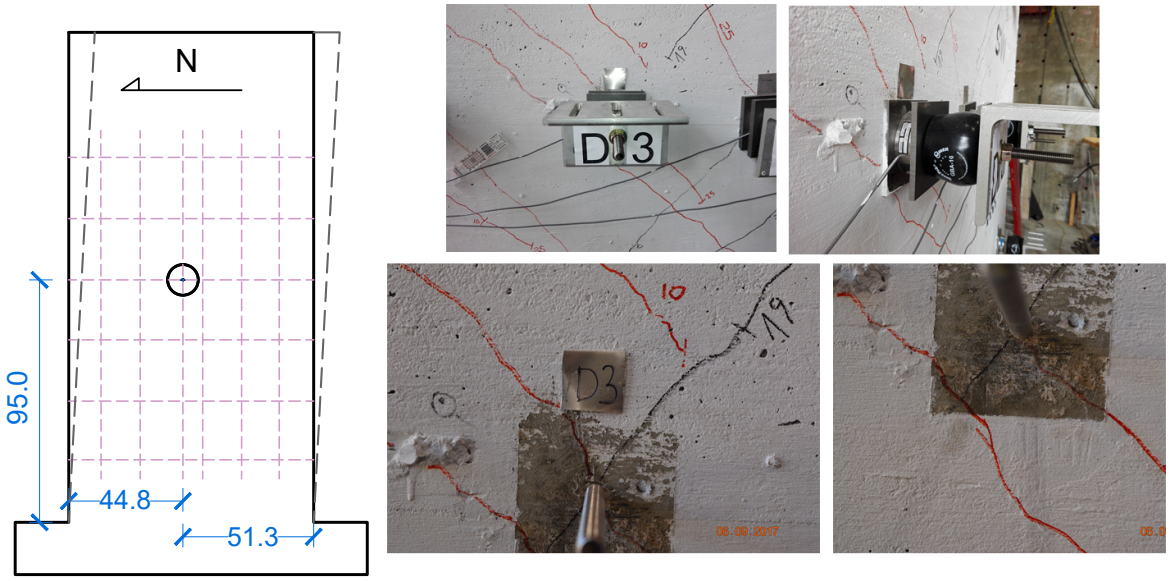


Figure E.40: Bonded anchor D2 in wall SL7.5: measured load and displacement histories and wall drift ratio history



(a) Anchor location. Units in inches

(b) Photograph of anchor and cracks at end of test

Figure E.41: Bonded anchor D3 in wall SL7.5: location and photographs. Wall residual drift is diagrammatically shown exaggerated for the purpose of illustrating the final context around the anchor

D3

Two shear cracks crossed bonded anchor D3, as shown in Fig.E.41. Anchor load progressively decreased up to 7% of the initial load, while displacement was small and almost constant. The maximum measured displacement was about zero.

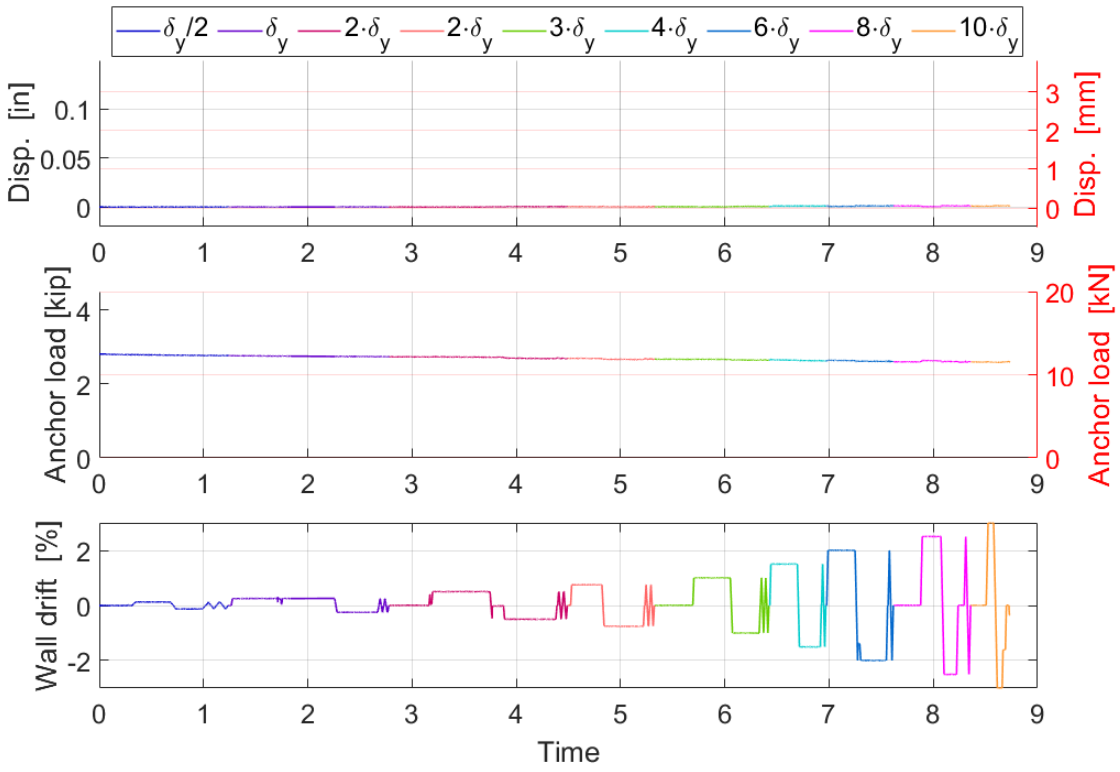
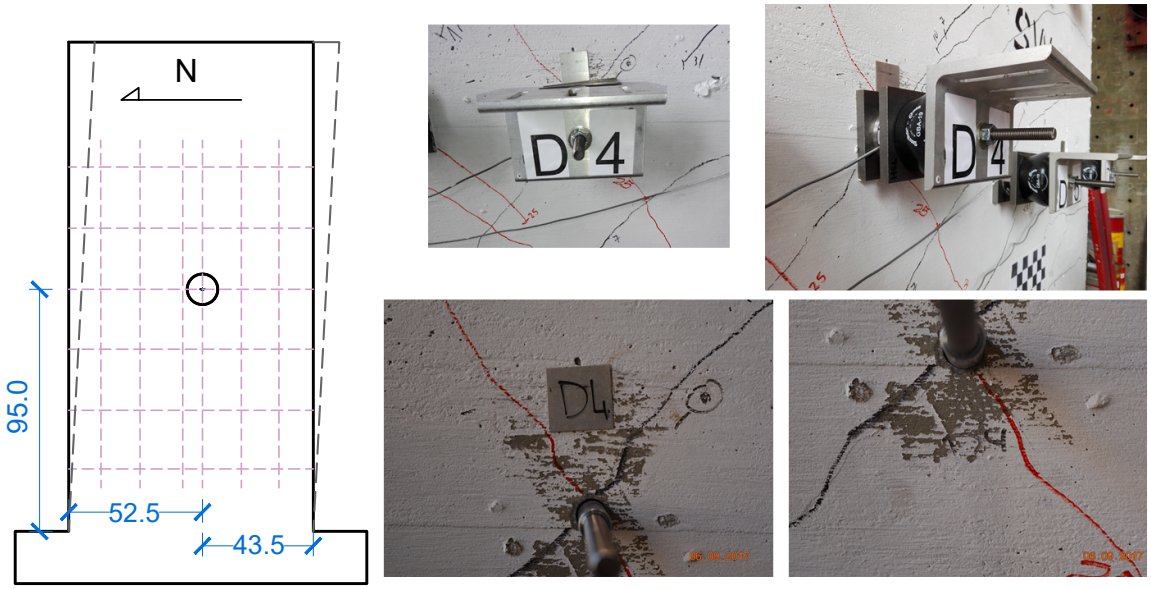


Figure E.42: Bonded anchor D3 in wall SL7.5: measured load and displacement histories and wall drift ratio history



(a) Anchor location. Units in inches

(b) Photograph of anchor and cracks at end of test

Figure E.43: Expansion anchor D4 in wall SL7.5: location and photographs. Wall residual drift is diagrammatically shown exaggerated for the purpose of illustrating the final context around the anchor

D4

Two shear cracks crossed torque-controlled expansion anchor D4, as shown in Fig.E.43. Measured anchor load and displacement were almost constant, except for the two reloads occurrences, at 0.75% and 2.0% drift ratio. The maximum displacement measured 0.03 in, and the total displacement at the end of test, calculated neglecting the displacement due the compression of the spring, was 0.16 in.

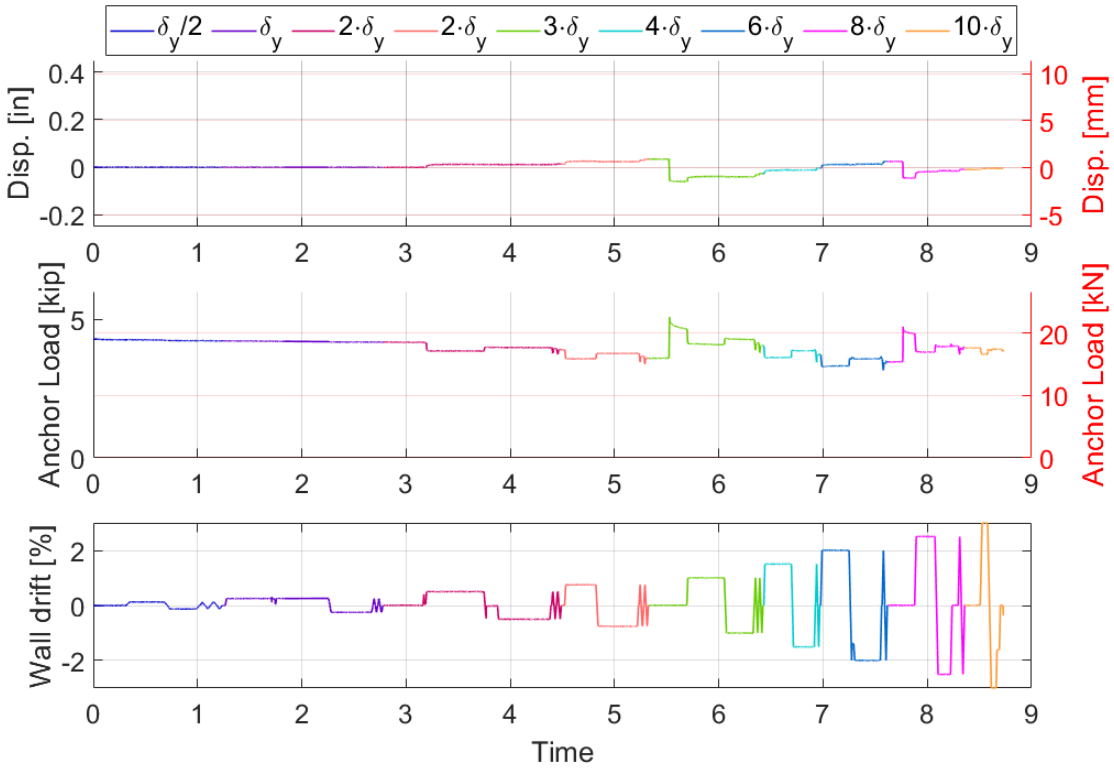
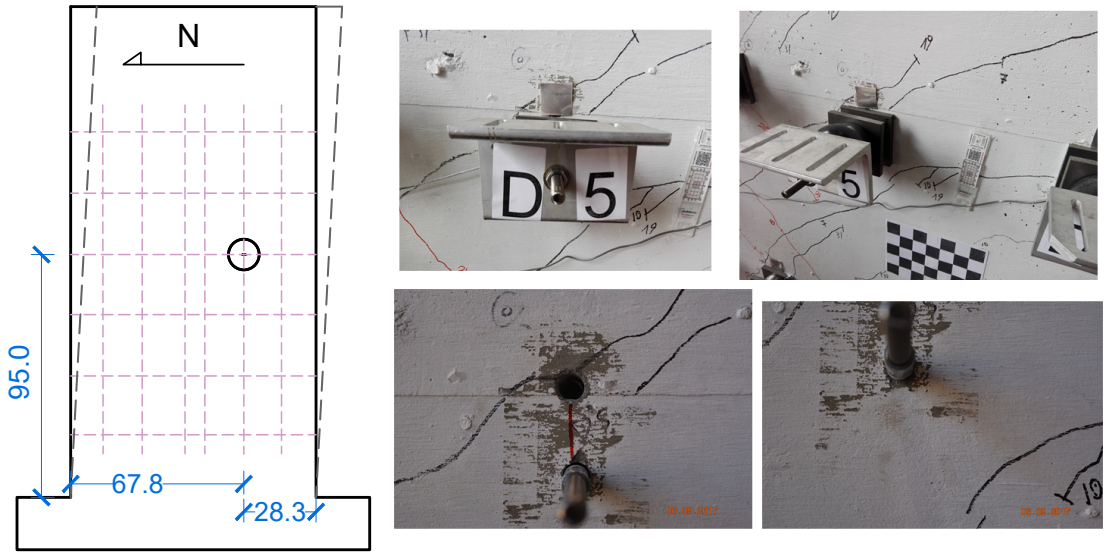


Figure E.44: Expansion anchor D4 in wall SL7.5: measured load and displacement histories and wall drift ratio history



(a) Anchor location. Units in inches

(b) Photograph of anchor and cracks at end of test

Figure E.45: Expansion anchor D5 in wall SL7.5: location and photographs. Wall residual drift is diagrammatically shown exaggerated for the purpose of illustrating the final context around the anchor

D5

Torque-controlled expansion anchor D5 was installed about 2 in below an abandoned installation hole resulting from a previous incorrect installation. This abandoned hole acted as stress concentration and attracted the shear crack in this region of the wall. As a consequence, no cracks crossed anchor D5, as shown in Fig.E.45. Measured load and displacement were almost constant. However, the anchor was reloaded two times, at 0.75% and 2.0% drift ratio. The maximum measured displacement was about zero.

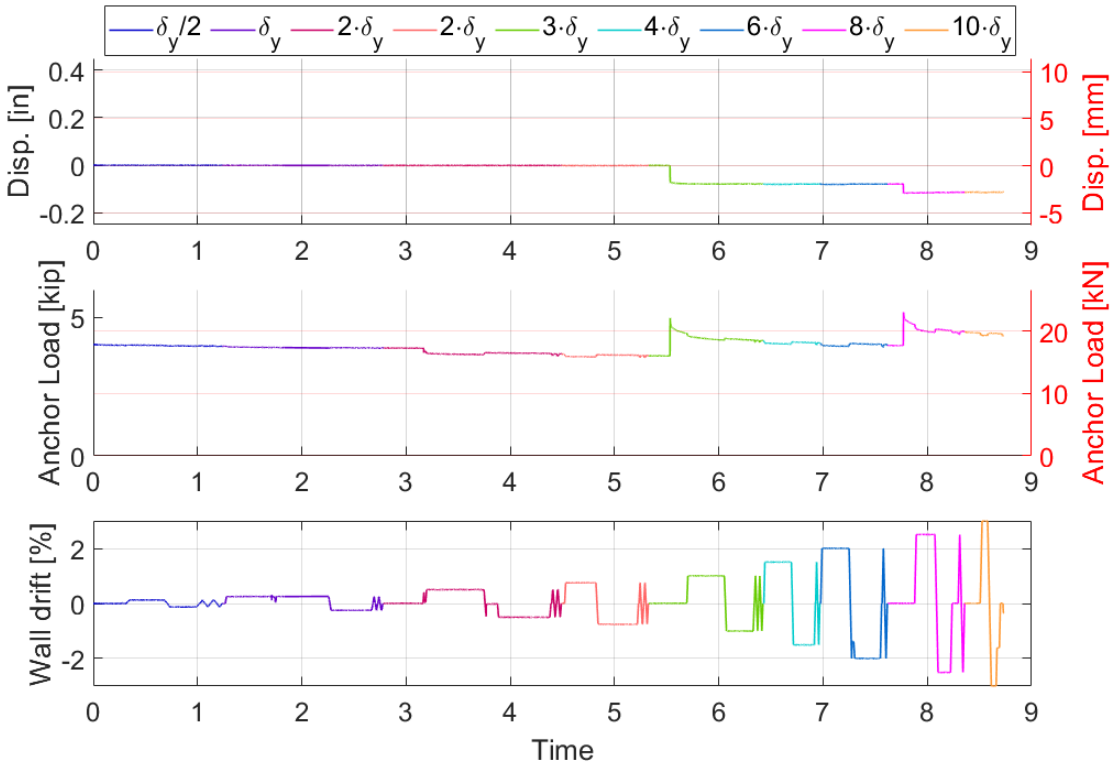
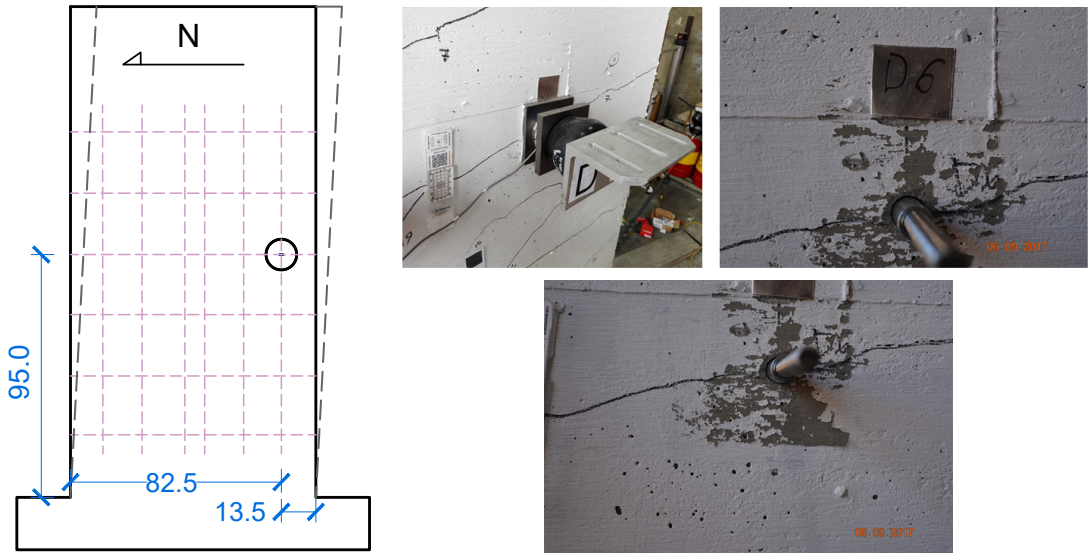


Figure E.46: Expansion anchor D5 in wall SL7.5: measured load and displacement histories and wall drift ratio history



(a) Anchor location. Units in inches

(b) Photograph of anchor and cracks at end of test

Figure E.47: Expansion anchor D6 in wall SL7.5: location and photographs. Wall residual drift is diagrammatically shown exaggerated for the purpose of illustrating the final context around the anchor

D6

One tension crack crossed torque-controlled expansion anchor D6, as shown in Fig.E.47. Measured anchor load and displacement were almost constant for great part of the test, although the anchor was reloaded two times, at 0.75% and 2.0% drift ratios. The maximum measured displacement was 0.03 in, and the total displacement at the end of test, calculated neglecting the displacement due the compression of the spring, was about 0.26 in.

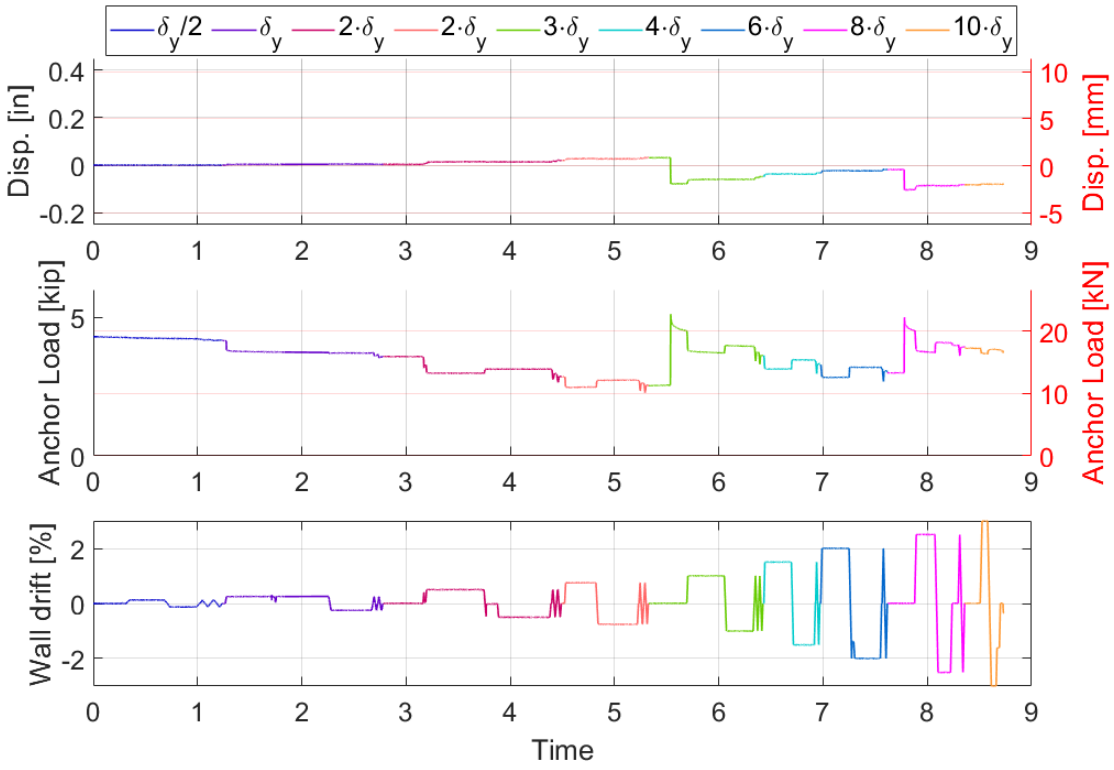


Figure E.48: Expansion anchor D6 in wall SL7.5: measured load and displacement histories and wall drift ratio history



(a) Anchor location. Units in inches

(b) Photograph of anchor and cracks at end of test

Figure E.49: Bonded anchor E1 in wall SL7.5: location and photographs. Wall residual drift is diagrammatically shown exaggerated for the purpose of illustrating the final context around the anchor

E1

No cracks crossed bonded anchor E1, as shown in Fig.E.49. Measured load and displacement were small and almost constant, with a maximum measured displacement of about zero.

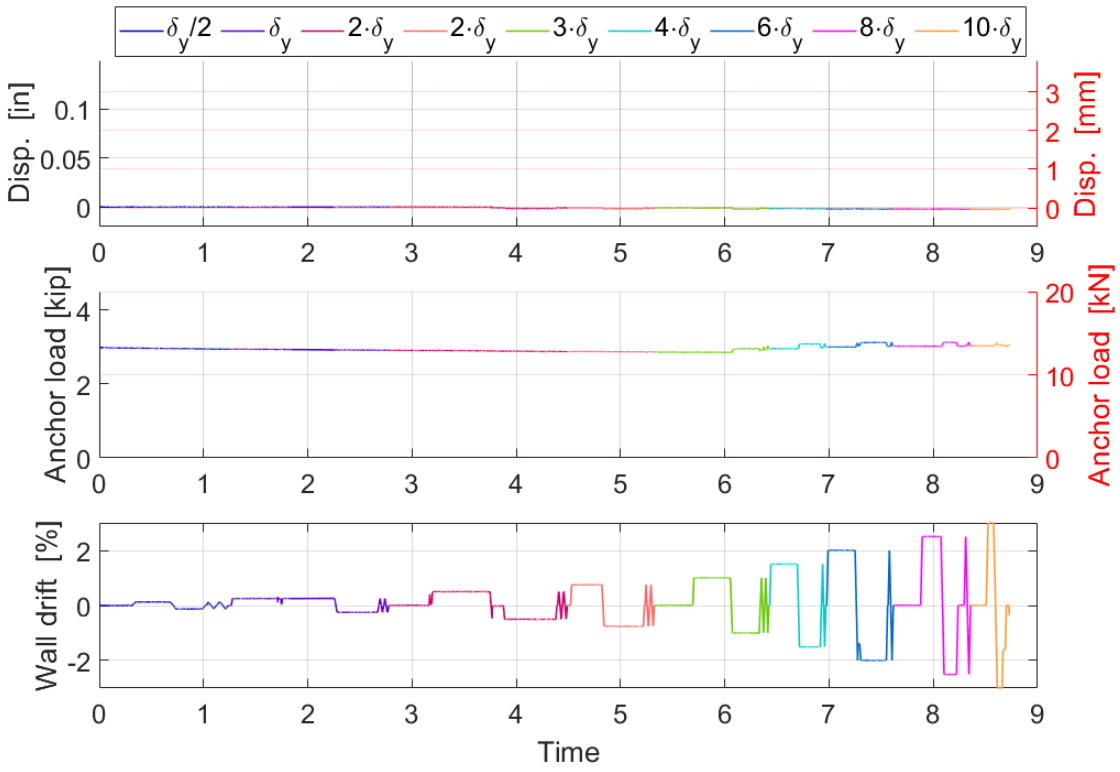
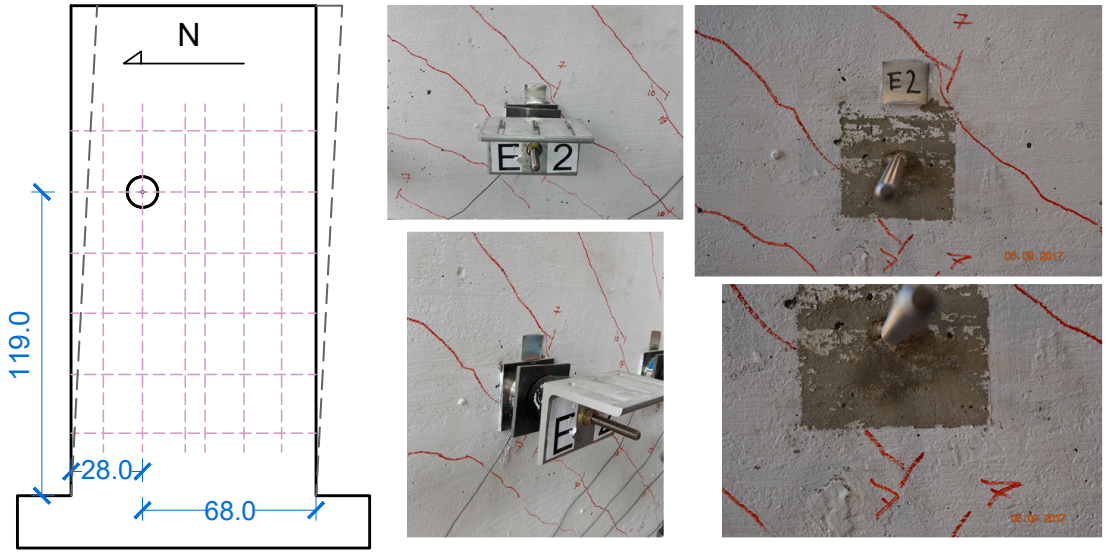


Figure E.50: Bonded anchor E1 in wall SL7.5: measured load and displacement histories and wall drift ratio history



(a) Anchor location. Units in inches

(b) Photograph of anchor and cracks at end of test

Figure E.51: Bonded anchor E2 in wall SL7.5: location and photographs. Wall residual drift is diagrammatically shown exaggerated for the purpose of illustrating the final context around the anchor

E2

No cracks crossed bonded anchor E2, as shown in Fig.E.51. Measured load and displacement were small and almost constant, with a maximum measured displacement of about zero.

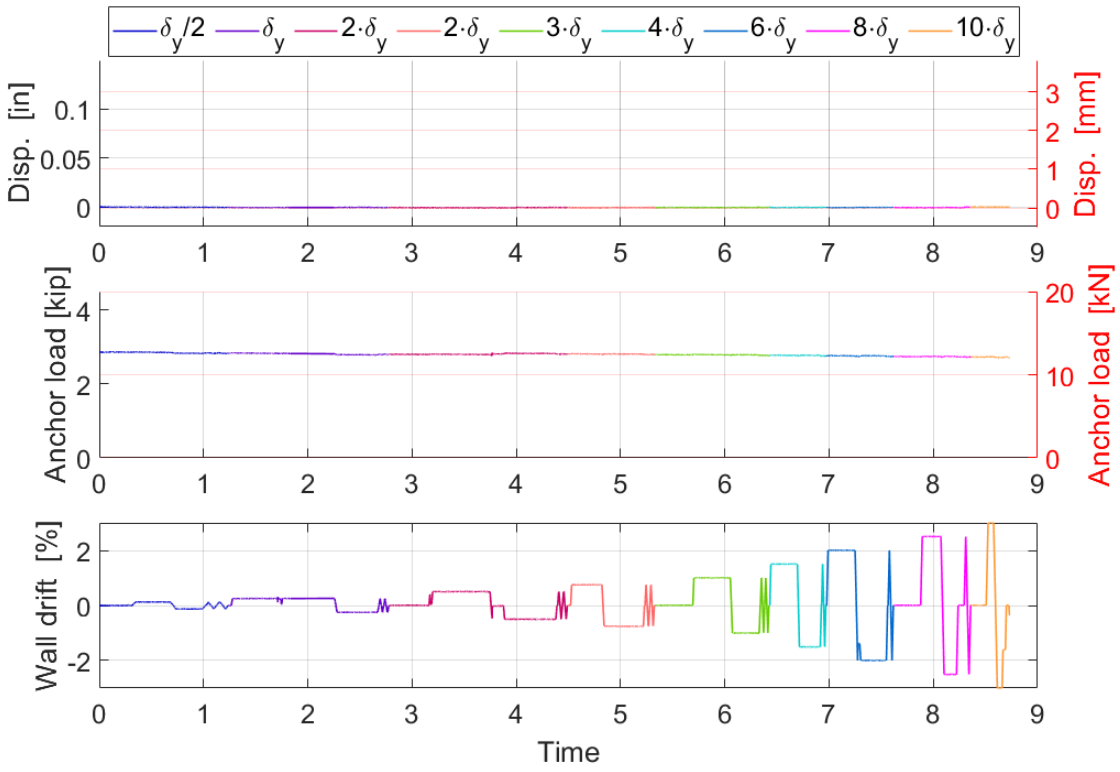
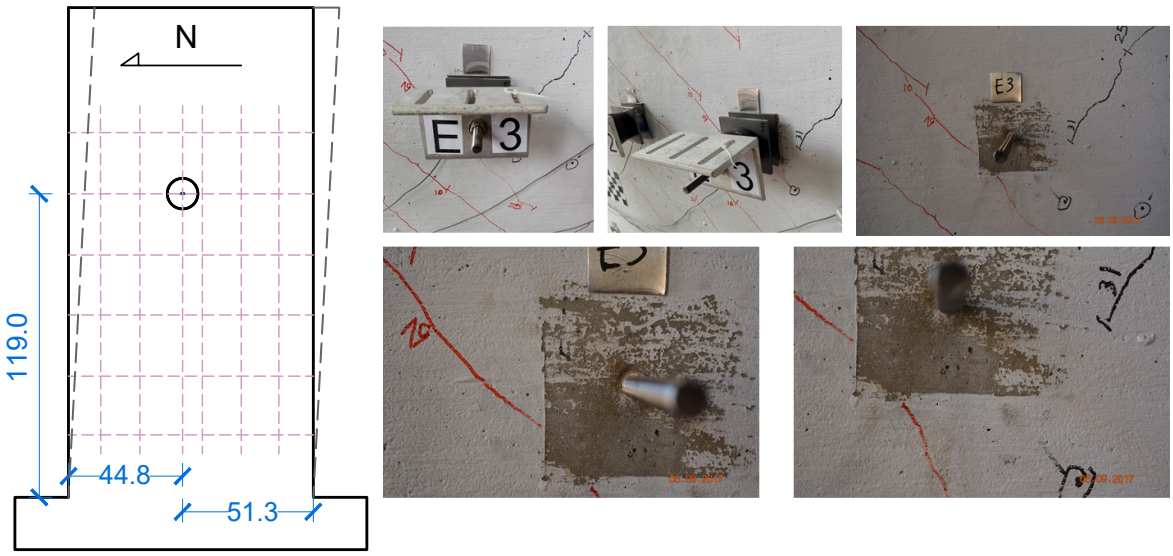


Figure E.52: Bonded anchor E2 in wall SL7.5: measured load and displacement histories and wall drift ratio history



(a) Anchor location. Units in inches

(b) Photograph of anchor and cracks at end of test

Figure E.53: Bonded anchor E3 in wall SL7.5: location and photographs. Wall residual drift is diagrammatically shown exaggerated for the purpose of illustrating the final context around the anchor

E3

No cracks crossed bonded anchor E3, as shown in Fig.E.53. Measured load and displacement were small and almost constant, with a maximum measured displacement of about zero.

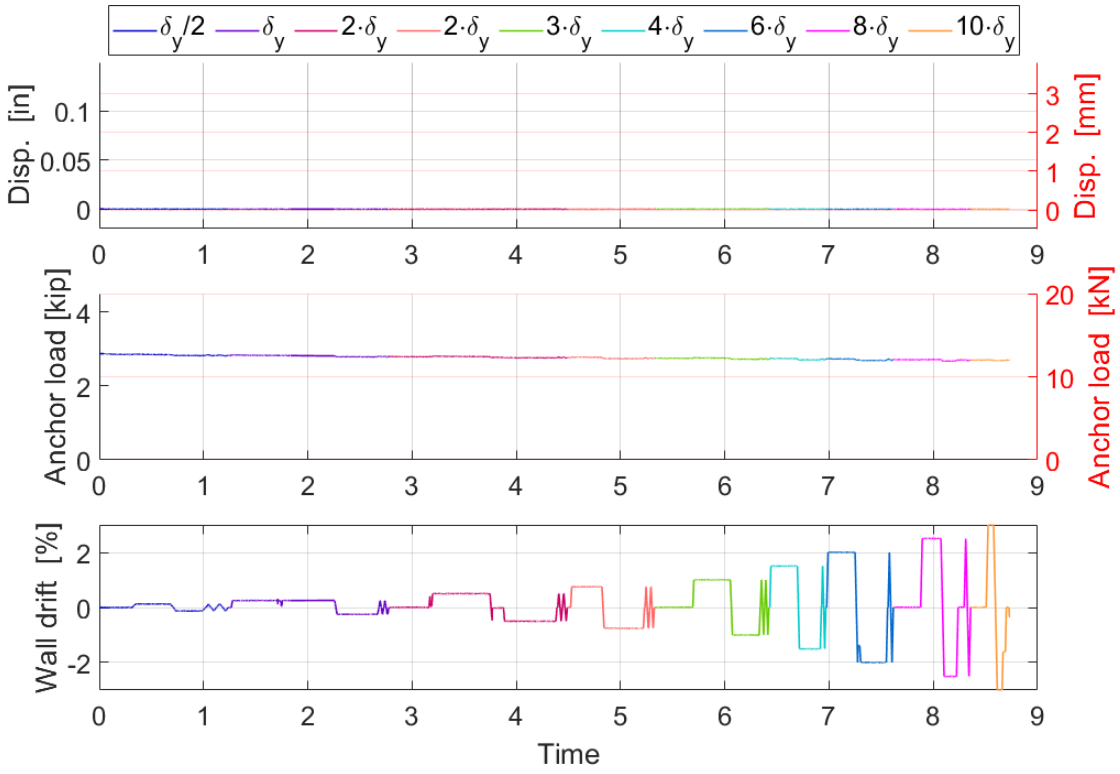
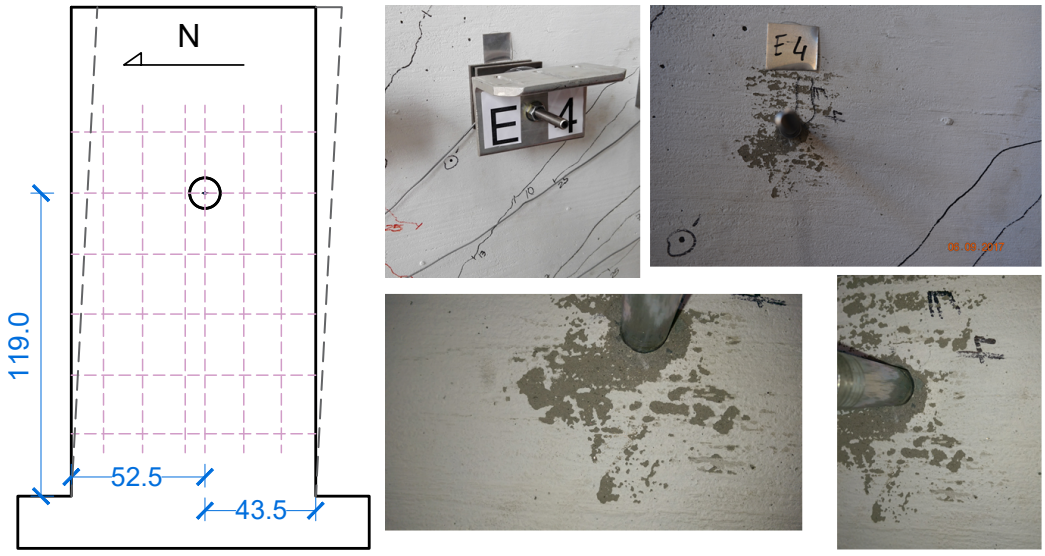


Figure E.54: Bonded anchor E3 in wall SL7.5: measured load and displacement histories and wall drift ratio history



(a) Anchor location. Units in inches

(b) Photograph of anchor and cracks at end of test

Figure E.55: Expansion anchor E4 in wall SL7.5: location and photographs. Wall residual drift is diagrammatically shown exaggerated for the purpose of illustrating the final context around the anchor

E4

No cracks crossed torque-controlled expansion anchor E4, as shown in Fig.E.55. Measured anchor load and displacement were almost constant during all the wall cycling history, although the anchor was reloaded twice, at 0.75% and 2.0% drift ratios. The maximum measured displacement was about zero.

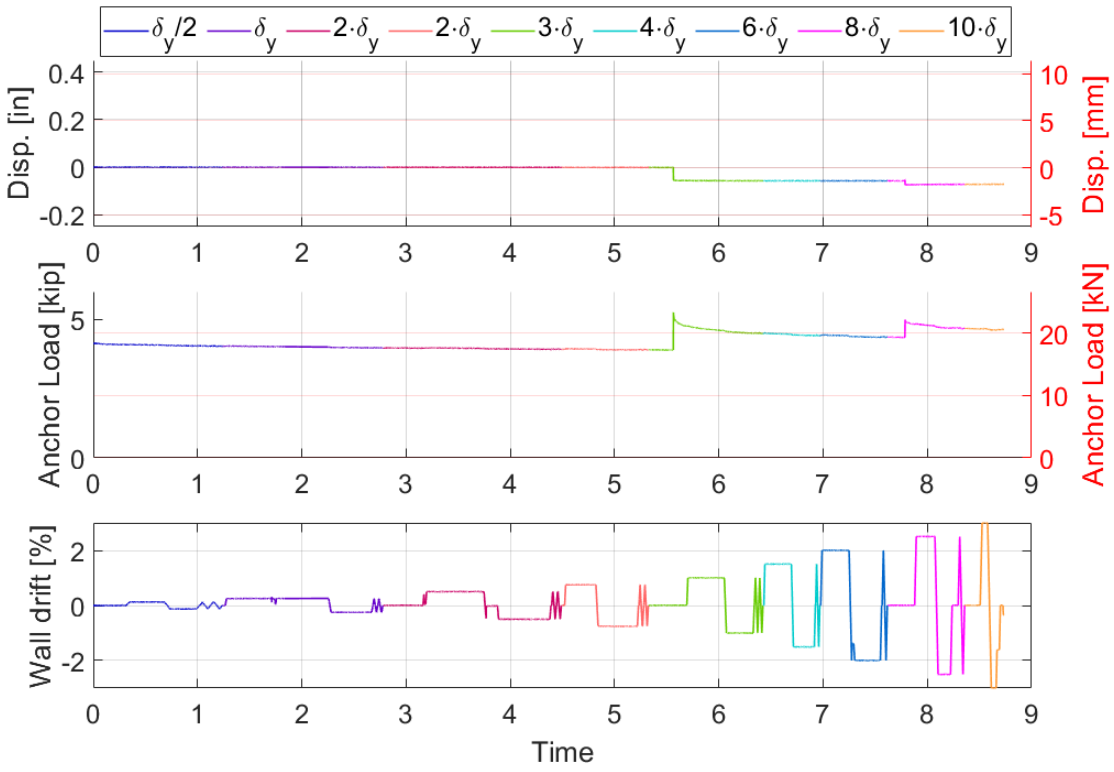
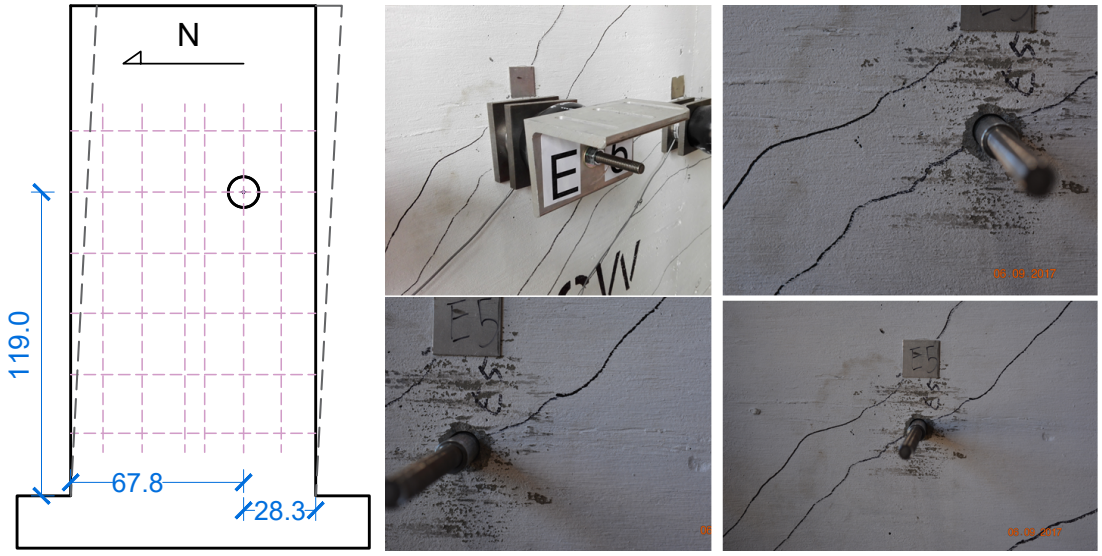


Figure E.56: Expansion anchor E4 in wall SL7.5: measured load and displacement histories and wall drift ratio history



(a) Anchor location. Units in inches

(b) Photograph of anchor and cracks at end of test.

Figure E.57: Expansion anchor E5 in wall SL7.5: location and photographs. Wall residual drift is diagrammatically shown exaggerated for the purpose of illustrating the final context around the anchor.

E5

One shear crack crossed torque-controlled expansion anchor E5, as shown in Fig.E.57. Measured load and displacement were almost constant during all the wall cycling history, although the anchor was reloaded twice, at 0.75% and 2.0% drift ratios. Small load drops and displacement increments were measured within each reloading. The maximum measured displacement was about zero.

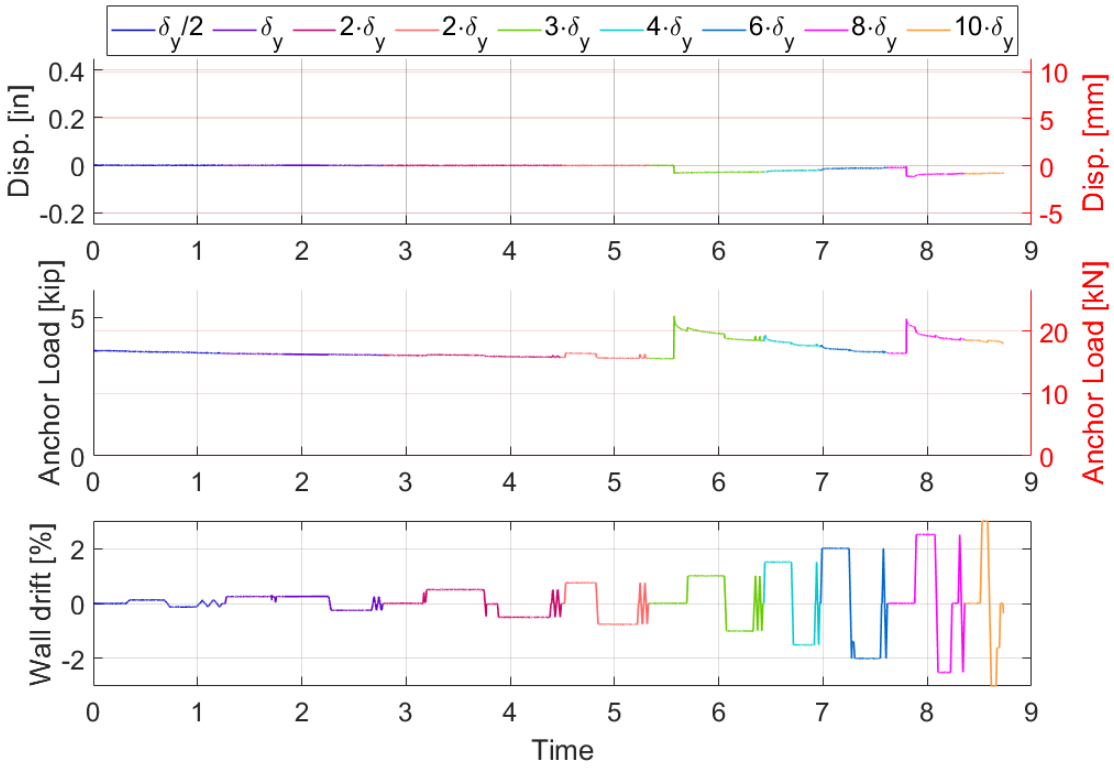
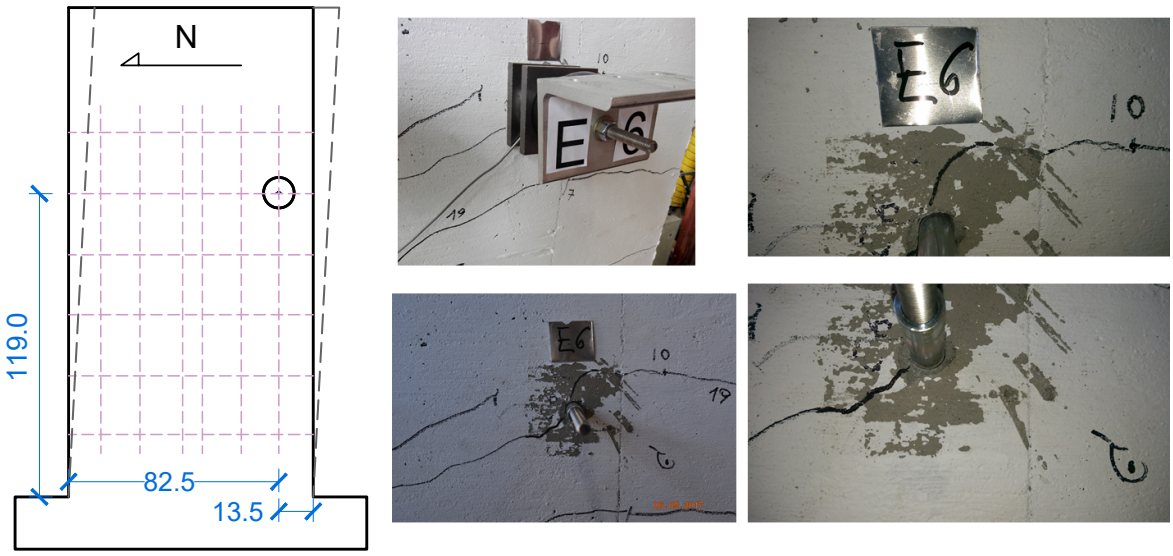


Figure E.58: Expansion anchor E5 in wall SL7.5: measured load and displacement histories and wall drift ratio history.



(a) Anchor location. Units in inches

(b) Photograph of anchor and cracks at end of test.

Figure E.59: Expansion anchor E6 in wall SL7.5: location and photographs. Wall residual drift is diagrammatically shown exaggerated for the purpose of illustrating the final context around the anchor.

E6

One tension crack crossed torque-controlled expansion anchor E6, as shown in Fig.E.59. Measured anchor load and displacement were almost constant throughout the test, although the anchor was reloaded two times, at 0.75% and 2.0% drift ratios. The maximum displacement measured 0.02 in, and the total displacement at the end of test, calculated neglecting the displacement due the compression of the spring, was about 0.12 in.

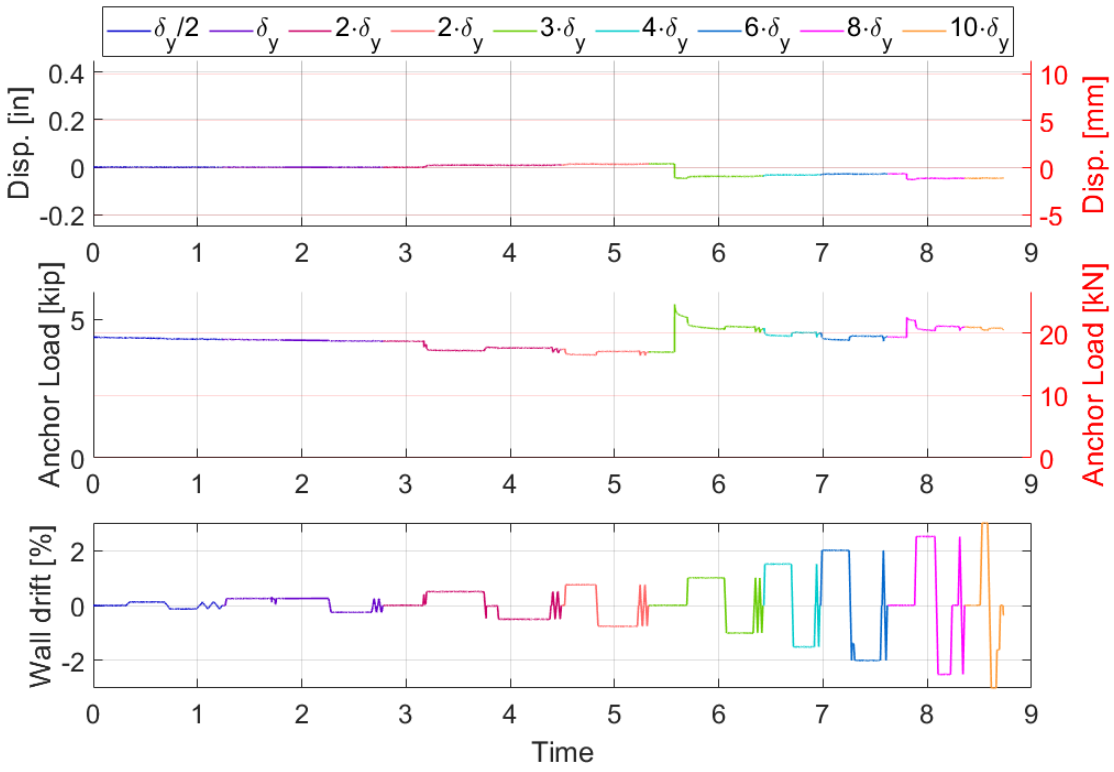
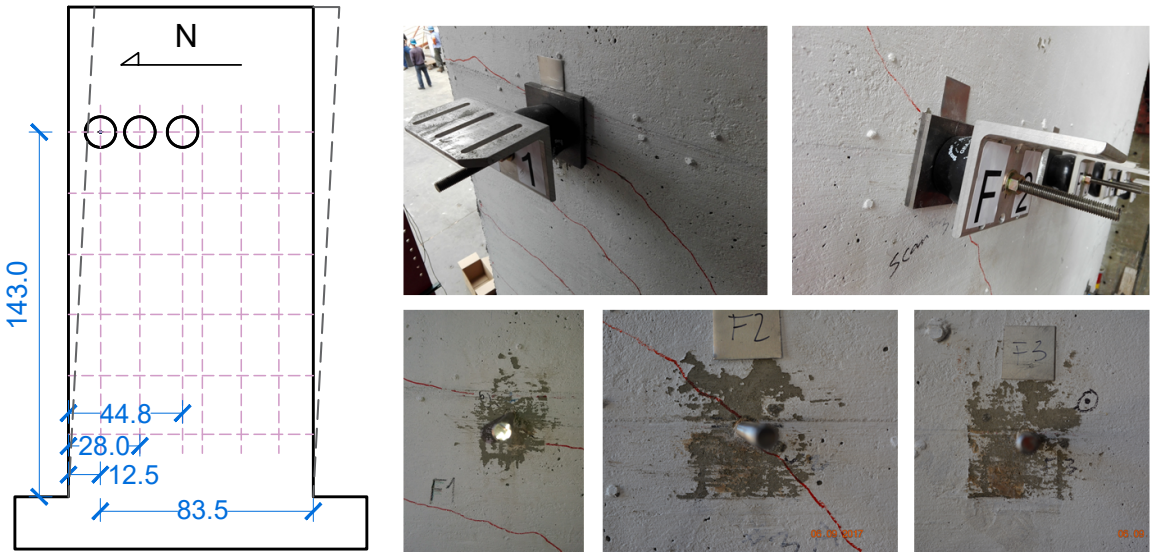


Figure E.60: Expansion anchor E6 in wall SL7.5: measured load and displacement histories and wall drift ratio history.



(a) Anchor location. Units in inches

(b) Photograph of anchors and cracks at end of test

Figure E.61: Bonded anchors F1, F2 and F3 in wall SL7.5: location and photographs. Wall residual drift is diagrammatically shown exaggerated for the purpose of illustrating the final context around the anchor

F1, F2 and F3

Bonded anchors *F1*, *F2* and *F3* were instrumented with displacement sensors only. One tension crack crossed anchor F1, one shear crack crossed anchor F2 and no cracks crossed F3, as shown in Fig.E.61. The measured displacement histories are reported in Fig.E.62. Displacements were small and almost constant around zero for the whole duration of the wall cycling test.

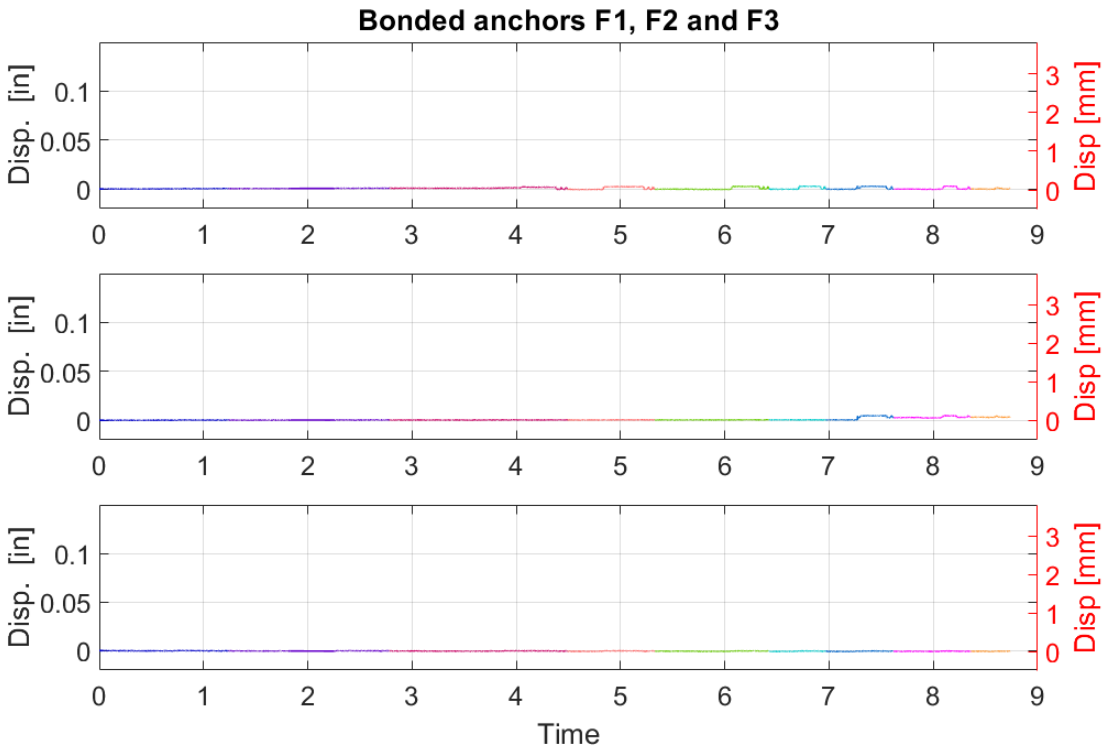
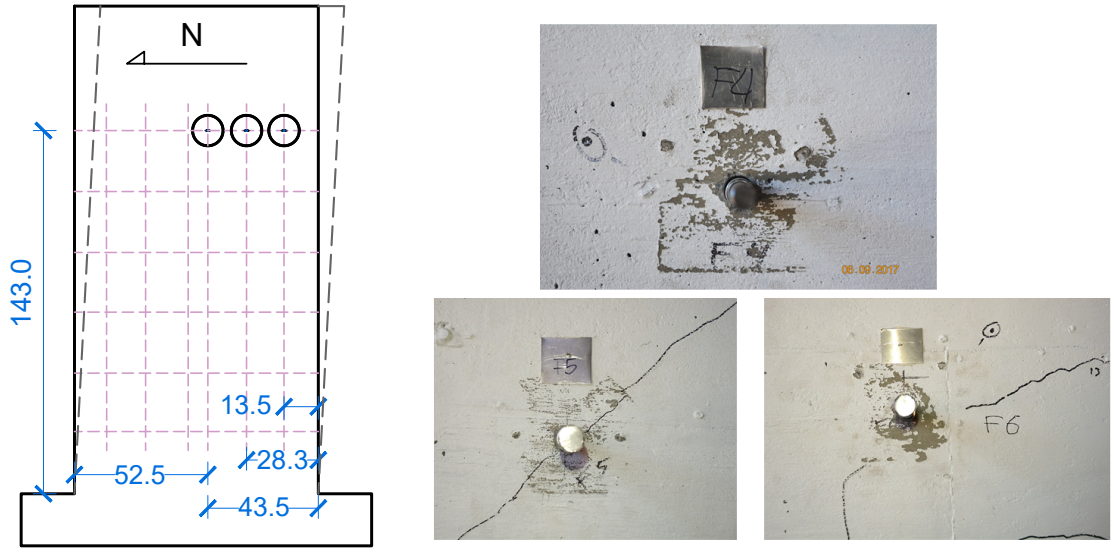


Figure E.62: Bonded anchors F1, F2 and F3 in wall SL7.5: measured displacement histories



(a) Anchor location. Units in inches

(b) Photograph of anchors and cracks at end of test

Figure E.63: Expansion anchor F4, F5 and F6 in wall SL7.5: location and photographs. Wall residual drift is diagrammatically shown exaggerated for the purpose of illustrating the final context around the anchor

F4, F5 and F6

Torque-controlled expansion anchors *F4*, *F5* and *F6* were instrumented with displacement sensors only. One shear crack crossed anchor F5, and no cracks crossed anchors F4 and F6, as shown in Fig.E.63. Displacements were small and almost constant around zero for the whole duration of the wall cycling test.

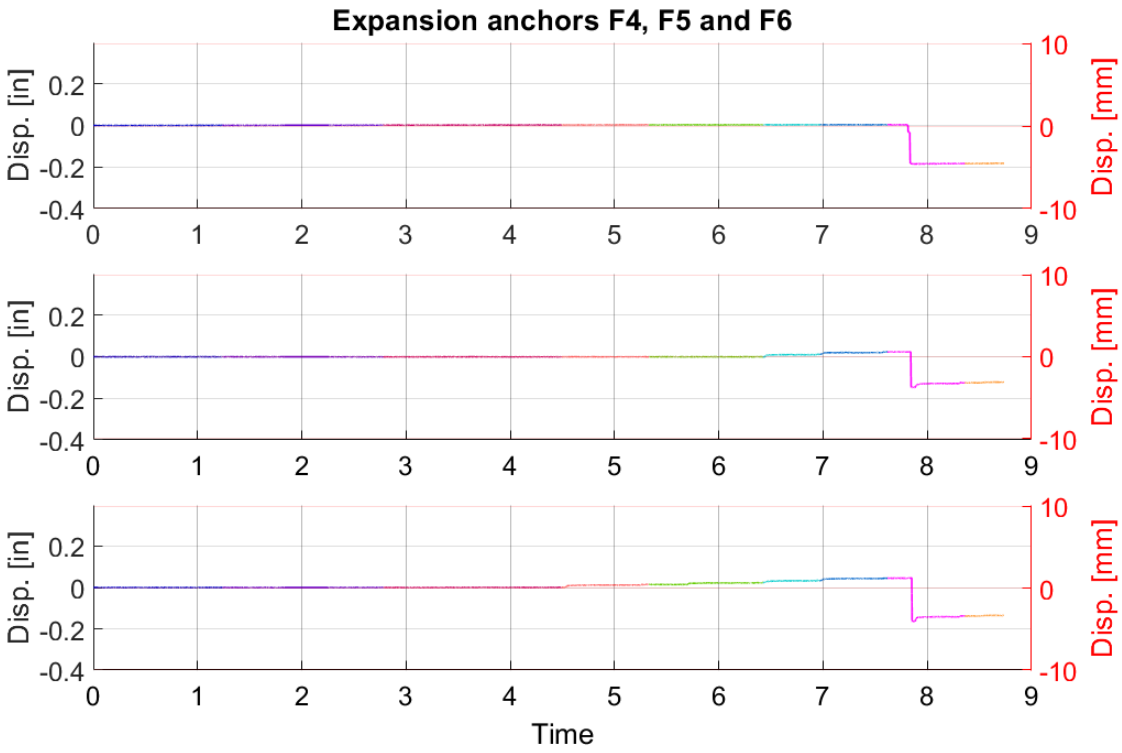


Figure E.64: Expansion anchor F4, F5 and F6 in wall SL7.5: measured displacement histories

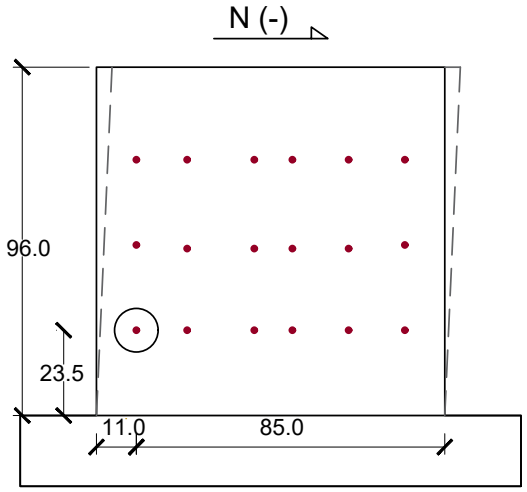
E.1.2 Anchors in Wall SQ7.5

Photographs presented in this section show anchor location and final crack situation for each anchor installed in the squat wall tested with axial load, denoted wall SQ7.5. Photographs of the damage evolution around the anchors during the wall cyclic test are also reported in this section. Measured crack width values of the cracks crossing the anchor plates are reported in Table E.1 as a function of the drift applied to the wall. In addition, anchor load and global displacement histories measured during the wall cycling test for each anchor installed in wall SQ7.5 are illustrated in this section.

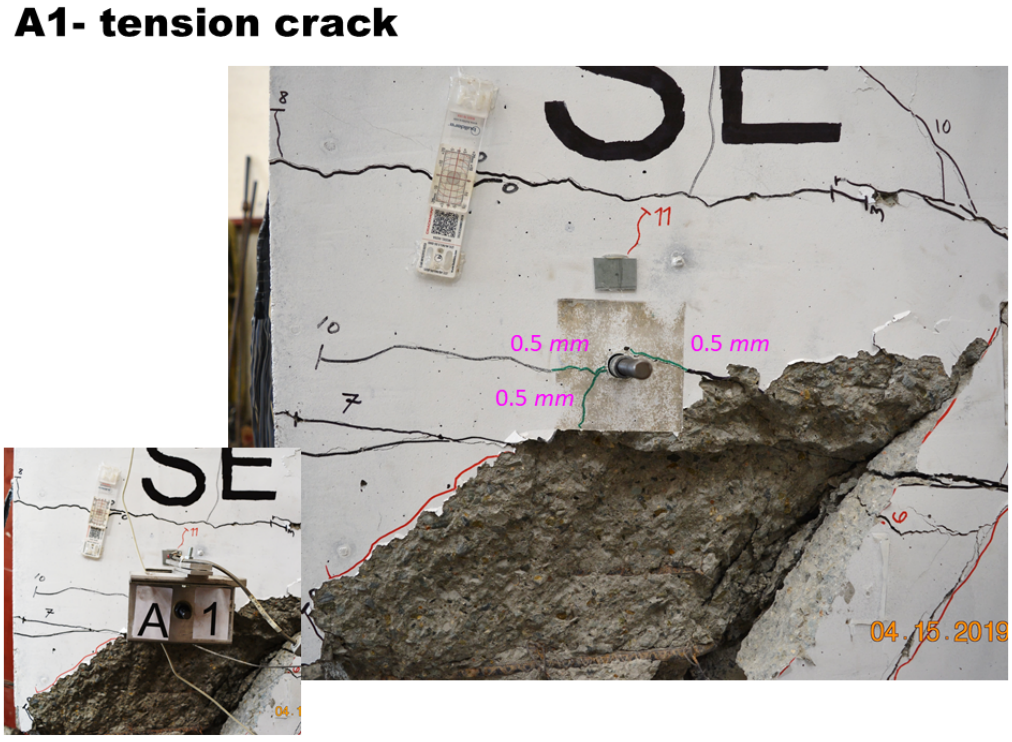
Anchor row A was located inside the theoretic plastic hinge of wall SQ7.5 at about 2 ft (0.25 h_w) from the wall-footing interface, and anchors A1 and A6 were located within the South and North end boundary elements of the wall, respectively. Anchor row B was located inside the theoretic plastic hinge of wall SQ7.5 at about 4 ft (0.5 h_w) from the wall-footing interface, and anchors B1 and B6 were located within the South and North end boundary elements of the wall, respectively. Finally, anchor row C was located outside the theoretic plastic hinge of wall SQ7.5 at about 6 ft (0.75 h_w) from the wall-footing interface, and anchors C1 and C6 were located within the South and North end boundary elements of the wall, respectively.

A1

Fig.E.65b shows one tension crack crossing torque-controlled expansion anchor A1 (see Fig.E.67) at 1.4% drift ratio. The late appearance of the crack is reflected in the approximately constant load and displacement histories (in Fig.E.67) up to the last but one cycle, when the crack crossed the anchor. The load drastically dropped and the global displacement increased at this stage. Residual crack width at the end of the test, after removal of the steel plates, measured approximately w_r =0.5 mm. The maximum measured displacement was 0.17 in.



(a) Anchor location. Units in inches



(b) Photograph of anchor and cracks at end of test

Figure E.65: Location and photograph of anchor A1 in wall SQ7.5. Wall residual drift is diagrammatically shown exaggerated for the purpose of illustrating the final context around the anchor



Figure E.66: Wall SQ7.5: photographs showing the crack evolution around anchor A1

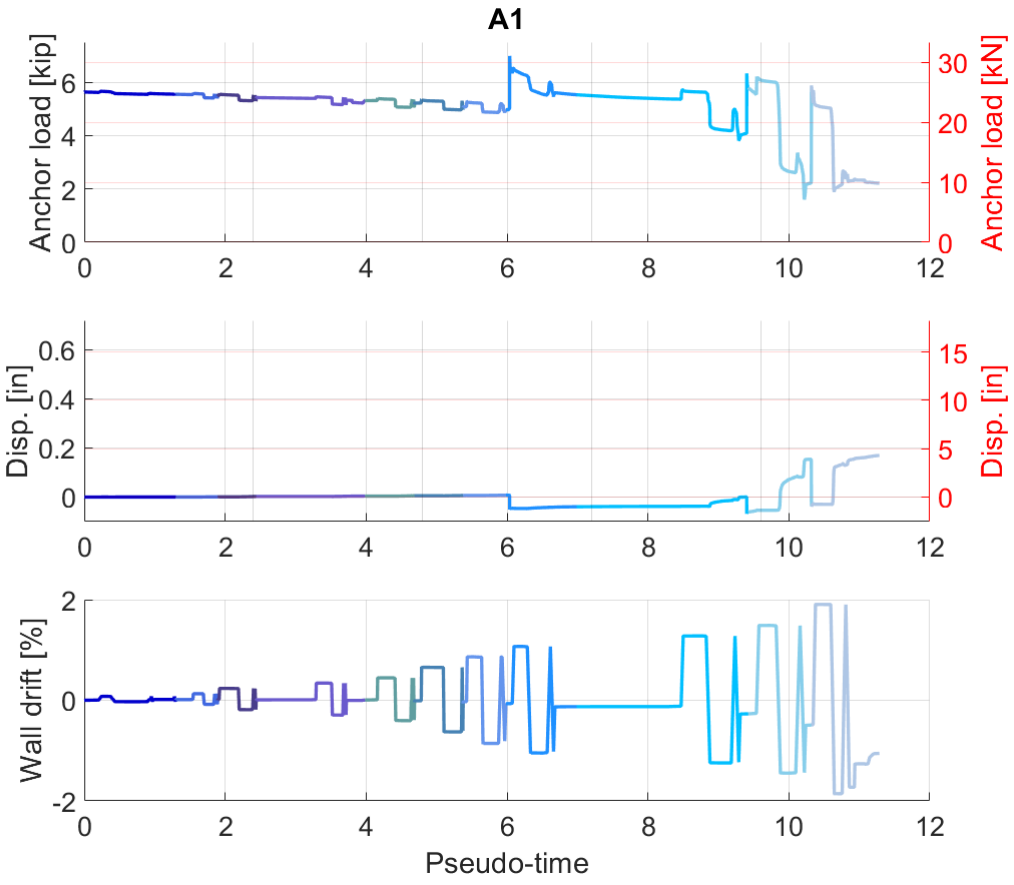
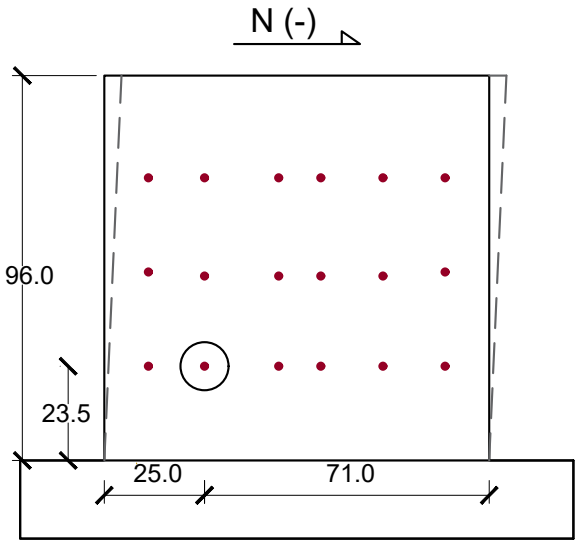


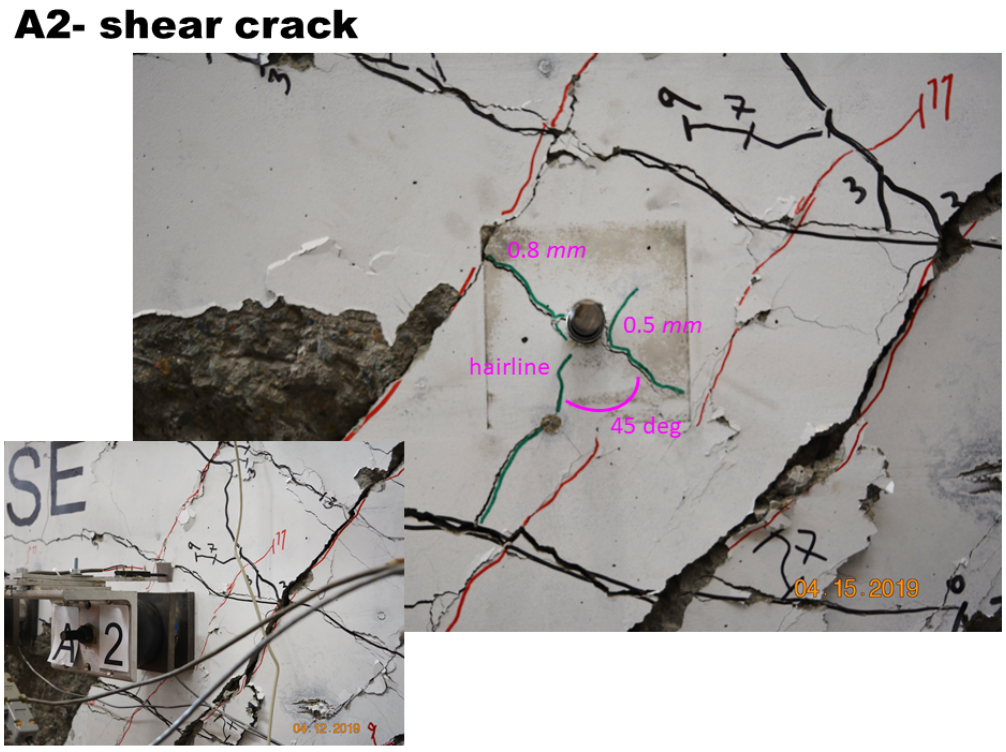
Figure E.67: Wall SQ7.5, anchor A1: measured load and displacement histories and wall drift history

A2

Fig.E.68b shows that torque-controlled expansion anchor A2 was located in a couple of shear cracks, hidden by the steel plates during the wall test, which spanned between two couples of parallel diagonal cracks in both directions (see Fig.E.70). These shear cracks crossing at the anchor location probably opened during the last drift amplitude applied to the wall, as only during the last wall cycle the load and displacement histories in Fig.E.70 show variations. Residual crack widths at the end of the test, after removal of the steel plates, measured approximately w_r = 0.8 and 0.5 mm in one direction and smaller than w_r = 0.1 mm in the opposite direction. The maximum measured displacement was 0.28 in.



(a) Anchor location. Units in inches



(b) Photograph of anchor and cracks at end of test

Figure E.68: Location and photograph of anchor A2 in wall SQ7.5. Wall residual drift is diagrammatically shown exaggerated for the purpose of illustrating the final context around the anchor

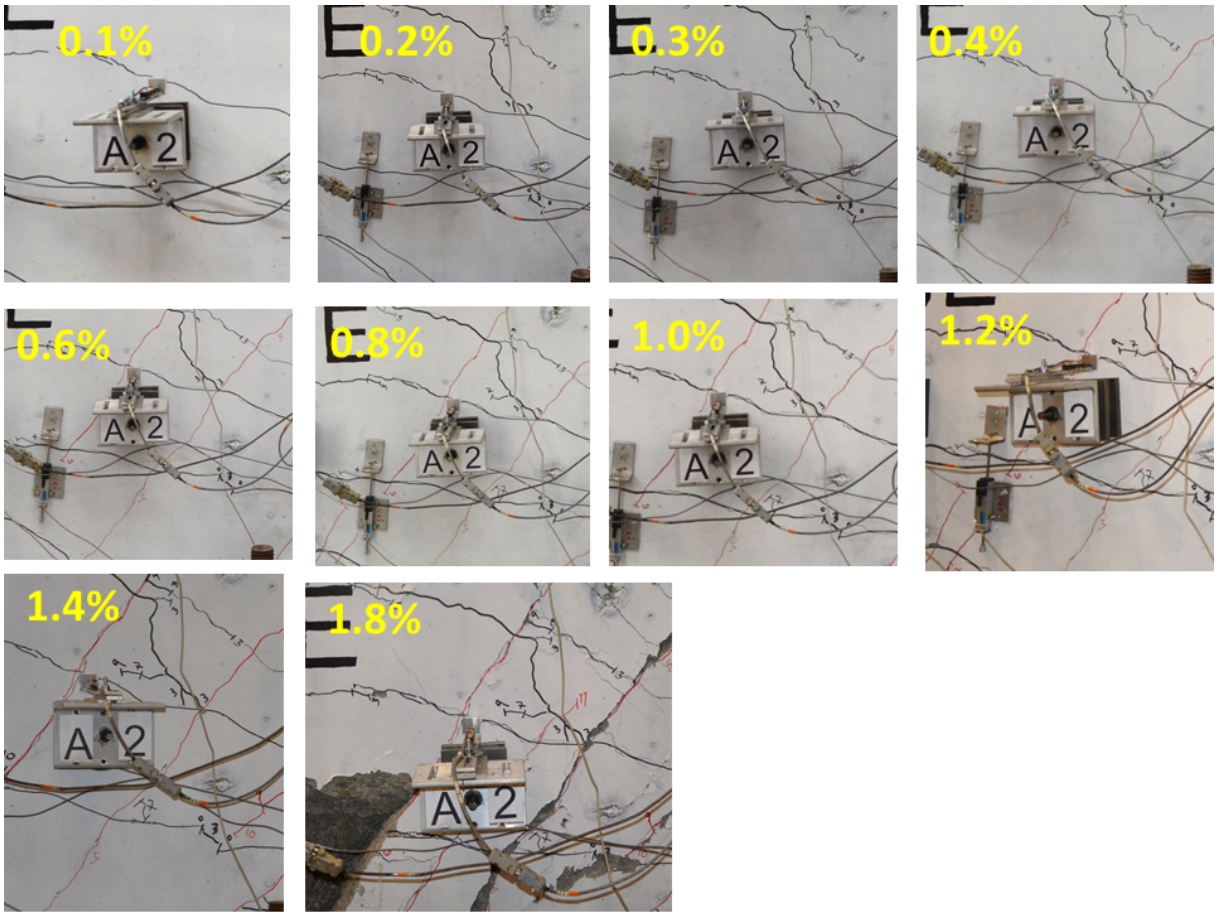


Figure E.69: Wall SQ7.5: photographs showing the crack evolution around anchor A2

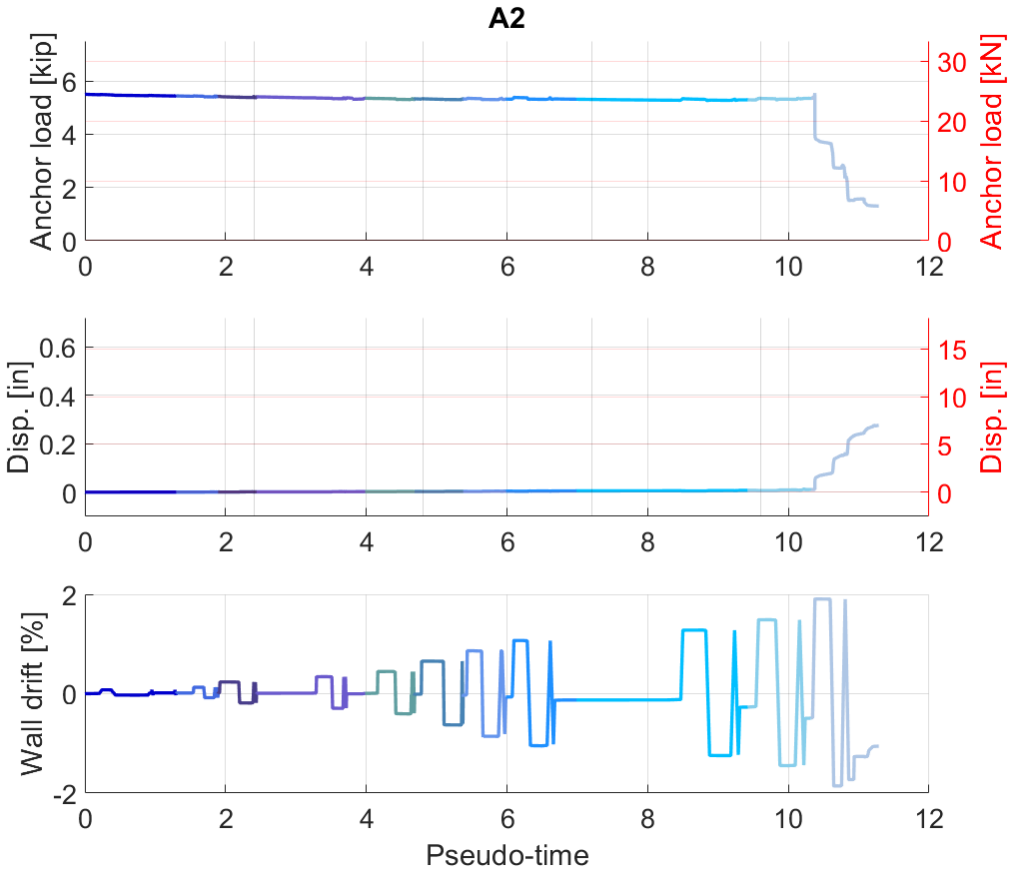
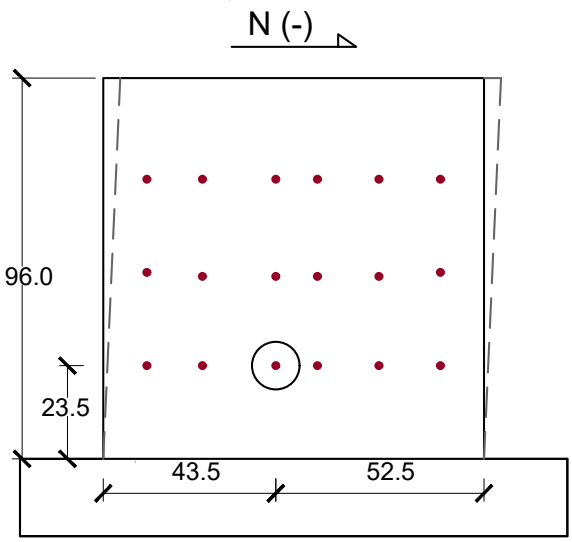


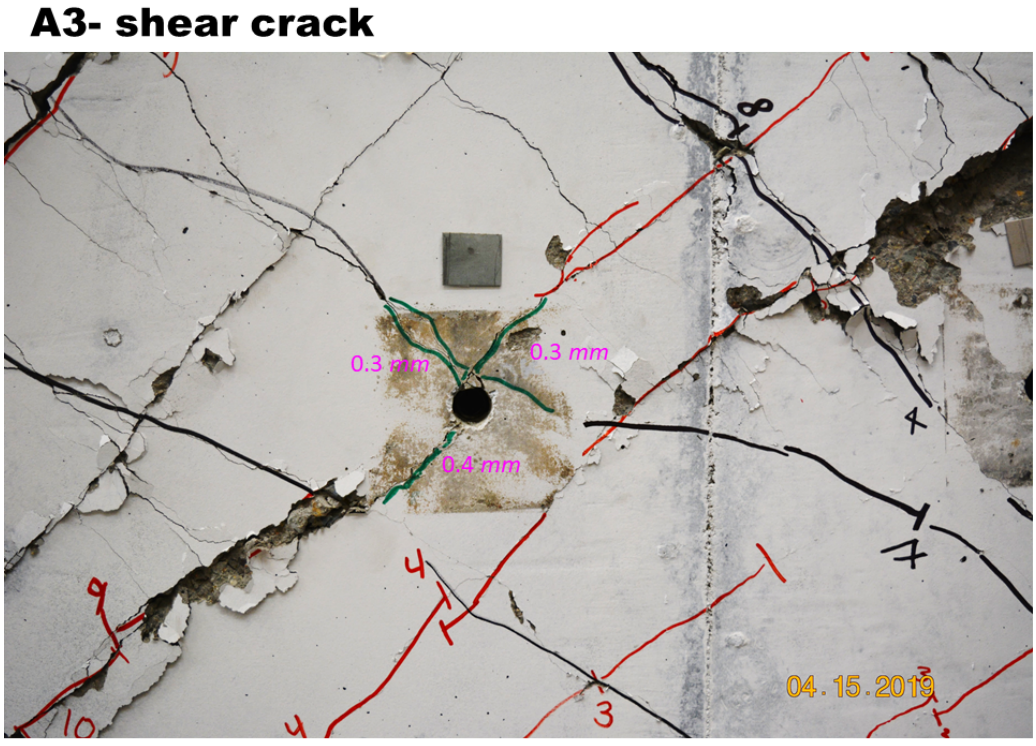
Figure E.70: Wall SQ7.5, anchor A2: measured load and displacement histories and wall drift history

A3

Fig.E.71b shows that torque-controlled expansion anchor A3 was located in a couple of shear cracks. One of these cracks opened at about 0.3% drift ratio in the Push direction, while the other one at about 0.6% drift ratio in the Pull direction. Similarly, the last branch of the diagonal shear crack in the Pull direction developed at about 1.4% drift ratio (see Fig.E.73). The load and displacement histories show the expected trend, characterized by increase in global displacement and load reduction when the crack opens around the anchor, at or right after these drift ratios, as a confirmation of the crack development illustrated in see Fig.E.73. Since anchor load dropped below the design level during the wall cyclic history, the anchor was reloaded three times, at the end of 0.8%, 1.2% and 1.4% drift ratio cycles. Residual crack widths at the end of the test, after removal of the steel plates, measured approximately 0.4 mm. The maximum measured displacement was 0.30 in.



(a) Anchor location. Units in inches



(b) Photograph of anchor and cracks at end of test

Figure E.71: Location and photograph of anchor A3 in wall SQ7.5. Wall residual drift is diagrammatically shown exaggerated for the purpose of illustrating the final context around the anchor

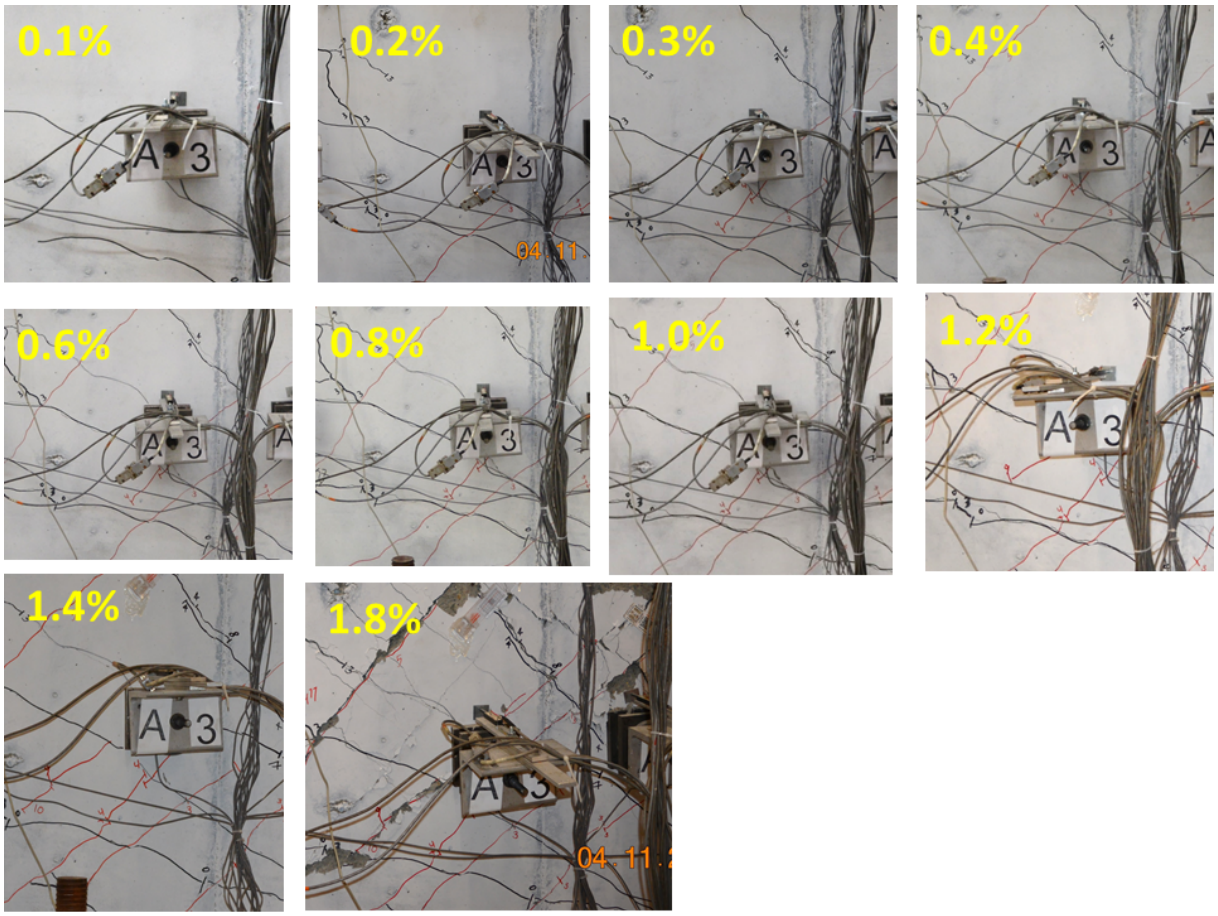


Figure E.72: Wall SQ7.5: photographs showing the crack evolution around anchor A3

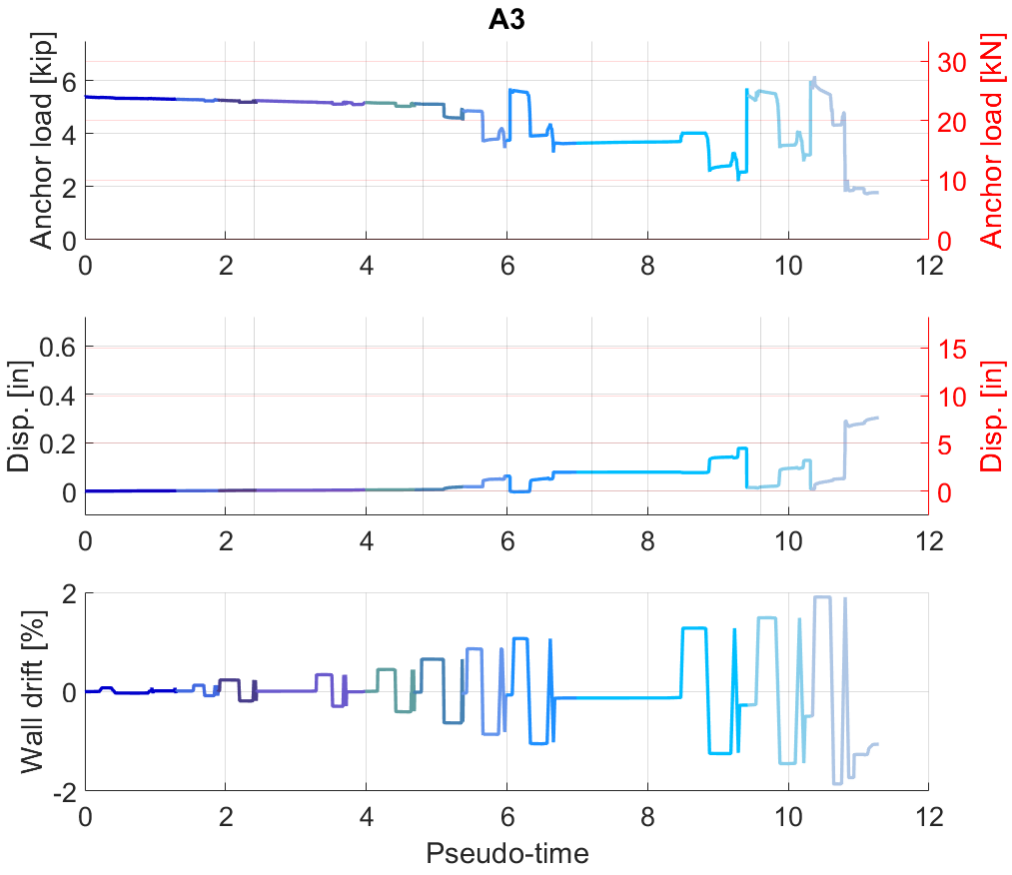
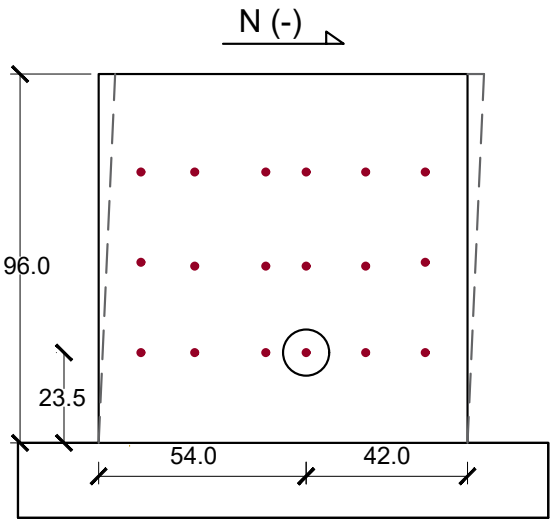


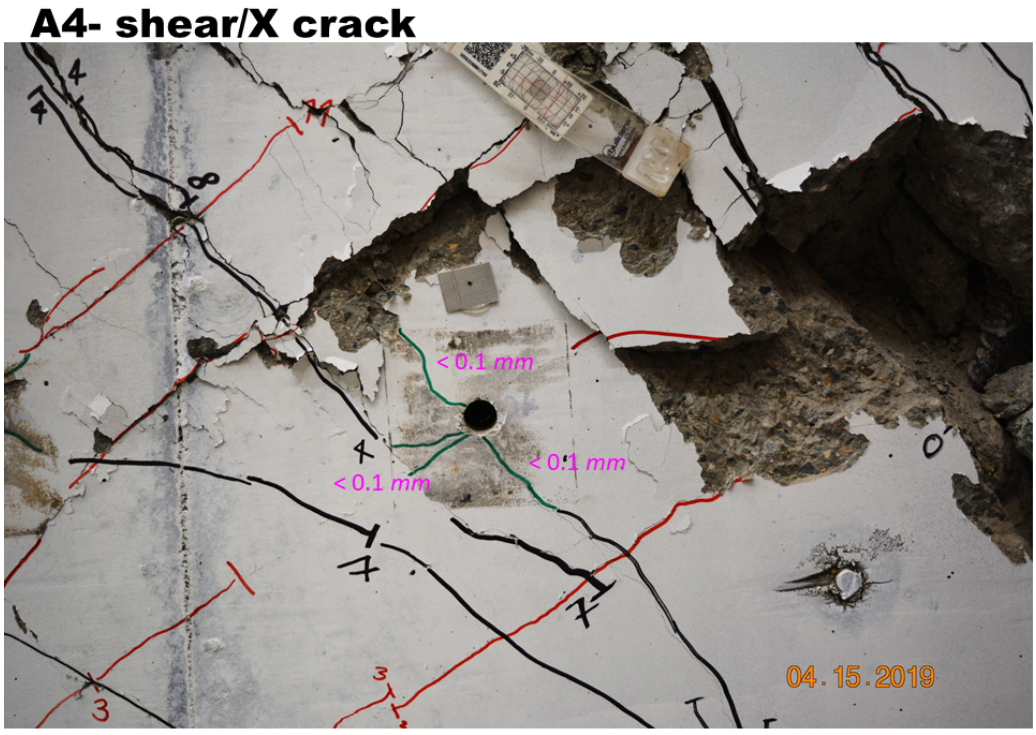
Figure E.73: Wall SQ7.5, anchor A3: measured load and displacement histories and wall drift history

A4

Fig.E.74b shows that torque-controlled expansion anchor A4 was located in a couple of shear cracks, which developed at the end of the wall cyclic test, when the load and displacement histories show the largest variation. Small load drops occurred also during the wall test, and the load was reapplied four times, at the end of 0.6%, 0.8%, 1.2% and 1.4% drift ratio cycles (see Fig.E.76). Residual crack widths at the end of the test, after removal of the steel plates, measured approximately less than 0.1 mm. The maximum measured displacement was 0.17 in.



(a) Anchor location. Units in inches



(b) Photograph of anchor and cracks at end of test

Figure E.74: Location and photograph of anchor A4 in wall SQ7.5. Wall residual drift is diagrammatically shown exaggerated for the purpose of illustrating the final context around the anchor

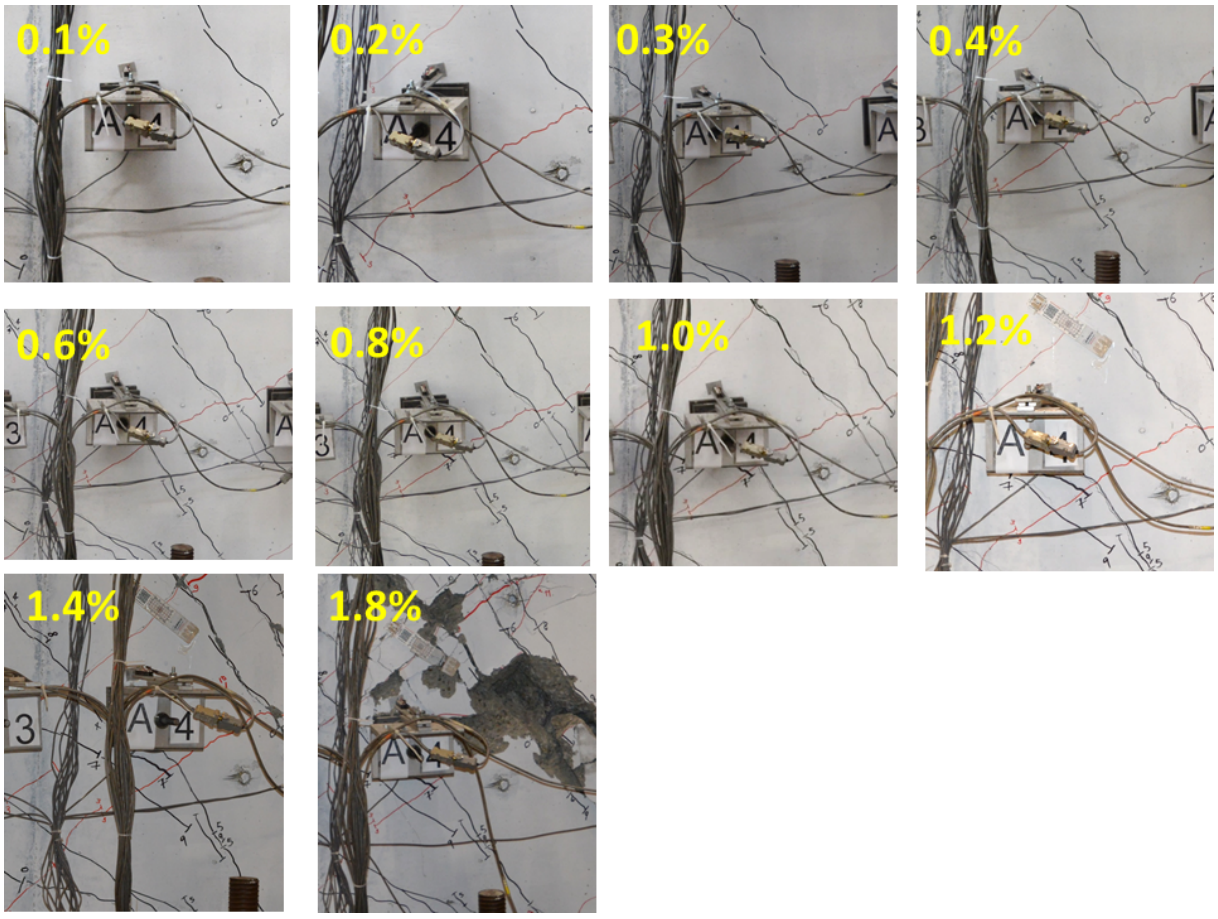


Figure E.75: Wall SQ7.5: photographs showing the crack evolution around anchor A4

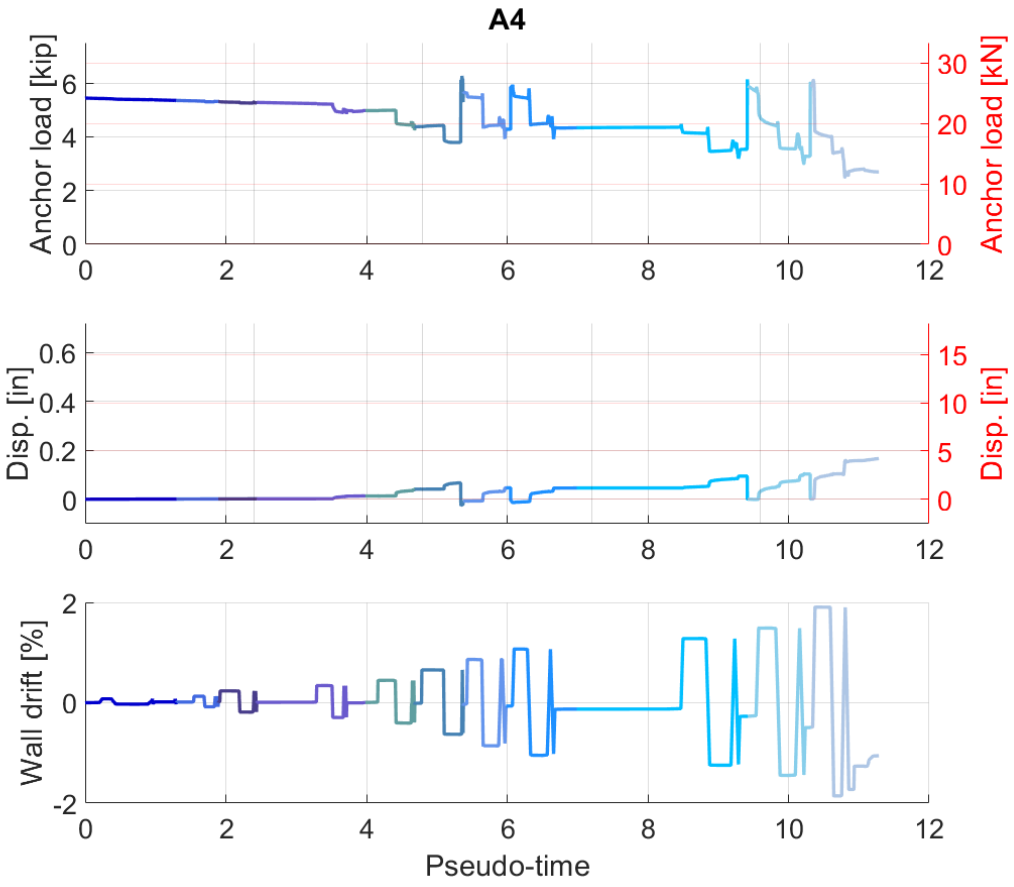
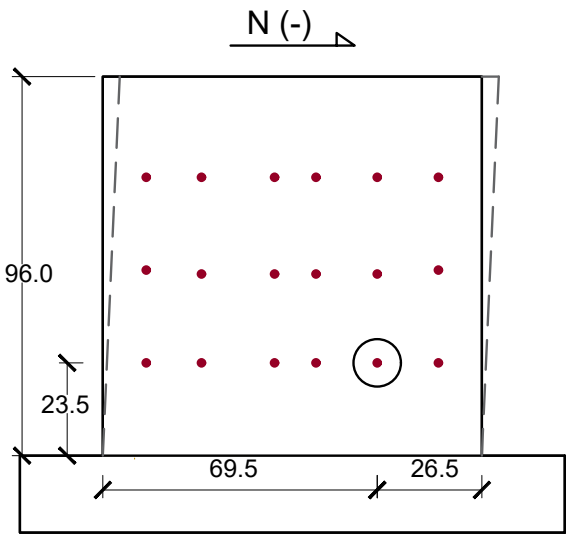


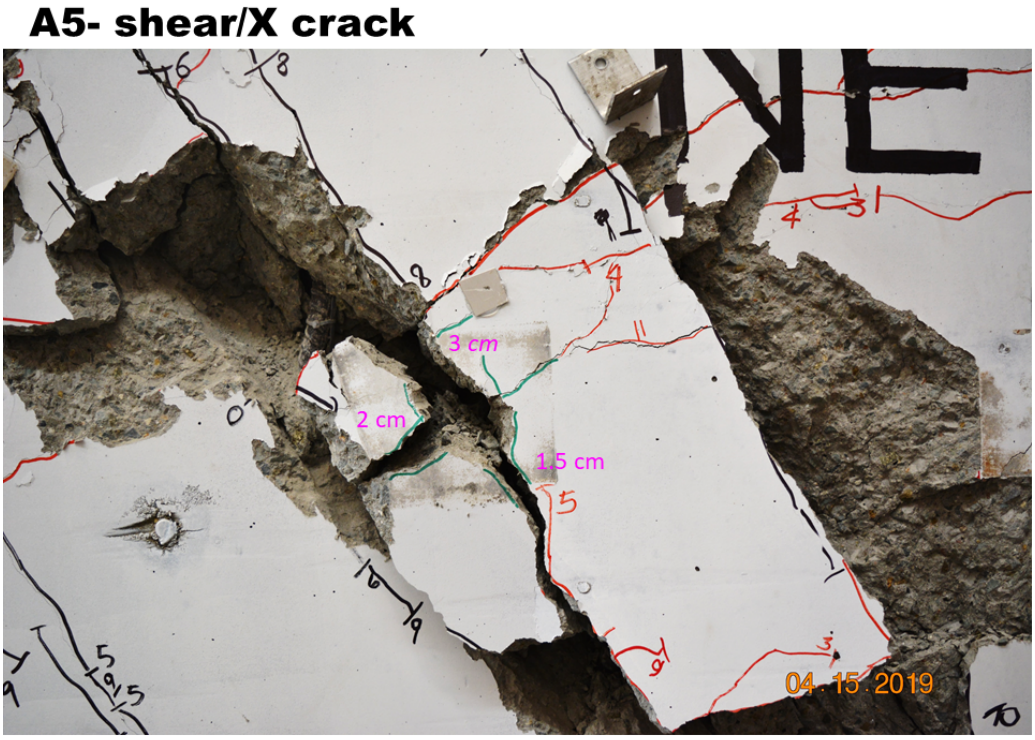
Figure E.76: Wall SQ7.5, anchor A4: measured load and displacement histories and wall drift history

A5

Fig.E.77b shows that torque-controlled expansion anchor A5 was located in a couple of shear cracks, before the accumulation of damage and concrete crushing in this region of the wall. These shear crack developed around the anchor at 0.4% and 1.0% drift ratio cycles, when small load reductions and displacement increments were measured (see Fig.E.79). To sustain constant tension load on the anchor, the load was reapplied twice, at the end of 1.2% and 1.4% drift ratio cycles. Anchor A5 failed at the end of the test when the nearby concrete crushed, as showed by the significant load drop and displacement increase in Fig.E.79. Residual crack widths at the end of the test were large, measuring as much as 3 cm. The maximum displacement measured before the concrete crushing was 0.29 in.



(a) Anchor location. Units in inches



(b) Photograph of anchor and cracks at end of test

Figure E.77: Location and photograph of anchor A5 in wall SQ7.5. Wall residual drift is diagrammatically shown exaggerated for the purpose of illustrating the final context around the anchor

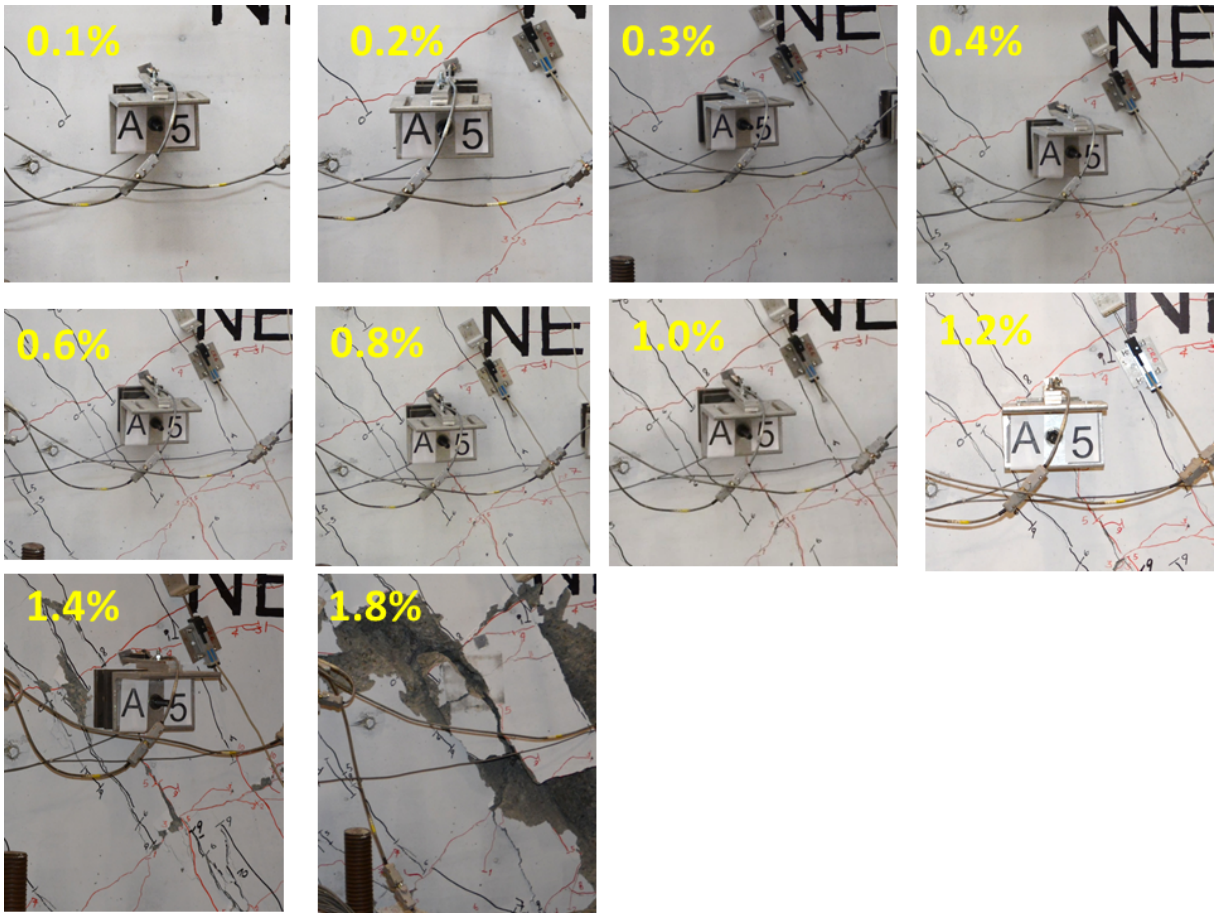


Figure E.78: Wall SQ7.5: photographs showing the crack evolution around anchor A5

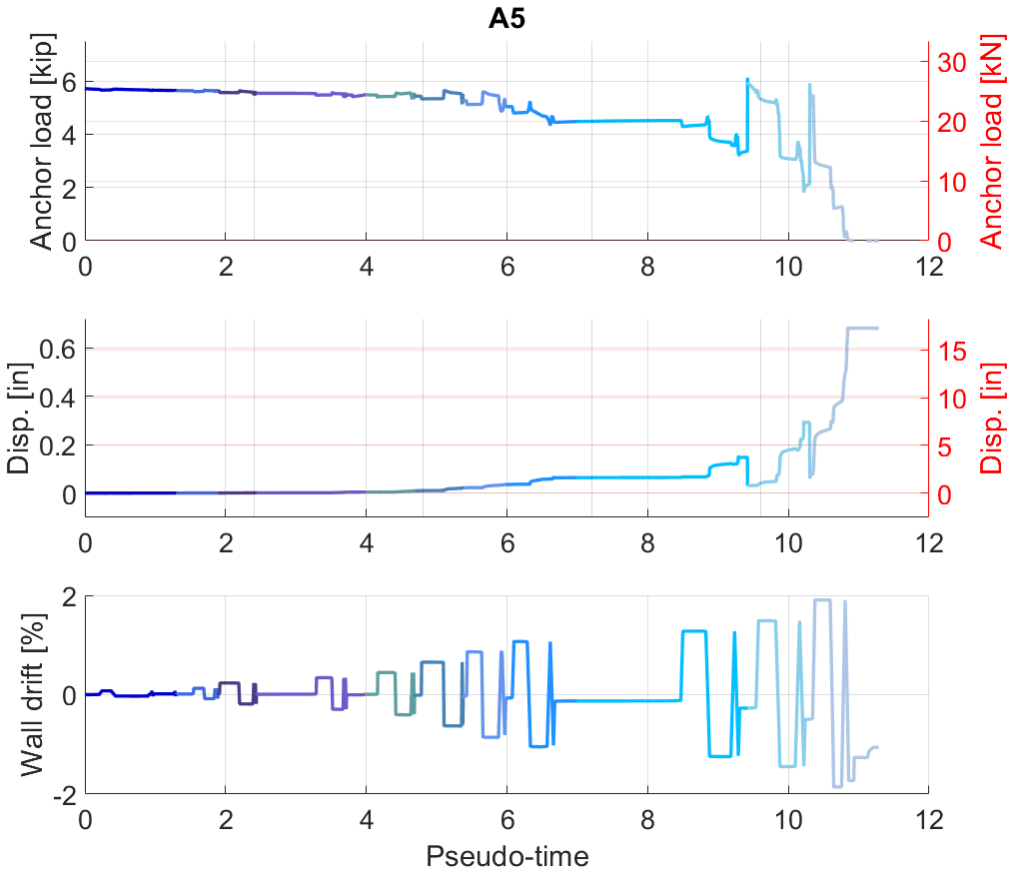
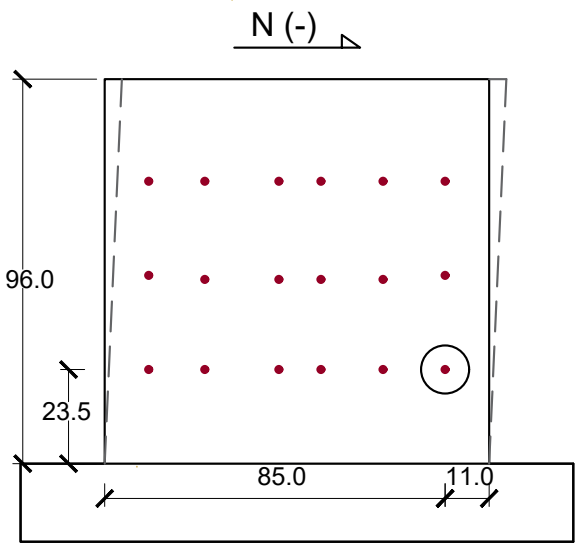


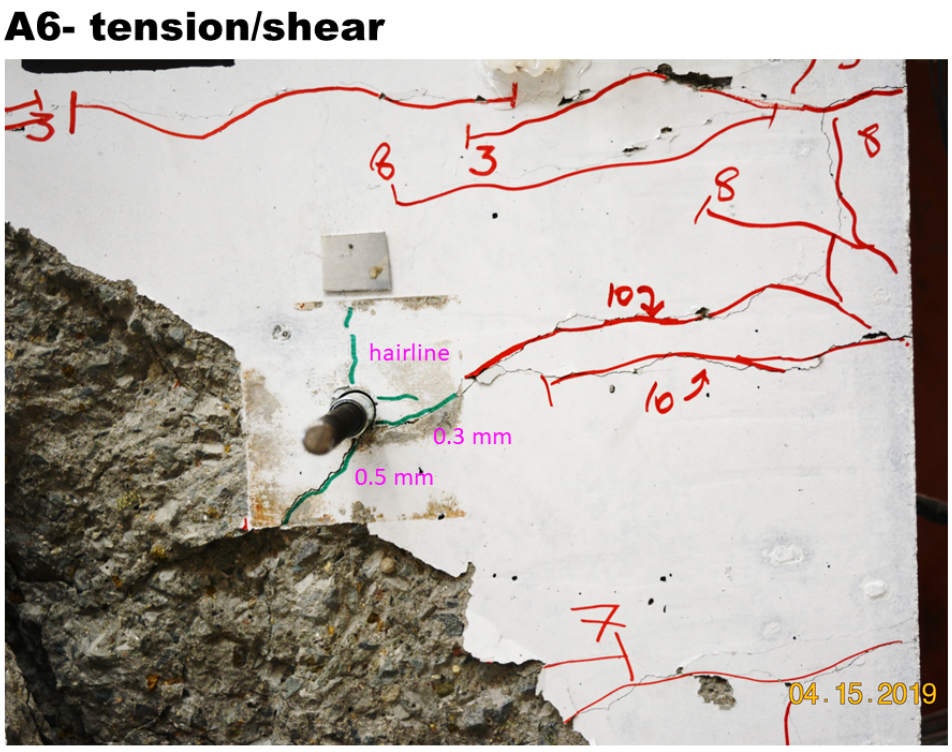
Figure E.79: Wall SQ7.5, anchor A5: measured load and displacement histories and wall drift history

A6

Fig.E.80b shows that torque-controlled expansion anchor A6 was located in a tension/shear crack, developed at 1.4% drift ratio. Moreover, extensive concrete crushing occurred right below the anchor during the last wall cycle. Anchor load and global displacement histories are relatively constant till the occurrence of the crack at 1.4% drift ratio amplitude (see Fig.E.82). The load was reapplied twice, at the end of 1.2% and 1.4% drift ratio cycles to maintain constant tension load on the anchor. It is noted that the anchor was reloaded before the crossing crack was marked on the wall surface, as a prove that smaller cracks within the embedment depth of the anchor were already open. Maximum residual crack widths at the end of the test measured w_r = 0.5 mm. The maximum displacement before the concrete crushing measured 0.17 in.



(a) Anchor location. Units in inches



(b) Photograph of anchor and cracks at end of test

Figure E.80: Location and photograph of anchor A6 in wall SQ7.5. Wall residual drift is diagrammatically shown exaggerated for the purpose of illustrating the final context around the anchor

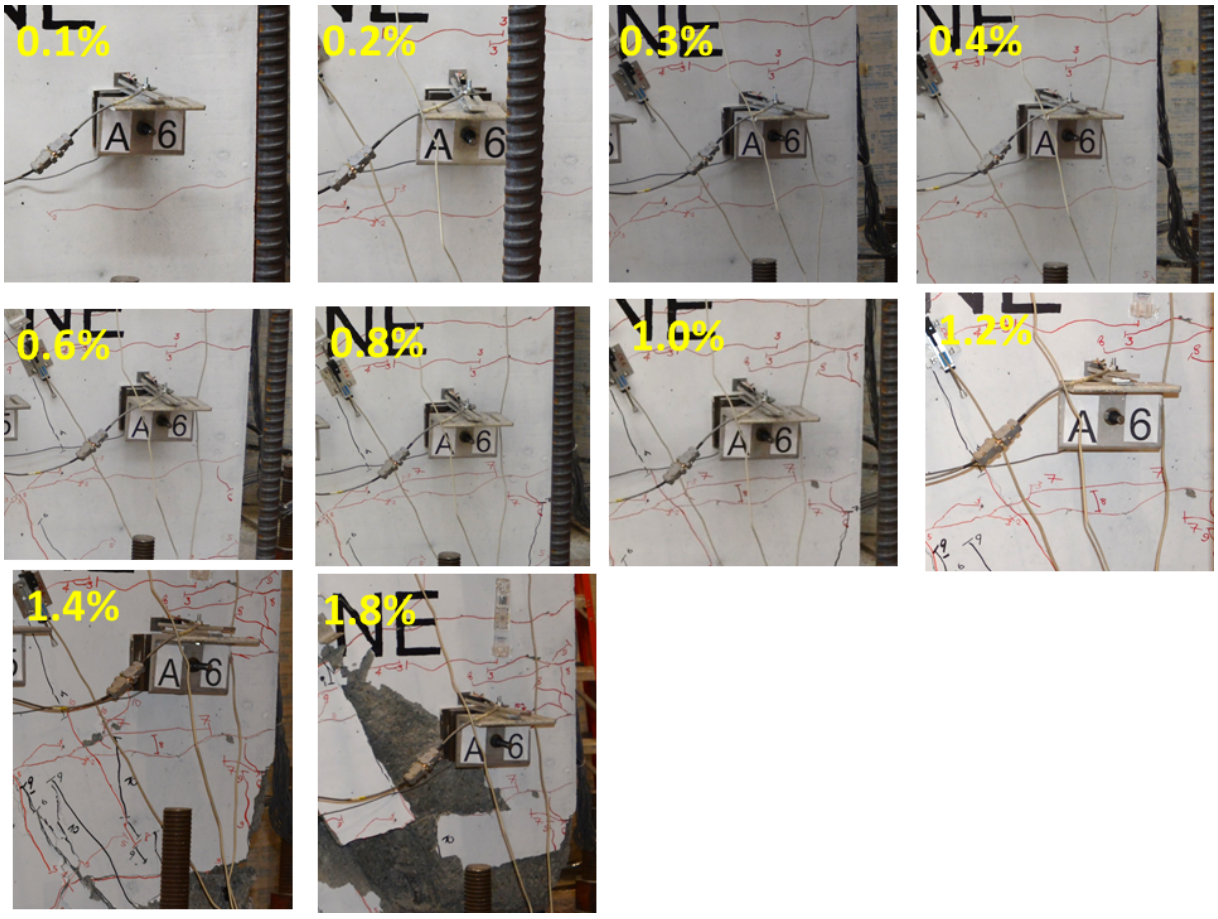


Figure E.81: Wall SQ7.5: photographs showing the crack evolution around anchor A6

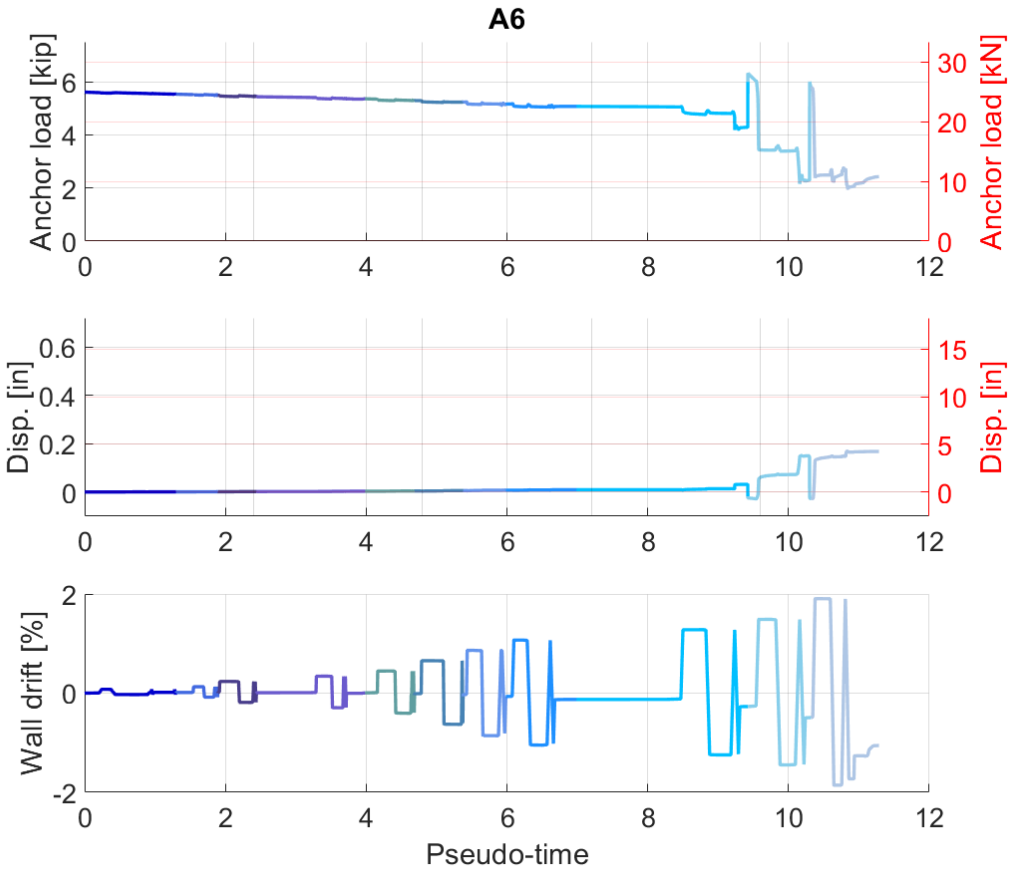
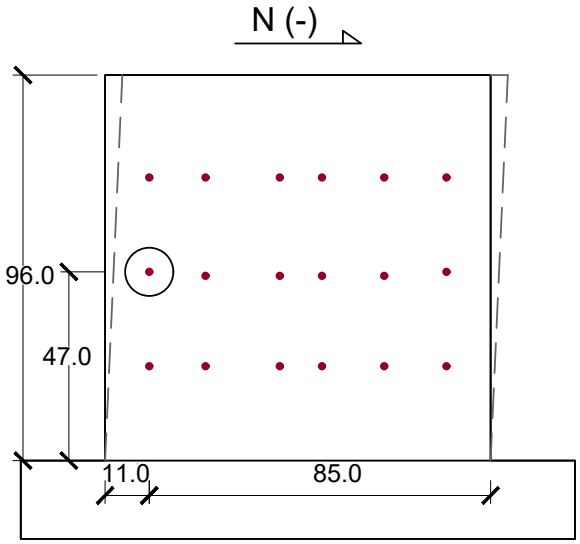


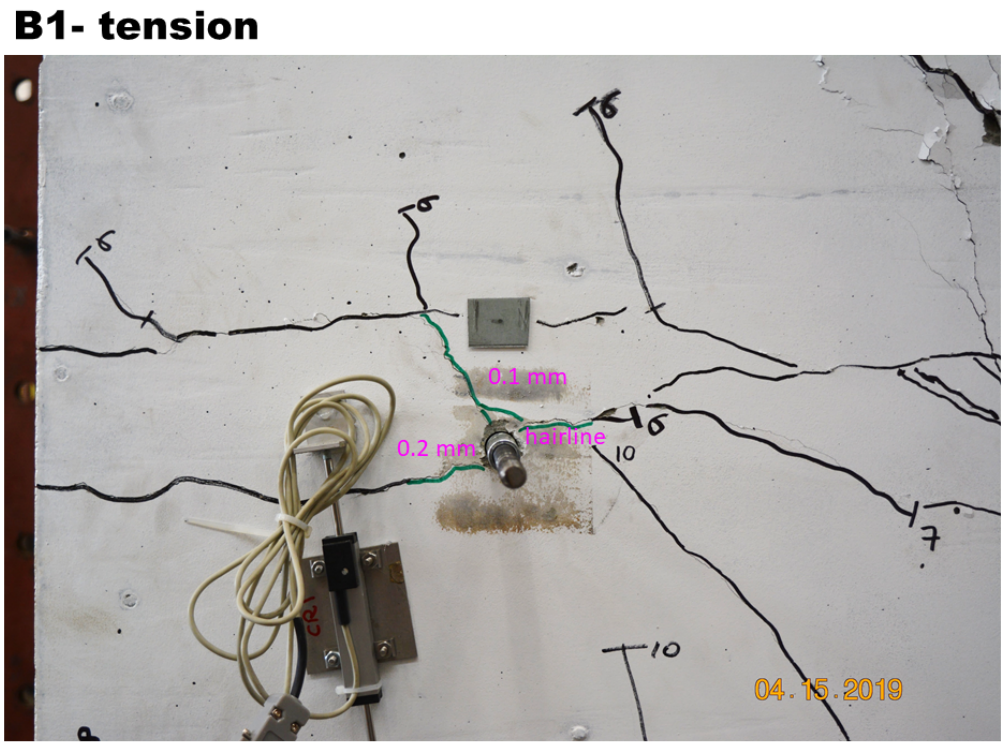
Figure E.82: Wall SQ7.5, anchor A6: measured load and displacement histories and wall drift history

B1

Fig.E.83b shows that torque-controlled expansion anchor B1 was located in a tension crack, which developed during the first wall pull at 0.2% drift. The crack width of this crossing tension crack was continuously measured by sensor CR1, installed at 0.2% drift ratio. Anchor load and global displacement histories were approximately constant for large part of the wall test, as in Fig.E.85. Appreciable load reduction and displacement increment were observed during the last two drift ratio cycles applied to the wall. The load was reapplied to anchor B1 three times, at the end of 0.4%, 0.8% and 1.2% drift ratio cycles to maintain constant tension load to the anchor. Residual crack widths at the end of the test measured about 0.2 mm. The maximum displacement measured at the end of the test was 0.24 in.



(a) Anchor location. Units in inches



(b) Photograph of anchor and cracks at end of test

Figure E.83: Location and photograph of anchor B1 in wall SQ7.5. Wall residual drift is diagrammatically shown exaggerated for the purpose of illustrating the final context around the anchor

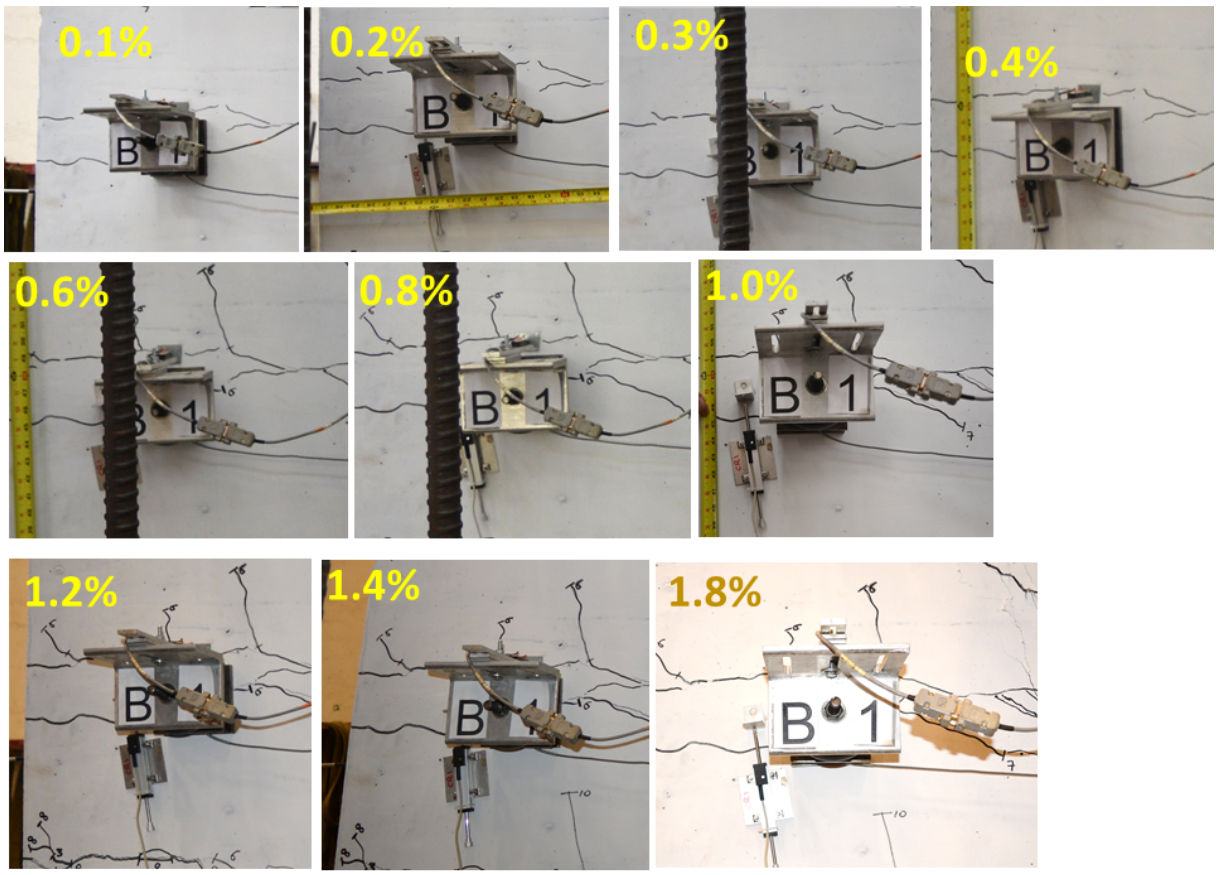


Figure E.84: Wall SQ7.5: photographs showing the crack evolution around anchor B1

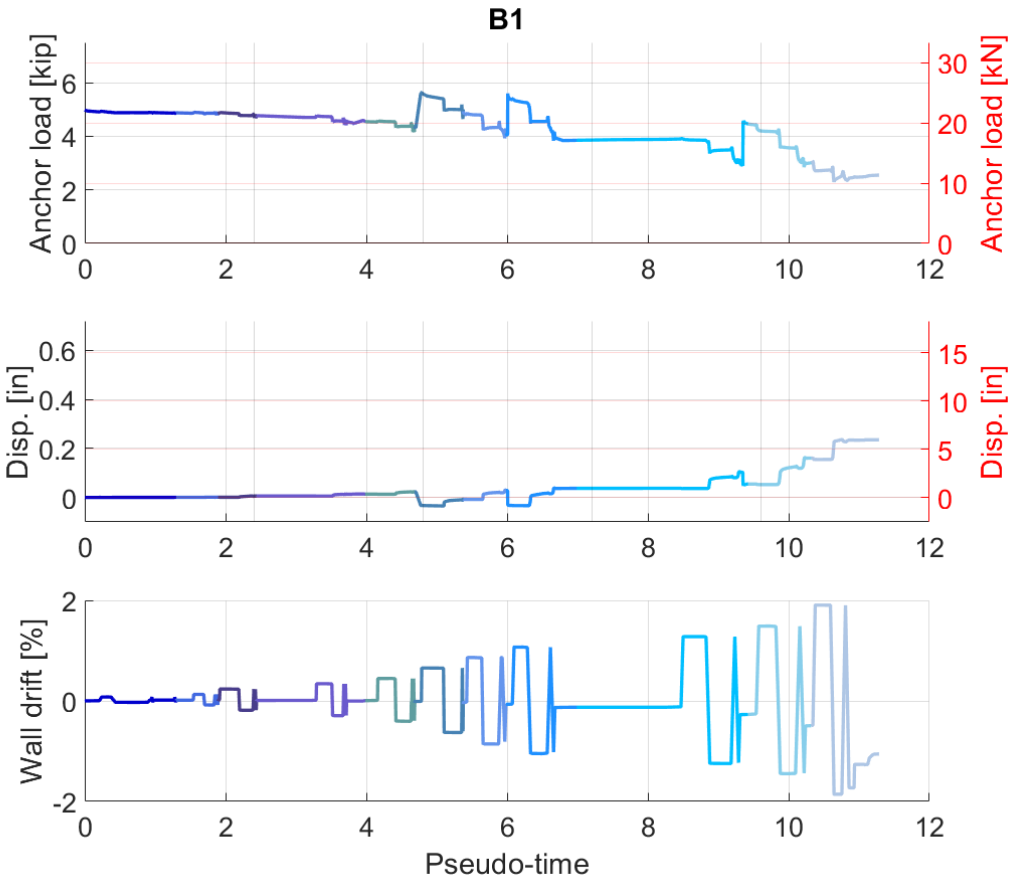
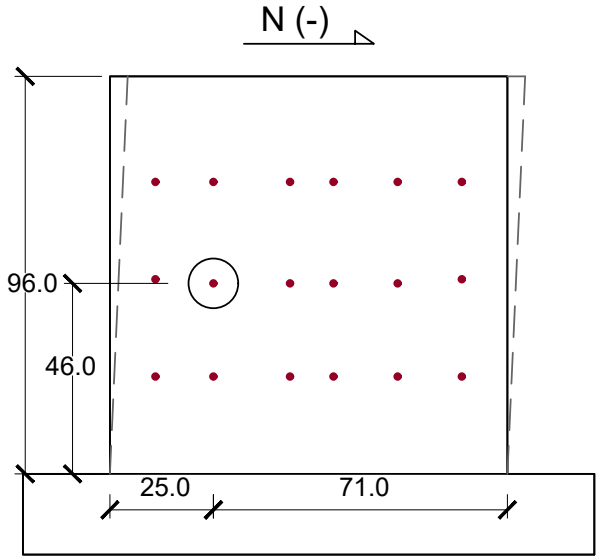


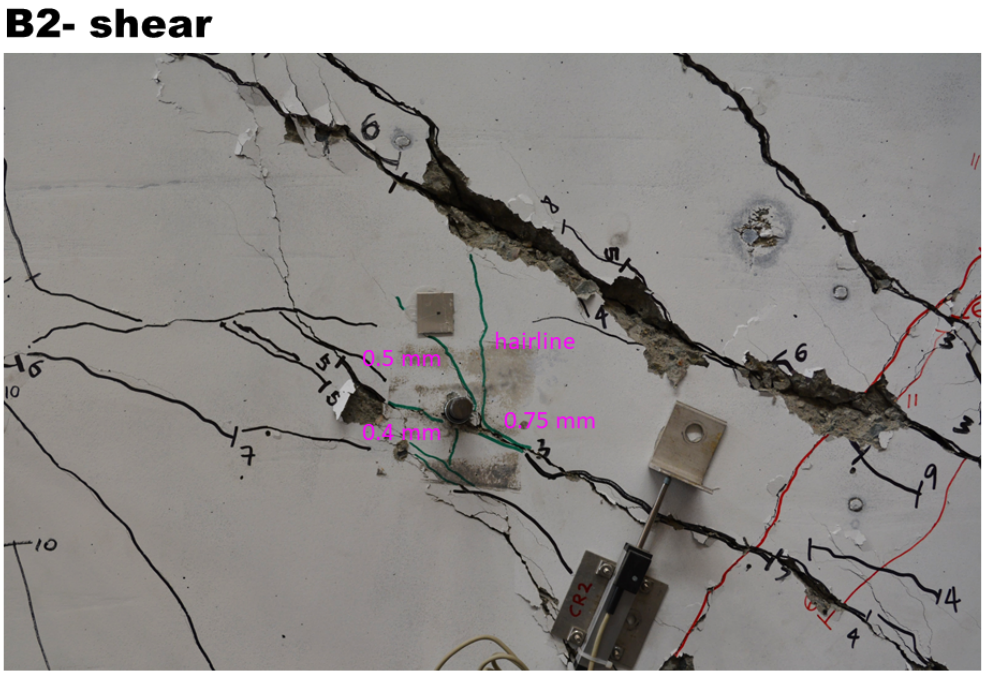
Figure E.85: Wall SQ7.5, anchor B1: measured load and displacement histories and wall drift history

B2

Fig.E.86b shows that torque-controlled expansion anchor B2 was located in a shear crack, which likely developed during the 0.2% drift ratio cycle. The crack width of this crossing shear crack was continuously measured by sensor CR2. Anchor load progressively reduced after the crack opened, as in Fig.E.88. The load was, hence, reapplied four times, at the end of 0.4%, 0.8%, 1.2% and 1.4% drift ratio cycles. Maximum residual crack width at the end of the test measured about 0.75 mm. The maximum displacement measured at the end of the test was 0.24 in.



(a) Anchor location. Units in inches



(b) Photograph of anchor and cracks at end of test

Figure E.86: Location and photograph of anchor B2 in wall SQ7.5. Wall residual drift is diagrammatically shown exaggerated for the purpose of illustrating the final context around the anchor

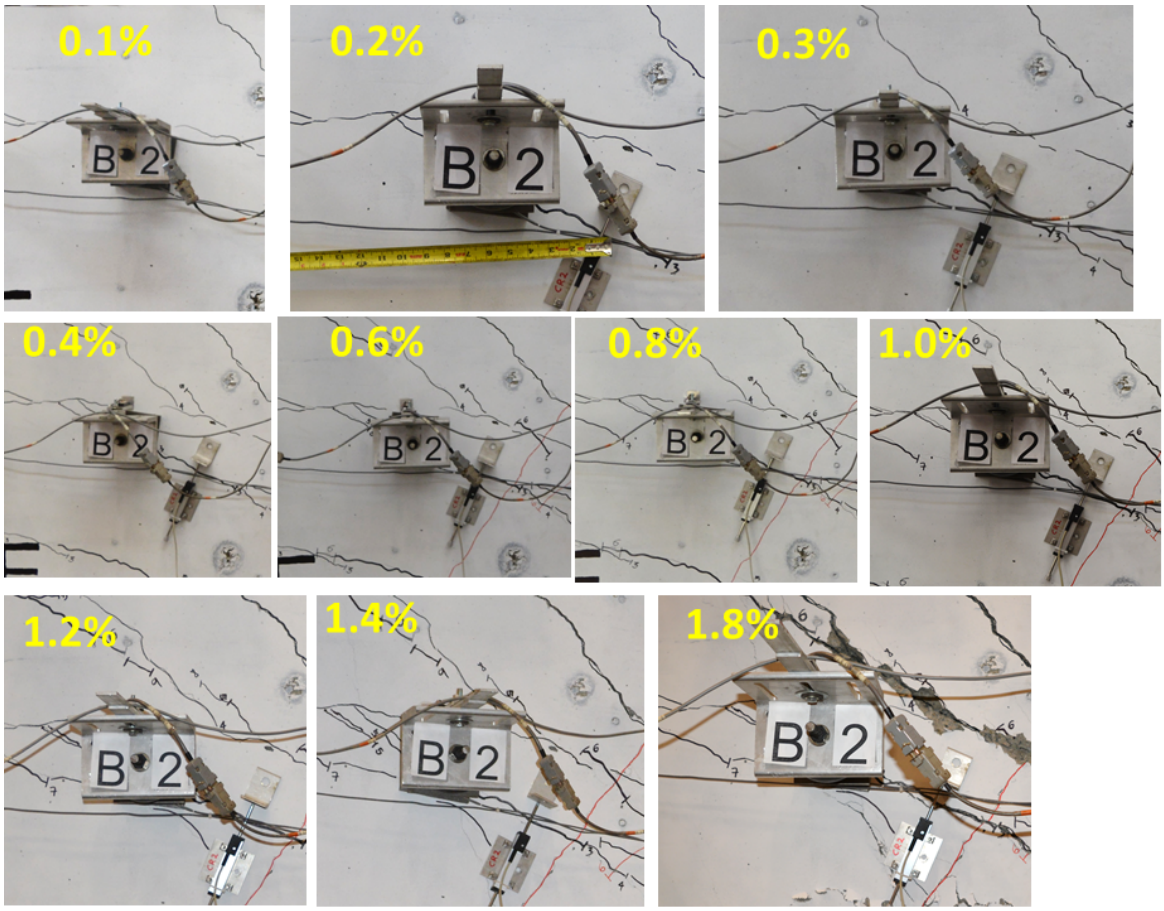


Figure E.87: Wall SQ7.5: photographs showing the crack evolution around anchor B2

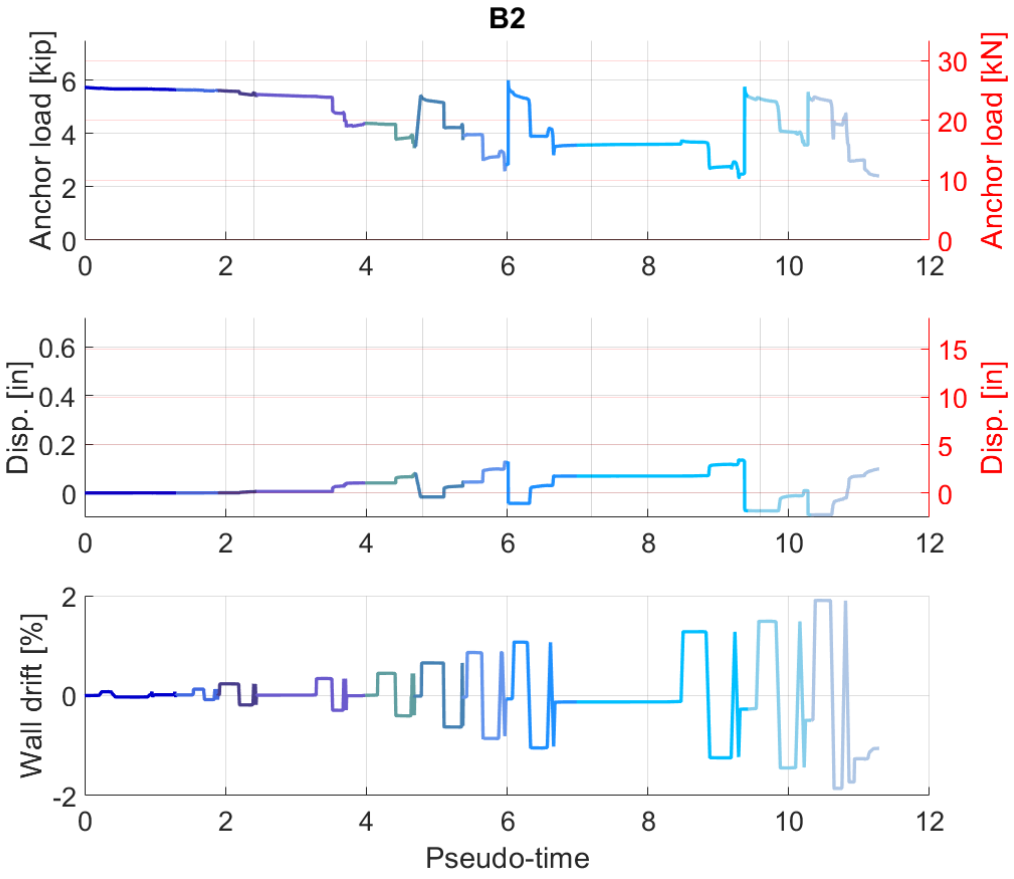
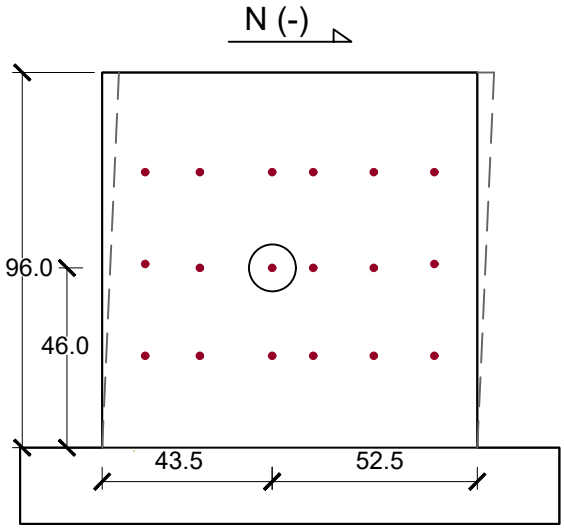


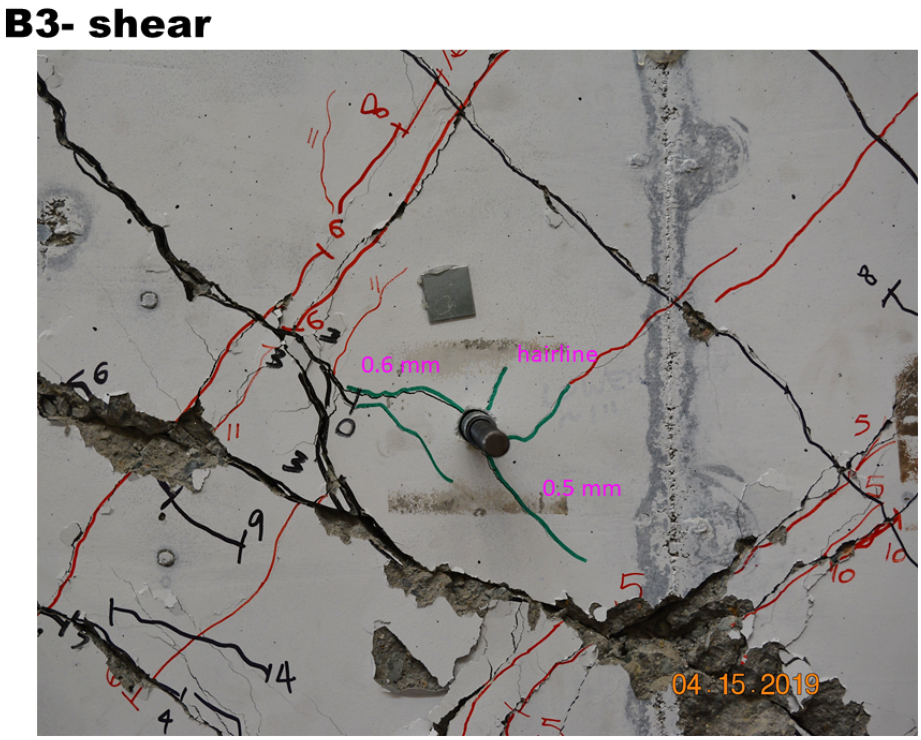
Figure E.88: Wall SQ7.5, anchor B2: measured load and displacement histories and wall drift history

B3

Fig.E.89b shows that torque-controlled expansion anchor B3 was located in a short shear crack, which was revealed after the steel plates were removed. The damage in the vicinity of the anchor was localized in a shear crack passing about 3 in below anchor B3. Concrete crushing of the sides of this crack was also observed by the end of the test. The anchor holds its tension design load approximately constant for all the duration of the test, therefore the load was reapplied only once, at the end of 0.4% drift ratio cycles. Only during last cycle concrete damage significantly reduced anchor load, as in Fig.E.91. The global displacement was considerably constant till the end of the test, when it measured 0.14 in. Maximum residual crack width at the end of the test was measured to be about 0.6 mm.



(a) Anchor location. Units in inches



(b) Photograph of anchor and cracks at end of test

Figure E.89: Location and photograph of anchor B3 in wall SQ7.5. Wall residual drift is diagrammatically shown exaggerated for the purpose of illustrating the final context around the anchor

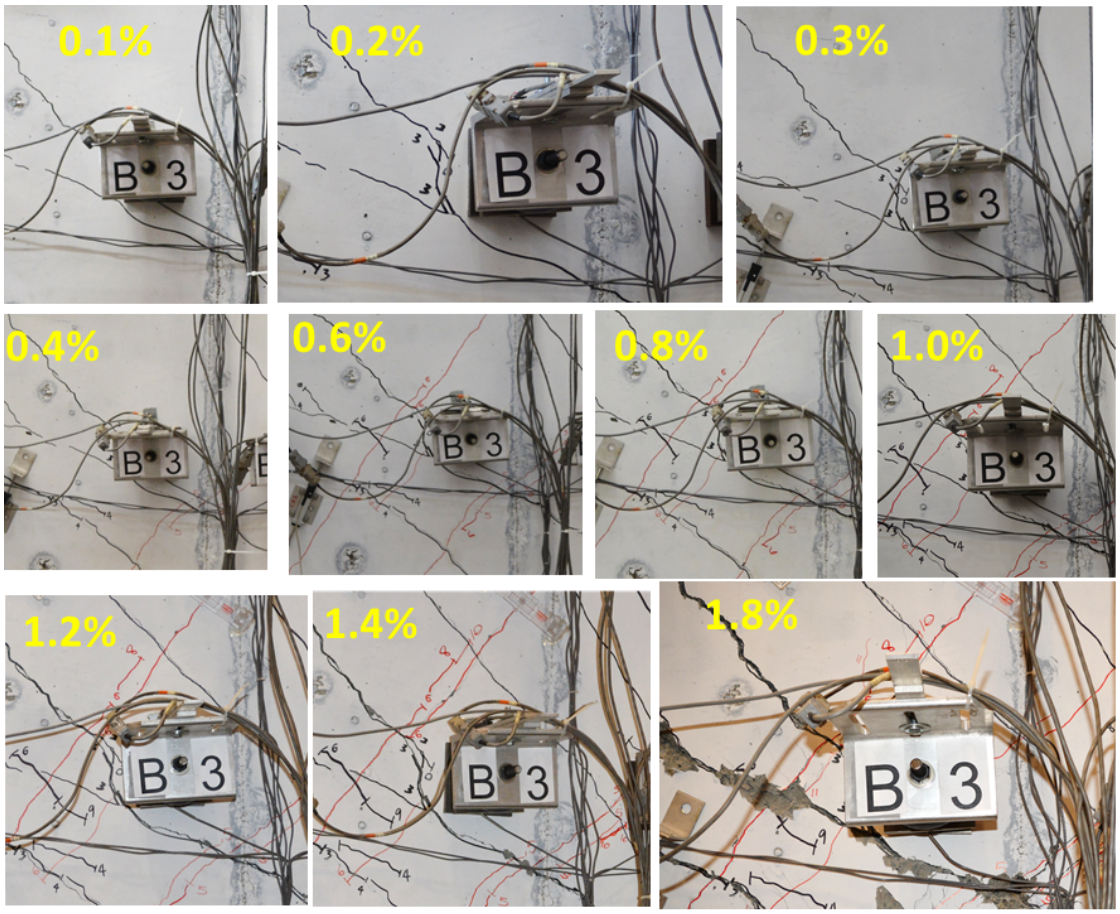


Figure E.90: Wall SQ7.5: photographs showing the crack evolution around anchor B3

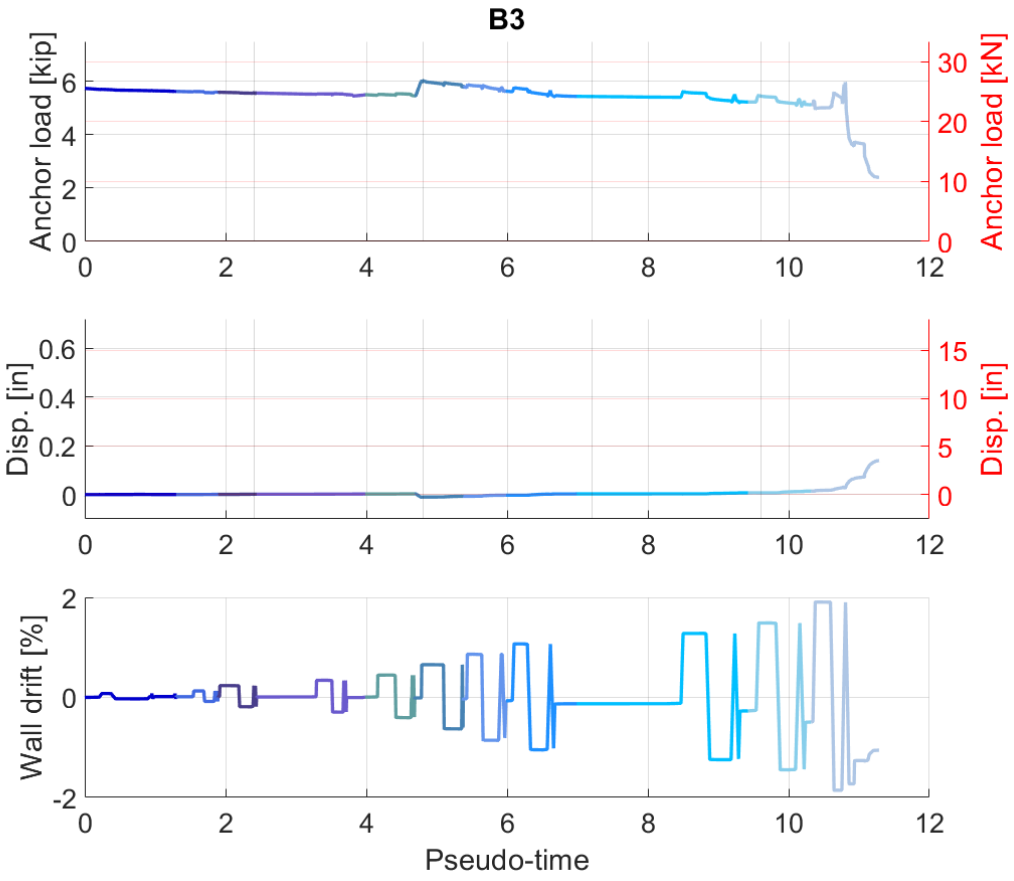
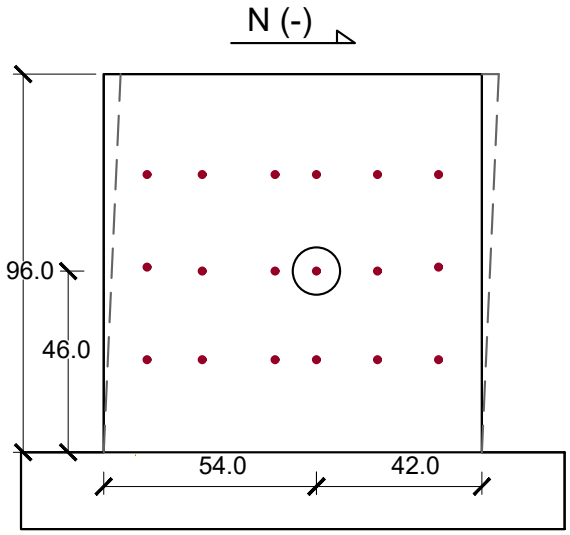


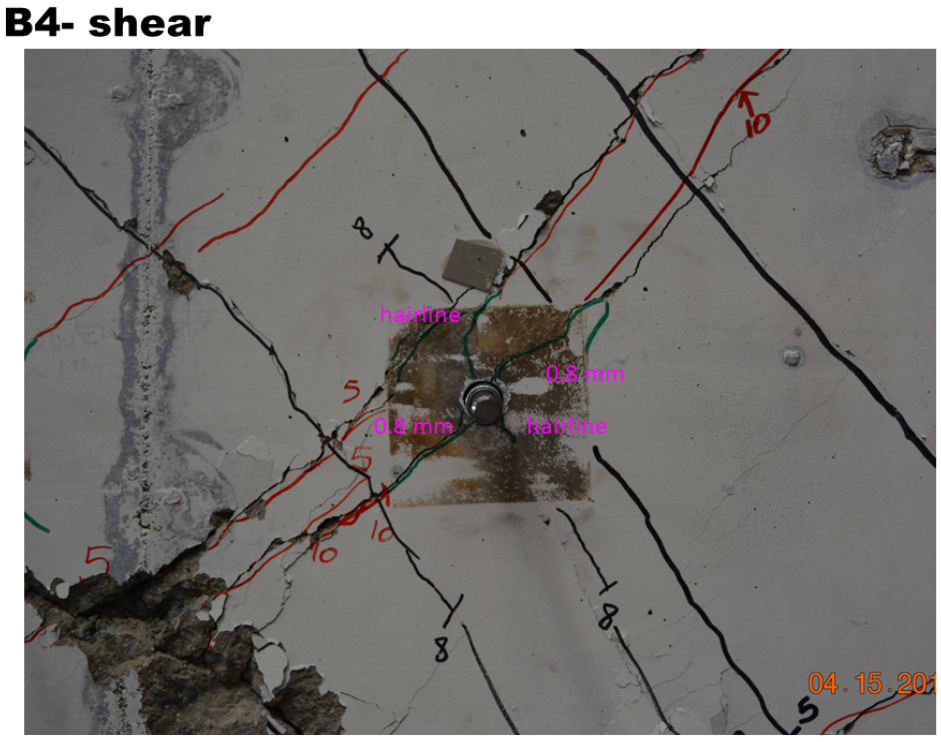
Figure E.91: Wall SQ7.5, anchor B3: measured load and displacement histories and wall drift history

B4

Fig.E.92b shows that torque-controlled expansion anchor B4 was located in a couple of crossing shear cracks, which opened at 1.00 and 1.4% drift ratio cycles. Several other parallel diagonal cracks in both directions developed in this region of the wall during the cyclic test. Anchor load history in Fig.E.94 presents a decreasing trend, therefore load was reapplied four times, at the end of 0.4%, 0.8%, 1.2% and 1.4% drift cycles. On the opposite side, measured anchor load shows an increasing trend (see Fig.E.94) with a maximum value of 0.40 in. at the end of the test. Maximum residual crack width at the end of the test measured about w_r = 0.8 mm.



(a) Anchor location. Units in inches



(b) Photograph of anchor and cracks at end of test

Figure E.92: Location and photograph of anchor B4 in wall SQ7.5. Wall residual drift is diagrammatically shown exaggerated for the purpose of illustrating the final context around the anchor

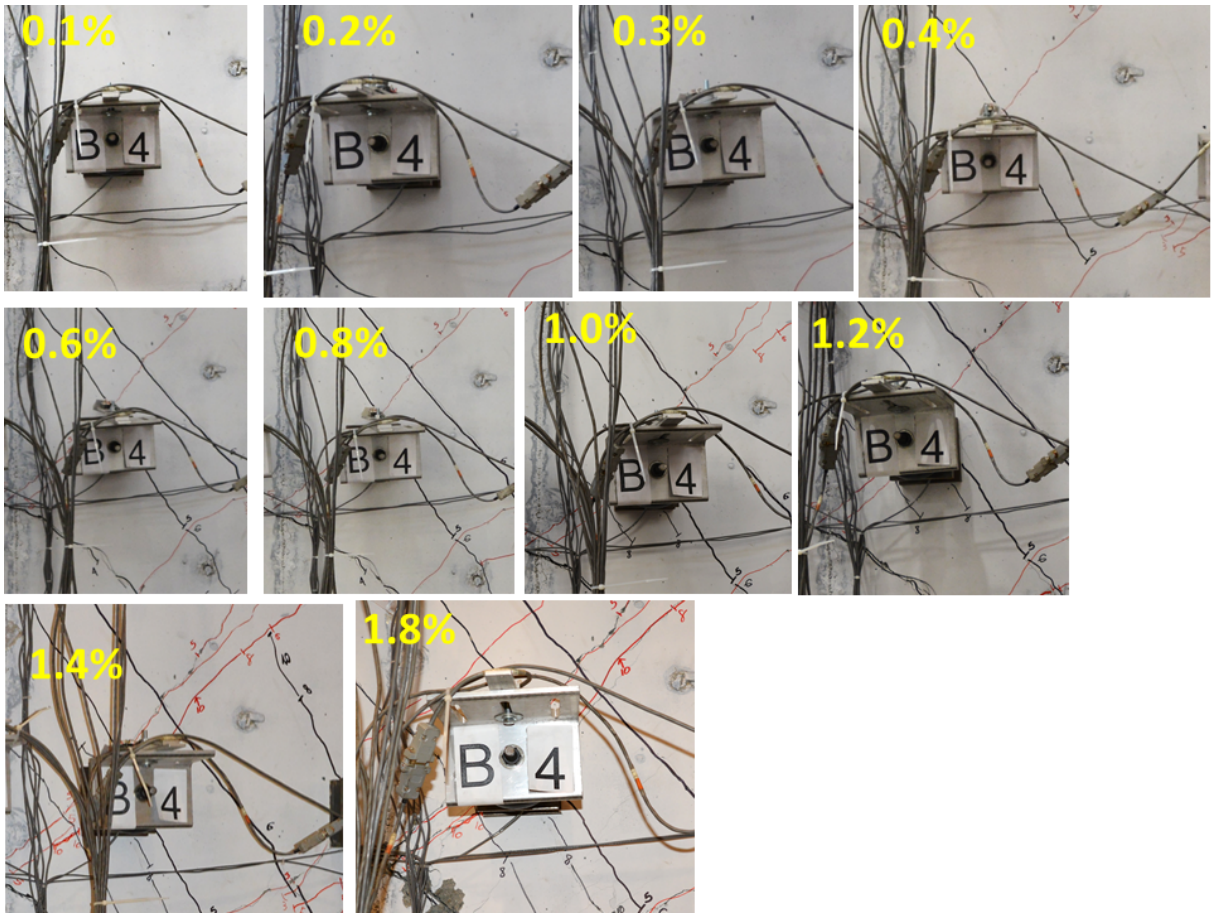


Figure E.93: Wall SQ7.5: photographs showing the crack evolution around anchor B4

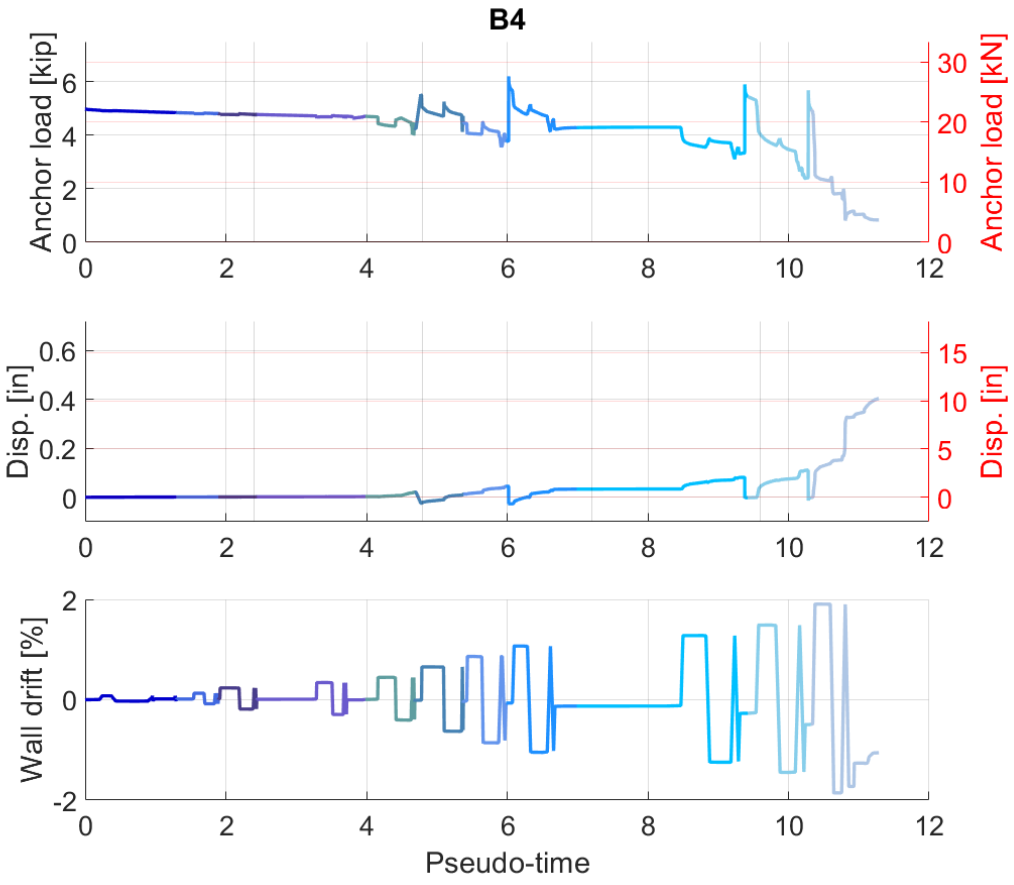
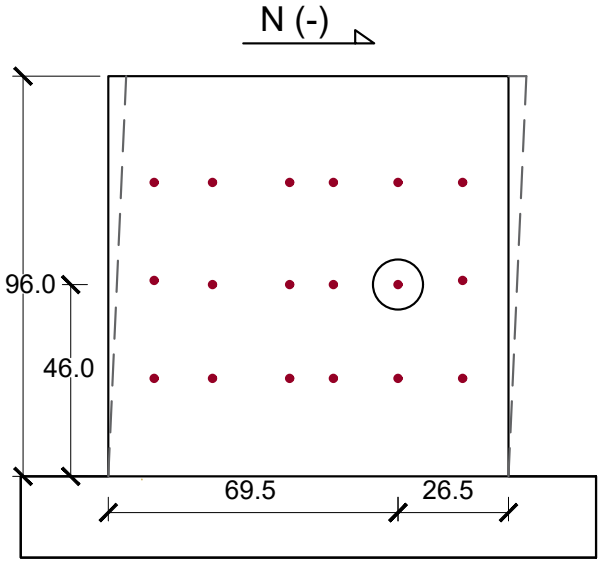


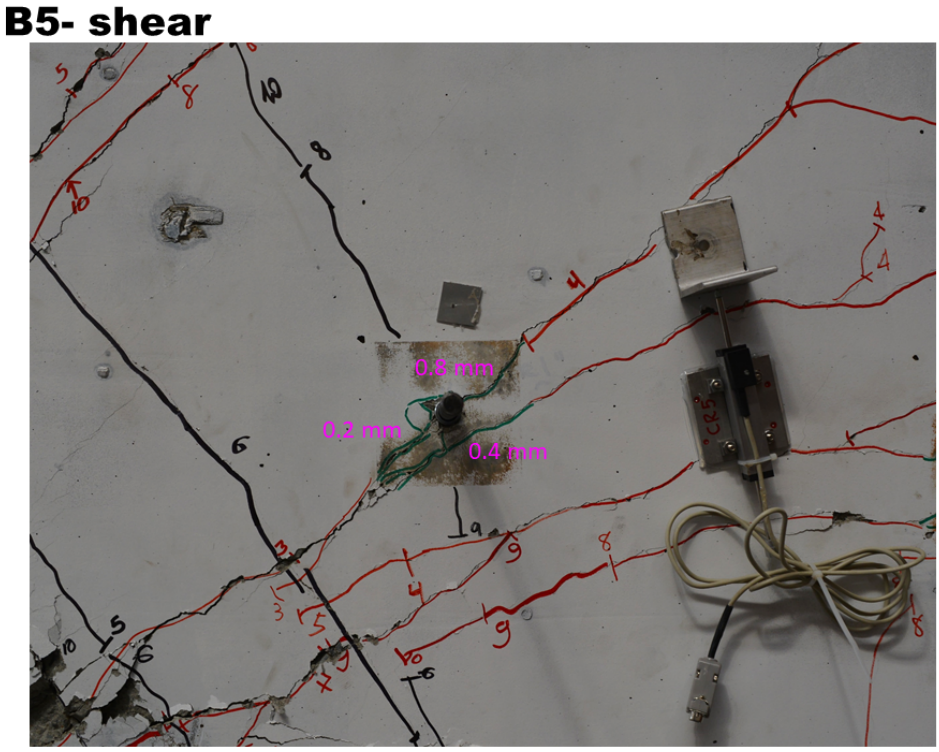
Figure E.94: Wall SQ7.5, anchor B4: measured load and displacement histories and wall drift history

B5

Fig.E.95b shows that torque-controlled expansion anchor B5 was located in a shear crack, which likely opened at 0.3% drift ratio cycles. The crack width sensor CR5 continuously monitored another shear crack, passing below the anchor. However, concrete damage in this region of the wall was significant, and anchor measured load history in Fig.E.97 shows a clear decreasing trend. To maintain anchor load approximately constant, the load was reapplied four times, at the end of 0.4%, 0.8%, 1.2% and 1.4% drift ratio cycles. Similarly, measured anchor load presents an increasing trend (see Fig.E.97) with a maximum value of 0.27 in reached at the end of the test. Maximum residual crack width at the end of the test measured about w_r= 0.8 mm.



(a) Anchor location. Units in inches



(b) Photograph of anchor and cracks at end of test

Figure E.95: Location and photograph of anchor B5 in wall SQ7.5. Wall residual drift is diagrammatically shown exaggerated for the purpose of illustrating the final context around the anchor

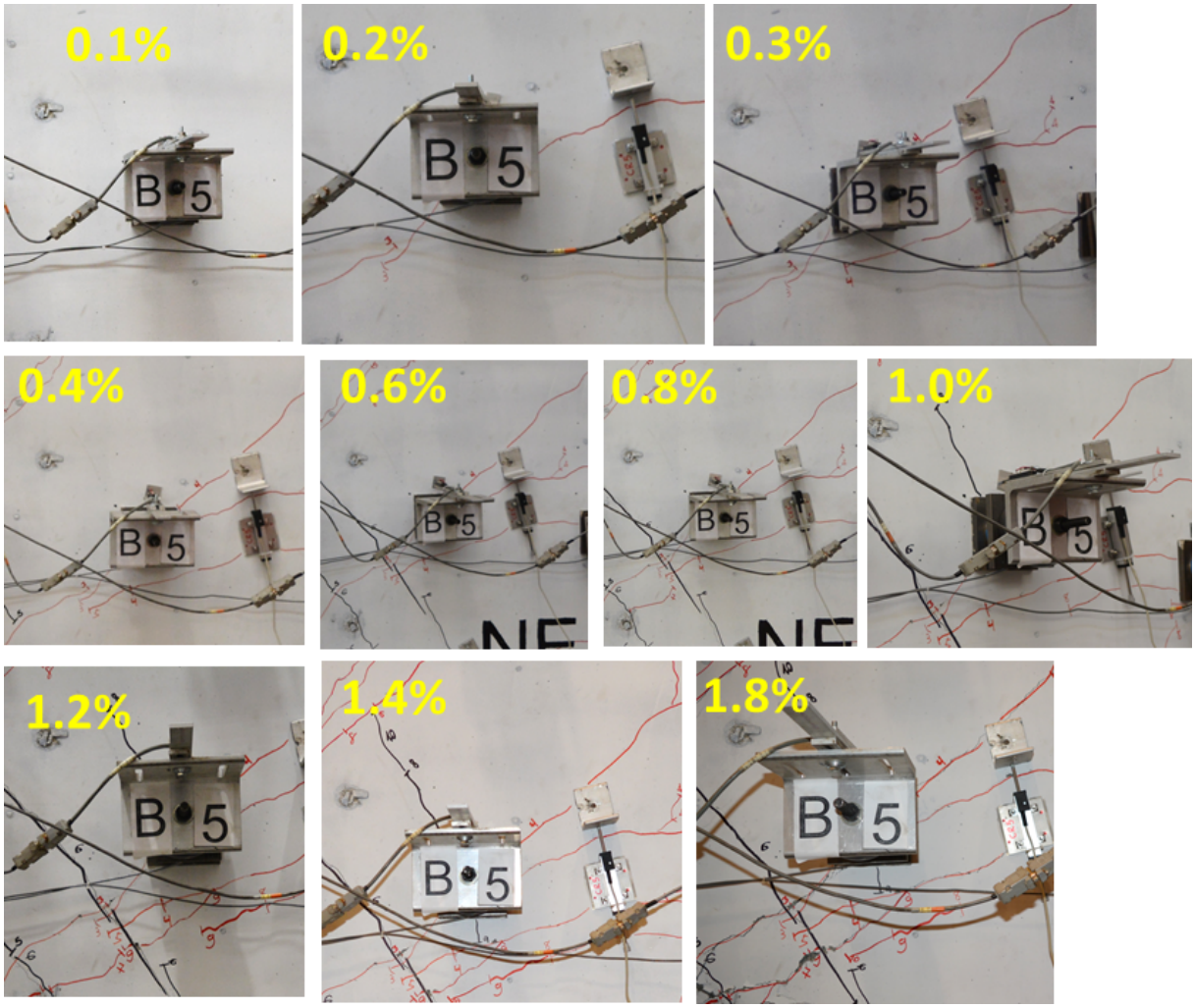


Figure E.96: Wall SQ7.5: photographs showing the crack evolution around anchor B5

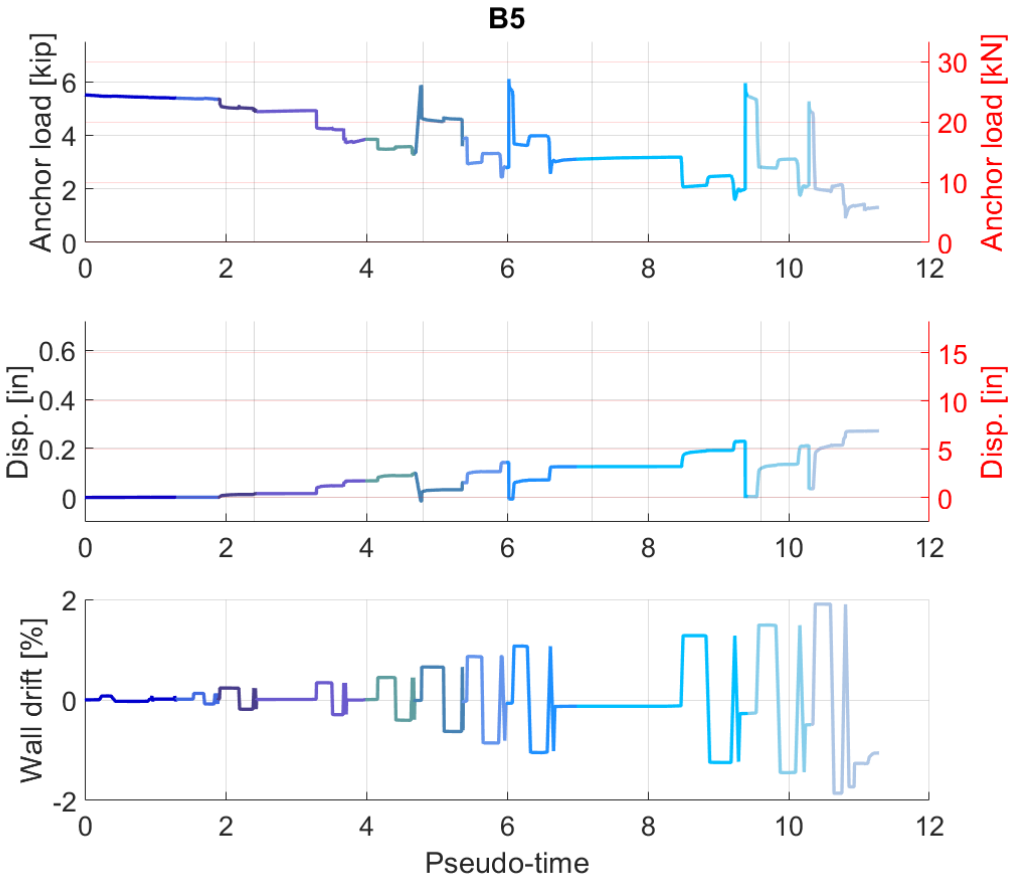
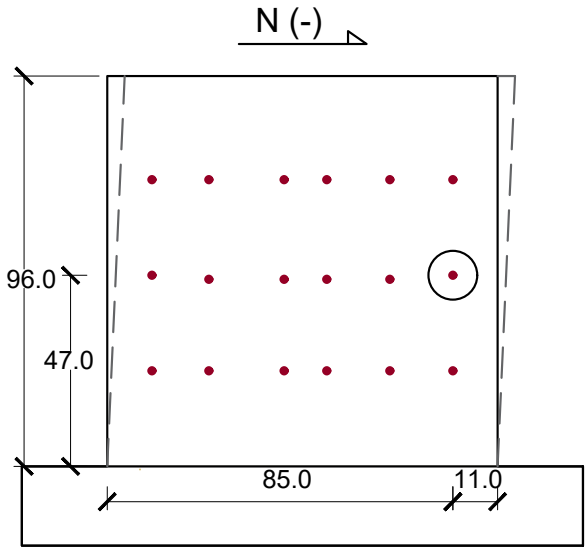


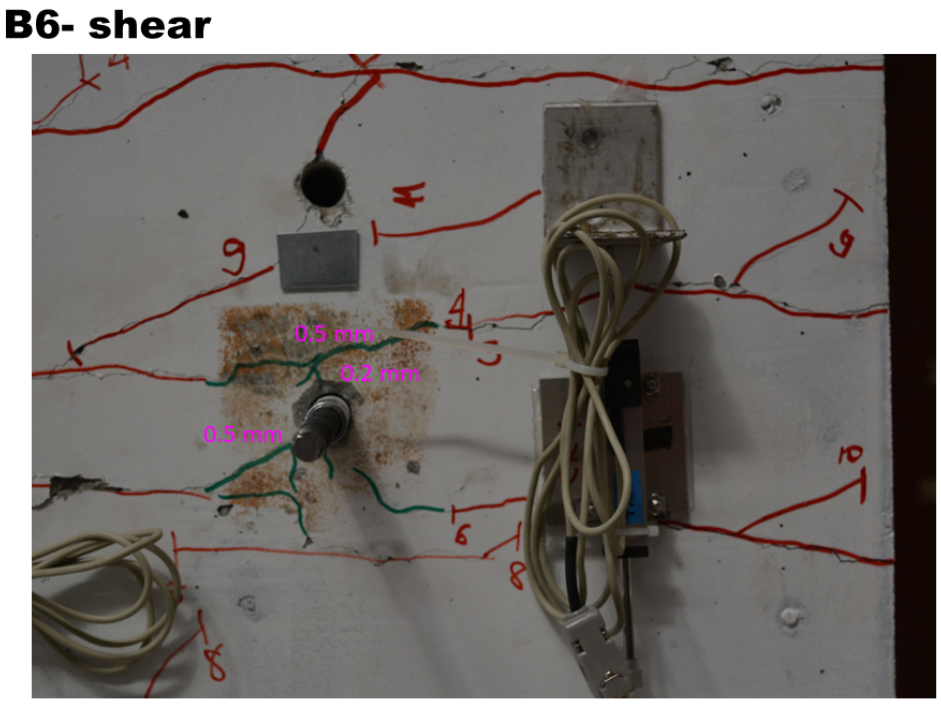
Figure E.97: Wall SQ7.5, anchor B5: measured load and displacement histories and wall drift history

B6

Fig.E.98b shows that torque-controlled expansion anchor B6 was located in one shear and several radial cracks, which likely opened at 1.00% drift ratio cycles. Additionally, two parallel tension cracks framed anchor B6. Anchor load history in Fig.E.100 shows a clear decreasing trend, reflecting the severe damage occurring in this end region of the wall. To maintain approximately constant tension on the anchor, load was reapplied four times, at the end of 0.4%, 0.8%, 1.2% and 1.4% drift ratio cycles. Similarly, measured anchor load shows an increasing trend (see Fig.E.100) with a maximum value of 0.21 in at the end of the test. Maximum residual crack width at the end of the test measured about w_r = 0.5 mm.



(a) Anchor location. Units in inches



(b) Photograph of anchor and cracks at end of test

Figure E.98: Location and photograph of anchor B6 in wall SQ7.5. Wall residual drift is diagrammatically shown exaggerated for the purpose of illustrating the final context around the anchor

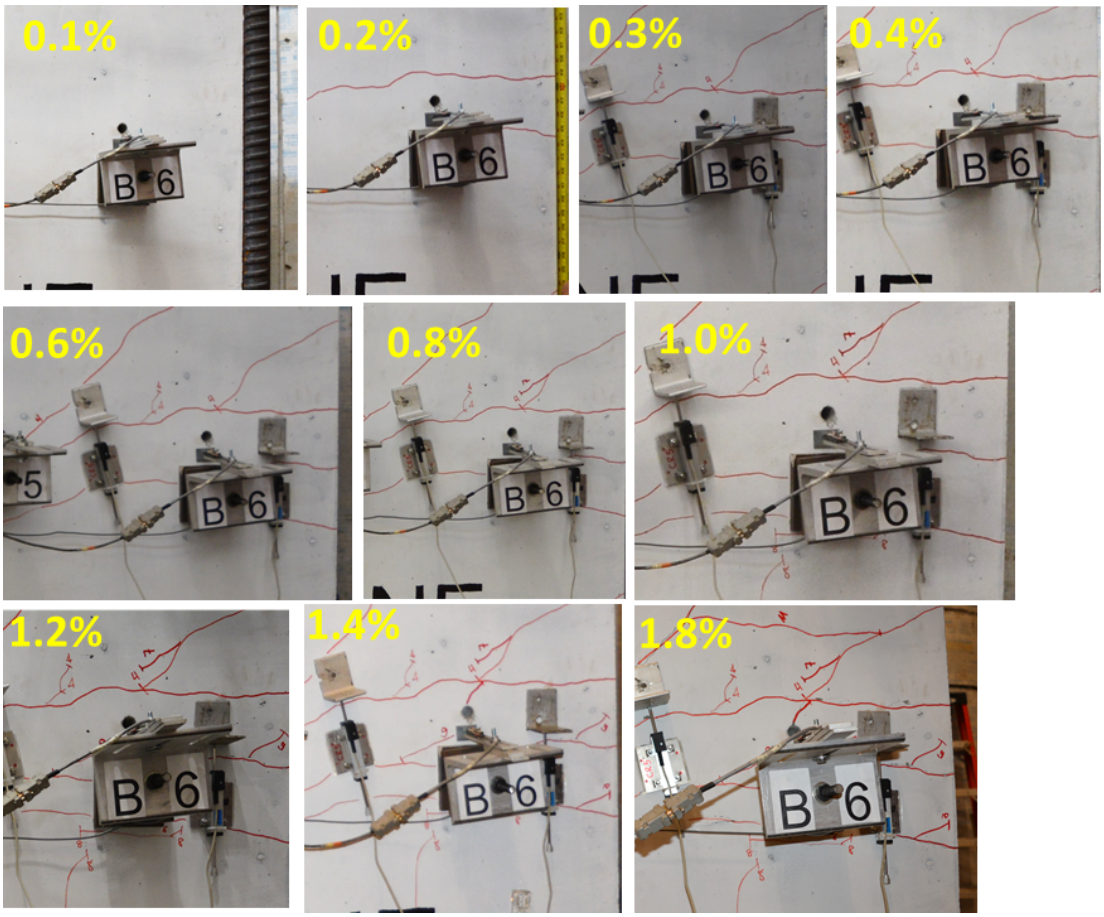


Figure E.99: Wall SQ7.5: photographs showing the crack evolution around anchor B6

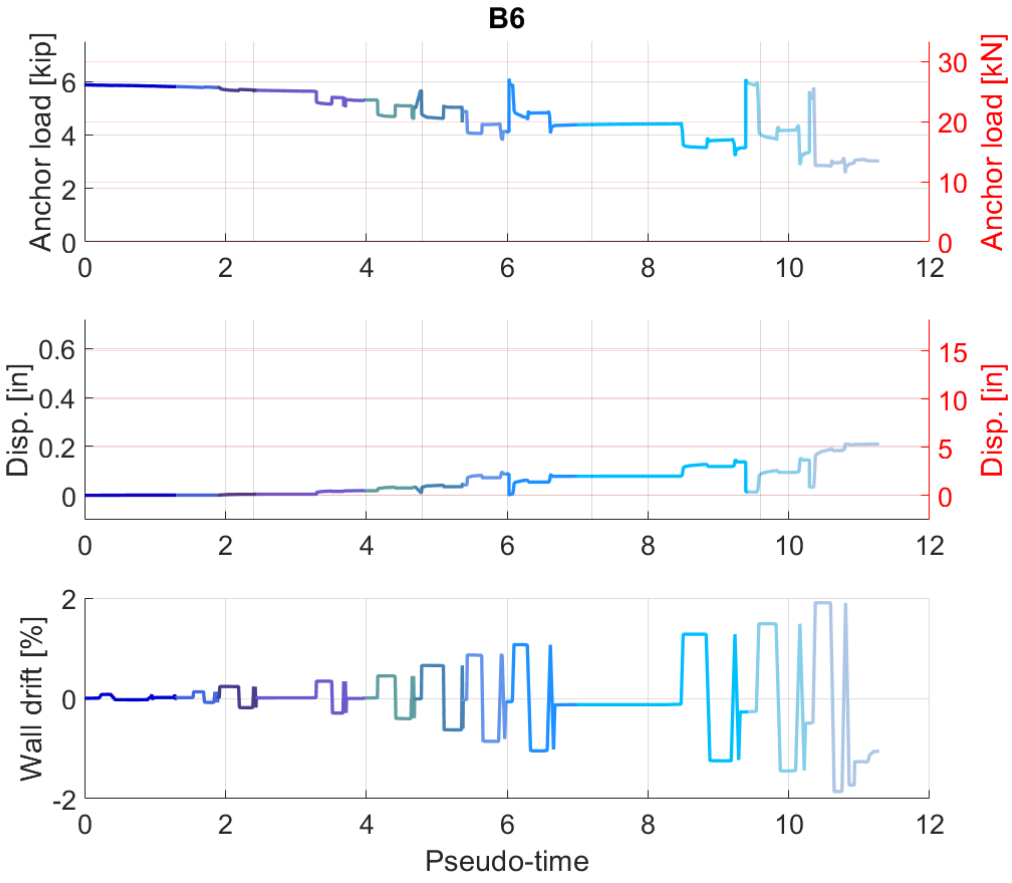
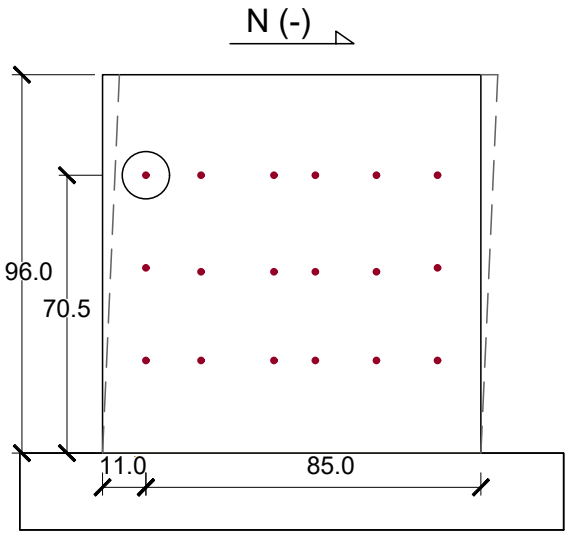


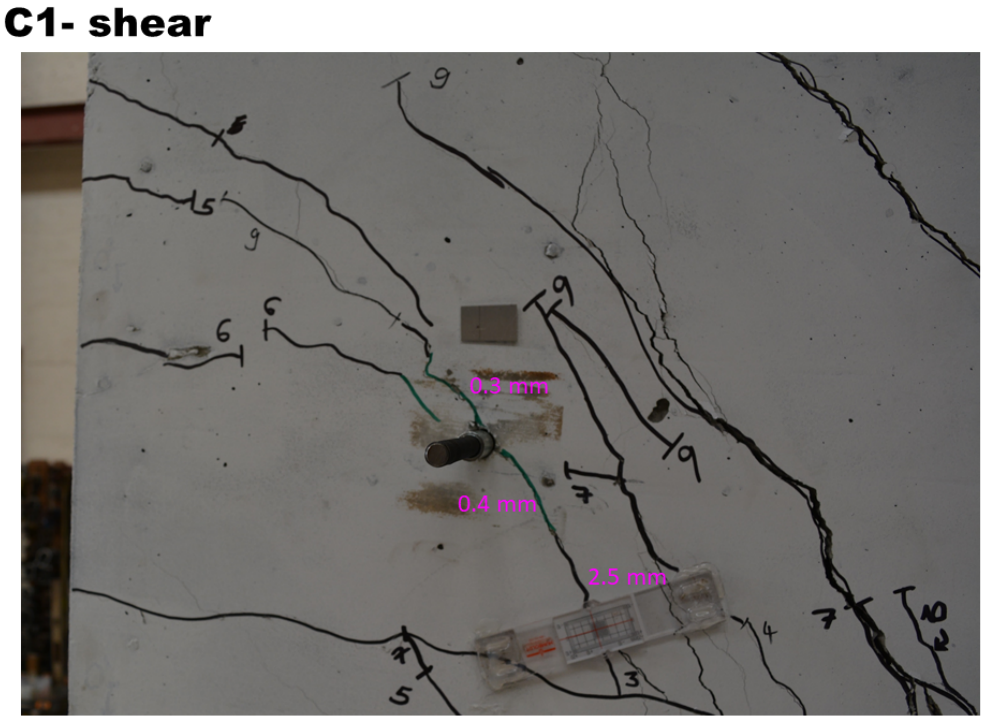
Figure E.100: Wall SQ7.5 anchor B6: measured load and displacement histories and wall drift history

C1

Fig.E.101b shows that torque-controlled expansion anchor C1 was located in one shear crack, which opened at 0.2% drift ratio. Several parallel diagonal-shear cracks developed near C1, being located inside the boundary element region of the wall. The width of the crossing crack was measured by the manual sensor installed after the formation of the crack. Anchor load visibly dropped at 0.3% drift ratio, and load was reapplied at 0.8% and 1.2% drift ratios, as in Fig.E.103. While the load decreased, the measured global displacement increased. Maximum displacement of 0.12 in was measured before the load was reapplied to the anchor at 0.8% drift ratio. Maximum residual crack width at the end of the test measured about w_r = 0.4 mm.



(a) Anchor location. Units in inches



(b) Photograph of anchor and cracks at end of test

Figure E.101: Location and photograph of anchor C1 in wall SQ7.5. Wall residual drift is diagrammatically shown exaggerated for the purpose of illustrating the final context around the anchor

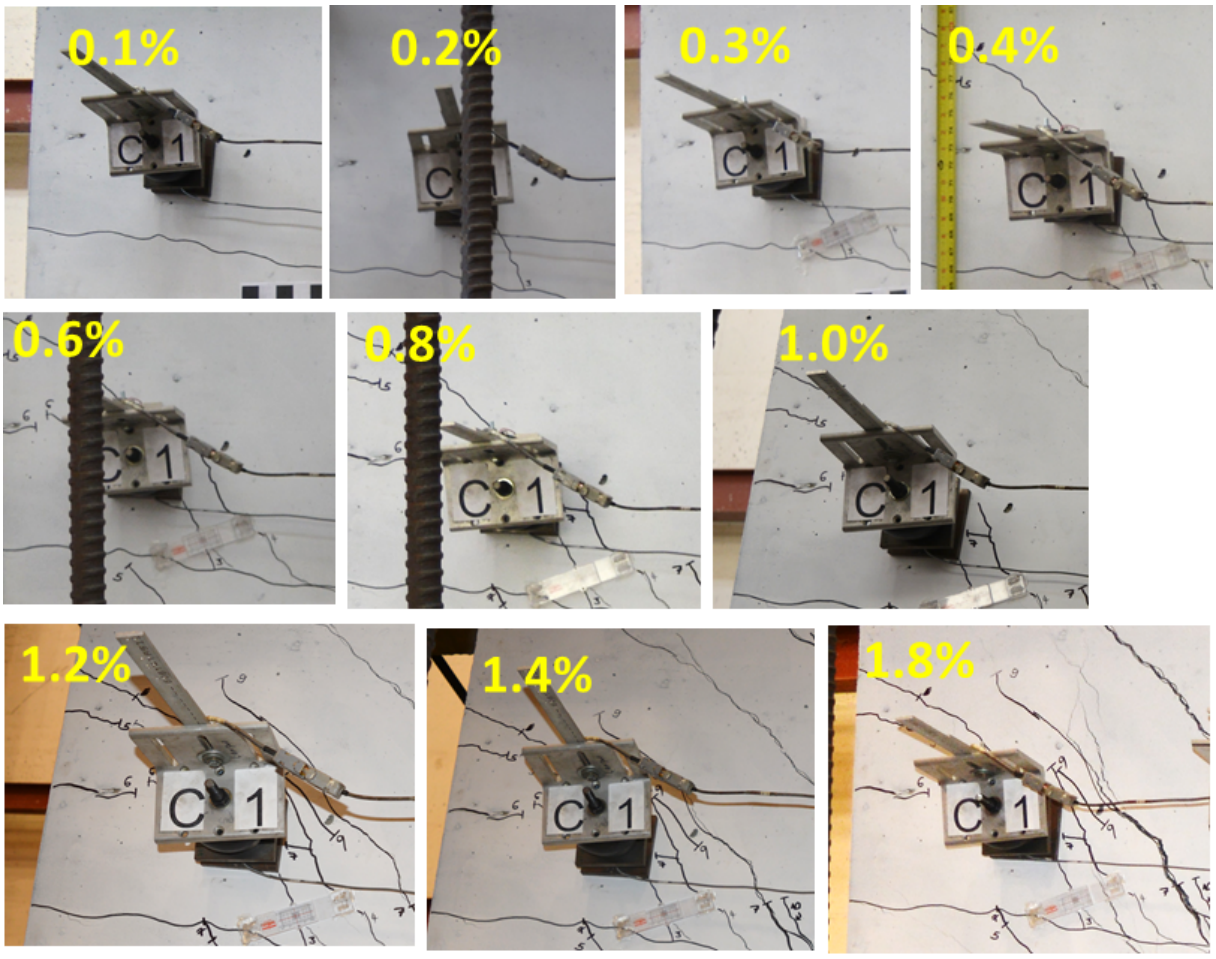


Figure E.102: Wall SQ7.5: photographs showing the crack evolution around anchor C1

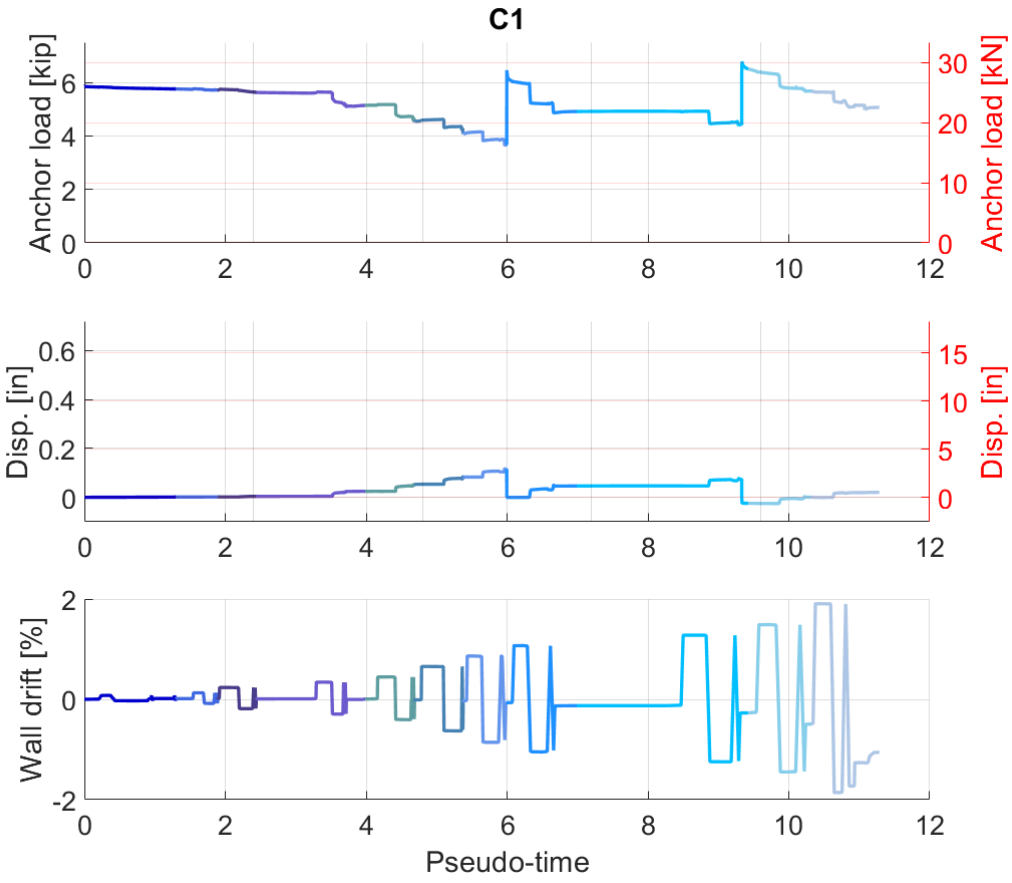
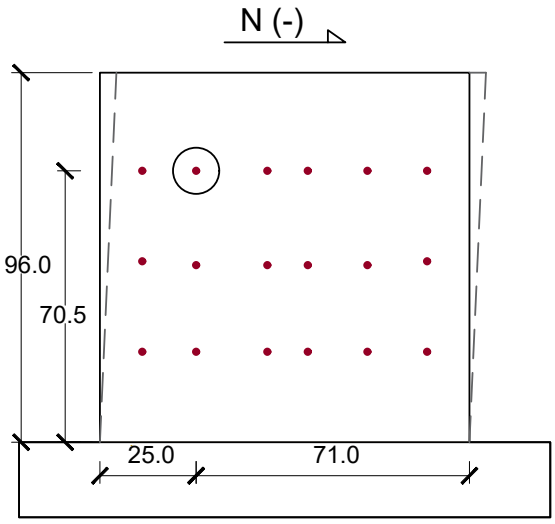


Figure E.103: Wall SQ7.5, anchor C1: measured load and displacement histories and wall drift history

C2

Fig.E.104b shows that torque-controlled expansion anchor C2 was located in one shear crack, which likely opened at 1.0% drift ratio. Shear-diagonal cracks in this region of the wall developed at an average stabilized crack spacing of about 7 in. Measured anchor load and global displacement histories in Fig. E.106 show overall constant trend up to the abrupt load drop/displacement increase at 1.0% drift ratio, which is the drift ratio at which the shear crack opened around anchor C2. The load was then reapplied at 1.2% and 1.4% drift ratios. Maximum measured displacement of 0.29 in occurred at the end of the test. Maximum residual crack width at the end of the test was considerably large, measuring about w_r= 1.2 mm, even if outside of the theoretical plastic hinge length.



(a) Anchor location. Units in inches



(b) Photograph of anchor and cracks at end of test

Figure E.104: Location and photograph of anchor C2 in wall SQ7.5. Wall residual drift is diagrammatically shown exaggerated for the purpose of illustrating the final context around the anchor

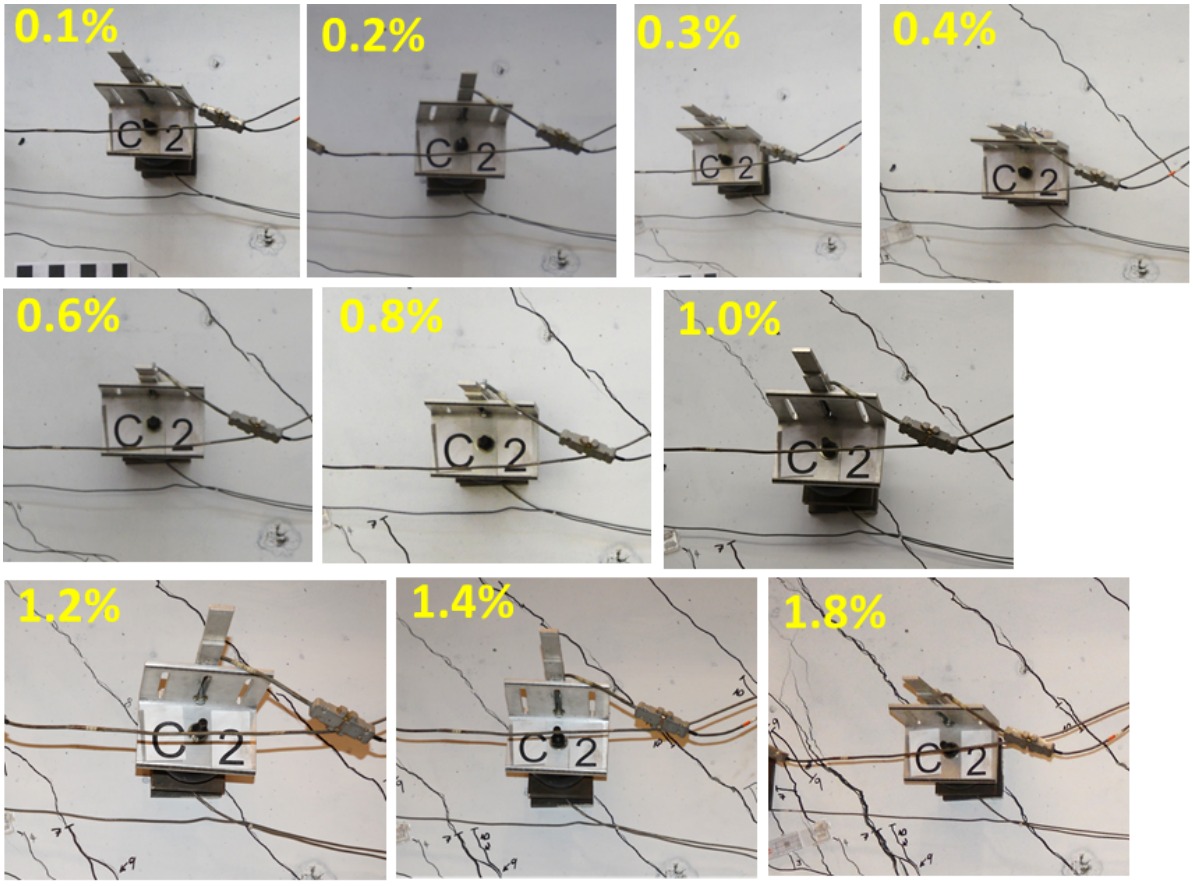


Figure E.105: Wall SQ7.5: photographs showing the crack evolution around anchor C2

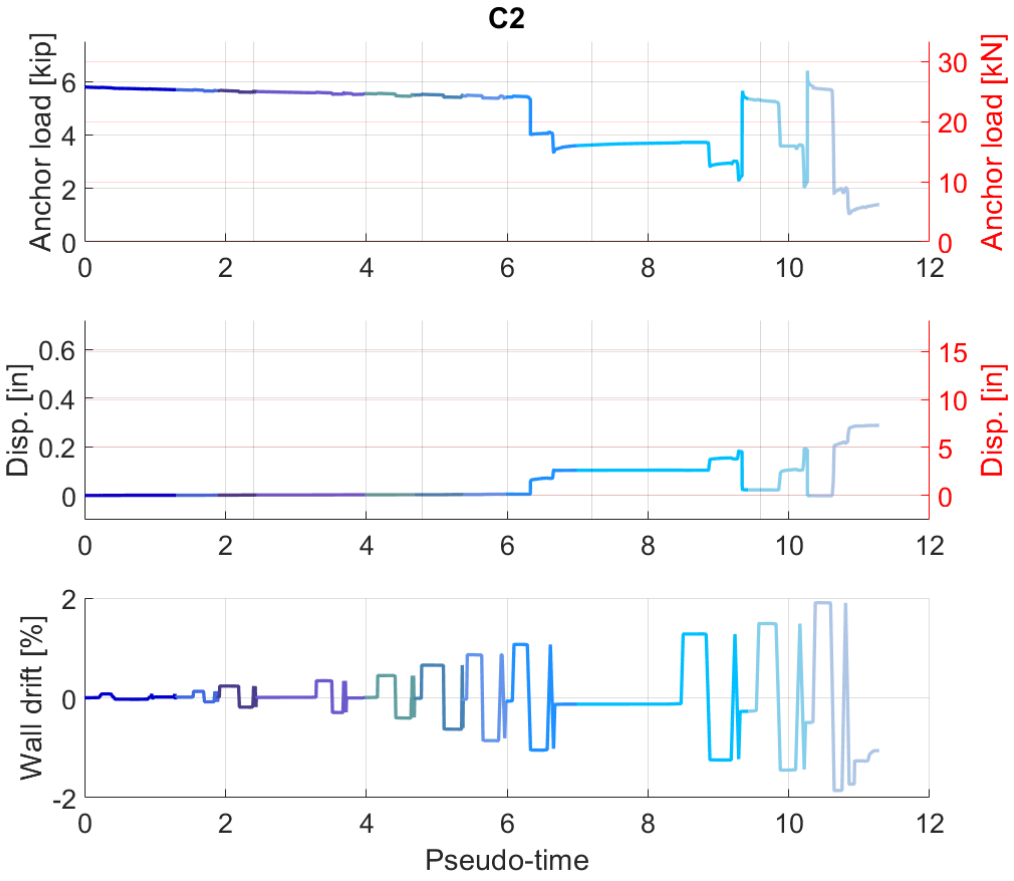
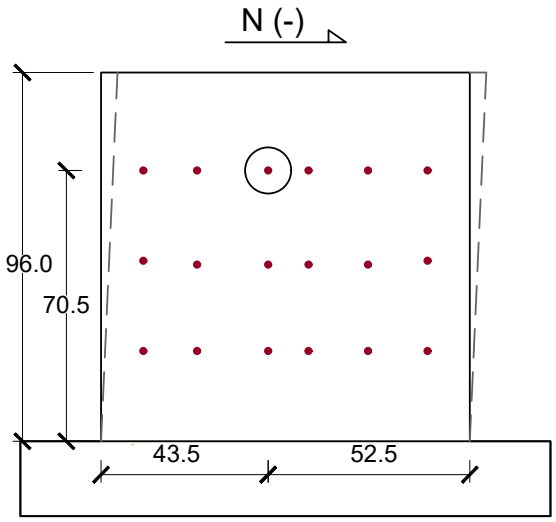


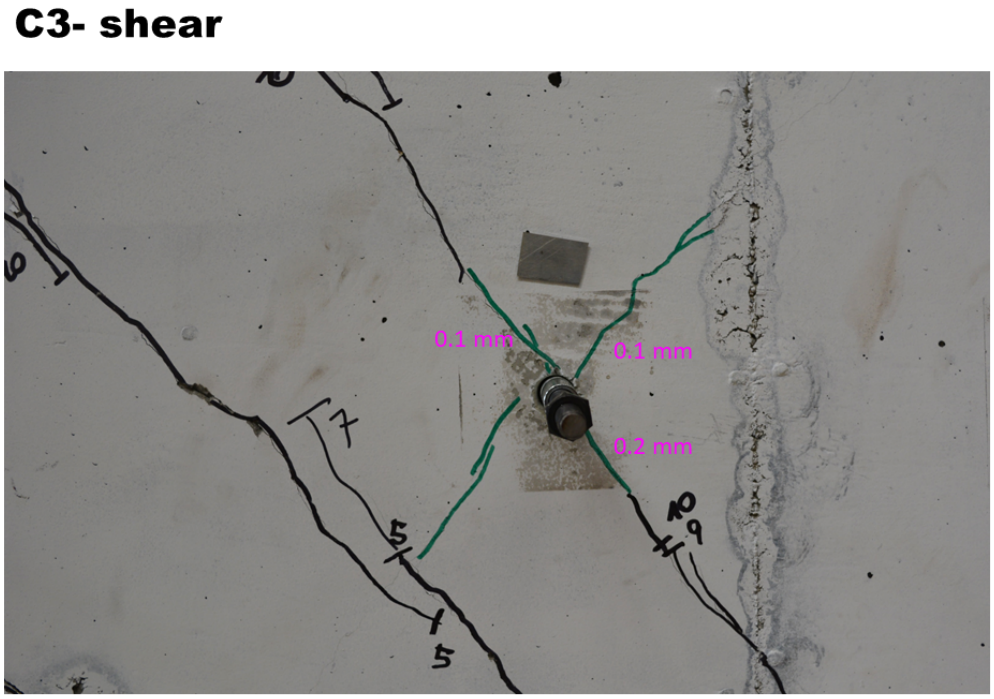
Figure E.106: Wall SQ7.5, anchor C2: measured load and displacement histories and wall drift history

C3

Fig.E.107b shows that torque-controlled expansion anchor C3 was located in a couple of shear crossing cracks. The diagonal crack in the Pull direction developed at 1.4% drift ratio, as indicated by the marks in the wall. The second opposite diagonal crack, instead, was only discovered when the steel plates were removed and the anchor unloaded. However, this second crack likely developed during the last wall cycle, as suggested by the small residual crack width measured at the end of the test (i.e., w_r = 0.1 mm as in Fig.E.107b). Cracks and damage around anchor C3 were less dense with respect to adjacent anchor C2. Measured anchor load and global displacement histories in Fig. E.109 show overall constant trend up to the abrupt load drop/displacement increase at 1.4% drift ratio, which is the drift amplitude at which the shear crack opened around anchor C3. At this drift amplitude the load was also reapplied to the anchor, before the final drift cycles. Fig. E.109 shows that both the anchor load and the measured global displacement returned to their "before reloading" values at the end of the last cycle, as an indicator of the compromised capacity of the anchor after the crack crossed. Maximum displacement measured 0.09 in at the end of the test and maximum residual crack width measured about w_r =0.2 mm.



(a) Anchor location. Units in inches



(b) Photograph of anchor and cracks at end of test

Figure E.107: Location and photograph of anchor C3 in wall SQ7.5. Wall residual drift is diagrammatically shown exaggerated for the purpose of illustrating the final context around the anchor

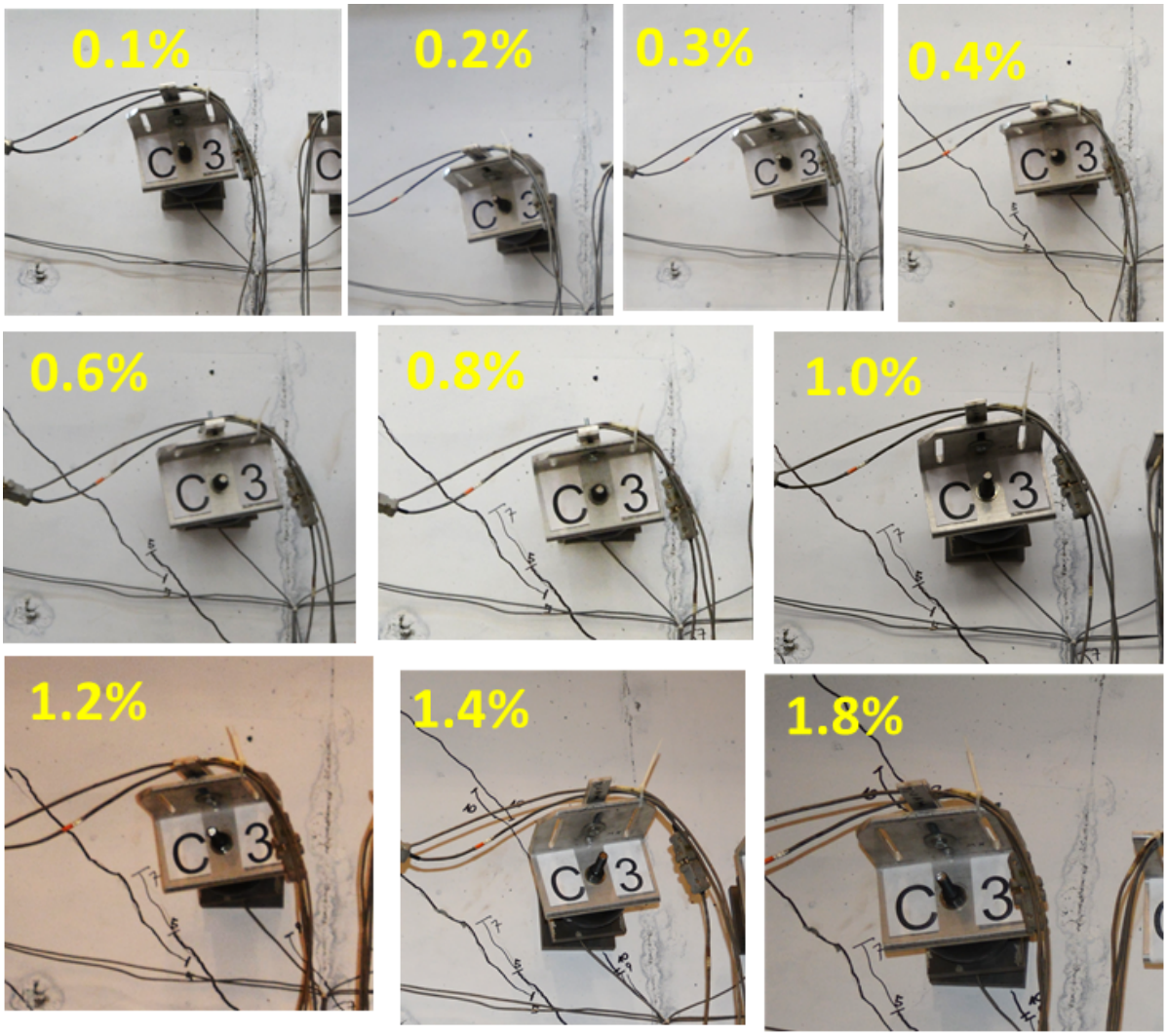


Figure E.108: Wall SQ7.5: photographs showing the crack evolution around anchor C3

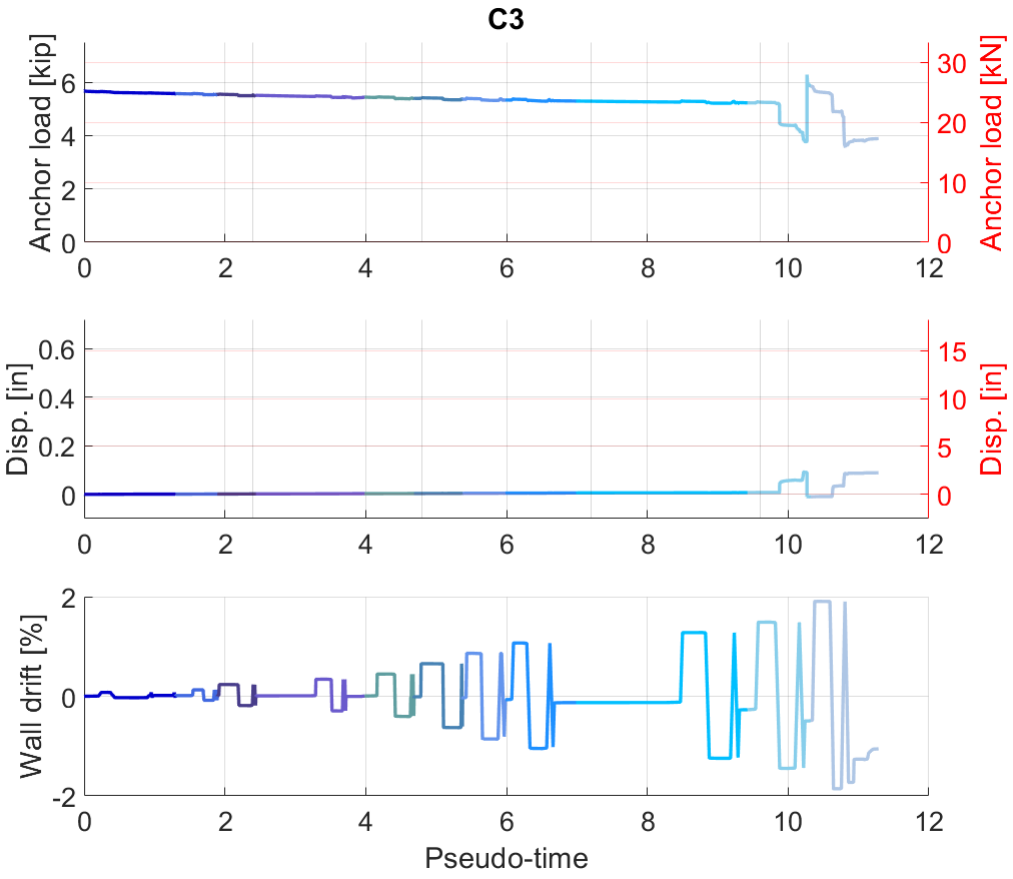
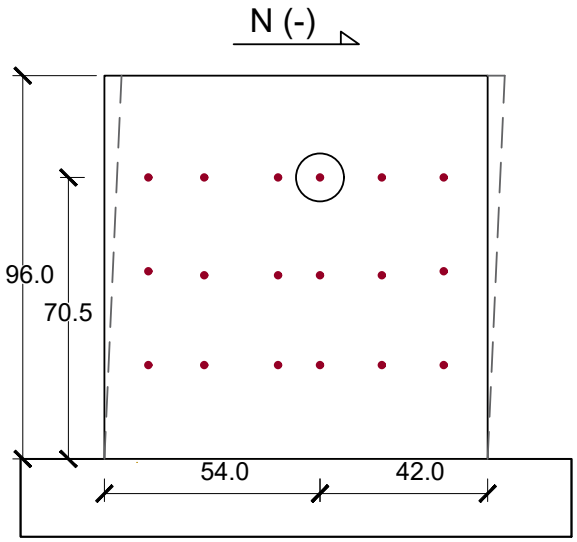


Figure E.109: Wall SQ7.5, anchor C3: measured load and displacement histories and wall drift history

C4

Fig.E.110b shows that torque-controlled expansion anchor C4 was relatively distant from superficial cracks. One diagonal shear crack in the Push direction passed at about 4 in from the anchor, but no superficial cracks visually intersected anchor location. Anchors load and measured global displacement were approximately constant for all the duration of the test, as in Fig.E.110b, and, as a consequence, the load was not reapplied during the test. The maximum global displacement measured 0.01 in.



(a) Anchor location. Units in inches

C4- NONE



(b) Photograph of anchor and cracks at end of test

Figure E.110: Location and photograph of anchor C4 in wall SQ7.5. Wall residual drift is diagrammatically shown exaggerated for the purpose of illustrating the final context around the anchor

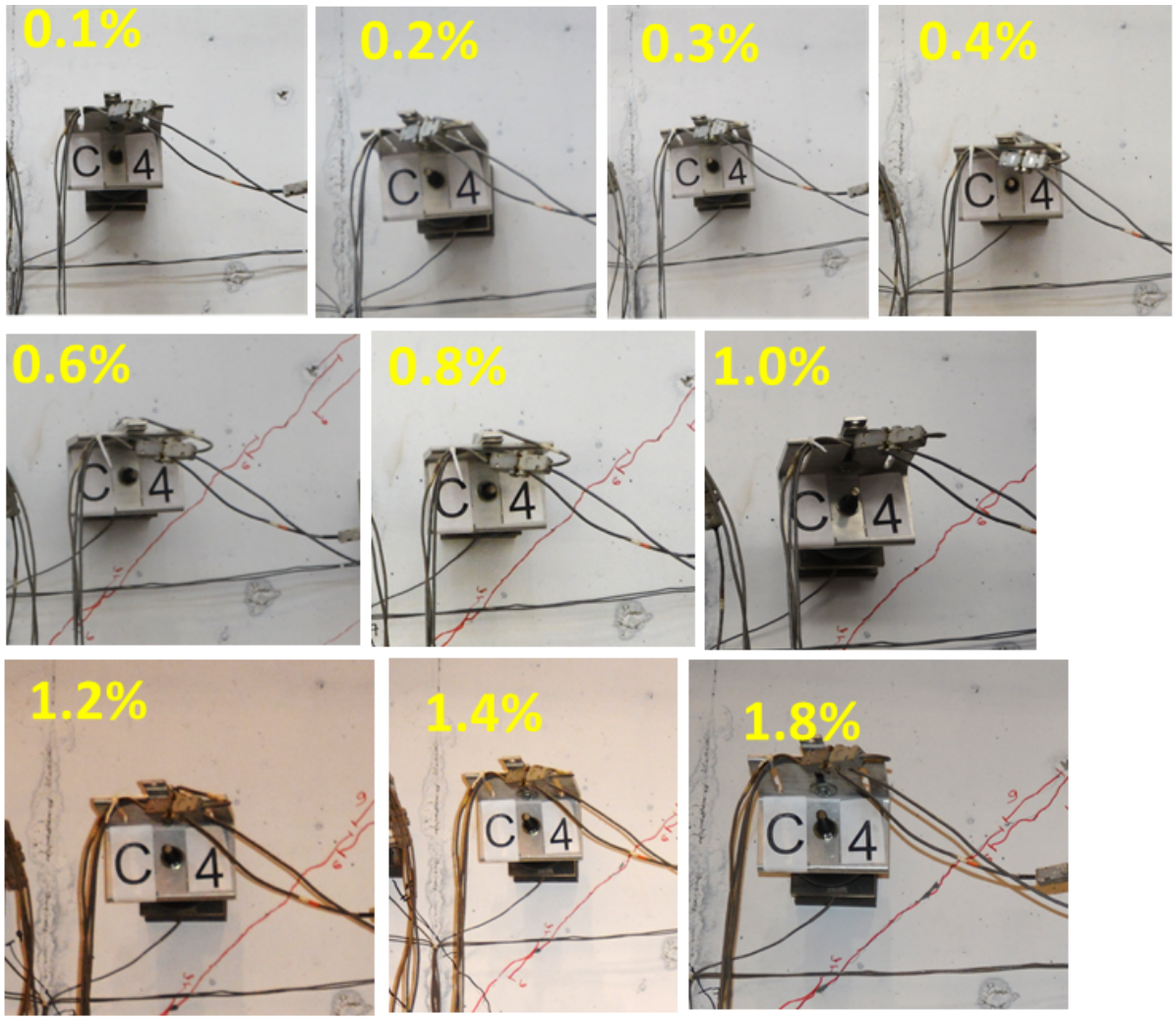


Figure E.111: Wall SQ7.5: photographs showing the crack evolution around anchor C4

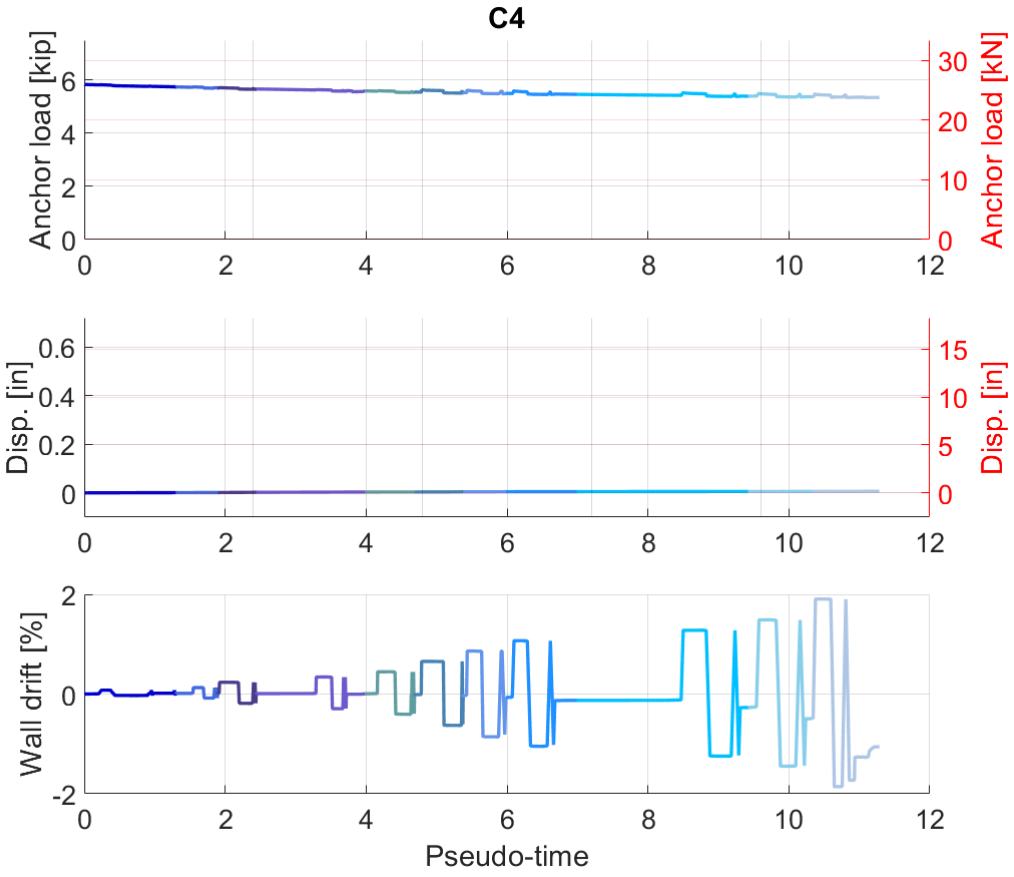
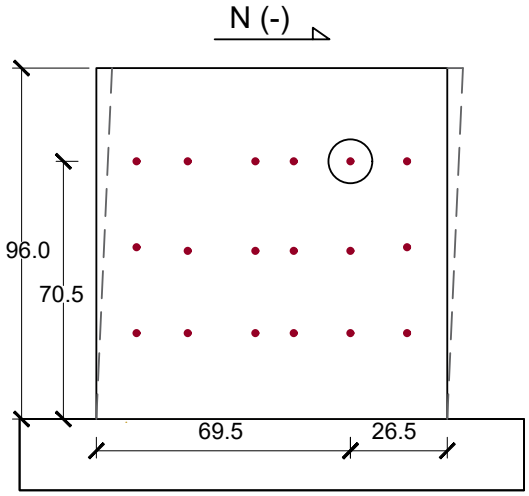


Figure E.112: Wall SQ7.5, anchor C4: measured load and displacement histories and wall drift history

C5

Fig.E.113b shows that torque-controlled expansion anchor C5 was relatively distant from superficial cracks. Although diagonal cracks formed during the Push cycles close to the anchor location, no superficial cracks visually intersected anchor location. It is noted that the anchor resulted located inside a concrete strut, where severe concrete damage was observed. Anchor load and measured global displacement were approximately constant for all the duration of the test, as in Fig.E.113b, and, as a consequence, the load was not reapplied during the test. The maximum global displacement measured 0.01 in.



(a) Anchor location. Units in inches



(b) Photograph of anchor and cracks at end of test

Figure E.113: Location and photograph of anchor C5 in wall SQ7.5. Wall residual drift is diagrammatically shown exaggerated for the purpose of illustrating the final context around the anchor

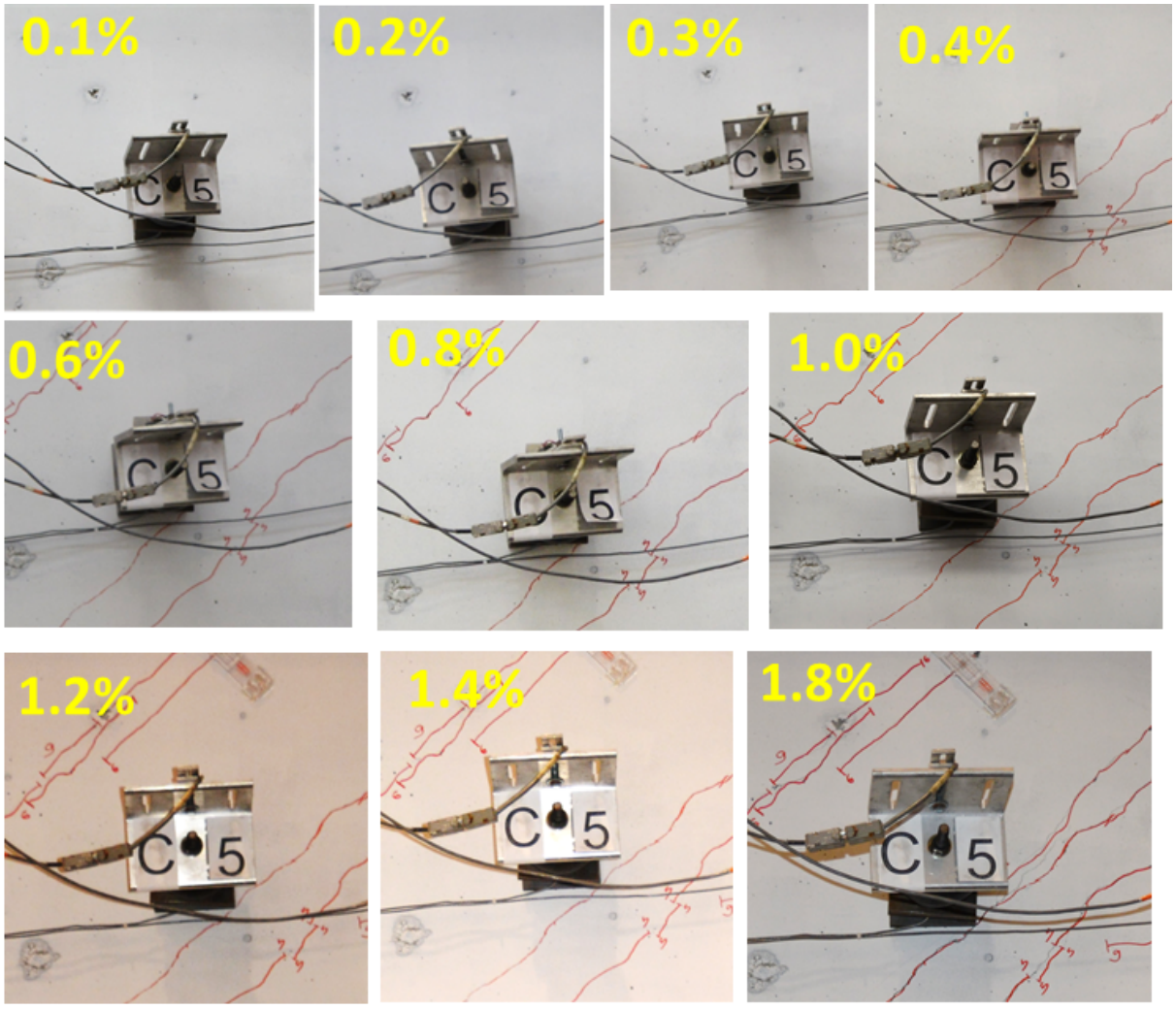


Figure E.114: Wall SQ7.5: photographs showing the crack evolution around anchor C5

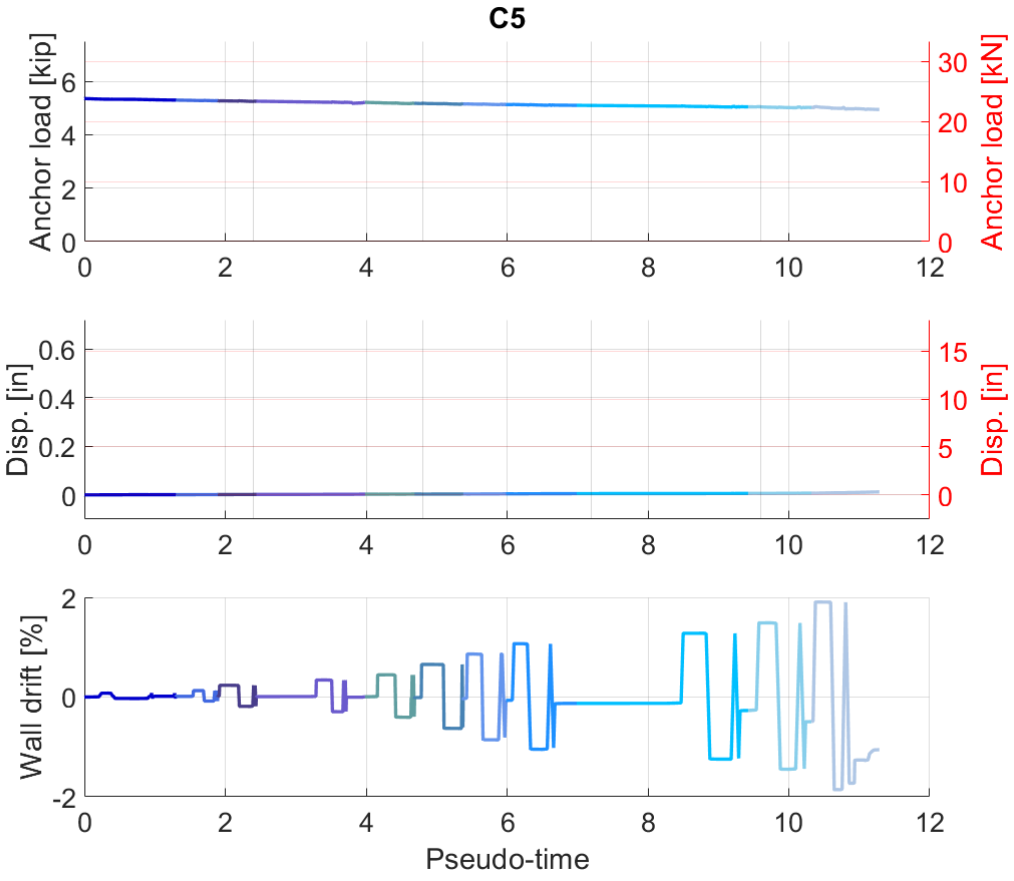
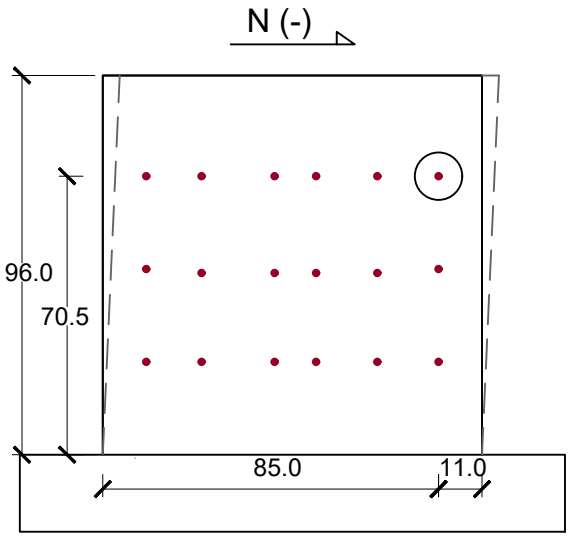


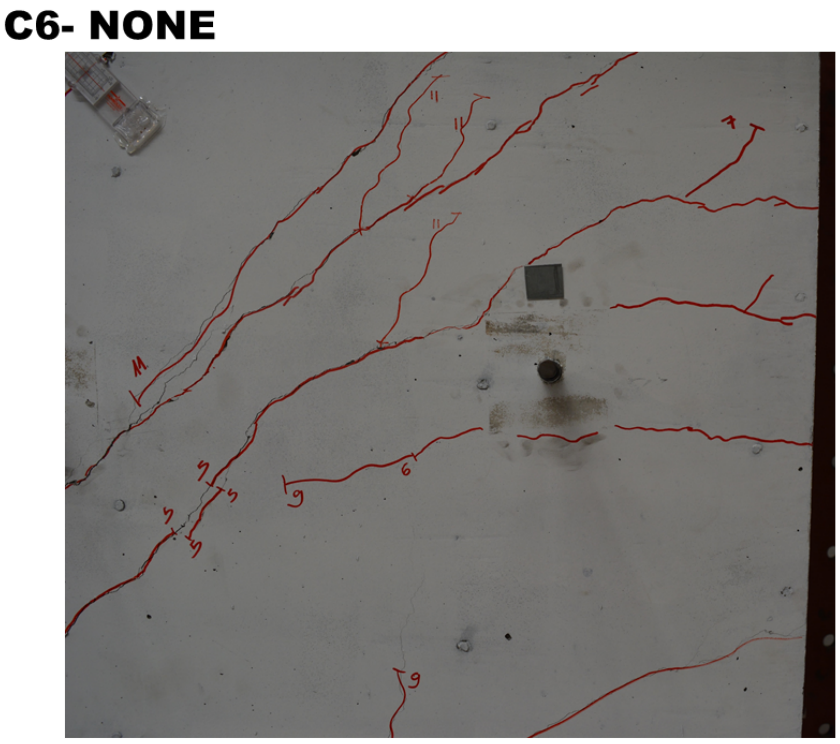
Figure E.115: Wall SQ7.5, anchor C5: measured load and displacement histories and wall drift history

C6

Fig.E.116b shows that torque-controlled expansion anchor C6 was relatively distant from superficial cracks. Although a dense crack pattern developed in this boundary region, no superficial cracks visually intersected anchor location and three tension cracks surrounded the anchor without crossing it. Anchor load and global displacement were approximately constant for all the duration of the test, as in Fig.E.116b, and, as a consequence, the load was not reapplied during the test. The maximum global displacement measured 0.03 in.



(a) Anchor location. Units in inches



(b) Photograph of anchor and cracks at end of test

Figure E.116: Location and photograph of anchor C6 in wall SQ7.5. Wall residual drift is diagrammatically shown exaggerated for the purpose of illustrating the final context around the anchor

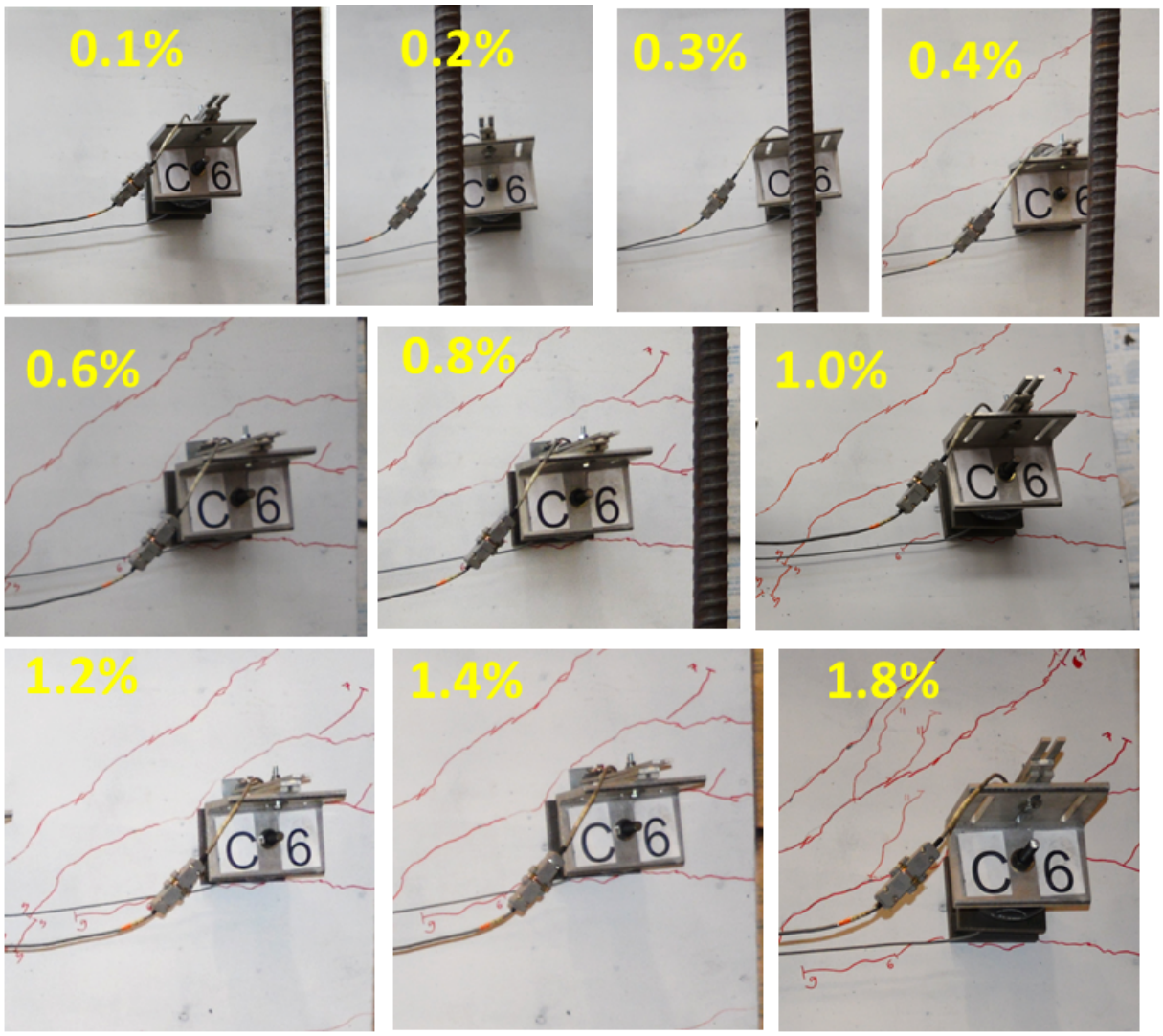


Figure E.117: Wall SQ7.5: photographs showing the crack evolution around anchor C6

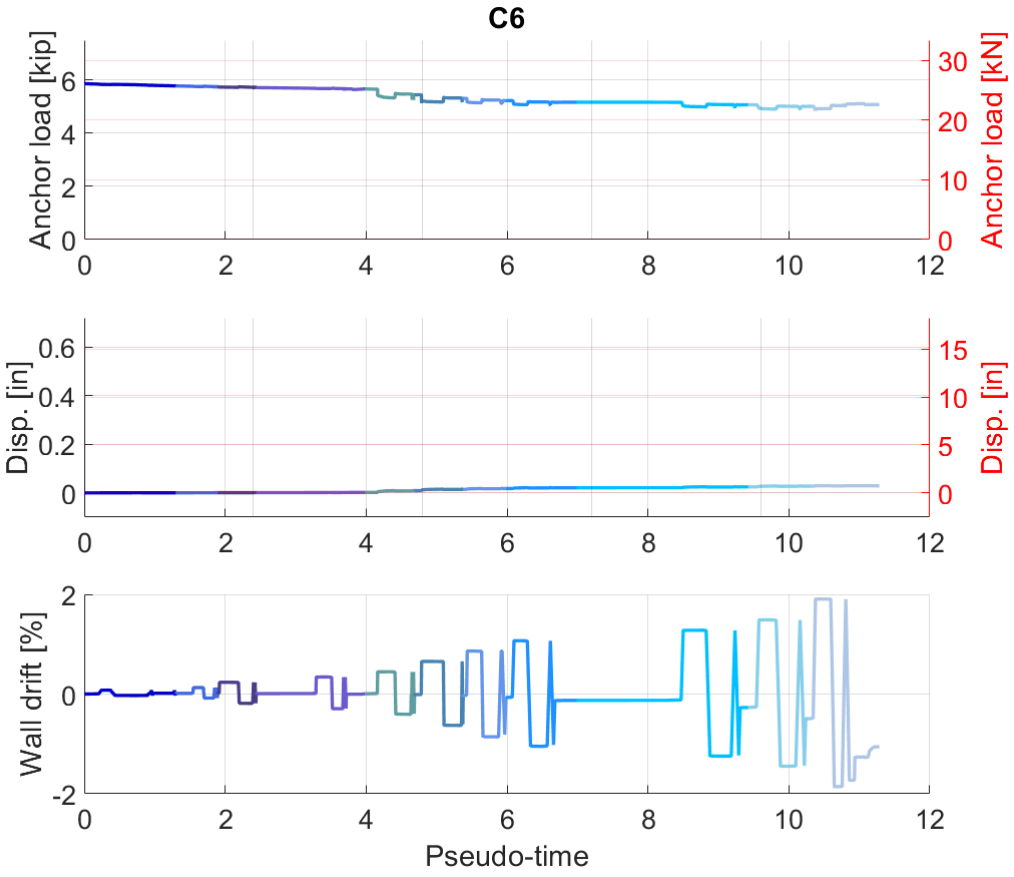


Figure E.118: Wall SQ7.5, anchor C6: measured load and displacement histories and wall drift history

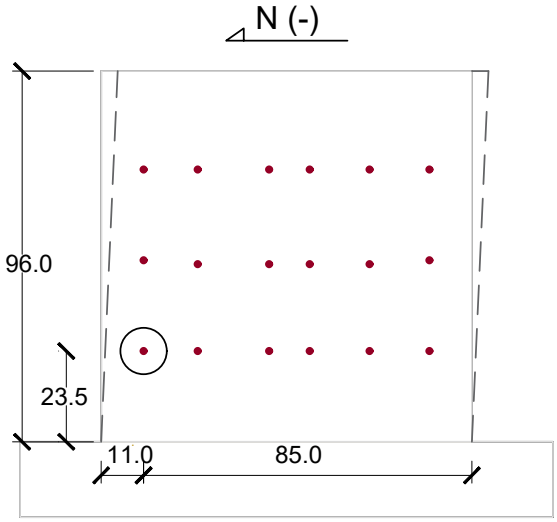
E.1.3 Anchors in Wall SQ0

Photographs presented in this section show anchor location and final crack situation for each anchor installed in wall SQ0, the squat wall tested absent axial load. Photographs of the damage evolution around each anchor during the wall cyclic test are also reported in this section. Measured crack width of the cracks crossing the anchor plates are reported in Table E.2 as a function of the drift applied to the wall. In addition, anchor load and global displacement histories measured during wall cycling history for each anchor installed in wall SQ0 are also illustrated in this section.

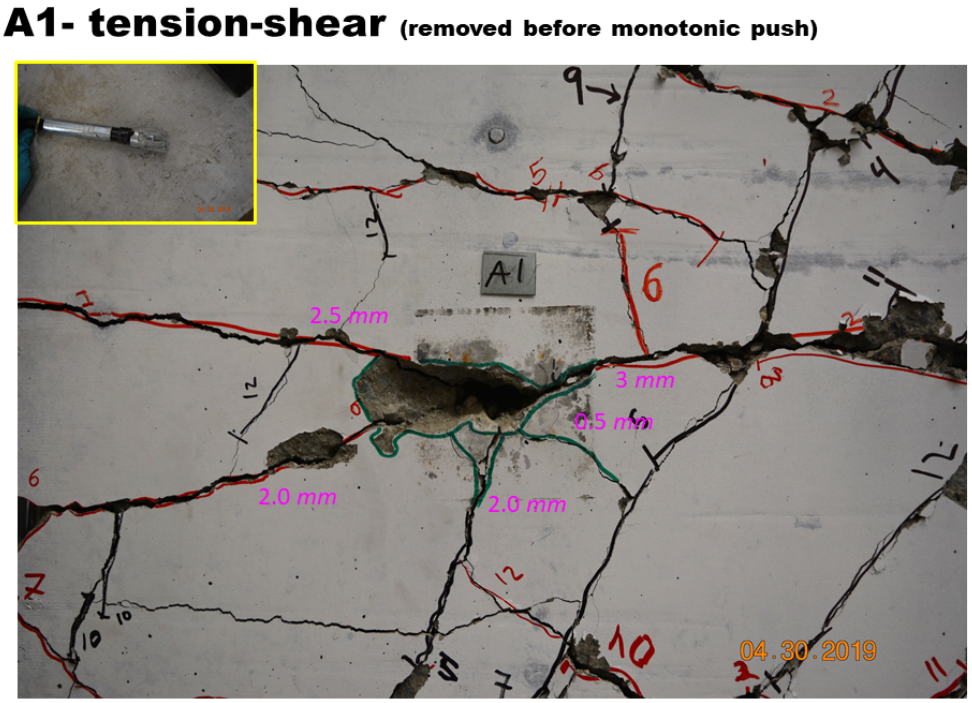
Anchor row A was located inside the theoretic plastic hinge of wall SQ0 at about 2 ft (0.25 h_w) from the wall-footing interface, and anchors A1 and A6 were located within the North and South end boundary elements of the wall, respectively. Anchor row B was located inside the theoretic plastic hinge of wall SQ0 at about 4 ft (0.5 h_w) from the wall-footing interface, and anchors B1 and B6 were located within the North and South end boundary elements of the wall, respectively. Finally, anchor row C was located outside the theoretic plastic hinge of wall SQ0 at about 6 ft (0.75 h_w) from the wall-footing interface, and anchors C1 and C6 were located within the North and South end boundary elements of the wall, respectively.

A1

Fig.E.119b shows that torque-controlled expansion anchor A1 was located in tension and shear cracks, which opened at 0.1% and 0.4% drift ratios, respectively (see Fig.E.120). Moreover, a dense crack pattern was observed around the anchor. Measured load history in Fig.E.121 follows a clear decreasing trend from the second drift cycle, up to approximately zero load at the end of the test, even though the load was reapplied five times (at the end of 0.4%, 0.8%, 1.0%, 1.2% and 1.4% drift ratios). It is noted that the anchor load returned to the "before reloading" value at the end of each displacement cycle after the load was reapplied, reflecting the compromised performance of this anchor. The measured global displacement shows an increasing trend, opposite to the load decreasing trend, and maximum global displacement at the end of the test measured 0.58 in. The anchor was removed before the monotonic push was performed to avoid damage to the load cell. By the end of the test, the nearby concrete crushed around the installation hole. Residual crack widths around the crushed region measured approximately w_r= 3 mm.



(a) Anchor location. Units in inches



(b) Photograph of anchor and cracks at end of test

Figure E.119: Location and photograph of anchor A1 in wall SQ0. Wall residual drift is diagrammatically shown exaggerated for the purpose of illustrating the final context around the anchor

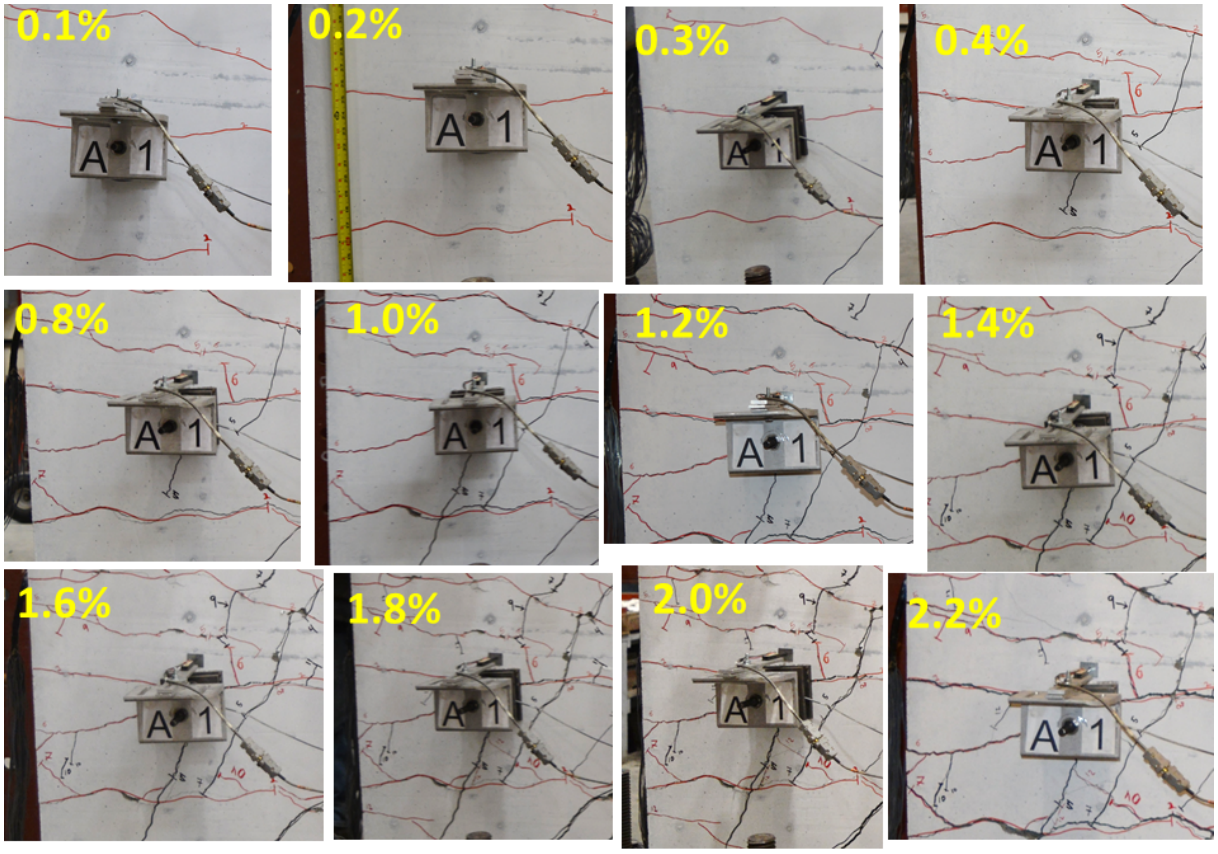


Figure E.120: Wall SQ0: photographs showing the crack evolution around anchor A1

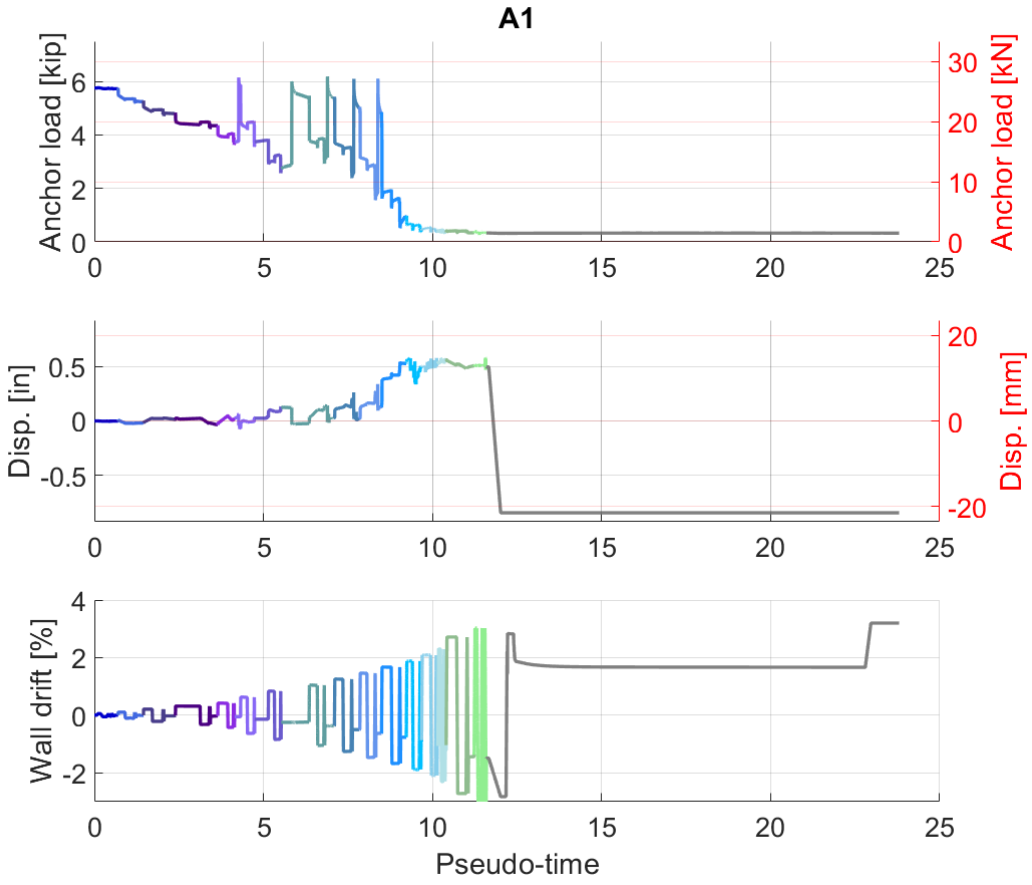
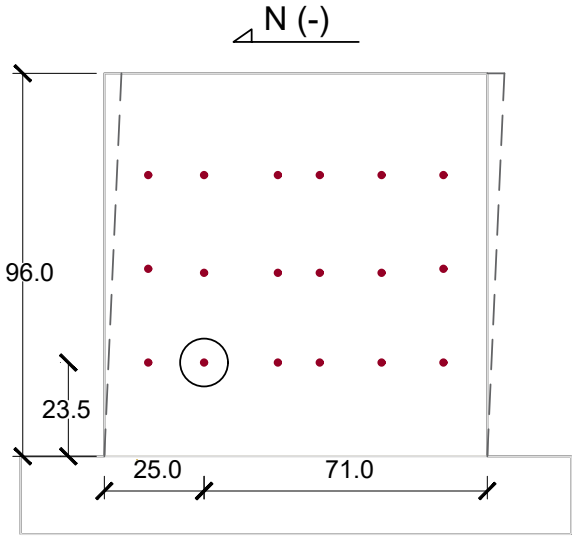


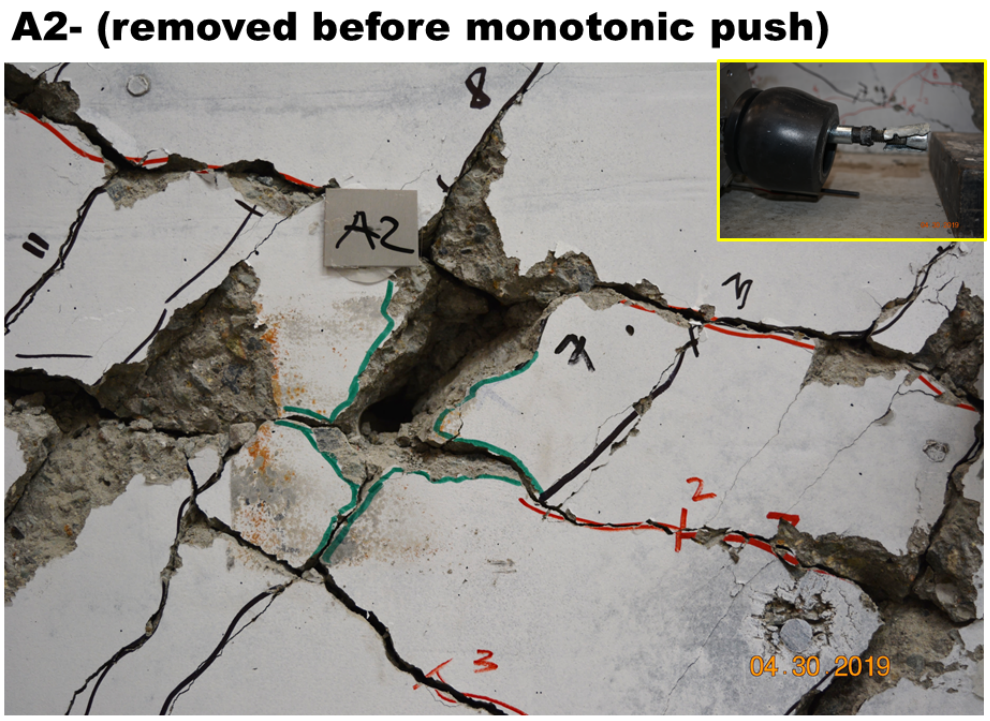
Figure E.121: Wall SQ0, anchor A1: measured load and displacement histories and wall drift history

A2

Fig.E.122b shows that torque-controlled expansion anchor A2 was located in a couple of shear cracks, which opened at 0.1% and 0.3% drift ratios, respectively (see Fig.E.69). Moreover, a dense crack pattern developed around the anchor. Measured load history (in Fig.E.124) follows a fast decreasing trend from the second drift cycle, up to approximately zero load at the end of the test, even though the load was reapplied four times (at the end of 0.4%, 0.8%, 1.0% and 1.2% drift ratios). It is noted that the anchor load returned to the "before reloading" value at the end of each displacement cycle after the load was reapplied, reflecting the compromised performance of this anchor. The measured global displacement shows an increasing trend, opposite to the load decreasing trend, and maximum global displacement at the end of the test measured 0.66 in. The anchor was removed before the monotonic push was performed to avoid damage to the load cell. By the end of the test, the nearby concrete crushed around the installation hole. Residual crack widths around the crushed region measured approximately w_r= 3 mm.



(a) Anchor location. Units in inches



(b) Photograph of anchor and cracks at end of test

Figure E.122: Location and photograph of anchor A2 in wall SQ0. Wall residual drift is diagrammatically shown exaggerated for the purpose of illustrating the final context around the anchor

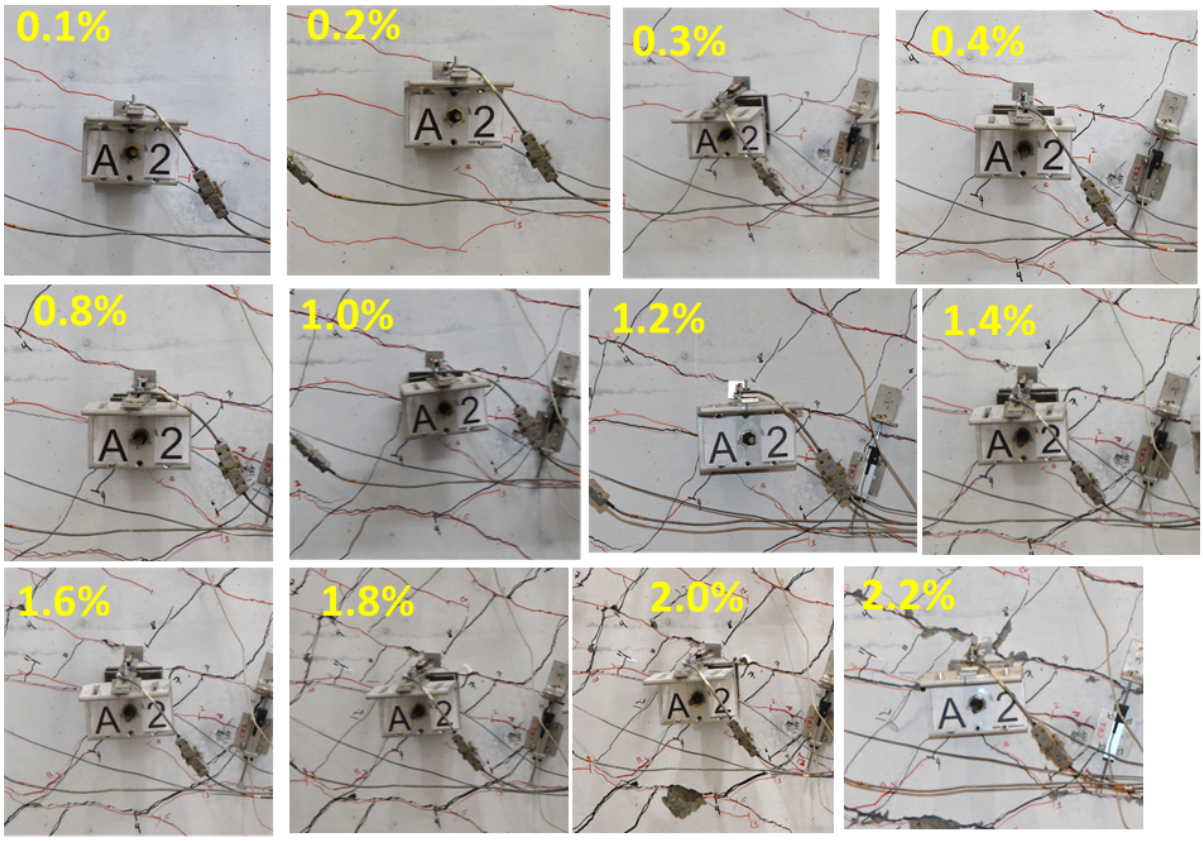


Figure E.123: Wall SQ0: photographs showing the crack evolution around anchor A2

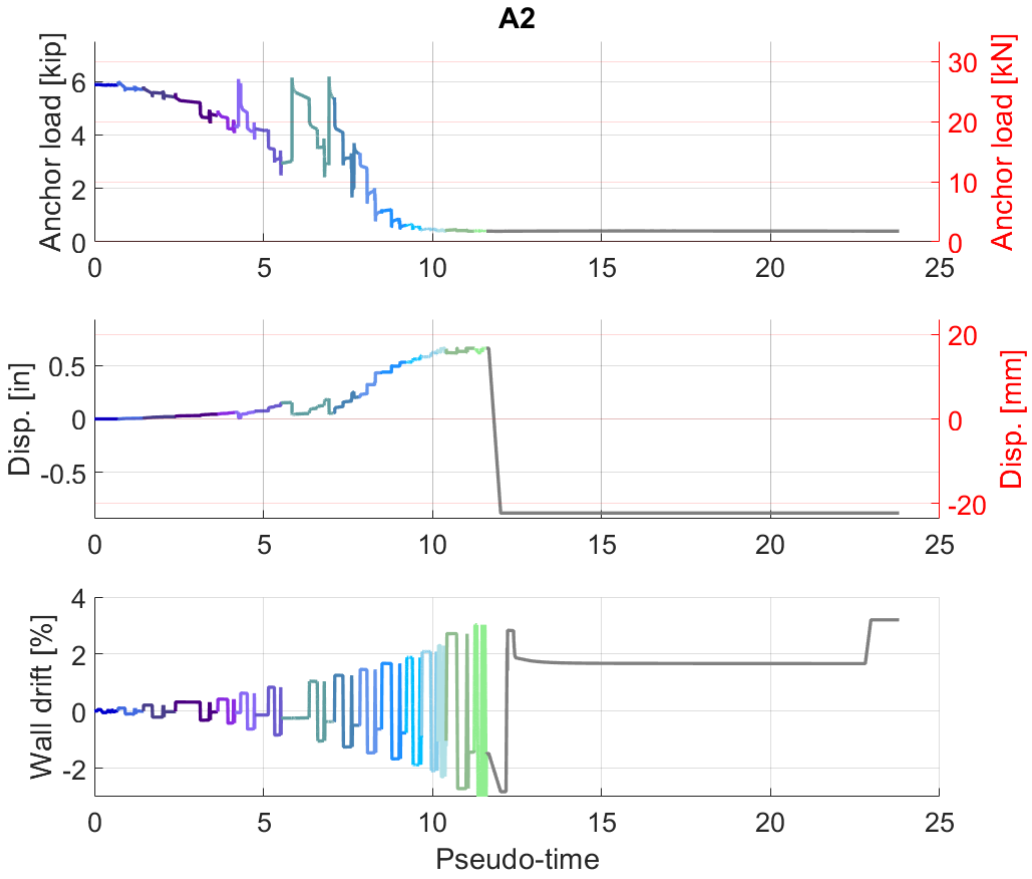
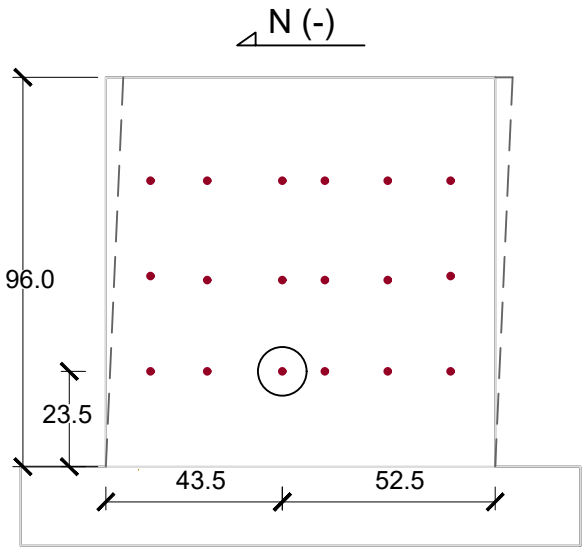


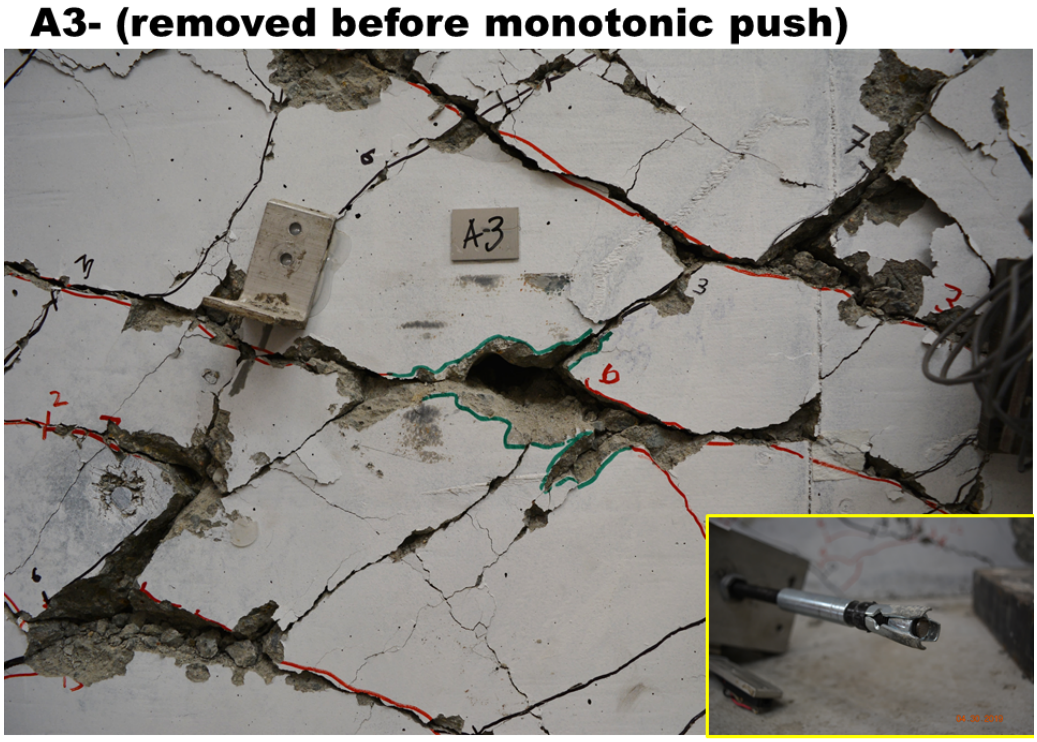
Figure E.124: Wall SQ0, anchor A2: measured load and displacement histories and wall drift history

A3

Fig.E.125b shows that torque-controlled expansion anchor A3 was located in a couple of shear cracks, which opened at 0.1% and 0.3% drift ratios, respectively (see Fig.E.72). Moreover, a dense crack pattern developed around the anchor. One of these cracks was monitored continuously by sensor CR2, installed at the end of 0.2% drift ratio. Measured load history (in Fig.E.127) follows a fast decreasing trend from the second drift cycle, up to approximately zero load at the end of the test, even though the load was reapplied three times (at the end of 0.6%, 0.8% and 1.0% drift ratios). Particularly, it is noted that the anchor load returned to the "before reloading" value at the end of each displacement cycle after the load was reapplied, reflecting the compromised performance of this anchor. The measured global displacement shows an increasing trend, opposite to the load decreasing trend, and maximum global displacement at the end of the test measured 0.71 in. The anchor was removed before the monotonic push was performed to avoid damage to the load cell. By the end of the test, the nearby concrete crushed around the installation hole. Residual crack widths around the crushed region measured approximately w_r= 3 mm.



(a) Anchor location. Units in inches



(b) Photograph of anchor and cracks at end of test

Figure E.125: Location and photograph of anchor A3 in wall SQ0. Wall residual drift is diagrammatically shown exaggerated for the purpose of illustrating the final context around the anchor

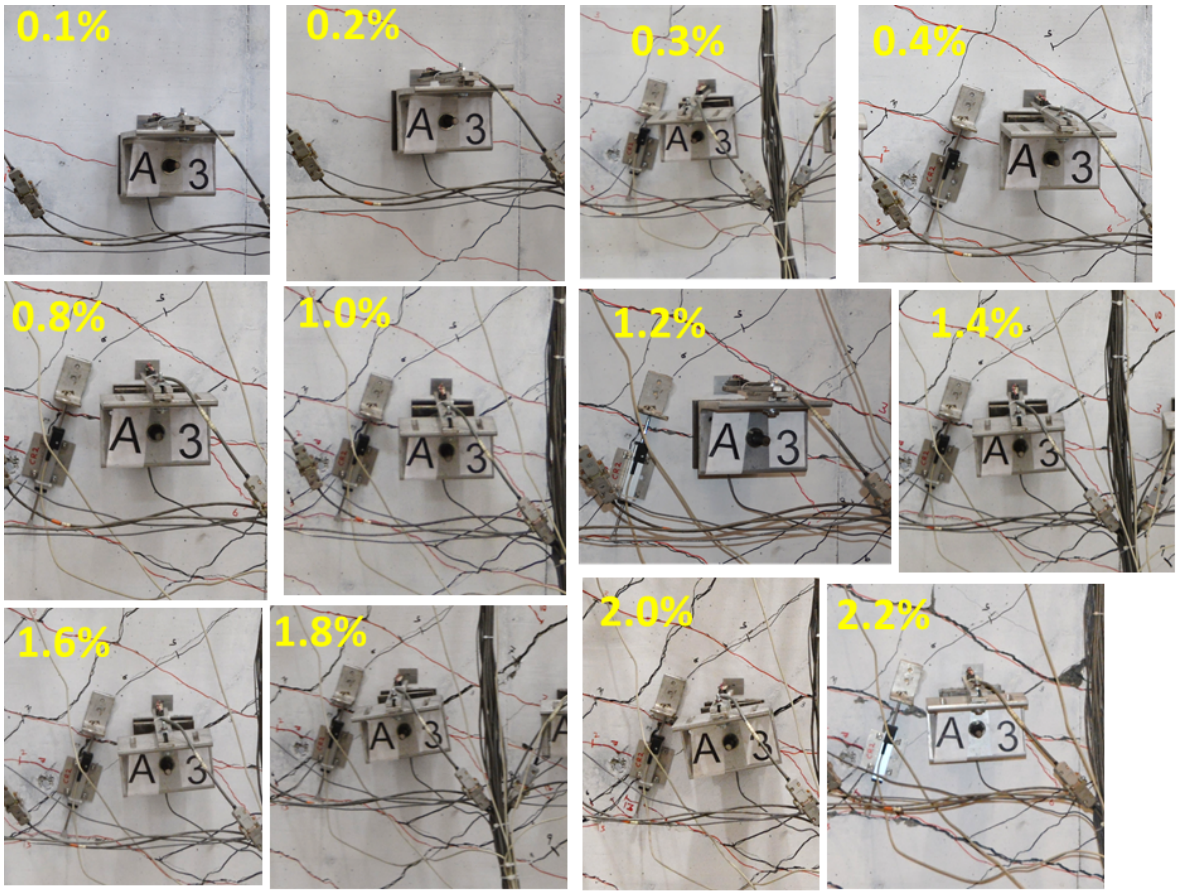


Figure E.126: Wall SQ0: photographs showing the crack evolution around anchor A3

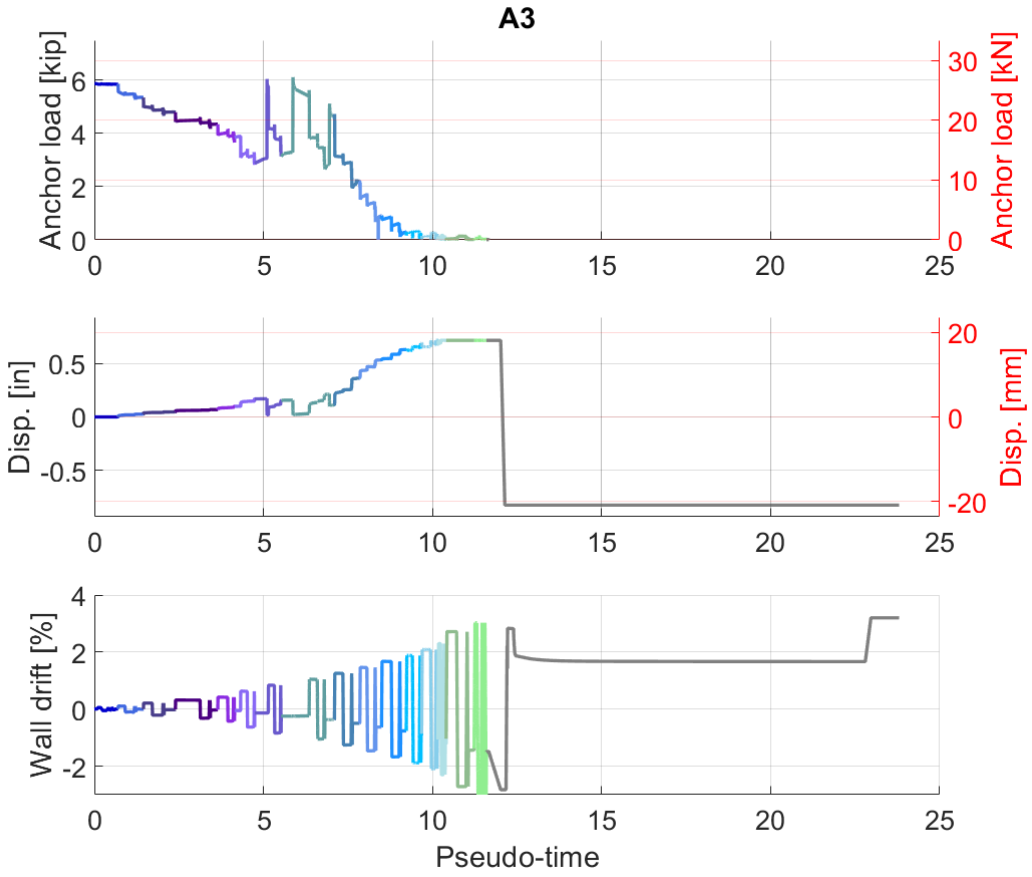
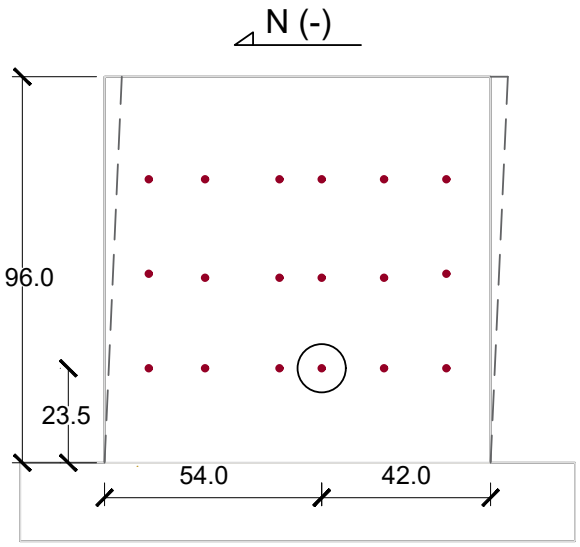


Figure E.127: Wall SQ0, anchor A3: measured load and displacement histories and wall drift history

A4

Fig.E.128b shows that torque-controlled expansion anchor A4 was located in a couple of shear cracks, which opened at 0.2% and 1.6% drift ratios, respectively (see Fig.E.75) and significantly widened during the test. Moreover, a dense crack pattern developed around the anchor. Measured load history (in Fig.E.130) follows a fast decreasing trend from the second drift cycle, up to approximately zero load at the end of the test, even though the load was reapplied three times (at the end of 0.4%, 0.8% and 1.0% drift ratios). It is noted that the anchor load returned to the "before reloading" value at the end of each displacement cycle after the load was reapplied, reflecting the compromised performance of this anchor. The measured global displacement shows an increasing trend, opposite to the load decreasing trend, up to the second time the load was reapplied (0.8% drift ratio). During the second reloading phase the displacement sensor was compromised, and subsequent displacement readings are considered not reliable. The maximum measured global displacement before the damage in the displacement sensor was 0.21 in, in line with the displacement measured at this drift amplitude for the other anchors in the A anchor row. A maximum global displacement of the order of 0.8 in can be expected for anchor A4, similarly to adjacent anchors. The anchor was removed before the monotonic push was performed to avoid damage to the load cell. By the end of the test, the nearby concrete around the anchor severely crushed and residual crack widths around the anchor could not be measured.



(a) Anchor location. Units in inches



(b) Photograph of anchor and cracks at end of test

Figure E.128: Location and photograph of anchor A4 in wall SQ0. Wall residual drift is diagrammatically shown exaggerated for the purpose of illustrating the final context around the anchor

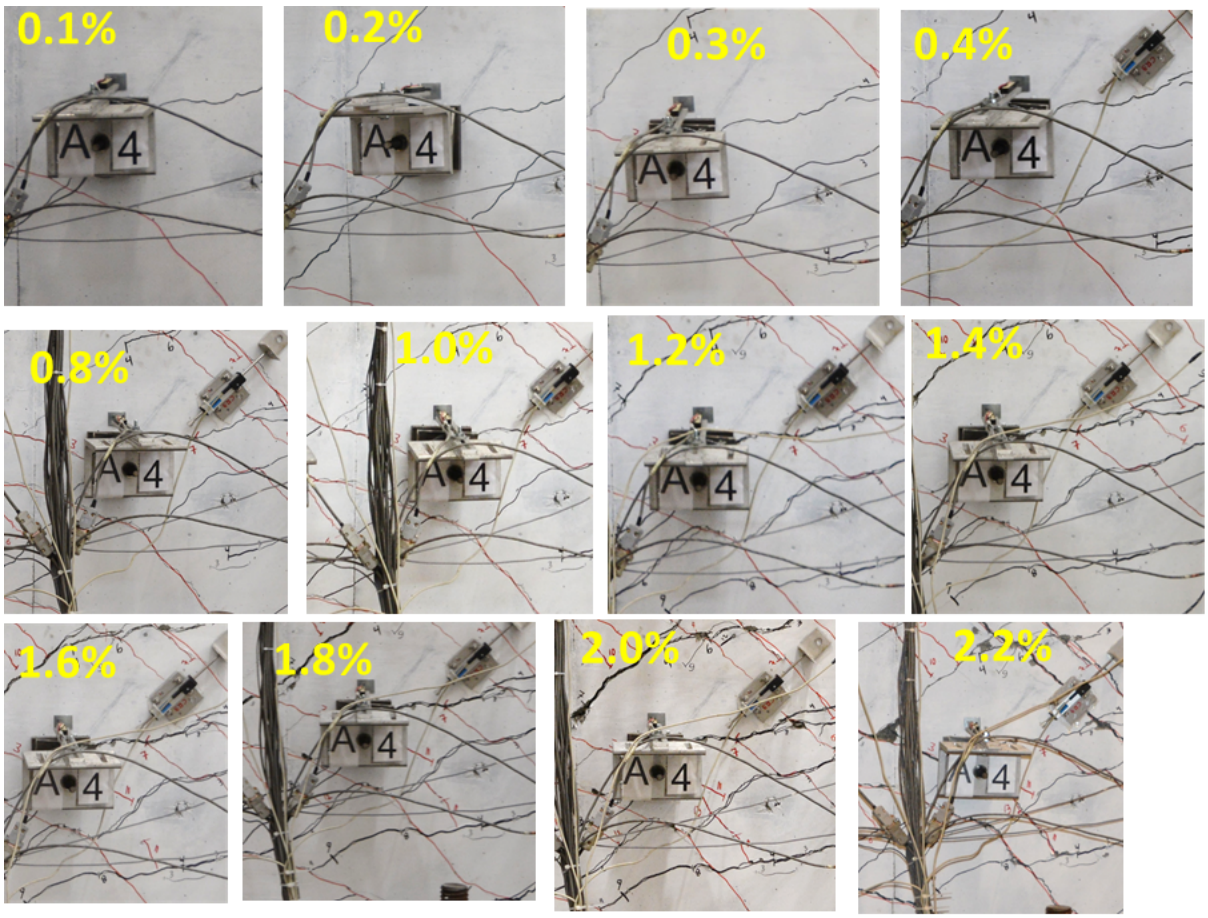


Figure E.129: Wall SQ0: photographs showing the crack evolution around anchor A4

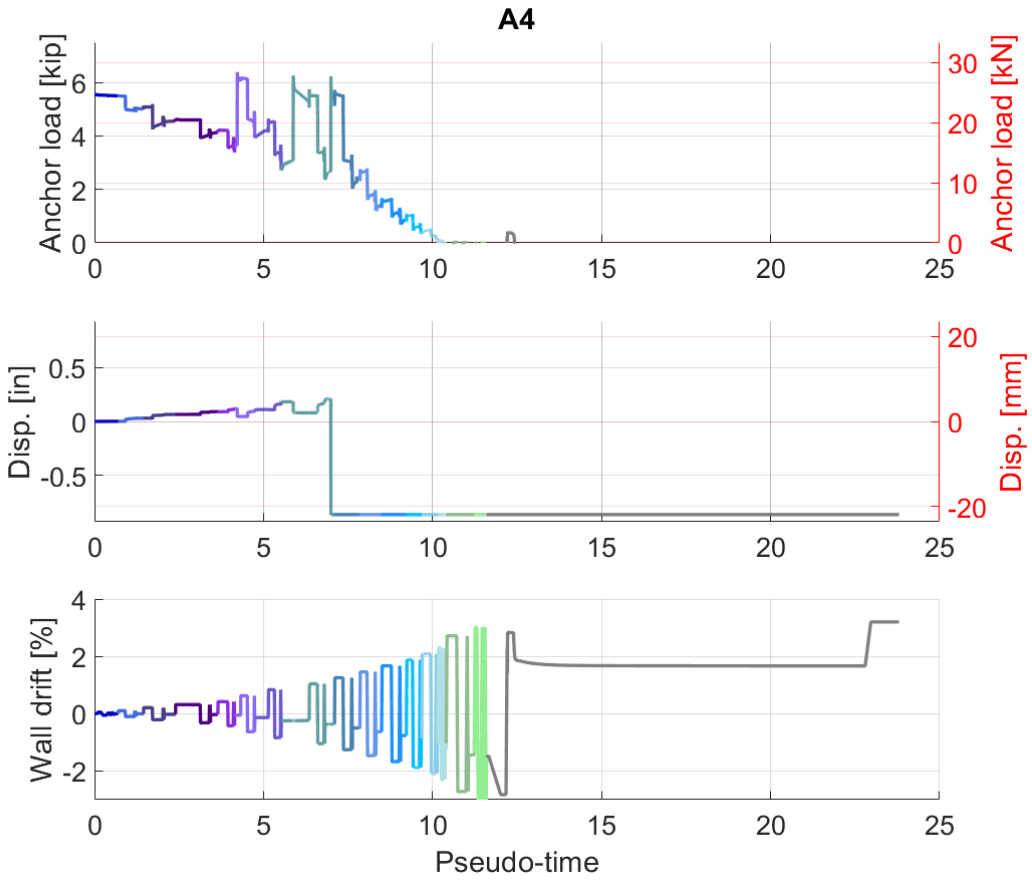
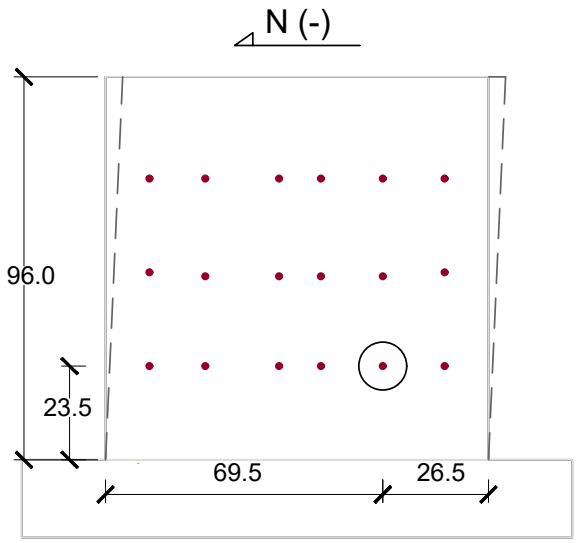


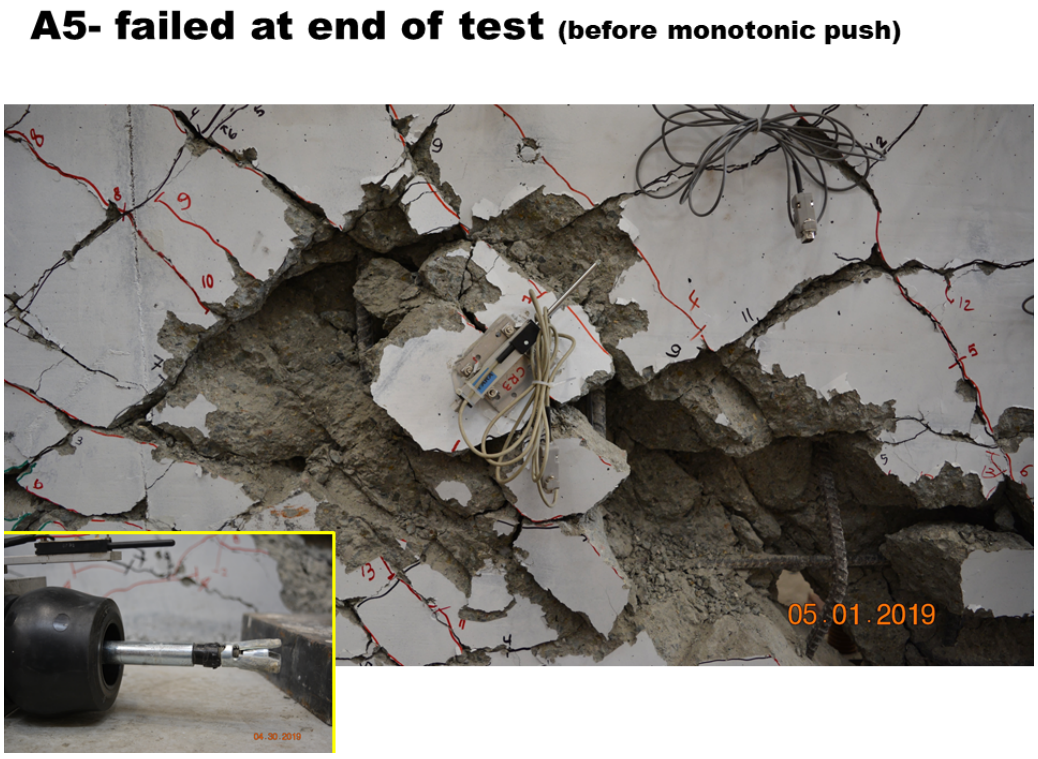
Figure E.130: Wall SQ0, anchor A4: measured load and displacement histories and wall drift history

A5

Fig.E.131b shows that torque-controlled expansion anchor A5 was located in the region of high damage and dense crack pattern, with at least one shear crack, which probably opened at 0.2% drift amplitude (see Fig.E.78) intersecting anchor location. However, no further considerations are possible, since the concrete around the installation hole crushed by the end of the test. Measured load history (in Fig.E.133) follows a fast decreasing trend from the second drift cycle, up to approximately zero load at the end of the test, even though the load was reapplied three times (at the end of 0.4%, 0.6% and 0.8% drift ratios). It is noted that the anchor load returned to the "before reloading" value at the end of each displacement cycle after the load was reapplied, reflecting the compromised performance of this anchor. The measured global displacement shows an increasing trend, opposite to the load decreasing trend, and maximum global displacement at the end of the test measured 0.77 in. The anchor failed when the concrete crushed, before the monotonic push was performed and residual crack widths were not measured.



(a) Anchor location. Units in inches



(b) Photograph of anchor and cracks at end of test

Figure E.131: Location and photograph of anchor A5 in wall SQ0. Wall residual drift is diagrammatically shown exaggerated for the purpose of illustrating the final context around the anchor

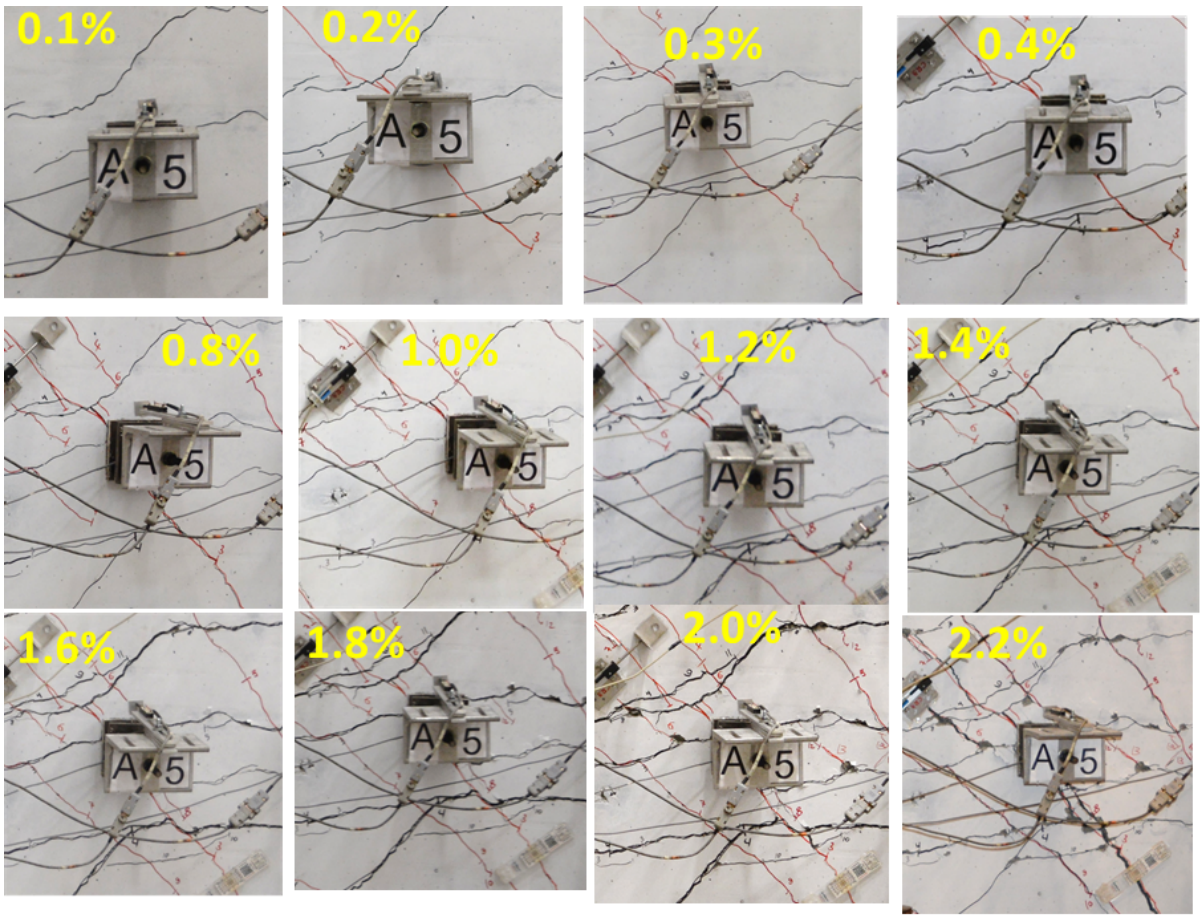


Figure E.132: Wall SQ0: photographs showing the crack evolution around anchor A5

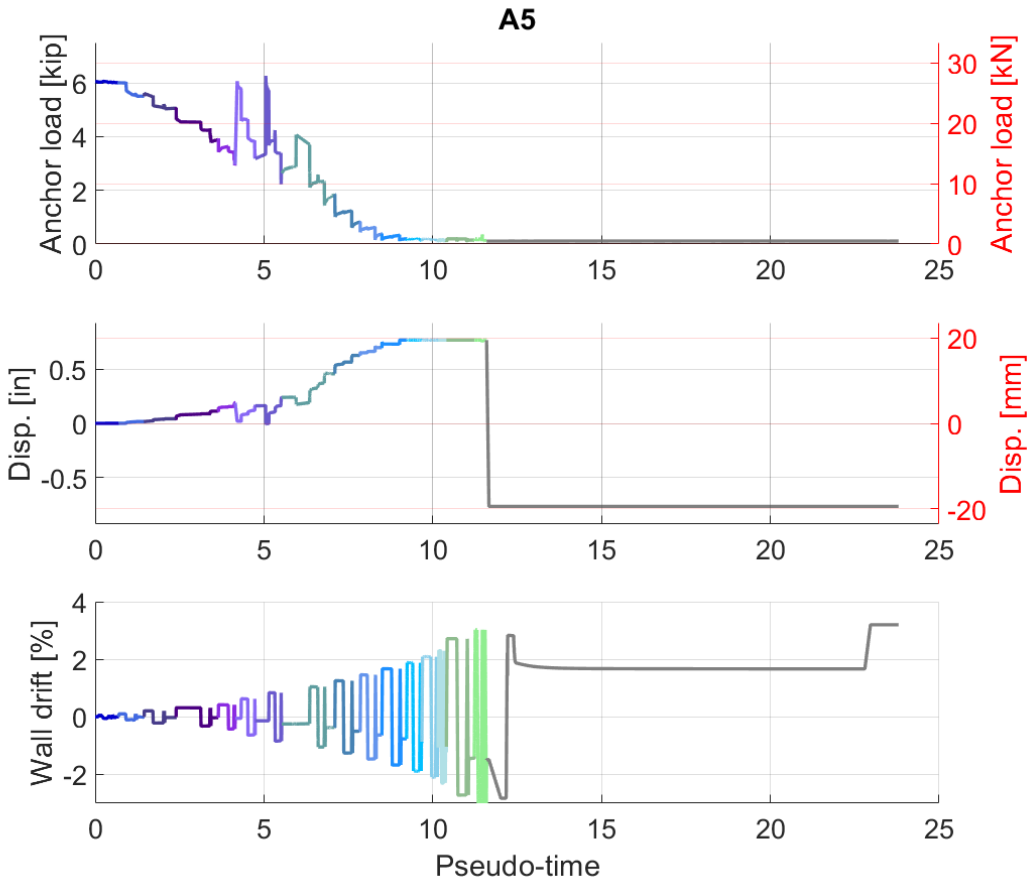
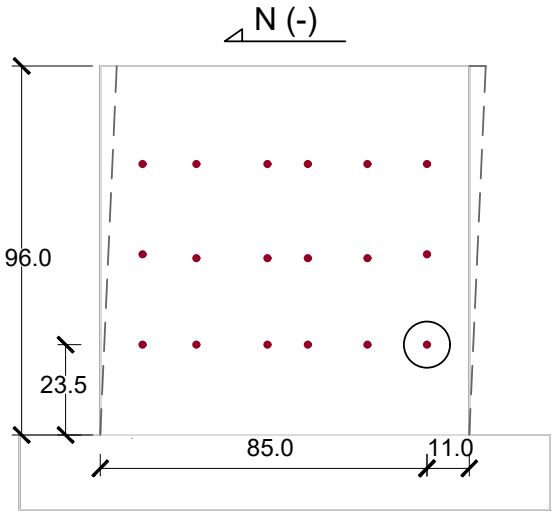


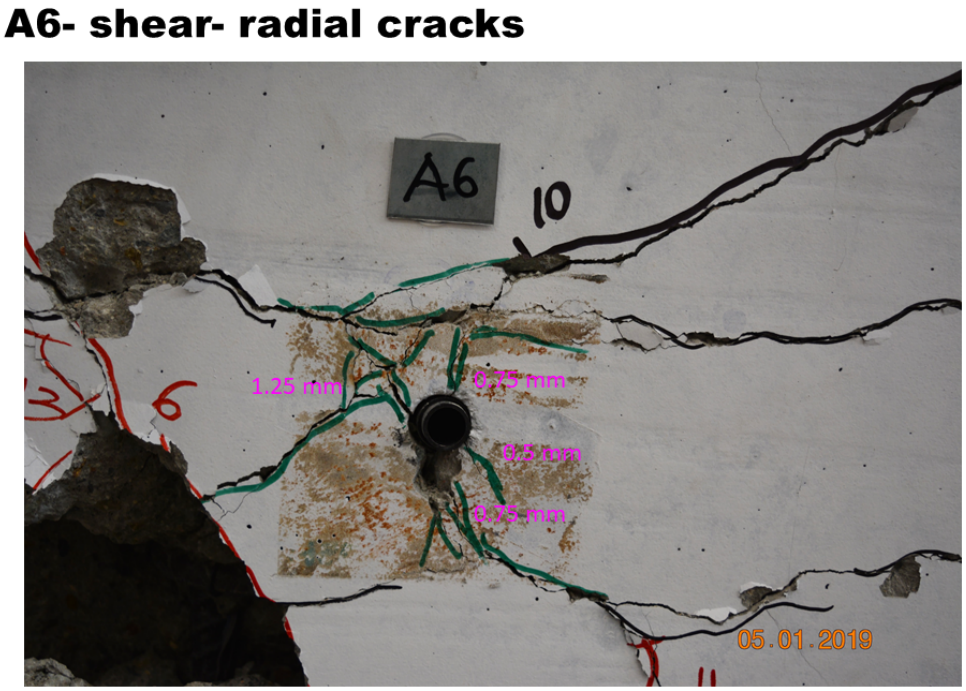
Figure E.133: Wall SQ0, anchor A5: measured load and displacement histories and wall drift history

A6

Fig.E.134b shows that two parallel tension cracks developed around torque-controlled expansion anchor A6 and deviated their path to cross the anchor location. This deviation of cracks trajectory resulted in radial/shear cracks crossing the anchor. Marks on the wall show that one of these cracks developed at 1.4% drift ratio (see Fig.E.81), but the load history in Fig.E.136 shows that earlier cracks opened at 1.0% drift ratio. Anchor A6 was close to the crushed concrete region, but it was not affected by the concrete damage as much as anchor A5. Measured load history (in Fig.E.136) follows a fast decreasing trend after 1.0% drift ratio, even though the load was reapplied three times (at the end of 0.6%, 1.2% and 1.6% drift ratios). The load cell cable was ripped off by the failure of adjacent anchor A5, hence the load measurement was interrupted before the monotonic push. It is noted that the anchor load returned to the "before reloading" value at the end of each displacement cycle after the load was reapplied, reflecting the compromised performance of this anchor. The measured global displacement shows an increasing trend, opposite to the load decreasing trend, and the maximum global displacement of 0.73 in was measured before the monotonic push. Maximum measured crack width at the end of the test was w_r= 1.25 mm.



(a) Anchor location. Units in inches



(b) Photograph of anchor and cracks at end of test

Figure E.134: Location and photograph of anchor A6 in wall SQ0. Wall residual drift is diagrammatically shown exaggerated for the purpose of illustrating the final context around the anchor

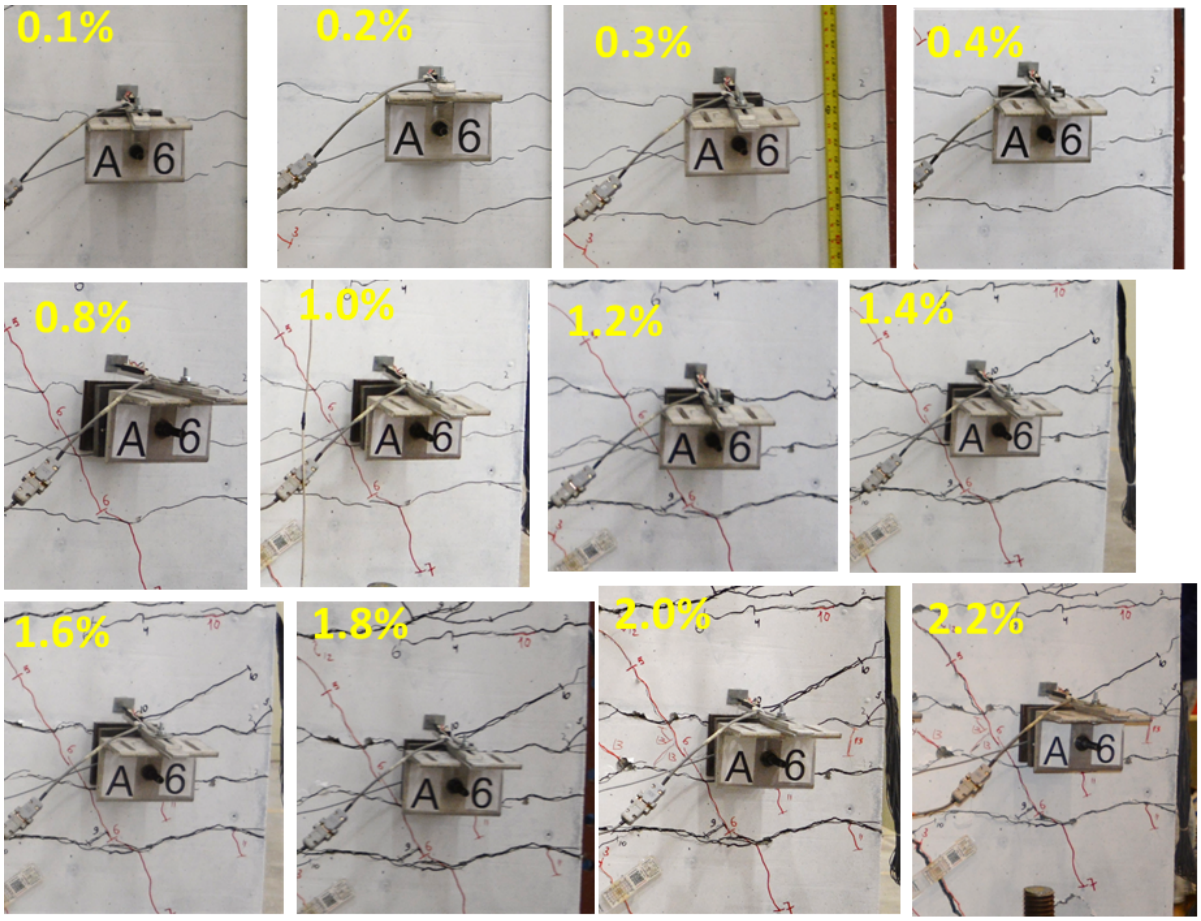


Figure E.135: Wall SQ0: photographs showing the crack evolution around anchor A6

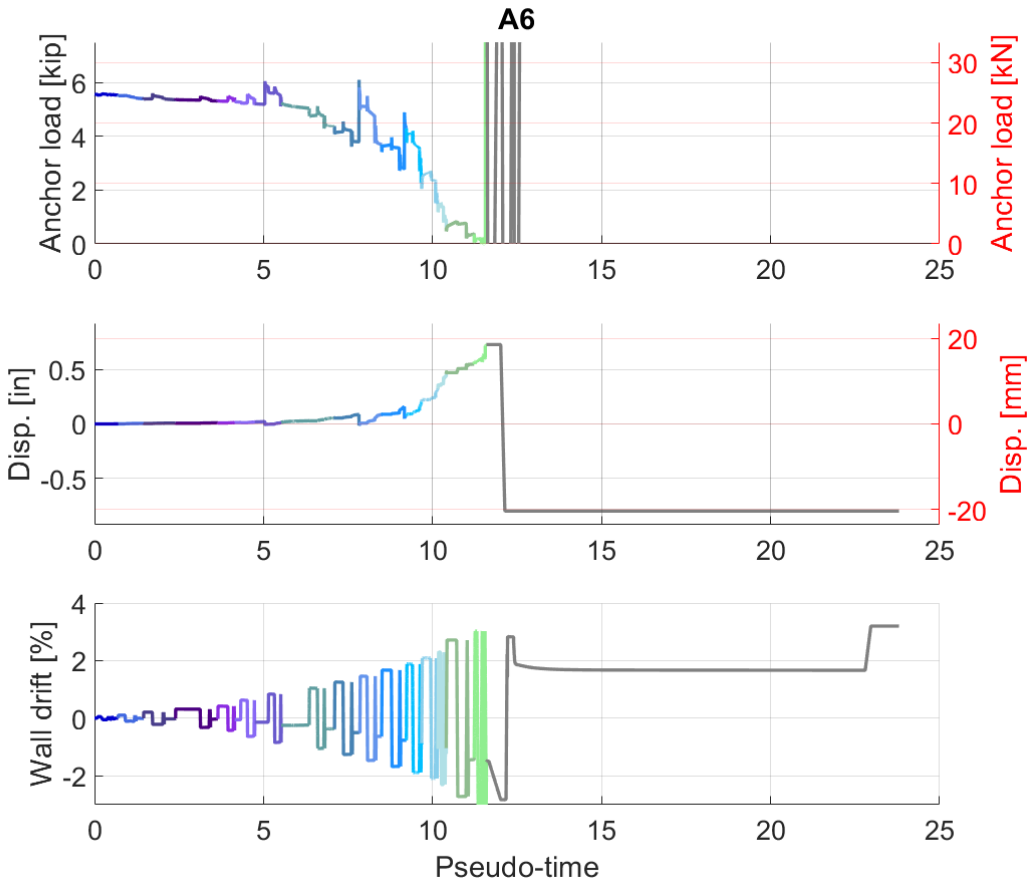


Figure E.136: Wall SQ0, anchor A6: measured load and displacement histories and wall drift history

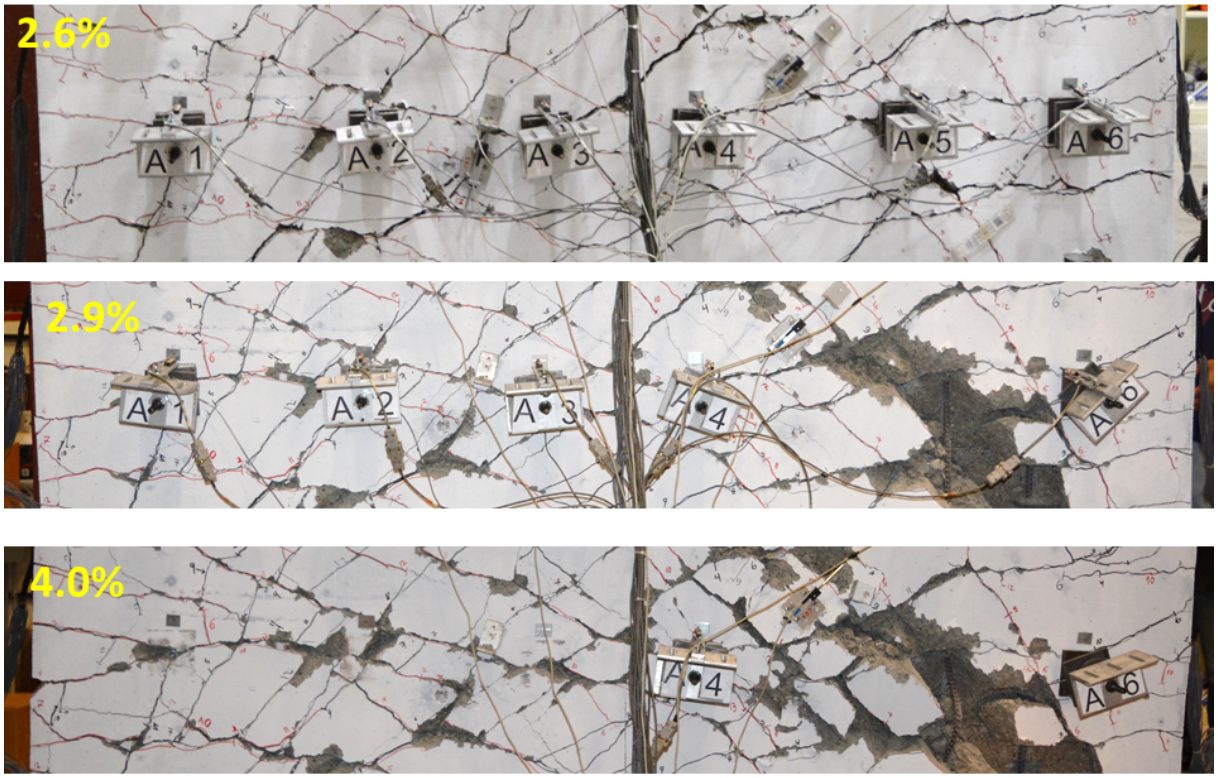
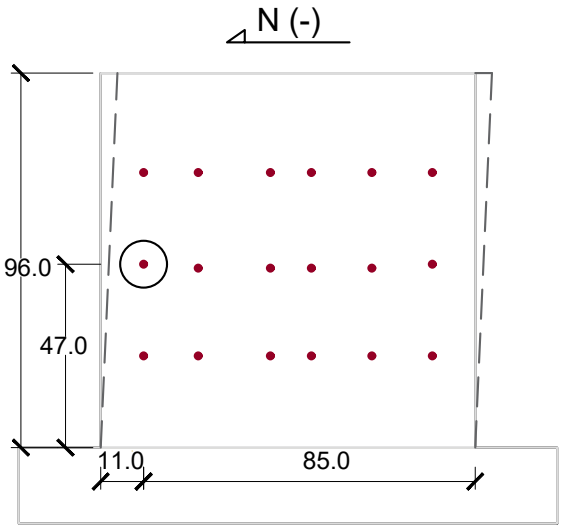


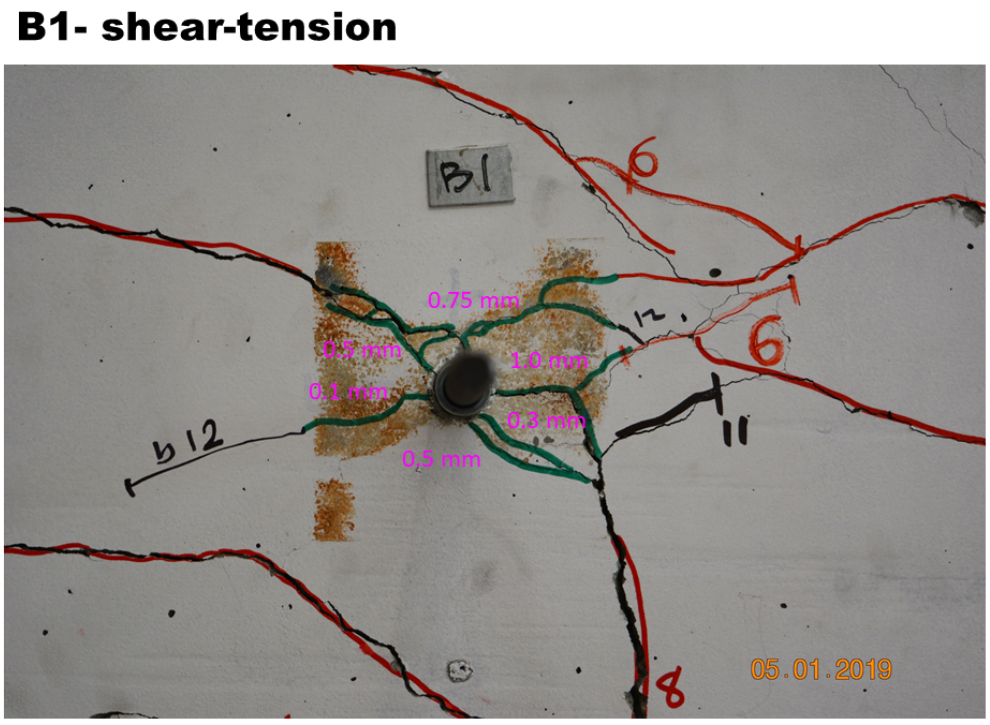
Figure E.137: Wall SQ0: photographs showing the crack evolution around row A during the last three drift demands

B1

Fig.E.138b shows that torque-controlled expansion anchor B1 was located in a tension crack, which formed at 0.2% drift ratio and increased in width as the drift demand on the wall increased (see Fig.E.84). Being inside the boundary element of the wall, anchor B1 had several other tension cracks around, forming a dense crack pattern. Measured load history (in Fig.E.140) shows a large load drop during the 1.0% drift ratio, which corresponds to the formation of a new crack going into the anchor (see Fig.E.84). Load was reapplied to the anchor at the end of this amplitude cycles. After the reloading, load rapidly dropped to zero and global displacement increased up to the maximum measured 0.54 in, before the monotonic push. Maximum measured crack width at the end of the test was w_r= 1.00 mm.



(a) Anchor location. Units in inches



(b) Photograph of anchor and cracks at end of test

Figure E.138: Location and photograph of anchor B1 in wall SQ0. Wall residual drift is diagrammatically shown exaggerated for the purpose of illustrating the final context around the anchor

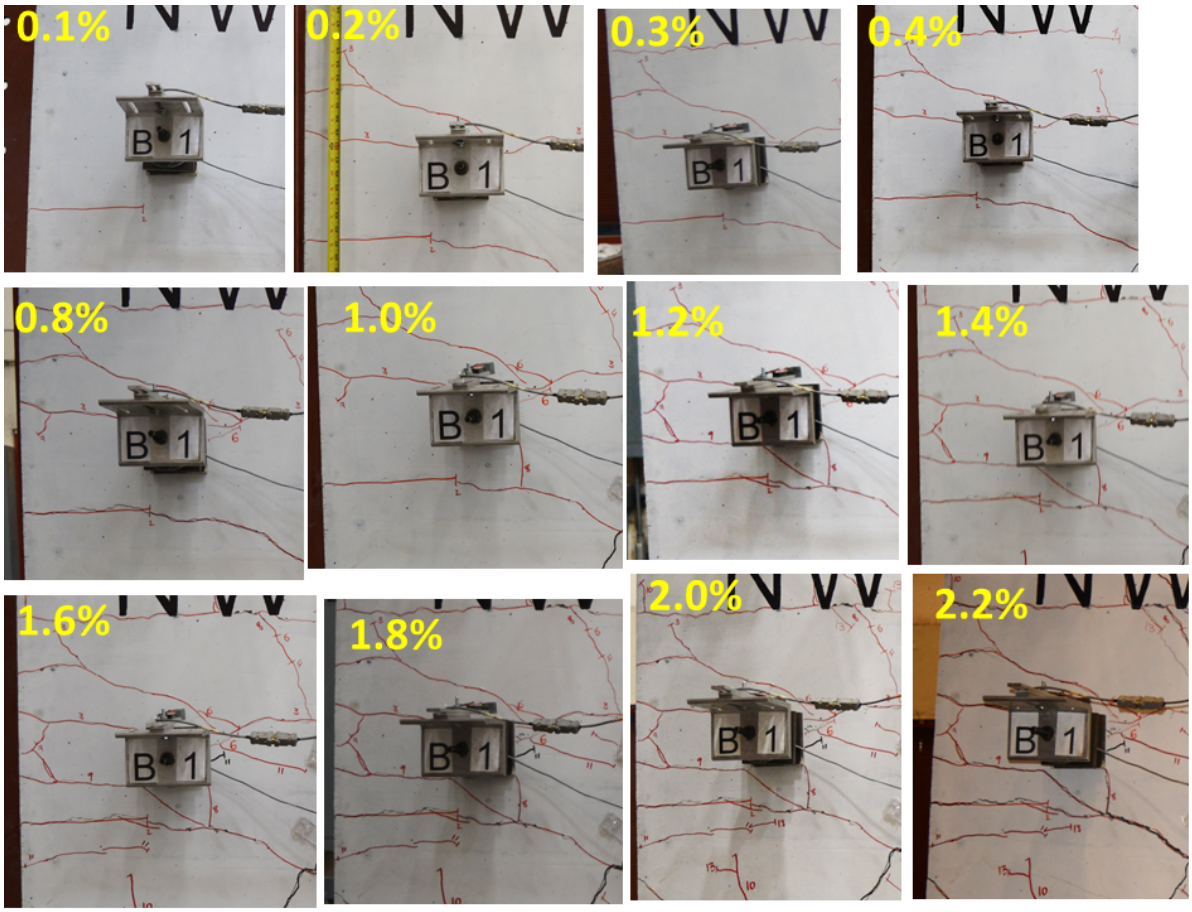


Figure E.139: Wall SQ0: photographs showing the crack evolution around anchor B1

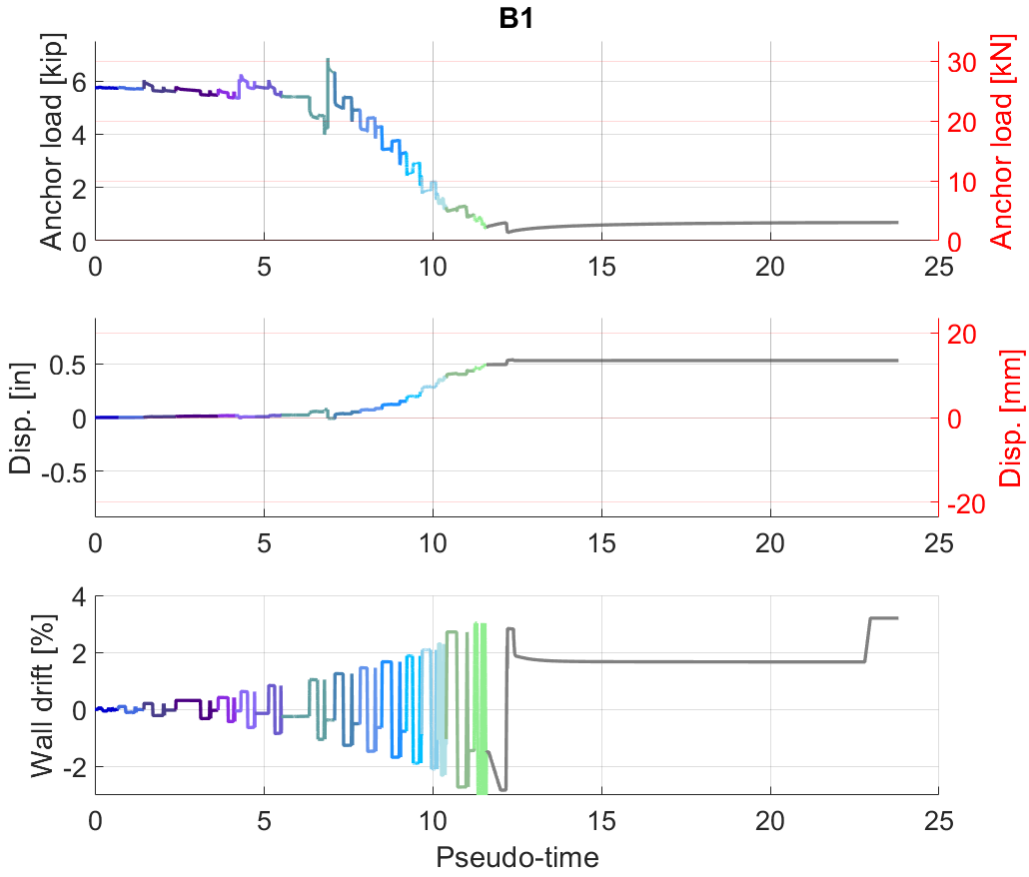
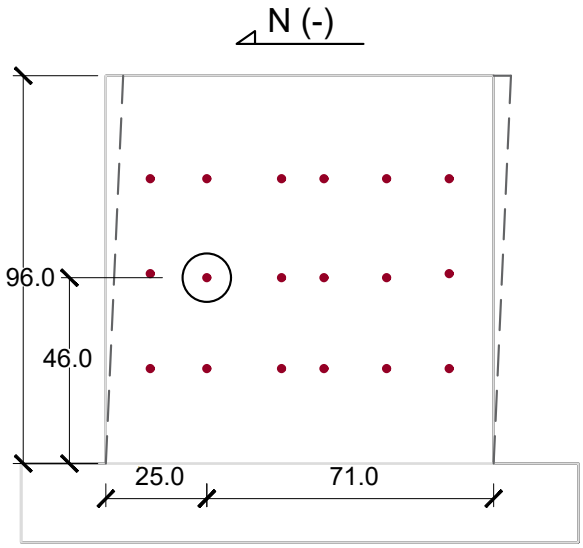


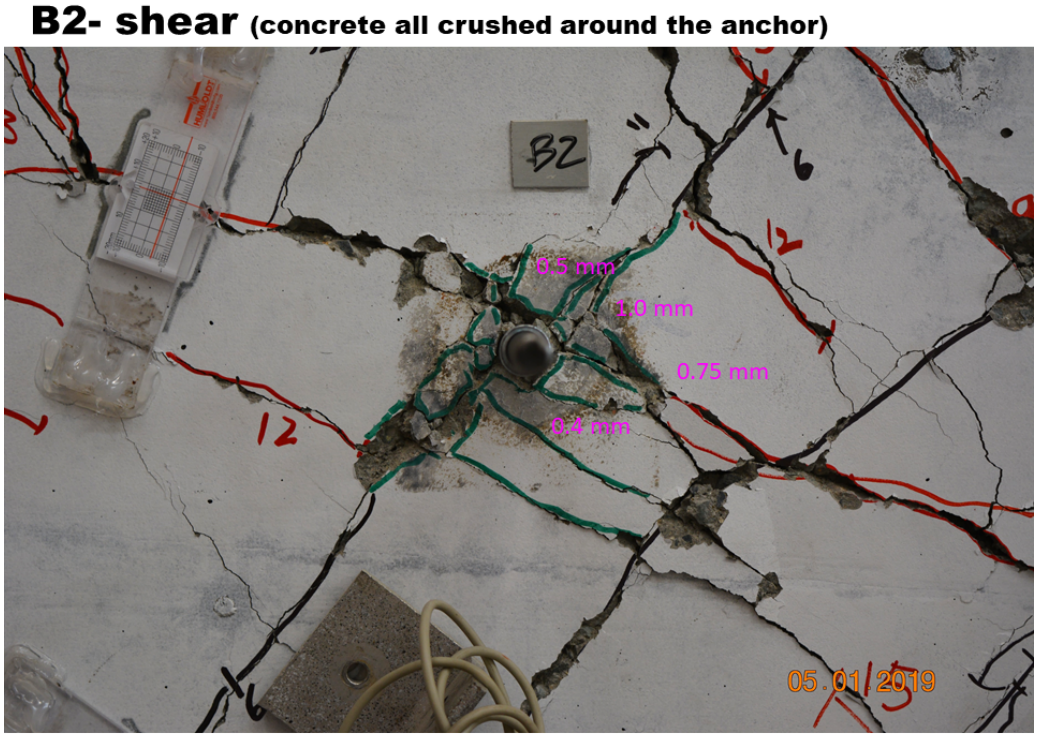
Figure E.140: Wall SQ0, anchor B1: measured load and displacement histories and wall drift history

B2

Fig.E.141b shows that torque-controlled expansion anchor B2 was located in a couple of shear crossing cracks, which formed at 0.4% and 1.0% drift ratios (see Fig.E.87) and increased in width with the drift demand. Other parallel diagonal shear cracks framed anchor B2 in a dense crack pattern. Measured load history in Fig.E.143 shows large load drops, which motivated the five reapplications of the load, at the end of 0.4%, 0.8%, 1.0%, 1.2%, 1.4% and 1.6% drift ratios. Global measured displacement shows increasing trend up to a maximum displacement of 0.68 in, measured before the monotonic push. Maximum measured crack width at the end of the test was w_r= 1.00 mm and local concrete crushing was observed in this region.



(a) Anchor location. Units in inches



(b) Photograph of anchor and cracks at end of test

Figure E.141: Location and photograph of anchor B2 in wall SQ0. Wall residual drift is diagrammatically shown exaggerated for the purpose of illustrating the final context around the anchor

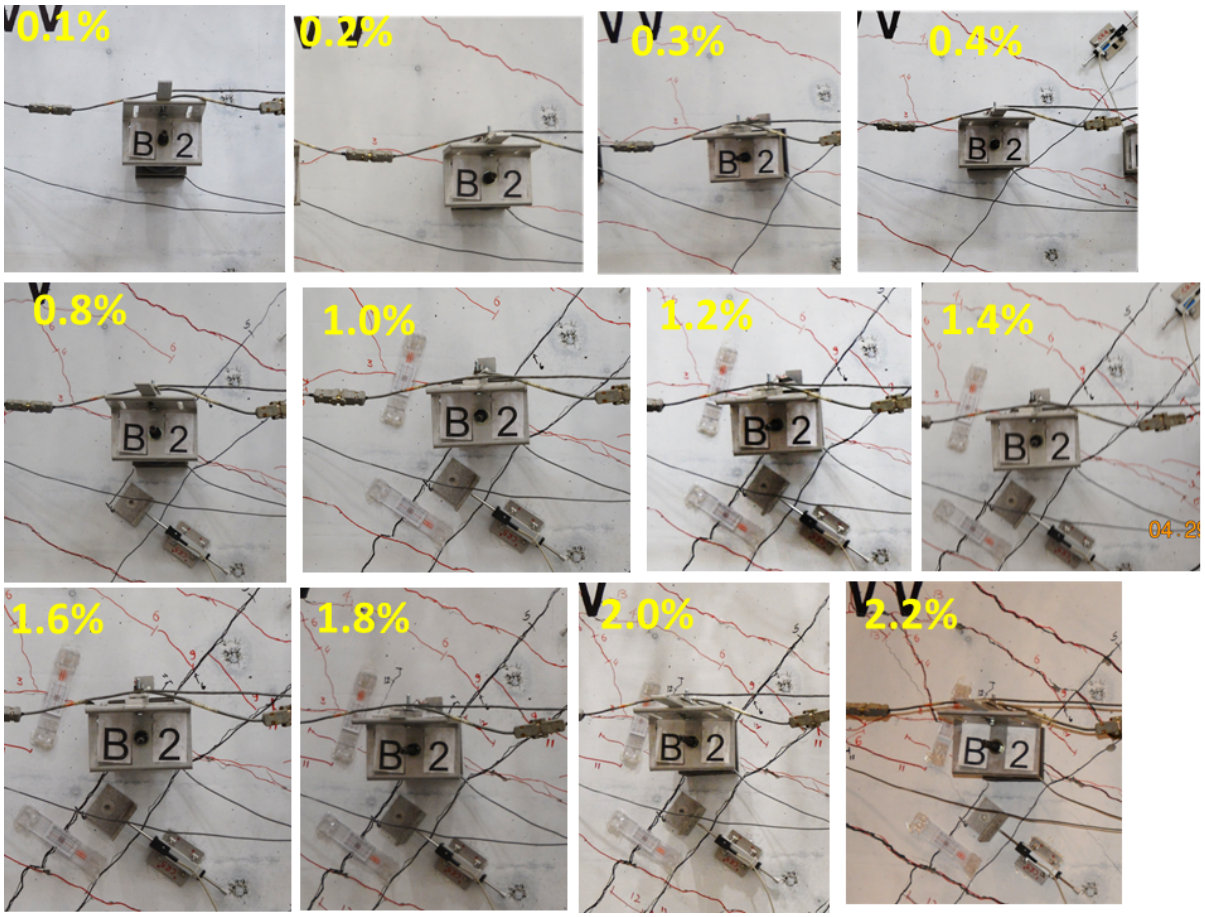


Figure E.142: Wall SQ0: photographs showing the crack evolution around anchor B2

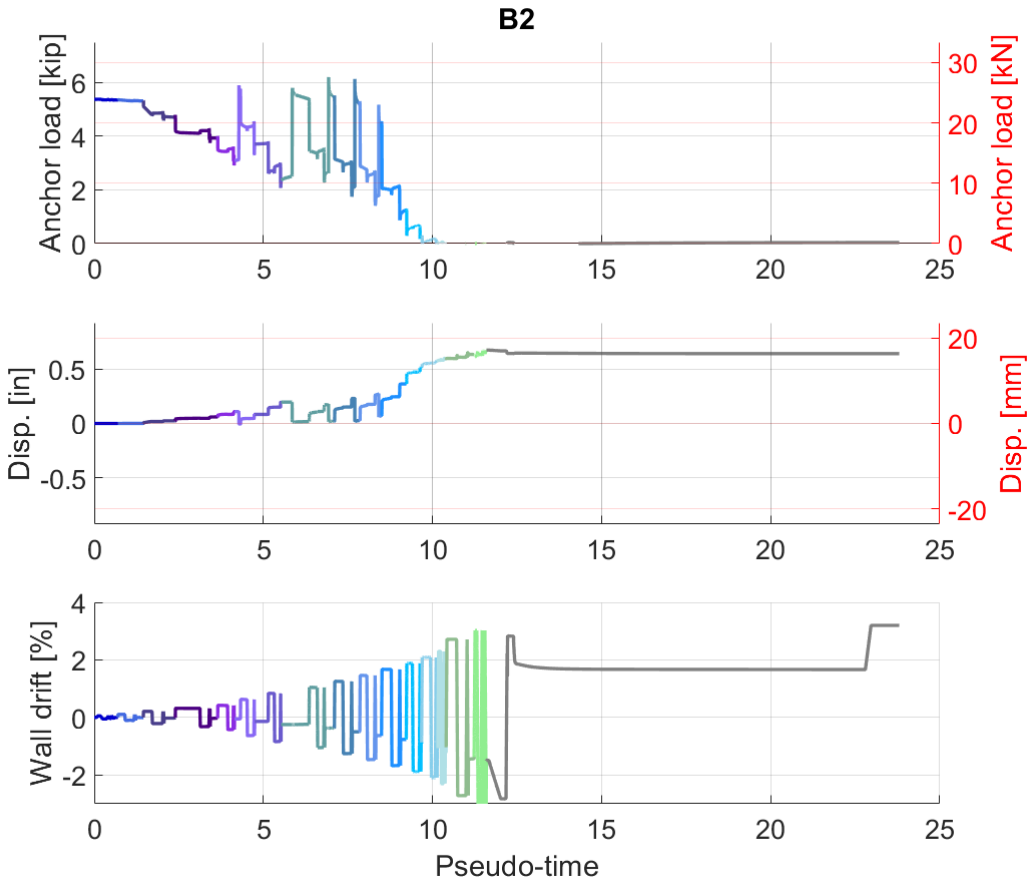
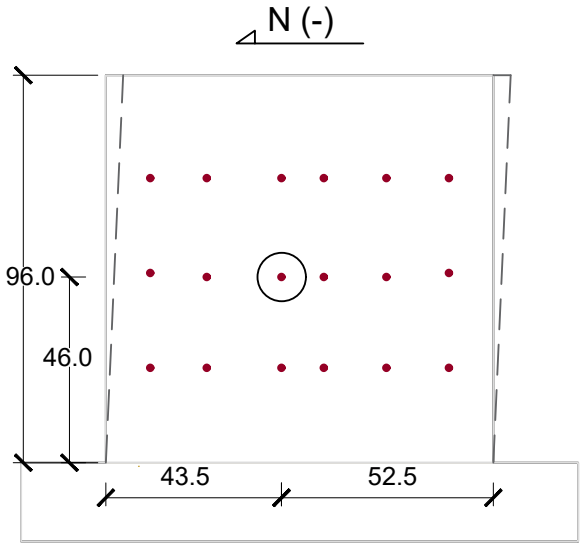


Figure E.143: Wall SQ0, anchor B2: measured load and displacement histories and wall drift history

B3

Fig.E.144b shows that torque-controlled expansion anchor B3 was located in a couple of shear crossing cracks, which fully developed between the 0.3% and 1.8% drift ratios (see Fig.E.90). However, crack pattern and damage were dense around this anchor also during previous cycles, being this anchor located along the main concrete strut. Measured load history (in Fig.E.146) shows that the load dropped significantly at 1.4% drift ratio, as a confirmation of the estimated formation of the crack. Anchor load was only reapplied twice (at the end of 0.6% and 1.0% drift ratios) to maintain constant tension load on the anchor. Global measured displacement shows increasing trend only after the 1.4% drift ratio and the maximum measured global displacement was 0.35 in before the monotonic push. Limited concrete crushed region was observed near to B3 at the end of the test and maximum measured crack width was w_r= 0.6 mm. It is also noted that when the load assembly was removed, the anchor sleeve was about 0.5 cm out of the installation hole due to the severe concrete damage.



(a) Anchor location. Units in inches



(b) Photograph of anchor and cracks at end of test

Figure E.144: Location and photograph of anchor B3 in wall SQ0. Wall residual drift is diagrammatically shown exaggerated for the purpose of illustrating the final context around the anchor

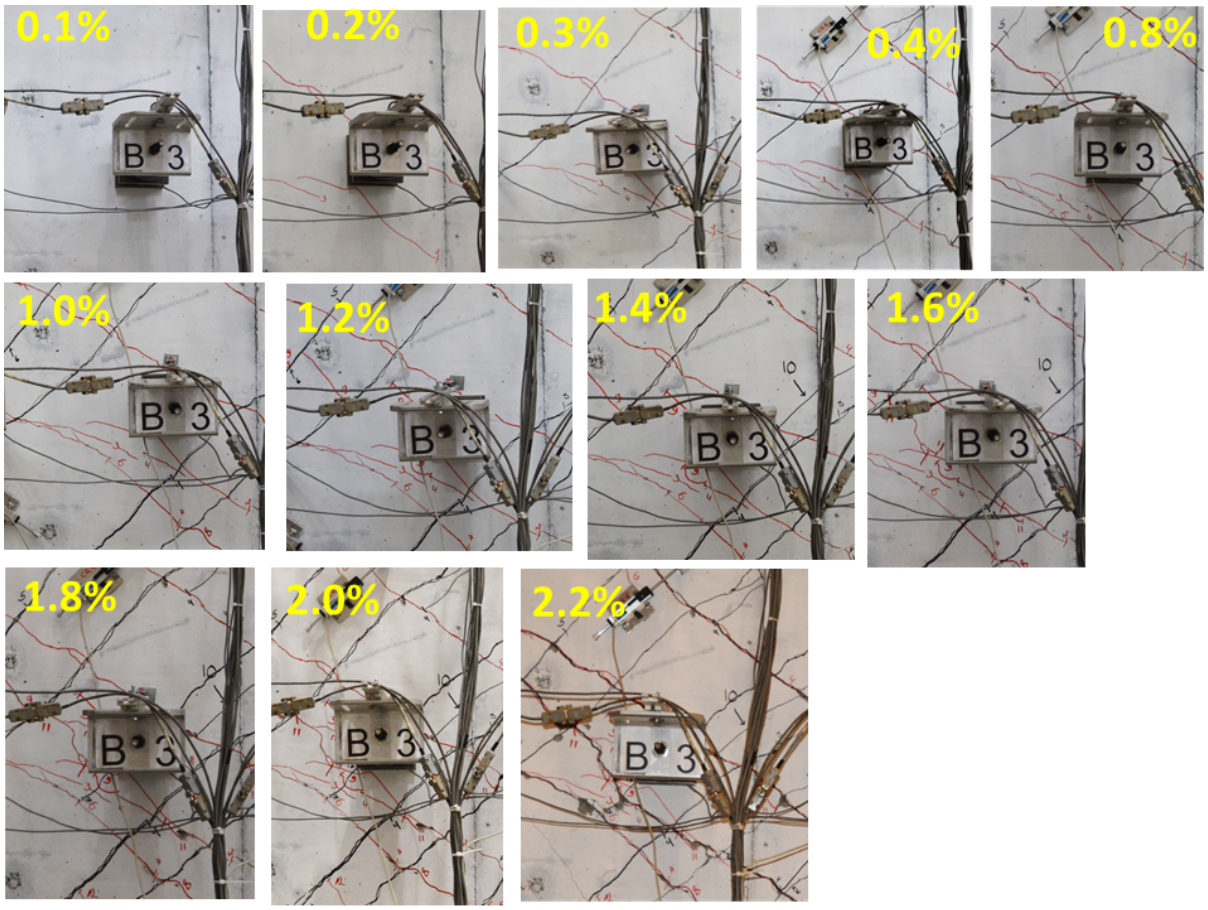


Figure E.145: Wall SQ0: photographs showing the crack evolution around anchor B3

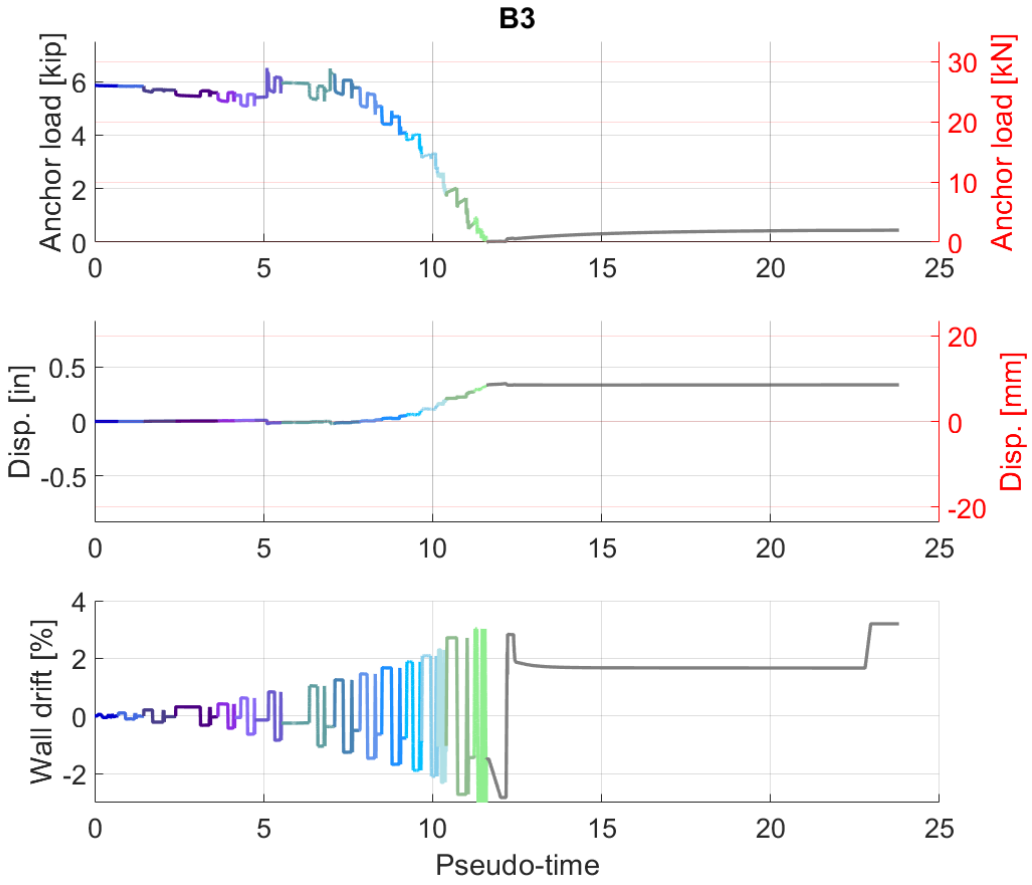
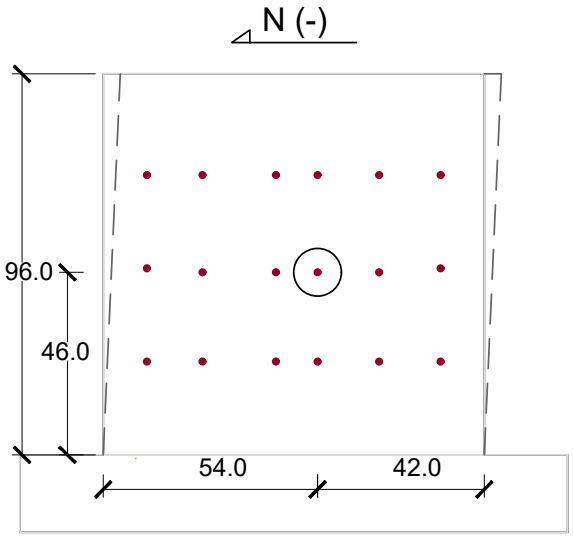


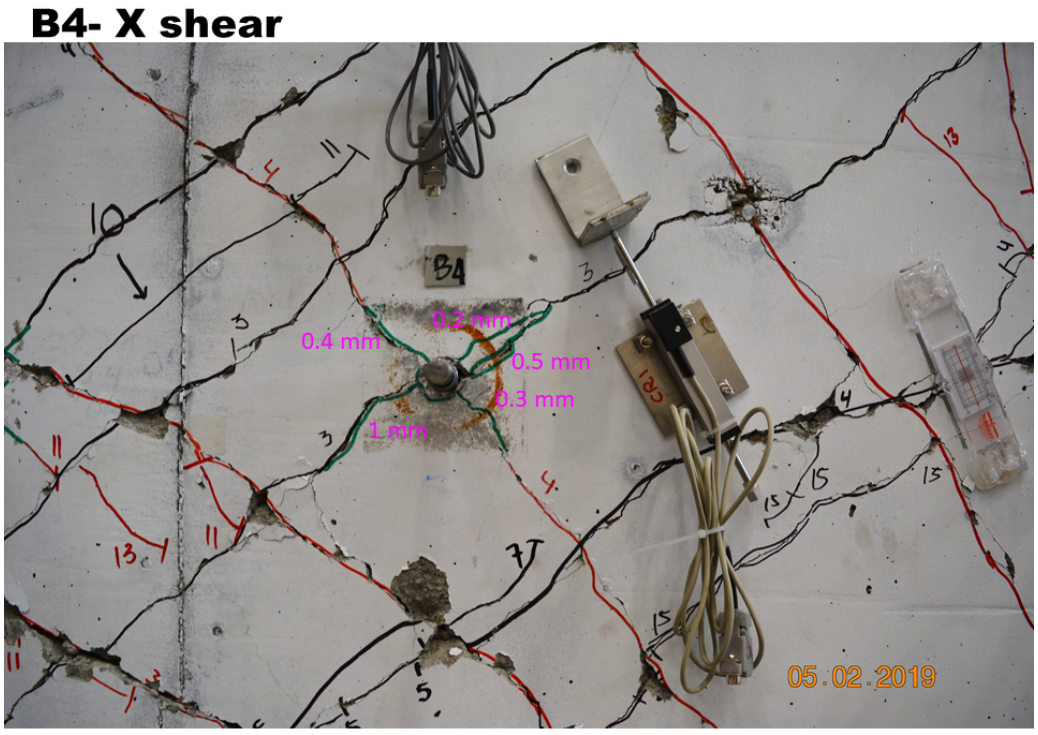
Figure E.146: Wall SQ0, anchor B3: measured load and displacement histories and wall drift history

B4

Fig.E.147b shows that torque-controlled expansion anchor B4 was located in a couple of shear crossing cracks, which formed in the early 0.3% drift ratio (see Fig.E.93). The width of one of these cracks was continuously monitored during the test by sensor CR1. Crack pattern and damage was dense around this anchor, being located at the center of the wall face. Measured load history in Fig.E.149 shows that the load dropped significantly at 1.4% drift ratio, as a confirmation of the estimated formation of the crack. Anchor load was reapplied three times (at the end of 0.6%, 1.0% and 1.2% drift ratios) to maintain constant tension load on the anchor. Global measured displacement shows increasing trend only before the second reapplication of load, when the displacement sensor was compromised by the reapplication of the load. Maximum global displacement measured 0.17 in before the damage of the displacement sensor. Maximum measured crack width at the end of the test was w_r= 0.6 mm. It is also noted that when the load assembly was removed, the anchor sleeve was about 0.5 cm out of the installation hole due to severe the concrete damage.



(a) Anchor location. Units in inches



(b) Photograph of anchor and cracks at end of test

Figure E.147: Location and photograph of anchor B4 in wall SQ0. Wall residual drift is diagrammatically shown exaggerated for the purpose of illustrating the final context around the anchor

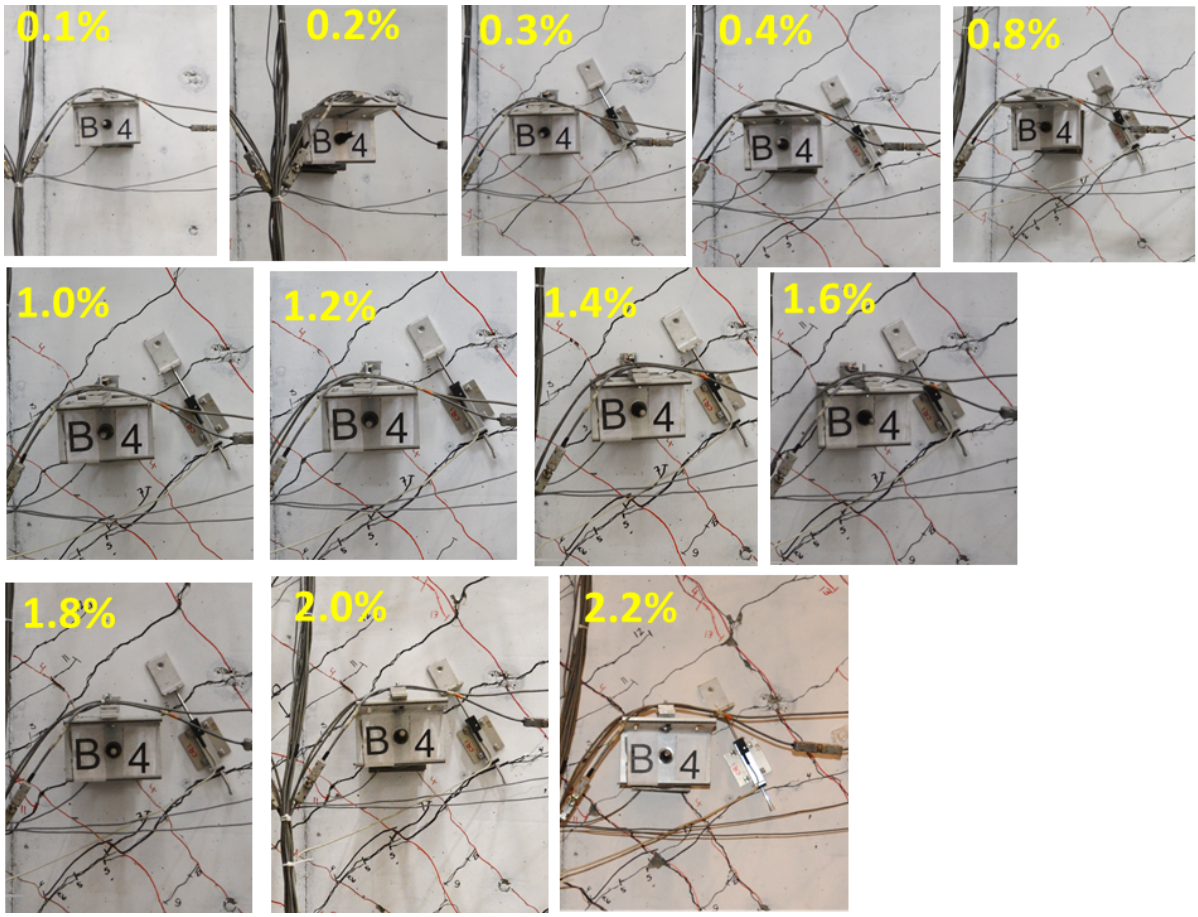


Figure E.148: Wall SQ0: photographs showing the crack evolution around anchor B4

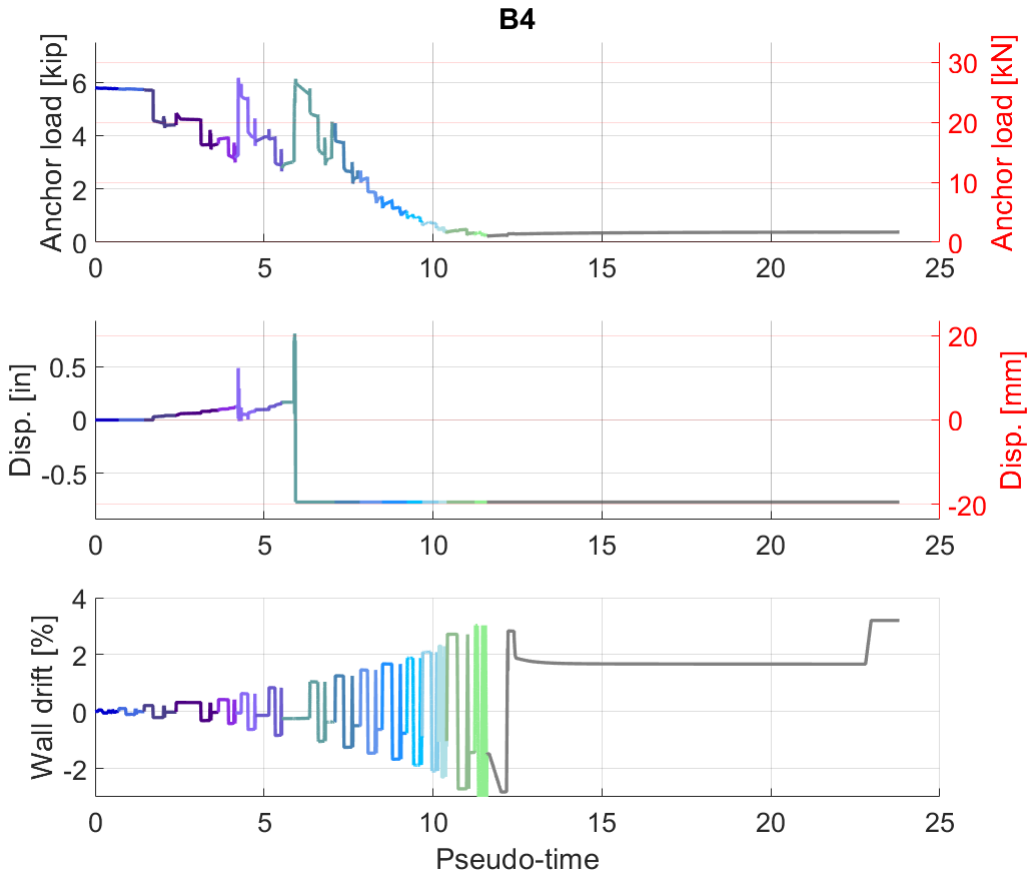
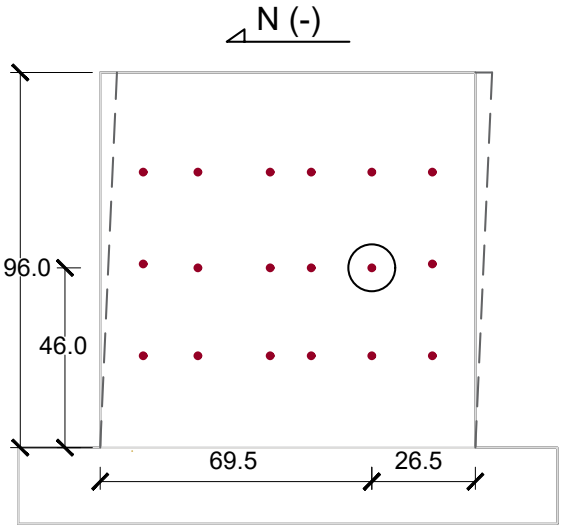


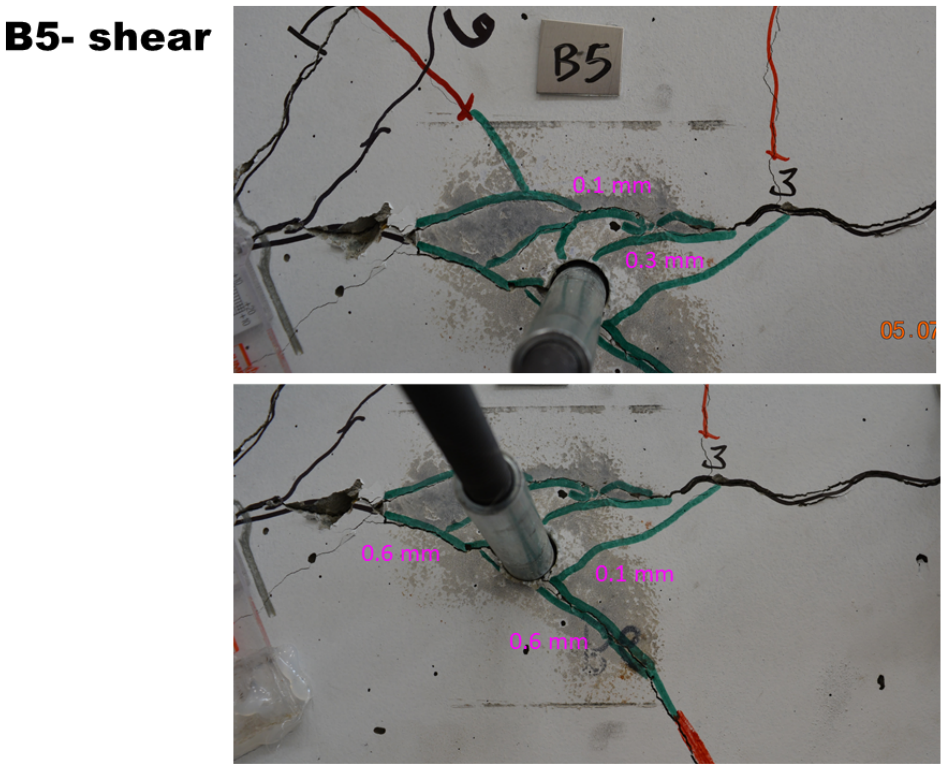
Figure E.149: Wall SQ0, anchor B4: measured load and displacement histories and wall drift history

B5

Fig.E.150b shows that torque-controlled expansion anchor B5 was located in one main shear crack and few radial cracks, which formed at 0.3% and 1.0% drift ratios (see Fig.E.96). The width of the main shear crack was continuously monitored during the test by the crack width sensor CR6 and by a manual sensor installed at 1.0% drift ratio. Crack pattern and damage were dense around this anchor, being located at the web-boundary element interface. Measured load history in Fig.E.152 shows that at the end of 1.0% drift ratio the load was significantly low, as a confirmation of the estimated opening of the shear crack. Even if the load was reapplied at the end of 1.0% and 1.2% drift ratios to maintain constant tension on the anchor, measured load was approximately zero before the monotonic push. Global displacement shows increasing trend after 1.4% drift ratio and the maximum global displacement measured 0.47 in before the monotonic push. Maximum crack width at the end of the test measured w_r= 0.6 mm.



(a) Anchor location. Units in inches



(b) Photograph of anchor and cracks at end of test

Figure E.150: Location and photograph of anchor B5 in wall SQ0. Wall residual drift is diagrammatically shown exaggerated for the purpose of illustrating the final context around the anchor

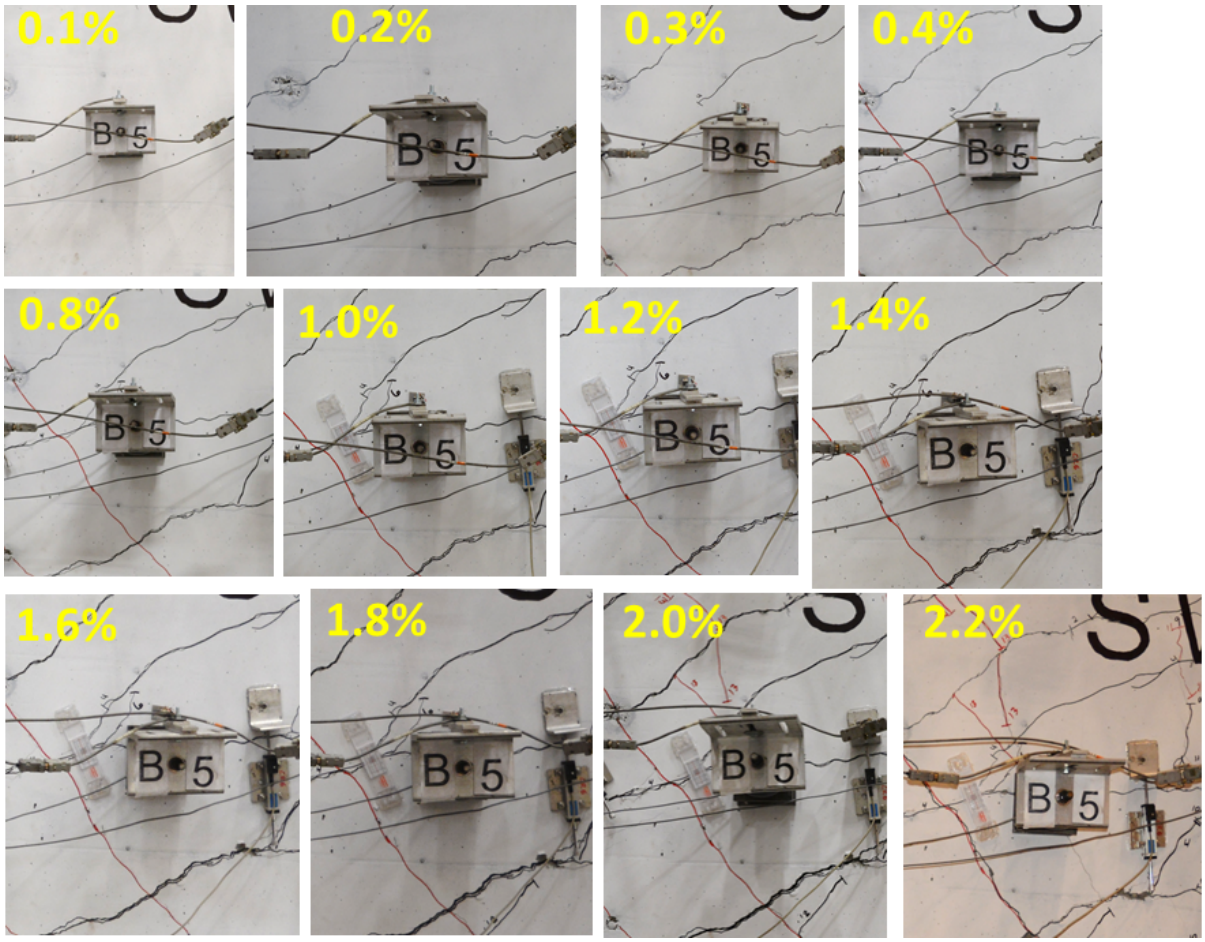


Figure E.151: Wall SQ0: photographs showing the crack evolution around anchor B5.

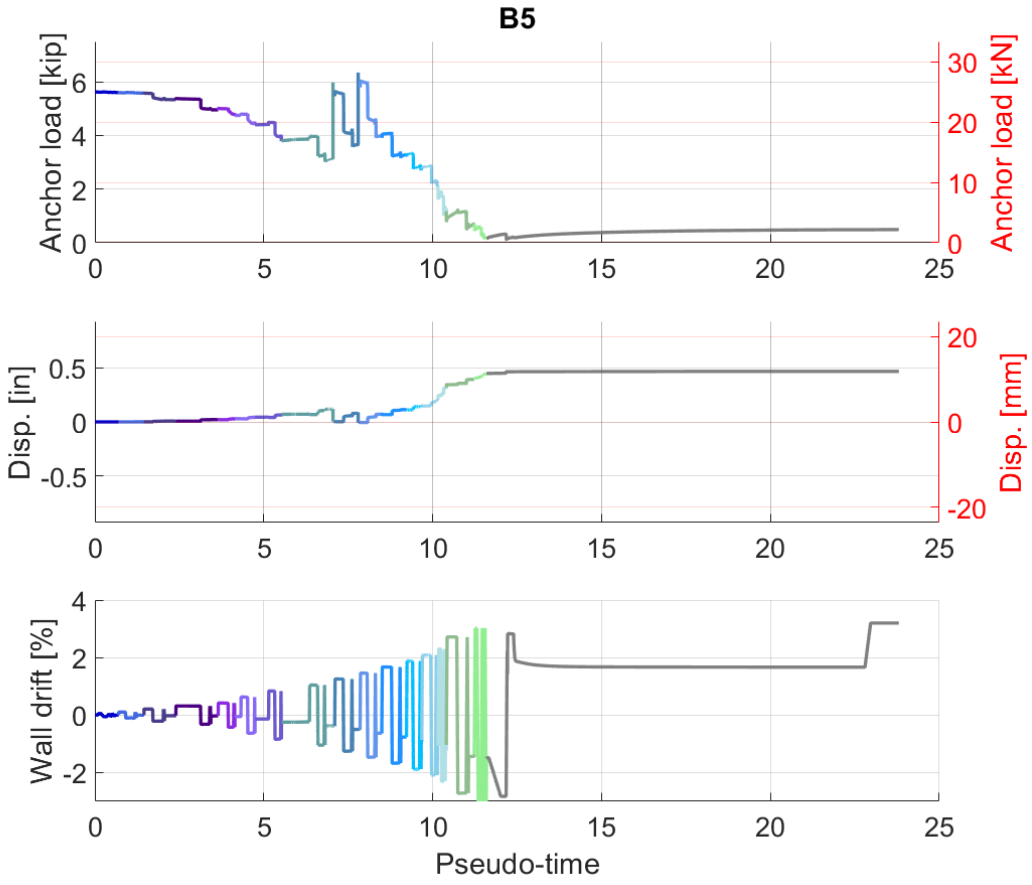
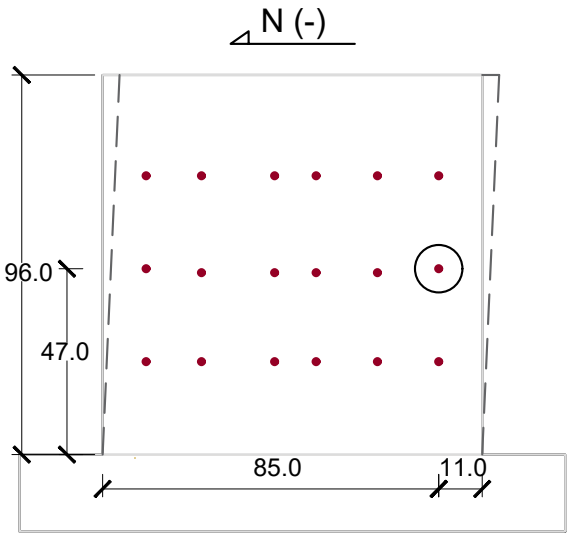


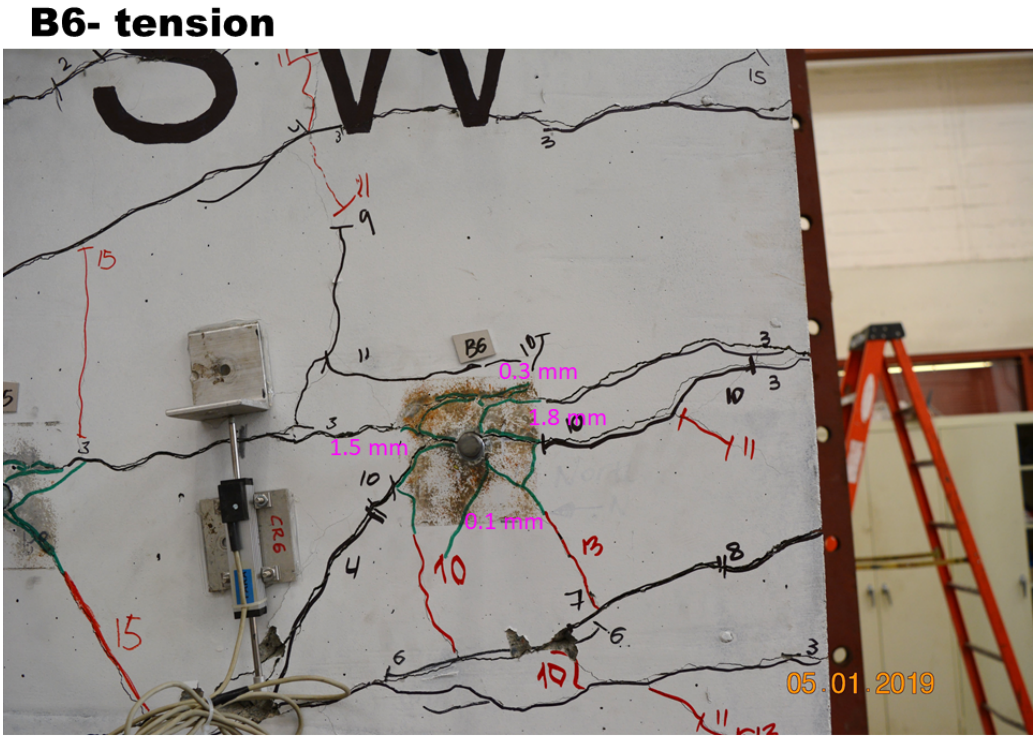
Figure E.152: Wall SQ0, anchor B5: measured load and displacement histories and wall drift history.

B6

Fig.E.153b shows that torque-controlled expansion anchor B6 was located in one main tension crack and few radial cracks, which formed at 0.3% drift ratio and evolved as the drift demand on the wall increased (see Fig.E.99). The width of the main tension crack was continuously monitored during the test by the crack width sensor CR6. It is noted that this crack crossed both anchors B5 and B6 and that the crack width was approximately measured at an equal distance between the two anchors. Crack pattern and damage was dense around anchor B6, being located inside the confined boundary element of the shear wall. Measured load history in Fig.E.155 shows that the load significantly decreased at 0.3% drift ratio, when the first crack opened around the anchor. Even if the load was reapplied four times (at the end of 0.6%, 1.0%, 1.2% and 1.4% drift ratios) to maintain constant tension on the anchor, measured load was approximately zero before the monotonic push. Similarly, significant increase in global displacement was measured after the 1.6% drift ratio, when new extensions of existing cracks crossed the anchor, and the maximum global displacement measured 0.63 in before the monotonic push. Maximum crack width at the end of the test measured w_r= 1.8 mm.



(a) Anchor location. Units in inches



(b) Photograph of anchor and cracks at end of test

Figure E.153: Location and photograph of anchor B6 in wall SQ0. Wall residual drift is diagrammatically shown exaggerated for the purpose of illustrating the final context around the anchor

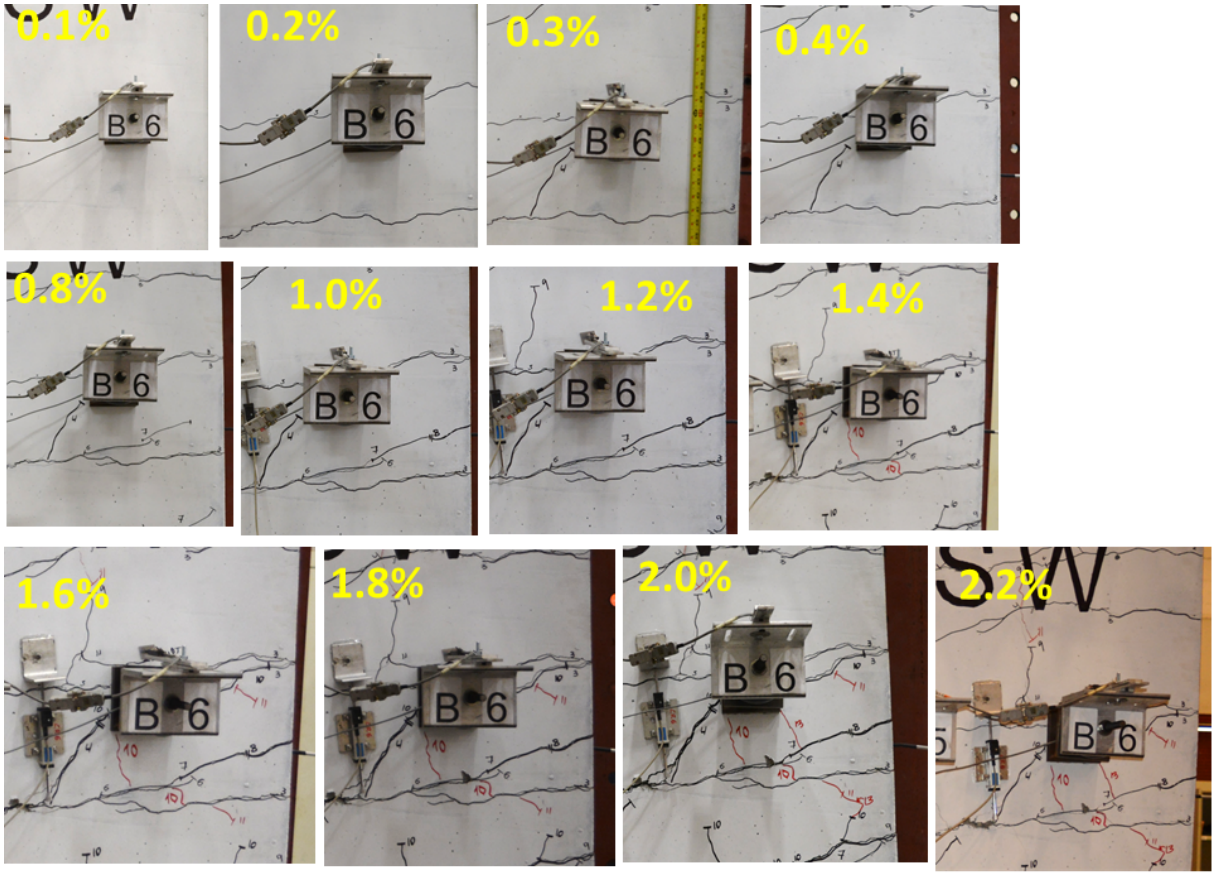


Figure E.154: Wall SQ0: photographs showing the crack evolution around anchor B6

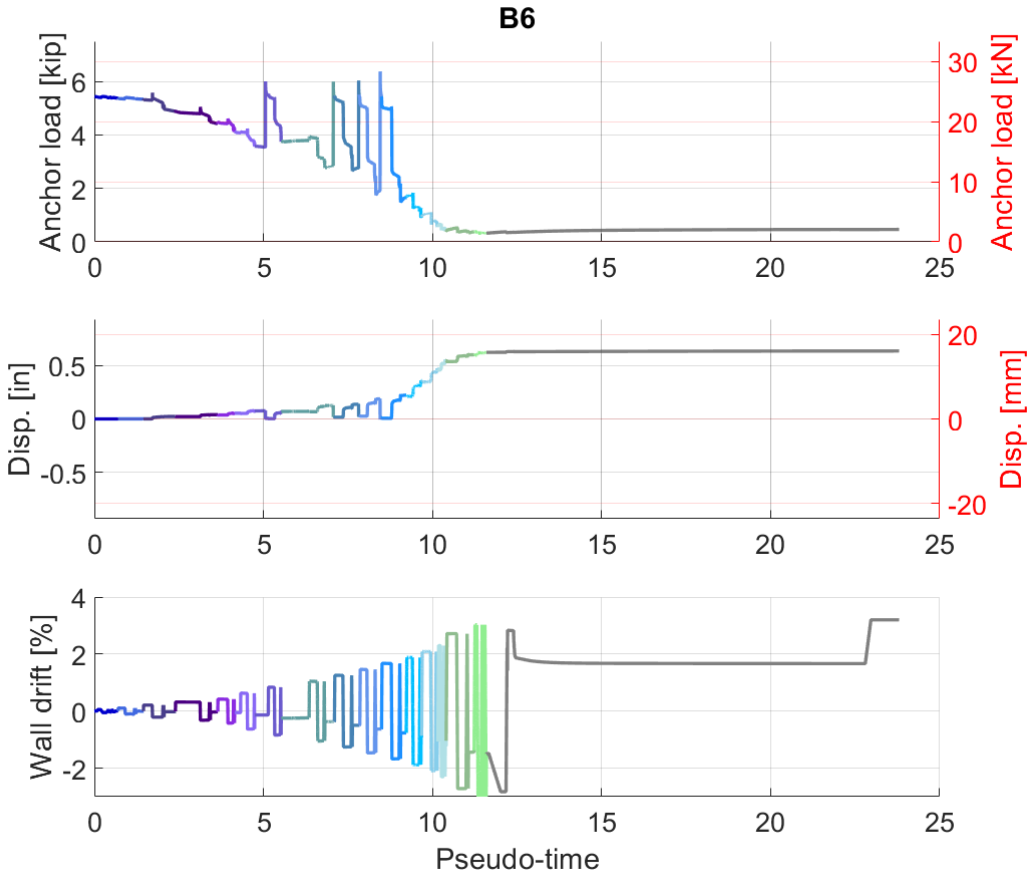


Figure E.155: Wall SQ0, anchor B6: measured load and displacement histories and wall drift history

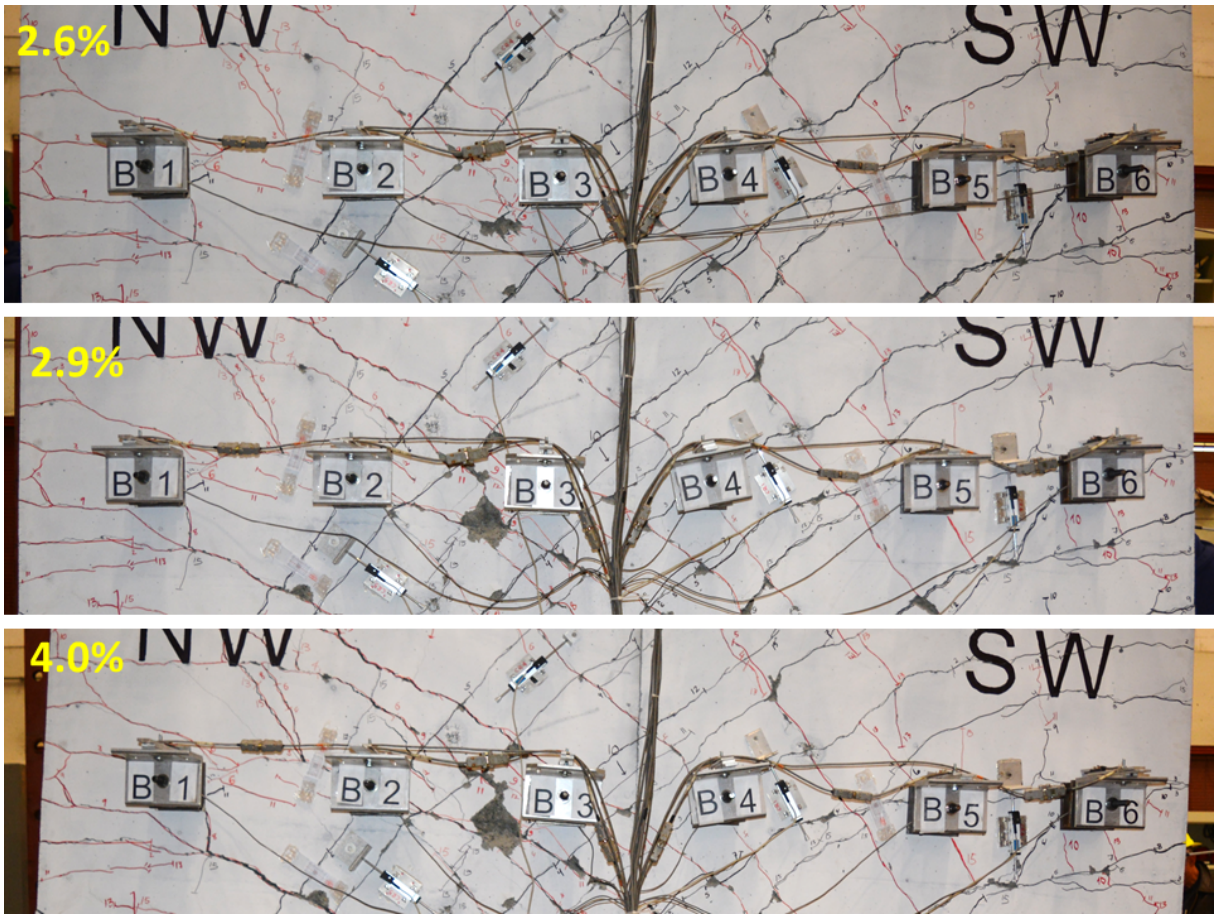
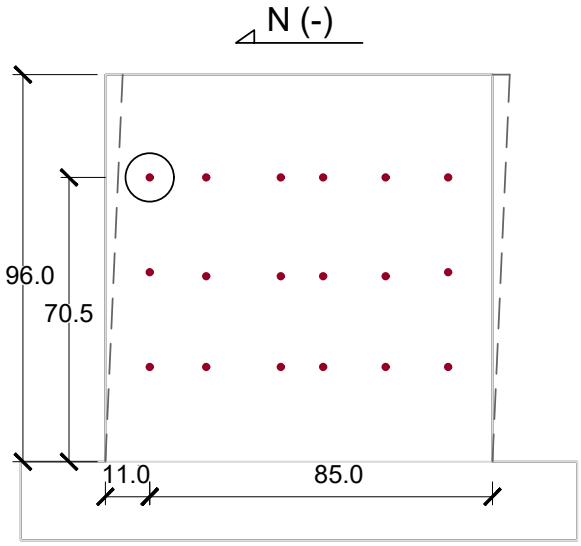


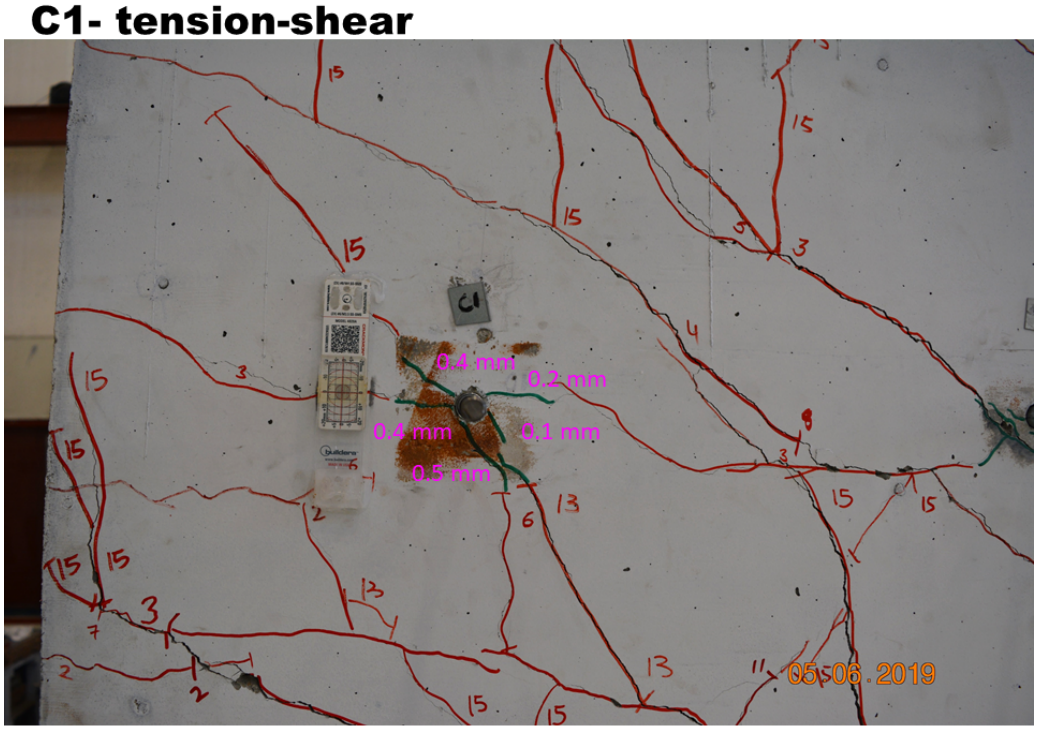
Figure E.156: Wall SQ0: photographs showing the crack evolution around row B during the last three drift demands

C1

Fig.E.157b shows that torque-controlled expansion anchor C1 was located in a tension crack (transitioning to a shear crack right after the anchor), which likely opened in the early cycles at 0.2% drift ratio and increased in width and extension as the wall cycled to large drift ratios. Several parallel tension-shear cracks developed near C1, being located inside the boundary element region and within the main diagonal concrete strut. The width of the crossing crack was measured by the manual sensor installed at 1.0% drift ratio. Anchor load visibly dropped at 0.2% drift ratio, when the first crack crossed the anchor, and it was reloaded at the end of 0.4% and 1.2% drift ratios, as shown in Fig.E.159. The measured global displacement slightly increased to the maximum measured value of 0.13 in, before the monotonic push. Maximum residual crack width at the end of the test measured about w_r= 0.5 mm.



(a) Anchor location. Units in inches



(b) Photograph of anchor and cracks at end of test

Figure E.157: Location and photograph of anchor C1 in wall SQ0. Wall residual drift is diagrammatically shown exaggerated for the purpose of illustrating the final context around the anchor

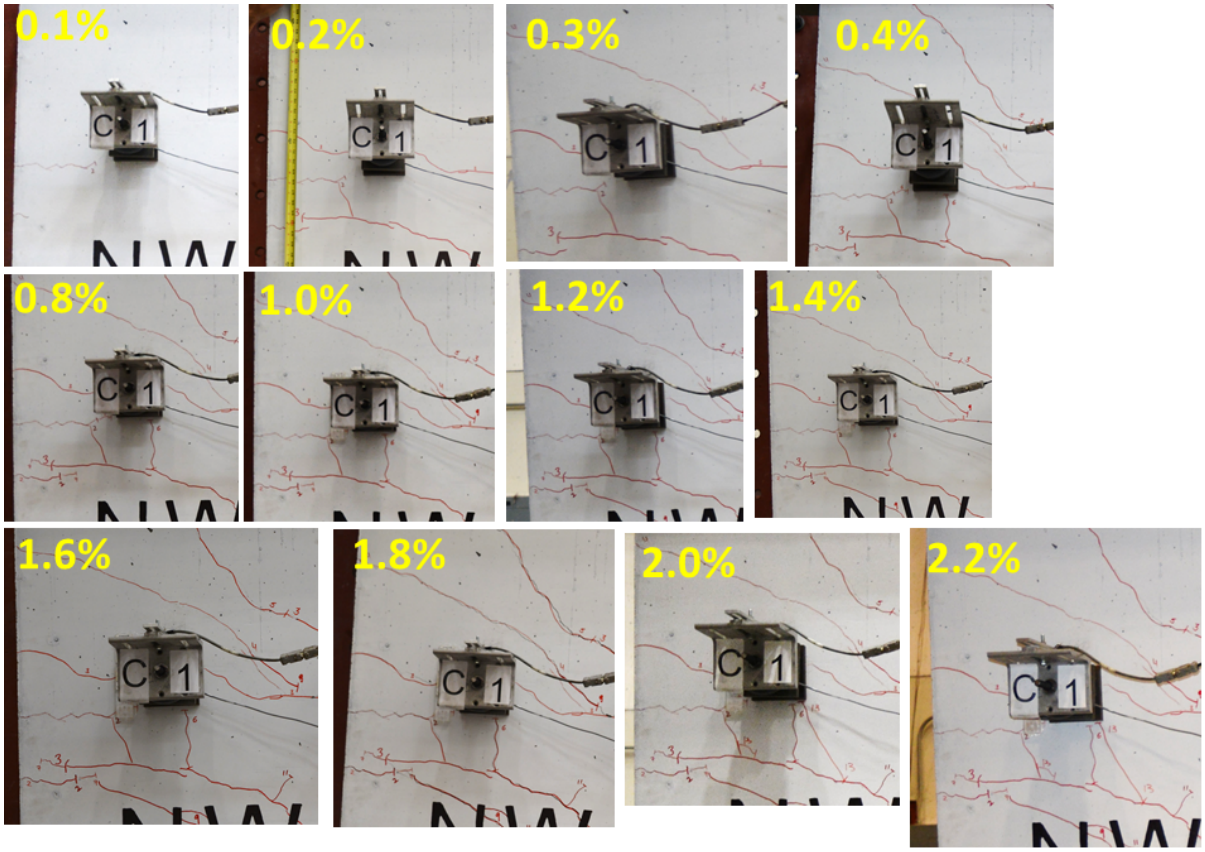


Figure E.158: Wall SQ0: photographs showing the crack evolution around anchor C1

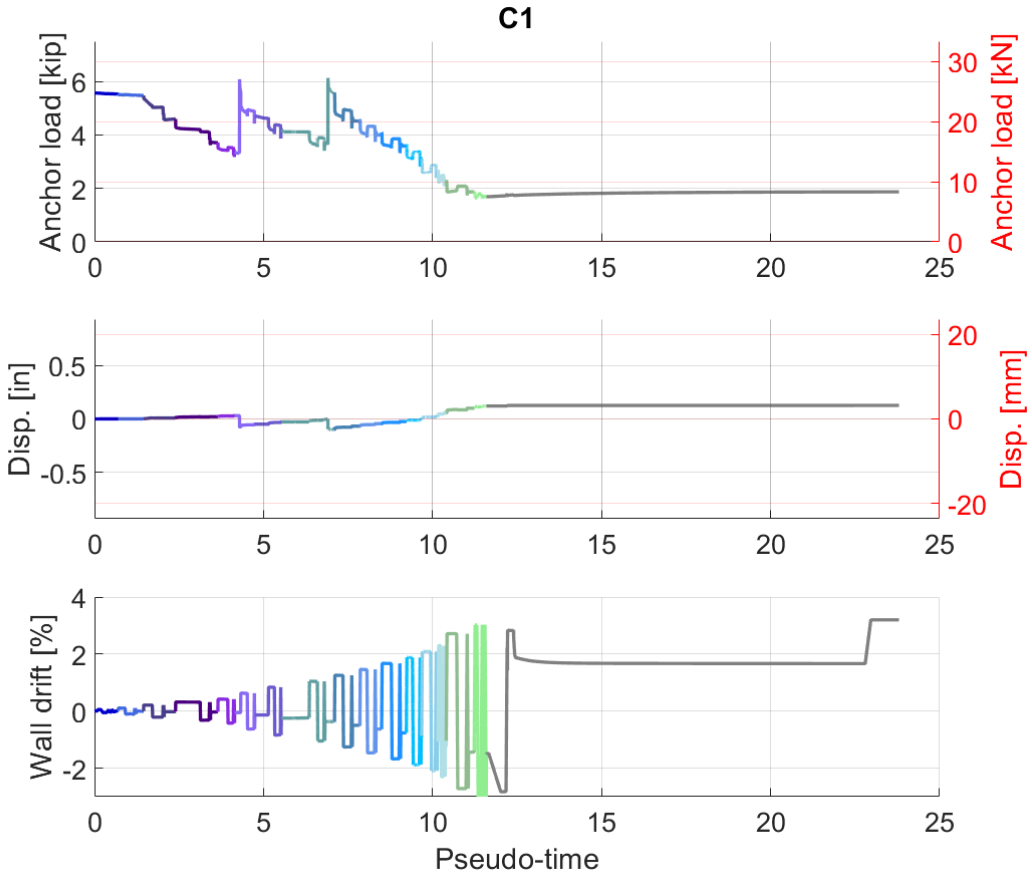
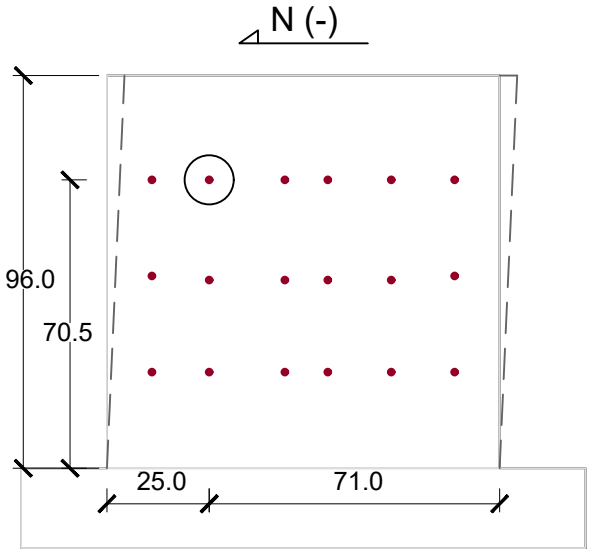


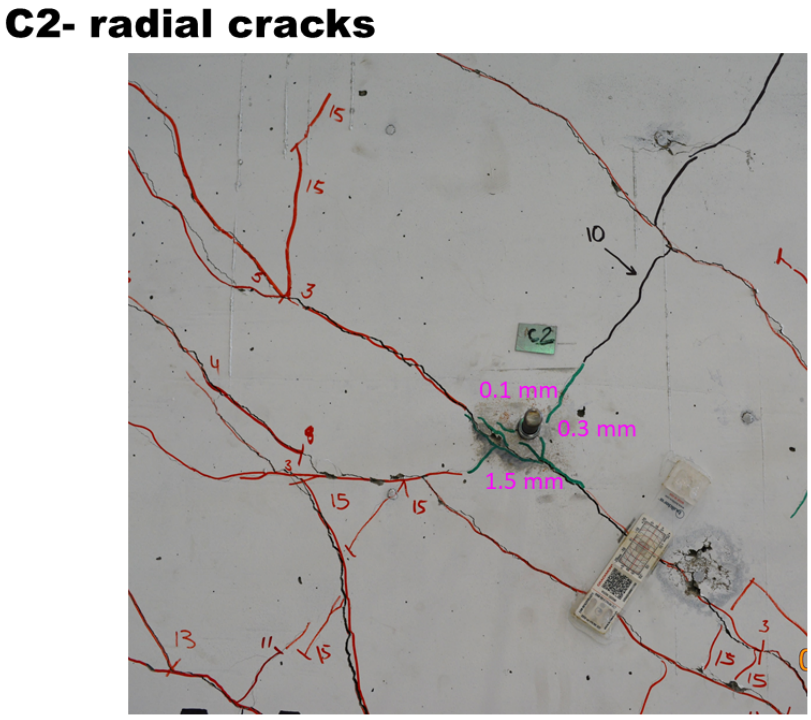
Figure E.159: Wall SQ0, anchor C1: measured load and displacement histories and wall drift history

C2

Fig.E.160b shows that radial cracks formed around torque-controlled expansion anchor C2, extending a shear crack opened during the 0.2% drift ratio. Several other parallel shear cracks framed the anchor and compromised the integrity of the surrounding concrete, despite the relatively high elevation of anchor C2 with respect to the wall-footing interface. The width of the shear crack near the anchor was measured by the manual sensor installed at 1.0% drift ratio. Anchor load visibly dropped at 0.4% drift ratio, and load was thus reapplied at the end of the 0.4%, 0.8%, 1.0%, 1.2% and 1.4% drift ratios, as shown in Fig.E.162. At the 0.4% drift ratio, the measured global displacement increased and reached the maximum value of 0.52 in at end of the cyclic wall test. Maximum residual crack width at the end of the test was significantly large, measuring about w_r= 1.5 mm.



(a) Anchor location. Units in inches



(b) Photograph of anchor and cracks at end of test

Figure E.160: Location and photograph of anchor C2 in wall SQ0. Wall residual drift is diagrammatically shown exaggerated for the purpose of illustrating the final context around the anchor

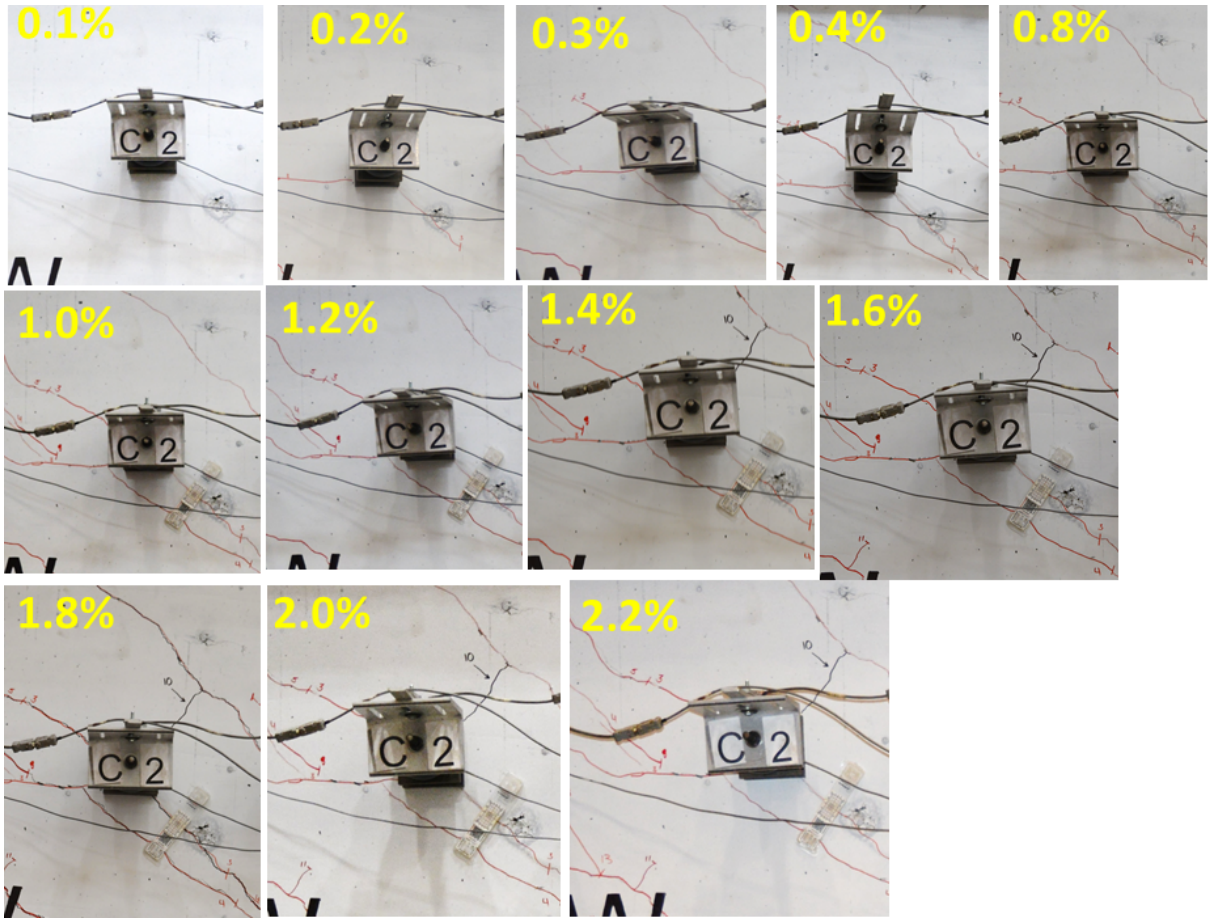


Figure E.161: Wall SQ0: photographs showing the crack evolution around anchor C2

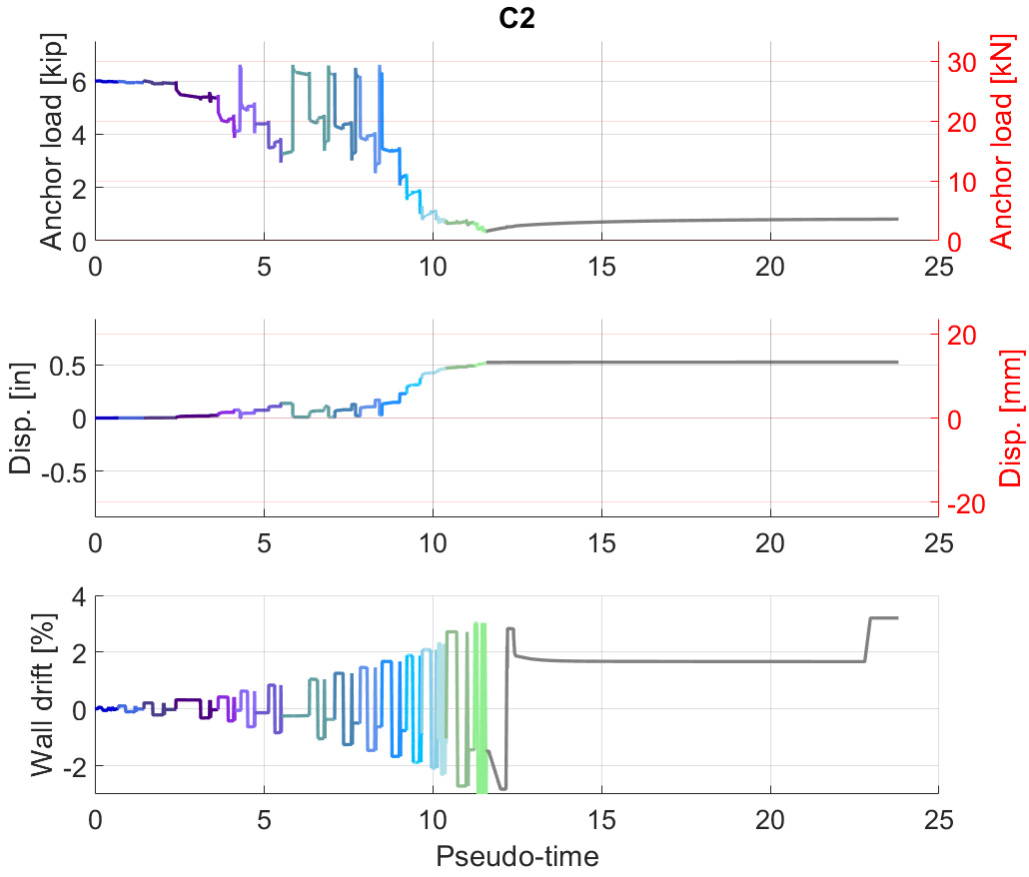
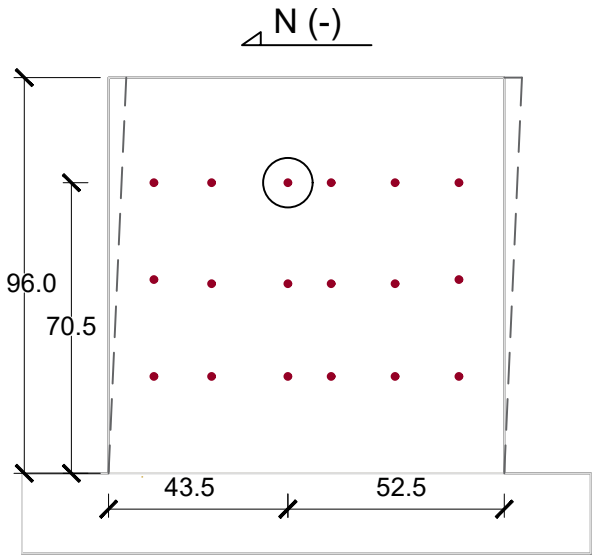


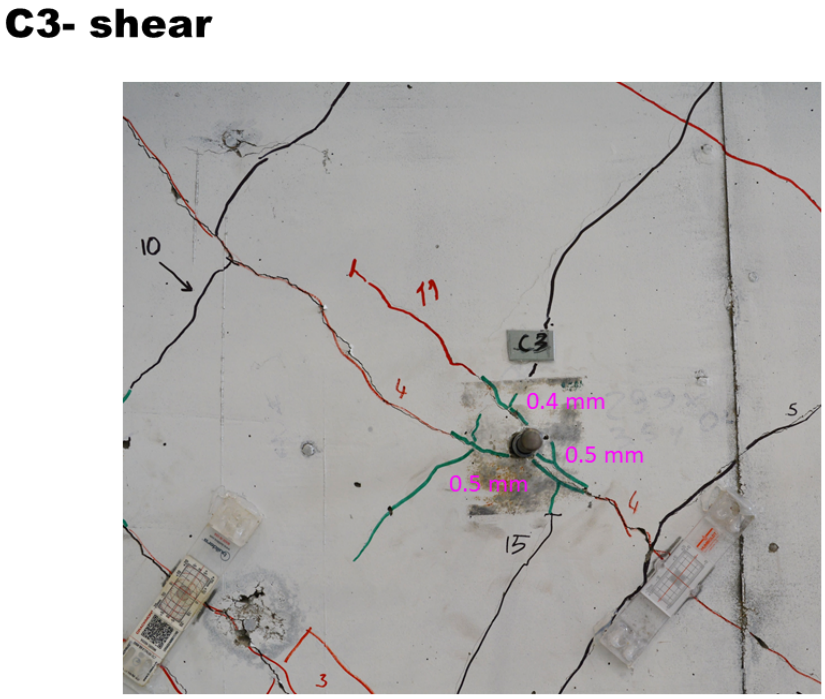
Figure E.162: Wall SQ0, anchor C2: measured load and displacement histories and wall drift history

C3

Fig.E.163b shows that one shear crossing crack and few radial cracks formed around torque-controlled expansion anchor C3 at 0.3% drift ratio. Several other parallel shear cracks in both the Push and Pull direction framed the anchor and compromised the integrity of the surrounding concrete, even at the relatively high elevation of anchor C3 with respect to the wall -footing interface. The width of the shear crossing crack was measured by the manual sensor installed at 1.0% drift ratio. Anchor load visibly dropped at 0.6% drift ratio, and it was thus reapplied at the end of the 0.6%, 1.0%, 1.2% and 1.6% drift ratios, as shown in Fig.E.165. At the 0.6% drift ratio, the measured global displacement increased and reached the maximum value of 0.42 in at end of the cyclic wall test. Maximum residual crack width at the end of the test measured about w_r= 0.5 mm.



(a) Anchor location. Units in inches



(b) Photograph of anchor and cracks at end of test

Figure E.163: Location and photograph of anchor C3 in wall SQ0. Wall residual drift is diagrammatically shown exaggerated for the purpose of illustrating the final context around the anchor

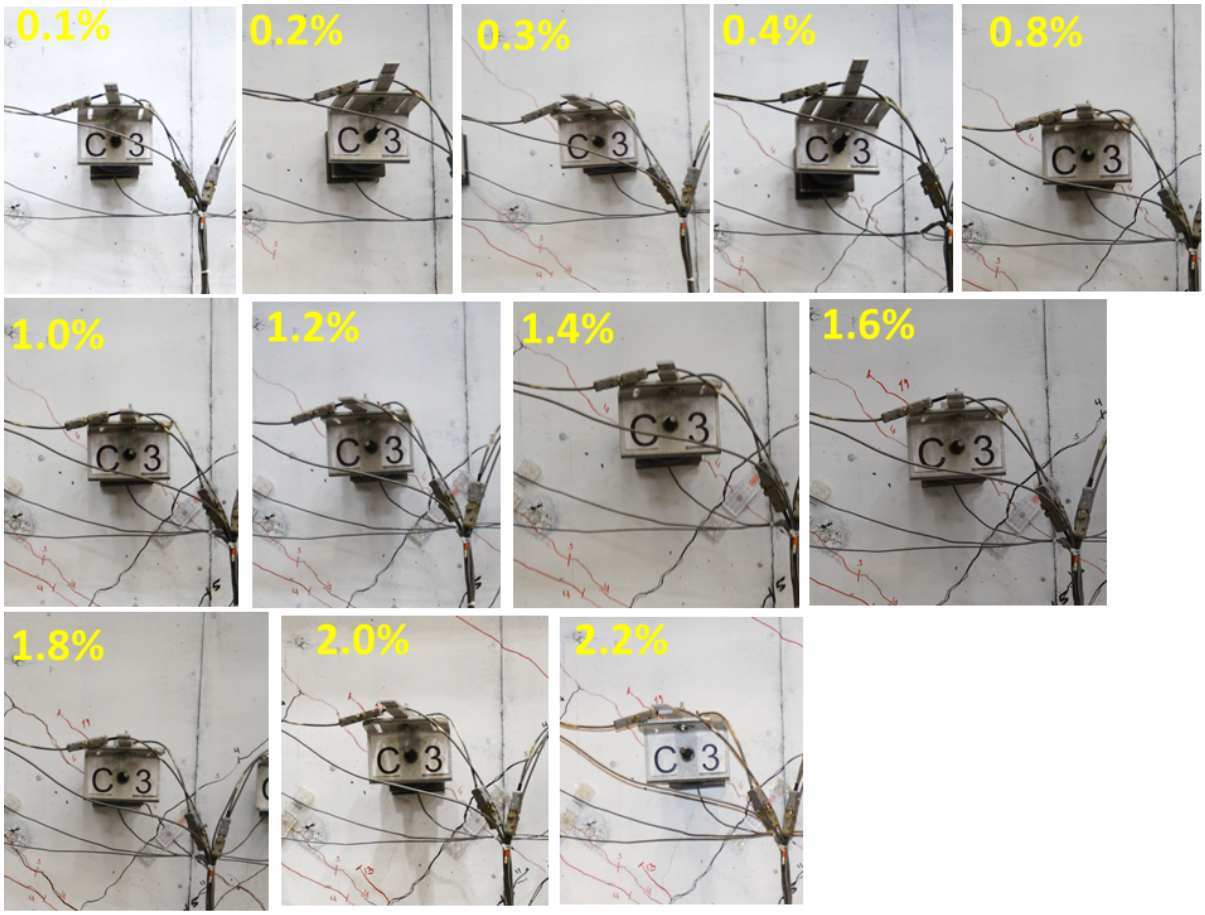


Figure E.164: Wall SQ0: photographs showing the crack evolution around anchor C3

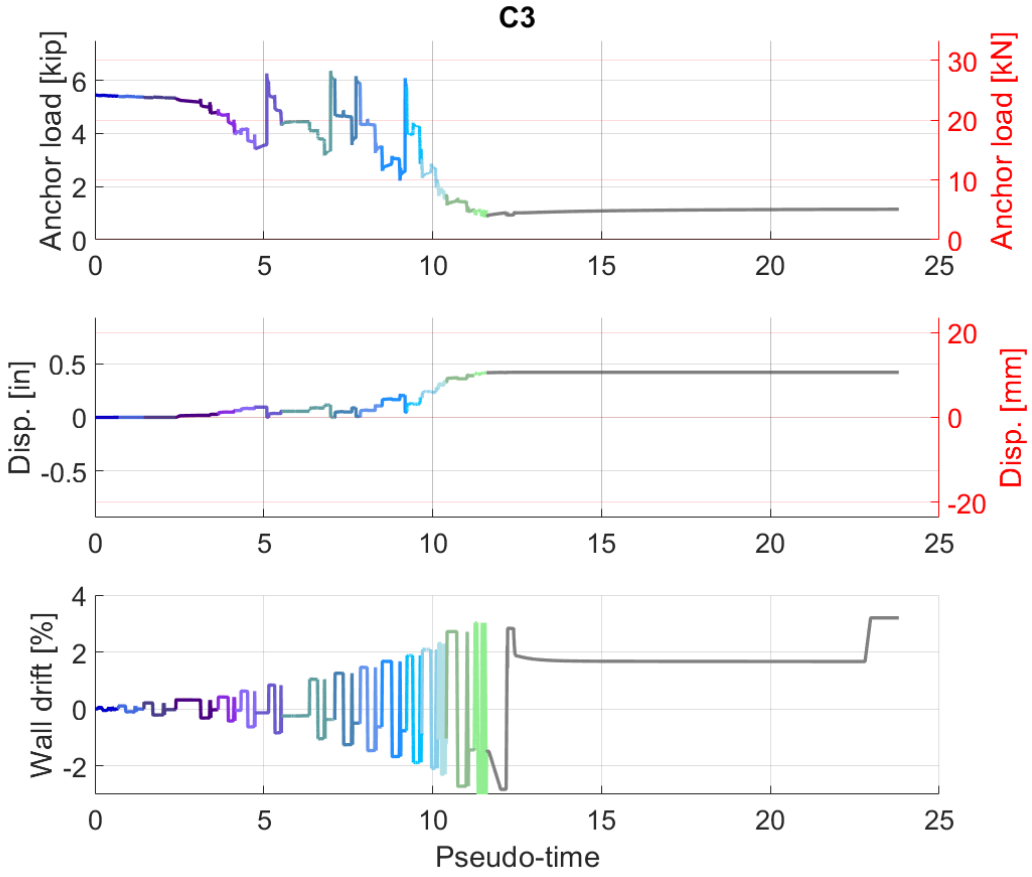
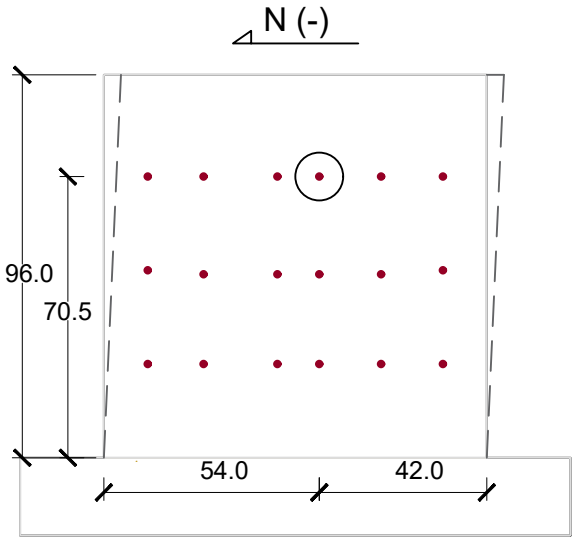


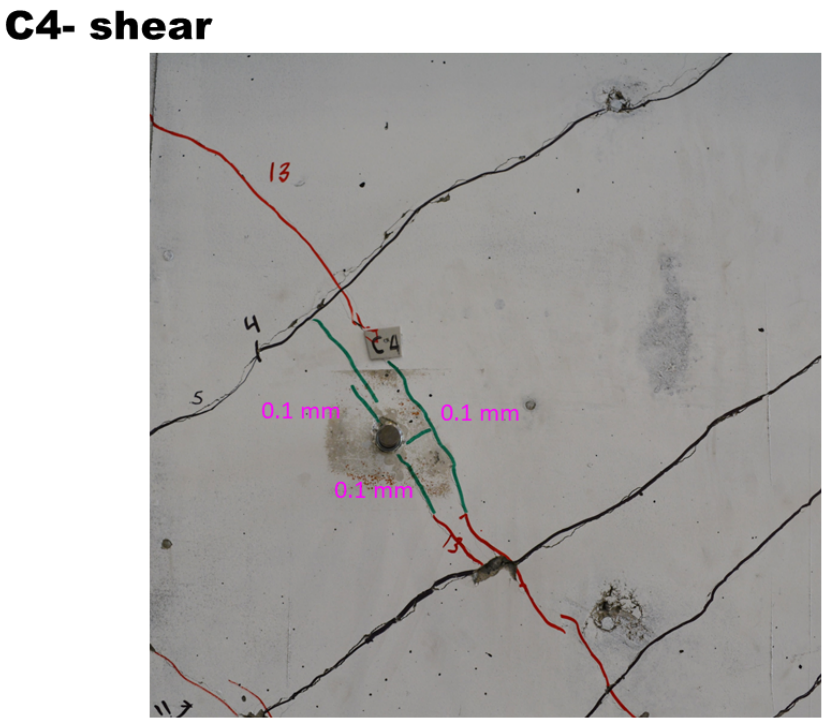
Figure E.165: Wall SQ0, anchor C3: measured load and displacement histories and wall drift history

C4

Fig.E.166b shows that one shear crack crossed torque-controlled expansion anchor C4 during at 2.0% drift cycles. Anchor C4 was located approximately in the middle of a concrete strut formed in the Pull direction, highlighted by two parallel diagonal cracks. Anchor load and global measure displacement remained approximately constant before 2.0% drift ratio, when the crossing shear crack opened around the anchor, as shown in Fig.E.168. At this stage, the load dropped to about 60% of its initial value. The measured global displacement reached its maximum value of 0.2 in. As opposed to the large cracks measured around the adjacent anchors, maximum residual crack width around anchor C4 measured only w_r= 0.1 mm at the end of the test.



(a) Anchor location. Units in inches



(b) Photograph of anchor and cracks at end of test

Figure E.166: Location and photograph of anchor C4 in wall SQ0. Wall residual drift is diagrammatically shown exaggerated for the purpose of illustrating the final context around the anchor

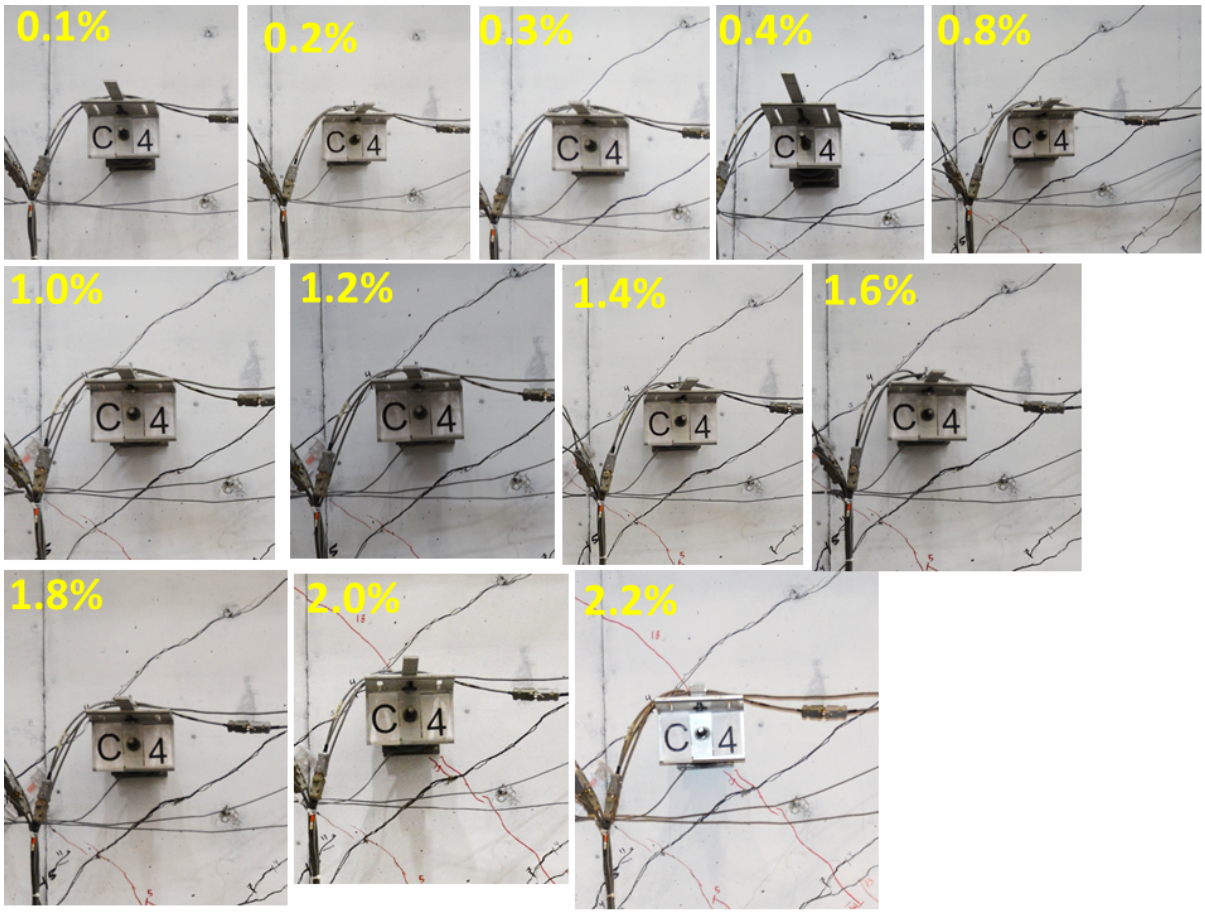


Figure E.167: Wall SQ0: photographs showing the crack evolution around anchor C4

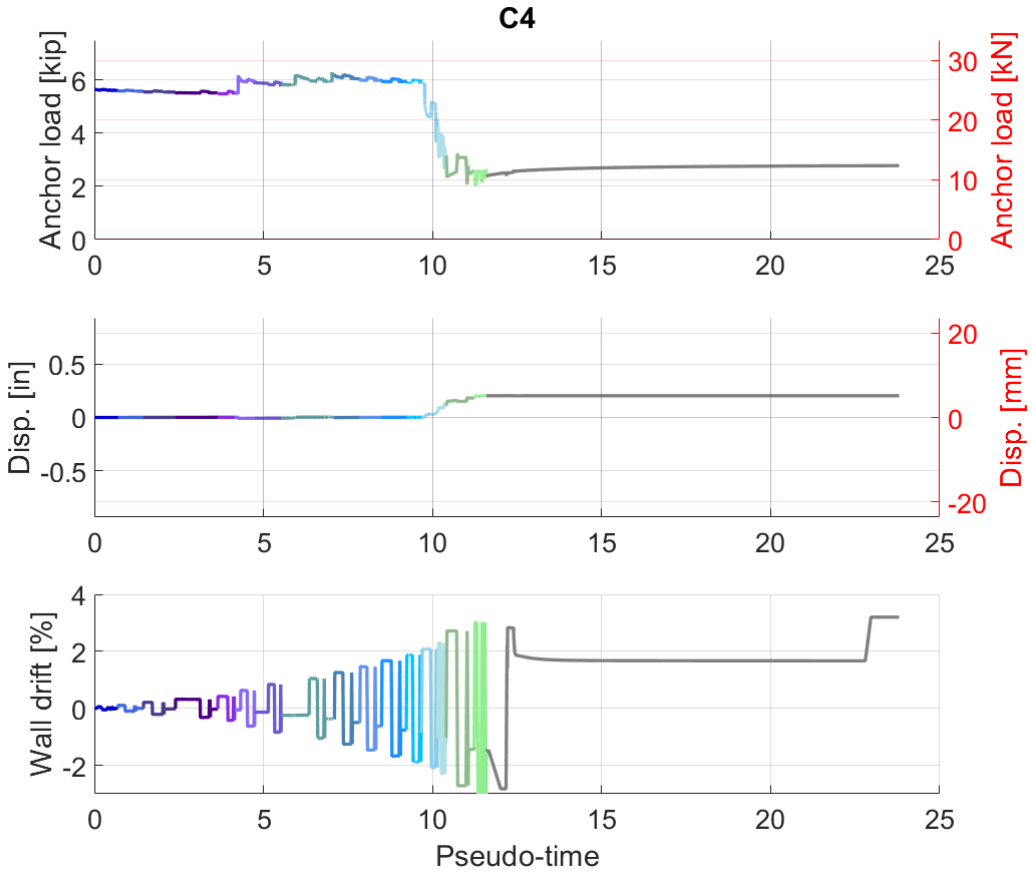
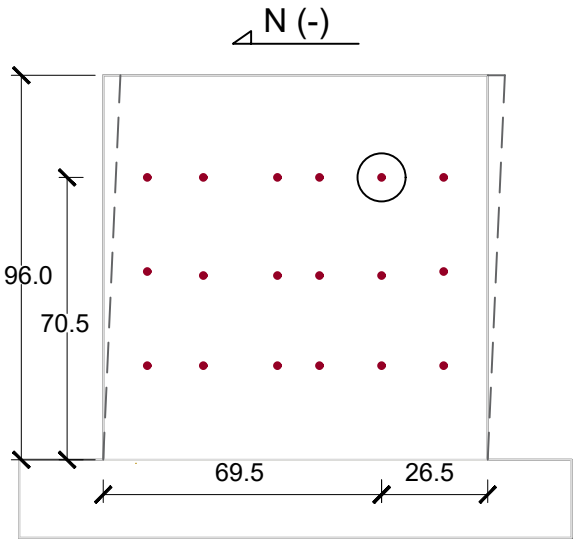


Figure E.168: Wall SQ0, anchor C4: measured load and displacement histories and wall drift history

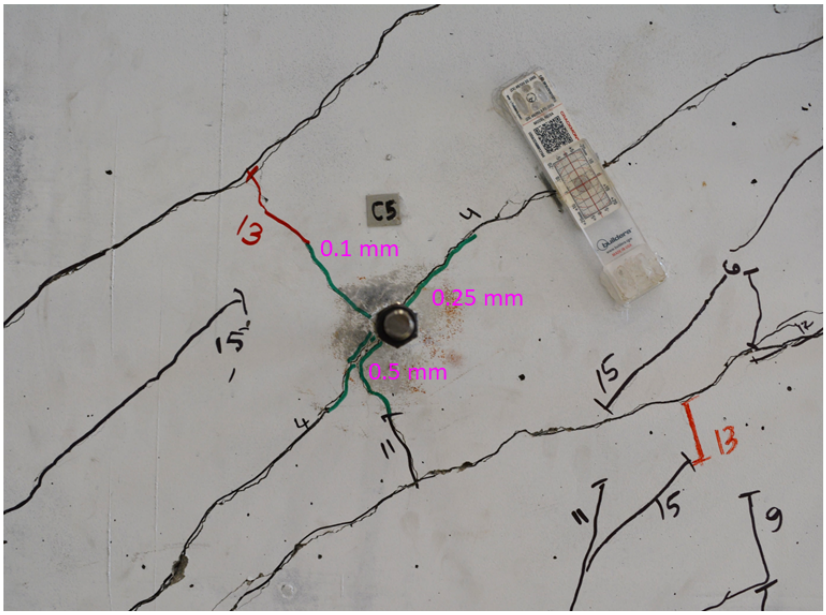
C5

Fig.E.169b shows that one shear crack crossed torque-controlled expansion anchor C5 at 0.3% drift ratio, and a second shear crack opened at 2.0% drift ratio. As for the anchor C4, anchor C5 was located approximately in the middle of the main concrete strut, highlighted by two large parallel diagonal cracks. As shown in Fig.E.171, anchor load was reapplied at the end of 1.0% and 1.2% drift ratios, and at 1.2% drift ratio a steep load reduction was measured. Global displacement presented a constant increasing trend, with maximum value of 0.42 in. Maximum residual crack width measured about 0.5 mm at the end of the test.



(a) Anchor location. Units in inches

C5- shear



(b) Photograph of anchor and cracks at end of test

Figure E.169: Location and photograph of anchor C5 in wall SQ0. Wall residual drift is diagrammatically shown exaggerated for the purpose of illustrating the final context around the anchor

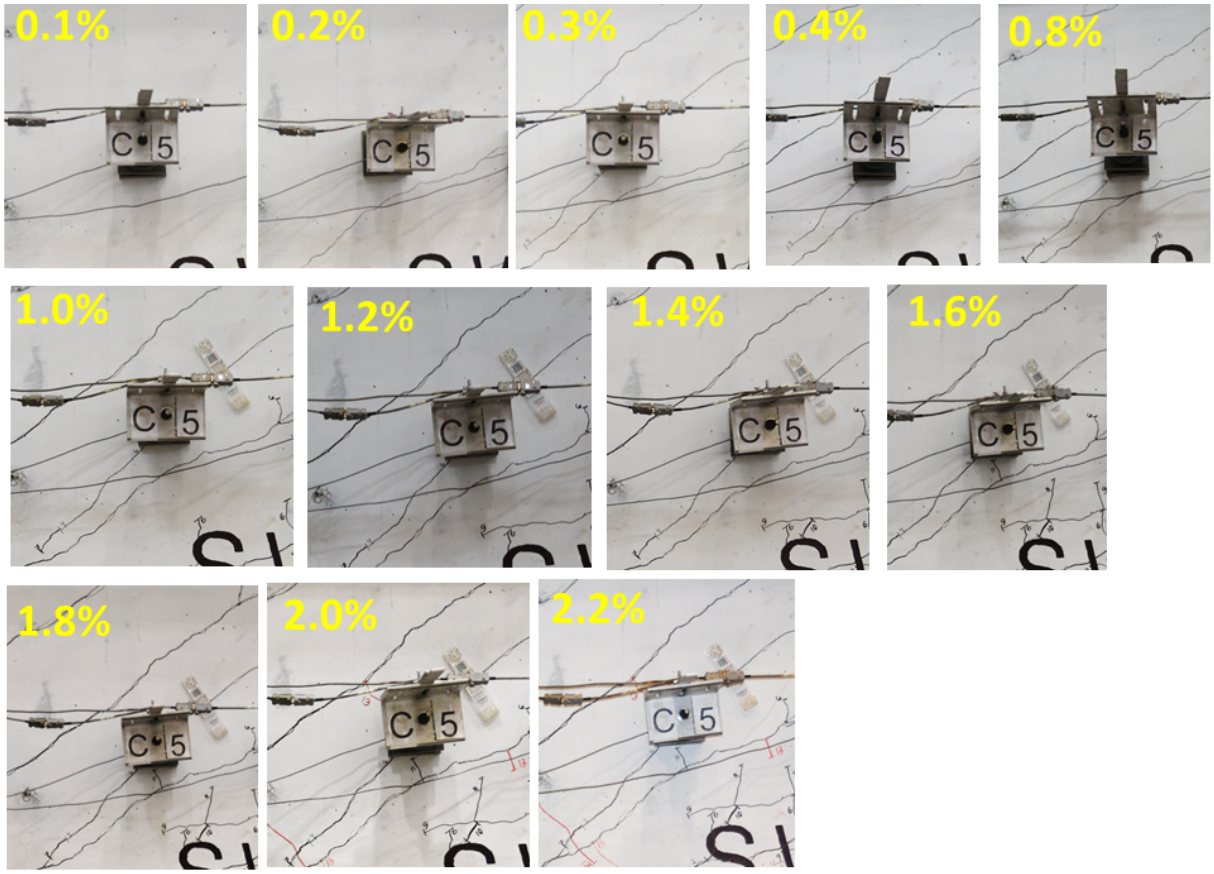


Figure E.170: Wall SQ0: photographs showing the crack evolution around anchor C5

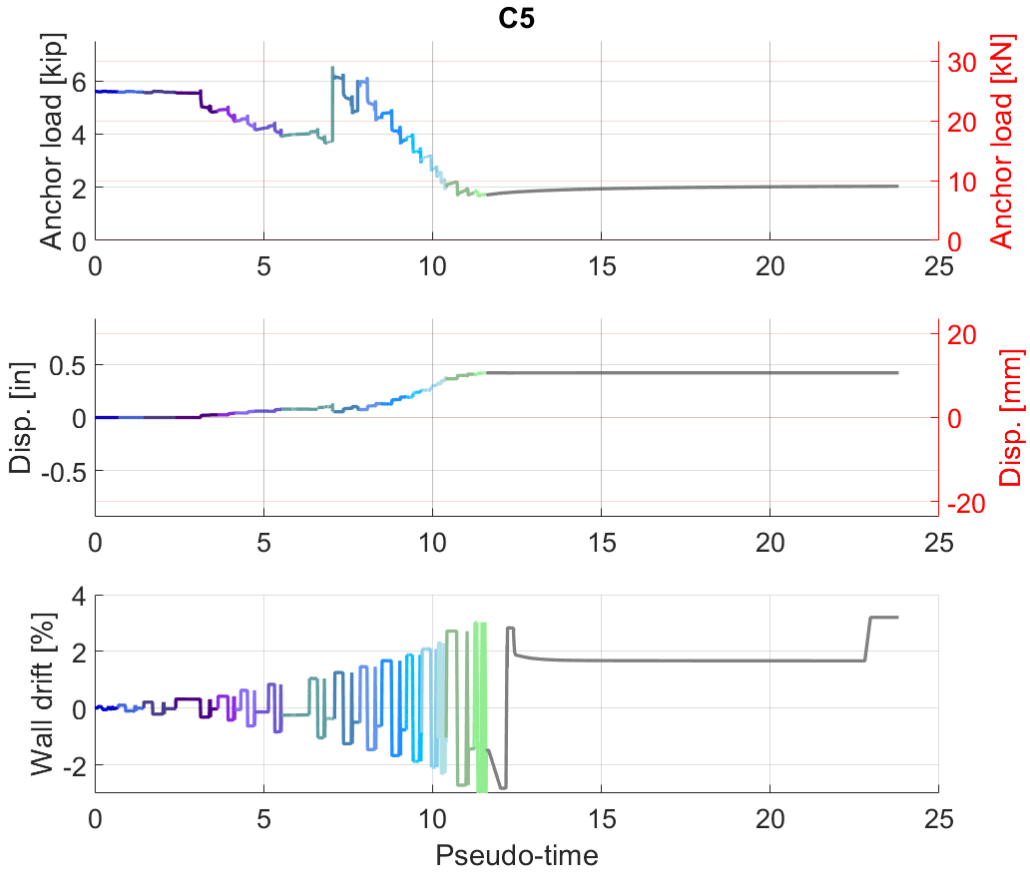
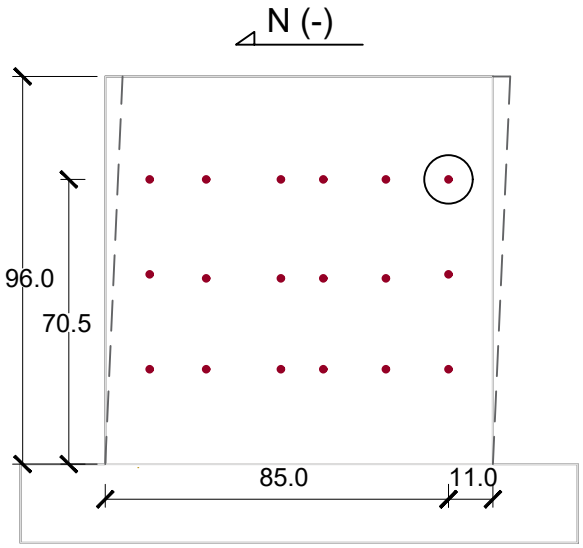


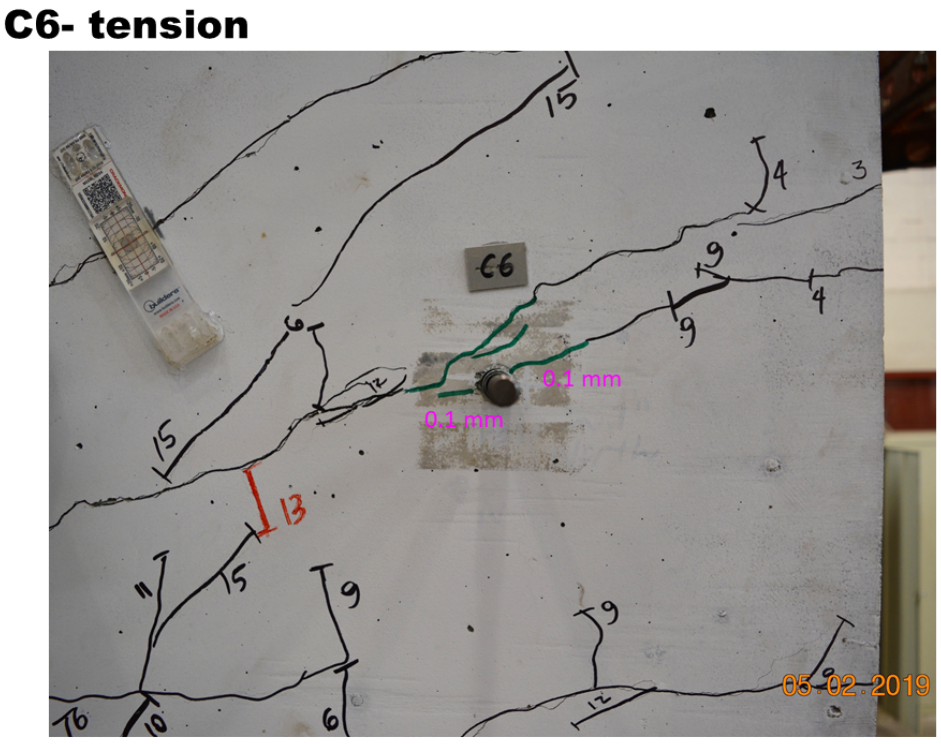
Figure E.171: Wall SQ0, anchor C5: measured load and displacement histories and wall drift history

C6

Fig.E.172b shows that one tension-shear crack crossed torque-controlled expansion anchor C6, during the 0.2% drift cycles. Small extension cracks developed as the wall drift demand increased. Fig.E.174 shows that anchor load reduced significantly as the drift demand on the wall increased, similarly to adjacent anchors. To maintain constant tension on the anchor, load was reapplied at the end of 0.6% and 1.2% drift ratios. Global displacement presented a constant increasing trend, and maximum value of 0.14 in was measured before reloading at 1.2% drift, when the displacement sensor was damaged. Maximum residual crack width at the end of the test was w_r= 0.1 mm.



(a) Anchor location



(b) Photograph of anchor and cracks at end of test

Figure E.172: Location and photograph of anchor C6 in wall SQ0. Wall residual drift is diagrammatically shown exaggerated for the purpose of illustrating the final context around the anchor

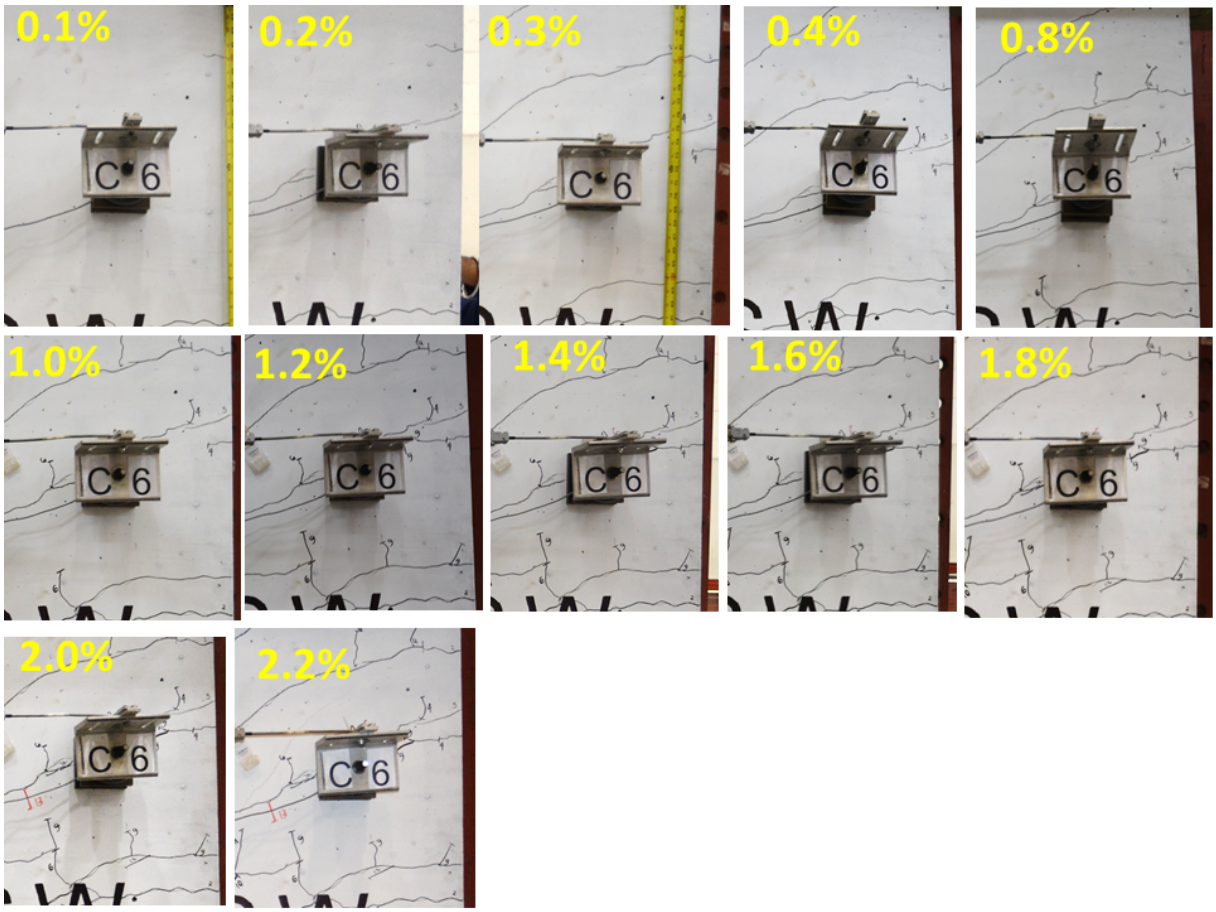


Figure E.173: Wall SQ0: photographs showing the crack evolution around anchor C6

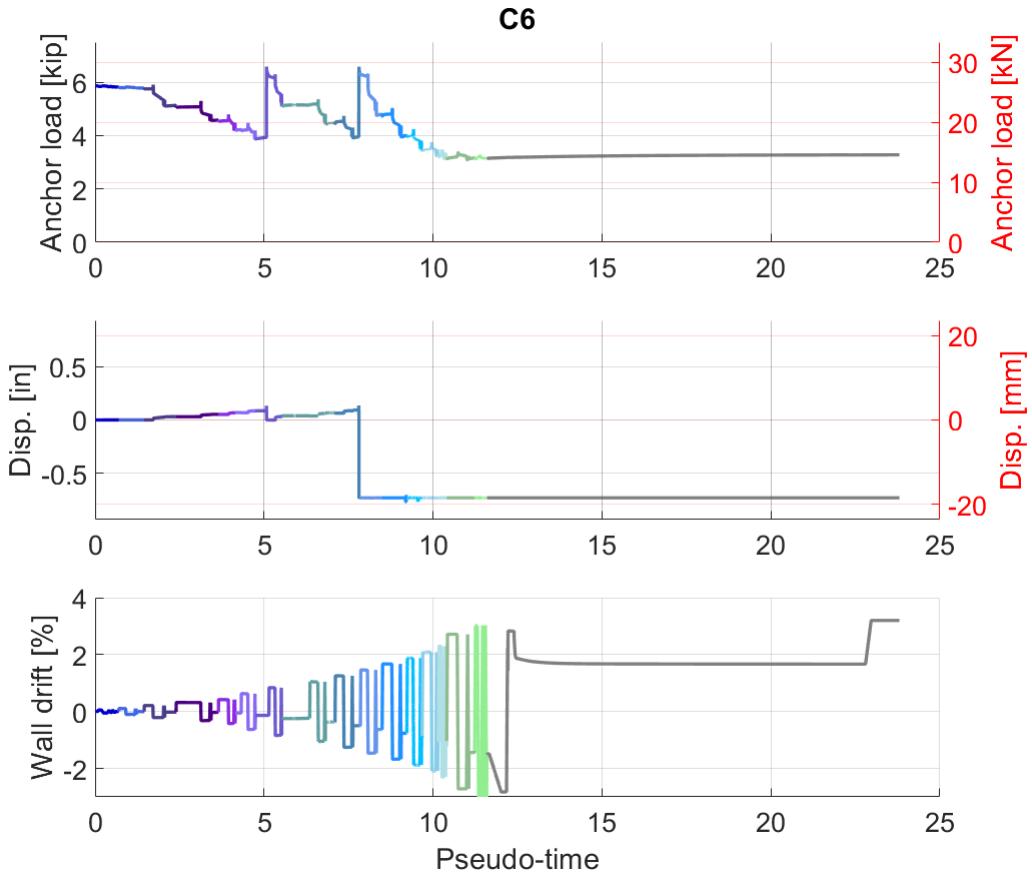


Figure E.174: Wall SQ0, anchor C6: measured load and displacement histories and wall drift history



Figure E.175: Wall SQ0: photographs showing the crack evolution around row C during the last three drift demands

E.2 Anchor Residual Capacity Curves

The load-displacement curves from pullout tests are reported in this section together with photographs of each anchor and of the concrete surface cone developed from the pullout. Summary and statistics of the load reduction for each anchor type and for each wall are also presented in this section.

E.2.1 Slender Wall SL7.5

Bonded Anchors

The load-displacement curves from pull-out tests (not normalized) are reported in Figs. E.176 to E.186. Normalized values to account for the two different concrete ages at time of tests are presented in the summaries of Figs. E.187 to E.190, where anchors are categorized in terms of crossing cracks. Note that the anchors that lied in residual crack widths larger than w_r= 0.1 mm (outliers) were excluded from the statistics. In particular, anchors A1, A2 and A3 were installed at 2 ft (0.125 h_w) from the wall-footing interface, where a dense crack pattern and large crack widths developed during the test. The residual capacity of these anchor tests was significantly lower compared to the other anchors of the same category (i.e., type of crossing crack), due to proximity to spalled regions of concrete, thus they were not considered in the calculation of the statistics. Anchor B1 load capacity was lower than anchors C1 and F1 (pulled-out in the second phase of testing).

Expansion Anchors

The load-displacement curves from pull-out tests (not normalized) are reported in Figs. E.191 to E.201. Anchors which lied in residual crack widths larger than w_r= 0.1 mm (outliers) are excluded from the statistics. Normalized values to account for the two different concrete ages at time of tests are presented in the summaries of Figs. E.202 to E.205, where anchors were categorized in terms of crossing cracks.

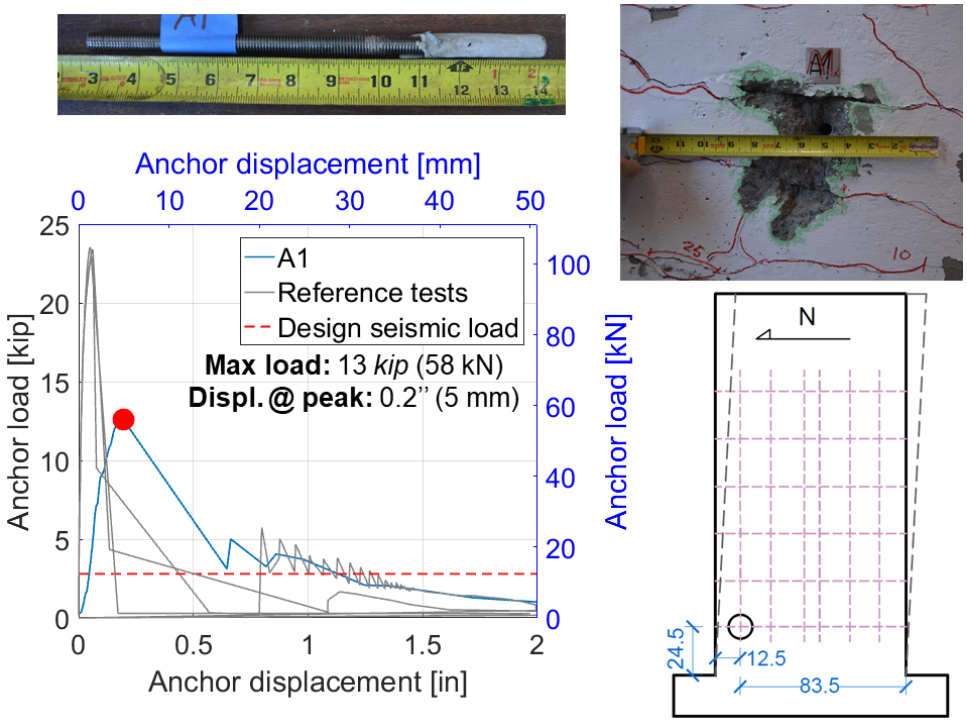


Figure E.176: Anchor A1 in wall SL7.5: Load-displacement pullout curve and photographs of the cone of failure and of the pulled anchor

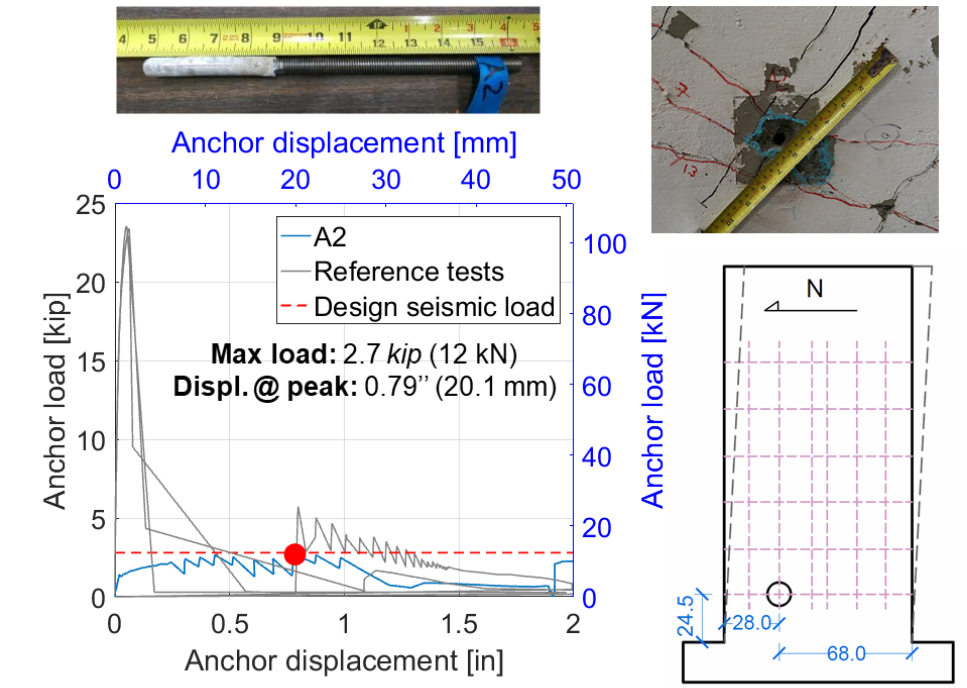


Figure E.177: Anchor A2 in wall SL7.5: Load-displacement pullout curve and photographs of the cone of failure and of the pulled anchor

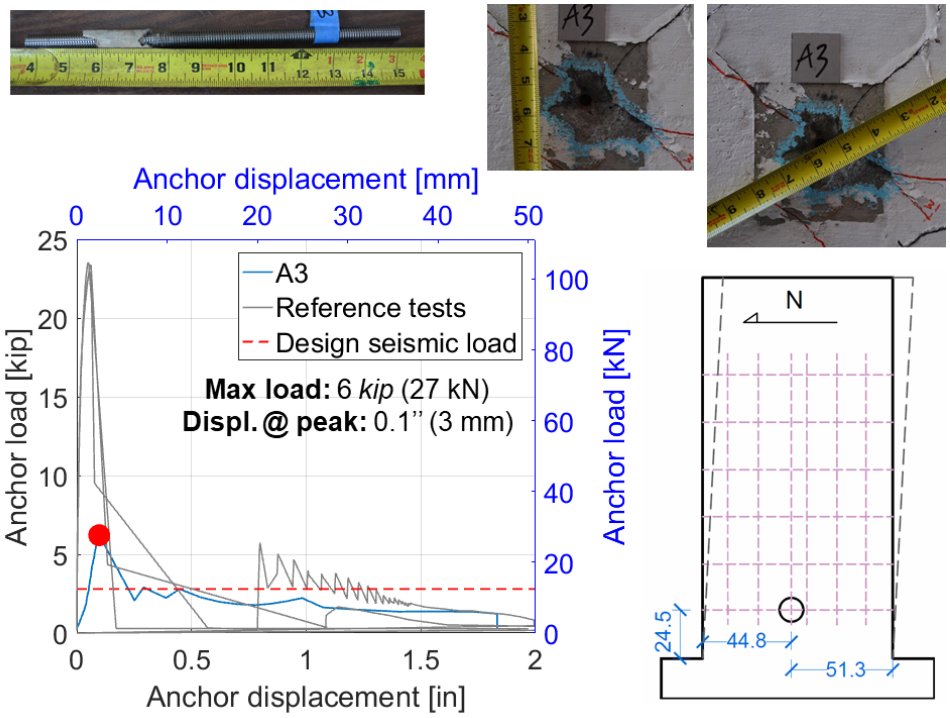


Figure E.178: Anchor A3 in wall SL7.5: Load-displacement pullout curve and photographs of the cone of failure and of the pulled anchor

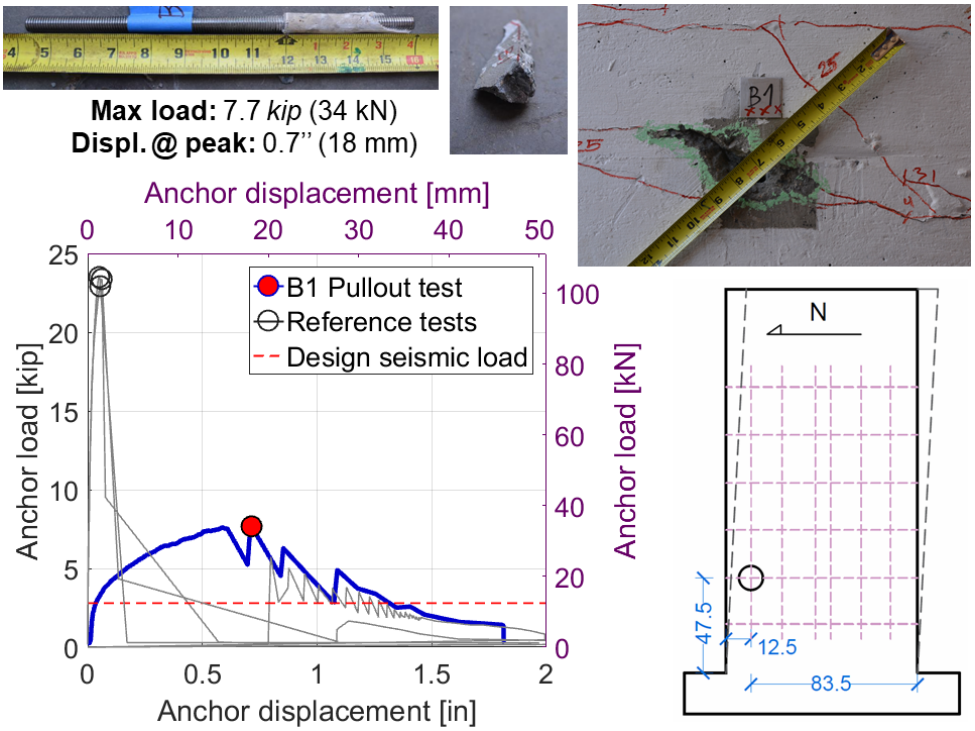


Figure E.179: Anchor B1 in wall SL7.5: Load-displacement pullout curve and photographs of the cone of failure and of the pulled anchor

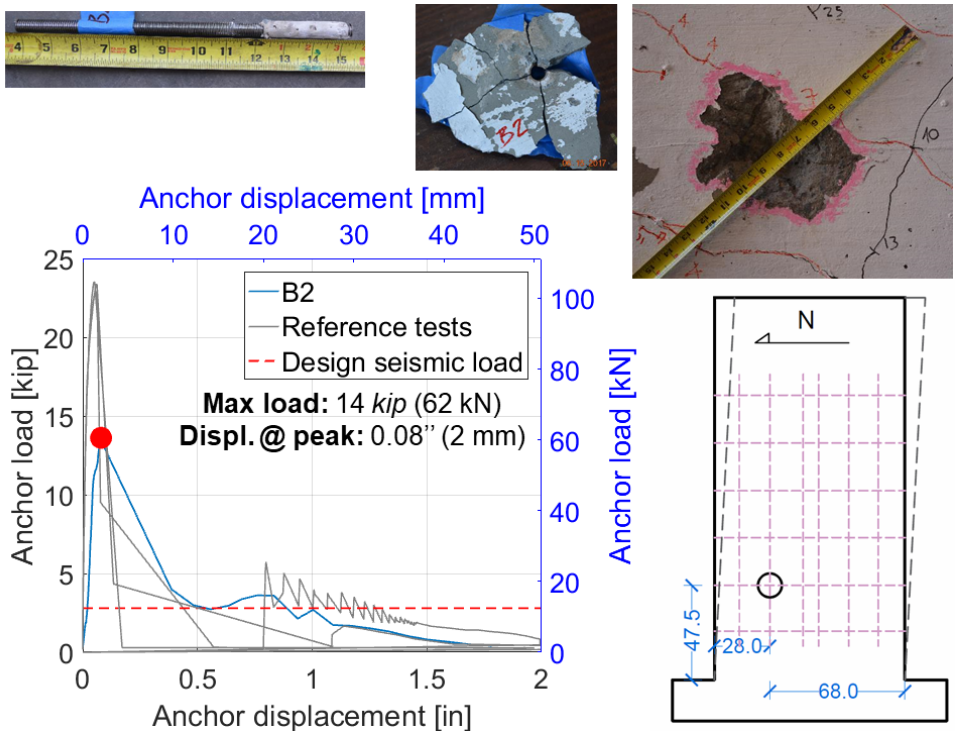


Figure E.180: Anchor B2 in wall SL7.5: Load-displacement pullout curve and photographs of the cone of failure and of the pulled anchor

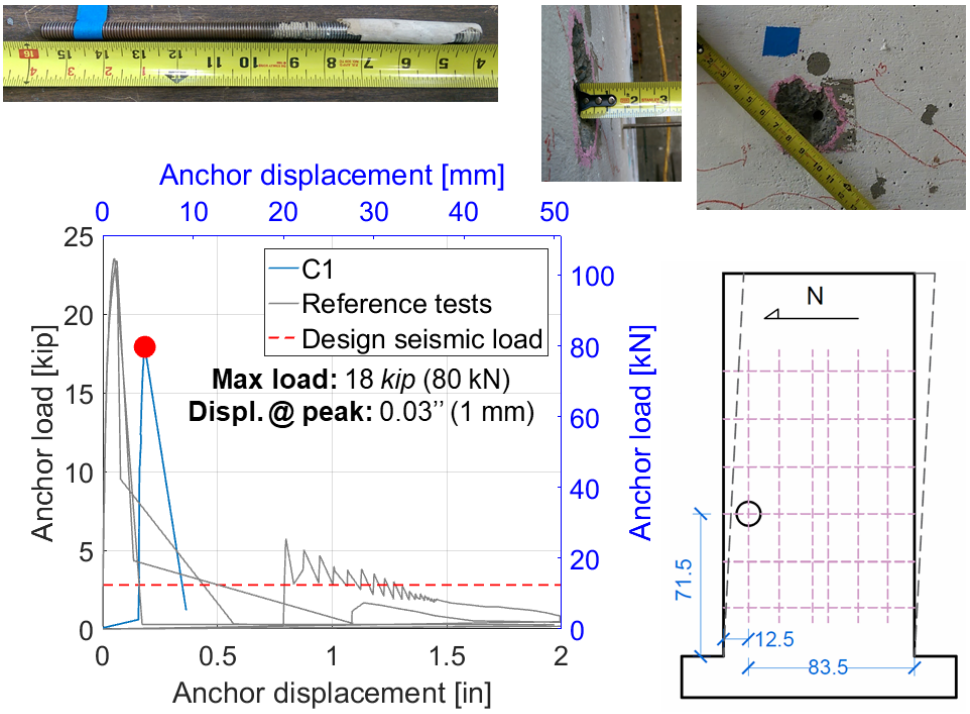


Figure E.181: Anchor C1 in wall SL7.5: Load-displacement pullout curve and photographs of the cone of failure and of the pulled anchor

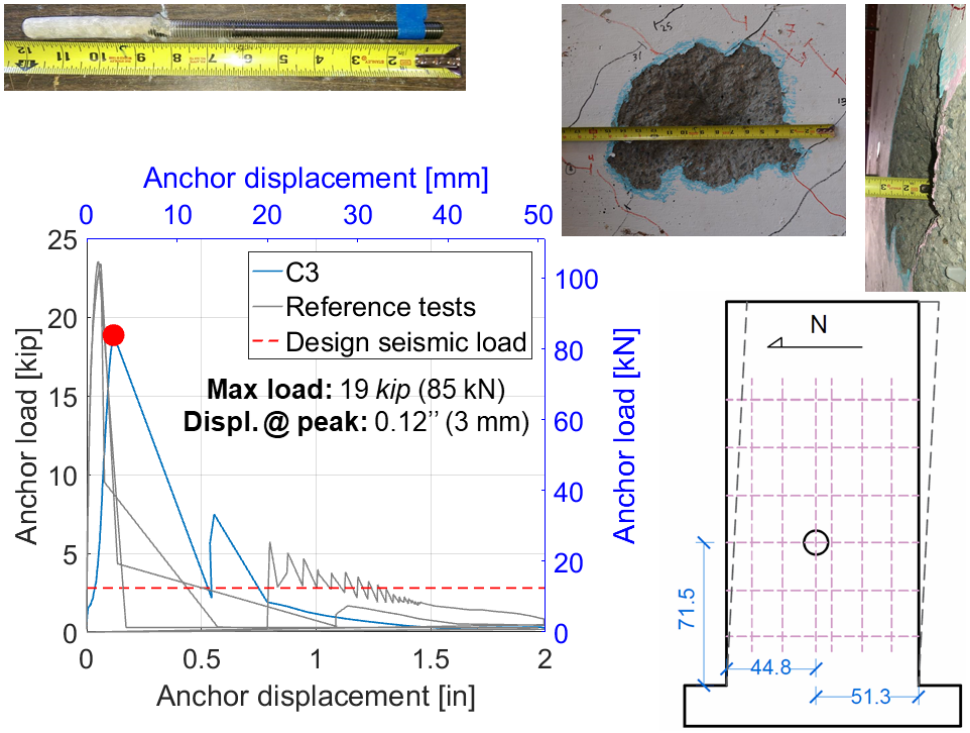


Figure E.182: Anchor C3 in wall SL7.5: Load-displacement pullout curve and photographs of the cone of failure and of the pulled anchor

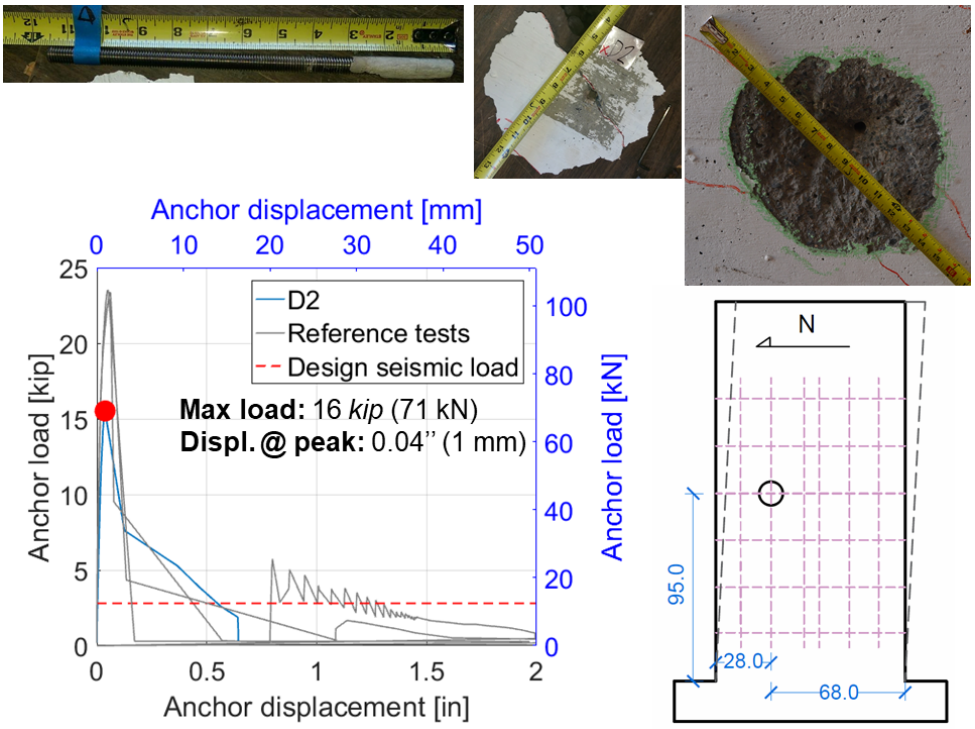


Figure E.183: Anchor D2 in wall SL7.5: Load-displacement pullout curve and photographs of the cone of failure and of the pulled anchor

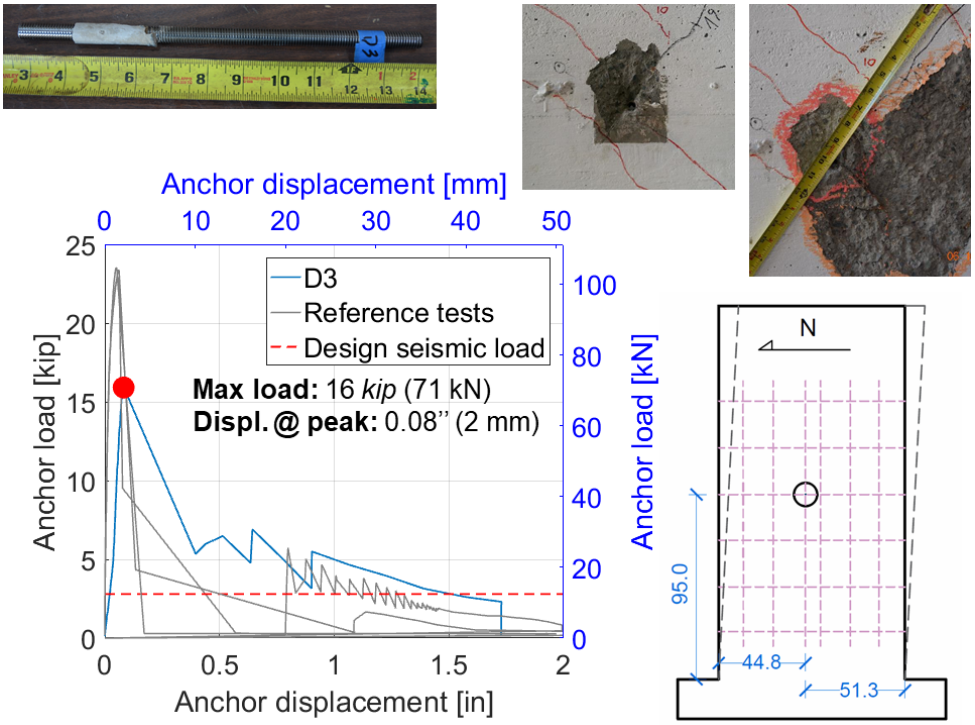


Figure E.184: Anchor D3 in wall SL7.5: Load-displacement pullout curve and photographs of the cone of failure and of the pulled anchor

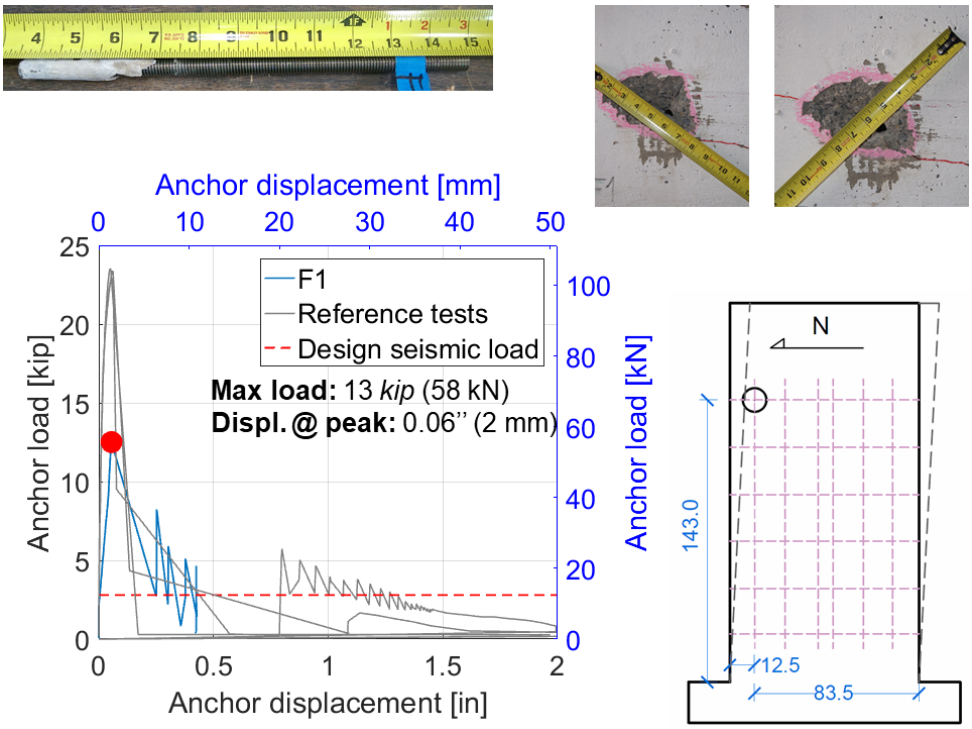


Figure E.185: Anchor F1 in wall SL7.5: Load-displacement pullout curve and photographs of the cone of failure and of the pulled anchor

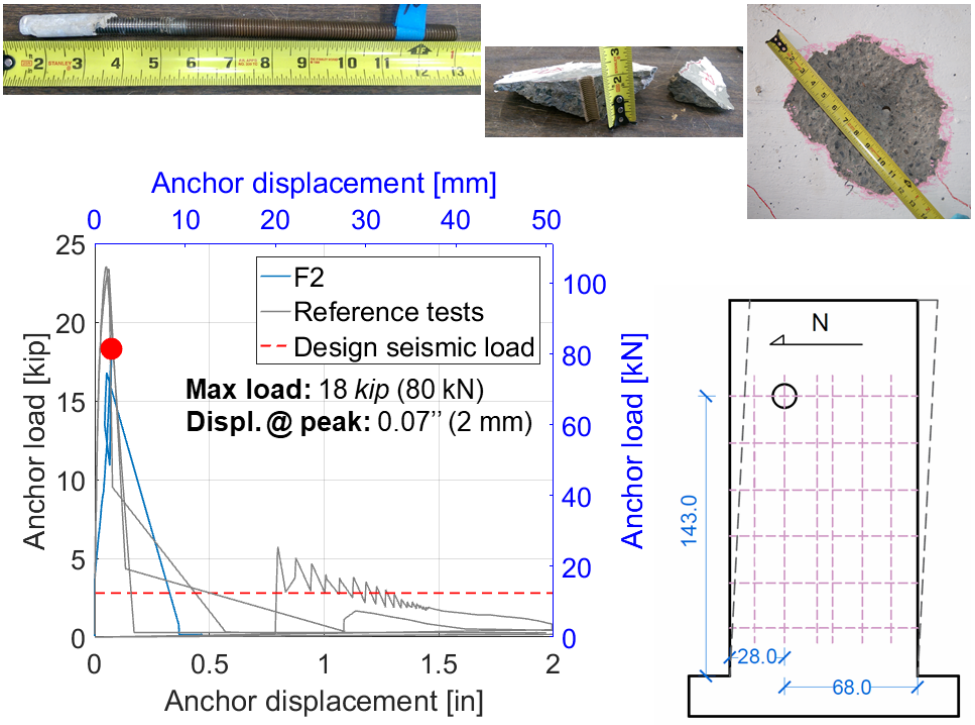
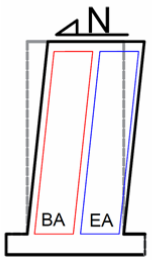


Figure E.186: Anchor F2 in wall SL7.5: Load-displacement pullout curve and photographs of the cone of failure and of the pulled anchor

	Displ.		Load	
Min	[in] [mm]	0.08 2	[kip] [kN]	13 56
Max	[in] [mm]	0.20 5	[kip] [kN]	19 84
Mean	[in] [mm]	0.13 3	[kip] [kN]	15 67
STD	[in] [mm]	0.06 2	[kip] [kN]	3 15
CV	[%]	45	[%]	22

Average from ref. tests (uncracked):
23.5 k *(104.5 kN)*, **0.06 "** (1 mm)



C3: Max load: 19 *kip* (85 kN)
Displ. @ peak: 0.12" (3 mm)

B2: Max load: 14 *kip* (62 kN)
Displ. @ peak: 0.08" (2 mm)

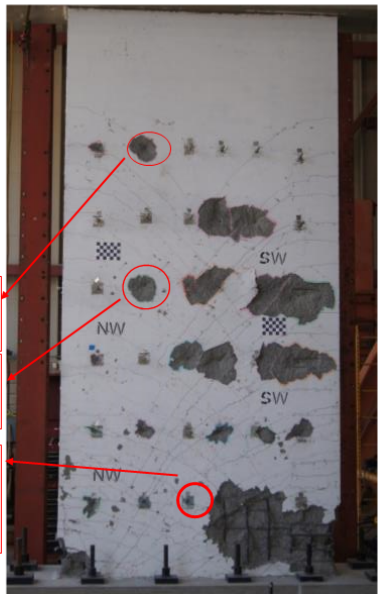
A1: Max load: 13 *kip* (58 kN)
Displ. @ peak: 0.2" (5 mm)

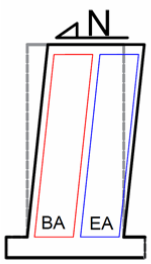


Figure E.187: Summary and statistics of the residual capacities of bonded anchors residing in no cracks at the end of the slender wall SL7.5 test. Note: the load values are normalized for the concrete strength

	Displ.		Load	
Min	[in] [mm]	0.04 1	[kip] [kN]	16 69
Max	[in] [mm]	0.07 2	[kip] [kN]	16 73
Mean	[in] [mm]	0.06 1	[kip] [kN]	16 71
STD	[in] [mm]	0.03 1	[kip] [kN]	1 3
CV	[%]	46	[%]	4

Average from ref. tests (uncracked):
23.5 k *(104.5 kN)*, **0.06 ‘’** (1 mm)





F2: Max load: 16 *kip* (73 kN)
Displ. @ peak: 0.07’’ (2 mm)

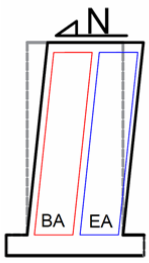
D2: Max load: 16 *kip* (69 kN)
Displ. @ peak: 0.04’’ (1 mm)

A3 (outlier): Max load: 6 *kip* (27 kN)
Displ. @ peak: 0.1’’ (3 mm)

Figure E.188: Summary and statistics of the residual capacities of bonded anchors residing in one or more shear cracks at the end of the slender wall SL7.5 test. Note: the load values are normalized for the concrete strength

	Displ.		Load	
Min	[in] [mm]	0.03 1	[kip] [kN]	11 50
Max	[in] [mm]	0.06 1	[kip] [kN]	16 72
Mean	[in] [mm]	0.04 1	[kip] [kN]	14 61
STD	[in] [mm]	0.02 0	[kip] [kN]	3 15
CV	[%]	47	[%]	25

Average from ref. tests (uncracked):
23.5 k *(104.5 kN)*, **0.06 ‘’** (1 mm)



F1: Max load: 11 *kip* (58 kN)
Displ. @ peak: 0.06” (2 mm)

C1: Max load: 16 *kip* (80kN)
Displ. @ peak: 0.03” (1 mm)

B1 (outlier): Max load: 7.7 *kip* (34 kN)
Displ. @ peak: 0.71” (18 mm)

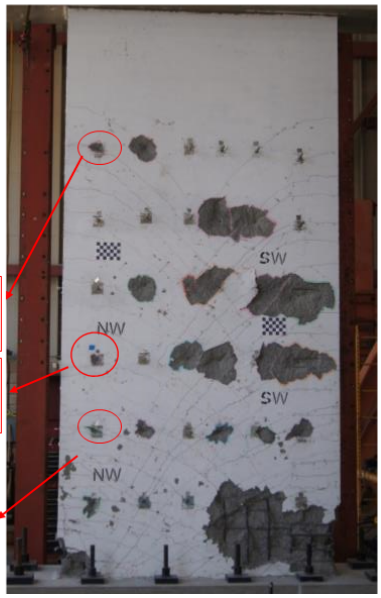


Figure E.189: Summary and statistics of the residual capacities of bonded anchors residing in one or more tension cracks at the end of the slender wall SL7.5 test. Note: the load values are normalized for the concrete strength

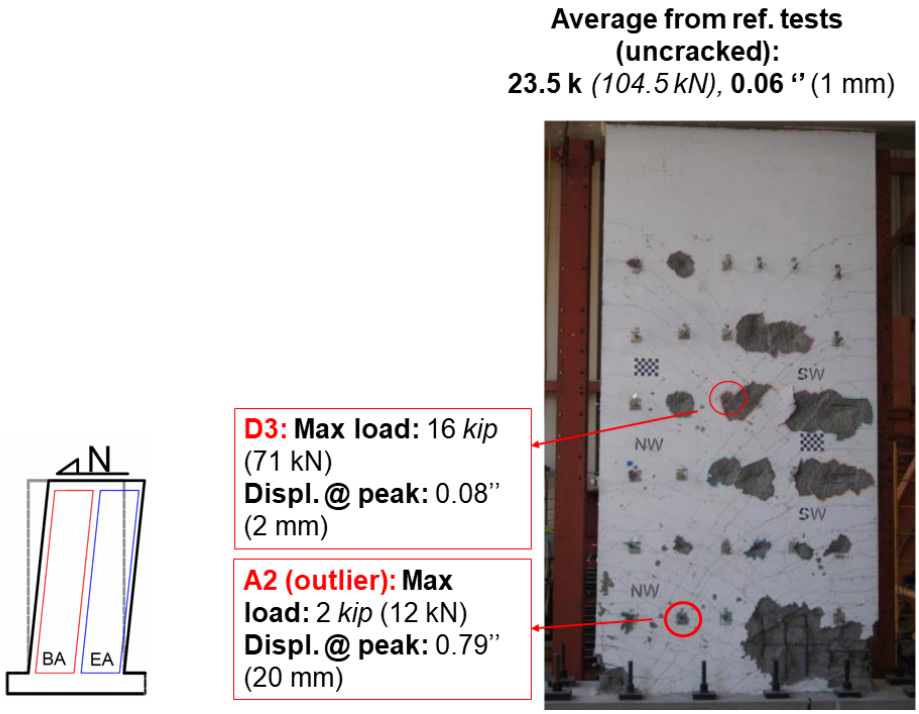


Figure E.190: Summary and statistics of the residual capacities of bonded anchors residing in X crossing shear cracks at the end of the slender wall SL7.5 test. Note: the load values are normalized for the concrete strength

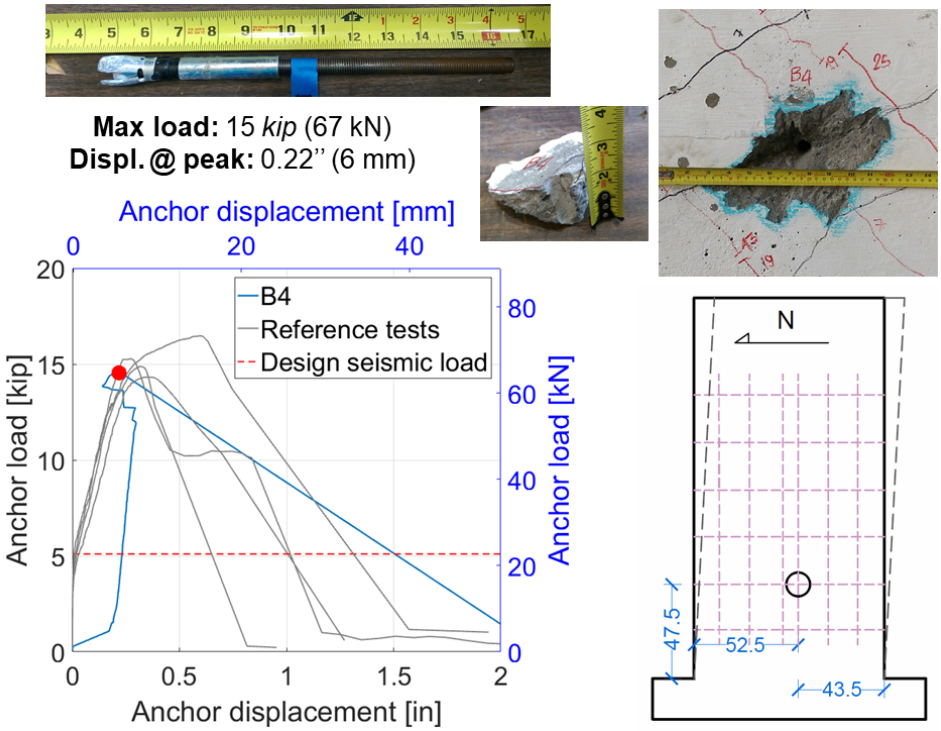


Figure E.191: Anchor B4 in wall SL7.5: Load-displacement pullout curve and photographs of the cone of failure and of the pulled anchor

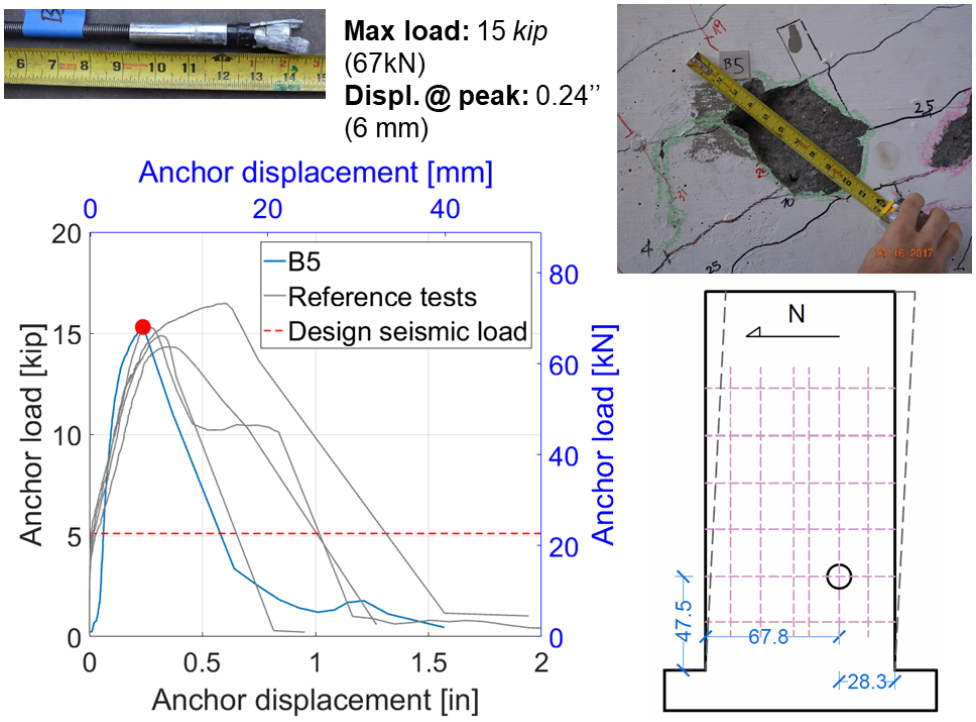


Figure E.192: Anchor B5 in wall SL7.5: Load-displacement pullout curve and photographs of the cone of failure and of the pulled anchor

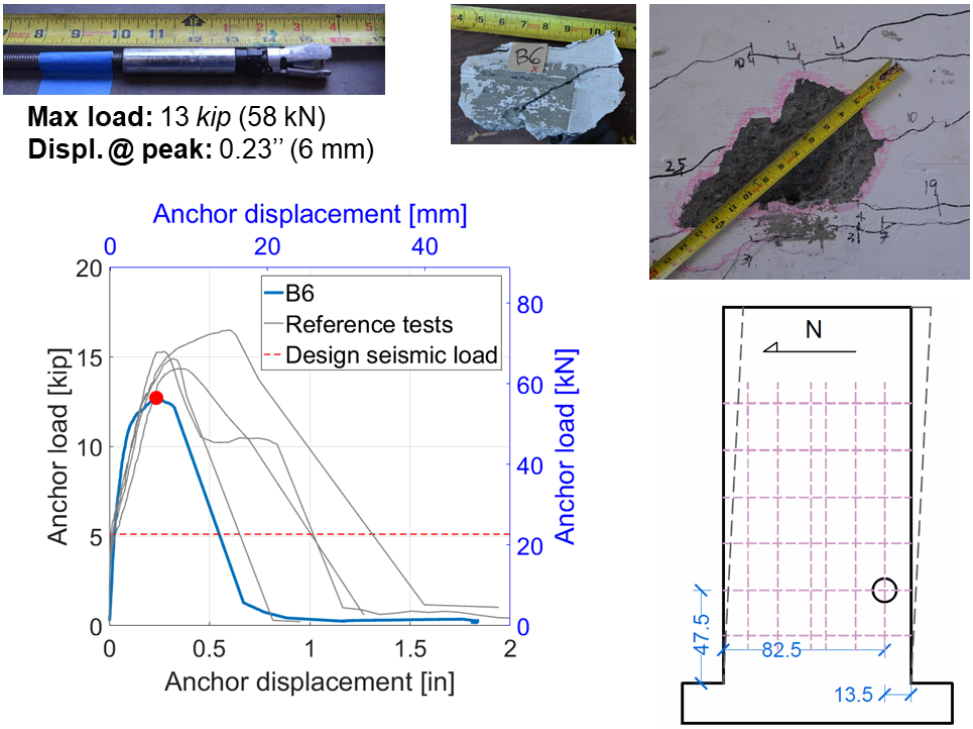


Figure E.193: Anchor B6 in wall SL7.5: Load-displacement pullout curve and photographs of the cone of failure and of the pulled anchor

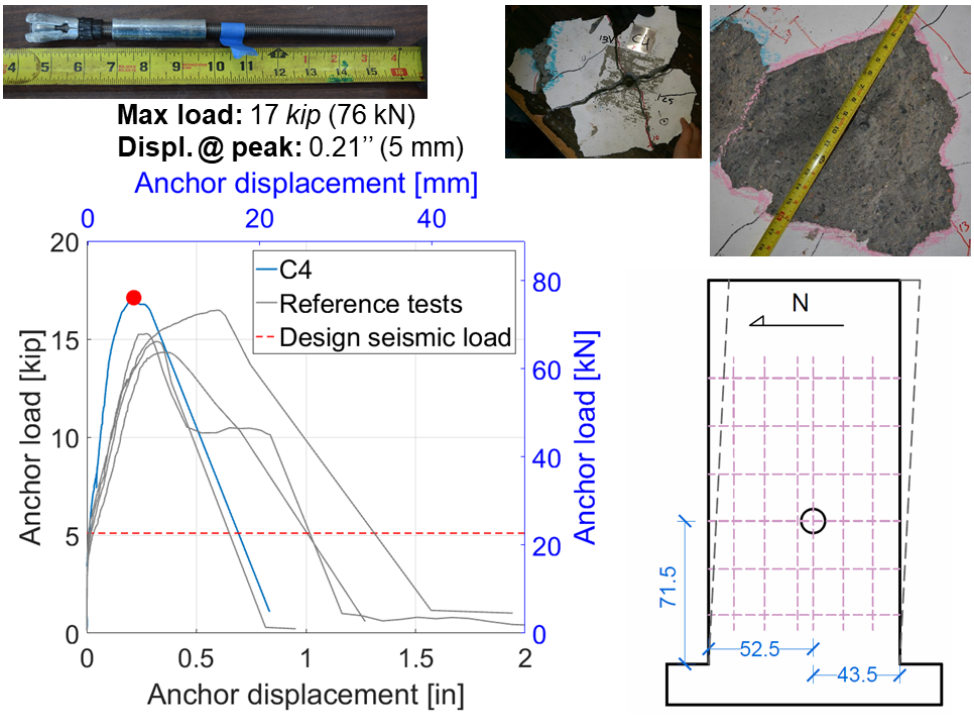


Figure E.194: Anchor C4 in wall SL7.5: Load-displacement pullout curve and photographs of the cone of failure and of the pulled anchor

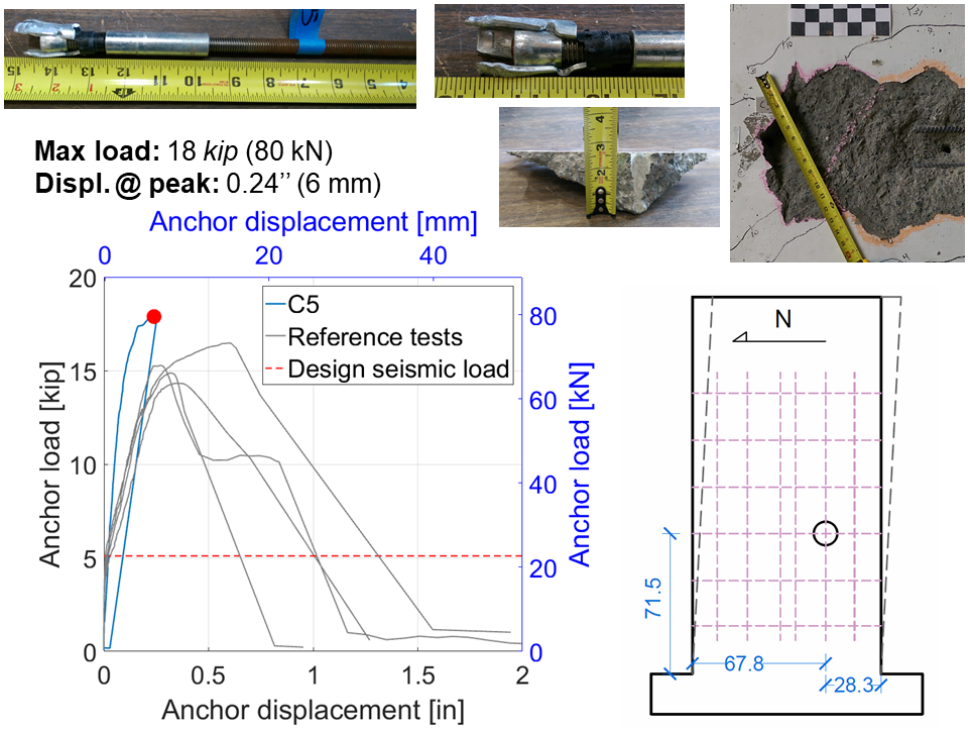


Figure E.195: Anchor C5 in wall SL7.5: Load-displacement pullout curve and photographs of the cone of failure and of the pulled anchor

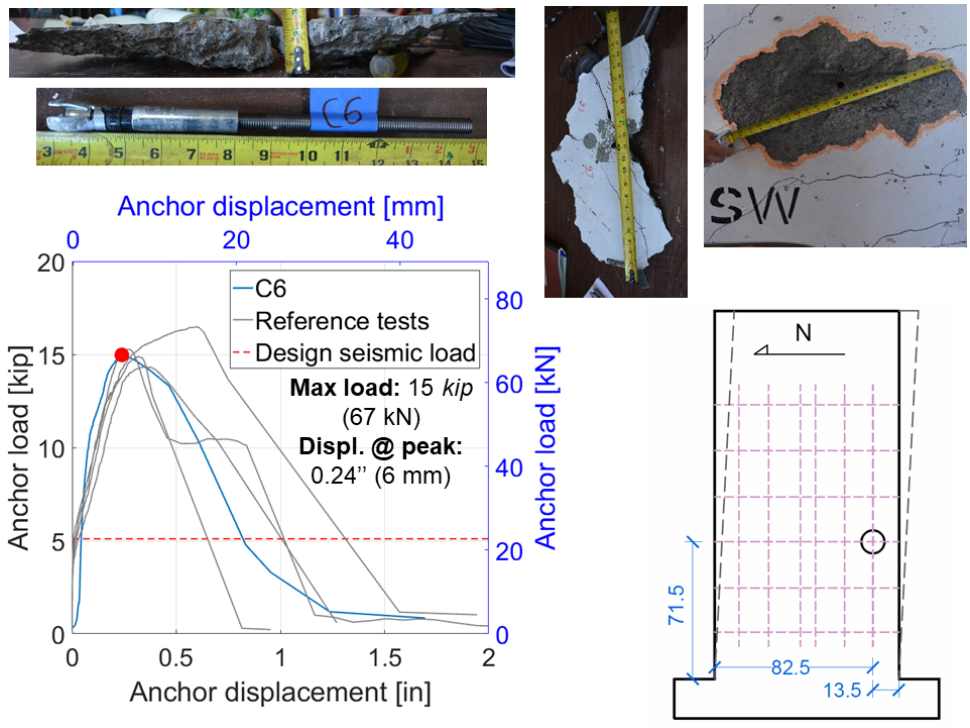


Figure E.196: Anchor C6 in wall SL7.5: Load-displacement pullout curve and photographs of the cone of failure and of the pulled anchor

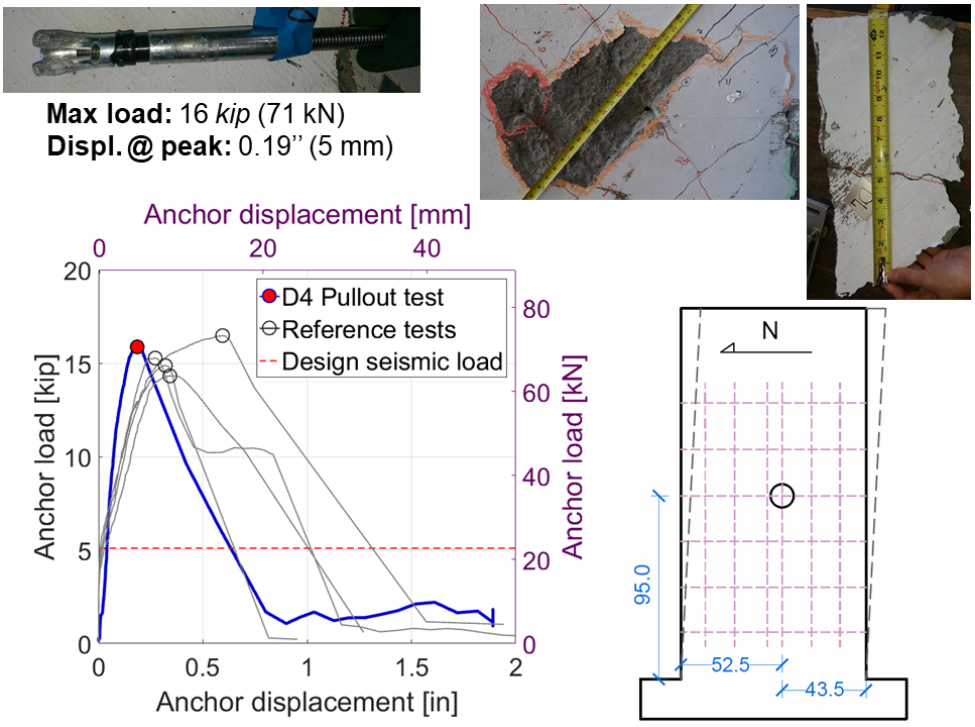


Figure E.197: Anchor D4 in wall SL7.5: Load-displacement pullout curve and photographs of the cone of failure and of the pulled anchor

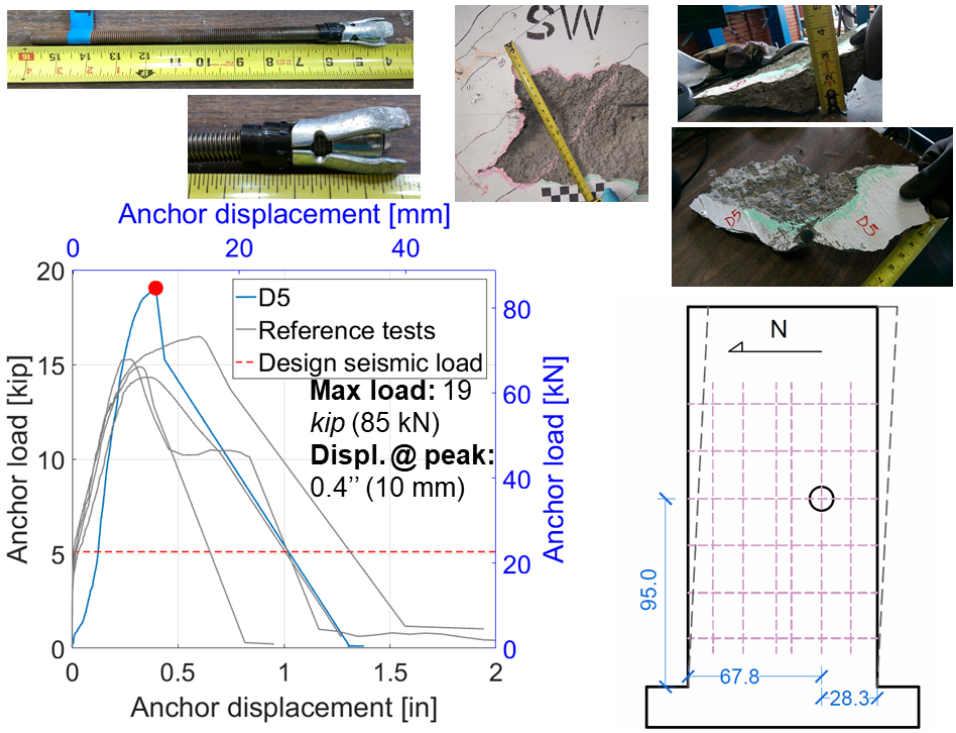


Figure E.198: Anchor D5 in wall SL7.5: Load-displacement pullout curve and photographs of the cone of failure and of the pulled anchor

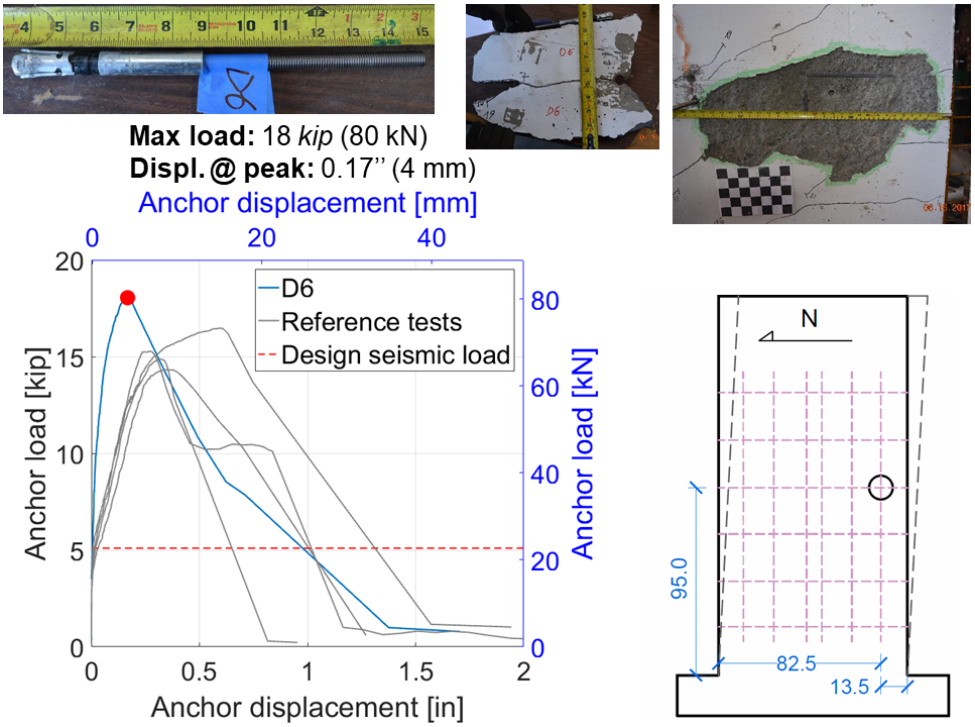


Figure E.199: Anchor D6 in wall SL7.5: Load-displacement pullout curve and photographs of the cone of failure and of the pulled anchor

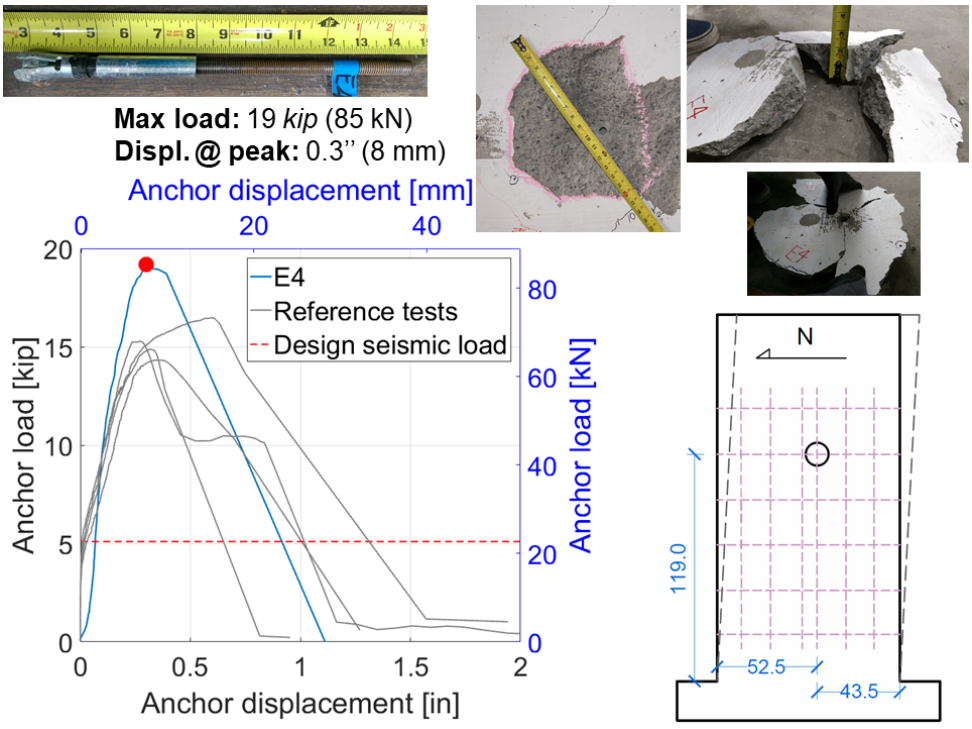


Figure E.200: Anchor E4 in wall SL7.5: Load-displacement pullout curve and photographs of the cone of failure and of the pulled anchor

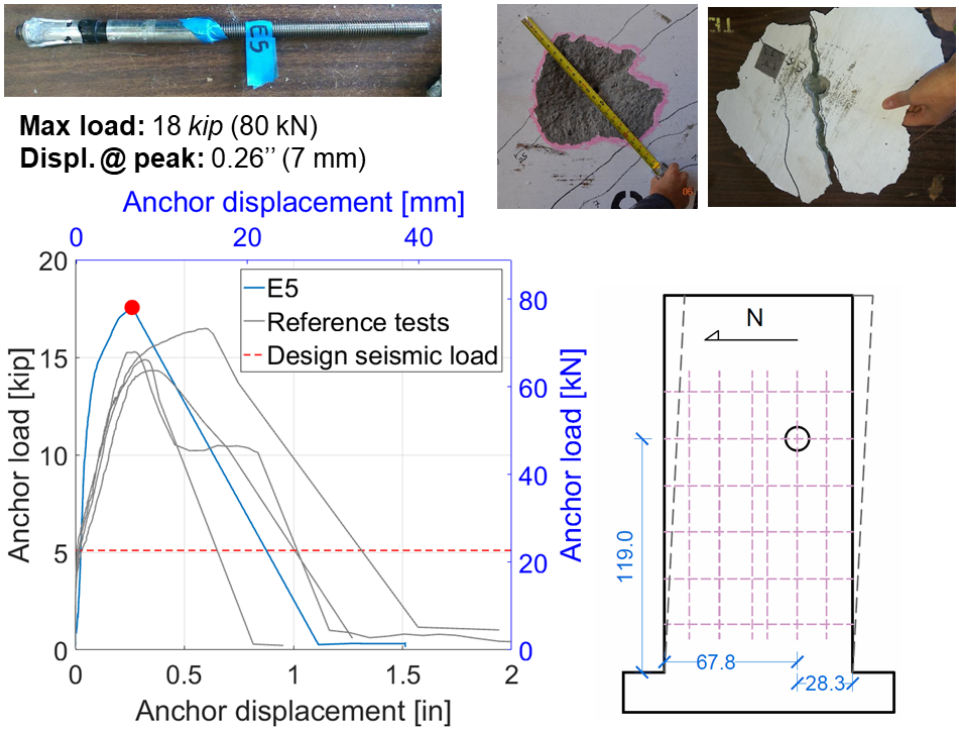
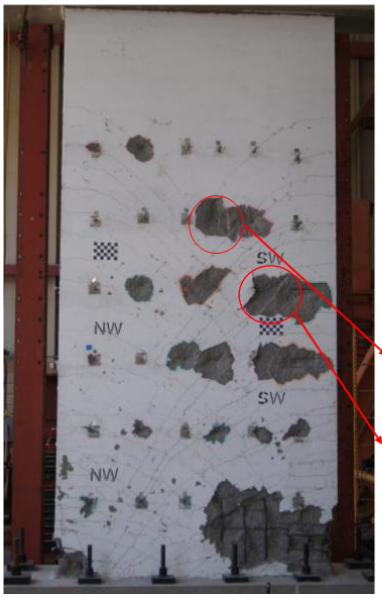


Figure E.201: Anchor E5 in wall SL7.5: Load-displacement pullout curve and photographs of the cone of failure and of the pulled anchor

Average from ref. tests (uncracked):
15 k *(68 kN),* **0.41 ‘’** (10 mm)



	Displ.		Load	
Min	[in] [mm]	0.30 8	[kip] [kN]	17 76
Max	[in] [mm]	0.40 10	[kip] [kN]	17 77
Mean	[in] [mm]	10.03 9	[kip] [kN]	17 76
STD	[in] [mm]	0.07 2	[kip] [kN]	0 1
CV	[%]	20	[%]	1

E4: Max load: 17 *kip* (76 kN)
Displ. @ peak: 0.3’’ (8 mm)

D5: Max load: 17 *kip* (76 kN)
Displ. @ peak: 0.4’’ (10 mm)

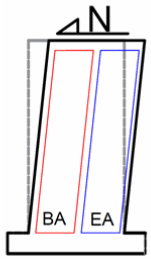
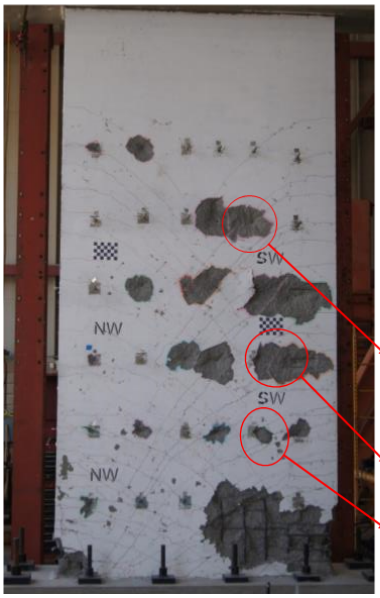


Figure E.202: Summary and statistics of the residual capacities of expansion anchors residing in no cracks at the end of the slender wall SL7.5 test. Note: the load values are normalized for the concrete strength

Average from ref. tests (uncracked):
15 k *(68 kN),* **0.41 ‘’** (10 mm)



	Displ.		Load	
Min	[in] [mm]	0.24 6	[kip] [kN]	16 72
Max	[in] [mm]	0.26 7	[kip] [kN]	18 78
Mean	[in] [mm]	0.25 6	[kip] [kN]	17 75
STD	[in] [mm]	0.01 0	[kip] [kN]	1 5
CV	[%]	6	[%]	6

E5: Max load: 18 *kip* (80 kN)
Displ. @ peak: 0.26’’ (7 mm)

C5: Max load: 16 *kip* (71 kN)
Displ. @ peak: 0.24’’ (6 mm)

B5 (outlier) : Max load: 15 *kip* (67 kN)
Displ. @ peak: 0.24’’ (6 mm)

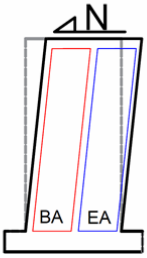


Figure E.203: Summary and statistics of the residual capacities of expansion anchors residing in one or more shear cracks at the end of the slender wall SL7.5 test. Note: the load values are normalized for the concrete strength

Average from ref. tests (uncracked):
15 k *(68 kN),* **0.41 ‘’** (10 mm)



	Displ.		Load	
Min	[in] [mm]	0.17 4	[kip] [kN]	13 58
Max	[in] [mm]	0.24 6	[kip] [kN]	18 80
Mean	[in] [mm]	0.21 5	[kip] [kN]	15 68
STD	[in] [mm]	0.04 1	[kip] [kN]	3 11
CV	[%]	18	[%]	16

D6: Max load: 18 *kip* (80 kN)
Displ. @ peak: 0.17’’ (4 mm)

C6: Max load: 15 *kip* (67 kN)
Displ. @ peak: 0.24’’ (6 mm)

B6 (outlier) : Max load: 13 *kip* (58 kN)
Displ. @ peak: 0.22’’ (6 mm)

B4: Max load: 13 *kip* (67 kN)
Displ. @ peak: 0.22’’ (6 mm)

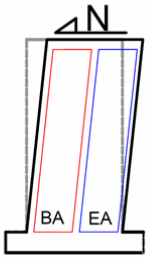
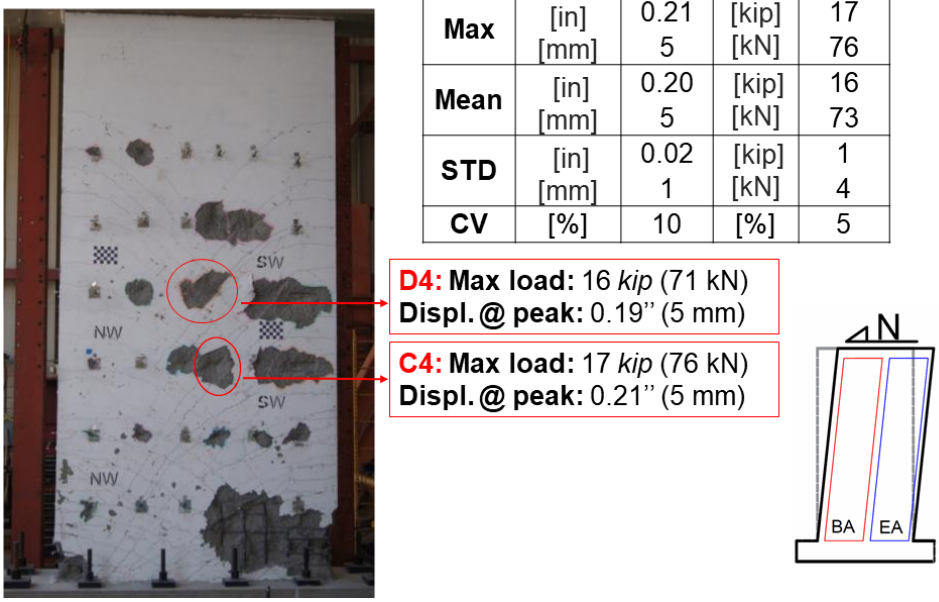


Figure E.204: Summary and statistics of the residual capacities of the expansion anchors residing in one or more tension cracks at the end of the slender wall SL7.5 test. Note: the load values are normalized for the concrete strength



	Displ.		Load	
Min	[in] [mm]	0.19 5	[kip] [kN]	16 71
Max	[in] [mm]	0.21 5	[kip] [kN]	17 76
Mean	[in] [mm]	0.20 5	[kip] [kN]	16 73
STD	[in] [mm]	0.02 1	[kip] [kN]	1 4
CV	[%]	10	[%]	5

Figure E.205: Summary and statistics of the residual capacities of expansion anchors residing in shear X crossing cracks at the end of the slender wall SL7.5 test. Note: the load values are normalized for the concrete strength

E.2.2 Wall SQ7.5

The load-displacement curves from pullout tests (not normalized) are reported in Figs. E.206 to E.219. It is noted that residual load capacity of anchors A2, B2, B3 and B4 did not reach the design seismic load for the severe concrete damage experienced in this lower region of the wall, as in Figs. E.206, E.209, E.210 and E.211. The residual capacity of these anchors was significantly lower compared to the anchors in the upper row C (see Figs. E.214, E.215, E.216, E.217, E.218 and E.219), where the cracks propagated only in the later cycles of the wall history and a light damage was finally recorded.

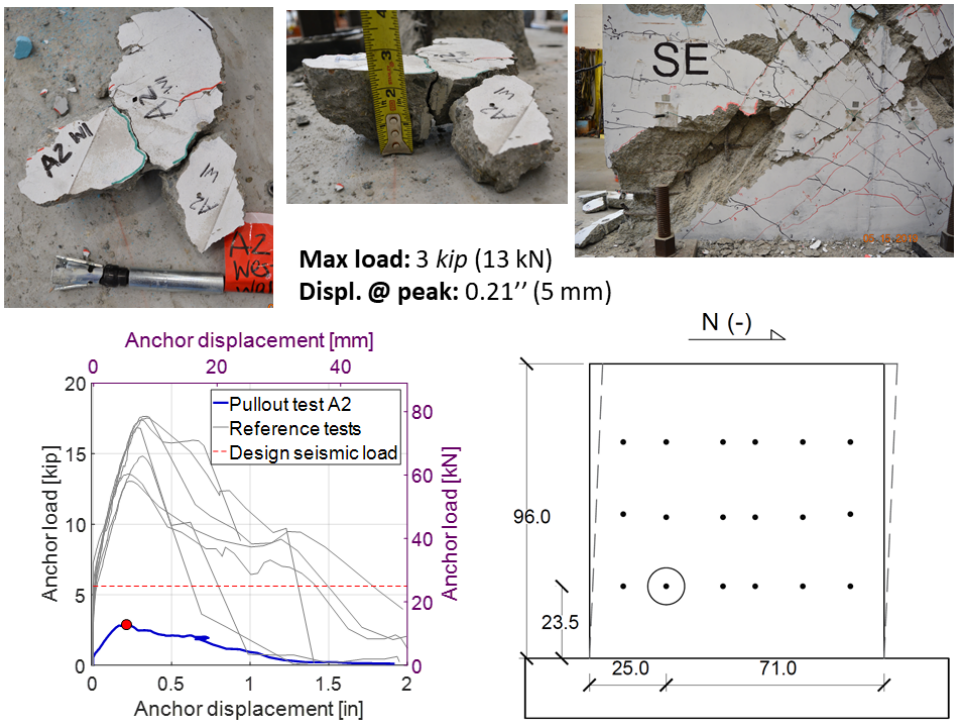


Figure E.206: Anchor A2 in wall SQ7.5: load-displacement pullout curve and photographs of the cone of failure and of the pulled anchor

Comparison of the normalized values with the reference tests results is presented in Fig. E.220. Statistics in Fig. E.220 show that the residual mean anchor load capacity was about half of the reference capacity in uncracked concrete. The loss of anchor capacity has to be attributed to the severe cyclic crack widths intersecting the anchors during the wall test. It is noted that anchors with the lowest residual load capacities were located inside the most damaged regions of the wall, such us the region inside the plastic hinge length and the boundary elements at the wall ends.

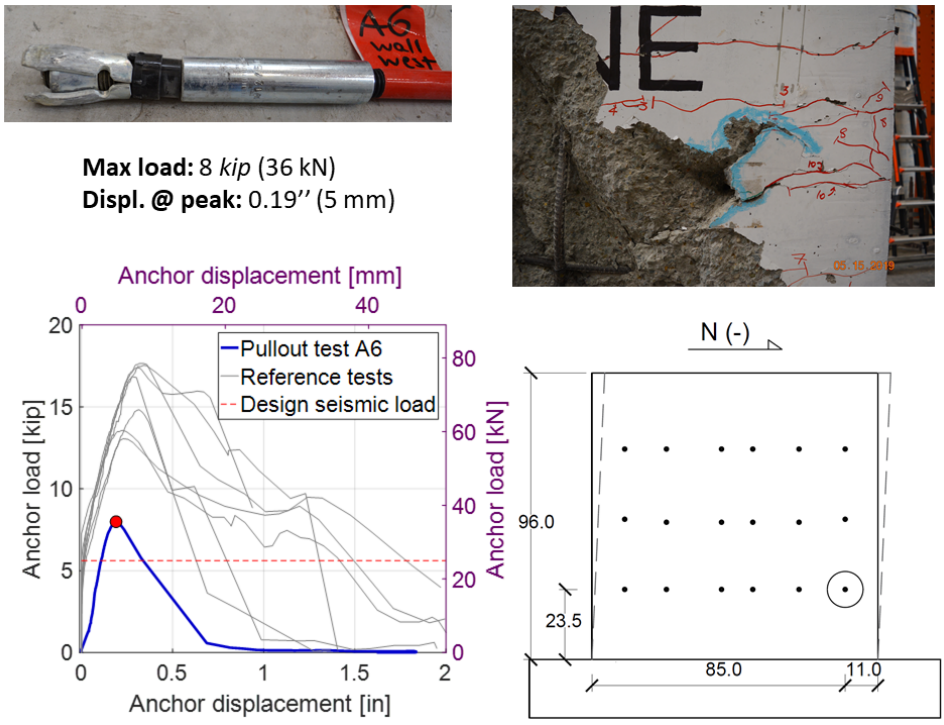


Figure E.207: Anchor A6 in wall SQ7.5: load-displacement pullout curve and photographs of the cone of failure and of the pulled anchor

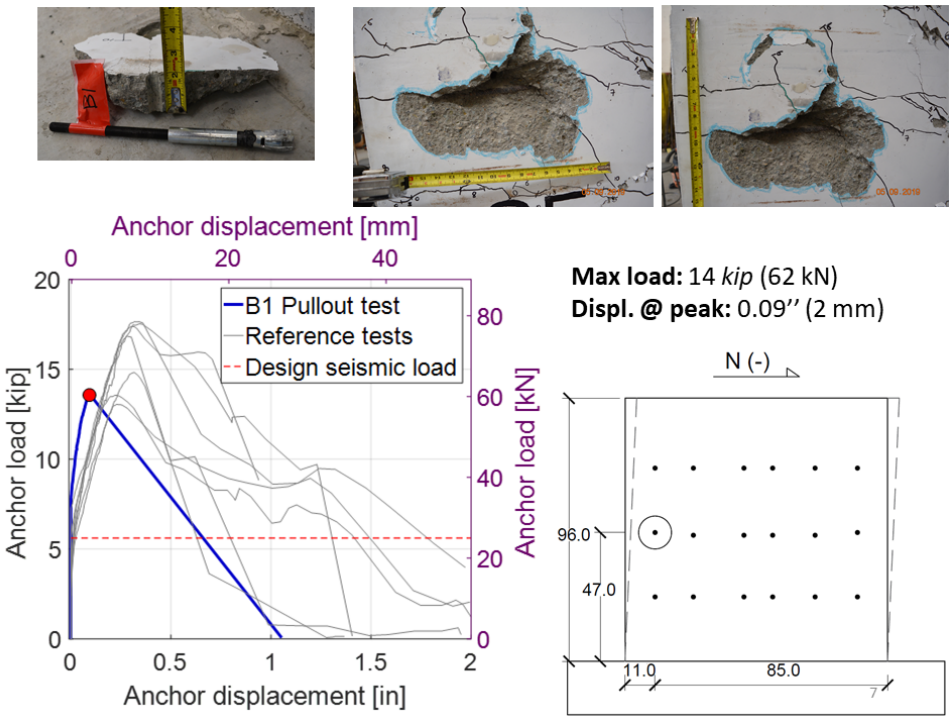


Figure E.208: Anchor B1 in wall SQ7.5: load-displacement pullout curve and photographs of the cone of failure and of the pulled anchor

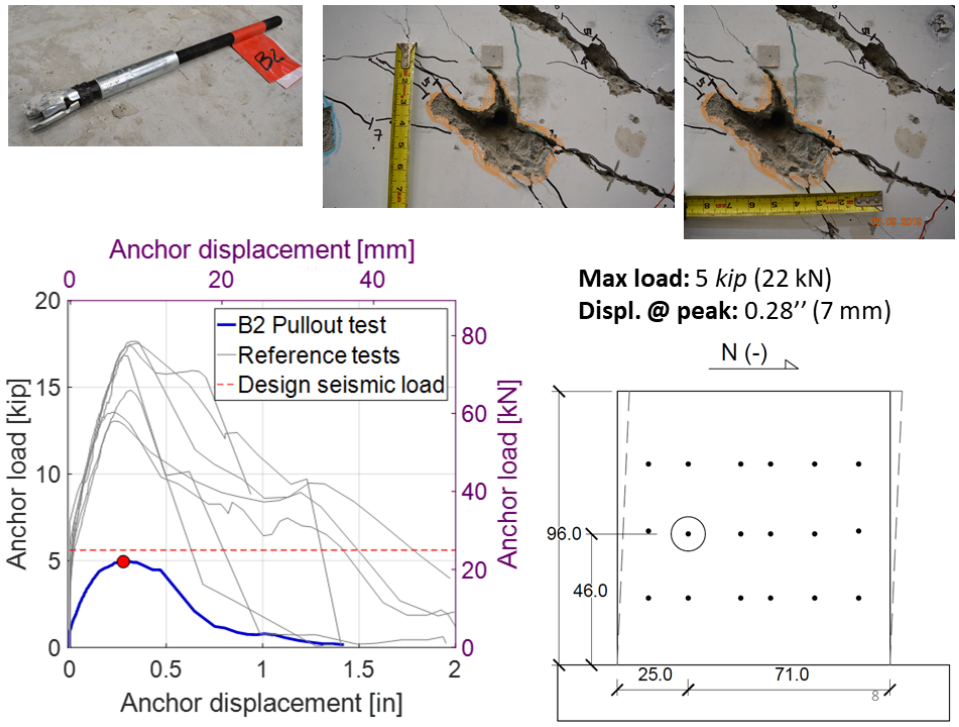


Figure E.209: Anchor B2 in wall SQ7.5: load-displacement pullout curve and photographs of the cone of failure and of the pulled anchor

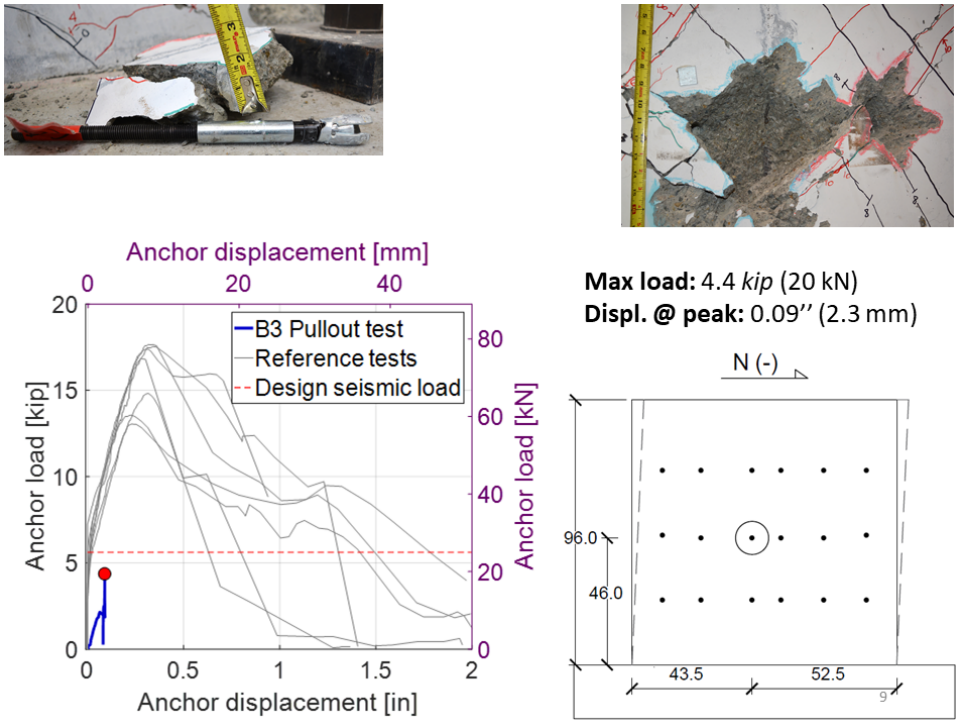


Figure E.210: Anchor B3 in wall SQ7.5: load-displacement pullout curve and photographs of the cone of failure and of the pulled anchor

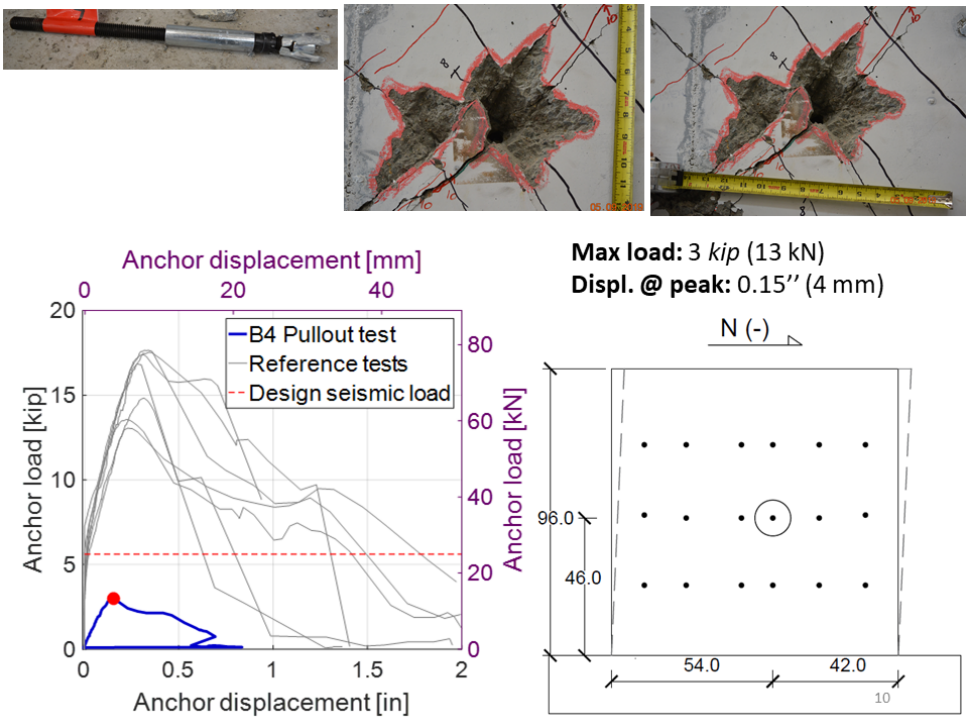


Figure E.211: Anchor B4 in wall SQ7.5: load-displacement pullout curve and photographs of the cone of failure and of the pulled anchor

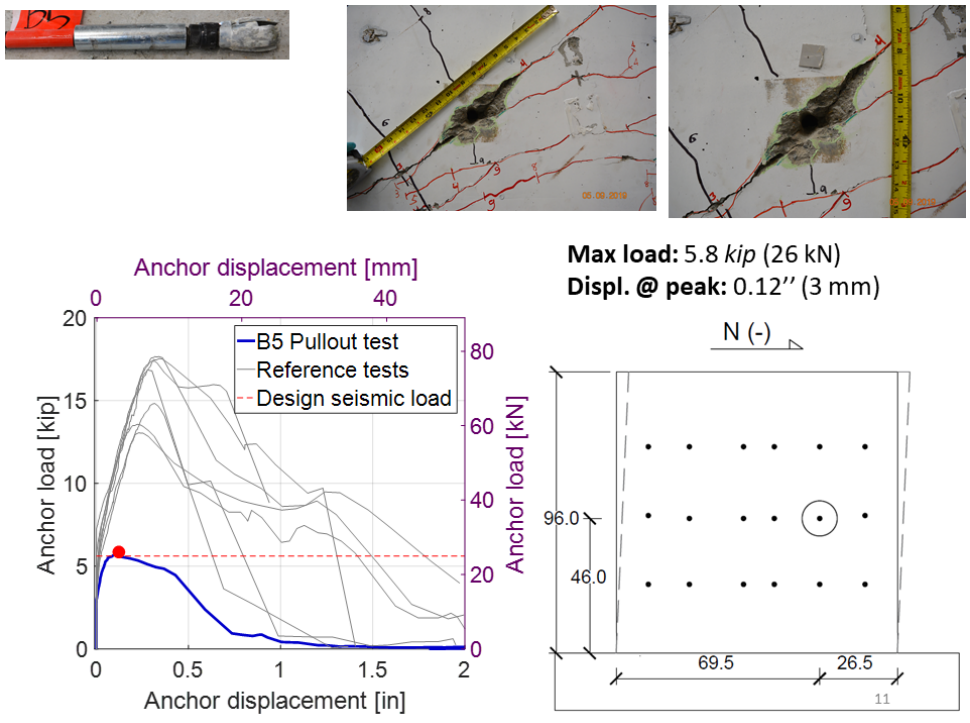


Figure E.212: Anchor B5 in wall SQ7.5: load-displacement pullout curve and photographs of the cone of failure and of the pulled anchor

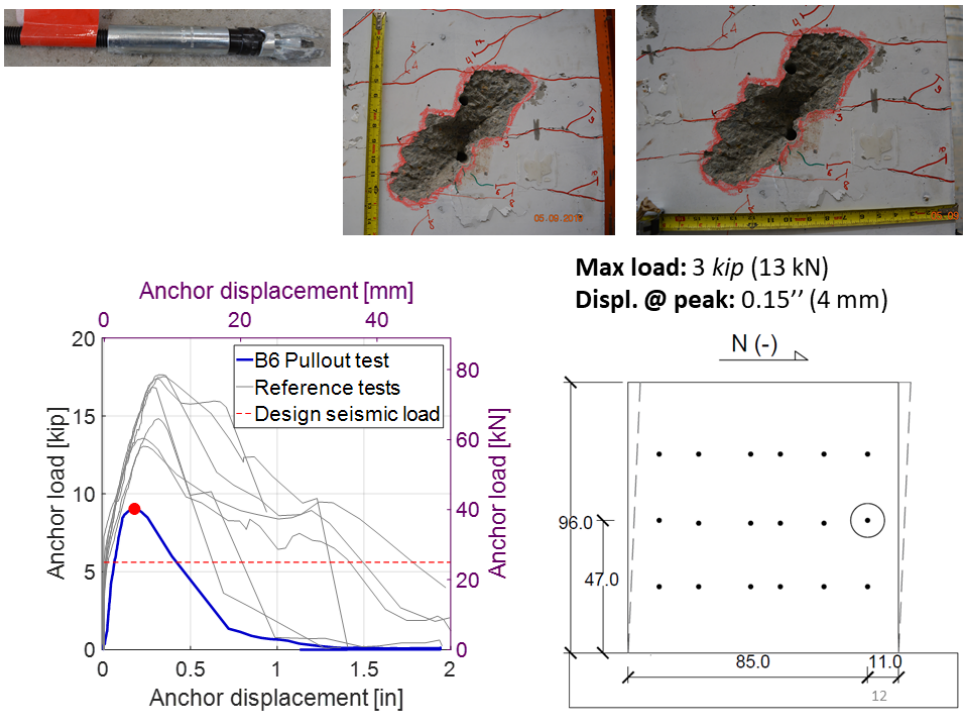


Figure E.213: Anchor B6 in wall SQ7.5: load-displacement pullout curve and photographs of the cone of failure and of the pulled anchor

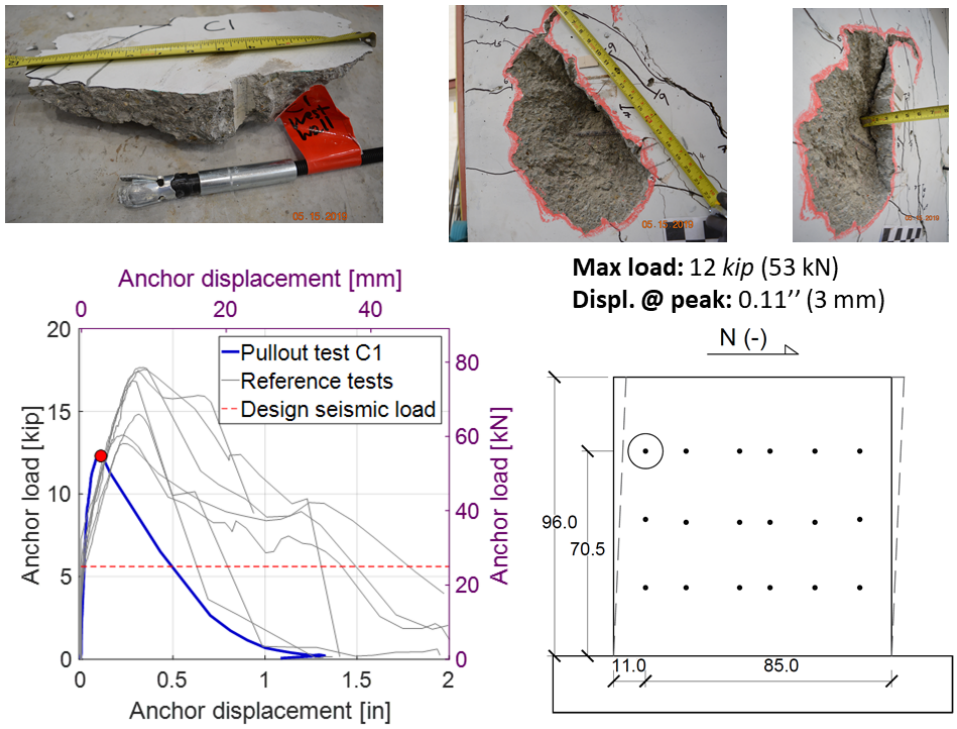


Figure E.214: Anchor C1 in wall SQ7.5: load-displacement pullout curve and photographs of the cone of failure and of the pulled anchor

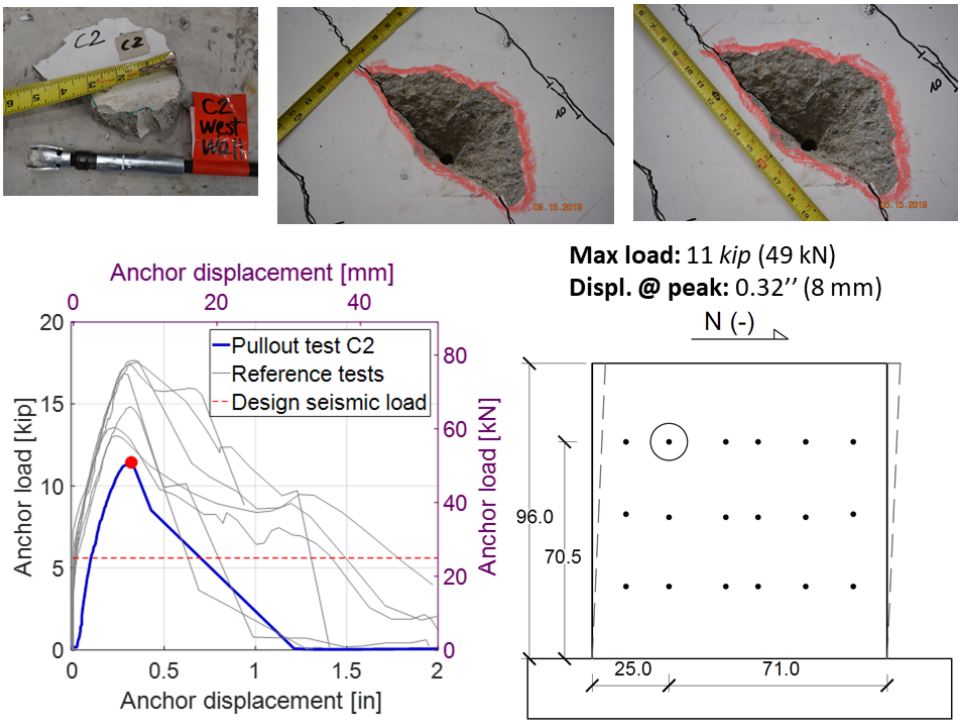


Figure E.215: Anchor C2 in wall SQ7.5: load-displacement pullout curve and photographs of the cone of failure and of the pulled anchor

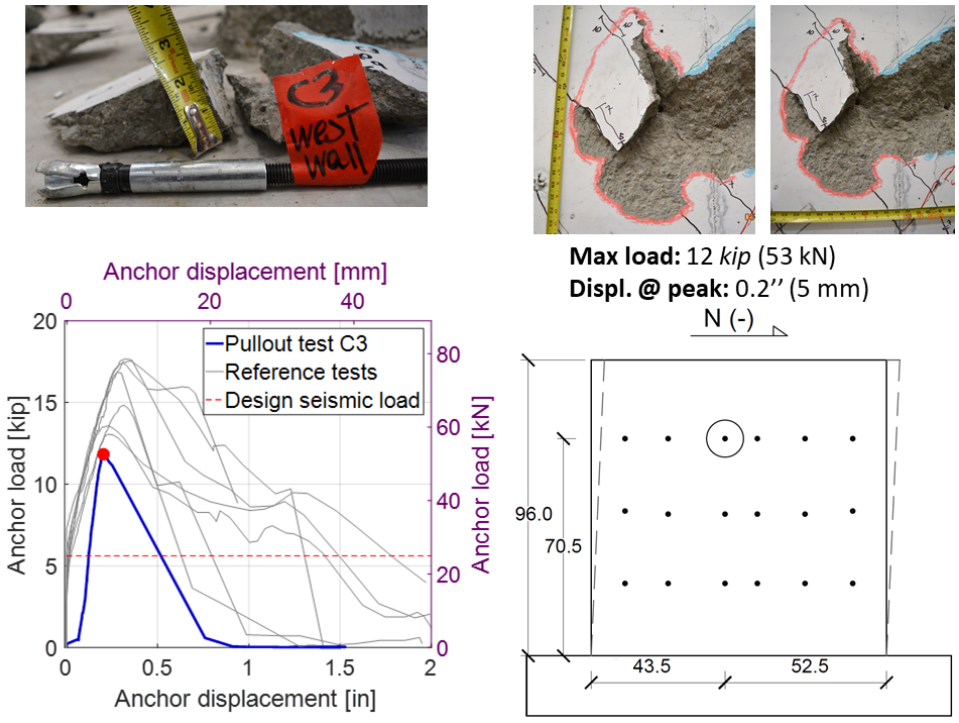


Figure E.216: Anchor C3 in wall SQ7.5: load-displacement pullout curve and photographs of the cone of failure and of the pulled anchor

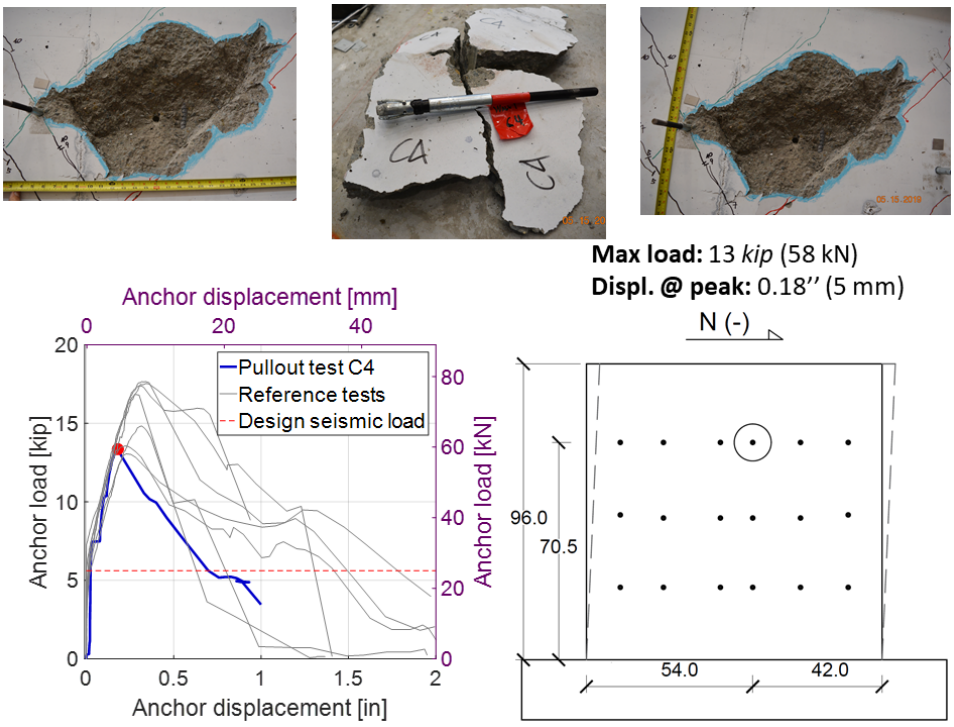


Figure E.217: Anchor C4 in wall SQ7.5: load-displacement pullout curve and photographs of the cone of failure and of the pulled anchor

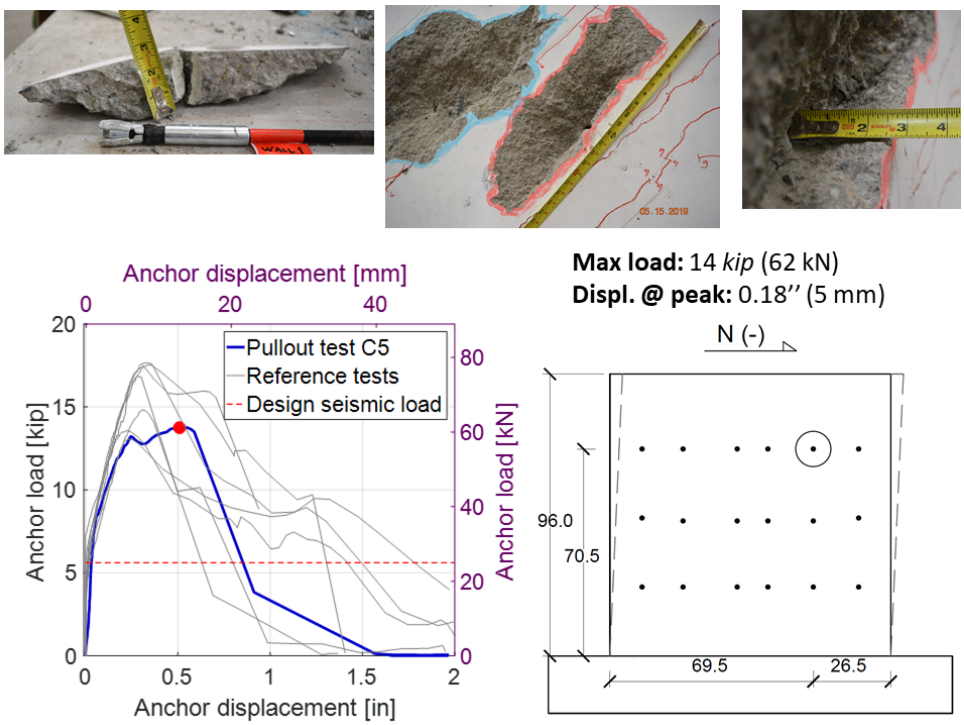


Figure E.218: Anchor C5 in wall SQ7.5: load-displacement pullout curve and photographs of the cone of failure and of the pulled anchor

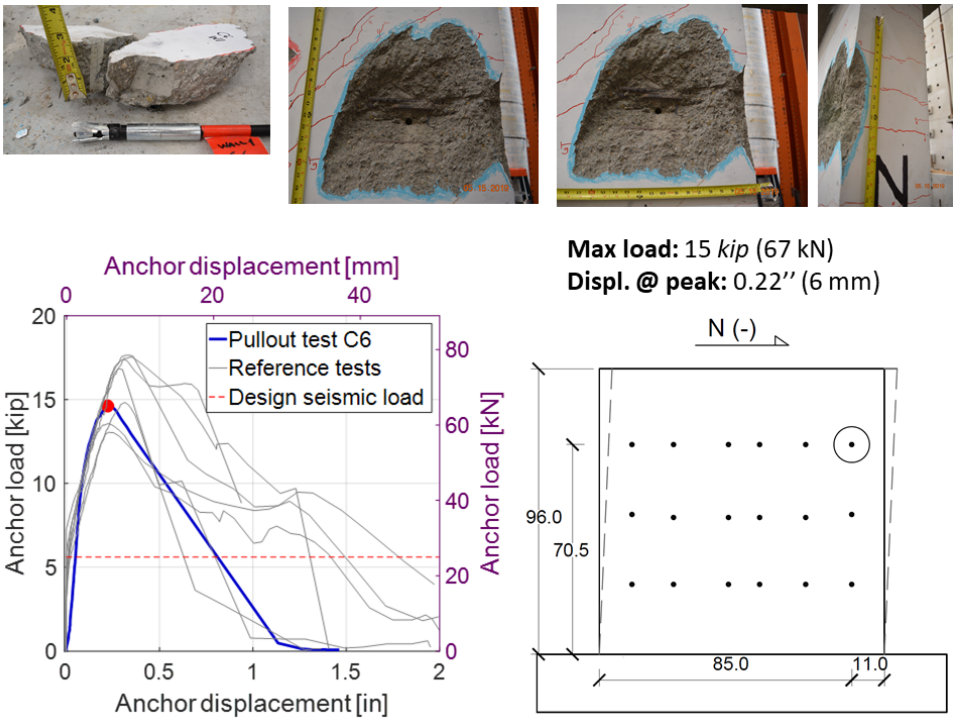


Figure E.219: Anchor C6 in wall SQ7.5: load-displacement pullout curve and photographs of the cone of failure and of the pulled anchor

Concrete strength @ day of reference tests (30 days): 6.9 ksi

	Mean	STD	CV [%]
Peak load	**16 kips (71 kN)**	2 kip (9 kN)	13
Disp. @ peak load	**0.29 in (7 mm)**	0.05 in (1 mm)	16

$Coeff_{norm}$ = Sqrt(6900/8300) = **0.912**

Concrete strength @ day of pullout (67 days): 8.3 ksi

	Mean	STD	CV[%]
Peak load	**8 kips (36 kN)**	4 kip (17 kN)	47
Disp. @ peak load	**0.24 in (6 mm)**	0.12 in (3 mm)	50

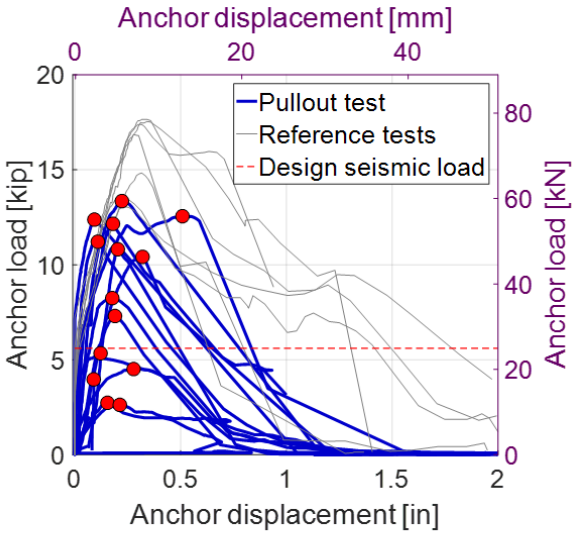


Figure E.220: Wall SQ7.5: summary of normalized data and comparison with anchor reference tests results

E.2.3 Wall SQ0

The load-displacement curves from pullout tests (not normalized) are reported in Figs. E.221 to E.231. It is noted that residual load capacity of all the anchors in the B row and anchor C2 did not reach the design seismic load for the severe concrete damage experienced in these regions of the wall specimen. It is noted that severe damage spread up to higher elevation with respect to wall SQ7.5, significantly affecting the residual load capacity of the anchors in the C row.

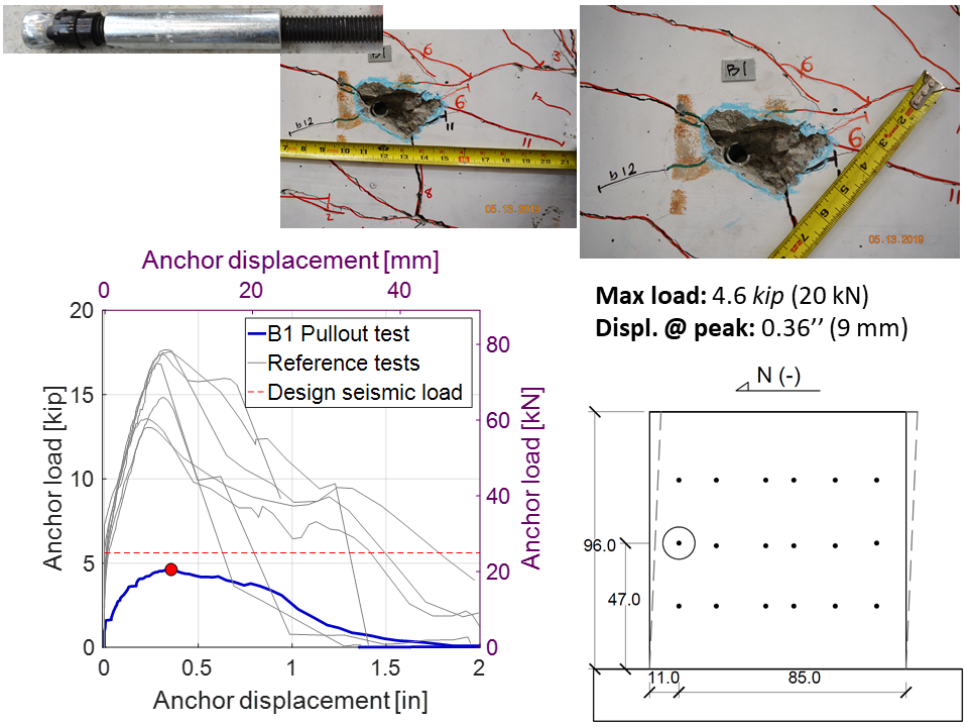


Figure E.221: Wall SQ0: anchor B1 load-displacement pullout curve and photographs of the cone of failure and of the pulled anchor

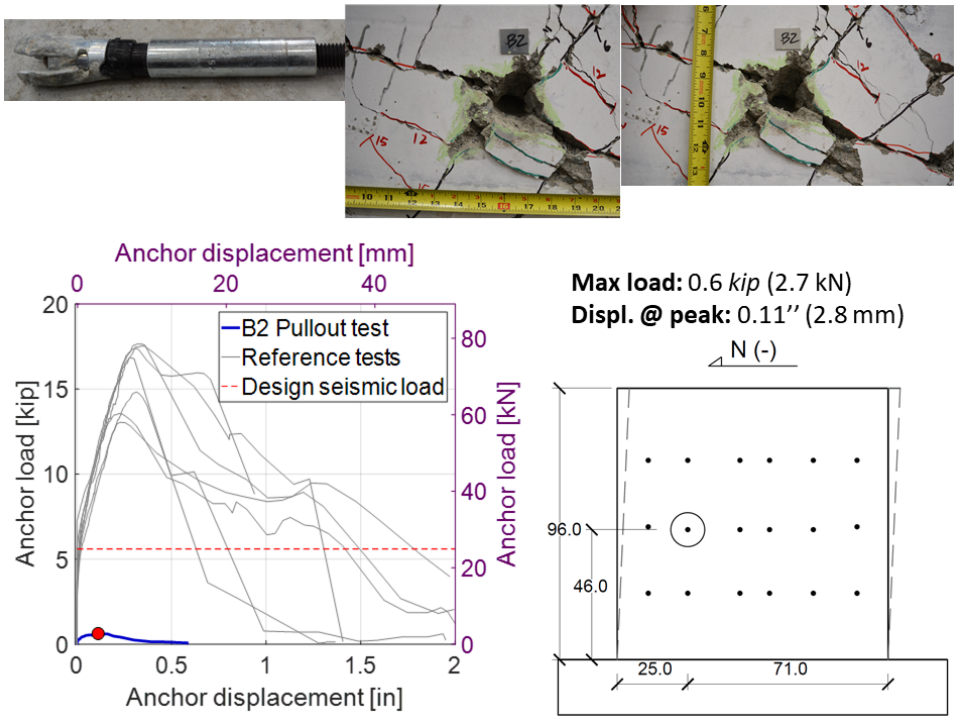


Figure E.222: Wall SQ0: anchor B2 load-displacement pullout curve and photographs of the cone of failure and of the pulled anchor

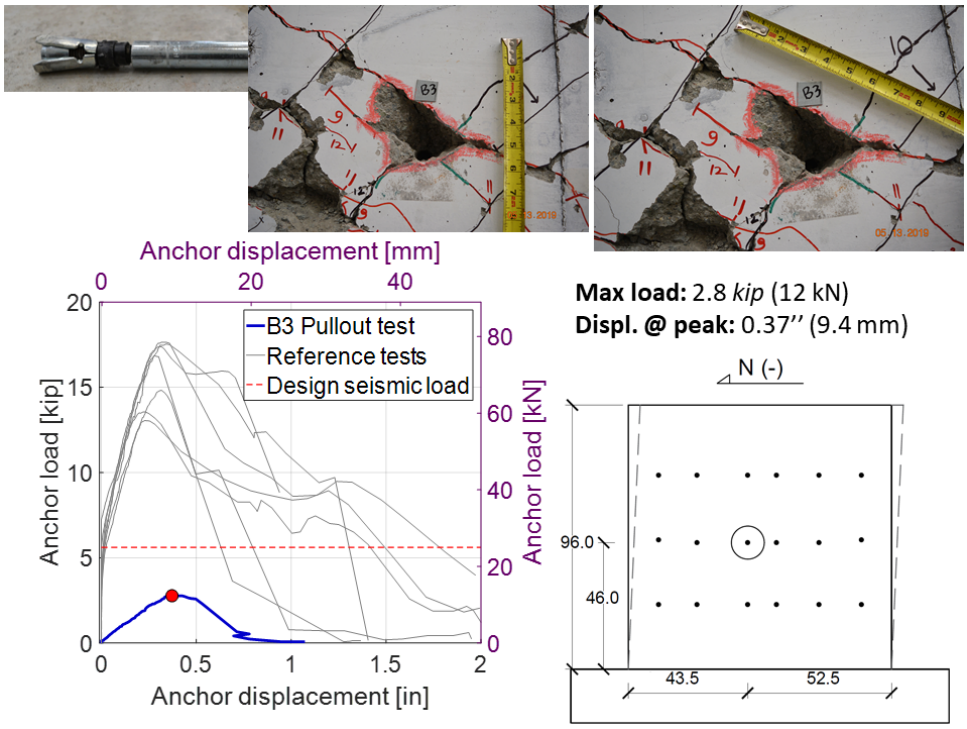


Figure E.223: Wall SQ0: anchor B3 load-displacement pullout curve and photographs of the cone of failure and of the pulled anchor

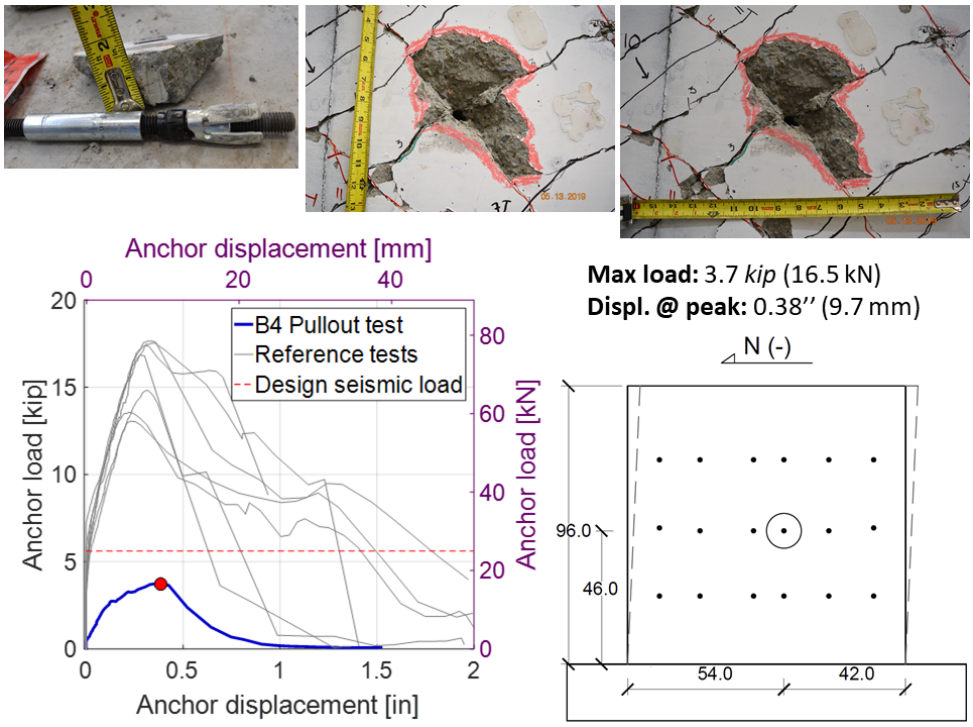


Figure E.224: Wall SQ0: anchor B4 load-displacement pullout curve and photographs of the cone of failure and of the pulled anchor

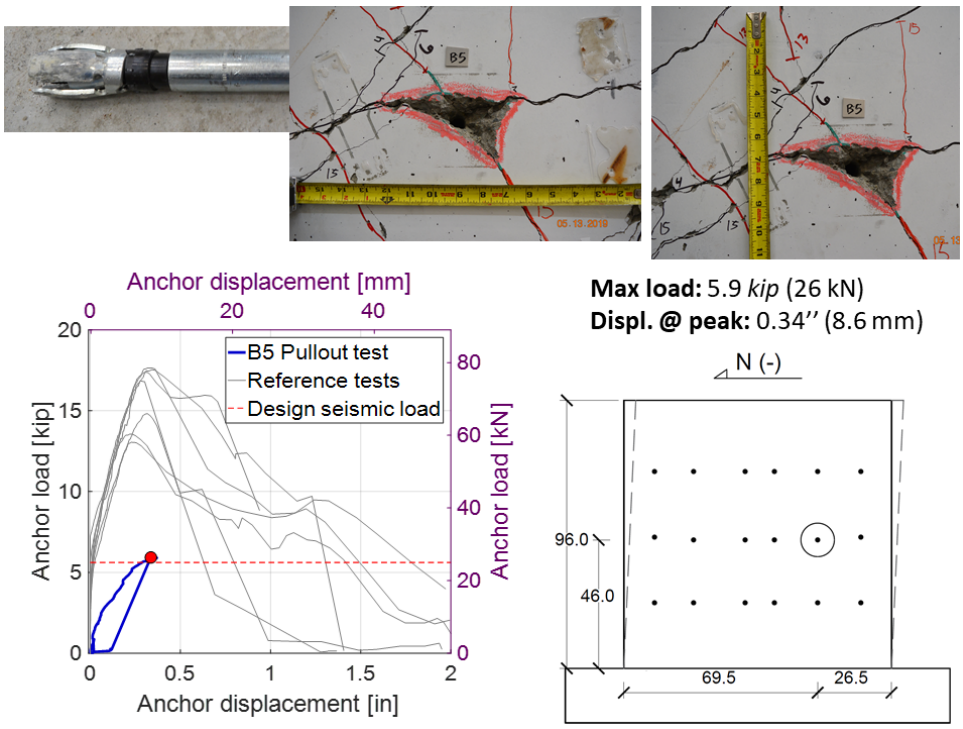


Figure E.225: Wall SQ0: anchor B5 load-displacement pullout curve and photographs of the cone of failure and of the pulled anchor

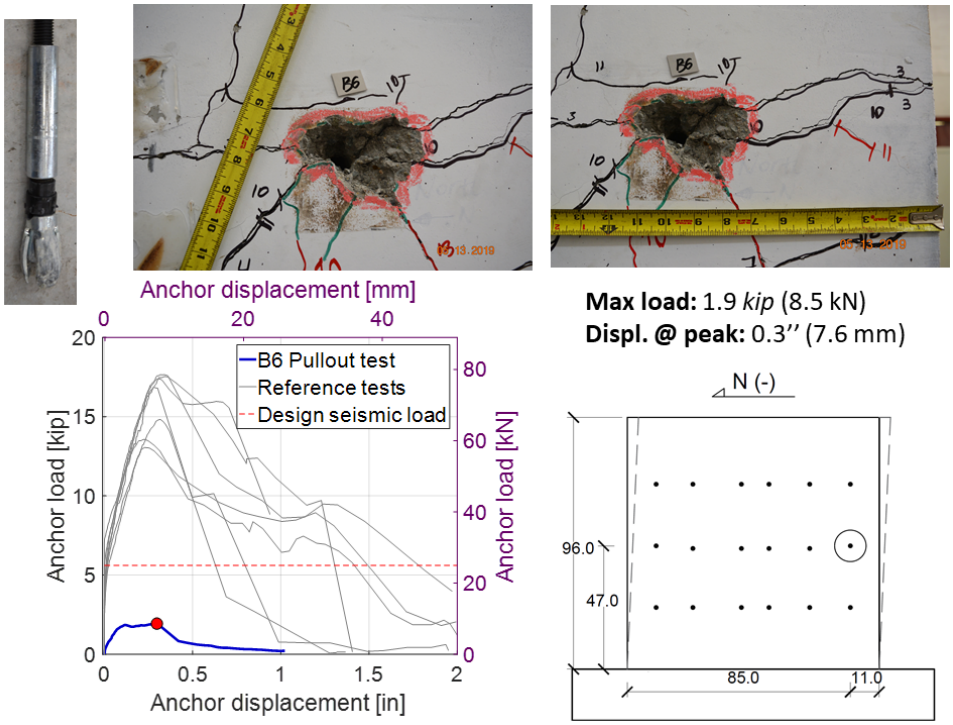


Figure E.226: Wall SQ0: anchor B6 load-displacement pullout curve and photographs of the cone of failure and of the pulled anchor

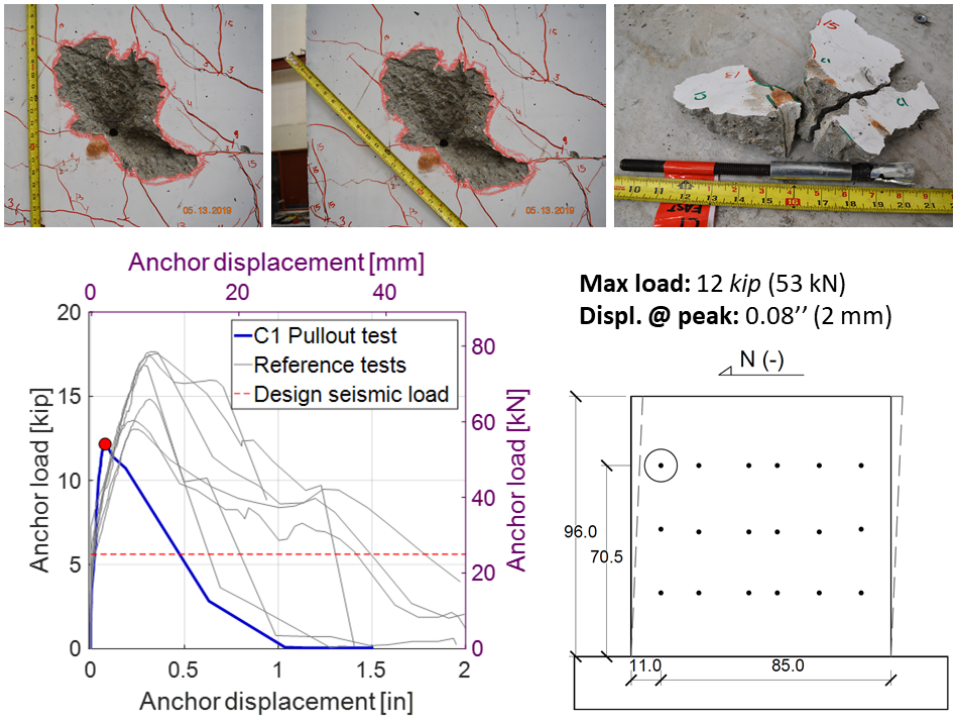


Figure E.227: Wall SQ0: anchor C1 load-displacement pullout curve and photographs of the cone of failure and of the pulled anchor

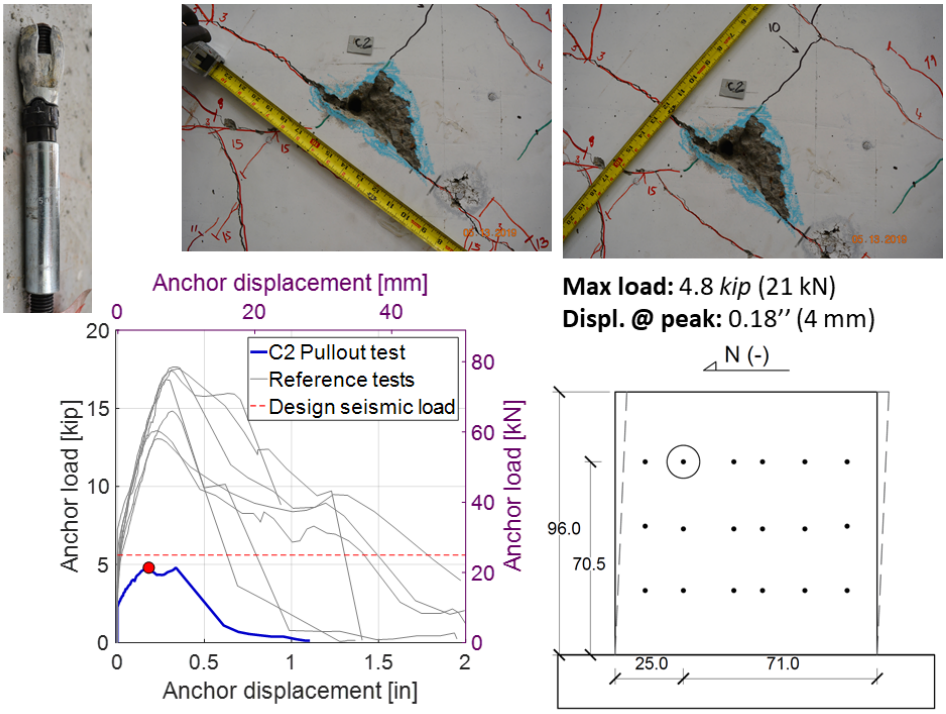


Figure E.228: Wall SQ0: anchor C2 load-displacement pullout curve and photographs of the cone of failure and of the pulled anchor

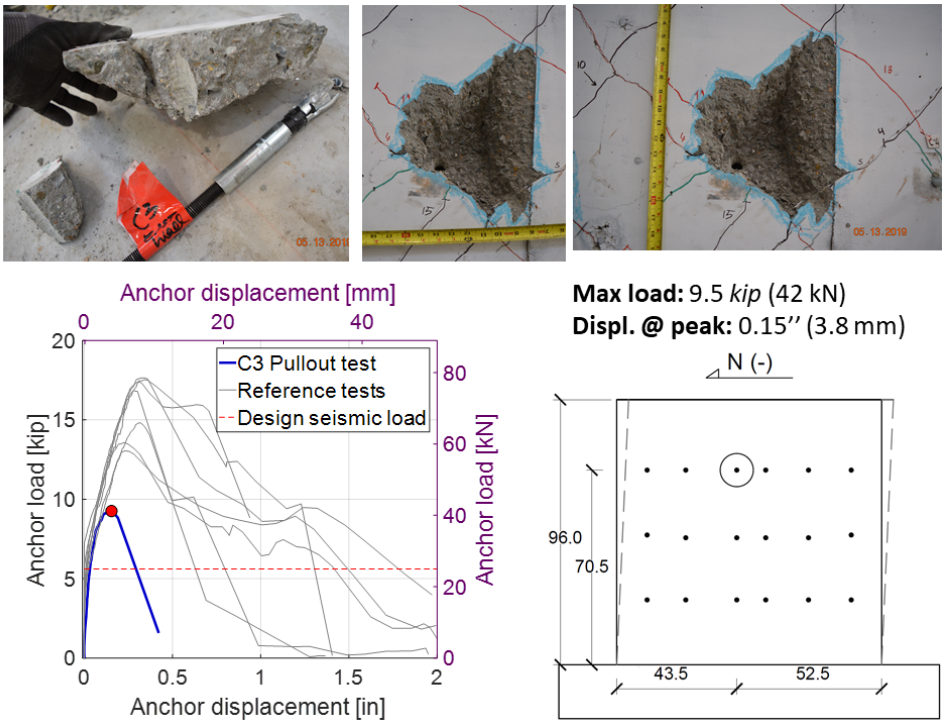


Figure E.229: Wall SQ0: anchor C3 load-displacement pullout curve and photographs of the cone of failure and of the pulled anchor

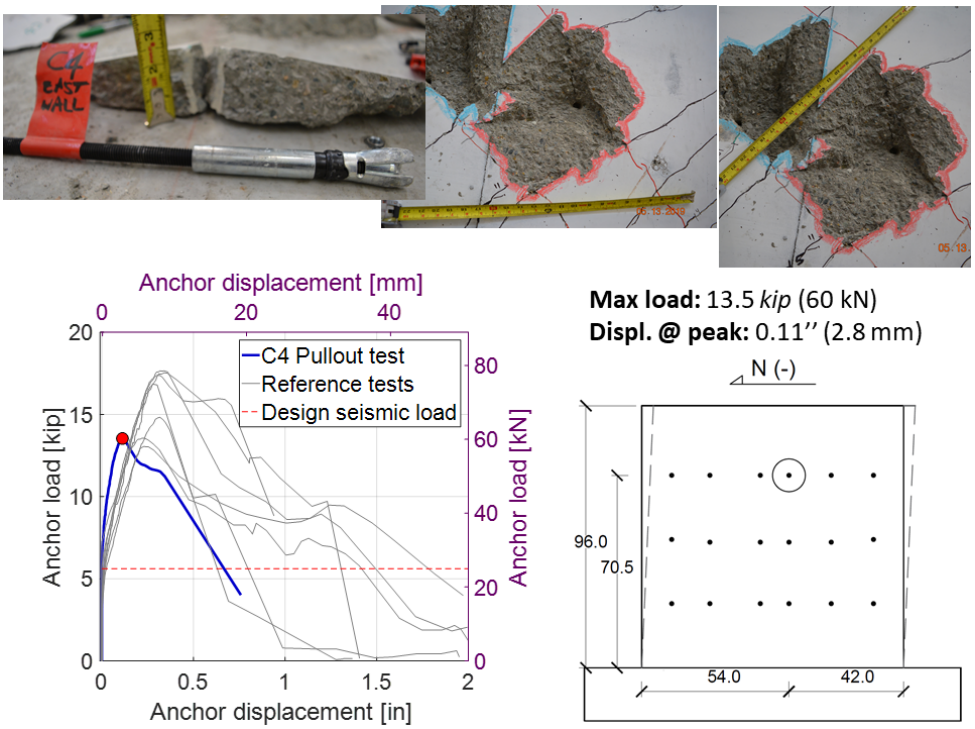


Figure E.230: Wall SQ0: anchor C4 load-displacement pullout curve and photographs of the cone of failure and of the pulled anchor

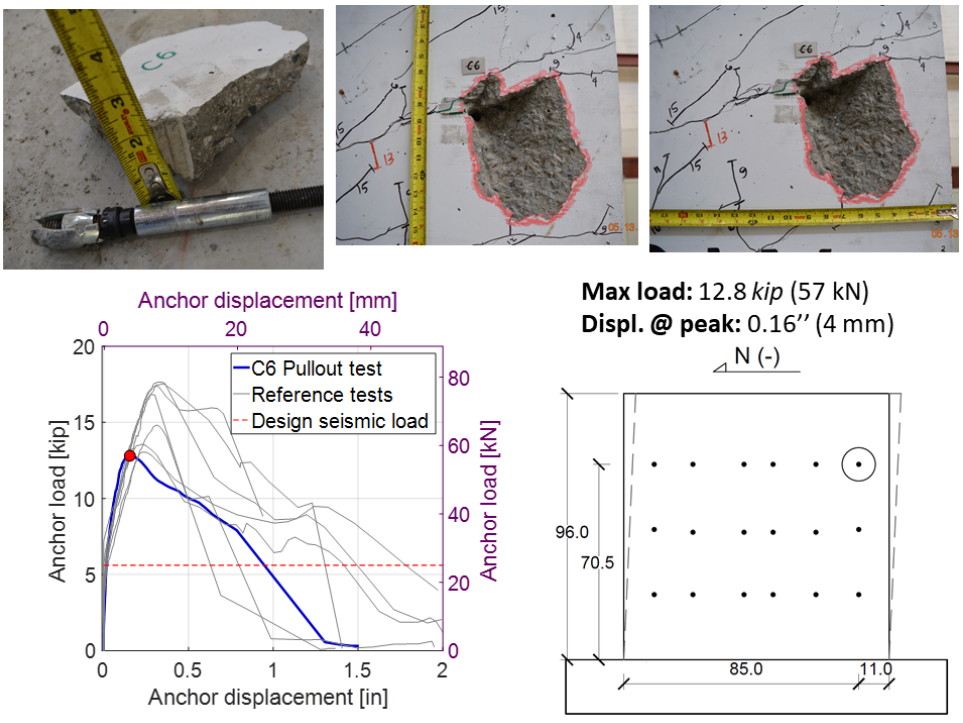


Figure E.231: Wall SQ0: anchor C6 load-displacement pullout curve and photographs of the cone of failure and of the pulled anchor

Concrete strength @ day of reference tests (30 days): 6.9 ksi

	Mean	STD	CV [%]
Peak load	**16 kips (71 kN)**	2 kip (9 kN)	13
Disp. @ peak load	**0.29 in (7 mm)**	0.05 in (1 mm)	16

$\mathbf{Coeff_{norm}}$ = Sqrt(6900/8300) = **0.912**

Concrete strength @ day of pullout (67 days): 8.3 ksi

	Mean	STD	CV[%]
Peak load	**6 kips (27 kN)**	4 kip (19 kN)	70
Disp. @ peak load	**0.2 in (5 mm)**	0.12 in (3 mm)	52

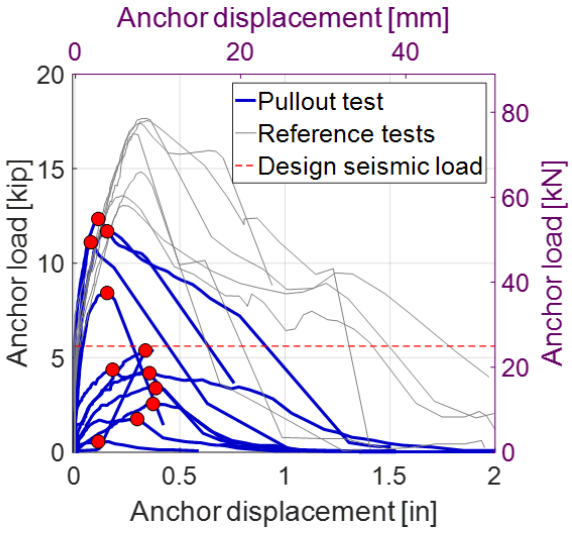


Figure E.232: Wall SQ0: summary of normalized data and comparison with anchor reference tests results

Appendix F

Structure from Motion Data

In photogrammetry, three-dimensional structures can be estimated from two-dimensional image sequences with the structure from motion (SfM) imaging technique. As illustrated by Ullman (1976), this technique is based on a fundamental theorem stating that "the structure of four non-coplanar points is recoverable from three orthographic projections". In other terms, the views in the structure from motion theorem are obtained by orthographic projection, similarly to the human visual system. To assist with documenting the physical characteristics of residual damage surrounding the anchor pullout locations, structure from motion was used and results are reported in this Appendix. A series of orthogonal images of the walls faces were collected at the completion of the tests, namely, about 300 pictures per wall were taken with high resolution cameras (SONY-ILCE-7RM3, with 31 mm focal length). These data allowed reconstruction of high-resolution surface geometric models of the damaged shear wall specimens. Figs.F.1 to F.4 and Figs. F.6 to F.7 show the principal global views of wall SQ7.5 and SQ0, respectively, represented as dense clouds of points.



Figure F.1: SfM model of wall SQ7.5- front view of West face



Figure F.2: SfM model of wall SQ7.5- front view of East face (anchor face)



Figure F.3: SfM model of wall SQ7.5- isometric view from South-West



Figure F.4: SfM model of wall SQ7.5- isometric view from North-East



Figure F.5: SfM model of wall SQ0- front view of West face (anchor face)

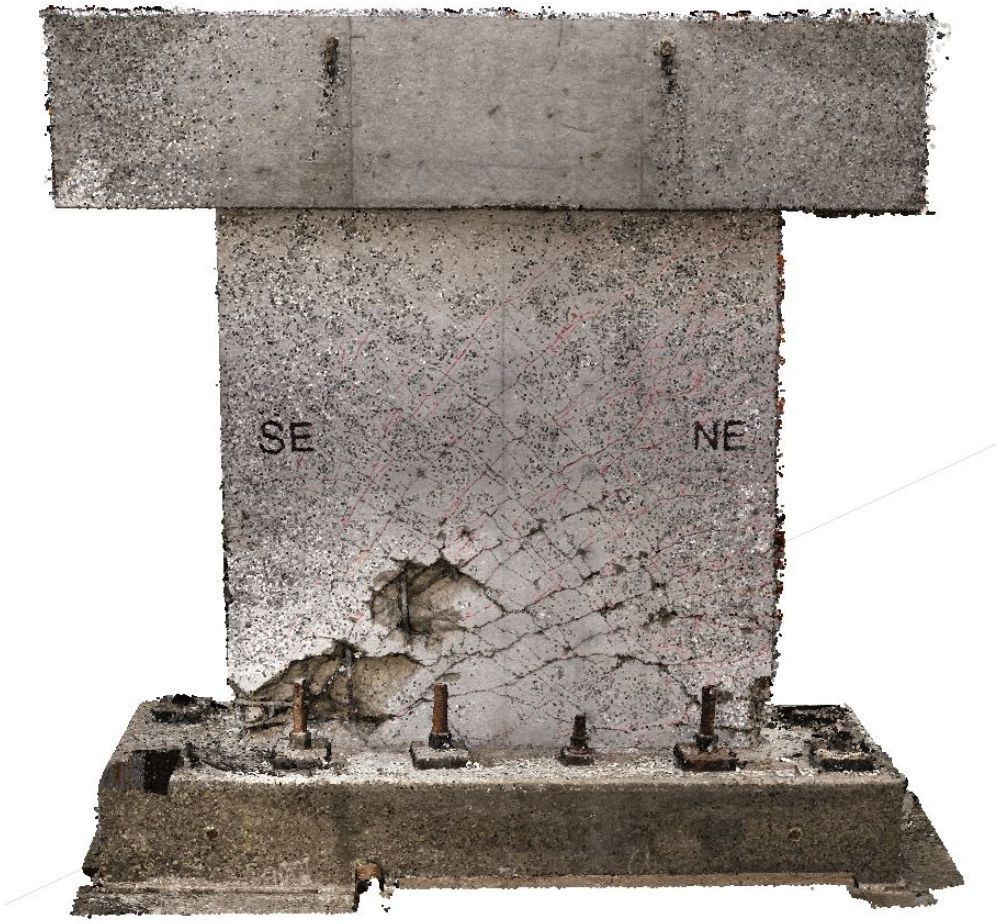


Figure F.6: SfM model of wall SQ0- front view of East face



Figure F.7: SfM model of wall SQ0- isometric view from South-West

Appendix G

Sample Code Used in the Numerical Validation Study

A sample code used in the validation of the SFI-MVLEM model presented in Chapter 5 is here reported. This example code describes the geometry and material properties of the AR=1 wall specimen tested with axial load. Similar codes are used to perform the parametric study presented in Chapter 6.

```
# ------------------------------------------------------------------
# Example code: Simulation of wall cyclic behavior using SFI_MVLEM
# Specimen: SQ7.5 (AR=1, 7.5 axial load ratio and boundary elements)
# Model by: Gloria Faraone (glfaraone@ucsd.edu)
# SFI_MVLEM model by Kristijan Kolozvari (kkolozvari@fullerton.edu)
# ------------------------------------------------------------------
# 500 kips of self-weight applied, dense mesh discretization
# ---------------------------------------------------------
# Start of model generation (Units: kip, in, sec, ksi)
# ---------------------------------------------------------

# Set Up Directories
set modelName "fine_mesh";              # Model Name
set dataDir sq8_$modelName; # Name of output folder
file mkdir $dataDir;

# Create ModelBuilder for 2D element (with two-dimensions and 2 DOF/node)
model BasicBuilder -ndm 2 -ndf 3

# ------------------------------------------
# Set geometry, nodes, boundary conditions
# ------------------------------------------

# Create nodes
# node nodeId xCrd yCrd
# Wall Geometry
set H 96.;  # Wall height
set t 10.;  # Wall thickness

# Create nodes
# node nodeId xCrd yCrd
node 1 0 0;
node 2 0 6;
node 3 0 12;
node 4 0 18;
node 5 0 24;
node 6 0 30;
node 7 0 36;
node 8 0 42;
node 9 0 48;
node 10 0 54;
node 11 0 60;
node 12 0 66;
node 13 0 72;
node 14 0 78;
node 15 0 84;
node 16 0 90;
node 17 0 $H;


# Boundary conditions
fix 1 1 1 1;    # Fixed condition at node 1

# Set Control Node and DOF
set IDctrlNode 17;
set IDctrlDOF 1;

# ------------------------------------------------------------------------
# Define uniaxial materials for 2D RC Panel Constitutive Model (FSAM)
# ------------------------------------------------------------------------

# STEEL .....................................................
# uniaxialMaterial SteelMPF $mattag  $fyp  $fyn  $E0  $bp  $bn   $R0  $a1  $a2
# steel X
set fyX 65;             # fy
set bx 0.009949;        # strain hardening

# steel Y web
set fyYw 65;            #fy
```

```
set byw 0.00927;        # strain hardening

# steel Y boundary
set fyYb 65;            # fy
set byb 0.00927;        # strain hardening

# steel misc
set Esy 29000.0;    # Young's modulus
set Esx $Esy;       # Young's modulus
set R0 20.0;        # initial value of curvature parameter
set A1 0.925;       # curvature degradation parameter
set A2 0.15;        # curvature degradation parameter

# Build steel materials
uniaxialMaterial    SteelMPF  1 $fyX $fyX $Esx $bx $bx $R0 $A1 $A2;     # steel X
uniaxialMaterial    SteelMPF  2 $fyYw $fyYw $Esy $byw $byw $R0 $A1 $A2; # steel Y web
uniaxialMaterial    SteelMPF  3 $fyYb $fyYb $Esy $byb $byb $R0 $A1 $A2; # steel Y
boundary


# CONCRETE ..........................................................
# uniaxialMaterial ConcreteCM $mattag  $fpcc  $epcc  $Ec  $rc  $xcrn   $ft  $et  $rt
$xcrp <-GapClose $gap>

# unconfined
set fpc 5.95;       # peak compressive stress - DATO NOTO
set ec0 -0.0022;    # strain at peak compressive stress
set ft 0.29;        # peak tensile stress
set et 0.0001;      # strain at peak tensile stress
set Ec 4815;        # Young's modulus - da concr07
set xcrnu 1.022;    # cracking strain - compression
set xcrp 10000;     # cracking strain - tension
set ru 6;           # shape parameter - compression
set rt 1.2;         # shape parameter - tension

# confined
set fpcc 7.80;      # peak compressive stress
set ec0c -0.006;    # strain at peak compressive stress (-0.0075)
set Ecc 5580;       # Young's modulus (5580 da concr07)
set xcrnc 1.023;    # cracking strain - compression
set rc 9.9;         # shape parameter - compression

# Build concrete materials
uniaxialMaterial ConcreteCM 4 -$fpc   $ec0   $Ec  $ru  $xcrnu  $ft  $et  $rt  $xcrp
-GapClose 0; # unconfined concrete
uniaxialMaterial ConcreteCM 5 -$fpcc  $ec0c  $Ecc $rc  $xcrnc  $ft  $et  $rt  $xcrp
-GapClose 0; # confined concrete


# ----------------------------------------
#  Define 2D RC Panel Material (FSAM)
# ----------------------------------------

# Reinforcing ratios
set rouXw 0.0027;   # X web
set rouYw 0.007;    # Y web
set rouYb 0.01;     # Y boundary
set rouXb 0.015;    # X boundary


# Shear resisting mechanism parameters
set nu 0.2;         # friction coefficient
set alfadow 0.012;  # dowel action stiffness parameter

# nDMaterial FSAM $mattag   $rho  $sX  $sY  $conc  $rouX  $rouY  $nu  $alfadow
nDMaterial FSAM         6    0.0   1     2     4  $rouXw $rouYw  $nu  $alfadow; # Web
(unconfined concrete)
nDMaterial FSAM         7    0.0   1     3     5  $rouXb $rouYb  $nu  $alfadow; #
Boundary (confined concrete only)
```

```
133
134
135   # ------------------------------
136   #  Define SFI_MVLEM elements
137   # ------------------------------
138   #element SFI_MVLEM eleTag iNode jNode m c -thick fiberThick -width fiberWidth -mat
      matTags
139
140
141   element SFI_MVLEM  1  1   2   16 0.4 -thick $t $t $t $t $t $t $t $t $t $t $t $t $t
      $t $t -width 6 6 6 6 6 6 6 6 6 6 6 6 6 6 6 6  -mat 7 7 7 6 6 6 6 6 6 6 6 6 7 7 7
142   element SFI_MVLEM  2  2   3   16 0.4 -thick $t $t $t $t $t $t $t $t $t $t $t $t $t $t
      $t $t -width 6 6 6 6 6 6 6 6 6 6 6 6 6 6 6 6  -mat 7 7 7 6 6 6 6 6 6 6 6 6 7 7 7
143   element SFI_MVLEM  3  3   4   16 0.4 -thick $t $t $t $t $t $t $t $t $t $t $t $t $t $t
      $t $t -width 6 6 6 6 6 6 6 6 6 6 6 6 6 6 6 6  -mat 7 7 7 6 6 6 6 6 6 6 6 6 7 7 7
144   element SFI_MVLEM  4  4   5   16 0.4 -thick $t $t $t $t $t $t $t $t $t $t $t $t $t $t
      $t $t -width 6 6 6 6 6 6 6 6 6 6 6 6 6 6 6 6  -mat 7 7 7 6 6 6 6 6 6 6 6 6 7 7 7
145   element SFI_MVLEM  5  5   6   16 0.4 -thick $t $t $t $t $t $t $t $t $t $t $t $t $t $t
      $t $t -width 6 6 6 6 6 6 6 6 6 6 6 6 6 6 6 6  -mat 7 7 7 6 6 6 6 6 6 6 6 6 7 7 7
146   element SFI_MVLEM  6  6   7   16 0.4 -thick $t $t $t $t $t $t $t $t $t $t $t $t $t $t
      $t $t -width 6 6 6 6 6 6 6 6 6 6 6 6 6 6 6 6  -mat 7 7 7 6 6 6 6 6 6 6 6 6 7 7 7
147   element SFI_MVLEM  7  7   8   16 0.4 -thick $t $t $t $t $t $t $t $t $t $t $t $t $t $t
      $t $t -width 6 6 6 6 6 6 6 6 6 6 6 6 6 6 6 6  -mat 7 7 7 6 6 6 6 6 6 6 6 6 7 7 7
148   element SFI_MVLEM  8  8   9   16 0.4 -thick $t $t $t $t $t $t $t $t $t $t $t $t $t $t
      $t $t -width 6 6 6 6 6 6 6 6 6 6 6 6 6 6 6 6  -mat 7 7 7 6 6 6 6 6 6 6 6 6 7 7 7
149   element SFI_MVLEM  9  9   10  16 0.4 -thick $t $t $t $t $t $t $t $t $t $t $t $t $t $t
      $t $t -width 6 6 6 6 6 6 6 6 6 6 6 6 6 6 6 6  -mat 7 7 7 6 6 6 6 6 6 6 6 6 7 7
      7

150   element SFI_MVLEM  10 10  11  16 0.4 -thick $t $t $t $t $t $t $t $t $t $t $t $t $t $t
      $t $t -width 6 6 6 6 6 6 6 6 6 6 6 6 6 6 6 6  -mat 7 7 7 6 6 6 6 6 6 6 6 6 7 7 7
151   element SFI_MVLEM  11 11  12  16 0.4 -thick $t $t $t $t $t $t $t $t $t $t $t $t $t $t
      $t $t -width 6 6 6 6 6 6 6 6 6 6 6 6 6 6 6 6  -mat 7 7 7 6 6 6 6 6 6 6 6 6 7 7 7
152   element SFI_MVLEM  12 12  13  16 0.4 -thick $t $t $t $t $t $t $t $t $t $t $t $t $t $t
      $t $t -width 6 6 6 6 6 6 6 6 6 6 6 6 6 6 6 6  -mat 7 7 7 6 6 6 6 6 6 6 6 6 7 7 7
153   element SFI_MVLEM  13 13  14  16 0.4 -thick $t $t $t $t $t $t $t $t $t $t $t $t $t $t
      $t $t -width 6 6 6 6 6 6 6 6 6 6 6 6 6 6 6 6  -mat 7 7 7 6 6 6 6 6 6 6 6 6 7 7 7
154   element SFI_MVLEM  14 14  15  16 0.4 -thick $t $t $t $t $t $t $t $t $t $t $t $t $t $t
      $t $t -width 6 6 6 6 6 6 6 6 6 6 6 6 6 6 6 6  -mat 7 7 7 6 6 6 6 6 6 6 6 6 7 7 7
155   element SFI_MVLEM  15 15  16  16 0.4 -thick $t $t $t $t $t $t $t $t $t $t $t $t $t $t
      $t $t -width 6 6 6 6 6 6 6 6 6 6 6 6 6 6 6 6  -mat 7 7 7 6 6 6 6 6 6 6 6 6 7 7 7
156   element SFI_MVLEM  16 16  17  16 0.4 -thick $t $t $t $t $t $t $t $t $t $t $t $t $t $t
      $t $t -width 6 6 6 6 6 6 6 6 6 6 6 6 6 6 6 6  -mat 7 7 7 6 6 6 6 6 6 6 6 6 7 7 7
157
158   # ------------------------------
159   # End of model generation
160   # ------------------------------
161
162   # Initialize
163   initialize
164
165   # ------------------------------
166   # Recorder generation
167   # ------------------------------
168
169   # set deltaT 10;-dT $deltaT
170
171   # Nodal recorders
172   recorder Node -file $dataDir/MVLEM_Dtop.out -time  -node $IDctrlNode -dof 1 disp
173   recorder Node -file $dataDir/MVLEM_DOFs.out -time  -node 1 2 3 4 5 6 7 8 9 10 11 12 13
      14 15 16 17 -dof 1 2 3 disp
174
175   # Element recorders
176   recorder Element -file $dataDir/MVLEM_Fgl.out -time  -ele 1 2 3 4 5 6 7 8 9 10 11 12 13
      14 15 16 globalForce
177   recorder Element -file $dataDir/MVLEM_Dsh.out -time  -ele 1 2 3 4 5 6 7 8 9 10 11 12 13
      14 15 16 ShearDef
178   recorder Element -file $dataDir/MVLEM_Curvature.out -time  -ele 1 2 3 4 5 6 7 8 9 10 11
      12 13 14 15 16 Curvature
```

```
179
180 # Single RC panel (macro-fiber) responses
181 recorder Element -file $dataDir/MVLEM_panel_strain_p1.out -time    -ele 1 2 3 4 5 6 7 8
    9 10 11 12 13 14 15 16  RCPanel 1 panel_strain
182 recorder Element -file $dataDir/MVLEM_panel_stress_p1.out -time    -ele 1 2 3 4 5 6 7 8
    9 10 11 12 13 14 15 16  RCPanel 1 panel_stress
183 recorder Element -file $dataDir/MVLEM_panel_strain_p8.out -time    -ele 1 2 3 4 5 6 7 8
    9 10 11 12 13 14 15 16  RCPanel 8 panel_strain
184 recorder Element -file $dataDir/MVLEM_panel_stress_p8.out -time    -ele 1 2 3 4 5 6 7 8
    9 10 11 12 13 14 15 16  RCPanel 8 panel_stress
185 recorder Element -file $dataDir/MVLEM_panel_strain_p16.out -time    -ele 1 2 3 4 5 6 7
    8 9 10 11 12 13 14 15 16  RCPanel 16 panel_strain
186 recorder Element -file $dataDir/MVLEM_panel_stress_p16.out -time    -ele 1 2 3 4 5 6 7
    8 9 10 11 12 13 14 15 16  RCPanel 16 panel_stress
187 recorder Element -file $dataDir/MVLEM_panel_stress_concrete.out -time -ele 1 2 3 4 5 6
    7 8 9 10 11 12 13 14 15 16  RCPanel 1 panel_stress_concrete
188 recorder Element -file $dataDir/MVLEM_panel_stress_steel.out -time   -ele 1 2 3 4 5 6 7
    8 9 10 11 12 13 14 15 16   RCPanel 1 panel_stress_steel
189
190 # Cracking angles for all panels
191 recorder Element -file $dataDir/MVLEM_cracking_angles1.out -time -ele 1 2 3 4 5 6 7 8 9
    10 11 12 13 14 15 16 RCPanel 1 cracking_angles
192 recorder Element -file $dataDir/MVLEM_cracking_angles2.out -time -ele 1 2 3 4 5 6 7 8 9
    10 11 12 13 14 15 16 RCPanel 2 cracking_angles
193 recorder Element -file $dataDir/MVLEM_cracking_angles3.out -time -ele 1 2 3 4 5 6 7 8 9
    10 11 12 13 14 15 16 RCPanel 3 cracking_angles
194 recorder Element -file $dataDir/MVLEM_cracking_angles4.out -time -ele 1 2 3 4 5 6 7 8 9
    10 11 12 13 14 15 16 RCPanel 4 cracking_angles
195 recorder Element -file $dataDir/MVLEM_cracking_angles5.out -time -ele 1 2 3 4 5 6 7 8 9
    10 11 12 13 14 15 16 RCPanel 5 cracking_angles
196 recorder Element -file $dataDir/MVLEM_cracking_angles6.out -time -ele 1 2 3 4 5 6 7 8 9
    10 11 12 13 14 15 16 RCPanel 6 cracking_angles
197 recorder Element -file $dataDir/MVLEM_cracking_angles7.out -time -ele 1 2 3 4 5 6 7 8 9
    10 11 12 13 14 15 16 RCPanel 7 cracking_angles
198 recorder Element -file $dataDir/MVLEM_cracking_angles8.out -time -ele 1 2 3 4 5 6 7 8 9
    10 11 12 13 14 15 16 RCPanel 8 cracking_angles
199 recorder Element -file $dataDir/MVLEM_cracking_angles9.out -time -ele 1 2 3 4 5 6 7 8 9
    10 11 12 13 14 15 16 RCPanel 9 cracking_angles
200 recorder Element -file $dataDir/MVLEM_cracking_angles10.out -time -ele 1 2 3 4 5 6 7 8
    9 10 11 12 13 14 15 16 RCPanel 10 cracking_angles
201 recorder Element -file $dataDir/MVLEM_cracking_angles11.out -time -ele 1 2 3 4 5 6 7 8
    9 10 11 12 13 14 15 16 RCPanel 11 cracking_angles
202 recorder Element -file $dataDir/MVLEM_cracking_angles12.out -time -ele 1 2 3 4 5 6 7 8
    9 10 11 12 13 14 15 16 RCPanel 12 cracking_angles
203 recorder Element -file $dataDir/MVLEM_cracking_angles13.out -time -ele 1 2 3 4 5 6 7 8
    9 10 11 12 13 14 15 16 RCPanel 13 cracking_angles
204 recorder Element -file $dataDir/MVLEM_cracking_angles14.out -time -ele 1 2 3 4 5 6 7 8
    9 10 11 12 13 14 15 16 RCPanel 14 cracking_angles
205 recorder Element -file $dataDir/MVLEM_cracking_angles15.out -time -ele 1 2 3 4 5 6 7 8
    9 10 11 12 13 14 15 16 RCPanel 15 cracking_angles
206 recorder Element -file $dataDir/MVLEM_cracking_angles16.out -time -ele 1 2 3 4 5 6 7 8
    9 10 11 12 13 14 15 16 RCPanel 16 cracking_angles
207
208
209 # ----------------------
210 # Define Axial Load
211 # ----------------------
212
213 set N [expr 500.0]; # kips
```

Bibliography

CEN (2004). *European Standard-Eurocode 8: Design of structures for earthquake resistance.*, European Committee for Standardization -prEN 1998-1 edition.

Abdullah, S. and Wallace, J. (2019). Drift Capacity of Reinforced Concrete Structural Walls with Special Boundary Elements. *ACI Structural Journal*, 116-S17(1):183–194.

ACI (1992). *Report on High Strength Concrete*. American Concrete Institute, ACI 363R-92 edition.

ACI 318 (2011). *Building Code Requirements for Structural Concrete and Commentary*. American Concrete Institute, Farmington Hills, MI, ACI 318-11 edition.

ACI 318 (2014). *Building Code Requirements for Structural Concrete and Commentary*. American Concrete Institute, Farmington Hills, MI, ACI 318-14 edition.

ACI 318 (2019). *Building Code Requirements for Structural Concrete and Commentary*. American Concrete Institute, Farmington Hills, MI, ACI 318-19 edition.

ACI 355 (2011). *Qualification of Post-Installed Adhesive Anchors in Concrete and Commentary*. American Concrete Institute, Farmington Hills, MI, ACI 355.4 edition.

ACI 355 (2019). *Qualification of Post-Installed Mechanical Anchors in Concrete and Commentary.* American Concrete Institute, Farmington Hills, MI, ACI 355.2-19 edition.

ACI 374 (2013). *Guide for Testing Reinforced Concrete Structural Elements Under Slowly Applied Simulated Seismic Loads*. American Concrete Institute, ACI 374.2R-13 edition.

Alarcon, C., Hube, M., and de la Llera, J. (2014). Effect of axial loads in the seismic behavior of reinforced concrete walls with unconfined wall boundaries. *Engineering Structures - ELSEVIER*, 73:13–23.

ASCE 356 (2000). *Prestandard and Commentary for the Seismic Rehabilitation of Buildings (FEMA 356)* . Washington, D.C.

ASCE 41 (2014). *ASCE/SEI 41-13 : Seismic Evaluation and Retrofit of Existing Buildings* . Reston, Va.

ASCE/SEI 7-16 (2016). *ASCE/SEI 7-16 : Minimum Design Loads for Buildings and Other Structures*, American Society of Civil Engineers ASCE/SEI 7-16 edition.

ASTM (2004). *Standard Test Method for Splitting Tensile Strength of Cylindrical Concrete Specimens*. ASTM International C496/C496M-04.

ATC-43 (1998). *FEMA 306: Evaluation of Earthquake Damaged Concrete and Masonry Wall Buildings. Basic Procedures Manual*. Redwood City, CA.

Barda, F. (1972). *Shear Strength of Low-Rise Walls with Boundary Elements*. PhD thesis, Lehigh University, Bethlehem.

Belarbi, A. and Hsu, T. (1994). Constitutive Laws of Concrete in Tension and Reinforcing Bars Stiffened by Concrete. *ACI Structural Journal*, 91(4):465–474.

Beyer, K., Dazio, A., and Priestley, M. (2008). Quasi-Static Cyclic Tests of Two U-Shaped Reinforced Concrete Walls. *Journal of Earthquake Engineering*, 12:7:1023–1053.

Beyer, K., Dazio, A., and Priestley, M. (2011). Shear Deformations of Slender Reinforced Concrete Walls under Seismic Loading. *ACI Structural Journal*, 108(2):167–177.

Birely, A. (2012). *Seismic Performance of Slender Reinforced Concrete Structural Walls*. PhD thesis, University of Washington, Washington.

Bohl, A. and Adebar, P. (2011). Plastic Hinge Lengths in High-Rise Concrete Shear Walls. *ACI Structural Journal*, 108-S15:148–157.

Brown, P., Ji, J., Sterns, A., Lehman, D., Lowes, L., Kuchma, D., and Zhang, J. (2006). Investigation of the seismic behavior and analysis of reinforced concrete walls. In *Proceedings, 8th US National Conference on Earthquake Engineering*.

BSI (1997). *BS 8110: Structural Use of Concrete- Part 1: Code of Practice for Design and Construction*. British Standards Institution, London, UK.

Calvi, G., Priestley, M., and Kowalsky, M. (May 2008). Displacement-Based Seismic Design of Structures. *Earthquake Spectra*.

CAN3-N287.2-M82 (1991). Material Requirements for Concrete Containment Structures for CANDU Nuclear Power Plants. Technical report, CAN/CSA-N287.2-M91.

Cannon, R. (1981). Expansion Anchor Performance in Cracked Concrete. *ACI Structural Journal*, 78-42:471–479.

Carrillo, J. and Alcocer, S. (2012). Seismic performance of concrete walls for housing subjected to shaking table excitations. *Engineering Structures - ELSEVIER*, 41:98–107.

Cattaneo, S. (2007). Wedge-type expansion anchors in high-performance concrete. *ACI Structural Journal*, 104(2):191–198.

CEN (2008). *Eurocode 2: Design of concrete structures*. British Standard Institution London.

Chopra, A. (2017). *Dynamics of Structures*. Pearson, University of California Berkeley.

Cook, R. (1993). Behavior of Chemically Bonded Anchors. *Journal of Structural Engineering*, 119(9):2744–2762.

Cook, R. and Konz, R. (2001). Factors Influencing Bond Strength of Adhesive Anchors. *ACI Structural*

Journal, 98(1):76–86.

CSA (2004). *Design of Concrete Structures: CSA A23.3-04 R2010 Standard.* Canadian Standard Association, Mississauga, ON.

Dazio, A., Beyer, K., and Bachmann, H. (2009). Quasi-static cyclic tests and plastic hinge analysis of RC structural walls. *Engineering Structures - ELSEVIER*, 31:1556–1571.

Eligehausen, R. (1992). Behavior, Design and Testing of Anchors in Cracked Concrete. SP-130 G. A. Senkiw and H. B. Lancelot III eds, American Concrete Institute, Farmington Hills, MI.

Eligehausen, R. and Balogh, T. (1995). Behavior of Fasteners Loaded in Tension in Cracked Reinforced Concrete. *ACI Structural Journal*, 92(3):365–379.

Eligehausen, R. and Hoehler, M. (2003). Testing of post-installed fastenings to concrete structures in seismic regions. In *Conference Proceedings of the fib Symposium on Concrete Structures in Seismic Regions*, Athens, Greece.

Eligehausen, R., Hutchinson, T., Mahrenholtz, P., Mahrenholtz, C., and Wood, R. (2010). Load and cyclic crack protocol for anchorage - Part 2: Alternate proposal. In *Presentation to EOTA WG 06.01/03 Meeting July 27, 2010*, Stuttgart, Germany.

Eligehausen, R., Mallee, R., and Silva, J. (2006). *Anchorage in Concrete Construction*. Ernst & Sohn, Berlin.

Elwood, K., Matamoros, A., Wallace, J., Lehman, D., Heintz, J., Mitchell, A., Moore, M., Valley, M., Lowes, L., and Comartin, C. (2007). Update to ASCE/SEI 41 concrete provisions. *Earthquake Spectra*, 23(3):493–523. https://doi.org/10.1193/1.2757714.

EOTA (2010). *Guideline for European Technical Approval of Metal Anchors for Use in Concrete. Annex C: Design Methods for Anchorages.* EOTA-European Organization for Technical Approvals.

EOTA (2013a). *Guideline for European Technical Approval of Metal Anchors for Use in Concrete. Annex A: Details of tests.* EOTA- European Organization for Technical Approvals.

EOTA (2013b). *Guideline for European Technical Approval of Metal Anchors for Use in Concrete. Annex E: Assessment of Metal Anchors under Seismic Action.* EOTA-European Organization for Technical Approvals.

EOTA (2013c). *Guideline for European Technical Approval of Metal Anchors for Use in Concrete. Part one: Anchors in General.* EOTA- European Organization for Technical Approvals.

EOTA TR 045 (2013). *Design of Metal Anchors for Use in Concrete Under Seismic Actions.* EOTA TR 045- European Organization for Technical Approvals.

Faraone, G. and Hutchinson, T. (2018). Behavior of Post-installed Anchors in Reinforced Concrete Shear Walls Subjected to Cyclic Lateral Loading. Part I: Slender Wall Test Program. Technical report, Structural Systems Research Project- Technical Report SSRP-2018/05, University of California San Diego.

Faraone, G. and Hutchinson, T. (2021). Behavior of Post-installed Anchors in Reinforced Concrete Shear Walls Subjected to Cyclic Lateral Loading. Part II: Squat Wall Test Program. Technical report, Structural Systems Research Project- Technical Report SSRP-2021/01, University of California San Diego.

Faraone, G., Hutchinson, T., Piccinin, R., and Silva, J. (2019). Back-Estimated Ductility and Response Modification Coefficient (R factor) for Concrete Shear Walls. In *Conference Proceedings of the 5th NBSC, ACI Italy Chapter*, Milan, Italy.

Faraone, G., Hutchinson, T., Piccinin, R., and Silva, J. (under review). Anchor Performance in Cyclically Loaded Shear Walls. *ACI Structural Journal*.

Fuchs, W., Eligehausen, R., and Breen, J. (1995). Concrete Capacity Design (CCD) Approach for Fastening in Concrete. *ACI Structural Journal*, 92(1):73–94.

Furche, J. (1994). *Load-bearing and displacement behavior of headed bolts under centric tension load*. PhD thesis, University of Stuttgart, Germany.

Ghobarah, A. (2004). On Drift Limits Associated with Different Damage Levels. In *Proceedings of the International Workshop on Performance-based Seismic Design*, pages 1–12, Bled Slovenia.

Ghosh, S. K. (2016). Significant changes from the 2011 to the 2014 edition of ACI 318. *PCI Journal*.

Gil, A., Segura, J., and Temme, N. (2007). *Numerical Methods for Special Functions*. SIAM Society for Industrial and Applied Mathematics.

Greifenhagen, C. and Lestuzzi, P. (2005). Static cyclic tests on lightly reinforced concrete shear walls. *Engineering Structures - ELSEVIER*, 27:1703–1712.

Gullu, M. and Orakcal, K. (2019). Nonlinear Finite Element Modeling of Reinforced Concrete Walls with Varying Aspect Ratios. *Journal of Earthquake Engineering*, 13632469.2019.1614498.

Henry, R. (2019). University of Auckland Lightly Reinforced Concrete Wall Tests. DesignSafe-CI.

Hidalgo, P., Jordan, R., and Martinez, M. (2001). An Analytical Model to Predict the Inelastic Seismic Behavior of Shear Wall Reinforced Structures. *Engineering Structures - ELSEVIER*, 24:85–98.

Hidalgo, P., Ledezma, C., and Jordan, R. (2002). Seismic Behavior of Squat Reinforced Concrete Shear Walls. *Earthquake Spectra*, 18(2):287–308.

Hines, E., Restrepo, J., and Seible, F. (2004). Force-Displacement Characterization of Well-Confined Bridge Piers. *ACI Structural Journal*, 101(4):537–547.

Hoehler, M. (2006). *Behavior and Testing of Fastenings to Concrete for use in Seismic Applications*. PhD thesis, University of Stuttgart, Germany.

Hutchinson, T. and Wang, T. (2009). Evaluation of Crack Spacing in Reinforced Concrete Shear Walls. *Journal of Structural Engineering*, 135(5):499–508.

Hwang, S., Fang, W., Lee, H., and Yu, H. (2001). Analytical Model for Predicting Shear Strength of Squat Walls. *Journal of Structural Engineering*, 127(1):43–50.

ICC (1995). Acceptance Criteria for Adhesive Anchors in Masonry Elements. Technical report, ICC-Evaluation Services.

Ince, R., Yalcin, E., and Arslan, A. (2007). Size-dependent response of dowel action in RC members. *Engineering Structures - ELSEVIER*, 29:955–961.

Jiang, H., Wang, B., and Lu, X. (2013). Experimental Study on Damage Behavior of Reinforced Concrete Shear Walls Subjected to Cyclic Loads. *Journal of Earthquake Engineering*, 17:7:958–971 DOI 10.1080/13632469.2013.791895.

Jünemann, R., de la Llera, J., Hube, M., Cifuentes, L., and Kausel, E. (2015). A statistical analysis of reinforced concrete wall buildings damaged during the 2010, Chile earthquake. *Engineering Structures - ELSEVIER*, 82:168–185.

Kassem, W. (2014). Shear Strength of Squat Walls: A Strut-and-Tie Model and Closed-form Design Formula. *Engineering Structures - ELSEVIER*, 84:430–438.

Kazaz, I. (2013). Analytical Study on Plastic Hinge Length of Structural Walls. *J. Struct. Eng.*, (10.1061/(ASCE)ST.1943-541X.0000770).

Kolozvari, K. (2013). *Analytical modeling of cyclic shear – Flexure interaction in reinforced concrete structural walls*. PhD thesis, University of California Los Angeles.

Kolozvari, K., Orakcal, K., and Wallace, J. (2014). Modeling of Cyclic Shear-Flexure Interaction in Reinforced Concrete Structural Walls. II: Experimental Validation. *J. Struct. Eng.*, (10.1061/(ASCE)ST.1943-541X.0001083,04014136).

Kolozvari, K., Orakcal, K., and Wallace, J. (2015). Shear-Flexure Interaction Modeling for Reinforced Concrete Structural Walls and Columns under Reversed Cycling Loading. Technical report, PEER Report No. 2015/12, University of California Berkeley.

Krolicki, J., Maffei, J., and Calvi, G. (2011). Shear Strength of Reinforced Concrete Shear Walls Subjected to Cyclic Loading. *Journal of Earthquake Engineering*, 15(S1):30–71 DOI 10.1080/13632469.2011.562049.

Kuang, J. and Ho, Y. (2008). Seismic Behavior and Ductility of Squat Reinforced Concrete Shear Walls. *ACI Structural Journal*, 105:225–231.

Lefas, I., Kotsovos, M., and Ambraseys, N. (1990). Behavior of Reinforced Concrete Structural Walls: Strength, Deformation Characteristics, and Failure Mechanism. *ACI Structural Journal*, 87(1):23–31.

Li, B., .Pan, Z., and Xiang, W. (2015). Experimental Evaluation of Seismic Performance of Squat RC Structural Walls with Limited Ductility Reinforcing Details. *Journal of Earthquake Engineering*, 19:313–331.

Looi, D., Su, R., Cheng, B., and Tsang, H. (2017). Effects of axial load on seismic performance of reinforced concrete walls with short shear span. *Engineering Structures - ELSEVIER*, 151:312–326.

Lotze, D. (1987). Investigation on the Probability of Fasteners being Located in Cracks- Influence of Transverse Reinforcement. Technical Report N0. 1/24-87/6, Institut fur Werkstoffe im Bauwesen, University of Stuttgart, Germany.

Lotze, D. (1993). *Load bearing behavior and applications for anchors under frequently repeated loads*. PhD thesis, University of Stuttgart, Germany.

Lu, Y., Henry, R., Gultom, R., and Ma, Q. (2016). Cyclic Testing of Reinforced Concrete Walls with Distributed Minimum Vertical Reinforcement. *J. Struct. Eng.*, (10.1061/(ASCE)ST.1943-541X.0001723):04016225.

Mahrenholtz, P. (2012). *Experimental Performance and Recommendations for Qualification of Post-installed Anchors for Seismic Applications*. PhD thesis, University of Stuttgart, Germany.

Mahrenholtz, P., Eligehausen, R., Hutchinson, T., and Hoehler, M. (2016). Behavior of Post-Installed Anchors Tested by Stepwise Increasing Cyclic Load Protocols. *ACI Structural Journal*, 113(5):997–1008.

Mahrenholtz, P., Wood, R., Eligehausen, R., Hutchinson, T., and Hoehler, M. (2017). Development and Validation of European Guidelines for Seismic Qualification of Post-Installed Anchors. *Engineering Structures*, 148:497–508.

Massone, L., Orakcal, K., and Wallace, J. (2006). Shear-Flexure Interaction for Structural Walls. *ACI Symposium Paper*, 236(5):127–150.

Massone, L., Orakcal, K., and Wallace, J. (2009). Modeling of Squat Structural Walls Controlled by Shear. *ACI Structural Journal*, 106(5):646–655.

Massone, L. and Wallace, J. (2004). Load-Deformation Responses of Slender Reinforced Concrete Walls. *ACI Structural Journal*, 101(1):103–113.

Mattock, A., Li, W., and Wan, T. (1976). Shear Transfer in Lightweight Reinforced Concrete. *PCI JOURNAL*, 21(1):20–39.

McKenna, F., Fenves, G., Scott, M., and Jeremic, B. (2000). Open system for earthquake engineering simulations (OpenSees).

Menegotto, M. and Pinto, E. (1973). Method of analysis for cyclically loaded reinforced concrete plane frames including changes in geometry and nonelastic behavior of elements under combined normal force and bending. In *IASBE Symposium on Resistance and Ultimate Deformability of Structures Acted on by Well-Defined Repeated Loads*, Lisbon, Portugal.

Moehle, J. (1992). Displacement-based Design of RC Structures Subjected to Earthquakes. *Earthquake Spectra*, 8(3):403–428.

Moehle, J., Ghodsi, T., Hooper, J., Fields, D., and Gedhada, R. (2011). Seismic Design of Cast-in-Place Concrete Special Structural Walls and Coupling Beams: A Guide for Practicing Engineers. Technical Report NIST GCR 11-917-11REV-1, NEHRP Seismic Design Technical Brief No. 6, Gaithersburg, MD.

NZS 3101 (2006). *Concrete Structures Standard. Part I- The Design of Concrete Structures*. Standards Council NZS 3101.

Oesterle, R., Fiorato, A., Johal, L., Carpenter, J., Russell, H., and Corley, W. (1976). Earthquake resistant structural walls- tests of isolated walls. Technical Report Grant No. GI-43880, Technical report to National Science Foundation (RANN).

Orakcal, K., Massone, L., and Wallace, J. (2009). Shear Strength of Lightly Reinforced Wall Piers and Spandrels. *ACI Structural Journal*, 106(4).

Orakcal, K. and Wallace, J. (2006). Flexural Modeling of Reinforced Concrete Walls- Experimental Verification. *ACI Structural Journal*, 103(5):196–206.

Orakcal, K., Wallace, J., and Conte, J. (2004). Flexural Modeling of Reinforced Concrete Walls- Model Attributes. *ACI Structural Journal*, 101(5):688–699.

P 3101 Concrete Design Committee (2006). *NZS 3101: Concrete structures standard* . New Zealand.

Panagiotou, M., Restrepo, J., Schoettler, M., and Kim, G. (2012). Nonlinear cyclic truss model for reinforced concrete walls. *ACI Structural Journal*, 109(2):205–214.

Park, R. (1998). Design Procedures for Achieving Ductile Behaviour of Reinforced Concrete Buildings. In *Proceedings of the International Workshop on Earthquake Engineering for Regions of Moderate Seismicity*, pages 45–50, Hong Kong, Cina.

Park, R. and Paulay, T. (1975). *Seismic Design of Reinforced Concrete and Masonry Buildings*. Jon Wiley and Sons Inc., New York.

Paulay, T. (2002). Displacement-based Design of RC Structures Subjected to Earthquakes. *Earthquake Spectra*, 18(4):689–718.

Paulay, T. and Priestley, J. (1993). Stability of ductile structural walls. *ACI Structural Journal*, 90(4):385–392.

Paulay, T., Priestley, J., and Synge, J. (1981). Ductility in Earthquake Resisting Squat Shearwalls. *ACI Structural Journal*, 79-26:257–299.

Paulay, T. and Priestley, M. (1992). *Seismic Design of Reinforced Concrete and Masonry Buildings*. John Wiley and Sons Inc., New York.

Paulay, T., Priestley, M., and Synge, A. (1982). Ductility in Earthquake Resisting Squat Shear Walls. *ACI Structural Journal*, 79-26.

Paulay, T. and Uzumeri, S. (1975). A Critical Review of the Seismic Design Provisions for Ductile Shear Walls of the Canadian Code and Commentary. *Canadian Journal of Civil Engineering*, 2(4).

Piccinin, R., Ballarini, R., and Cattaneo, S. (2010). Linear Elastic Fracture Mechanics Pull Out Analyses of Headed Anchors in Stressed Concrete. *J. Eng. Mech.*, (10.1061/(ASCE)EM.1943-7889.0000120).

Priestley, M., Calvi, G., and Kowalsky, M. (2007). *Displacement-Based Seismic Design of Structures*.

IUSS Press, New York.

Priestley, M., Seible, F., and Calvi, G. (1996). *Seismic Design and Retrofit of Bridges*. John Wiley and Sons Inc., New York.

Rasoolinejad, M. and Bazant, P. (2019). Size Effect of Squat Shear Walls Extrapolated by Microplane Model M7. *ACI Structural Journal*, 116(3):75–84.

Riva, P., Meda, A., and Giuriani, E. (2003). Cyclic behavior of a full scale RC structural wall. *Engineering Structures - ELSEVIER*, 25:835–845.

Saatcioglu, M., Palermo, D., Ghobarah, A., Mitchell, D., Simpson, R., Adebar, P., Tremblay, R., Ventura, C., and Hong, H. (2013). Performance of reinforced concrete buildings during the 27 February 2010 Maule (Chile) earthquake. *NRC Research Press- Canadian Journal of Civil Engineering*, 40(8):693–710.

Salonikios, T., Kappos, A., Tegos, I., and Penelis, G. (1999). Cyclic Load Behavior of Low-Slenderness Reinforced Concrete Walls: Design Basis and Test Results. *ACI Structural Journal*, 96(4):649–661.

Salonikios, T., Kappos, A., Tegos, I., and Penelis, G. (2000). Cyclic Load Behavior of Low-Slenderness Reinforced Concrete Walls: Failure Modes, Strength and Deformation Analysis, and Design Implications. *ACI Structural Journal*, 97(1):132–142.

Schlaich, J., Schafer, K., and Jennewein, M. (1987). Toward a consistent design of structural concrete. *PCI Journal*, 32(3).

Scott, M. and Fenves, G. (2010). A Krylov Subspace Accelerated Newton Algorithm: Application to Dynamic Progressive Collapse Simulation of Frames. *J. Struct. Eng.*, (10.1061/(ASCE)ST.1943-541X.0000143).

Seghezzi, H. (1985). Interactions between testing technology and development of fastening elements. In *Presentation 15.01*, Stuttgart, Germany.

SEOAC (1999). *Recommended Lateral Force Requirements and Commentary.* SEAOC blue book - Seismic design recommendations, Seismology Committee, Structural Engineers Association of California, Sacramento, CA.

Silva, J. (2001). Test methods for seismic qualification of post-installed anchors. *International Symposium on Connections between Steel and Concrete, RILEM Proceedings PRO 21*, 1:551–563.

Su, R. and Wong, S. (2007). Seismic behaviour of slender reinforced concrete shear walls under high axial load ratio. *Engineering Structures - ELSEVIER*, 29:1957–1965.

Tran, A. (2012). *Experimental and analytical studies of moderate aspect ratio reinforced concrete structural walls*. PhD thesis, University of California Los Angeles.

Tran, T. and Wallace, J. (2015). Cyclic Testing of Moderate-Aspect-Ratio Reinforced Concrete Structural Walls. *ACI Structural Journal*, 112(6):653–665.

Ullman, S. (1976). The Interpretation of Structure from Motion. In *Proceedings of the Royal Society of*

London, Massachusetts Institute of Technology.

Veletsos, A. and Newmark, N. (1960). Effect of inelastic behavior on the response of simple systems to earthquake motions. In *Proceedings of the Second World Conference on Earthquake Engineering*, volume II, pages 895–912, Tokyo, Japan.

Vulcano, A., Bertero, V., and Colotti, V. (1988). Analytical Modeling of RC Structural Walls. In *Proceedings, 9^{th} World Conference on Earthquake Engineering*, pages 41–46, Tokyo-Kyoto, Japan.

Wallace, J. and Moehle, J. (1992). Displacement-based Design of RC Structures Subjected to Earthquakes. *Journal of Structural Engineering*, 118(6):1625–44.

Watkins, D. (2011). *Seismic Behavior and Modeling of Anchored Nonstructural Components Considering the Influence of Cyclic Cracks*. PhD thesis, University of California San Diego.

Wood, R., Hutchinson, T., and Hoehler, M. (2010). Cyclic load and crack protocols for anchored nonstructural components and systems. Technical Report SSRP-2009/12, University of California San Diego.

Xu, S. and Zhang, J. (2010). Hysteretic shear-flexure interaction model of reinforced concrete columns for seismic response assessment of bridges. *Earthq. Eng. Struct. Dyn.*, 4(3):315–337.

Yanez, F., Park, R., and Paulay, T. (1989). Strut and tie models for reinforced concrete design and analysis. In *New Zealand Concrete Society Silver Jubilee Conference*, pages 43–45, Wairakei, New Zealand.

Zhang, Y. and Wang, Z. (2000). Seismic Behavior of Reinforced Concrete Shear Walls Subjected to High Axial Loading. *ACI Structural Journal*, 97(5):739–750.